

SYNTHESIS AND CHARACTERIZATION OF A FEW ORGANIC SMALL MOLECULES AS OLED MATERIALS FOR DEVICE APPLICATIONS

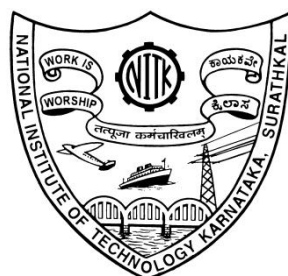
Thesis

Submitted in partial fulfilment of the requirements for the degree of

DOCTOR OF PHILOSOPHY

by

MAKESH M.



DEPARTMENT OF PHYSICS

NATIONAL INSTITUTE OF TECHNOLOGY KARNATAKA,

SURATHKAL, MANGALURU-575025

September, 2020

DECLARATION

by the Ph.D. Research Scholar

I hereby *declare* that the Research Thesis entitled

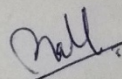
**SYNTHESIS AND CHARACTERIZATION OF A FEW
ORGANIC SMALL MOLECULES AS OLED MATERIALS FOR
DEVICE APPLICATIONS**

Which is being submitted to the National Institute of Technology
Karnataka, Surathkal in partial fulfilment of the requirements for the
award of the Degree of Doctor of Philosophy in

PHYSICS

is a *bonafide report of the research work carried out by me*. The material
contained in this Research Thesis has not been submitted to any
University or Institution for the award of any degree.

148043PH14F06, MAKESH M



(Register Number, Name & Signature of the Research Scholar)

Department of **PHYSICS**

Place: NITK-Surathkal

Date: 03-10-2019

Note: Declaration to be signed by the Scholar and incorporated as part of the Ph.D. Research Thesis /Synopsis

CERTIFICATE

This is to certify that the Research Thesis entitled

**SYNTHESIS AND CHARACTERIZATION OF A FEW
ORGANIC SMALL MOLECULES AS OLED MATERIALS FOR
DEVICE APPLICATIONS**

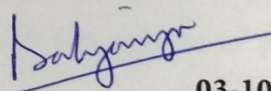
submitted by **MAKESH M**

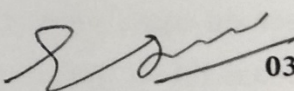
(Register Number: **148043PH14F06**) as the record of the research work carried out by him, is *accepted as the Research Thesis submission* in partial fulfilment of the requirements for the award of degree of Doctor of Philosophy.

Dr. M. N. Satyanarayan
डॉ. एम एन सत्यनारायण
Professor, Department of Physics,
प्रोफेसर, भौतिकी विभाग,
National Institute of Technology Karnataka
राष्ट्रीय प्रौद्योगिकी संस्थान कर्नाटक,
Srinivasnagar P.O., Mangaluru - 575025
श्रीनिवासनगर पी ओ, मंगलुरु - 575025

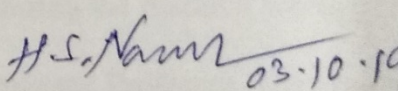
डॉ.दर्शक आर त्रिवेदी (JSPS Fellow)
सह - प्राध्यापक
रसायन शास्त्र विभाग
राष्ट्रीय प्रौद्योगिकी संस्थान कर्नाटक, सूरतकल
मंगलुरु - 575025, कर्नाटक

Dr. H.S. Nagaraja
ASSOCIATE PROFESSOR & HEAD
Physics Department
NITK Surathkal, Mangalore- 575025
KARNATAKA


03-10-2019
Prof. M. N. Satyanarayan


03-10-2019
Dr. Darshak R Trivedi

Research Guide(s)
(Name and
Signature with Date
and Seal)


03-10-19
Chairman - DRPC
(Signature with Date and Seal)

**DEDICATED
TO
MY SPIRITUAL TEACHER**



ACKNOWLEDGEMENT

“Experience is the best teacher”

It has been a great experience pursuing research career at National Institute of Technology Karnataka (NITK) Surathkal with proficient and unique individuals who have helped me to achieve what I have up to this point. I would like to express my deepest appreciation for the help and support of the kind people around me, to only some of whom it is possible to give a particular mention here.

I express my gratitude to my research supervisors Prof. M. N. Satyanarayan and Dr. Darshak R. Trivedi for their research guidance and inspiration. Throughout my doctoral work they have been a constant source of encouragement and sound advice. I thank them for having instilled in me the work ethic and determination to achieve this goal. Be it failure and success, trial and error, ennui and exuberance, they were there for all of it. Their unstained support throughout the course of my research work has made my thesis appear in the present form.

I am grateful to NITK for the research infrastructure and fellowship that allowed me to work at a smoother pace. I am grateful to Dr. H. S. Nagaraja, Head, Department of physics and Chairman – DRPC and Prof. M. N. Satyanarayan, Former Head, Department of physics for their kind support.

I am thankful to the RPAC members, Prof. A. Nityananda Shetty, Department of Chemistry for the continuous guidance during my seminars that helped me shape my research work. I am also thankful to Prof. Kartick Tarafder, Department of Physics for his encouragement and inspiration all throughout my work.

I thank Prof. G. Umesh, Prof. N. Udayshankar, Prof. H. D. Shashikala, Prof. Kasthuri V Bangera, Dr. H. S. Nagaraja, Dr. Ajith K M, Dr. Kartick Tarafder, Dr. Deepak Vaid, Dr. Partha Pratim Das, and Dr. Shahjahan T K for their support during the research work.

I wish to convey my sincere thanks to Dr. Ajith K. M., Assistant Professor, Department of Physics, NITK Surathkal for his support in providing access to Gaussian 09 package.

I extend my gratitude to Department of Science and Technology, Govt. of India for providing SCXRD facility to Department of Chemistry, NITK Surathkal, under FIST program.

I am thankful to MIT Manipal, IISc Bangalore, for the timely analytical support.

I would like to express my special thanks to my friends and colleagues, Mr. Nimith K M, Mr. Achyutha K, Ms. Sherin Thomas, Mr. Venkatadri Tekuri , Ms. Archana Singh and Mr.

Nagaraj who have helped and supported me in many ways. I also thank the postgraduate project students of our group.

I extend my thanks to the nonteaching staff of the department, Mrs. Ashalatha, Mrs. Venna, Mr. Harshith, Mr. Dhanraj, Mr. Karthik and Mr. Pradeep for their timely assistance in the departmental work.

I earnestly yearn to thank my parents, Mr. Mohan R. and Mrs. Brinda M and my in-laws Mr. P. Venkatramana Pangannaya and Mrs. Varada P for their love and sacrifice that motivated me to achieve this goal. They have given up many things for me to be at NITK; they have cherished with me every great moment and supported me whenever I needed it. I am extremely thankful to my sister Mrs. Rekha M, my brother-in-law Mr. Krishna Kripa Das, my niece Sriya for their love, prayers and support. I am ceaselessly grateful to all of you and pray for your continued mercy upon me.

I owe my deepest gratitude to my wife, Dr. Srikala pangannaya, for being very supportive and encouraging all throughout my PhD course. She has been a strong and steady source of inspiration for me and there have been countless moments while pursuing my research that, without her, I feel I would have succumbed to defeat. I thank her from the bottom of my heart for the undivided support and being a witness for every step of the way. I thank her for all the sacrifices she has gone through to give me the best of the best things in life.

Makesh M.

ABSTRACT

Efficient molecular design and synthesis of novel fluorescent organic small molecules have attracted significant attention among the researchers for their promising solid-state lighting applications. Precise bandgap engineering of an organic molecule achieved by various chemical routes have shown significant progress in the past few decades by generation of different color emission, sweeping over the entire visible spectrum. Ease of functionalization, a good stability under wider range of operating conditions and a low-cost synthetic route have always motivated researchers in developing novel molecules for optoelectronic applications.

The present work is aimed at design and synthesis of few organic small molecules to uncover some of its interesting photophysical phenomena. Solvatochromic behavior of all the molecules of the series were studied under solvents of varying dielectric constants. Precise bandgap tuning achieved by variation of ancillary substituents on the core system was successful in generation of vivid emission colors. Solid-state emission of few of the molecules of the series exhibited an emission intensity higher in comparison with their solution state supporting aggregation induced emission (AIE) phenomena. Single crystal X-ray analysis on few of the molecules resulted in system adopting a larger intermolecular π - π stacking that would in turn block all the non-radiative channels leading to enhanced emission upon aggregation. Design strategies of few of the synthesized molecules resulting in an optimal HOMO and LUMO energy levels were successfully realized for OLED device applications. Density functional calculations on series were carried out to understand the nature of geometry at its ground state along with their electronic orbital information. Estimated electronic transitions for few of the series correlate well with the experimental absorption and emission energy transitions. Theoretical calculations uncovering excited state proton transfer dynamics resulting in estimation of excited state proton transfer barrier, questionable step-wise or hypothetical simultaneous double proton transfer for few of the molecular series were well discussed.

Keywords: Aggregation induced emission, Density functional theory, Excited state intramolecular proton transfer, Fluorescence, OLED, Potential energy surface, Tautomerism

CONTENTS

CONTENTS	i
LIST OF FIGURES	vii
LIST OF SCHEMES	xxi
LIST OF TABLES	xxiii
NOMENCLATURE	xxv
SYMBOLS AND UNITS	xxvii

CHAPTER 1

INTRODUCTION

1.1	ORGANIC ELECTRONICS	1
1.2	CONDUCTION MECHANISM	3
1.3	EXCITONS	6
1.4	LUMINESCENCE	12
1.4.1	Spin orbit coupling (SOC)	14
1.5	AGGREGATION INDUCED EMISSION (AIE)	16
1.5.1	Restriction of intramolecular rotation (RIR)	19
1.5.2	Restriction of intramolecular vibration (RIV)	19
1.5.3	Restriction of intramolecular motion (RIM)	19
1.6	EXCITED STATE INTRAMOLECULAR PROTON TRANSFER (ESIPT)	20
1.7	ORGANIC LIGHT EMITTING DIODES	23
1.7.1	OLED Efficiency	28
1.7.1.1	Injection efficiency (γ)	29
1.7.1.2	Internal quantum efficiency (IQE) η_r	29
1.7.1.3	Quantum yield η_{PL}	29
1.7.1.4	Out coupling efficiency η_{out}	30
1.8	LITERATURE REVIEW	31
1.9	SCOPE OF THE PRESENT WORK	41
1.10	OBJECTIVES OF THE WORK	42

CHAPTER 2

PHOTOPHYSICAL AND ELECTROCHEMICAL PROPERTIES OF ORGANIC MOLECULES: SOLVATOCHROMIC EFFECT AND DFT STUDIES

2.1	INTRODUCTION	45
2.2	EXPERIMENTAL SECTION	47
2.2.1	Materials and methods	47
2.2.2	Synthesis of molecules	47
2.2.3	Characterization results	50
2.3	RESULTS AND DISCUSSION	56
2.3.1	UV-Vis studies	56
2.3.2	Photoluminescence studies	62
2.3.3	Quantum Yield measurement	66
2.3.4	Fluorescent lifetime measurement	67
2.3.5	Cyclic voltammetry	69
2.3.6	DFT studies	71
2.4	CONCLUSIONS	76

CHAPTER 3

MULTICOLOURED THIOPHENE BASED AIEGENS: SINGLE CRYSTAL STRUCTURE ELUCIDATION, SPECTRAL BEHAVIOUR AND DFT STUDIES

3.1	INTRODUCTION	77
3.2	EXPERIMENTAL SECTION	79
3.2.1	Materials and methods	79
3.2.2	Synthesis of molecules	79
3.2.3	Characterization data	83
3.3	RESULTS AND DISCUSSION	96
3.3.1	UV-Vis studies	96
3.3.2	Photoluminescence Studies	102
3.3.3	Quantum yield measurement	108
3.3.4	Solid-state photoluminescence studies	109
3.3.5	Fluorescent lifetime measurement	110

3.3.6	Aggregation induced emission studies	112
3.3.7	Cyclic Voltammetry	117
3.3.8	X-ray crystal structure analysis	119
3.3.9	DFT studies	122
3.4	CONCLUSIONS	130

CHAPTER 4

DESIGN AND SYNTHESIS OF BITHIOPHENE BASED AIE EMITTERS: EXPERIMENTAL AND THEORETICAL ANALYSIS

4.1	INTRODUCTION	131
4.2	EXPERIMENTAL SECTION	132
4.2.1	Materials and methods	132
4.2.2	Synthesis	132
4.2.3	Characterization data	134
4.3	RESULTS AND DISCUSSION	138
4.3.1	Photophysical studies	138
4.3.2	Quantum Yield measurement	144
4.3.3	Aggregation induced emission studies	144
4.3.4	Cyclic voltammetry	147
4.3.5	DFT Studies	149
	4.3.5.1 Spectral studies and orbital analysis	151
	4.3.5.2 Reorganization and dimer interaction energies	155
4.4	Conclusions	161

CHAPTER 5

PHOTOPHYSICS OF PROTON TRANSFER IN HYDRAZIDES: A COMBINED THEORETICAL AND EXPERIMENTAL ANALYSIS TOWARDS OLED DEVICE APPLICATION

5.1	INTRODUCTION	163
5.2	EXPERIMENTAL SECTION	165
5.2.1	Materials and methods	165

5.2.2	Synthesis	167
5.2.3	Characterization data	169
5.3	RESULTS AND DISCUSSION	177
5.3.1	UV-Vis Studies	177
5.3.2	Photoluminescence studies	180
5.3.3	Solid-state studies	186
5.3.4	Quantum yield measurement	187
5.3.5	Ratiometric studies	188
5.3.6	Cyclic Voltammetry	193
5.3.7	DFT Studies	195
	5.3.7.1 Geometry	197
	5.3.7.2 Spectral quality and frontier molecular orbitals	199
	5.3.7.3 Potential energy curve	205
	5.3.7.4 PES Surface studies	211
5.3.8	Device fabrication and characterization	213
5.4	CONCLUSIONS	216

CHAPTER 6

EXPLORING THE POSSIBILITIES OF DOUBLE PROTON TRANSFER IN HYDRAZIDES: A THEORETICAL APPROACH

6.1	INTRODUCTION	219
6.2	EXPERIMENTAL SECTION	221
	6.2.1 Materials and methods	221
	6.2.2 Synthesis of molecule P4	222
	6.2.5 Characterization data	223
6.3	RESULTS AND DISCUSSION	224
	6.3.1 UV-Vis studies	224
	6.3.2 Quantum yield measurement	228
	6.3.3 Solid-state photoluminescence studies	228
	6.3.4 Ratiometric studies	229
	6.3.5 Cyclic voltammetry	232

6.3.6	DFT studies	233
	6.3.7 Structural analysis	235
	6.3.8 Electronic spectra and molecular orbitals analysis	240
	6.3.9 Potential Energy Scan	248
	6.3.10 Potential Energy Surface Scan	256
6.4	CONCLUSIONS	260

CHAPTER 7

SUMMARY AND CONCLUSIONS

7.1	SUMMARY	261
7.2	CONCLUSIONS	262
7.3	SCOPE FOR FUTURE WORK	263
	<i>REFERENCES</i>	265
	<i>PUBLICATIONS</i>	295
	<i>CURRICULUM VITAE</i>	297

LIST OF FIGURES

CHAPTER 1

Fig. 1.1	Molecular structure of few organic semiconductors	2
Fig. 1.2	Schematic representation of orbital overlap and energy level diagram	5
Fig. 1.3	Illustration of charge hopping in HOMO and LUMO energy states	5
Fig. 1.4	Frenkel type of excitons wherein distance $r < a$	7
Fig. 1.5	Charge transfer type of excitons wherein distance $r = a$	7
Fig. 1.6	Wannier-Mott type of excitons wherein distance $r > a$	7
Fig. 1.7	Illustration of Förster and Dexter energy transfer process with initial and final state	9
Fig. 1.8	Mechanism illustrating singlet-singlet annihilation	10
Fig. 1.9	Mechanism illustrating singlet-triplet annihilation	11
Fig. 1.10	Mechanism illustrating triplet-triplet annihilation	11
Fig. 1.11	Schematic representation of Jablonski diagram	13
Fig. 1.12	Examples of planar type ACQ molecules	17
Fig. 1.13	Fluorescence of solutions with increasing water fractions exhibiting ACQ effect	17
Fig. 1.14	Few of the most prominent AIEgens	18
Fig. 1.15	Fluorescence of solutions with increasing water fractions exhibiting AIE effect	18
Fig. 1.16	Illustration of intramolecular rotation, vibration and motion	20
Fig. 1.17	Four level photo-cyclic process of ESIPT	21
Fig. 1.18	Generic structure of an OLED	24
Fig. 1.19	A generic working mechanism of single layer OLED device	25
Fig. 1.20	Working mechanism of double layer OLED device	26
Fig. 1.21	Scheme of the electroluminescence mechanism in an OLED	27
Fig. 1.22	Flowchart illustrating overall device efficiency of an OLED	30

CHAPTER 2

Fig. 2.1	FT-IR spectrum of molecule M1	50
Fig. 2.2	FT-IR spectrum of molecule M2	51

Fig. 2.3	FT-IR spectrum of molecule M3	51
Fig. 2.4	FT-IR spectrum of molecule M4	52
Fig. 2.5	FT-IR spectrum of molecule M5	52
Fig. 2.6	¹ H NMR spectra of molecule M1	53
Fig. 2.7	¹ H NMR spectra of molecule M2	53
Fig. 2.8	¹ H NMR spectra of molecule M3	54
Fig. 2.9	¹ H NMR spectra of molecule M4	54
Fig. 2.10	¹ H NMR spectra of molecule M5	55
Fig. 2.11	Differential Scanning calorimetry of molecules M1 to M5	55
Fig. 2.12	Fluorescent response of molecules M1 to M5 (10^{-5} M) in solvents of varying polarity under UV illumination	57
Fig. 2.13	UV-Vis spectra of molecule M1 (10^{-5} M) in various solvents	58
Fig. 2.14	UV-Vis spectra of molecule M2 (10^{-5} M) in various solvents	59
Fig. 2.15	UV-Vis spectra of molecule M3 (10^{-5} M) in various solvents	59
Fig. 2.16	UV-Vis spectra of molecule M4 (10^{-5} M) in various solvents	60
Fig. 2.17	UV-Vis spectra of molecule M5 (10^{-5} M) in various solvents	60
Fig. 2.18	Photoluminescence spectra of molecule M1 (10^{-5} M) in various solvents	62
Fig. 2.19	Photoluminescence spectra of molecule M2 in solvents of varying polarity	63
Fig. 2.20	Photoluminescence spectra of molecule M3 (10^{-5} M) in various solvents	63
Fig. 2.21	Photoluminescence spectra of molecule M4 (10^{-5} M) in various solvents	64
Fig. 2.22	Photoluminescence spectra of molecule M5 (10^{-5} M) in various solvents	64
Fig. 2.23	Variation in the emission wavelength of molecules M1-M5 under solvents of varying polarity	65
Fig. 2.24	Solid-state emission of molecules M1 to M5 under UV lamp.	66
Fig. 2.25	Solid-state photoluminescence spectra of molecule M2 and M4 .	66
Fig. 2.26	Fluorescence decay curve of molecules M1 to M5 excited with a source of 346 nm	68

Fig. 2.27	Standard deviation profile for decay curve fitting for molecules M1 to M5	69
Fig. 2.28	Cyclic voltammogram of molecules M1 to M5	70
Fig. 2.29	HOMO, LUMO and band gap of molecule M1 to M5 by cyclic voltammetry	71
Fig. 2.30	DFT optimized structures of the molecules M1 to M5 with their dihedral angle.	72
Fig. 2.31	Representation of energy distribution in molecules M1 to M5 in gas phase	73
Fig. 2.32	Theoretical UV-Vis spectra of molecule M1 in various solvent.	73
Fig. 2.33	Theoretical UV-Vis spectra of molecule M2 in various solvents	74
Fig. 2.34	Theoretical UV-Vis spectra of molecule M3 in various solvents	74
Fig. 2.35	Theoretical UV-Vis spectra of molecule M4 in various solvents	75
Fig. 2.36	Theoretical UV-Vis spectra of molecule M5 in various solvents	75

CHAPTER 3

Fig. 3.1	FT-IR spectra of D1	83
Fig. 3.2	FT-IR spectra of D2	83
Fig. 3.3	FT-IR spectra of D3	84
Fig. 3.4	FT-IR spectra of D4	84
Fig. 3.5	FT-IR spectra of D5	85
Fig. 3.6	FT-IR spectra of D6	85
Fig. 3.7	FT-IR spectra of D7	86
Fig. 3.8	FT-IR spectra of D8	86
Fig. 3.9	FT-IR spectra of D9	87
Fig. 3.10	¹ H NMR spectra of D1	87
Fig. 3.11	¹ H NMR spectra of D2	88
Fig. 3.12	¹ H NMR spectra of D3	88
Fig. 3.13	¹ H NMR spectra of D4	89
Fig. 3.14	¹ H NMR spectra of D5	89
Fig. 3.15	¹ H NMR spectra of D6	90
Fig. 3.16	¹ H NMR spectra of D7	90
Fig. 3.17	¹ H NMR spectra of D8	91

Fig. 3.18	^1H NMR spectra of D9	91
Fig. 3.19	ESI-MS spectrum of molecule D1	92
Fig. 3.20	ESI-MS spectrum of molecule D2	92
Fig. 3.21	ESI-MS spectrum of molecule D3	92
Fig. 3.22	ESI-MS spectrum of molecule D4	93
Fig. 3.23	ESI-MS spectrum of molecule D5	93
Fig. 3.24	ESI-MS spectrum of molecule D6	93
Fig. 3.25	ESI-MS spectrum of molecule D7	94
Fig. 3.26	ESI-MS spectrum of molecule D8	94
Fig. 3.27	ESI-MS spectrum of molecule D9	94
Fig. 3.28	Differential Scanning calorimetry of molecules D2, D3, D4 and D6	95
Fig. 3.29	Differential Scanning calorimetry of molecules D5, D7 and D9	95
Fig. 3.30	UV-Vis absorbance spectra of molecule D1 in solvent of varying polarity.	98
Fig. 3.31	UV-Vis absorbance spectra of molecule D2 in solvent of varying polarity.	98
Fig. 3.32	UV-Vis absorbance spectra of molecule D3 in solvent of varying polarity.	99
Fig. 3.33	UV-Vis absorbance spectra of molecule D4 in solvent of varying polarity.	99
Fig. 3.34	UV-Vis absorbance spectra of molecule D5 in solvent of varying polarity.	100
Fig. 3.35	UV-Vis absorbance spectra of molecule D6 in solvent of varying polarity.	100
Fig. 3.36	UV-Vis absorbance spectra of molecule D7 in solvent of varying polarity.	101
Fig. 3.37	UV-Vis absorbance spectra of molecule D8 in solvent of varying polarity.	101
Fig. 3.38	UV-Vis absorbance spectra of molecule D9 in solvent of varying polarity.	102
Fig. 3.39	Photoluminescence spectra of molecule D1 in solvent of varying polarity.	103

Fig. 3.40	Photoluminescence spectra of molecule D2 in solvent of varying polarity	104
Fig. 3.41	Photoluminescence spectra of molecule D3 in solvent of varying polarity	104
Fig. 3.42	Photoluminescence spectra of molecule D4 in solvent of varying polarity	105
Fig. 3.43	Photoluminescence spectra of molecule D5 in solvent of varying polarity.	105
Fig. 3.44	Photoluminescence spectra of molecule D6 in solvent of varying polarity	106
Fig. 3.45	Photoluminescence spectra of molecule D7 in solvent of varying polarity	106
Fig. 3.46	Photoluminescence spectra of molecule D8 in solvent of varying polarity	107
Fig. 3.47	Photoluminescence spectra of molecule D9 in solvent of varying polarity	107
Fig. 3.48	Emission wavelength of molecule D1-D9 in solvent of varying polarity.	108
Fig. 3.49	Solid state emission of molecule D2-D9 under UV illumination	109
Fig. 3.50	Solid state photoluminescence spectra of molecule D2-D9	110
Fig. 3.51	Fluorescence Lifetime decay of molecule D1-D9 in methanol medium	111
Fig. 3.52	Standard deviation profiles for the determination of fluorescence lifetime values for molecule D1-D9	112
Fig. 3.53	Photographs of molecules D2-D9 in methanol/water mixtures with different f_w taken under UV illumination at a wavelength of 365 nm	114
Fig. 3.54	Fluorescence emission spectrum of D2 with varying f_w and inset gives the intensity value with varying f_w	115
Fig. 3.55	Fluorescence emission spectrum of D5 with varying f_w and inset gives the intensity value with varying f_w	115
Fig. 3.56	Fluorescence emission spectrum of D6 with varying f_w and inset gives the intensity value with varying f_w	116

Fig. 3.57	Fluorescence emission spectrum of D7 with varying f_w and inset gives the intensity value with varying f_w	116
Fig. 3.58	Fluorescence emission spectrum of D9 with varying f_w and inset gives the intensity value with varying f_w	117
Fig. 3.59	Cyclic voltammogram representing (a) oxidation cycle and (b) reduction cycle for the molecules D1 to D9	118
Fig. 3.60	HOMO and LUMO energy levels of molecule D1 to D9	119
Fig. 3.61	ORTEP diagram of molecule D6	120
Fig. 3.62	ORTEP diagram of molecule D7	120
Fig. 3.63	Molecular packing arrangement of molecule of D7 obtained by single crystal XRD	121
Fig. 3.64	Molecular packing arrangement of molecule of D7 obtained by single crystal XRD	121
Fig. 3.65	Optimized geometry of molecules D1 - D9 using DFT B3LYP functional.	124
Fig. 3.66	Molecular spatial orbitals of molecule D1 to D9 with their oscillator strength	125
Fig. 3.67	TD-DFT absorbance spectra of molecule D1 in solvent of varying polarity	126
Fig. 3.68	TD-DFT absorbance spectra of molecule D2 in solvent of varying polarity	126
Fig. 3.69	TD-DFT absorbance spectra of molecule D3 in solvent of varying polarity	127
Fig. 3.70	TD-DFT absorbance spectra of molecule D4 in solvent of varying polarity	127
Fig. 3.71	TD-DFT absorbance spectra of molecule D5 in solvent of varying polarity	128
Fig. 3.72	TD-DFT absorbance spectra of molecule D6 in solvent of varying polarity	128
Fig. 3.73	TD-DFT absorbance spectra of molecule D7 in solvent of varying polarity	129

Fig. 3.74	TD-DFT absorbance spectra of molecule D8 in solvent of varying polarity	129
Fig. 3.75	TD-DFT absorbance spectra of molecule D9 in solvent of varying polarity	130

CHAPTER 4

Fig. 4.1	FT-IR spectra of B1	134
Fig. 4.2	FT-IR spectra of B2	134
Fig. 4.3	FT-IR spectra of B3	135
Fig. 4.4	¹ H-NMR spectra of B1	135
Fig. 4.5	¹ H-NMR spectra of B2	136
Fig. 4.6	¹ H-NMR spectra of B3	136
Fig. 4.7	ESI-Mass spectra of B1	137
Fig. 4.8	ESI-Mass spectra of B2	137
Fig. 4.9	ESI-Mass spectra of B3	137
Fig. 4.10	UV-Vis spectra of molecule B1 in solvents of varying polarity	138
Fig. 4.11	UV-Vis spectra of molecule B2 in solvents of varying polarity	139
Fig. 4.12	UV-Vis spectra of molecule B3 in solvents of varying polarity	139
Fig. 4.13	UV-Vis spectra of molecules B1 , B2 and B3 in the presence and absence of acid	140
Fig. 4.14	Photoluminescence spectra of molecule B1 in solvents of varying polarity	141
Fig. 4.15	Photoluminescence spectra of molecule B2 in solvents of varying polarity	142
Fig. 4.16	Photoluminescence spectra of molecule B3 in solvents of varying polarity	142
Fig. 4.17	Fluorescence emission of molecules in day light and at UV-irradiation	143
Fig. 4.18	Solid-state UV-Vis and PL spectra of molecule B1 , B2 and B3	143
Fig. 4.19	Fluorescence spectrum of B1 with varying f_w % and inset show intensity vs f_w	145
Fig. 4.20	Fluorescence spectrum of B2 with varying f_w % and inset show intensity vs f_w	146

Fig. 4.21	Fluorescence spectrum of B3 with varying f_w % and inset show intensity vs f_w	146
Fig. 4.22	Photographs of molecules in THF/water mixtures with different f_w under UV illumination	147
Fig. 4.23	Cyclic voltammogram representing oxidation peak for molecules B1 , B2 and B3	148
Fig. 4.24	Cyclic voltammogram representing reduction peak for molecules B1 , B2 and B3	148
Fig. 4.25	Electronic energy levels for the molecules B1 , B2 and B3	149
Fig. 4.26	Optimized geometry of all the molecules with B3LYP/6-311+G (d,p) with their side view showing structural planarity	150
Fig. 4.27	Electronic orbital representation of the molecules B1 to B3	152
Fig. 4.28	Theoretically derived absorption and fluorescence emission spectrum of all the molecules with experimental values.	153
Fig. 4.29	Definition of reorganization energy in organic systems	156
Fig. 4.30	Illustration of face to face (FF), edge to face (EF) and slip stacking (SS) modes.	158
Fig. 4.31	Interaction energy of B1 dimer for different stacking arrangement with variation in dimer separation distance	158
Fig. 4.32	Interaction energy of B2 dimer for different stacking arrangement with variation in dimer separation distance	159
Fig. 4.33	Interaction energy of B3 dimer for different stacking arrangement with variation in dimer separation distance	159
Fig. 4.34	Interaction energy of all the molecules for slip-stacking arrangement with variation in dimer angular distance	160
Fig. 4.35	Computed dimer geometries in slip-stacking mode with their stacking distance and slip angle	160

CHAPTER 5

Fig. 5.1	Generic mechanism of keto-enol tautomerism exhibited in acid hydrazides	164
Fig. 5.2	FT-IR spectra of T2	169
Fig. 5.3	FT-IR spectra of P2	169

Fig. 5.4	FT-IR spectra of F2	170
Fig. 5.5	FT-IR spectra of T3	170
Fig. 5.6	FT-IR spectra of P3	171
Fig. 5.7	FT-IR spectra of F3	171
Fig. 5.8	¹ H NMR spectra of T2	172
Fig. 5.9	¹ H NMR spectra of P2	172
Fig. 5.10	¹ H NMR spectra of F2	173
Fig. 5.11	¹ H NMR spectra of T3	173
Fig. 5.12	¹ H NMR spectra of P3	174
Fig. 5.13	¹ H NMR spectra of F3	174
Fig. 5.14	ESI-MS spectra of T2	175
Fig. 5.15	ESI-MS spectra of P2	175
Fig. 5.16	ESI-MS spectra of F2	175
Fig. 5.17	ESI-MS spectra of T3	176
Fig. 5.18	ESI-MS spectra of P3	176
Fig. 5.19	ESI-MS spectra of F3	176
Fig. 5.20	UV-Vis absorbance spectra of molecule T2 in solvent of varying polarity.	177
Fig. 5.21	UV-Vis absorbance spectra of molecule P2 in solvent of varying polarity.	178
Fig. 5.22	UV-Vis absorbance spectra of molecule F2 in solvent of varying polarity.	178
Fig. 5.23	UV-Vis absorbance spectra of molecule T3 in solvent of varying polarity.	179
Fig. 5.24	UV-Vis absorbance spectra of molecule P3 in solvent of varying polarity.	179
Fig. 5.25	UV-Vis absorbance spectra of molecule F3 in solvent of varying polarity.	180
Fig. 5.26	PL spectra of molecule T2 in solvent of varying polarity.	183
Fig. 5.27	PL spectra of molecule P2 in solvent of varying polarity.	183
Fig. 5.28	PL spectra of molecule F2 in solvent of varying polarity.	184
Fig. 5.29	PL spectra of molecule T3 in solvent of varying polarity.	184

Fig. 5.30	PL spectra of molecule P3 in solvent of varying polarity.	185
Fig. 5.31	PL spectra of molecule F3 in solvent of varying polarity.	185
Fig. 5.32	Solid State UV-Vis absorbance spectra of all the molecules of the series	186
Fig. 5.33	Solid state PL spectra of molecules. Inset shows solid state emission under UV illumination	187
Fig. 5.34	Photographs of molecules in THF/water mixtures with different f_w under UV illumination	189
Fig. 5.35	Fluorescence emission spectrum of T2 with varying f_w and inset gives the intensity value with varying f_w	190
Fig. 5.36	Fluorescence emission spectrum of P2 with varying f_w and inset gives the intensity value with varying f_w	190
Fig. 5.37	Fluorescence emission spectrum of F2 with varying f_w and inset gives the intensity value with varying f_w	191
Fig. 5.38	Fluorescence emission spectrum of T3 with varying f_w and inset gives the intensity value with varying f_w	191
Fig. 5.39	Fluorescence emission spectrum of P3 with varying f_w and inset gives the intensity value with varying f_w	192
Fig. 5.40	The fluorescence emission spectrum of F3 with varying f_w and inset gives the intensity value with varying f_w	192
Fig. 5.41	Cyclic voltammogram for the molecules T2 , P2 , and F2 with their energy levels	194
Fig. 5.42	Cyclic voltammogram for the molecules T3 , P3 , and F3 with their energy levels	194
Fig. 5.43	Probable tautomeric structures with keto (k), enol (e) and double enol (o) form	195
Fig. 5.44	Vibrational stretching frequency of T1 , P1 and F1 in S_0 and S_1 states; specifically focusing N-H stretching frequency	197
Fig. 5.45	Intermolecular associations of molecules of the series with O--H bond distances. Color code: O-atoms, red; C-atoms, grey; N-atom: blue, S- atoms, green).	198

Fig. 5.46	Electronic orbital representations of all the molecules with their energy levels	200
Fig. 5.47	Vibrational stretching frequency of all the molecules in S_0 and S_1 states; specifically focusing N-H stretching frequency	202
Fig. 5.48	Experimentally observed and theoretically estimated absorption and emission spectra for keto and enol forms of all the molecules.	204
Fig. 5.49	Single point energies of molecule T2 , P2 and F2 as a function of rotation of dihedral angle for both S_0 and S_1 . Black colored atom - Thiophene, Furan or Pyridine	206
Fig. 5.50	Single point energies of molecule T3 , P3 , and F3 as a function of rotation of dihedral angle for both S_0 and S_1 . Black colored atom - Thiophene, Furan or Pyridine	207
Fig. 5.51	Single point energies of molecule T2 in the S_0 and S_1 states calculated by B3LYP and CAM-B3LYP	208
Fig. 5.52	Single point energies of molecule P2 in the S_0 and S_1 states calculated by B3LYP and CAM-B3LYP	209
Fig. 5.53	Single point energies of molecule F2 in the S_0 and S_1 states calculated by B3LYP and CAM-B3LYP	209
Fig. 5.54	Single point energies of molecule T3 in the S_0 and S_1 states calculated by B3LYP and CAM-B3LYP	210
Fig. 5.55	Single point energies of molecule P3 in the S_0 and S_1 states calculated by B3LYP and CAM-B3LYP	210
Fig. 5.56	PES scan of T3 in S_0 and S_1 states with their contour profile	212
Fig. 5.57	PES scan of P3 in S_0 and S_1 states with their contour profile	212
Fig. 5.58	Device architecture for molecule T2 , P2 , and F2 as an emitter layer	214
Fig. 5.59	J-V characteristics of the device with T2 , P2 , and F2 as emitter material. Inset showing the EL spectrum and image showing the light emission from the device.	214
Fig. 5.60	Voltage luminous flux characteristics of molecule T2 and P2	215
Fig. 5.61	Current Efficiency and power efficiencies of the device with T2 as an emitter layer	215

Fig. 5.62	Current Efficiency and power efficiencies of the device with P2 as an emitter layer	216
------------------	--	-----

CHAPTER 6

Fig. 6.1	FT-IR spectra of P4	223
Fig. 6.2	¹ H NMR spectra of P4	223
Fig. 6.3	Experimental UV-Vis absorbance spectra and fluorescence emission spectra of T4 , P4 and F4 in THF solvent	226
Fig. 6.4	Photoluminescence spectra of T4 in solvents of varying dielectric constants	226
Fig. 6.5	Photoluminescence spectra of P4 in solvents of varying dielectric constants	227
Fig. 6.6	Photoluminescence spectra of F4 in solvents of varying dielectric constants	227
Fig. 6.7	Fluorescence emission spectra of T4 , P4 and F4 thin films	229
Fig. 6.8	Photographs of molecules in THF/water mixtures with different f_w under UV illumination	230
Fig. 6.9	Fluorescence emission spectrum of T4 with varying f_w and inset gives the intensity value with varying f_w	231
Fig. 6.10	Fluorescence emission spectrum of P4 with varying f_w and inset gives the intensity value with varying f_w	231
Fig. 6.11	Fluorescence emission spectrum of F3 with varying f_w and inset gives the intensity value with varying f_w	232
Fig. 6.12	Cyclic voltammogram of molecule P4 in acetonitrile solvent	233
Fig. 6.13	Possible conformations of TX , PX , and FX where X=4,5,6 at its S0 and S1 state,	234
Fig. 6.14	Ground state geometry optimized normal form (k) of TX , PX , FX , where X=4, Color code: O-atoms, red; C-atoms, grey; N-atom: blue, S-atoms, yellow; H-atoms, white.	236
Fig. 6.15	Ground state geometry optimized normal form (k) of TX , PX , FX , where X=5 Color code: O-atoms, red; C-atoms, grey; N-atom: blue, S-atoms, yellow; H-atoms, white.	237

Fig. 6.16	Ground state geometry optimized normal form (k) of TX , PX , FX , where X=6, Color code: O-atoms, red; C-atoms, grey; N-atom: blue, S-atoms, yellow; H-atoms, white	237
Fig. 6.17	Vibrational stretching frequency of TX , PX , FX , where X=4, in S0 and S1 states; specifically focusing N-H stretching frequency	238
Fig. 6.18	Vibrational stretching frequency of TX , PX , FX , where X=5,6, in S0 and S1 states; specifically focusing N-H stretching frequency	239
Fig. 6.19	Frontier molecular orbitals of T4 , P4 and F4 in keto form	242
Fig. 6.20	Frontier molecular orbitals of T5 , P5 and F5 in keto form	243
Fig. 6.21	Frontier molecular orbitals of T6 , P6 and F6 in keto form	244
Fig. 6.22	Absorption and Fluorescence emission spectrum of all the TX , PX and FX , where X=4 with experimental values	245
Fig. 6.23	Absorption and Fluorescence emission spectrum of all the TX , PX and FX , where X=5,6 with experimental values	246
Fig. 6.24	SP energies of T4 , P4 , F4 as a function of rotation of dihedral angle for S0 and S1	249
Fig. 6.25	SP energies of T5 , P5 , F5 as a function of rotation of dihedral angle for S0 and S1	249
Fig. 6.26	SP energies of T6 , P6 , F6 as a function of rotation of dihedral angle for S0 and S1	250
Fig. 6.27	SP energies of T4 in the S0 and S1 states calculated by B3LYP and CAM-B3LYP	251
Fig. 6.28	SP energies of P4 in the S0 and S1 states calculated by B3LYP and CAM-B3LYP	252
Fig. 6.29	SP energies of F4 in the S0 and S1 states calculated by B3LYP and CAM-B3LYP	252
Fig. 6.30	SP energies of T5 in the S0 and S1 states calculated by B3LYP and CAM-B3LYP	253
Fig. 6.31	SP energies of P5 in the S0 and S1 states calculated by B3LYP and CAM-B3LYP	253
Fig. 6.32	SP energies of F5 in the S0 and S1 states calculated by B3LYP and CAM-B3LYP	254

Fig. 6.33	SP energies of T6 in the S0 and S1 states calculated by B3LYP and CAM-B3LYP	254
Fig. 6.34	SP energies of P6 in the S0 and S1 states calculated by B3LYP and CAM-B3LYP	255
Fig. 6.35	SP energies of F6 in the S0 and S1 states calculated by B3LYP and CAM-B3LYP	255
Fig. 6.36	PES scan of T4 in S0 and S1 states with their contour profile	257
Fig. 6.37	PES scan of P4 in S0 and S1 states with their contour profile	258
Fig. 6.38	PES scan of F4 in S0 and S1 states with their contour profile	258
Fig. 6.39	PES scan of T6 in S0 and S1 states with their contour profile	259
Fig. 6.40	PES scan of P6 in S0 and S1 states with their contour profile	259
Fig. 6.41	PES scan of F6 in S0 and S1 states with their contour profile	260

LIST OF SCHEMES

Scheme 2.1	Structure of molecules M1, M2, M3, M4 and M5	48
Scheme 3.1	Structure of molecules D1-D9	82
Scheme 4.1	Synthetic scheme of molecules B1, B2 and B3	133
Scheme 5.1	Synthesized molecular structures of T2, P2, F2, T3, P3 and F3 for the present study	167
Scheme 6.1	Synthesis of molecule P4	223

LIST OF TABLES

CHAPTER 2

Table 2.1	Photophysical aspects of molecules M1 to M5 in solvents of varying polarity	61
Table 2.2	Photoluminescence parameters of molecule M2 and M4 in solid state	66
Table 2.3	Measured quantum yield for molecule M1 , M2 and M4	67
Table 2.4	The lifetime of molecules M1 to M5 and its XSQR value.	68
Table 2.5	Estimation of HOMO, LUMO and bandgap of molecule M1 to M2 from electrochemical studies	70

CHAPTER 3

Table 3.1	Photophysical studies of molecules D1 to D9 under various solvents and its optical band gap for UV-Vis absorption spectra	96
Table 3.2	Fluorescence quantum yield of molecule D1-D9 in methanol solvent	108
Table 3.3	Photophysical studies for molecule D2-D9 in solid state	110
Table 3.4	Fluorescence Lifetime for the molecules D1 to D9	111
Table 3.5	Electrochemical results for the molecules D1 to D9	118
Table 3.6	Crystallographic data of molecule D6	122

CHAPTER 4

Table 4.1	Photophysical parameters of molecules in solvents of varying dielectric constant	141
Table 4.2	Solid state photophysical properties of all the molecules	143
Table 4.3	Measured quantum yield of molecules in methanol solvent	144
Table 4.4	Electrochemical parameters with their energy levels for all the molecules	149
Table 4.5	Theoretically estimated optical parameters pertaining to energy transition, oscillator strength, configuration interaction using CAM-B3LYP 6-31G(d,p) in methanol medium	154
Table 4.6	Theoretically estimated optical parameters pertaining to energy transition, oscillator strength, configuration interaction using CAM-B3LYP 6-311+G(d,p) in methanol medium	154

Table 4.7 Theoretically estimated optical parameters pertaining to energy transition, oscillator strength, and configuration interaction using Def2TZVP in methanol medium 155

Table 4.8 Computational evaluation of the reorganization energies k (eV) for hole and electron transport in all the molecules 156

CHAPTER 5

Table 5.1 Photophysical parameters of the molecules in solvents of different polarities 182

Table 5.2 Photophysical parameters of the molecules in thin film 187

Table 5.3 The measured quantum yield of all the molecules 188

Table 5.4 Electrochemical parameters and their electronic energy levels of all the molecules 193

Table 5.5 Geometrical parameters of the molecules at S_0 and S_1 198

Table 5.6 Vibrational –NH stretching frequency of all molecules at S_0 and S_1 201

Table 5.7 Computed optical parameters of molecules, keto absorbance and emission, enol emission, oscillator strengths, composition and CI(%) calculated at DFT/B3LYP and TD-DFT/CAM-B3LYP for ground and excited state 205

CHAPTER 6

Table 6.1 Photophysical parameters of **T4**, **P4** and **F4** in solvent of varying polarities 225

Table 6.2 Photoluminescence parameters of thin films of **T4**, **P4** and **F4** 229

Table 6.3 Geometrical parameters of the molecules at S_0 and S_1 238

Table 6.4 Computed vibrational NH stretching frequency at ground and excited state 240

Table 6.5 Computed optical parameters of molecules: keto absorbance and emission, enol emission, oscillator strengths, composition and CI(%) calculated at DFT/B3LYP and TD-DFT/CAM-B3LYP for ground and excited state 247

Table 6.6 Forward and Reverse potential barrier at ground state S_0 and excited state S_1 for all the molecules of the series 256

NOMENCLATURE

Abbreviation

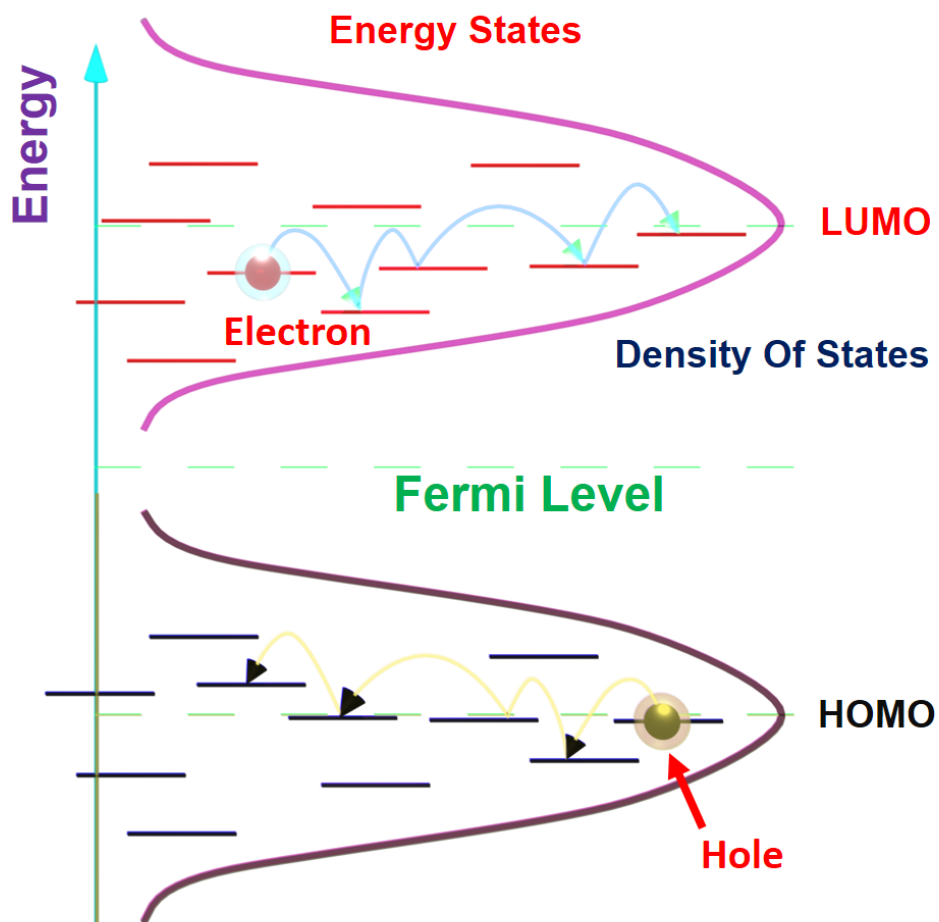
ACN	Acetonitrile
ACQ	Aggregation caused quenching
AIE	Aggregation Induced Emission
B3LYP	Becke 3-parameter Lee–Yang–Parr
CAM-B3LYP	Coulomb attenuated model Becke 3-parameter Lee–Yang–Parr
DFT	Density Functional Theory
DCM	Dichloromethane
DMF	Dimethylformamide
DMSO	Dimethylsulfoxide
DMSO-d ₆	Dimethylsulfoxide-deuterated
ESI	Electron Spray Ionized
EtOH	Ethyl alcohol
ESIPT	Excited state intramolecular proton transfer
EQE	External quantum efficiency
FT-IR	Fourier Transform Infra-Red
HOMO	Highest Occupied Molecular Orbital
LUMO	Lowest un-occupied molecular orbital
MS	Mass Spectra
M.p.	Melting point
MeOH	Methanol
ORTEP	Oak Ridge Thermal Ellipsoid Plot
PEC	Potential energy curve
PES	Potential energy surface
HNMR	Proton Nuclear Magnetic Resonance
QY	Quantum Yield
RT	Room Temperature
RIM	Rotation of intramolecular motion
RIR	Rotation of intramolecular rotation
RIV	Rotation of intramolecular vibration
SCXRD	Single Crystal X-Ray Diffraction
SSA	Singlet singlet annihilation
STA	Singlet triplet annihilation
SOC	Spin orbit coupling
THF	Tetrahydrofuran
TLC	Thin Layer Chromatography
TDDFT	Time Dependent Density Functional Theory
TTA	Triplet triplet annihilation
TZVP	Triple zeta valence potential
UV-Vis	Ultraviolet-Visible

SYMBOLS AND UNITS

Å	Angstrom
Cd	Candela
cm	Centimetre
°	Degree
°C	Degree Celsius
φ	Efficiency
eV	Electron volt
E _G	Energy bandgap
ν	Frequency
>	Greater than
h	Hour
Hz	Hertz
⁻¹	Inverse
λ	Lambda
<	Lesser than
τ	Lifetime
L	Litre
lm	Luminous flux
MHz	Megahertz
mg	Milligram
mA	Milliampere
mL	Millilitre
mmol	Millimole
min	Minute
M	Molar
nm	Nanometre
ns	Nano-second
h	Planck's constant
C	Speed of light
T	Temperature
V	Volt

CHAPTER 1

INTRODUCTION



1.1 ORGANIC ELECTRONICS

Organic electronics has attracted greater attention amongst academic and industrial research owing to its wide infra of applications in the field of organic light emitting diodes (OLED), organic field effect transistors (OFETs) and organic photovoltaics (OPVCs) (Müllen and Scherf 2006). Organic electronics is a branch of material science that deals in design and synthesis of novel organic molecules aiming towards various optoelectronics device applications (Brütting 2006). Organic molecules serving as an active component in organic devices possess a good amount of conjugation in their structure (Brütting and Adachi 2012). Organic systems are mainly composed of carbon and hydrogen, and often contains various other elements like oxygen, nitrogen and sulphur. These may also contain various metal atoms like aluminium, zinc, platinum or iridium that are generally termed as organo-metallic complexes (Brütting 2006). This is in contrast with conventional electronics that basically rely on two most prominent materials such as silicon and germanium for various inorganic device applications. Organic semiconductors are classified into two different classes, a class of small organic molecules and a class of organic polymers, i.e. long chain molecules composed of repeating structural units. Though the classes of both materials are purely organic, however, their basic difference lies in the techniques and methodology adopted for device processing. Organic polymers are generally solution processed and hence can be deposited onto the substrates either by spin-coating or by printing. On the other, organic small molecules are generally deposited by sublimation process, wherein, organic molecules tend to crystallize into ordered arrays forming thin films. Some of the well-explored organic molecules used in device applications are illustrated in the Fig. 1.1. Organic molecules interact with one another through Van der Waals forces that are comparatively much weaker than forces arise out of covalent bonds (Tang and VanSlyke 1998). Van der Waals forces acting on these materials adopt a good amount of structural flexibility and possess a relatively low melting temperature. Organic semiconductors are often amorphous in nature and hence their device functioning doesn't rely upon crystalline nature of the system (Forrest et al. 1997). Whereas the devices constructed using inorganic semiconductors demands a high amount of structural crystallinity and a strong covalent bond between the lattice atoms. Amorphous nature of organic molecules exhibits a tremendous amount of structural flexibility, that rules out epitaxial growth at the organic-organic or organic-metal interface and thus can be

easily mounted on flexible substrates. Conversely, inorganic semiconductors demand a good lattice matching between the substrate and the film being deposited on it. Lattice mismatching in inorganic semiconductors lead to defects that are highly detrimental resulting in shallow and deep traps. Ease of molecular synthesis and chemical versatility benefits tuning of optical and electronic properties in organic system owing towards a specific application (Brütting 2006). Further, for OLED devices, emission colour tuning in active organic materials is easily achieved by mere chemical synthesis (Montes et al. 2004). Organic device processing techniques is by far much simpler and cost-effective method in comparison with that required for processing inorganic devices. Structural flexibility facilitates organic molecules to be processed using various printing technologies such as ink-jet printing, stamping and roll-to-roll printing for large area devices, have been proven successful in device fabrication (Zhang et al. 2013).

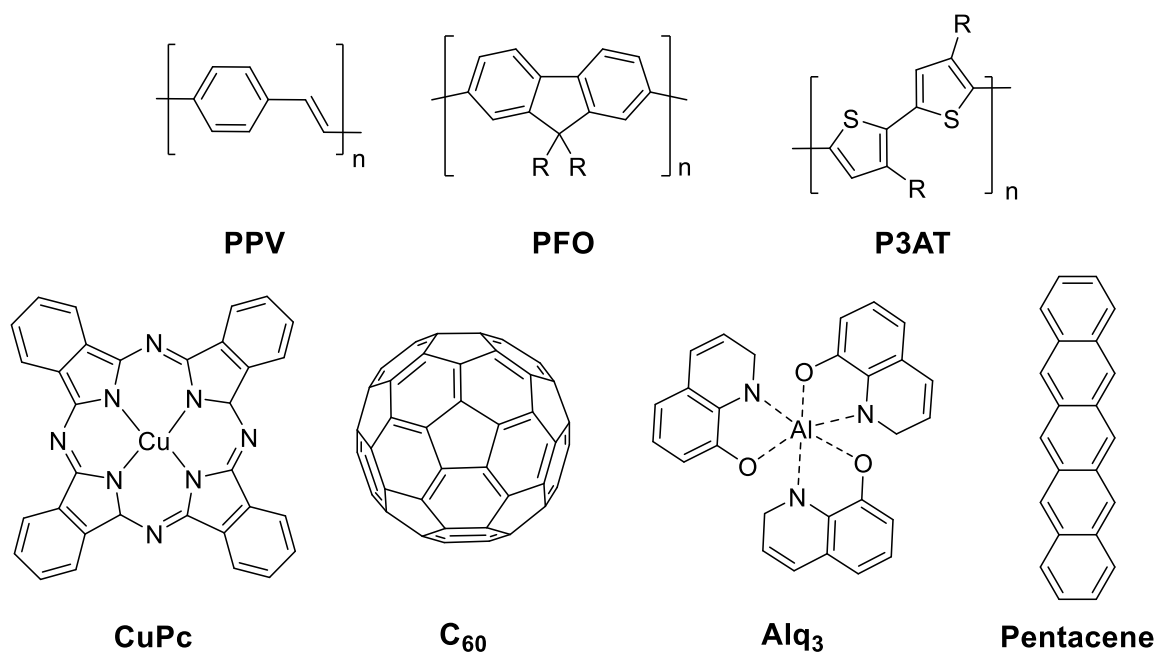


Fig. 1.1 Molecular structure of few organic semiconductors

Organic light emitting diodes have revolutionized lighting and display technology since the advent of organic luminescent materials. Tang and Van Slyke at Eastman Kodak reported their first organic light emitting diodes in 1987 (Tang and VanSlyke 1987). Soon after their first report, Eastman Kodak and Sanyo Electric launched Kodak's LS633 digital camera with active-matrix-driven OLED (AMOLED). OLED based displays were developed since then for mobile cellular phones, GPS devices, and portable multimedia players. OLED displays offer improved image quality with better contrast, higher-

brightness, a wider range of colours, and faster refreshing rates. Simpler in design, offering ultrathin flexible displays with low power consumption and wide range of operating temperature have made OLED displays advantageous over conventional light sources.

1.2 CONDUCTION MECHANISM

Atomic orbitals in organic molecules fuse to form new hybridized orbitals possessing a mixed behaviour of s-shell and p-shell, and accordingly sp , sp^2 and sp^3 hybridization are the three major classifications. Organic molecules possessing sp^2 hybridization overall controls the activity of charge conduction and charge transport in organic systems. The sp^2 constitutes hybridization of a single 2s orbital with three 2p orbitals, wherein, the three 2p orbitals formed in a plane possess a 120° angular separation between them as shown in Fig. 1.2. The remaining un-hybridized 2p orbital orient orthogonal to the plane containing three 2p orbitals. Hybridized carbon atoms when bonded to each other forms a head-on bond also called as σ bond developed over the two 2p orbitals. The remaining two perpendicular p orbitals interact to form a more diffusely overlapping bond, termed as π bond that further delocalizes electronic density in the system. In general, the σ bond is much stronger than a π bond as the head-on overlapping is more direct and effective. This combination of a stronger σ and weaker π bond describes the ubiquitous carbon-carbon double bond. Hence, the nature of electronic transition pertaining to π - π^* orbital requires a minimal energy in comparison with that of electronic transition involved in σ - σ^* orbital. Bonding π orbitals are formed by constructive interference of their individual wave function, whereas, antibonding π^* is formed by destructive interference. The molecules upon condensation undergo an overlap of their delocalized π -electronic system forming a channel to guide charges through it. The term highest occupied molecular orbital (HOMO) represents highest filled orbital formed by overlapping of bonding π -orbitals (π) and lowest unoccupied molecular orbital (LUMO) is an empty orbital formed by overlapping of anti-bonding π -orbitals (π^*) (Li and Kwok 2012). Owing to partially filled p_z orbital, there exist a significant energy gap between the HOMO and LUMO energy levels, generally referred as energy band gap. Hence, the band gap energy E_g , is the minimum energy required to excite an electron from HOMO to LUMO orbital, or in other words, it is the difference between HOMO and LUMO energy levels. Organic semiconductors typically possess a band gap value ranging between 1 – 3 eV (Brütting 2006).

Organic molecules, whose photophysical properties can be tuned at ease by means of chemical synthesis have attracted greater interest amongst the researchers. Results prove that organic molecules possessing carbon backbone as a main constituent exhibits semiconducting properties that are exciting for various device applications (Li and Kwok 2012). Semiconducting properties in organics is highly predominant for system possessing alternate single and double bond along the carbon backbone. Alternate single and double bond in organic molecules governs some of the most prominent parameters like conductivity, chemical nature and optical properties of the system (Karimov et al. 2008). Charge transport and conduction in an organic system is through the π bonded orbitals that exhibits a large amount of delocalization along the conjugation length. Charge transfer occurring between the donor and acceptor species in a molecule is known as intramolecular charge transfer, while charge transfer between two adjacent molecules is termed as intermolecular charge transfer. Condensation of organic molecules leads to stacking of molecular system that readily alters the charge transfer behaviour in the system. Presence of strong intermolecular overlapping between π orbital of interacting molecules leads to weaker charge transport in organics (Datt 1969).

Mechanism of charge conduction in organic semiconducting materials is far different than the conventional valence band theory applicable for inorganic semiconductor materials. Conduction mechanism in organics primarily describes the movement of mobile charge carriers inside the solids under the influence of external electric field. In accordance with inorganic band theory, charge carriers are permitted to transport only in allowed orbitals. In organic systems charge carriers are generated within the delocalized π orbitals due to overlap of individual atomic orbitals. Irregularity in molecular structures greatly affects the charge carrier mobility in organic systems (Li and Kwok 2012). Energy distribution in organics hold a Gaussian distribution pattern and are referred to as density of states (DOS). Owing to the presence of high charge trap density and defects due to irregularity, band theory fails to support charge transport in organic system. Instead, organic system support charge hopping mechanism, wherein, charges hop from one energy state to another energy state within an orbital. Hole charge carriers are guided along HOMO orbital while the electron charge carriers are transported along LUMO orbital as shown in the Fig. 1.3.

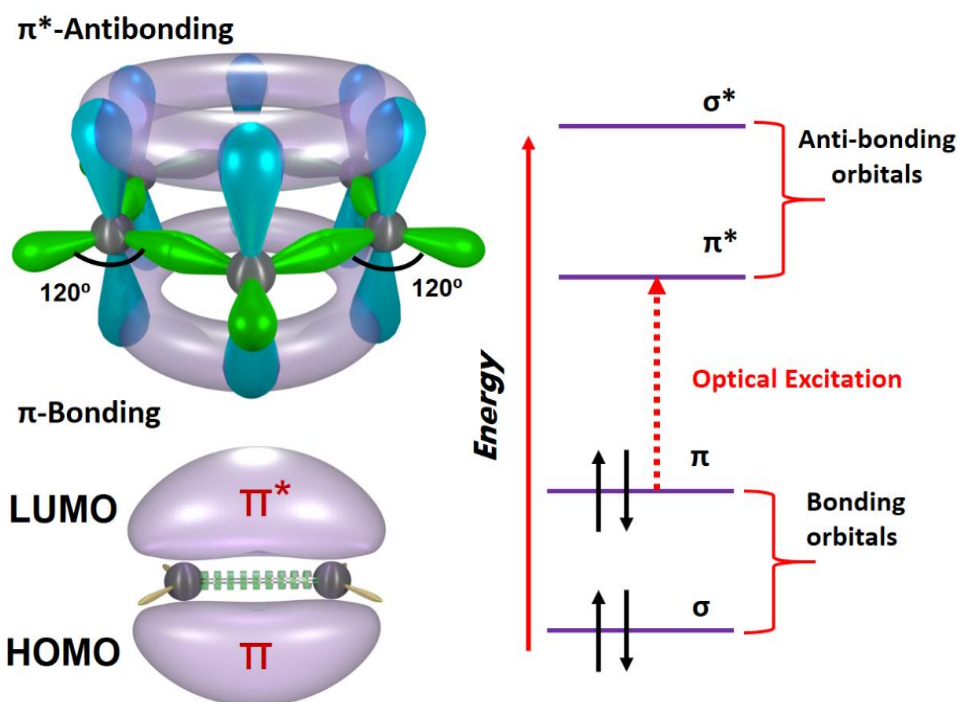


Fig. 1.2 Schematic representation of orbital overlap and energy level diagram

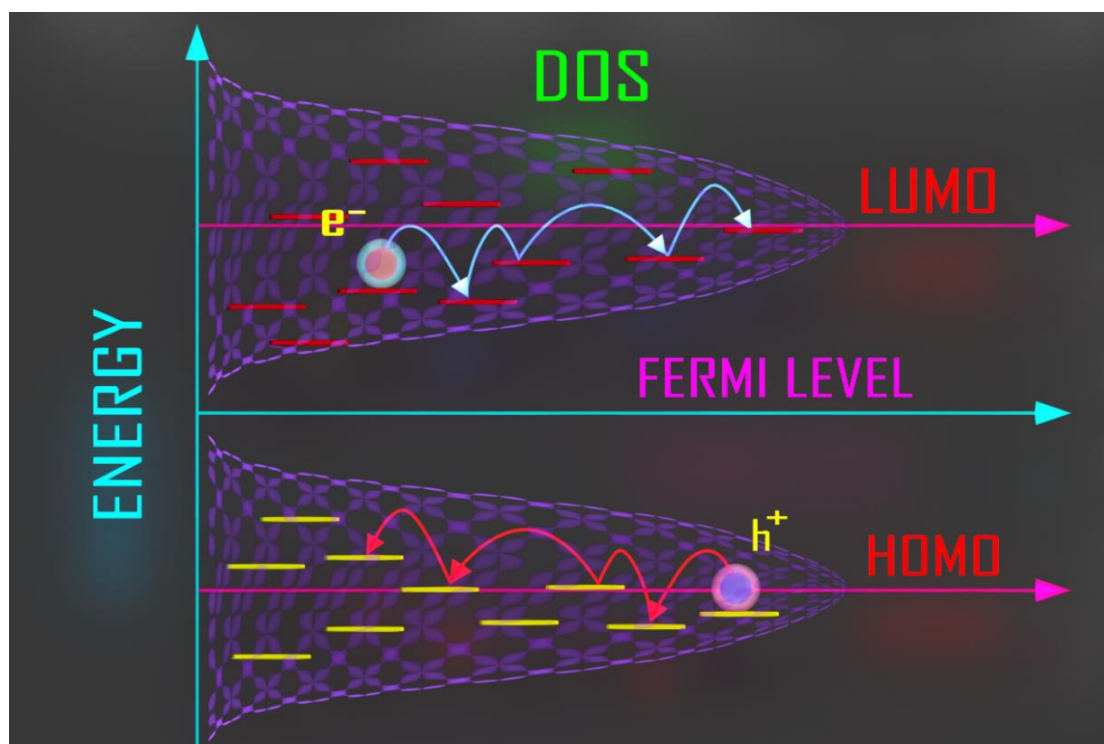


Fig. 1.3 Illustration of charge hopping in HOMO and LUMO energy states

1.3 EXCITONS

Photoexcitation in organic semiconductor induces an electron to get excited from HOMO to LUMO energy level and in turn leaves a localized hole in the HOMO energy level. Thus the localized hole and the excited electron pair forms a bound energy state and this bound pair is called an exciton. The minimum energy required to separate the bound electron-hole pair into discrete charges is defined as exciton binding energy. Exciton binding energy is the energy that corresponds to the sum of energy gap between the HOMO-LUMO and the exciton energy (Bulović et al. 2001). On the basis of distance between the bound electron-hole pair, excitons can be classified into Frenkel type or Wannier-mott type. Frenkel type excitons are the one whose bound electron-hole pair possesses the shortest intramolecular distance as shown in Fig. 1.4. Frenkel excitons possess a relatively stronger binding energy as they are highly localized on a single molecule. Charge transfer excitons, that is quite similar to that of Frenkel type excitons is also observed at some cases in organic systems. Supposing, if the exciton binding distance is enhanced by two or more lattice constants, then that would result in electron residing on donor species, while the hole residing on the acceptor species of a molecule as illustrated in Fig. 1.5. Such a formation is achieved with an increased delocalization of charges in the system, and are generally termed as charge transfer exciton (CT). Binding energy of charge transfer exciton and Frenkel type excitons typically fall in the range between $\sim 0.1 - 1$ eV (Alvarado et al. 1998; Barth and Bäessler 1997; Hill et al. 2000; Knupfer et al. 1998). Frenkel and charge transfer excitons are generally found in organic small molecules owing to weak Van der waals intermolecular force that are localized on a molecule (Bulović et al. 2001). Wannier-Mott type of excitons are generally perceived in inorganic semiconductors, that are highly delocalized possessing a fairly large electron-hole binding distance as shown in Fig. 1.6. The typical binding energy of Wannier-Mott type of exciton falls in orders of few millielectron volt and hence the dielectric constant of the material are high enough to easily separate the bound charges (Ashcroft and Mermin 1976).

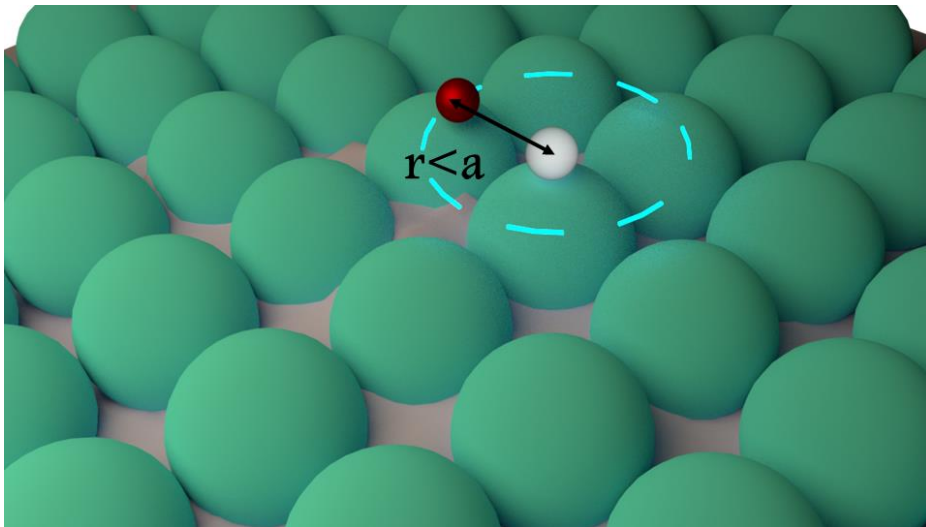


Fig. 1.4 Frenkel type of excitons wherein distance $r < a$

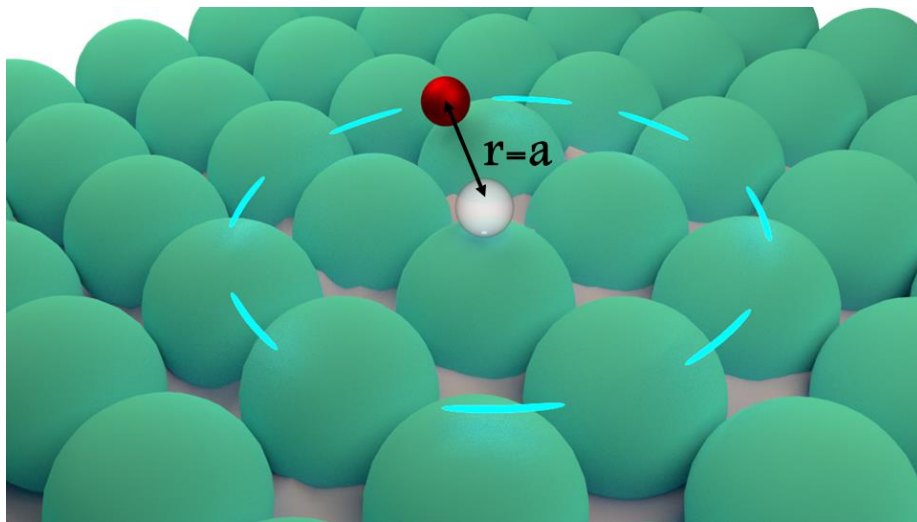


Fig. 1.5 Charge transfer type of excitons wherein distance $r = a$

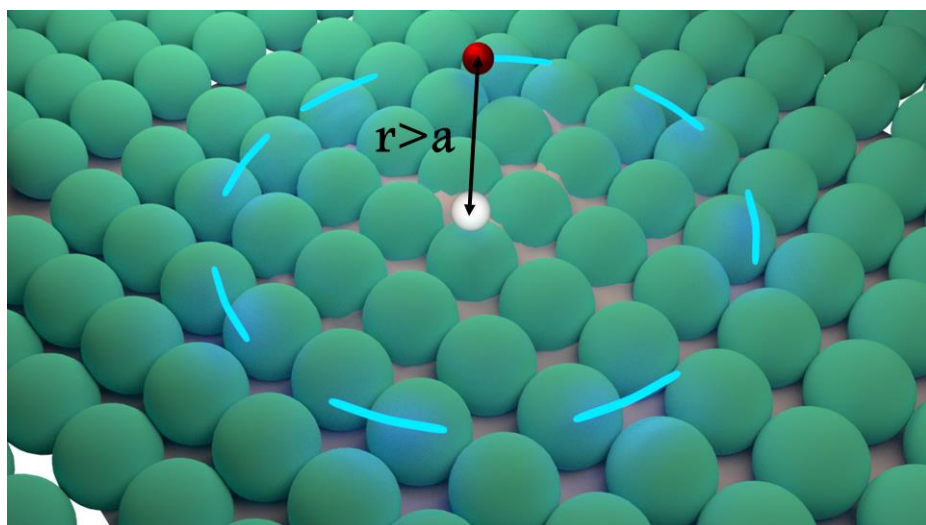


Fig. 1.6 Wannier-Mott type of excitons wherein distance $r > a$

Generated excitons at the active layer undergo recombination transferring energy in the form of vibrational relaxation or radiative relaxation. If the energy transfer between molecules whose intermolecular distance falls above 10 nm, i.e., $d > 10$ nm, then such energy transfer would be radiative in nature. One of the main reason would be that the energy transfer between the molecules emerge without direct interaction between the molecules (Gaspar and Polikarpov 2015). Columbic forces acting on the bound exciton pair, assists in recombination, resulting in an exciton energy transfer in the form of generated photon. The photons that are generated by exciton recombination at donor molecules may be reabsorbed by the acceptor molecules. Reabsorption by the system may occur provided, if the emitted photonic energy of donor molecules overlaps with the absorption energy of acceptor molecules. This photon reabsorption process maybe unending if there exists a strong overlap between the absorption and emission spectrum of the system (Pope and Swenberg 1999).

Energy transfer can also be non-radiative in nature and are realized within short range of distances, where $d < 10$ nm, between the donor and acceptor molecules (Gaspar and Polikarpov 2015). Accordingly, there are two kinds of non-radiative energy transfer, Förster energy transfer and Dexter energy transfer. Förster energy transfer is a resonant energy transfer mechanism that occurs via dipole-dipole coupling between the interacting molecules (Braslavsky et al. 2008). Förster energy transfer strongly relies on emission-absorbance overlap between the donor and the acceptor molecule. Photoexcitation causes the donor molecule to get excited while the acceptor molecule remains at the ground state. Energy transfer from the donor to the acceptor occurs when the wavefunction of interacting molecule interact coherently causing acceptor wavefunction to oscillate at the same frequency. Förster energy transfer can be thought of radiative photon transfer process between the donor and the acceptor molecules, without the emitted photon being seen (Gaspar and Polikarpov 2015). After a successful energy transfer process, the acceptor molecule gets excited and the donor transit back to ground state as illustrated in Fig. 1.7. In contrast to Förster energy transfer, Dexter energy transfer involves in physical exchange of electrons between the donor and an acceptor molecule. Dexter energy transfer is less probable, unlike Förster energy transfer, which is highly dominant in organic systems. Dexter transfer is highly predominant for triplet-triplet interaction as the molar extinction coefficient of triplet levels are significantly low in comparison with that of the singlet levels. Further, physical exchange of electrons between the molecules is a time consuming

process, and hence, long-lived triplet states are apt for Dexter transfer mechanism providing sufficient interaction time for exchange. Dexter energy transfer occurs at short range of interaction distances much lesser than the Förster energy transfer distance, typically a few nanometers. Photoexcited donor molecule transfers an electron to the acceptor molecule and simultaneously ground state acceptor transfers an electron to the donor molecule accomplishing an energy transfer.

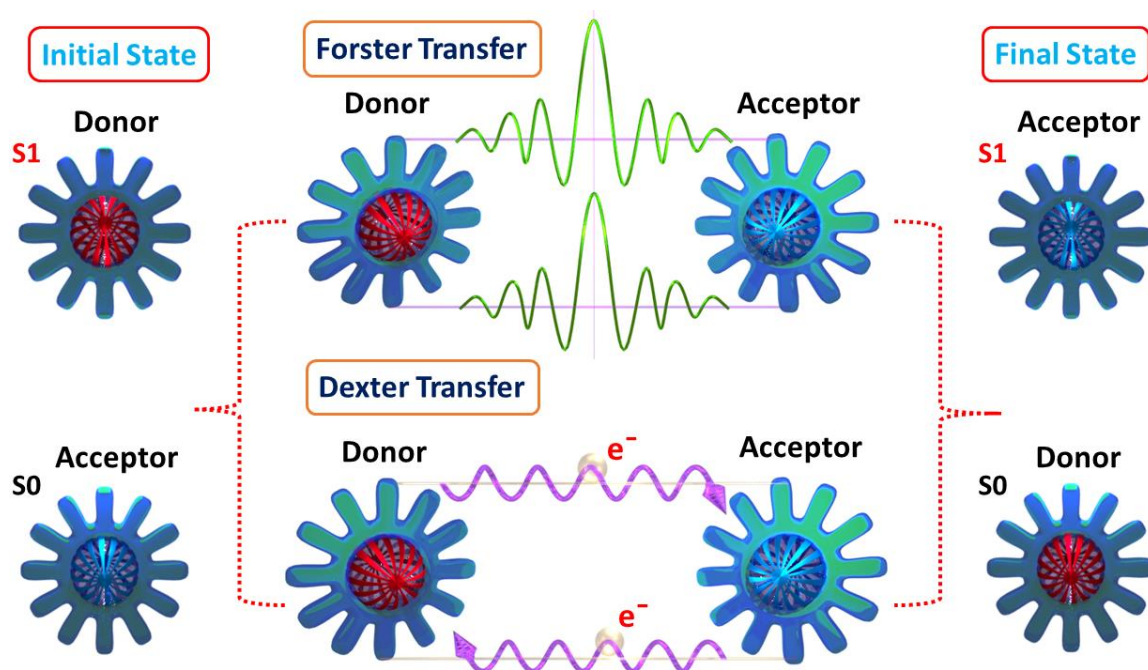


Fig. 1.7 Illustration of Förster and Dexter energy transfer process with initial and final state

Exciton energy transfer can also occur between the two excited states of a system provided if the excitation density of the system is very high. Annihilation or exciton energy transfer is a process involved in transfer of energy from one excited state to another excited state resulting in a higher excited state and a ground state of the molecular system. Energy exchange can occur between an exciton and a polaron or it can occur between a singlet-singlet exciton or between a singlet-triplet exciton (Gutman and Lyons 1981). Accordingly, there are three classifications, singlet-singlet annihilation (SSA), triplet-triplet annihilation (TTA) and singlet-triplet annihilation (STA). Annihilation occurring between excitons in an organic play significant role in altering the optical properties of the system.

Singlet-singlet annihilation involves in two singlet excitons annihilating resulting in a combination of a higher excited singlet exciton and a singlet ground state. Excited singlet exciton then undergoes recombination providing a first excited singlet state and a

singlet ground state with the remaining energy spent over vibrational relaxation in generation of heat in the system. Fig. 1.8 illustrates this mechanism, wherein, S_0 , S_1 and S_n represents singlet ground state, first excited singlet state and higher excited singlet state respectively. An excited singlet state exciton can also annihilate with excited triplet state exciton resulting in higher excited triplet exciton and a ground singlet state. Higher excited triplet exciton then relaxes to the first excited state by vibrational relaxation in the form of heat, and the process involved is termed as internal conversion. First excited triplet energy state may then relax back to ground state by vibrational relaxation or radiative emission provided if the triplet to singlet energy levels are favourable for radiative emission as shown in Fig. 1.9. Singlet-triplet annihilation mechanism occurs via Förster energy transfer, whereas, triplet-triplet annihilation is based on dexter energy transfer. TTA involves in energy transfer between two excited triplet excitons, resulting in the energy being transferred either by radiative or by non-radiative means. Two triplet state exciton recombines to result in generation of singlet ground state and a higher excited singlet state. Excited singlet state further relaxes to the ground state via radiative emission, since the system has to transit from excited triplet to excited singlet state, the whole process is relatively delayed and hence coined delayed fluorescence. The other outcome of TTA can be non-radiative relaxation, wherein, the TTA can result in generation of a singlet ground state and a higher excited triplet state. This higher excited triplet state then further relaxes back to the ground state via internal conversion also termed as triplet quenching and the mechanism is as shown in the Fig. 1.10.

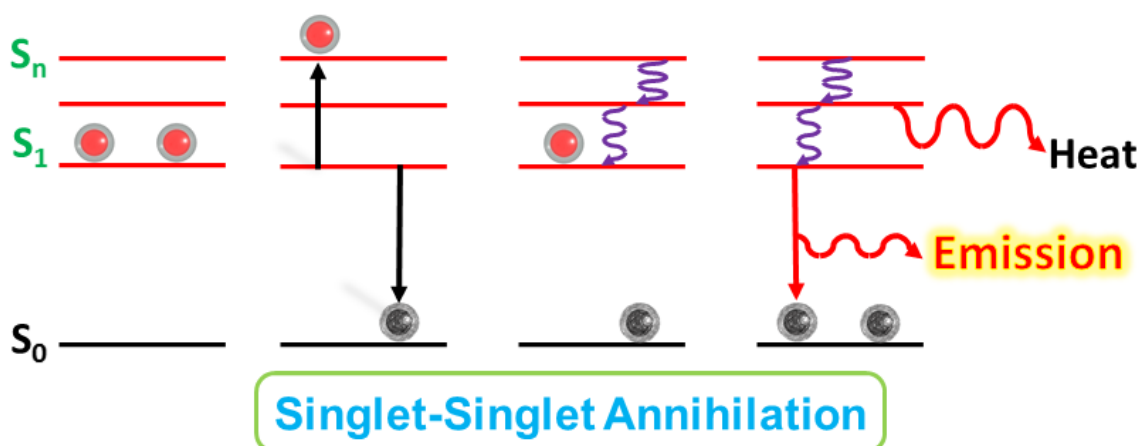


Fig. 1.8 Mechanism illustrating singlet-singlet annihilation

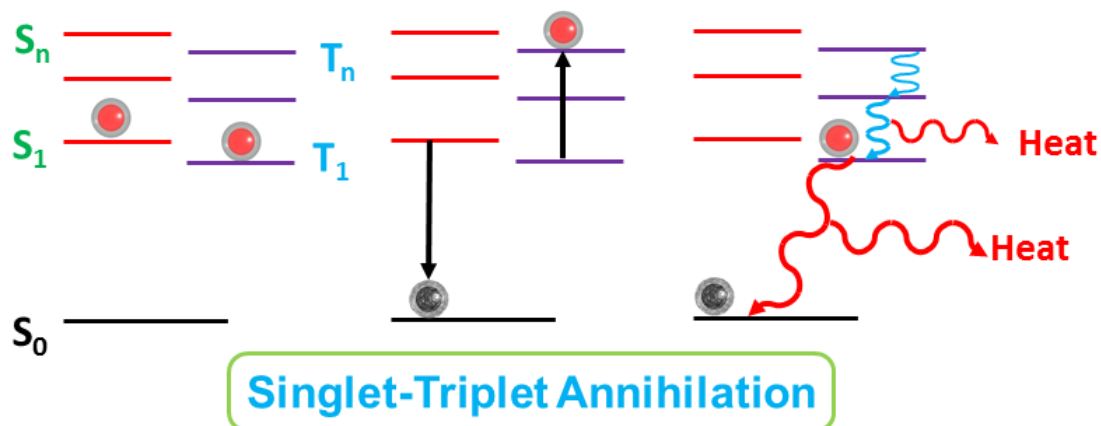


Fig. 1.9 Mechanism illustrating singlet-triplet annihilation

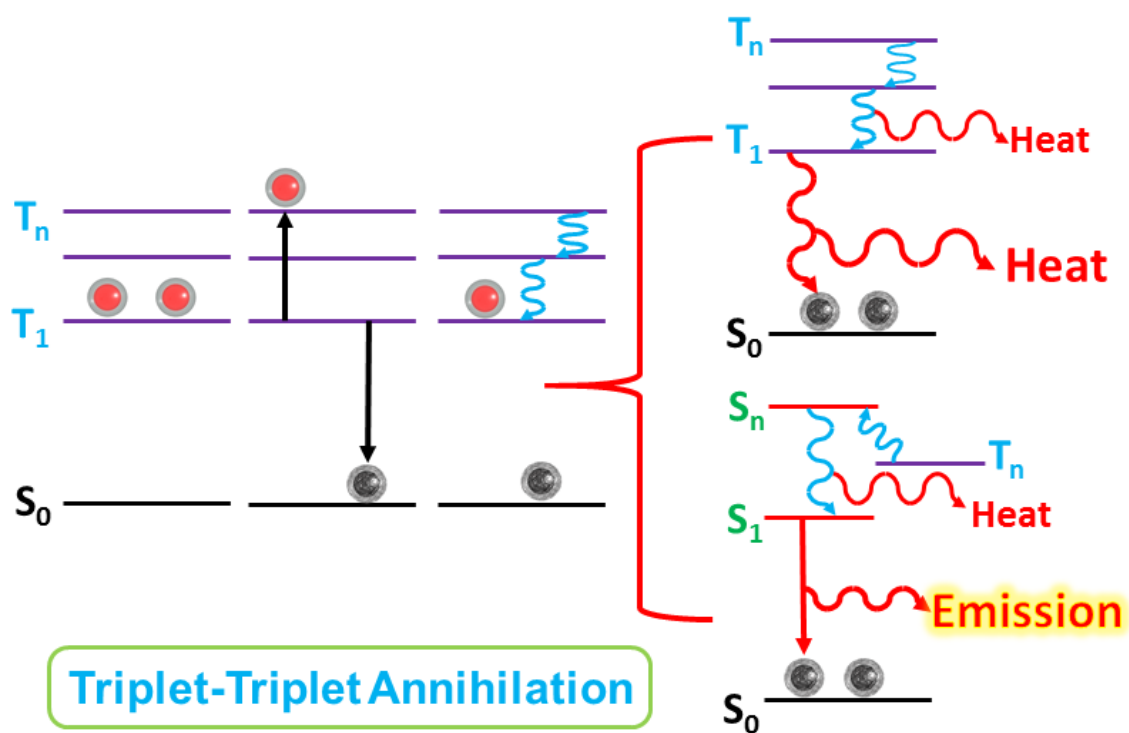
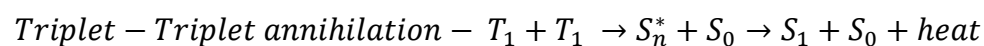
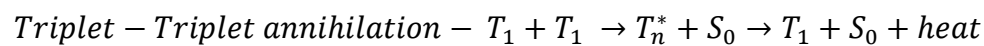
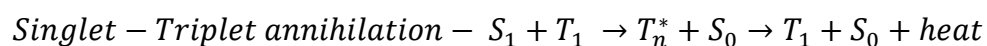
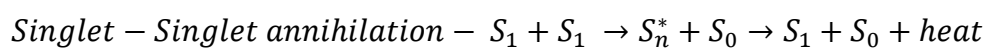


Fig. 1.10 Mechanism illustrating triplet-triplet annihilation

The mechanism involved in exciton energy transfer is provided below



1.4 LUMINESCENCE

Radiative de-excitation and non-radiative de-excitation are the two different possibilities of deactivation of excited state in an organic molecular system. Radiative de-excitation involves in emission of visible photons while the non-radiative de-excitation losses its energy in the form of vibration, rotation and translation of neighbouring molecules. Photoluminescence is a radiative process involving in absorption of higher energy photons by a molecule followed by the emission of photons of lower energy (Harris et al. 2008). Unlike conventional sources, luminescence is a mechanism not involved in light generation that are solely conditioned by the rise in temperature. Bioluminescence, cathodoluminescence, photoluminescence, radioluminescence, sonoluminescence, thermoluminescence, chemiluminescence, triboluminescence are a few different types of luminescence. The classification and type of luminescence is in accordance to their mode of excitation in a system. Fluorescence and phosphorescence are two major classifications of photoluminescence, classified purely based on their mode of excitation.

Fluorescence is spontaneous emission of visible radiation that lasts for few nanoseconds after photo-excitation. Photons of suitable energy when absorbed by a molecule experiences excitation in a system. Excited molecules then undergoes vibrational relaxation to arrive at the lowest vibrational level of the excited state. Relaxation from these excited states finally ends up in radiative decay via fluorescence. Phosphorescence is a phenomenon in which the materials that are phosphorescent in nature does not re-emit the absorbed photons immediately and there is a certain amount of delay observed in their emission behaviour. The delay in time is mainly associated with the energy emission from triplet energy levels that are quantum mechanically forbidden. Since, transitions occur from triplet energy states, the emission energy would be of lower intensity with longer duration of phosphorescence emission from the molecules. Phosphorescent lifetime of these energy transitions is of the order of 10^{-6} seconds to tens of seconds. Unlike fluorescence, phosphorescence is majorly realized at lower temperatures as the internal conversion and radiation less energy transfer overrule phosphorescence phenomena from triplet energy states.

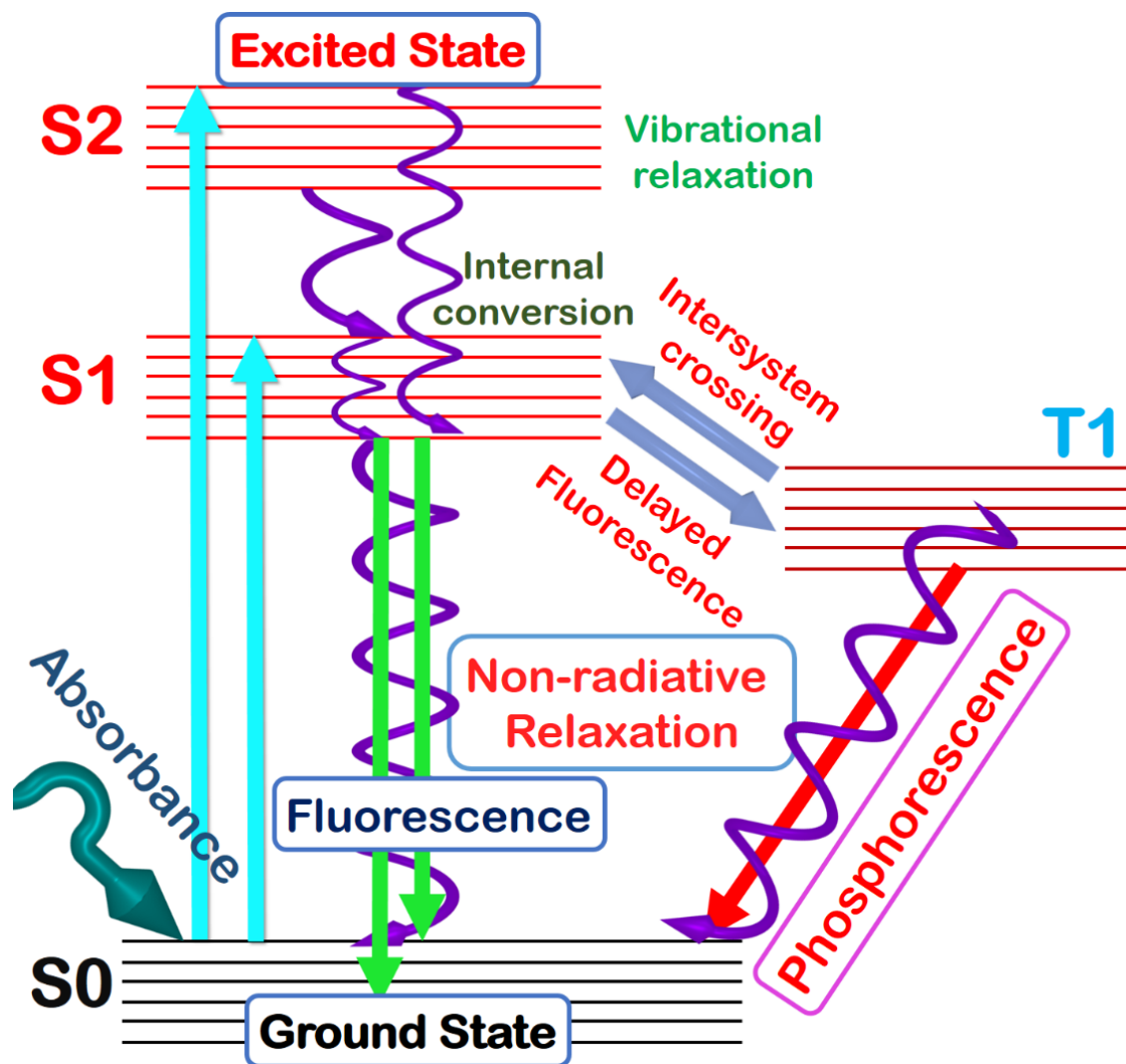


Fig. 1.11 Schematic representation of Jablonski diagram

Jablonski diagram as shown in the Fig. 1.11, provides a detailed mechanism supporting the fundamentals of electronic energy levels and electronic transitions in an organic material (Frackowiak 1988). The ground state of an organic molecule is its singlet ground state denoted as S0 corresponds to electronic ground state. Photoexcitation causes the system to achieve excited singlet state, wherein, S1 and S2 denotes the first and second excited states while T1 represents first excited triplet state. The process begins when a photon gets absorbed by a molecule which initially at the ground state gets excited to singlet state. Transitions from the topmost level of singlet excited state to the next immediate singlet level occurs at a time duration of 10^{-15} seconds. This process involves in vibrational energy loss and during the process the molecules starts to collide with the neighbouring molecules. Process continues as the molecules keep transiting from every vibrational level until it reaches the bottom of the singlet excited state, this process is also called as internal

conversion. Internal conversion from the top of singlet excited state to the bottom of the singlet excited state happens at a rate of 10^{-13} to 10^{-14} seconds. Following which the molecules come down to the lowest of the excited singlet state and either undergoes a radiative relaxation (fluorescence) or a non-radiative relaxation. Excited molecules at singlet state can also undergo intersystem crossing from singlet excited state to triplet excited state T1 at a rate of 10^{-10} to 10^{-8} seconds. Transition into triplet states is quantum mechanically forbidden but still their occurrence is highly perceived and inevitable. Relaxation from triplet excited state can then be either radiative transition termed as phosphorescence or a non-radiative relaxation. The rate of transition from excited triplet to singlet ground state occurs at a time duration of 10^{-3} to 100 seconds.

1.4.1 Spin orbit coupling (SOC)

Excitons are formed by columbic interaction between the negatively charged electrons and positively charged holes. Exciton confinement efficiently confines generated excitons to the emissive layer of OLED. Spin angular momentum of an electron at an unoccupied orbital can either be parallel or antiparallel with the occupied orbitals of the system. Antiparallel spin state would give rise to singlet excitons, whereas, parallel spin states would give rise to triplet excitons. Singlet excited state transitions are quite efficient and their excited state lifetime is of the order of few nanoseconds. Since longer time durations of 0.1 to 1 μ s are associated with intersystem crossing, the deactivation of excited triplet states undergo non-radiative emission. This leads to 75% of the excitons, namely the triplet excitons, are lost without radiative energy emission. However, 100% quantum yield in organic fluorescent molecules can also be achieved by preventing triplet intersystem crossing. This mechanism is achieved by designing fluorescent system to possess a faster singlet de-excitation decay time, thus avoiding intersystem crossing to a triplet state (Kalinin et al. 2001; Langhals et al. 1998). Electrical excitations in electroluminescent materials results in poorer radiative emission in comparison to their optical excitation. Unlike optical excitation, electrical excitation of a molecule is brought about by charge hopping mechanism that are not energetic enough to support electron-electron spin correlation in fluorescent material. This inefficiency limits the number of generated radiative singlet excitons in material to 25% while that of non-radiative triplet excitons to 75%. Device efficiency will enhance if those 75% of non-radiative triplet excitons are made radiative, and that is made possible by spin-orbit coupling of electrons.

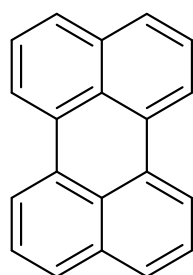
Spin-orbit coupling is an interaction existent between spin and orbit associated with the electron by the action of induced magnetic field. Pure organic molecules possess a very weak spin-orbit coupling. Weaker SOC of the system exhibits a small energy splitting between the singlet and triplet charge transfer states. Further, the longer time duration associated with the intersystem crossing from singlet to triplet states doesn't occur and system chooses to relax to the lower levels of excited state without spin flipping. However, such weaker interaction can be strengthened by incorporating heavy metal atoms like platinum, osmium, iridium and gold into the organic molecules. In principle, heavier atoms possessing enhanced magnetic field, influences an electron to achieve greater acceleration during its motion. Enhanced acceleration of electrons influenced by induced magnetic field changes the spin angular momentum of electron causing spin flip. Overall, a strong spin-orbit coupling of an electron in a system can influence radiative emission from triplet state by promoting significant intersystem crossing (Goushi et al. 2004; Sajoto et al. 2009). Researchers have reported phosphorescence mechanism on iridium doped organometallic complex and established phosphorescent lifetimes of the orders of microseconds (Baldo et al. 2000; Kalinowski et al. 2002). Since then various different organometallic complexes using heavy atoms were designed to completely harvest triplet excitons for radiative emission. In organometallic complexes, initially hole is trapped at the HOMO of emitter material and an electron is drawn subsequently toward the hole (Lamansky et al. 2001). Heavier atom present at its central core then induces significant coupling between spin and orbit of an electron, leading to an increased occurrence of intersystem crossing. Heavy metal complex are usually very efficient that at a suitable energy separation between the S1 and T1 states, an emission from a singlet excited state is highly quenched. SOC in principle can gather and convert all the singlet and triplet excitons formed by electron-hole pair into radiative emission. Yersin proposed a new electroluminescent mechanism wherein both the singlet and triplet excitons can be harvested for radiative emission (Yersin 2008). The phenomenon known as thermally activated delayed fluorescence, which can occur only if the energy gap between the triplet and the singlet state is lesser than 0.025 eV (Brown et al. 1972; Parker and Hatchard 1961). Spin orbit coupling favours ISC that in turn pushes the electrons from excited singlet to triplet states. Since, the energy gap between the singlet and excited triplet states are very small, the electrons are pumped back into the excited singlet state at room temperature. In summary, the acronym TADF harvest both the singlet

and triplet excitons, the triplet excitons generated undergoes reverse intersystem crossing and that introduces a minor time delay in fluorescence emission.

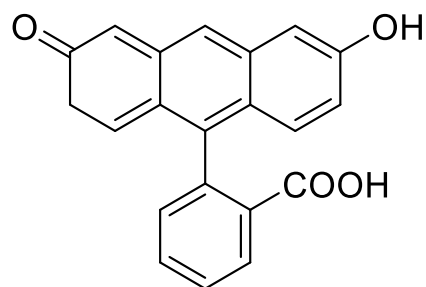
1.5 AGGREGATION INDUCED EMISSION (AIE)

Organic luminescent materials were extensively studied by researchers owing to their multitude of application in the field of light emitting diodes, fluorescence chemical sensors and fluorescence bio-imaging (Kwok et al. 2015). Organic fluorescent molecules generally tend to exhibit good emission in non-aggregated state and rather show a weaker emission upon aggregation. Luminophores exhibiting fluorescence emission quenching upon aggregation, the mechanism known as aggregation caused quenching (ACQ) has been documented for more than few couple of decades (Förster and Kasper 1954). Though organic molecules with ACQ characteristics have been employed for various practical applications, however, their full potential in solid state haven't been realized (Bünau 1970). Since their solid state emission is quite weak in comparison to the solution state, their practical applications are greatly restrained (Sensors 2006; Tang and VanSlyke 1987; Zhelev et al. 2006). However, the AIE phenomenon have revitalized the whole concept, wherein, the traditionally accepted AIE inactive materials can be made AIE active by mere structural modification. AIE has opened up new avenues to explore various numerous possibilities in practical applications (Ding et al. 2013; Kwok et al. 2015; Mei et al. 2014).

Weaker emission of organic luminescent materials in aggregated state limits their practical use in applications demanding solid state emission properties. Organic luminophores upon aggregation are in close vicinity with one another as they tend to stack in a tight molecular packing arrangement. The aromatic rings of nearby luminophores that resembles disc-like or rod-like shapes, experience intense intermolecular π - π stacking. This π - π stacking interactions in aggregates is highly responsible in governing the solid state quantum efficiency of the system (Mei et al. 2015). Excited state of luminophores possessing a smaller π - π stacking distance often relax back to ground state via non-radiative pathways, resulting in fluorescence emission quenching. Perylene and fluorescein are good examples for system supporting ACQ and their structure is presented in Fig. 1.12. Perylene in pure solvents e.g., tetrahydrofuran (THF), exhibits strong fluorescence, and with gradual increase in ratio of poor solvent via 10%, 20% and so on, the emission is quenched as illustrated in Fig. 1.13. The structural planarity possessed by polycyclic aromatic perylene when aggregated involves in smaller intermolecular π - π stacking, results in ACQ.



Perylene



Fluorescein

Fig. 1.12 Examples of planar type ACQ molecules

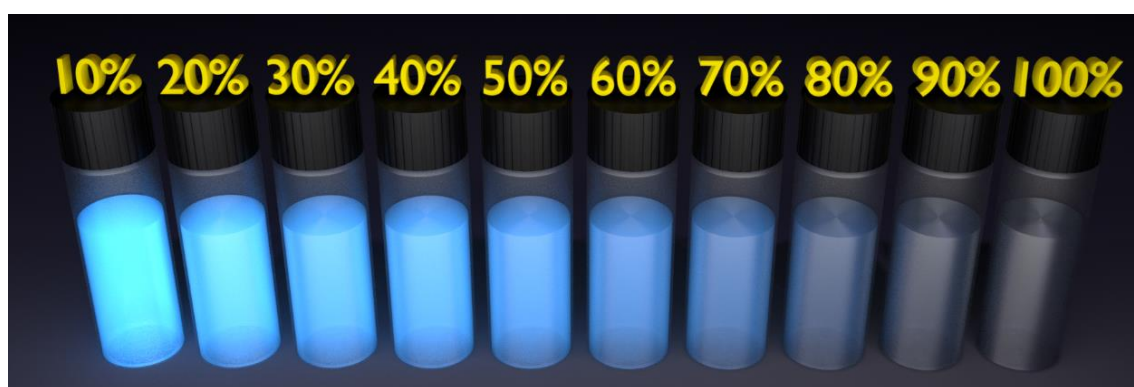


Fig. 1.13 Fluorescence of solutions with increasing water fractions exhibiting ACQ effect

In contrast to ACQ, aggregation induced emission materials are the one whose emission is enhanced upon aggregation in comparison with that of non-aggregated state (Luo et al. 2001; Tang et al. 2001). AIE emitters are highly desired and intensive research is being carried out to design and synthesize new materials for solid state device application (Hong et al. 2009; Hu et al. 2009). Few of the well-known AIE luminogen is provided in Fig. 1.14 and their emission behaviour with varying water fraction is provided in Fig. 1.15. Tertraphenyl ethylene (TPE) for example possesses a central core olefin stator surrounded by four peripheral phenyl rings or the aromatic rotors (Wang et al. 2010; Zhao et al. 2012b). The non-aggregated TPE in dilute solvent does not show any emission. The intramolecular rotations of the phenyl rings against the olefin, deactivate the exciton energy non-radiatively in the form of rotational and vibrational motion. Owing to intense π - π stacking upon aggregation, intramolecular rotation of the phenyl rings is restricted. Restriction of rotation of phenyl rings in TPE utilizes the deactivation energy into enhanced radiative emission upon aggregation.

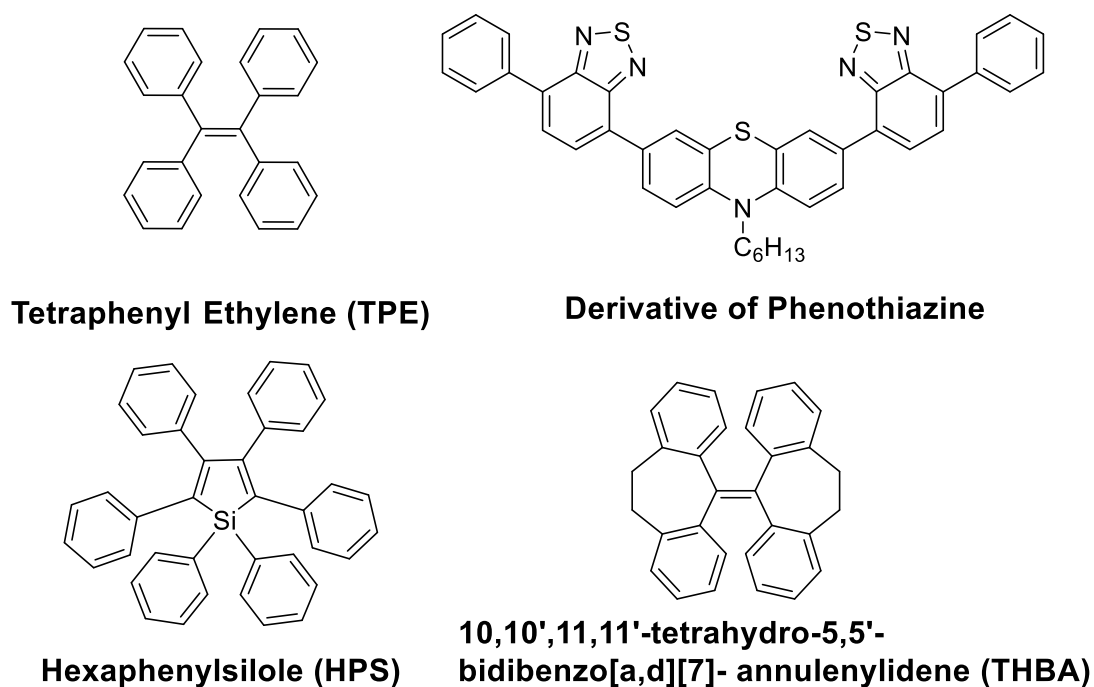


Fig. 1.14 Few of the most prominent AIEgens

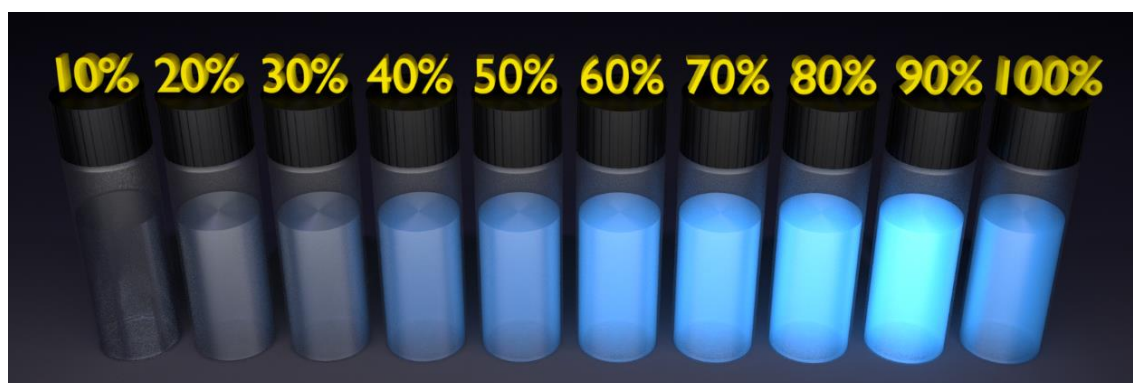


Fig. 1.15 Fluorescence of solutions with increasing water fractions exhibiting AIE effect

Since the discovery of AIE chromophores, researchers have shown interest in developing concepts that support some of the fundamentals of AIE in a system. Formation of J-aggregates, E/Z isomerization, twisted intramolecular charge transfer (TICT), conformational planarization and ESIPT are few of the theories hypothesized that support the AIE mechanism. These hypotheses only provide theoretical understanding of aggregated emission and cannot be realized by experimental techniques. However, three main hypotheses have been validated both by theoretical and experimental works to provide proof for AIE mechanism. The three main mechanisms for AIE are illustrated in the Fig. 1.16.

1.5.1 Restriction of intramolecular rotation (RIR)

Restriction of intramolecular rotation was proposed based on systematic study of hexaphenylsilole (HPS) (Chen et al. 2003; ZhongáTang 2008), wherein the highly flexible phenyl rings that are attached to the central silole moiety can freely rotate around the central core. Crystal structure reported for HPS confirms the existence of good amount of torsion present between the central core and the peripheral phenyl rings. Results from XRD further reveals HPS possessing a large amount of intermolecular π - π stacking between the adjacent molecule (Chen et al. 2003). In diluted state, these phenyl rings deactivate the energy of excited state via non-radiative means by rotation of phenyl rings around silole group. Aggregation of HPS restricts these rotation, hindering all the non-radiative relaxation pathway leading to enhanced emission in the solid state (Ren et al. 2005).

1.5.2 Restriction of intramolecular vibration (RIV)

Restriction of intramolecular vibration was hypothesized based on AIE luminogen 10,10',11,11'-tetrahydro-5,5'-bidibenzo[a,d][7]-annulenylidene (THBA) (Leung et al. 2014; Mei et al. 2014), wherein, the rotation of the phenyl rings are locked by a pair of ethylene tethers. In HPS, the rotating phenyl rings around the core, relaxes the excited state by non-radiative pathways, in a similar manner relaxation of excited state can also occur by vibrational motion. Experimental evidences on THBA validate the exciton energy consumption is due to the vibrational motion of attached phenyl rings. Analysis of the vibrational modes on THBA molecule clearly highlights the reduction in intensity of vibrational modes for a clustered THBA in comparison with that of isolated THBA molecule.

1.5.3 Restriction of intramolecular motion (RIM)

Restriction of intramolecular rotation and vibration in a system would undoubtedly help system achieve enhanced emission in aggregated state (Kamaldeep et al. 2014; Liu et al. 2013; Yao et al. 2014). This particular aspect is realized on a system that contain a vibrating core and a rotating peripheral ring. The derivative of phenothiazine follows this mechanism, wherein, the system possesses a non-planar molecular configuration with rotating peripheral rings (Banal et al. 2014; Liu et al. 2013; Mei et al. 2015). Isolated phenothiazine is non-luminescent in solution but emits bright red fluorescence in solvent-poor-solvent mixture at a volumetric ratio of 70% establishing AIE phenomena.

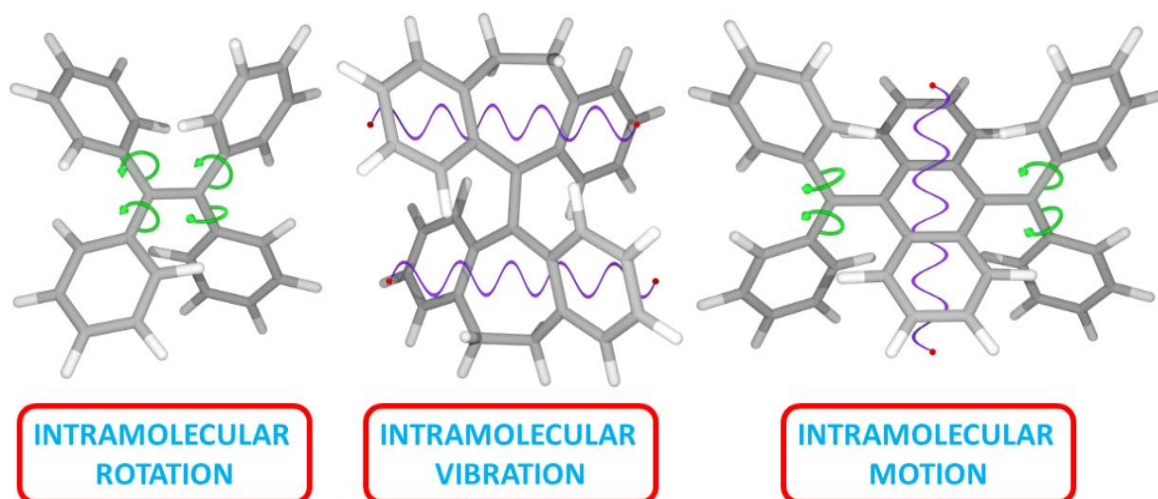


Fig. 1.16 Illustration of intramolecular rotation, vibration and motion

Overall, restrictions of intramolecular rotation, vibration and motion would surely block all the non-radiative deactivation pathway and help the system to exhibit an enhanced emission upon aggregation.

1.6 EXCITED STATE INTRAMOLECULAR PROTON TRANSFER (ESIPT)

Organic chromophores that exhibit a phenomenon of excited state intramolecular proton transfer (ESIPT), have gathered immense attention amongst researchers in recent years. ESIPT is a four-level photochemical process in which the original excited system produces a tautomer system with a different electronic structure (Gao et al. 2010; Hsieh et al. 2010; Wu et al. 2011; Zhao et al. 2012a). Organic molecules that readily form intramolecular hydrogen bonding with the neighbouring species are highly attractive for novel optoelectronic applications (Padalkar and Seki 2015). The pre-requisite of ESIPT in a system is the presence of proton donor moiety ($-OH$ or $-NH$) and a proton acceptor moiety ($=N-$ and $-C=O$) linked by intramolecular hydrogen bonding between them. Photoexcitation of the molecule causes the proton to translocate from a proton donor to a proton acceptor species via a pre-linked hydrogen bonding (Zhao et al. 2012a). The whole process is illustrated in the Fig. 1.17, wherein, the normal form of the molecule (N) at ground state gets excited to (N^*) upon photoexcitation. At this point the proton is ready to translocate from a donor to acceptor in a time span of femtoseconds. The transferred proton alters the N^* geometry to a tautomer T^* form, which then relaxes to T ground state and back to normal form via ground state intramolecular proton transfer (GSIPT), realizing a four-level photo-cyclic process ($N \rightarrow N^* \rightarrow T^* \rightarrow T \rightarrow N$) (Padalkar and Seki 2015). Large

Stokes shift is achieved for ESIPT chromophores wherein the tautomer emission is highly red shifted with respect to normal absorption. Dual fluorescence emission is uniqueness of ESIPT chromophores as there is an emission from normal form (N^*) as well as the tautomer form (T^*) (Mutai et al. 2008). ESIPT molecules find its applications in designing fluorescence sensors, UV filters, and aggregation-induced emissive materials (Arnaut and Formosinho 1993; Barbara et al. 1980, 1989; Douhal et al. 1996; Hsieh et al. 2010; Kwon and Park 2011). Researchers were successful in generating white light emission from a single molecule gelator by careful control and tuning of normal and tautomer emission (Maity et al. 2015).

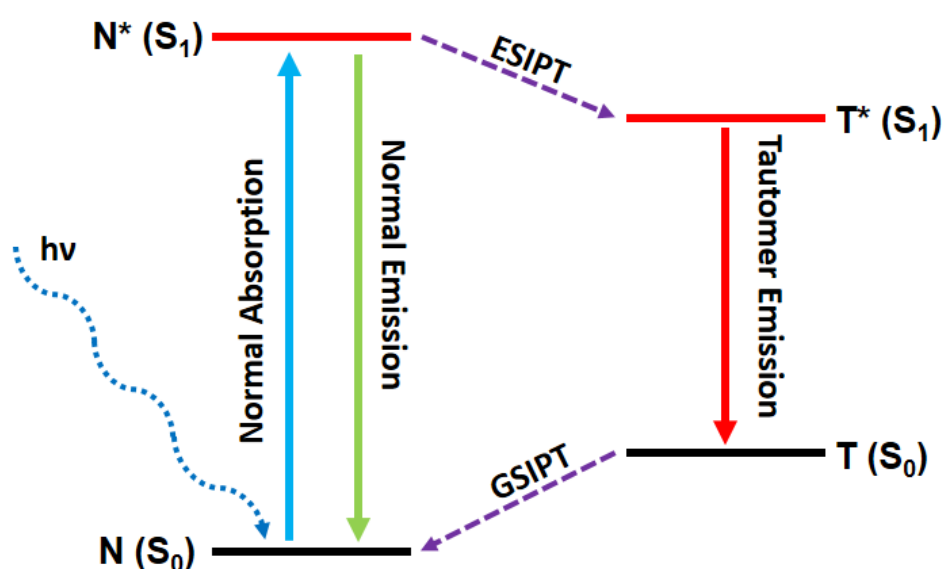


Fig. 1.17 Four level photo-cyclic process of ESIPT

Excited state proton transfer phenomenon was first observed by Waller in 1950s for salicylic acid. This observation led researchers to explore deep into some of the fundamental concepts of proton transfer dynamics, time-resolved ESIPT fluorophores, kinetics and thermodynamics at the singlet state, pico-second kinetics and vibronically resolved spectroscopy. The remarkable properties of ESIPT fluorophores are the existence of large Stokes shift (~ 200 nm), an ultrafast proton transfer process, dual emission peak and high amount of spectral sensitivity to the surrounding medium. Proton transfer at the excited state involves in generation of various transition structure and hence their spectral response is highly affected by microenvironmental changes. Spectral properties of the system is highly dependent on the nature of hydrogen bonding, rotamerisation process, acidity or

basicity of the surrounding medium and on the substituents present on donor and acceptor groups.

Some of the most promising ESIPT fluorophores are the derivatives of 2-(2'-hydroxyphenyl) benzimidazole (HBI) (Benelhadj et al. 2013; Furukawa et al. 2012), 2-(2'-hydroxyphenyl) benzoxazole (HBO) (Padalkar et al. 2012, 2014) and 2-(2'-hydroxyphenyl) benzothiazole (HBT) (Cheng et al. 2015; Padalkar et al. 2012; Patil et al. 2013). Further, the derivatives of benzophenone (Ignasiak et al. 2015), flavones (Ghosh et al. 2015; Jin et al. 2015), hydroxyquinolones (Padalkar et al. 2014), quinoxalines (Nakane et al. 2015), anthraquinones (Schmidtke et al. 2004), benzotriazoles (Paterson et al. 2004), thiodiazoles (Oliveira et al. 2010), salicylidene aniline (Hadjoudis and Mavridis 2004), benzazoles (Iijima et al. 2010), chromones (Das et al. 2014), coumarins (Barman et al. 2015; Xiao et al. 2014) and naphthalimides (Ma et al. 2012; Wilbraham et al. 2014) have been well reported for ESIPT. Most of the reported fluorophores are highly emissive in solution state and tend to show a weaker emission in solid state. Aggregation induced enhanced emitters are highly desired for solid state optoelectronic applications. Large number of ESIPT chromophores that have been designed show good emission in solution state, however, very few reports are available on ESIPT chromophores that exhibit solid state emission. Solid state emission in organic chromophore is achieved by suppressing all the non-radiative deactivation pathways. Aggregation induced emission, aggregation induced emission enhancement, precise control over molecular packing arrangement and restriction of intramolecular rotation are few techniques employed to achieve solid state emission in ESIPT system (Douvali et al. 2015; Hong et al. 2011; Li et al. 2015; Zhou et al. 2009).

Solid state ESIPT chromophores are highly preferred over the solution state and there are numerous shortcomings that needs to be addressed when designing a solid state ESIPT system. Hydrogen bonding plays a crucial role in governing proton transfer process in a system, as the hydrogen bonding is capable of forming a cyclization of five or six membered ring that highly alters the property of ESIPT chromophore (Hsieh et al. 2010; Kwon and Park 2011; Wu et al. 2011). In polar solvents, in addition to intramolecular hydrogen bonding, intermolecular hydrogen bonding with solvent molecules is likely to occur (Cheng et al. 2015). This intermolecular hydrogen bonding between the solute and solvent molecules further suppresses tautomeric emission in the system (Kasha 1986). However, in solid state, ESIPT process is undisturbed and thus enhances tautomeric

emission in the system. Restriction of intramolecular rotation (RIR) nullifies all the non-radiative deactivation pathways, thus leading to an enhanced emission in solid state (Kwon and Park 2011). Careful design of system that restricts intramolecular rotation upon aggregation would surely exhibit higher efficiency in solid state. RIR in ESIPT system would help the system attain a favorable geometry that would further support ESIPT and AIEE. ESIPT system that possess a cis-conformation, upon photoexcitation may turn to trans-conformation breaking the intramolecular hydrogen bonding in solution state. However, such cis-trans conformal changes are restricted in tight molecular packing in solid state (Cai et al. 2012; Ikegami and Arai 2002). Aggregation effect on the efficiency of ESIPT is highly crucial, wherein, J-aggregates (slip stacking arrangement) are highly preferred over H-aggregates (face to face arrangement) (Qian et al. 2007; Wu et al. 2015). The packing arrangement totally depend on the nature of the groups present in the system, and thus, results prove that structure possessing bulky group and good amount of steric hindrance would surely form J-aggregates enhancing AIEE of ESIPT (Kwon and Park 2011). ESIPT is a four-level photo-cyclic process and thus the structural stability of tautomer depends on torsion between the proton donor and proton acceptors rings. In solution state, the torsional motion between the proton donor and proton acceptor brings down the tautomer emission through vibrational relaxation (Shigemitsu et al. 2012; Wu et al. 2012). However, in most of the reported literatures, the torsion between the proton donor and proton acceptor ring is coplanar leading to an enhanced fluorescence emission in solid state (Shigemitsu et al. 2014).

1.7 ORGANIC LIGHT EMITTING DIODES

Organic light emitting diodes that makes use of electroluminescent materials, are of two types, small molecule organic light emitting diodes (SM-OLED) and polymer light emitting diodes (PLED). In small molecule based LED, the electroluminescent active material used is of organic small molecules, whereas, in PLED it is an organic polymer. The basic electroluminescent working principle of these two types is quite similar, however, the difference is in the techniques involved in device processing and device fabrication. Generally, SM-OLEDs are fabricated using physical thermal vapour deposition technique under high vacuum conditions, whereas, wet processing or solution processing techniques are employed for PLED fabrication under inert conditions. Fabrication

techniques used for small organic molecule based devices provide access for stacking multiple layers with good control over layer engineering in comparison with PLEDs.

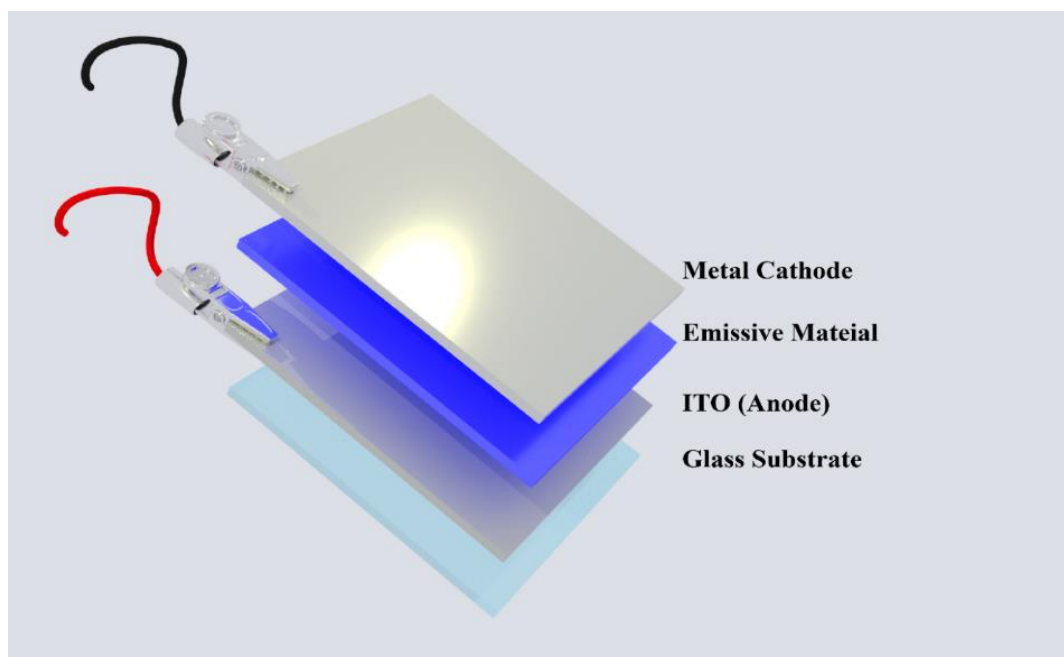


Fig. 1.18 Generic structure of an OLED

A generic structure of OLED with an emissive material sandwiched between anode and cathode is as shown in the Fig. 1.18. Light emission from these active organic materials is by electron-hole recombination injected at the respective electrodes. OLEDs can be categorized based on the emission at a surface and hence can be of top-emitting, bottom-emitting or a transparent-type. OLEDs demand at least one of the electrodes must be transparent for the photons to escape from the device, this is true for both top-emitting and the bottom emitting type devices. However, transparent type emitting OLEDs have both of their anode and cathode material transparent and such configurations allow light emission from both the sides of their electrodes. Indium tin oxide coated glass substrate is optically transparent allowing the emitted photons to escape out of device and hence generally used as anode material in OLEDs. Cathode layer is formed by a metal of good conductivity with high values of optical reflectivity. Organic electroluminescent material that forms the active part of OLEDs is usually deposited with a thickness ranging between 50~150 nm. When a potential is applied across the device, holes from anode and electron from cathode get injected into the adjacent layers. Injected charges further move into organic emitter material and recombine to form an exciton. Exciton recombination window is defined by the charge

mobility of an organic material and the electric field distribution across the device. Excitons formed at the active layer further diffuses to undergo radiative emission and the mechanism is as shown in the Fig. 1.19. Emission wavelength of an OLED is a function of energy difference between the HOMO and LUMO energy levels of an organic electroluminescent material. Precise control over the conjugation length in a molecular network can efficiently tune the bandgap of an organic system.

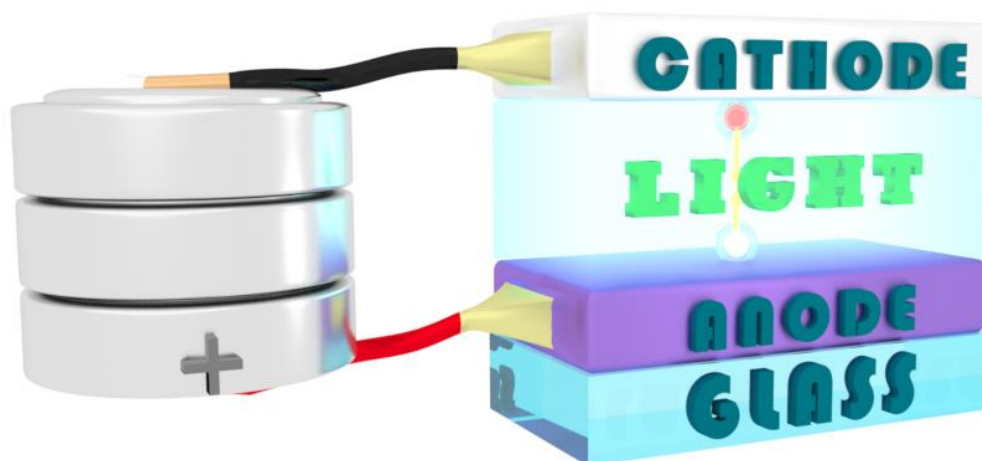


Fig. 1.19 A generic working mechanism of single layer OLED device

OLEDs functioning solely on single layer organic material for light emission suffer from poor device performance, and hence, different layers are introduced to enhance the overall device efficiency. In a two layered device, electron transport layer (ETL) and hole transport layer (HTL) are sandwiched between the anode and cathode electrodes as shown in the Fig. 1.20. Electrons are injected from the cathode into the LUMO of the ETL and holes are injected from anode into HOMO of the HTL, and recombination of holes and electrons generates radiative excitons. The three-layered OLED is formed by a combination of organic emitter material sandwiched between ETL, HTL and electrodes. When a potential is applied, anode is relatively at a higher electrical potential with respect to the cathode. This electric potential gradient at the anode-organic interface drives the holes into HOMO of HTL and electrons are injected from cathode to LUMO of ETL. Localization of few of the holes and electrons on a single emissive material recombine to form an exciton. Some of these excitons further decay spontaneously to ground state via radiative relaxation or via non-radiative relaxation.

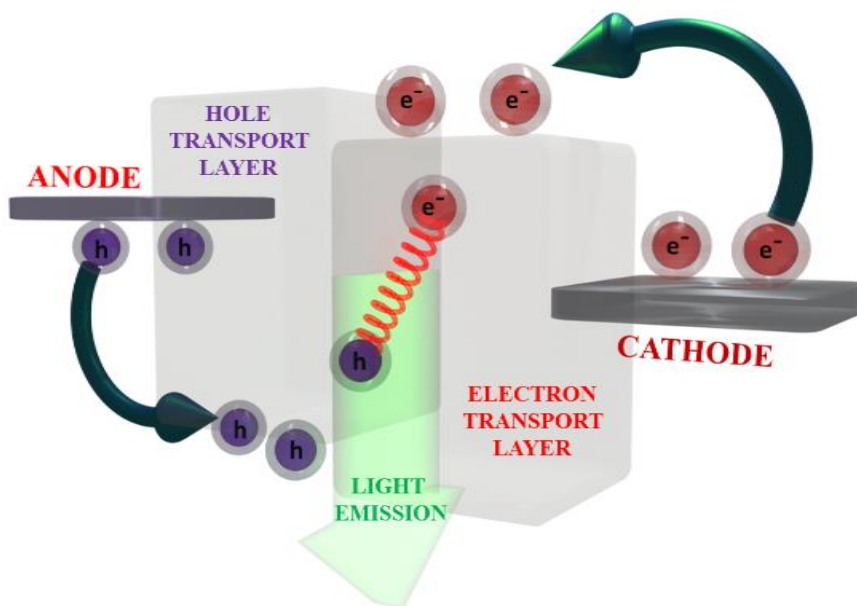


Fig. 1.20 Working mechanism of double layer OLED device

Two layered and three layered devices suffer from charges diffusing through the organic materials and reaching the other side of the electrodes. Such discrepancies are overcome by introducing organic layers that blocks the charges reaching the other side of the electrodes. Accordingly hole blocking layer (HBL) and electron blocking layer (EBL) are introduced in multi-layered device architecture. Further, in order to enhance and boost the charges being injected to the electrodes, electron injection layer (EIL) and hole injection layer (HIL) is also introduced. Overall, a multi-layered device architecture consists of HIL, HTL, HBL, and an organic emissive material, EBL, ETL and EIL as shown in the Fig. 1.21. Researchers have strived to improve the OLED device performance by adopting various different layers into device architecture (Ohmori et al. 1993; So and Forrest 1991). Fabrication of a multi-layered OLED can be achieved by either solution processing technique or by physical vapour deposition technique. One of the main advantages of a multi-layered architecture is that the carrier confinement within the organic emissive material is intense and this improves the chances of generation of radiative excitons. Understanding of basic functioning of these different layers in a multi-layered architecture is highly necessary to extract maximum efficiency out of a device. In general, ITO anode and aluminium cathode injects hole and electrons respectively into the adjacent layer. Hole injection layer injects the hole received from anode into hole transporting layer. Hole transport layer then transfers the hole into the HOMO of emissive material. Electron injection material on the other hand helps in better injection of electrons from the cathode,

while electron transport layer transport electrons to LUMO of the emissive material. Hole blocking and electron blocking layers assist in confining the charges within the emissive material, that has reached the emissive layer via hopping. Further, HBL and EBL introduced in the device architecture will help to minimize ohmic losses arising due to the imbalance in the hole and electron current across the emissive layer (Huang et al. 2002; Qiu et al. 2002). Negating such discrepancies in a well-designed architecture would drastically improve the OLED device efficiency. However, adding up of such additional layers would evidently build-up huge charge densities at organic interfaces, overall affecting the device lifetime (Yu et al. 2015). Additionally, a very thin layer of lithium fluoride (LiF) or cesium fluoride (CsF) is introduced that eases the electron injection process from the cathode to the electron injection material. LiF and CsF further prevents the metallic cathode undergoing chemical reactions with the organic ETL material (Priyat and Plais 2001).

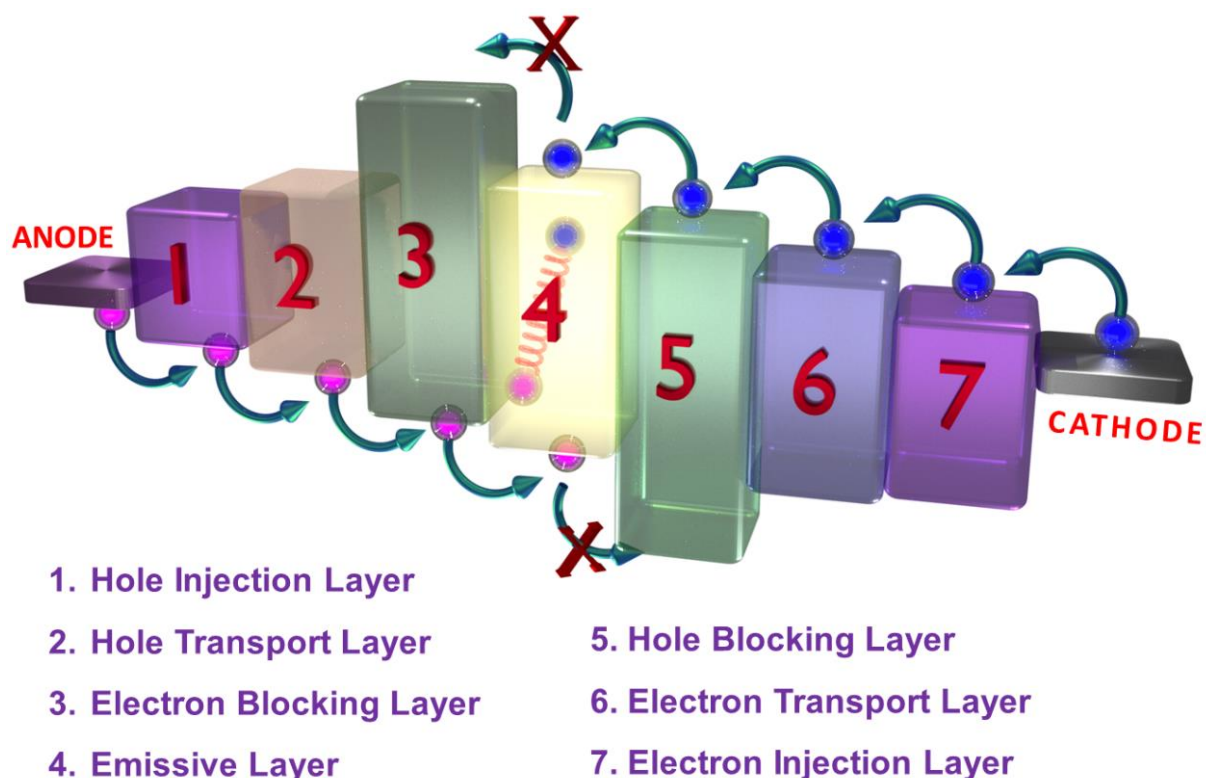


Fig. 1.21 Scheme of the electroluminescence mechanism in an OLED

1.7.1 OLED Efficiency

Efficiency of an organic light emitting diodes is defined by external quantum efficiency (EQE). EQE is defined as the number of photons that is generated out of the device surface to the number of charges injected from the source.

$$\text{EQE \%} = \frac{N_p}{N_e} \times 100$$

where, N_p – Number of photons emitted out of device surface

N_e – Number of charges injected into the OLED device

External quantum efficiency (η_{ext}) is also defined as

$$\eta_{\text{ext}} = (\gamma) \cdot (\eta_r) \cdot (\eta_{\text{PL}}) \cdot (\eta_{\text{out}})$$

where, γ is the charge injection efficiency, η_r is the internal quantum efficiency, η_{PL} is the solid-state quantum yield of the emitter material and η_{out} is the device out-coupling efficiency.

1.7.1.1 Injection efficiency (γ)

Injection efficiency refers to the charge balance factor (Geffroy et al. 2006; Kafafi 2018). It is a ratio of exciton recombination relative to the number of charge carriers injected into the device from the electrodes. An injection efficiency value closer to 1 can be achieved for a well optimized device architecture (Adachi et al. 2001). Charge balance in a device strongly depends on current density across the device. Lighting applications demands higher brightness in OLEDs and this in turn depends on higher current densities in devices. Higher current densities generate large number of excitons approaching a value of injection efficiency closer to 1 (Giebink and Forrest 2008; Reineke et al. 2007). The main disadvantage would be that the materials degrade faster due to constant exposure to higher current densities. Thus, injection efficiency is the ratio of number of charges that recombine to the number of charges injected into the device as provided in the equation.

$$\text{Injection efficiency} = \frac{\text{Number of charges recombine}}{\text{Number of charges injected into the device}}$$

1.7.1.2 Internal quantum efficiency (IQE) η_r

Internal quantum efficiency (IQE) is the amount of luminescent exciton recombination to the total number of exciton recombined within the device. Organic luminescent material that are purely fluorescent, a maximum internal quantum efficiency of value $\eta_r = 0.25$ is achievable, whereas, materials that harvest both singlet and triplet excitons should reach a value of $\eta_r = 1$. In general, IQE is the ratio of radiative excitons to the total number of excitons recombined as given below.

$$\text{IQE} = \frac{\text{Number of excitons radiatively recombined}}{\text{Total number of excitons recombined}}$$

1.7.1.3 Quantum yield η_{PL}

Quantum yield is a measure of number of photons emitted from an organic luminescent material to the number of photons absorbed by that material.

$$\text{Quantum yield} = \frac{\text{Number of photons emitted by a system}}{\text{Total number of photons absorbed by it}}$$

$$\text{Quantum yield} = \frac{k^r}{k^r + k^{nr}}$$

Where, k_r is radiative rate constant, while k_{nr} is a non-radiative rate constant.

1.7.1.4 Out coupling efficiency η_{out}

In a generic OLED device, a simple planar glass is used as a substrate material. These materials act like photon reflectors and hence most of the generated photons at the active layer are guided back to the material. Surface plasmon losses at the metal organic interface may also affect the out-coupling efficiency of the device. Practical outcoupling efficiencies are too low ($\eta_{\text{out}} < 20\%$), hence the OLEDs still suffer to function as conventional light sources.

Out-coupling efficiency is generally defined as the ratio of number of photons collected at the surface of a device to the total number of photons generated within the device.

$$\text{Out coupling efficiency} = \frac{\text{Number of photons coming out of the device}}{\text{Number of photons generated within the device}}$$

The whole process indicating the efficiency of the device is illustrated in the Fig. 1.22

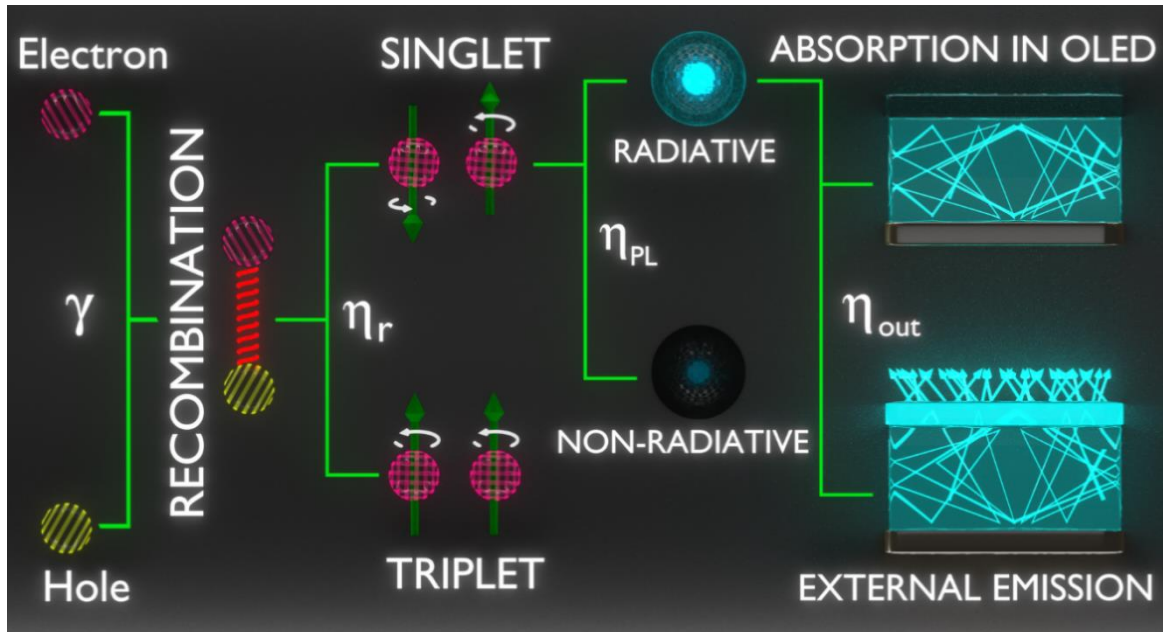
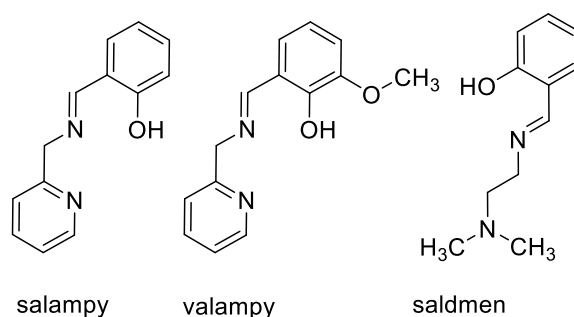


Fig. 1.22 Flowchart illustrating overall device efficiency of an OLED

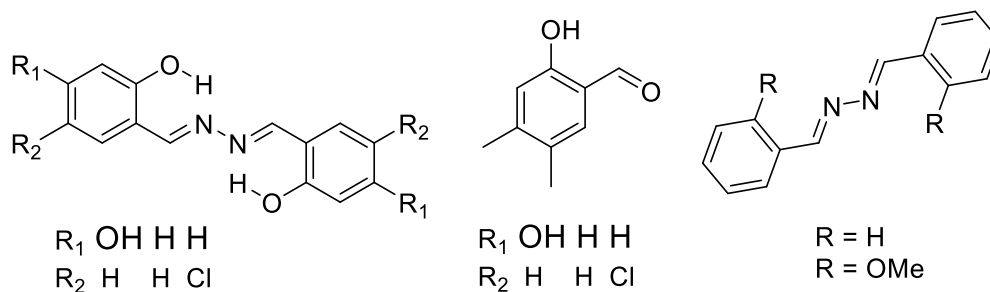
1.8 LITERATURE REVIEW

Maxim and co-workers (2008) have synthesized Schiff base copper (II) and zinc(II) complexes (S1.1) N- [(2-pyridyl)-methyl]-salicylimine (Hsalampy), N-[2-(N,N-dimethyl-amino)-ethyl]-salicylimine (Hsaldmen), and N-[(2-pyridyl)-methyl]-3-methoxy-salicylimine (Hvalampy). Four new coordination compounds $[\text{Cu}(\text{salampy})(\text{H}_2\text{O})(\text{ClO}_4)]_1$, $[\text{Cu}_2(\text{salampy})_2(\text{H}_2\text{trim})_2]_2$ (H_2trim^- = the mono-anion of the trimesic acid), $[\text{Cu}_4(\text{valampy})_4](\text{ClO}_4)_4 \cdot 2\text{CH}_3\text{CN}_3$, and $[\text{Zn}_3(\text{saldmen})_3(\text{OH})](\text{ClO}_4)_{2-0.25}\text{H}_2\text{O}_4$ that were synthesized and structurally characterized. Compound 4 exhibits a solid-state photoluminescence at room temperature.



S1.1

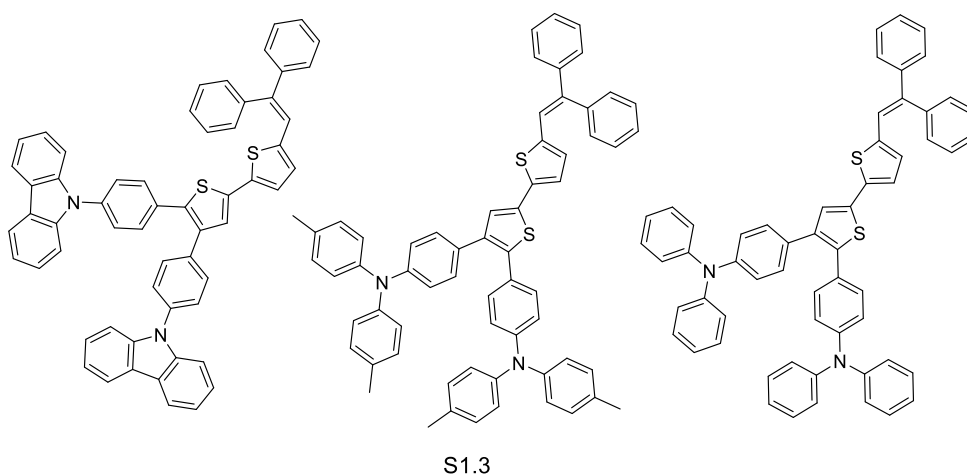
Tang and co-workers (2009) have reported a series of salicylaldehyde azine derivatives (S1.2) exhibiting interesting aggregation-induced emission enhancement (AIEE) characteristics. All these compounds displayed very weak fluorescence in good solvents, while strong emission was observed when they were placed in poor solvent. Moreover, the aggregation induced emission enhancement colour of these compounds varied from green to red depending on the substituents on azines.



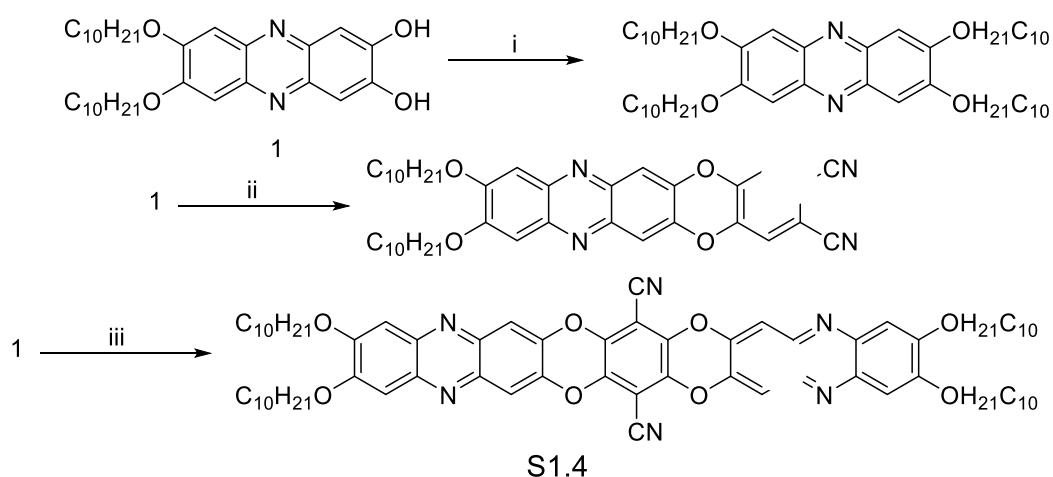
S1.2

Song and co-workers (2013) have designed and synthesized a series of green dopants for organic light emitting device applications based on arylamine 2,3-disubstituted bithiophene derivatives (S1.3) by Suzuki and witting coupling reactions.

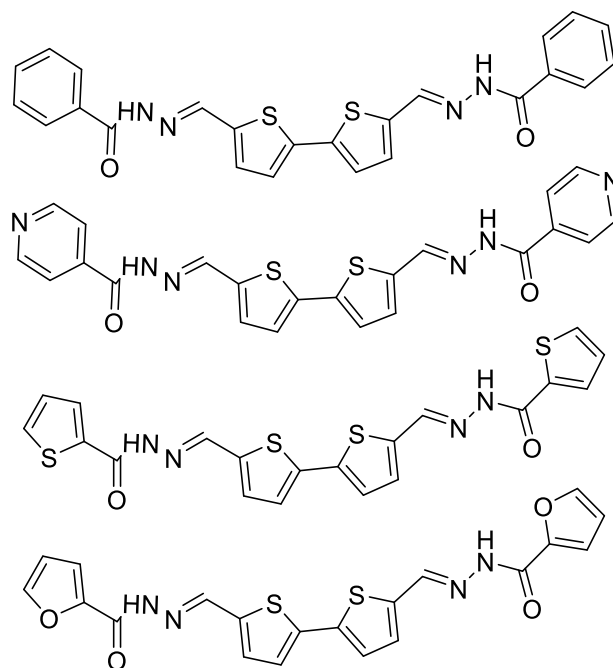
Photoluminescence reports reveal that molecule with 9-phenylcarbazole moiety exhibited a highest quantum yield among the series and thus has been chosen for OLED device application. The device exhibited a yellowish green emission with a maximum brightness and luminous efficiency of 5,100 cd/m² and 2.56 cd/A with colour co-ordinates of CIE (0.42, 0.54).



Gu and co-workers (2015) have synthesized three novel phenazine derivatives (2,3,7,8-tetrakis(decyloxy)phenazine, 2,3-didecyloxy-5,14-diaza-7,12-dioxo-9,10-dicyanopentacene and 2,3,13,14-tetradecyloxy-5,11,16,22-tetraaza-7,9,18,20-tetraoxo-8,19-dicyanoenneacene (S1.4) realizing the importance of controlled emission colours of single molecules in the development of full-colour emitting materials. Compound emit blue light in toluene solution (450 nm), green light in the powder/film state (502/562 nm), and red light in the TFA state (610 nm). The OLED with compound as an emitter material emits a strong green light at a peak of 536 nm with a maximum luminance of about 8600 cd m⁻² finding its potential as emitters in OLEDs.



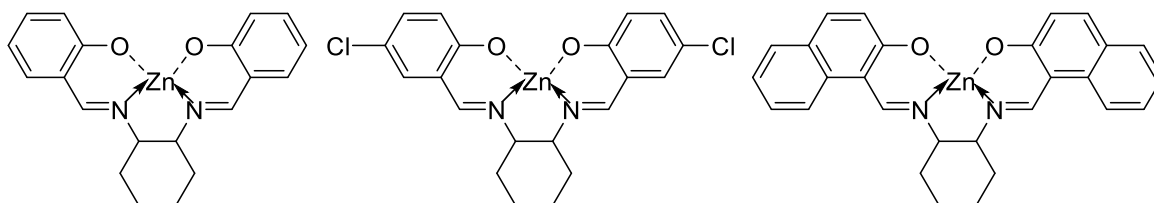
Jarczyk-Jedryka and co-workers (2016) have synthesized four symmetrical N-acylsubstituted dihydrazones containing bithiophene core by condensation of 2,2'-bithiophene-5,5'-dicarboxylaldehyde with benzoic, isonicotinoyl, 2-thiophenic and 2-furoic hydrazide (S1.5). The compounds were characterized by various standard spectroscopic techniques such as $^1\text{H-NMR}$, IR and elemental analysis. UV-Vis spectroscopy and photoluminescence spectroscopy were carried out in order to study their photophysical response. The molecules exhibited an emission wavelength in the range of 499 - 530 nm in solution and blue emission in blend with PMMA. DFT studies were carried out to estimate the electronic orbitals supporting the electronic transitions in the system. Further, these selected compounds were tested preliminary as component of active layer in organic photovoltaic cells. The highest value of power conversion efficiency equals to 1.68% under simulated 100 mW/cm^2 for device architecture of ITO/PEDOT:PSS/P3HT:PCBM:FBTH (1:2:2)/Al.



S1.5

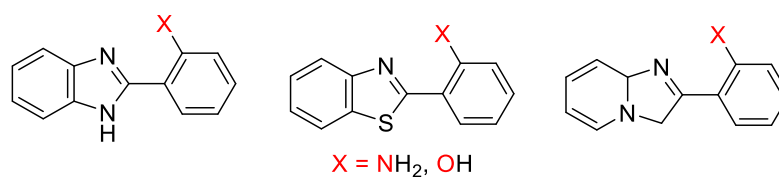
Srinivas and co-workers (2017) have synthesized various azomethine-zinc (II) complexes (S1.6) of bis(salicylidene)cyclohexyl-1,2-diamino organic ligands by one pot reaction of salicylaldehydes/2-hydroxy-1-naphthaldehyde, cyclohexyl-1,2-diamine and zinc acetate. Their photophysical properties such as Photoluminescence (PL) and Diffused Reflectance Spectra (DRS) were studied. PL studies revealed that the emission peaks of the

complexes in both solution and solid states appeared to occur at 395 - 600 nm. The band gap energies determined from DRS were 2.98 eV, 2.91 eV, and 2.73 eV. These complexes can serve as a suitable non-dopant blue light emitting compound for flat panel display applications.



S1.6

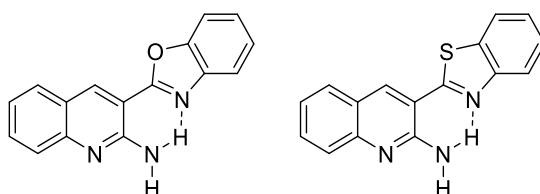
Kanlayakan and co-workers (2017) investigated the effect of proton donors on the excited state intramolecular proton transfer of hydrogen bonding using DFT and TDDFT on system (S1.7). ESIPT process is strongly dependent on the reaction and activation energy, and thus the system that are thermodynamically stable and kinetically labile would in turn support ESIPT. The results involving bond parameters and stronger red-shift in the vibrational spectra clearly establishes the stronger nature of O-H to donate proton in comparison with N-H donors. Potential energy surface studies show that the proton transfer occurring in O-H type possesses a small proton transfer barrier in comparison with that of N-H type of donors. Proton transfer time were also simulated for all the system using on-the-fly dynamic simulations for the first excited state. The results of proton transfer time reveals the O-H proton donor type to support faster proton transfer of 80 fs in comparison with N-H type.



S1.7

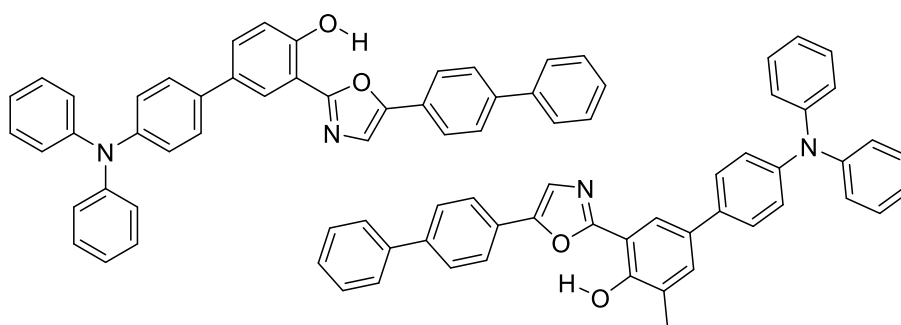
Khimich and co-workers (2017) have designed and synthesized 2-amino-3-(2'-benzoxazolyl)-quinoline (ABO) and 2-amino-3-(2'-benzothiazolyl)-quinoline (ABT) (S1.8) that support proton transfer at the excited state. Fluorescence spectra of the system exhibited dual emission bands arising from normal and tautomer emission. Tautomer emission intensity depends on the basicity of the proton acceptor group and the temperature

of the system. Theoretical calculations predicts the system supports ESIPT only by overcoming a significant potential barrier. It is important to note that the increasing potential barrier would further decrease the basicity of the proton accepting benzazole moiety. Proton transfer time determined using femtosecond absorption and nanosecond fluorescence spectroscopy show a faster proton transfer time upon decreasing temperature.



S1.8

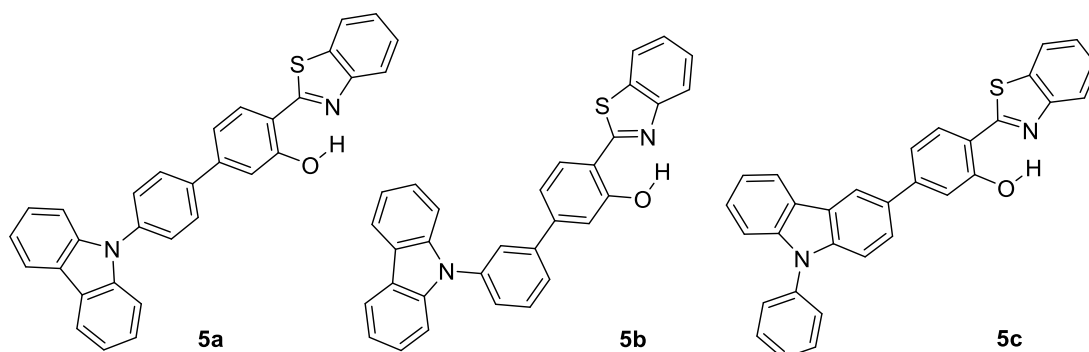
Li and co-workers (2017) have studied the photoluminescence and electroluminescence behaviour of 2-(20-hydroxyphenyl)oxazoles containing one triphenylamine (TPA) (1) and two TPAs (2) (S1.9) ESIPT molecules. Device fabricated using TPA(1) exhibited a greenish-white emission with CIE colour coordinates of (0.25, 0.41). The external quantum efficiency (EQE) of device using TPA(1) exhibited up to 5.3% and is the highest recorded for a single molecule white light-emitting diode. Device with TPA(2) showed a sky-blue emission with CIE coordinates of (0.18, 0.16) with an EQE of 8.0% and a highest recorded for reported HLCT materials. Enolic emission intensities are higher in comparison with that of their keto counterpart. Theoretical and experimental analysis reveal the system to support reverse intersystem crossing process. The reverse intersystem crossing of the enol-form from the triplet state to the singlet triggers a larger number of enol singlet excitons leading to a shift in ESIPT equilibrium towards an enhanced enol emission.



S1.9

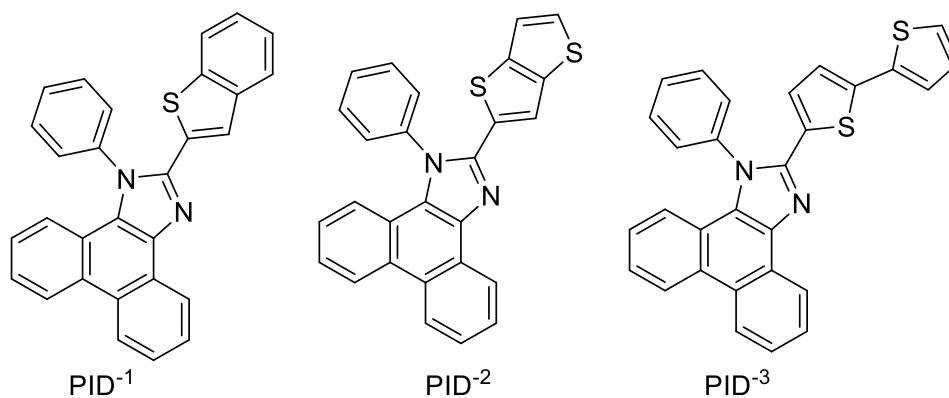
Padalkar and co-workers (2017) have designed and synthesized molecules based on carbazole (Cz) and hydroxyl benzothiazole (HBT) (S1.10) by Suzuki coupling reaction.

Position substitution of the side chain on the core group readily alters the structural and photophysical properties significantly. The molecules of the series exhibited an enhanced emission in solid state in comparison with that in the solution. A solid state quantum yield of value 0.4 is achieved in comparison with that in the solution exhibiting 0.026 to 0.17. Density functional theory calculations performed on the system well correlates with the experimental results and supports some of the geometrical concepts.



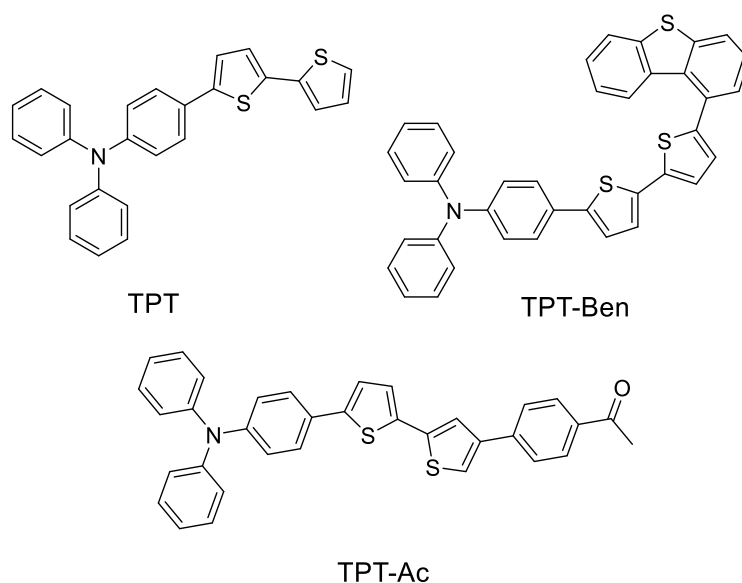
S1.10

Kula and co-workers (2018) have synthesized a series of phenanthro[9,10-*d*]imidazole (S1.11) derivatives containing thiophene units aiming towards organic light emitting device application. All phenanthro[9,10-*d*]imidazole derivatives were luminescent both in solution and solid state. Emission maximum for all the molecules were centred around 414 - 461 nm in solution state with their quantum yields ranging from 56% to 64% in chloroform. Solid state quantum yields recorded for the molecules showed a range between 12 to 23% with their emission in blue region. The device application was successfully carried out using PID-3 containing bithiophene unit as the active emitting layer.



S1.11

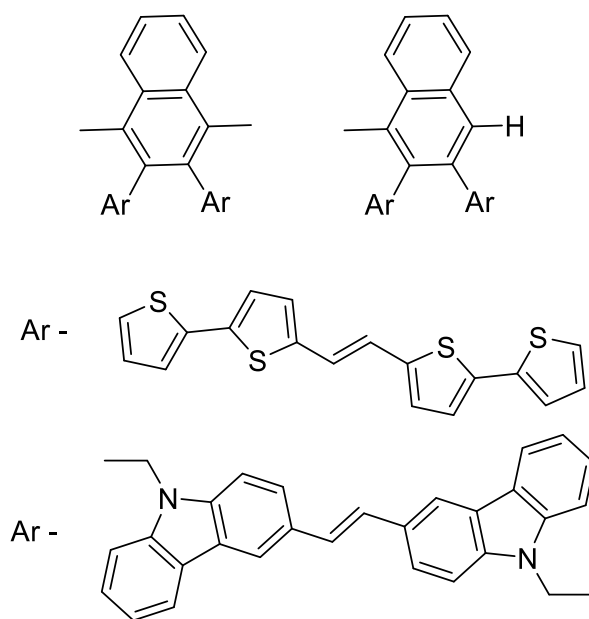
Krishna and co-workers (2018) have designed and synthesized a set of donor-acceptor based triphenylamine-bithiophene dyes TPT, TPT-Ben and TPT-Ac (S1.12) as RGB emitters for white light generation. The effect of substituents on the triphenylamine moiety induces a change in the emission wavelength of the molecules. The molecules were found to emit in Blue, Green and Orange-Red regions of the visible spectrum owing to the differences in their Stokes shift values. A mixture of all the three molecules with a ratio of 3:2:1 resulted in white light generation with a colour coordinate of (0.32, 0.36) in both at solution and solid state.



TPT-Ac

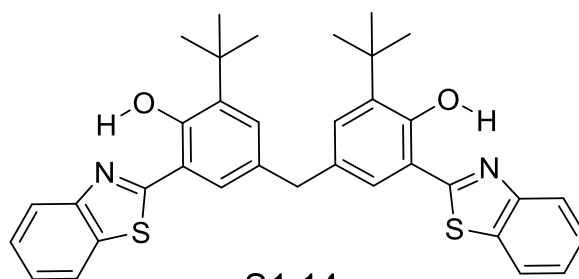
S1.12

Szlapa-kula and co-workers (2018) have synthesized tetrasubstituted naphthalene derivatives bearing thiophene or carbazole (S1.13) for organic light emitting applications. The naphthalene derivatives were electrochemically active and exhibited a very low energy bandgap between 1.64 and 1.85 eV. Molecules exhibited an emission wavelength in the range of 379-436 nm with their photoluminescence quantum yield ranging between 9.5 to 19.8% in solution. Electroluminescence enhancement was observed with increase in the blend ratio with PVK. Devices exhibited an emission band centred on 593 to 637 nm. Highest emission intensity was observed for the devices that bears carbazole derivative with one methyl group.



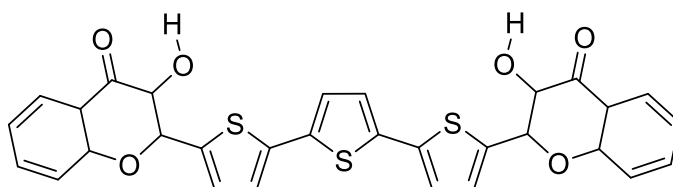
S1.13

Xuemei Lu co-workers (2018) have investigated the intramolecular hydrogen bonds occurring between (O1-H2...N3 and O4-H5...N6) of a new photochemical sensor 4-(3-(benzo[d]thiazol-2-yl)-5-tert-butyl-4-hydroxybenzyl)-2-(benzo[d]thiazol-2-yl)-6-tertbutyl phenol (Bis-HPBT) (S1.14) through DFT and TD-DFT methods. Bond lengths estimated of (O1- H2...N3 and O4-H5...N6) at the excited state clearly affirms the strengthening of intramolecular hydrogen bond. Theoretical results corresponding to absorption and emission spectra well reproduces the experimental results, and hence approves the use of the level of theory effective for the studied system. Analysis of the frontier orbitals supports proton transfer process in the system. Frontier molecular orbitals depict the nature of electronically excited state to well support the proton transfer reaction. Proton transfer barrier of 1.399 kcal/mol is observed at S1 state, this further supports single proton transfer at its excited state.



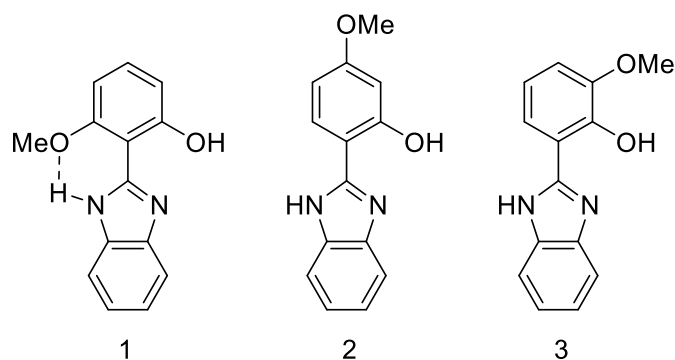
S1.14

Yusheng Wang and co-workers (2018) have theoretically investigated 3-hydroxy-2-(5-(5-(5-(3-hydroxy-4-oxo-4H-chromen-2-yl)thiophene-2-yl)thiophen-2-yl) thiophen-2-yl)-4H-hromen-4-one (S1.15) based on DFT and TDDFT methods. Formation of dual intramolecular hydrogen bonds existing between (O1—H2···O3 and O4—H5···O6) were confirmed with reduced density gradient (RDG) map. Structural parameters and their corresponding vibrational spectra of ground and excited state clearly affirms the strengthening of the intramolecular hydrogen bonds on both the arms at excited state. Theoretical level of B3LYP/TZVP used herein well reproduces the experimental results and validates the use of functional to accurately predict the nature of excited state of the system. Potential energy curves predicted clearly shows the system to support single proton transfer at the excited state, in spite of structure possessing intramolecular hydrogen bonding on both the arm.



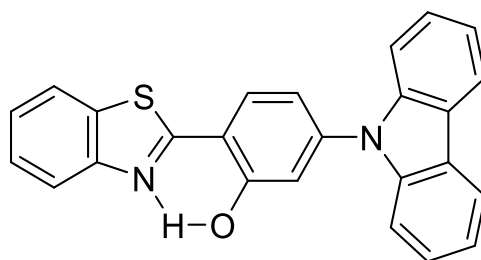
S1.15

Takagi and co-workers (2018) have designed and synthesized three 2-hydroxyphenylbenzimidazole isomers **1**, **2**, and **3** (S1.16) possessing methoxy group at 6, 4, and 3-position. Substitution of methoxy group at various position designed in the system exhibited various distinct characters. Molecule **1** showed excited state proton transfer behaviour irrespective of the solvent medium in comparison with molecule **2** that showed ESIPT emission in only THF and MeCN. However, molecule **3** exhibited a dual emission band and demonstrated strange behaviour in protic solvents. Crystal packing of the system purely contributes to the emission behaviour observed in the solid state.



S1.16

Qiaoli Zhang and co-workers (2019) have theoretically explored the excited state proton transfer dynamics of novel (benzo[d]thiazol-2-yl)-5-(9H-carbazol-9-yl)phenol (HBT-Cz) (S1.17) system based on DFT and TDDFT methods. Electrostatic potential mapping estimated clearly for the system confirms the existence of intramolecular hydrogen bond O2—H3···N4 in the S0 state. Structural parameters of the system at the excited state, further confirms the strengthening of intramolecular hydrogen bonding resulting in proton transfer at excited state. The charge transfer characteristics of the system around the hydrogen bonding overall facilitates ESIPT process. Further, transition state structure was determined along the proton transfer pathway by simulating intrinsic reaction coordinate (IRC) path. ESIPT process were further confirmed by molecular dynamic simulation using atom-centered density matrix propagation (ADMP).



S1.17

1.9 SCOPE OF THE WORK

Owing to the availability of wide variety of organic materials, electronic properties of organic systems can be precisely tuned by various chemical means have attracted the attention of researchers. The simplicity in organic device processing, cost-effective manufacturing techniques and versatile molecular design enhances their use in organic light emitting diodes. OLEDs are self-illuminating and easy disposable devices when compared to the conventional incandescent bulbs and fluorescent lights that contain mercuric toxin. OLEDs are potential light sources, that minimizes energy requirement by their improved power efficiency several times in contrast with the existing incandescent and fluorescent lighting technologies. Ultrathin and flexible panels could be manufactured of varying size and shapes have made OLEDs suitable for lighting applications.

OLEDs of present generation fail to exhibit a good external quantum efficiency caused due to various losses in the devices and hence improvement regarding device efficiency is of greater need for lighting sources with acceptable standards. Issues related to shorter device lifetime, high turn-on voltage and faster device degradation still remains a challenge. One of the main reasons is that the organic materials forming an active layer in the device fails to exhibit enhanced fluorescence in solid state. Organic molecules generally tend to exhibit weaker emission in solid state in comparison with the solution state. This general tendency of organic molecules can be easily curbed by careful design of fluorescent AIE emitters to show enhanced solid-state emission, a strategy to improvise OLED device efficiency. Further, organic system that exhibit excited state intramolecular proton transfer (ESIPT) has been a hot topic of research interests lately. Researchers have designed organic emitters that exhibit ESIPT phenomenon to generate energy over a broad range of spectrum. This phenomenon has directed to realize white light emission from a single molecule.

Research areas focussing on design and synthesis of new organic molecules exhibiting high quantum yield in solid state is highly desirable for solid state lighting applications. Extensive research in this field is vital to gain insight into some of the fundamental processes that govern the operation of these devices. Hence, this provides numerous interesting challenges to precisely design materials aiming towards greater efficiency for OLED applications.

1.10 OBJECTIVES OF THE WORK

1. To design and synthesize new small organic molecules aiming towards an efficient active layer for OLEDs.
2. To characterize and analyse molecules through FT-IR, ¹H-NMR and Mass spectrometry.
3. To study the photo-physical properties of synthesized molecules by UV-Vis spectrophotometry and Photo Luminescence spectrometry.
4. To study electrochemical characteristics of synthesized molecules.
5. To study theoretical aspects of the designed and synthesized molecules and to corroborate with the experimental results.
6. To study the OLED device applications of the synthesized molecules as an active emitter material.

Overall, the present research is focused on design and synthesis of small organic fluorescent molecules that exhibit a mechanism of aggregation induced emission and excited state intramolecular proton transfer aiming toward OLED device application. In this regard, few molecular series were designed and synthesized to study their optoelectronic properties towards device application. **Chapter 2** deals with the syntheses of Schiff's base salicylaldehyde with substituted hydrazide derivatives to study their photophysical properties. DFT and TDDFT correlates well with the experimental results. **Chapter 3** deals with the design and syntheses of multi-coloured emitter materials based on thiophene core to study its optoelectronic properties. Synthesized molecules exhibited emission enhancement upon aggregation in condensed state with that of the solution state. SCXRD analysis validated the observed AIE effect is due to the larger intermolecular π - π stacking distance. DFT and TDDFT performed on the molecular series supports experimental results. **Chapter 4** deals with the design and syntheses of orange and red emitter materials based on bithiophene core to study its optoelectronic properties. All the molecules synthesized exhibited aggregation induced emission enhancement effect. DFT and TDDFT performed on the molecular series supports experimental results. **Chapter 5** deals with the design and syntheses of organic fluorescent materials based on single and bi-thiophene core appended with hetero-substituted hydrazides. Synthesized molecules clearly support the mechanism of excited state intramolecular proton transfer.

Photoluminescence study performed for solid and solution state exhibiting double peak clearly validates the excited state intramolecular proton transfer mechanism in the system. Theoretical studies were extensively carried out to corroborate with the experimental results and to estimate the proton transfer barrier in a system. Few of the synthesized molecules were then successfully employed as an emitter material in organic light emitting diodes. *Chapter 6* deals with the detailed theoretical calculation involving dynamics of proton transfer with few supporting experimental evidences for bi-thiophene core with acyl-substituted hydrazides. Results reveal the system with bithiophene core exhibited good ES IPT mechanism supporting experimental evidences. Further, theoretical calculations performed on an extended central thiophene core reveals a much harder proton transfer at the excited state. *Chapter 7* summarizes the conclusion of the present research work and highlights the scope for future work.

Design of the molecules in each of the series were rooted on the structural aspects of the molecules more related to the functionalities present on it. Following are few of the design criteria adopted to successfully synthesize the chemical product.

1. Substitution: The presence of electron donating group such as hydroxyl, methoxy, ethoxy and dimethyl amino and electron withdrawing group such as nitro substituents in the molecules could alter and fine tune the optical properties of the system. Molecules possessing substituents with –OH moiety can also involve in intermolecular hydrogen bonding with the solvent molecules either in polar protic solvent or at solvents of higher polarity. Such species exhibited a well pronounced AIE effect.
2. Nature of the heterocyclic atom and mono/di/tri substituted heterocyclic rings: The presence of lone pair electrons on the heteroatoms is known to influence the optoelectronic properties in the system, in specific absorption and emission behaviour of the system is readily altered. Lone pair electron gained via heteroatoms would contribute to the overall electronic π -orbital density, thus altering property of the system. Apart from this, the heterocyclic rings with substituted hydrazides is certain to alter the effect of excited state proton transfer explored in the system.
3. Influence of the planarity in inducing AIE effect: The sterically hindered peripheral groups of the molecules would certainly disrupt the proton transfer at excited state. Planar structure would better support proton translocation at the excited state.

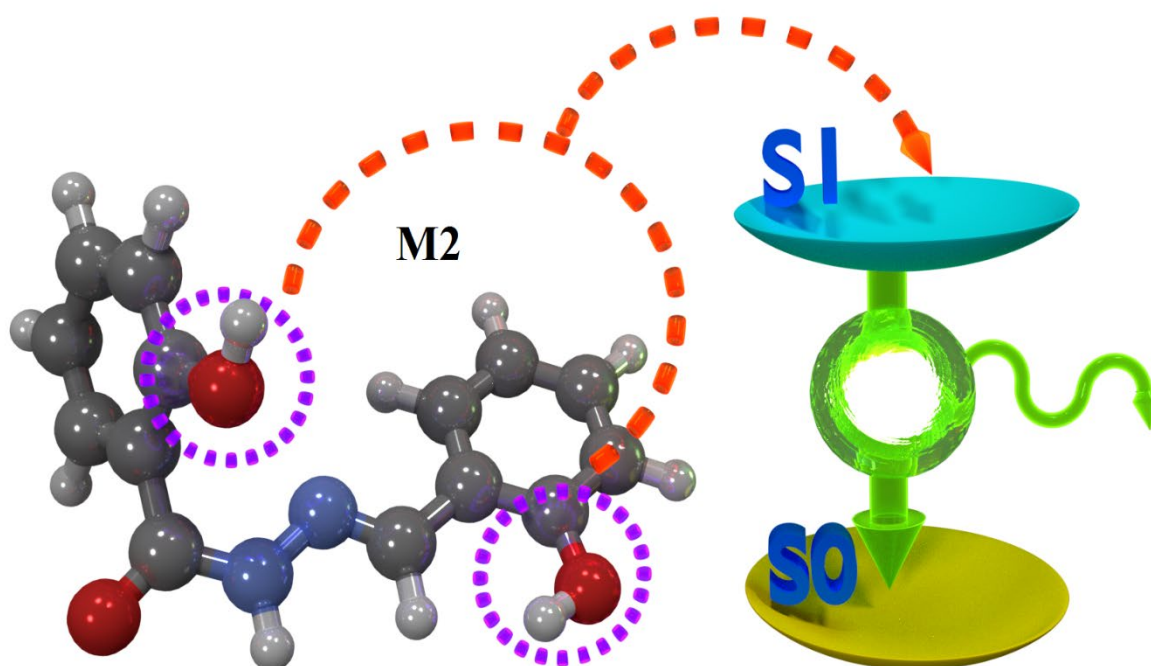
Hence, design criteria involving bithiophene as the central core moiety would uproot the possibilities of steric hindrance in the structure. Further, symmetrical molecules were also designed and synthesized, that could further adopt planarity in the structure. This in turn would alter the emission behaviour of the molecule and forms a critical factor while designing structurally planar system. Having considered planarity to be a key factor in inducing AIE effect, design criteria involves in introducing different groups to understand its role in favouring/disfavouring planarity.

4. Nature of solute-solvent interactions: Solvents of higher polarity tend to generally stabilize the excited state of the molecule yielding a characteristic pattern in the solvatochromic studies. Molecules are carefully designed with different functionalities to induce positive-solvatochromic effect through the solute-solvent interaction. Such interaction would drastically alter the optical properties of the system and help us to understand the subtleties of the system for its optical property tuning by mere solvent effect.

Having considered all the above key points as the basis of the design criteria, nearly 24 molecules has been synthesized and presented in the thesis.

CHAPTER 2

PHOTOPHYSICAL AND ELECTROCHEMICAL PROPERTIES OF ORGANIC MOLECULES: SOLVATOCHROMIC EFFECT AND DFT STUDIES



Mohan, M., Pangannaya, S., Satyanarayan, M. N., and Trivedi, D. R. (2018). "Photophysical and electrochemical properties of organic molecules: Solvatochromic effect and DFT studies." Opt. Mater., 77, 211–220

Abstract

A series of five Schiff base fluorescent molecules have been designed, synthesized and characterized by standard spectroscopic techniques. The solvatochromic behavior of molecules in solvents of varying polarity were investigated by UV-Vis and fluorescence spectroscopy.

2.1 INTRODUCTION

The design and synthesis of organic luminescent materials have attracted considerable attention in academic and industrial circles ever since the pioneering work of Tang et al. in 1987 (Tang and VanSlyke 1987). Extensive research by the scientific community have unveiled the wide range of applications of organic luminescent materials such as organic light-emitting diodes (OLEDs) (Hung and Chen 2002; Mitschke and Bäuerle 2000; Xiang et al. 2013; Yersin 2008), light-emitting electrochemical cells (LECs) (Costa et al. 2011; Slinker et al. 2007), triplet–triplet annihilation based upconversion (Singh-Rachford and Castellano 2010; Zhao et al. 2011a, 2013), fluorescence probes (Cheng et al. 2015; Feng et al. 2012; Kaur et al. 2012; Kim et al. 2008; Martínez-Máñez and Sancenón 2003; Nolan and Lippard 2008; Yang et al. 2013; Zhang et al. 2011; Zhao et al. 2010), therapy (Feng et al. 2013; Sun and Che 2009), and bio-imaging (Fernández-Moreira et al. 2009; Malleshm et al. 2014; Zhao et al. 2011b; Zhu and Yang 2013). OLEDs have thrived in the field of organic electronics leading to practical applications such as flat-panel displays and solid-state lighting resources, due to their low cost (Bünau 1970; Luo et al. 2001; Yoo et al. 2013). Most widely used organic luminescent material is composed of a polycyclic aromatic molecule with one plane of π -conjugated system, which would be favorable to the larger wavelength of absorption (λ_{abs}) and emission (λ_{em}) bands with the stronger absorption intensity and higher luminescence quantum yield (Φ). Nevertheless, luminescence is often weakened or quenched at high concentration or in solid state induced by the phenomenon of aggregation-caused quenching (ACQ) effect (Bünau 1970) that is usually arisen from the intermolecular π – π stacking interactions of π -conjugated plane molecules. ACQ effect in organic molecules is quite severe and challenging for applications demanding solid-state fluorescence emission. More recently, Tang et al have discovered a phenomenon opposed to ACQ effect known as phenomenon of aggregation-induced emission (AIE) (Luo et al. 2001). AIE active materials have seen progressive path in the field of organic electronics and has attracted great research interest (Hong et al. 2009, 2011;

Tang and Qin 2013; Wang et al. 2010).

Organic functional materials, by virtue of their ease of processing and tunability of properties through a simple chemical modification, lead to myriads of applications in comparison with inorganic materials. The incorporation of functional groups in organic materials have enriched the molecular materials with unique and interesting optoelectronic properties (Leclerc et al. 2005; Morin et al. 2004; Wong et al. 2003). Gondek and co-workers have investigated the effect of nitrogen and methyl substituent on the photophysical properties of organic molecules (Gondek et al. 2006). Kouari and coworkers have studied the effect of hydroxyl and methoxyl substituents on anthocyanidin and their effect on UV-Vis absorption spectra, with decreasing bandgap and increasing the ground state dipole moment enhancing NLO coefficient in the system (El Kouari et al. 2015). Small organic molecules possessing electron donor and electron acceptor species have proven to exhibit interesting optical and spectral properties aided by intramolecular charge transfer (ICT). The charge transfer transitions have brought in wide infra of applications in photoelectronic and nonlinear optical devices (Arias et al. 2010; Rahulan et al. 2014), chemical sensing (Singh et al. 2014) and revealing the photochemical and photobiological processes (Grabowski et al. 2003). Moreover, an azobenzene based iminopyridine ligand has been synthesized by condensation reaction between N,N-dimethyl-4,4'-azodianiline and 2-formylpyridine to study its practical application in the field of non-linear optics (Guezguez et al. 2014). Researchers have investigated structure-property relationship on tetrathiafulvalene–quinones and their effect on third-order optical nonlinearity properties (Karakas et al. 2013). The unique properties of small organic molecules such as strong solvent polarity dependent changes in their photophysical characteristics have made them quite interesting owing to their resultant large red shifts in their emission spectra, Stokes shifts between absorption and fluorescence spectra, significant reduction in the fluorescence quantum yield and lifetime on increasing the solvent polarity (Huang et al. 2002; Pham and Clarke 2008; Shaikh et al. 2010).

Salicylaldehyde derivatives have received considerable attention for their facile preparation, good stabilities, biological activities, and rich photophysical properties. Five derivatives of salicylaldehyde **M1**, **M2**, **M3**, **M4** and **M5** have been designed and synthesized. **M1** possesses salicylaldehyde covalently attached through an imine linkage to benzohydrazide moiety without any ancillary substituent in its structure. **M2** and **M4** possess an additional –OH functionality and an additional benzene ring on benzohydrazide

group respectively covalently attached through an imine linkage to salicylaldehyde moiety whereas **M4** comprises of an –OH functionality on the naphthoic hydrazide unit. **M5** comprises of nitro (NO₂) functionality on the benzohydrazide unit at position *para* to the imine linked salicylaldehyde. The aim of the present work is focused towards detailed investigation on the spectral behavior and photophysical properties of Schiff base salicylaldehyde derivatives in solvents of varying polarity. The effect of solvation on the photophysical properties of molecules **M1** to **M5** have been investigated to understand the excited state properties in solvents of varying polarity. It was observed under present study that the presence of ancillary substituent, like –OH, naphthyl and NO₂ had profound influence on the physicochemical properties. UV-Vis absorption studies, photoluminescence studies and cyclic voltammetric studies performed on the molecules reveal the utility in OLED applications. Realization of ground state geometry and the nature of electronic transitions in the system through density functional studies (DFT) in support of the experimental techniques has been the main theme of the present work.

2.2 EXPERIMENTAL SECTION

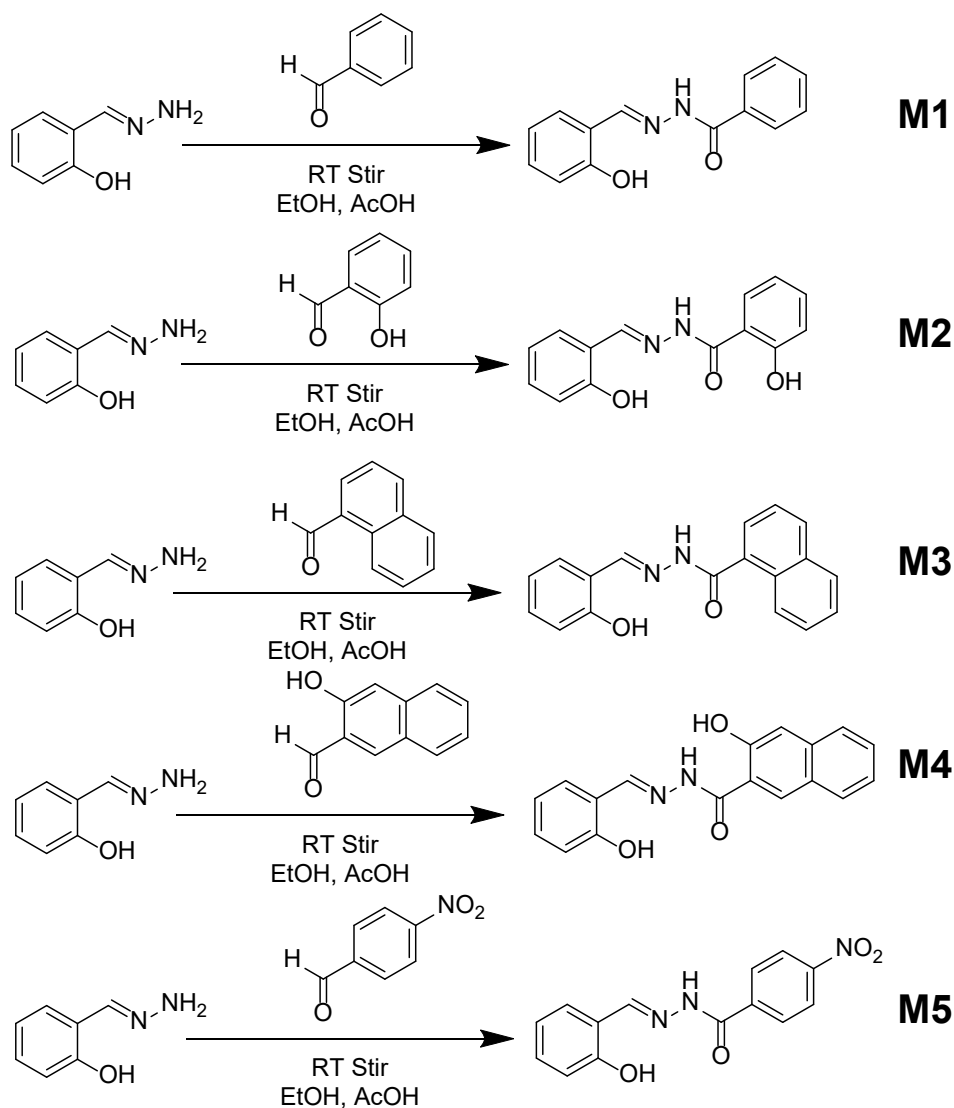
2.2.1 Materials and methods

All the chemicals used in the present study were procured from Sigma-Aldrich and Alfa Aesar and were used as received without further purification. All the solvents were purchased from SD Fine, India, were of HPLC grade and used without further distillation. Melting point was measured on Stuart SMP3 melting-point apparatus in open capillaries. Infrared spectrum was recorded on Bruker Apex FTIR spectrometer. UV-Vis spectroscopy was performed with analytik jena Specord S600 spectrometer in standard 3.0 mL quartz cell with 1 cm path length. The ¹H-NMR spectra were recorded on Bruker Ascend (400 MHz) instrument using TMS as internal reference and DMSO-d₆ as solvent. Resonance multiplicities are described as s (singlet), d (doublet), t (triplet) and m (multiplet). Cyclic voltammogram was recorded on IVIUM electrochemical workstation (Vertex) at a scan rate of 20 mV/s with the potential range -2.5 V to 2.5 V. DSC was performed using Shimadzu DSC-60.

2.2.2 Synthesis of molecules

The molecules **M1**, **M2**, **M3**, **M4** and **M5** were synthesized by simple condensation reaction between salicylaldehyde and different substituted hydrazides. The compounds

have been characterized by various spectral techniques such as DSC, FT-IR and $^1\text{H-NMR}$ analysis. The structures of the molecules **M1** to **M5** are shown in Scheme 2.1. DSC analysis were carried out to measure the melting point of all the molecules and the result is provided in the Fig. 2.11.



Scheme 2.1 Structure of molecules **M1**, **M2**, **M3**, **M4** and **M5**

Synthesis of (E)-N'-(2-hydroxybenzylidene)benzohydrazide (**M1**)

Benzohydrazide (0.11 g, 0.81 mmol) and salicylaldehyde (0.1 g, 0.81 mmol) were appropriately weighed and transferred to a round bottom flask. 5 ml of ethanol and a drop of acetic acid was added and the mixture was refluxed for about 4 h at 78 $^{\circ}\text{C}$. The progress of reaction was confirmed by TLC. After cooling to room temperature, the reaction mixture was filtered through filter paper, washed with ethanol to obtain pure product.

M1 (E)-N'-(2-hydroxybenzylidene)benzohydrazide White solid (75%). M.p. 173.06 °C. FT-IR (ATR, cm⁻¹) v: 3587(OH), 3264 (NH), 1669 (-CH=N-). ¹HNMR (400 MHz, DMSO-d₆, δ ppm): 12.10 (s, NH), 11.31 (s, OH), 8.66 (s, -CH=N), 7.96 (d, 2Ar-H), 7.60 (dt, 4Ar-H), 6.95 (t, Ar-CH), 7.32 (t, 2Ar-H)

Synthesis of (E)-N'-(2-hydroxybenzylidene)-2-hydroxybenzohydrazide (M2)

Salicylhydrazide (0.124 g, 0.81 mmol) and salicylaldehyde (0.1 g, 0.81 mmol) were appropriately weighed and transferred to a round bottom flask. 5 ml of ethanol and a drop of acetic acid was added and the mixture was refluxed for about 4 h at 78 °C. The progress of reaction was confirmed by TLC. After cooling to room temperature, the reaction mixture was filtered through filter paper, washed with ethanol to obtain pure product.

M2 (E)-N'-(2-hydroxybenzylidene)-2-hydroxybenzohydrazide Pale yellow solid (82%). M.p. 293 °C. FT-IR (ATR, cm⁻¹) v: 3686(OH), 3427 (NH), 1612 (-CH=N-). ¹HNMR (400 MHz, DMSO-d₆, δ ppm): 12.04 (s, NH), 11.77 (s, OH), 11.18 (s, OH), 8.68 (s, -CH=N-), 7.89 (dd, Ar-H), 7.57 (dd, Ar-H), 7.46 (ddd, Ar-H), 7.32 (td, Ar-H), 6.99 (m, Ar-H), 6.95(m, Ar-H)

Synthesis of (E)-N'-(2-hydroxybenzylidene)-1-naphthohydrazide (M3)

Naphthohydrazide (0.152 g, 0.81 mmol) and salicylaldehyde (0.1 g, 0.81 mmol) were appropriately weighed and transferred to a round bottom flask. 5 ml of ethanol and a drop of acetic acid was added and the mixture was refluxed for about 4 h at 78 °C. The progress of reaction was confirmed by TLC. After cooling to room temperature, the reaction mixture was filtered through filter paper, washed with ethanol to obtain pure product.

M3 (E)-N'-(2-hydroxybenzylidene)-1-naphthohydrazide Pale yellow solid (85%). M.p. 242.54 °C. FT-IR (ATR, cm⁻¹) v: 3649(OH), 3427 (NH), 3001(CH stretching), 1644 (-CH=N-). ¹HNMR (400 MHz, DMSO-d₆, δ ppm): 12.25 (s, NH), 11.22 (s, OH), 8.55 (s, -CH=N-), 8.25 (m, Ar-H), 8.09 (m, Ar-H), 7.80 (dd, Ar-H), 7.62 (m, 6Ar-H), 7.32 (m, Ar-H), 6.95 (m, 2Ar-H)

Synthesis of (E)-3-hydroxy-N'-(2-hydroxybenzylidene)-2-naphthohydrazide (M4)

3-hydroxy,2-naphthohydrazide (0.165 g, 0.81 mmol) and salicylaldehyde (0.1 g, 0.81 mmol) were appropriately weighed and transferred to a round bottom flask. 5 ml of ethanol and a drop of acetic acid was added and the mixture was refluxed for about 4 h at 78 °C. The progress of reaction was confirmed by TLC. After cooling to room temperature, the reaction mixture was filtered through filter paper, washed with ethanol to obtain pure product.

M4 (E)-3-hydroxy-N'-(2-hydroxybenzylidene)-2-naphthohydrazide: White solid (77%). M.p. 299.69 °C. FT-IR (ATR, cm^{-1}) v: 3251(OH), 3165 (NH), 3051(CH stretching), 1642(-CH=N-). ^1H NMR (400 MHz, DMSO- d_6 , δ ppm): 12.16 (s, NH), 11.26 (s, OH), 11.19 (s, OH), 8.68 (s, -CH=N-), 8.46 (s, Ar-H), 7.85 (dd, 2Ar-CH), 7.55 (m, 1Ar-CH), 7.34 (m, 4Ar-H), 6.95 (m, 2Ar-H)

Synthesis of (E)-N'-(2-hydroxybenzylidene)-4-nitrobenzohydrazide (M5)

4-Nitrobenzohydrazide (0.148 g, 0.81 mmol) and salicylaldehyde (0.1 g, 0.81 mmol) were appropriately weighed and transferred to a round bottom flask. 5 ml of ethanol and a drop of acetic acid was added and the mixture was refluxed for about 4 h at 78 °C. The progress of reaction was confirmed by TLC. After cooling to room temperature, the reaction mixture was filtered through filter paper, washed with ethanol to obtain pure product.

M5 (E)-N'-(2-hydroxybenzylidene)-4-nitrobenzohydrazide Pale yellow solid (83%). M.p. 299.58 °C. FT-IR (ATR, cm^{-1}) v: 3215 (OH), 3062 (NH), 3001(CH stretching), 1647 (-CH=N-). ^1H NMR (400 MHz, DMSO- d_6 , δ ppm): 12.36 (s, NH), 11.09 (s, OH), 8.69 (s, -CH=N-), 8.39 (d, 2Ar-H), 8.18 (d, 2Ar-H), 7.61 (m, Ar-H), 7.32 (t, Ar-H), 6.94 (m, Ar-H)

2.2.2.6 Characterization results

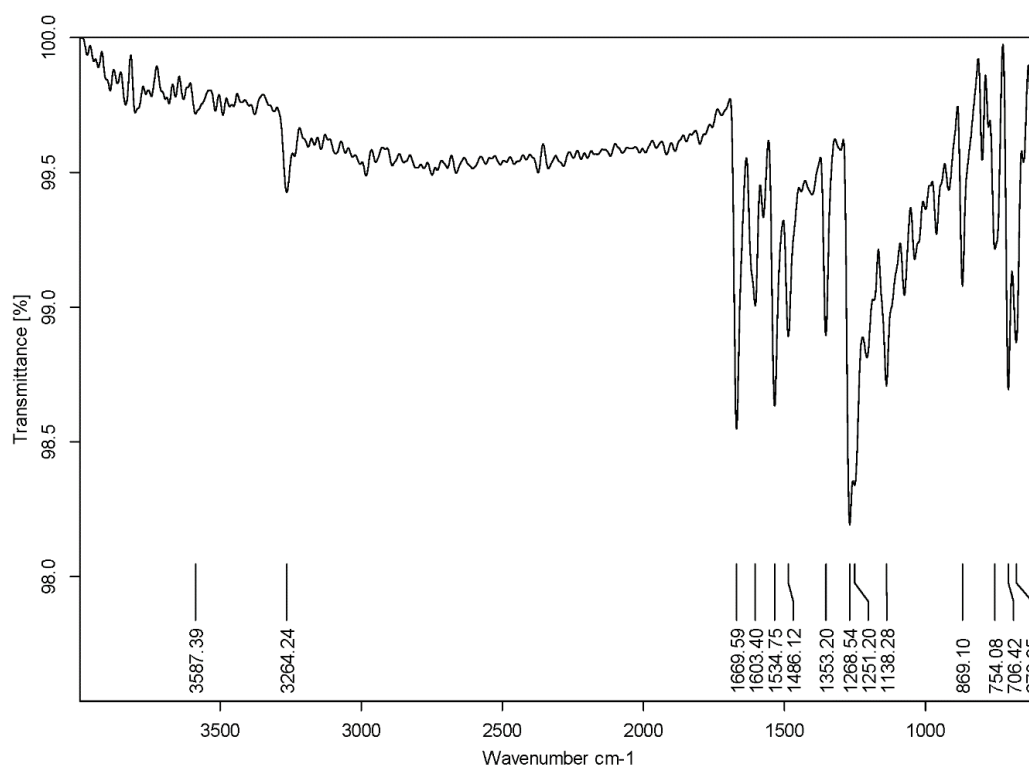


Fig. 2.1 FT-IR spectrum of molecule **M1**

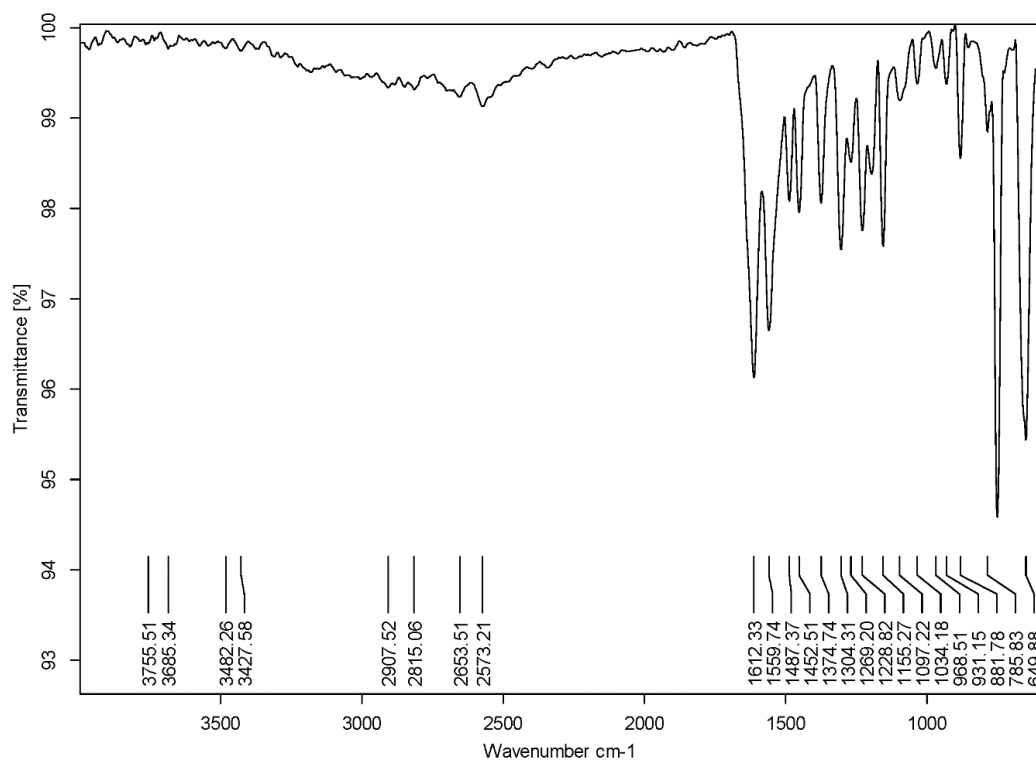


Fig. 2.2 FT-IR spectrum of molecule M2

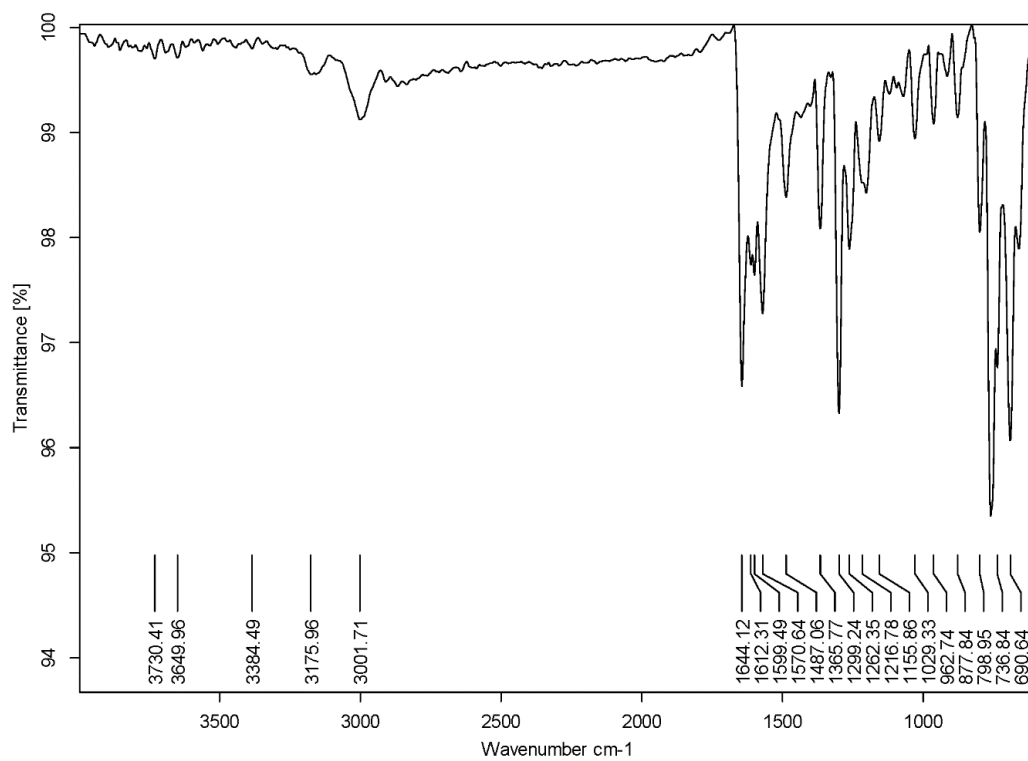


Fig. 2.3 FT-IR spectrum of molecule M3

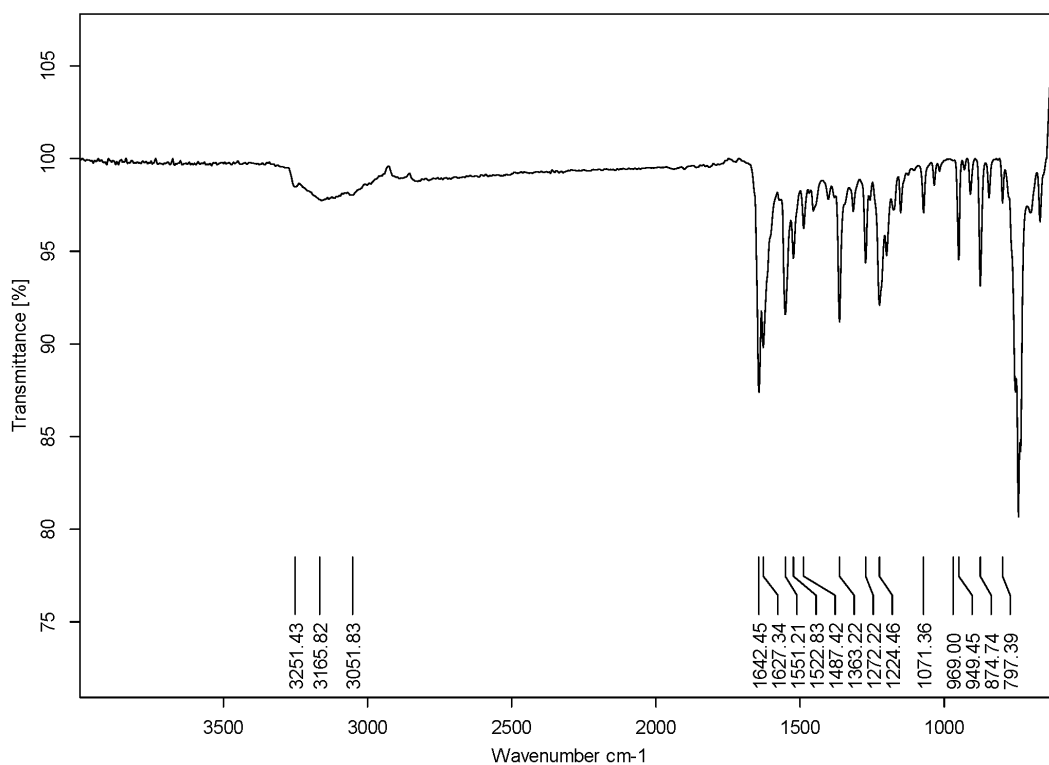


Fig. 2.4 FT-IR spectrum of molecule **M4**

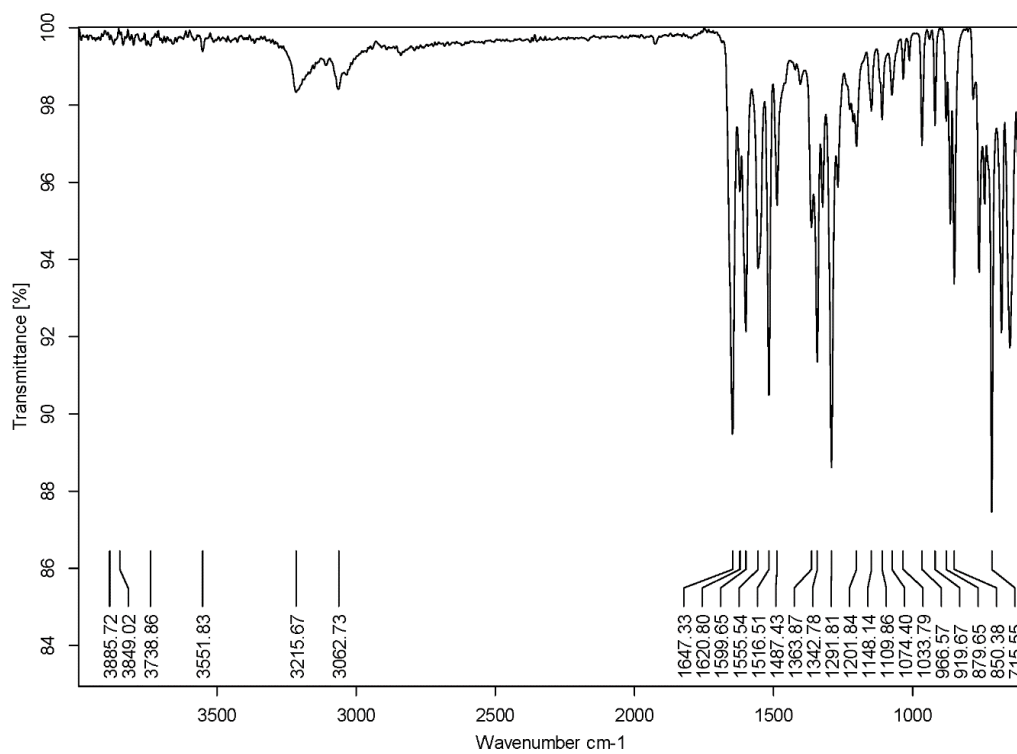


Fig. 2.5 FT-IR spectrum of molecule **M5**

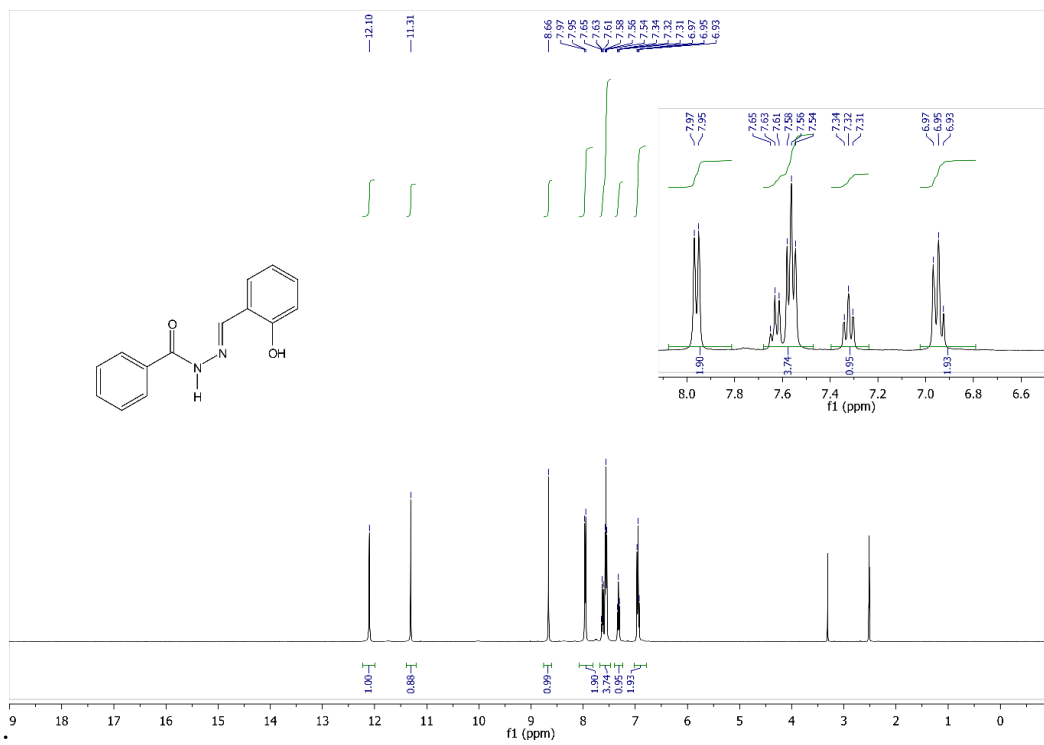


Fig. 2.6 ^1H NMR spectra of molecule M1

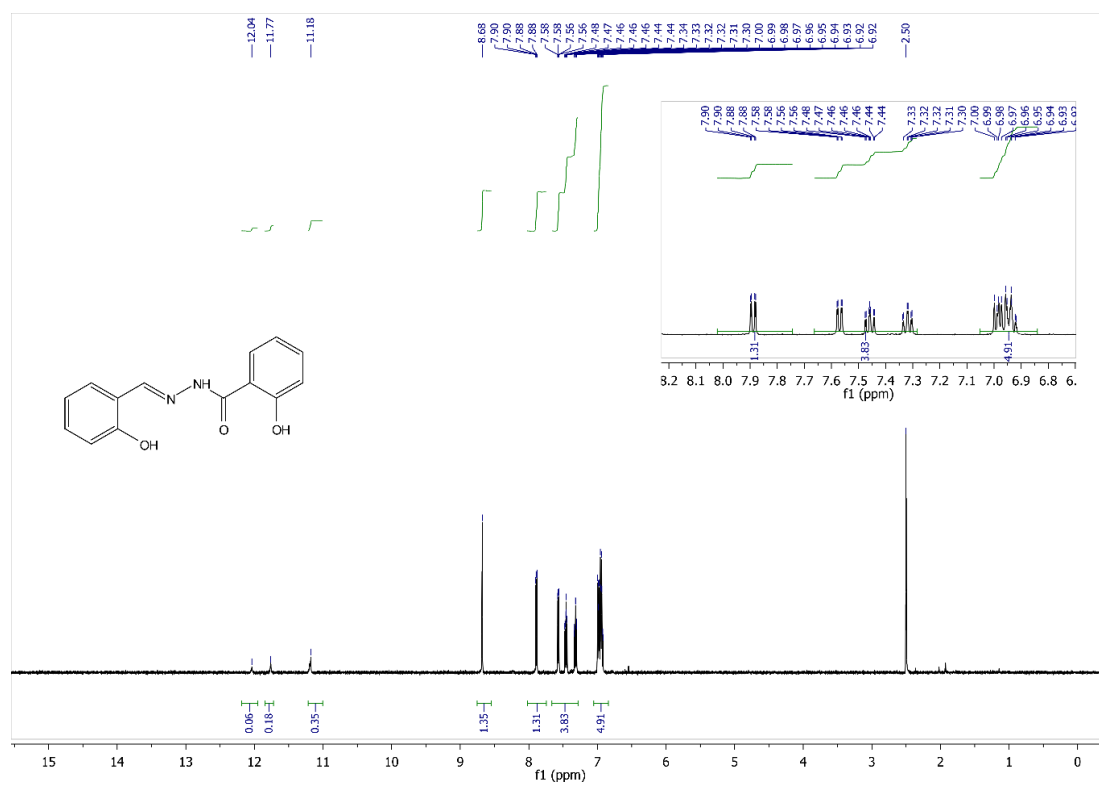


Fig. 2.7 ^1H NMR spectra of molecule M2

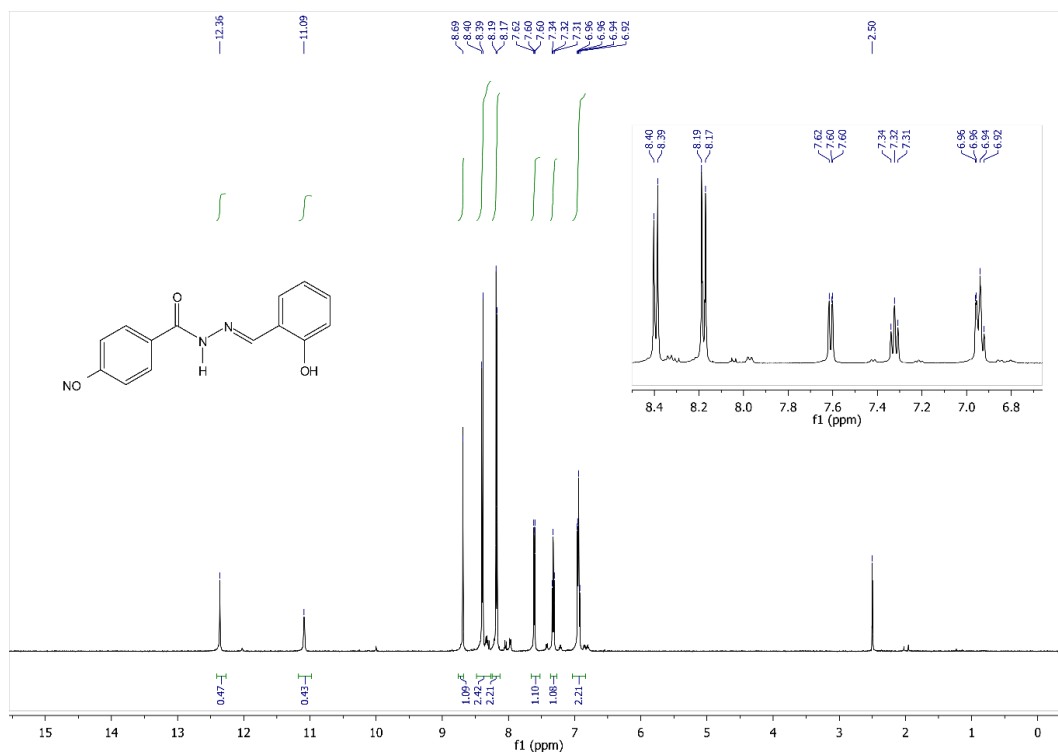


Fig. 2.10 ¹H NMR spectra of molecule M5

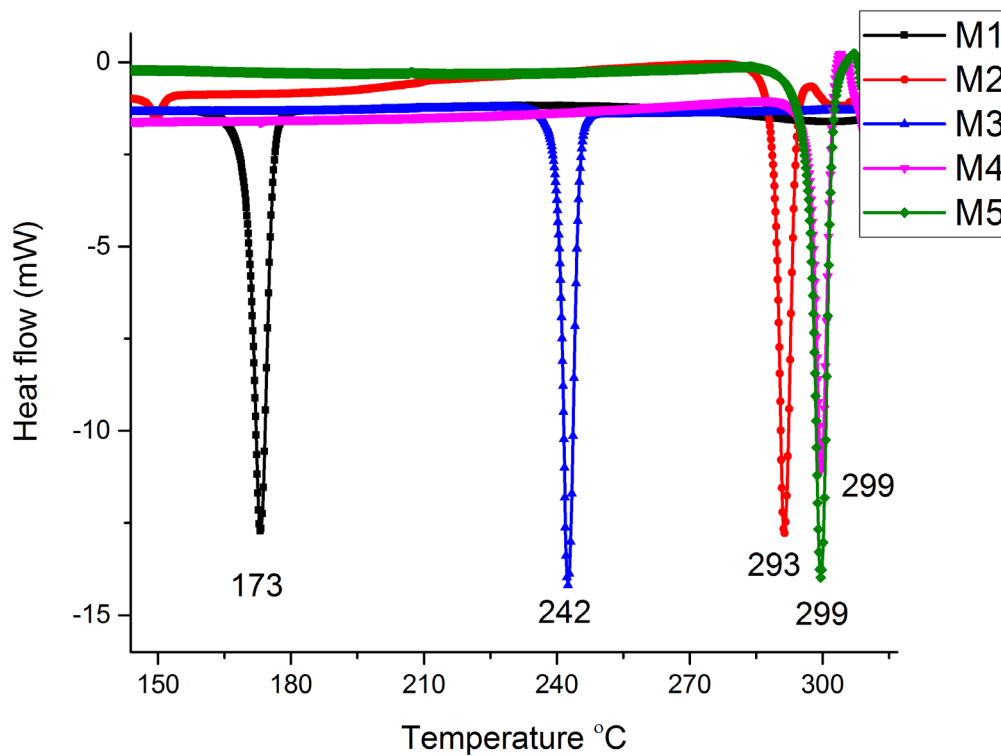


Fig. 2.11 Differential Scanning calorimetry of molecules M1 to M5

2.3 RESULTS AND DISCUSSION

2.3.1 UV-Vis studies

The optical properties of synthesized molecules were studied in order to probe the influence of substituents such as extension of π conjugation or increasing donor character on the photophysical properties of salicylaldehyde derivatives. With a view to evaluate the effect of polarities and hydrogen bond forming abilities of various organic solvents on the fluorescence and absorption spectra of molecules, UV-Vis spectra and fluorescence spectra of **M1** to **M5** have been recorded. 10^{-5} M solution of the molecules were prepared in solvents of varying polarity such as THF, DCM, acetone, EtOH, ACN, DMF and DMSO. Molecules **M2** and **M4** exhibited significant fluorescence in solution phase when illuminated with UV lamp as shown in Fig. 2.12.

The UV-Vis spectra of these molecules reveal that the absorption band in the region ~ 300 nm corresponds to the transition between the p-orbital localized on the central bond of azomethine (HC=N-) and the carbonyl (C=O) group. The second band located in the range of ~ 350 to 400 nm refers to an intramolecular charge transfer (CT) transition within the molecule (Gabr 1990). Furthermore, the band at 400 nm is highly significant in salicylaldehyde derivatives which indicates the occurrence of strong intramolecular hydrogen bond between the hydroxyl group and the azomethine nitrogen that causes planarity of the molecules. This further facilitates the charge transfer bands which are more sensitive to solvent changes than bands which are resulting from local transition (Gabr 1990). The results are shown in Table 2.1. The role of solvent is significant in spectroscopic analysis as it induces predominant changes in the position, intensity and shape of the absorption and fluorescence bands (Wirth 1982). The effect of changes in the polarity of the solvents is reflected in changes in the excitation and emission wavelengths on whether S1 or S0 is more stabilized by the solvent (Mishra and Dogra 1983). Among all the solvents used in the present study, each molecule showed highest Stokes shift values in a specific solvent. This reveals the influence of solvent polarity in promoting or nullifying the solute-solvent interactions. 10^{-5} M solution of molecule **M1** in DMSO, **M2** in EtOH, **M3** and **M4**, in DMF and **M5** in ACN exhibited maximum Stokes shift differing by 223, 162, 165, 188 and 111 units respectively. This proved the complex nature of solute solvent interactions dominated by the hydrogen bond accepting nature of the solvents to have a prominent role in inducing red shift. The red shift and the Stokes shift observed for the molecules with the increase in solvent polarity reveals that the long wavelength band of the molecule is due to

n- π^* transitions existing in the neutral molecules.

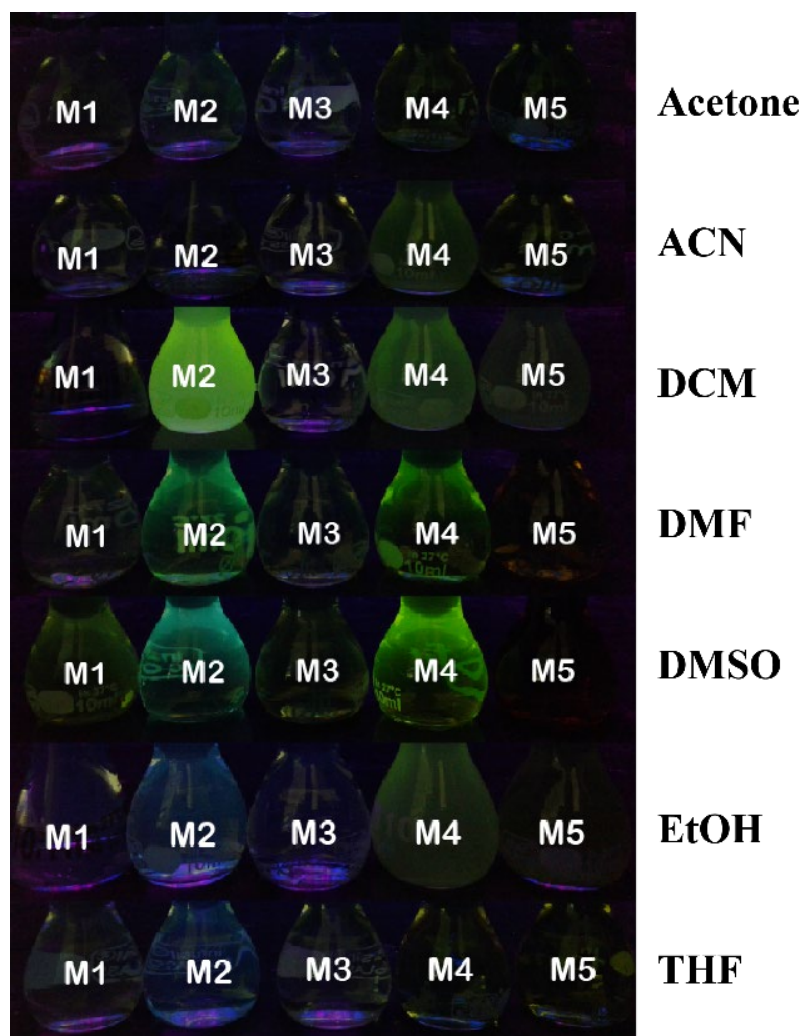


Fig. 2.12 Fluorescent response of molecules **M1** to **M5** (10^{-5} M) in solvents of varying polarity under UV illumination

The UV-Vis spectral studies of the molecules **M1** to **M5** in solvents of varying polarity reveals the following results. The molecules **M1** and **M5** exhibited linear correlation between the solvent polarity and red shift in the absorption bands in solvents such as THF, DCM and acetone. The absorption band for **M1** and **M5** exhibited a red shift in solvents of increasing polarity following an order THF < DCM < acetone differing by 50 units respectively. THF and acetone being polar aprotic solvents, DCM being a non-polar solvent exhibited less prevalent solute-solvent interactions on the molecules. Molecules **M1** and **M5** did not exhibit any linear correlation between solvent polarity and red shift in absorption band in solvents of higher dielectric constants such as EtOH, DMF, ACN, and

DMSO. The UV-Vis spectra of molecules **M1** and **M5** is as shown in the Fig. 2.13 to Fig. 2.17. Ethanol being a polar protic solvent, DMF, ACN and DMSO being polar aprotic solvent introduced complex nature of solute solvent interactions dominated by the hydrogen bond accepting nature of the solvents. The hydrogen bonding capacity of the solvents is necessary to be considered from a view point of its importance over polarity. This is justified with the anomalous behavior observed in the case of ACN which is more polar than DMF, yet exclusively a hydrogen-bond acceptor. Molecules **M2** and **M4** by virtue of the presence of an additional -OH functionality did not show any linear dependence on the solvent polarity and the red shift, yet indicating complex nature of solute solvent interactions. This justifies the role of -OH functionality as a hydrogen bond donor site aiding the solute-solvent interactions with hydrogen bond acceptor solvents such as DMSO, ACN and EtOH. Molecules **M2** and **M4**, possessing two -OH functionalities, exhibited a significant red shift at 385 nm and 400 nm respectively in DMSO which is attributed to the hydrogen bond interactions dominating over the solute-solvent interactions.

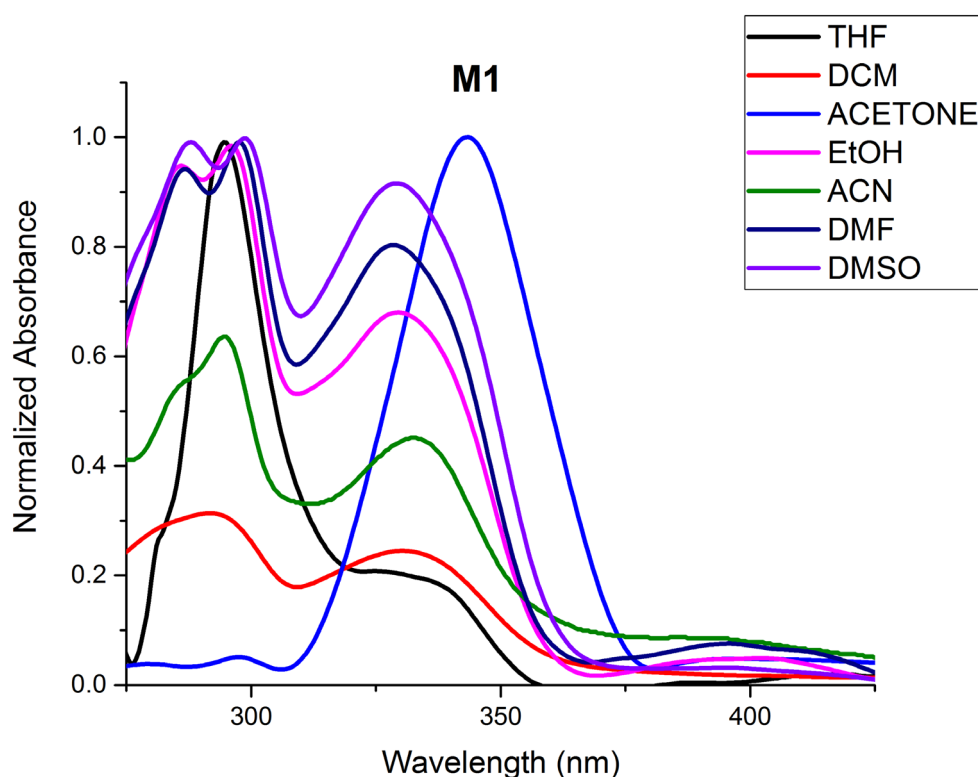


Fig. 2.13 UV-Vis spectra of molecule **M1** (10^{-5} M) in various solvents

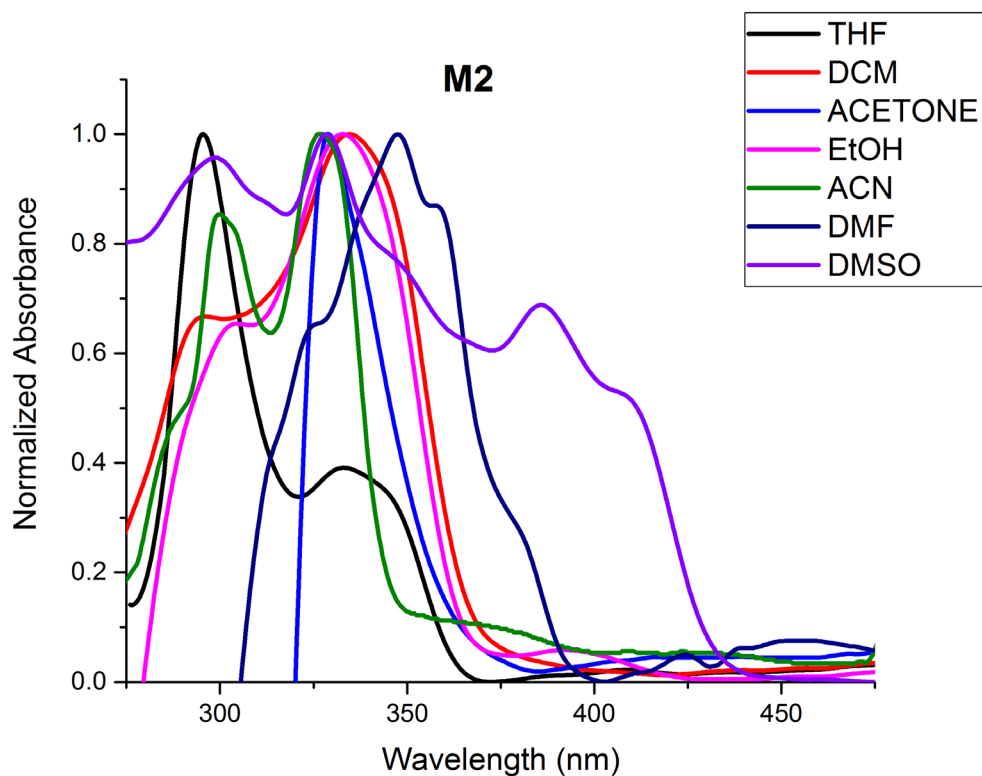


Fig. 2.14 UV-Vis spectra spectra of molecule **M2** (10^{-5} M) in various solvents

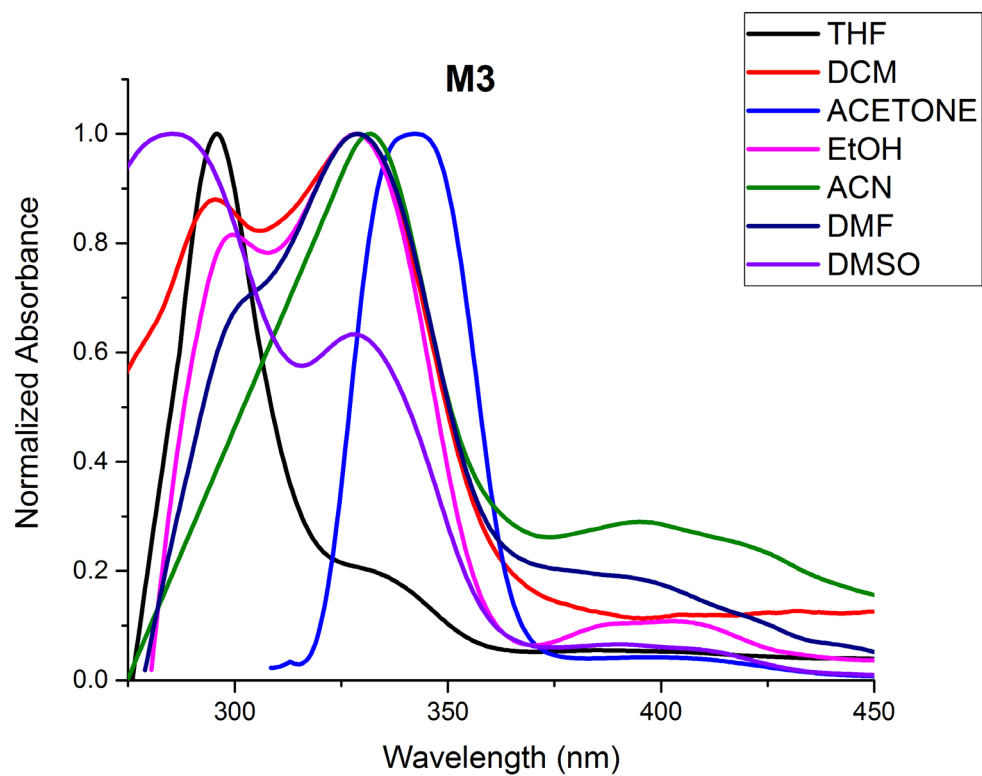


Fig. 2.15 UV-Vis spectra of molecule **M3** (10^{-5} M) in various solvents

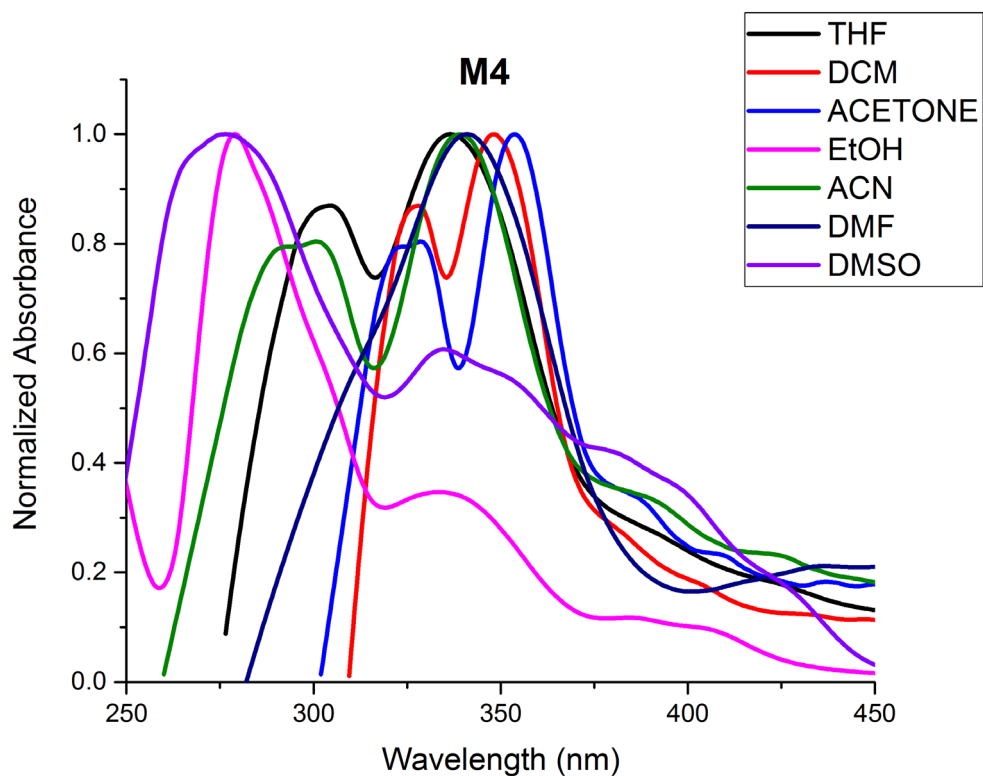


Fig. 2.16 UV-Vis spectra of molecule **M4** (10^{-5} M) in various solvents

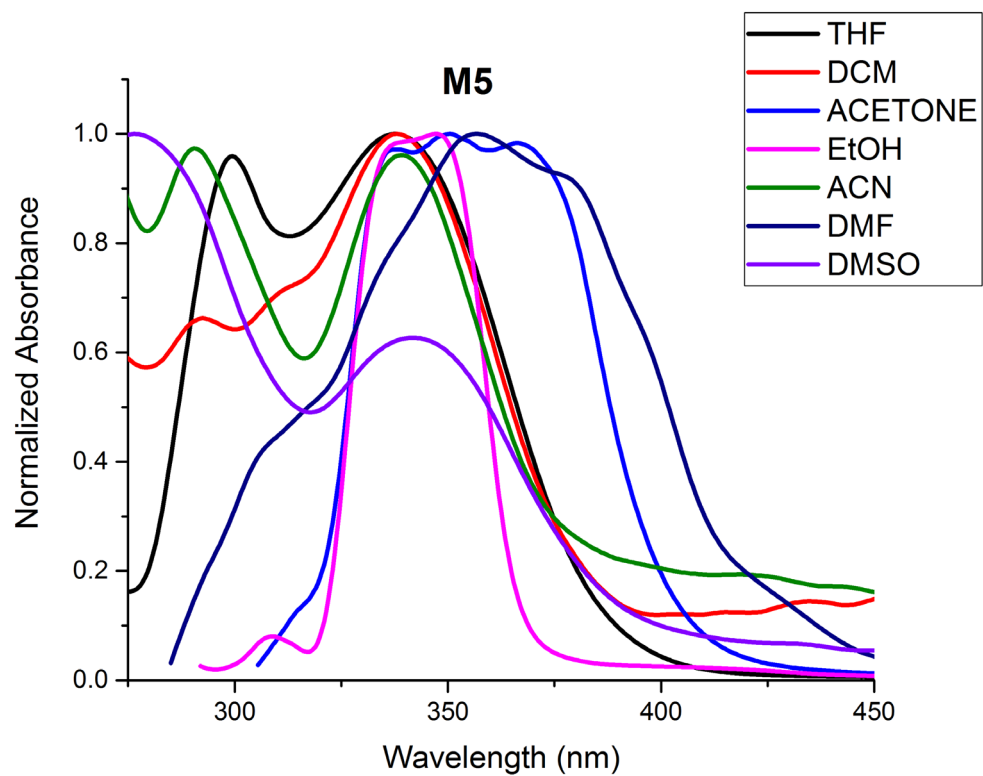


Fig. 2.17 UV-Vis spectra of molecule **M5** (10^{-5} M) in various solvents

Table 2.1 Photophysical aspects of molecules **M1** to **M5** in solvents of varying polarity

Molecule		λ_{abs} (nm)	λ_{ex} (nm)	λ_{ems} (nm)	Stoke Shift	FWHM
THF	M1	250, 295, 334	250	306	56	34
	M2	250, 295, 334	334	446	112	75
	M3	250, 295, 334	334	436	102	69
	M4	250, 295, 305, 335	250	311	61	38
	M5	250, 295, 338	250	311	61	39
DCM	M1	285, 294, 330	294	392	98	99
	M2	293, 335	293	392	99	102
	M3	294, 328	294	393	99	103
	M4	308, 334	308	394	86	59
	M5	292, 340	292	393	101	78
Acetone	M1	345, 415	345	426	81	79
	M2	331	331	484	153	150
	M3	343	343	428	85	124
	M4	350	350	513	163	86
	M5	350	350	427	77	77
EtOH	M1	285, 296, 330, 400	330	429	99	68
	M2	301, 333, 400	301	463	162	80
	M3	297, 329, 400	329	429	100	65
	M4	275, 337, 400	400	557	157	125
	M5	345	345	430	85	64
ACN	M1	271, 285, 295, 333	271	373	102	105
	M2	291, 335	335	474	139	102
	M3	294, 332	294	376	82	121
	M4	290, 303, 339	290	360	70	121
	M5	267, 290, 339	267	378	111	96
DMF	M1	286, 298, 329, 397	397	458, 553	61, 156	105
	M2	330, 364, 381, 412	330	455	125	82
	M3	300, 329, 395	395	560	165	95
	M4	340	340	528	188	104
	M5	357, 380	380	453	73	73
DMSO	M1	288, 299, 329	329	552	223	175
	M2	329, 385	385	458	73	78
	M3	285, 329	285	336	51	51
	M4	276, 333, 400	400	557	157	104
	M5	276, 342	276	330	54	55

2.3.2 Photoluminescence studies

Photoluminescence studies were performed for the molecules **M1** to **M5** in solvents of varying polarity. Furthermore, all the materials show good solvatochromic effect in wide range of solvent polarities. The probability of absorption is greater in polar solvents in contrast with the fluorescence intensity which is affected by other processes such as internal conversion and intersystem crossing. These processes are favored by greater hydrogen bond accepting character of ACN relative to other polar and hydrogen-bond donor solvents such as methanol which inhibit these non-radiative processes. Fluorescence emission is favored in solvents of higher dielectric constants such EtOH and DMF. **M2**, by virtue of the presence of two OH functionalities which is in direct conjugation with the imine linkage, further favors delocalization of electrons. This in turn influences the electronic transition in the molecule leading to emission intensity greater in comparison with the other molecules of the series. The fluorescence emission spectrum of **M1** to **M5** in various solvents is provided in Fig. 2.18 to Fig. 2.22. Variation of emission wavelengths of the molecules **M1** to **M5** in solvents of varying polarity is shown in Fig. 2.23.

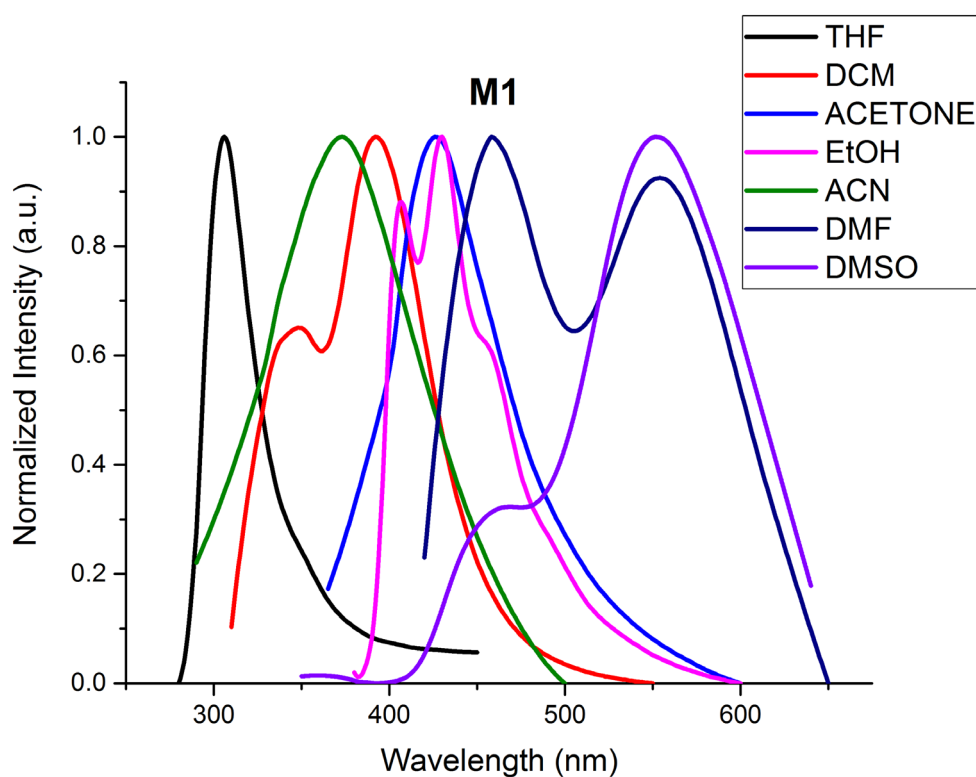


Fig. 2.18 Photoluminescence spectra of molecule **M1** (10^{-5} M) in various solvents

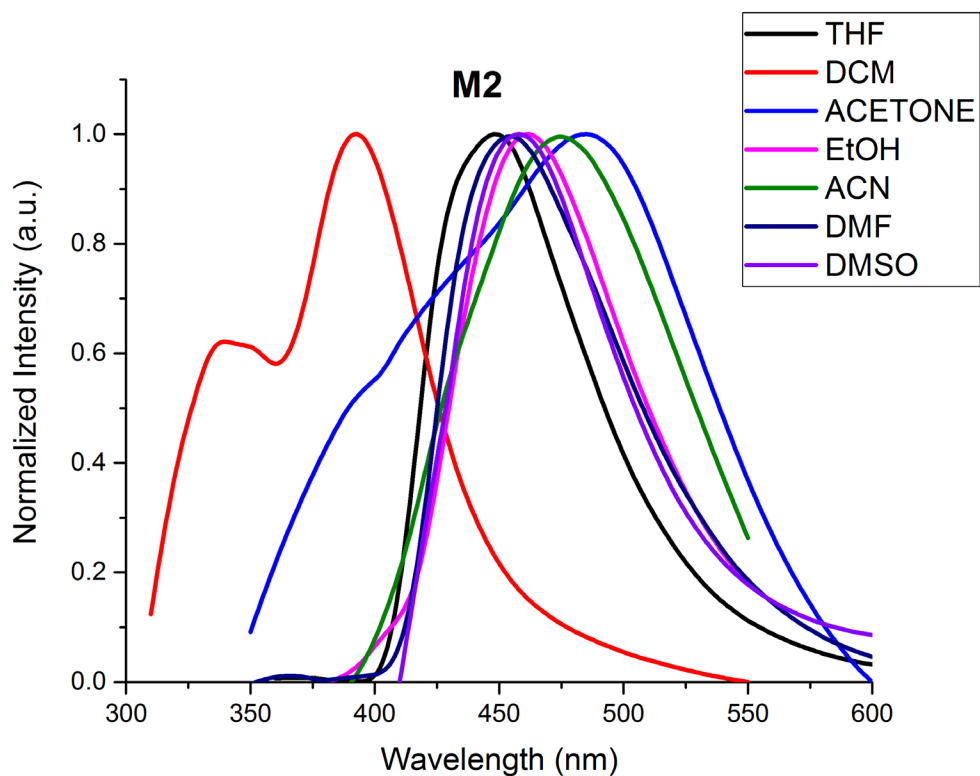


Fig. 2.19 Photoluminescence spectra of molecule **M2** in solvents of varying polarity

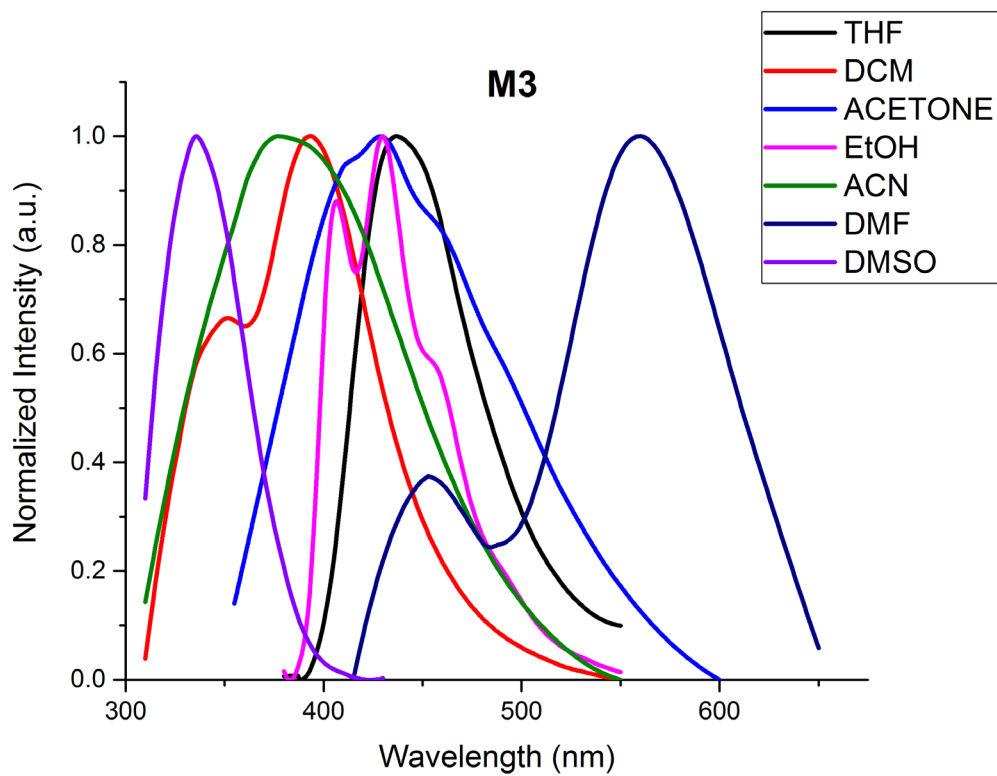


Fig. 2.20 Photoluminescence spectra of molecule **M3** (10^{-5} M) in various solvents

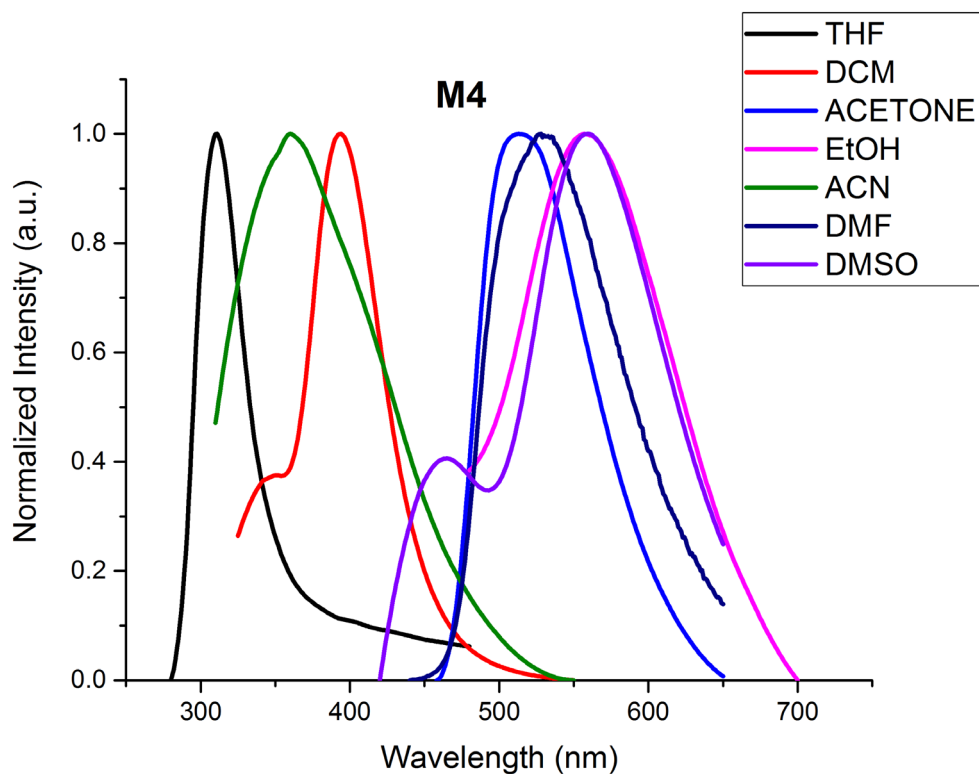


Fig. 2.21 Photoluminescence spectra of molecule **M4** (10^{-5} M) in various solvents

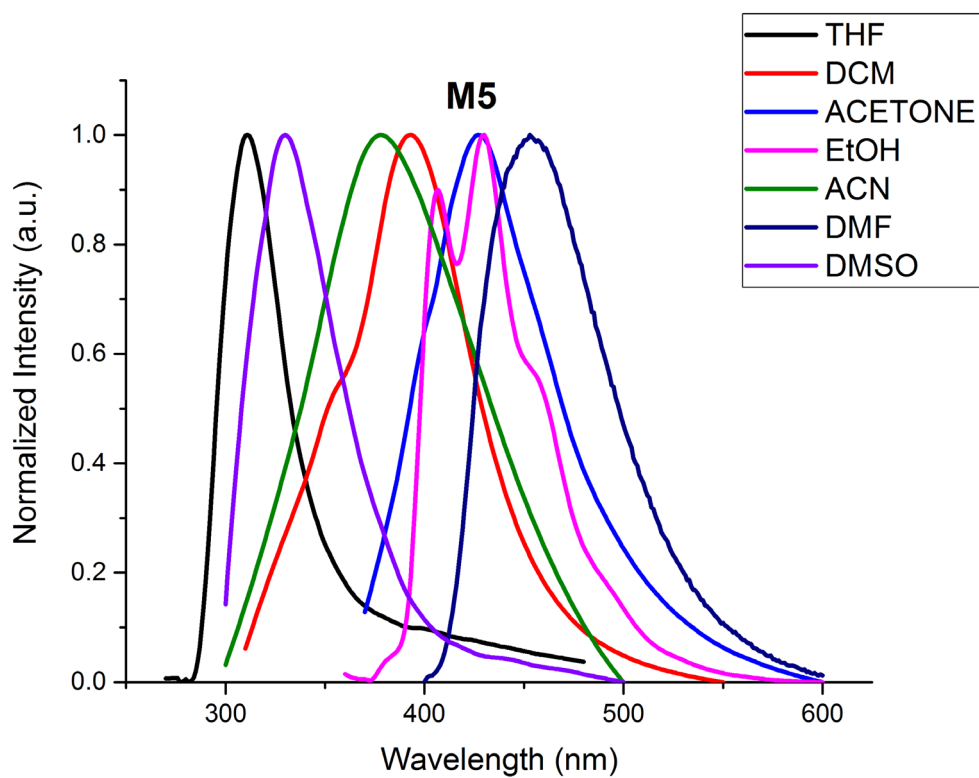


Fig. 2.22 Photoluminescence spectra of molecule **M5** (10^{-5} M) in various solvents

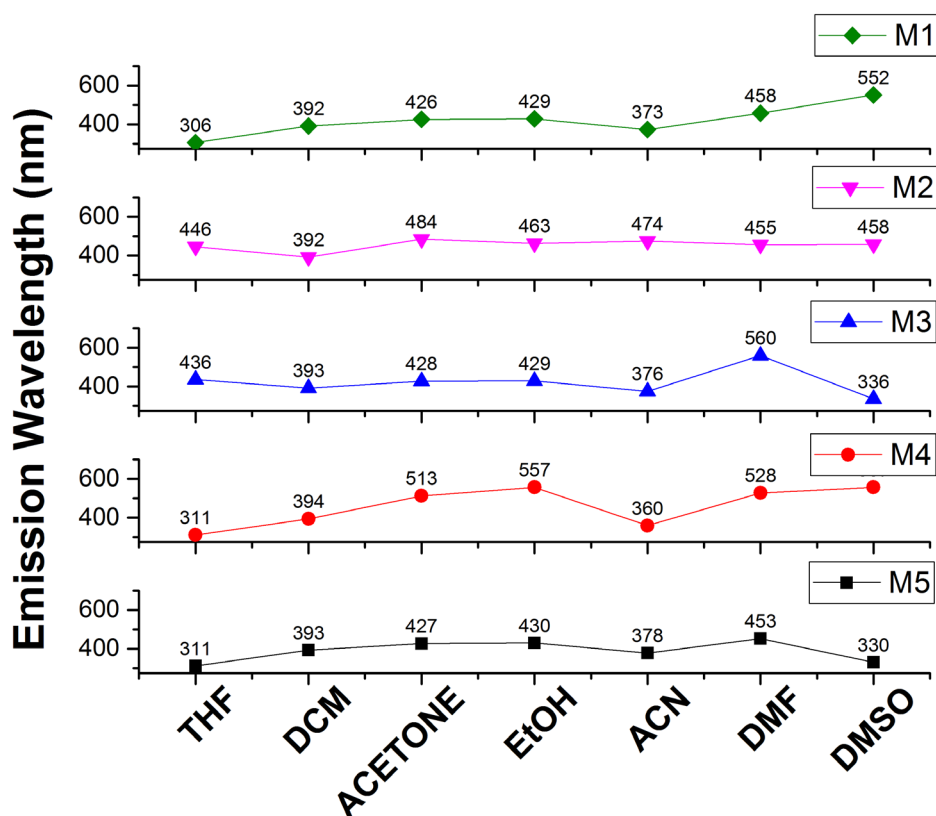


Fig. 2.23 Variation in the emission wavelength of molecules **M1-M5** under solvents of varying polarity

Molecules **M1** to **M5** were deposited onto chemically cleaned glass substrates with the help of thermal vacuum deposition to study its solid-state emission properties. **M4** exhibited a weaker emission as compared to **M2** under UV illumination as shown in the Fig. 2.24. The -OH functionality in **M2** and **M4** are known to have prominent role in exhibiting solid state luminescent property. **M1** and **M3** devoid of -OH substitution on one of the aromatic counterparts did not exhibit solid state emission. Further, molecule **M5**, due to the presence of -NO₂ group quenched the emission intensity and hence no significant solid-state emission was observed. Photoluminescence spectra of thin films of molecules **M2** and **M4** is provided in the Fig. 2.25 with their photophysical parameters tabulated in Table 2.2. Molecule **M2** exhibited a solid-state emission at 512 nm red shifted in comparison with the solution state whereas **M4** exhibited an emission at 520 nm with a FWHM of 88. A good color purity would imply in achieving a value of FWHM lesser than 60 and molecule **M2** exhibited a value of 70.

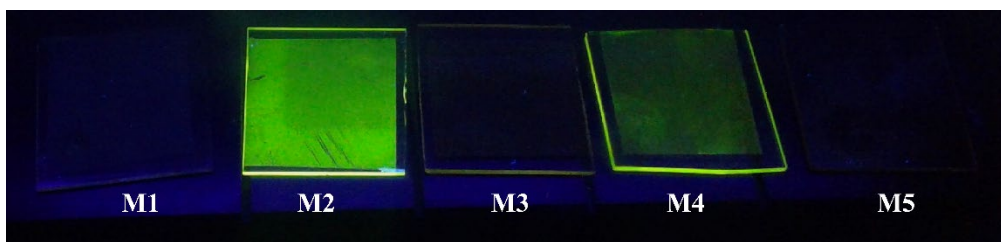


Fig. 2.24 Solid-state emission of molecules **M1** to **M5** under UV lamp.

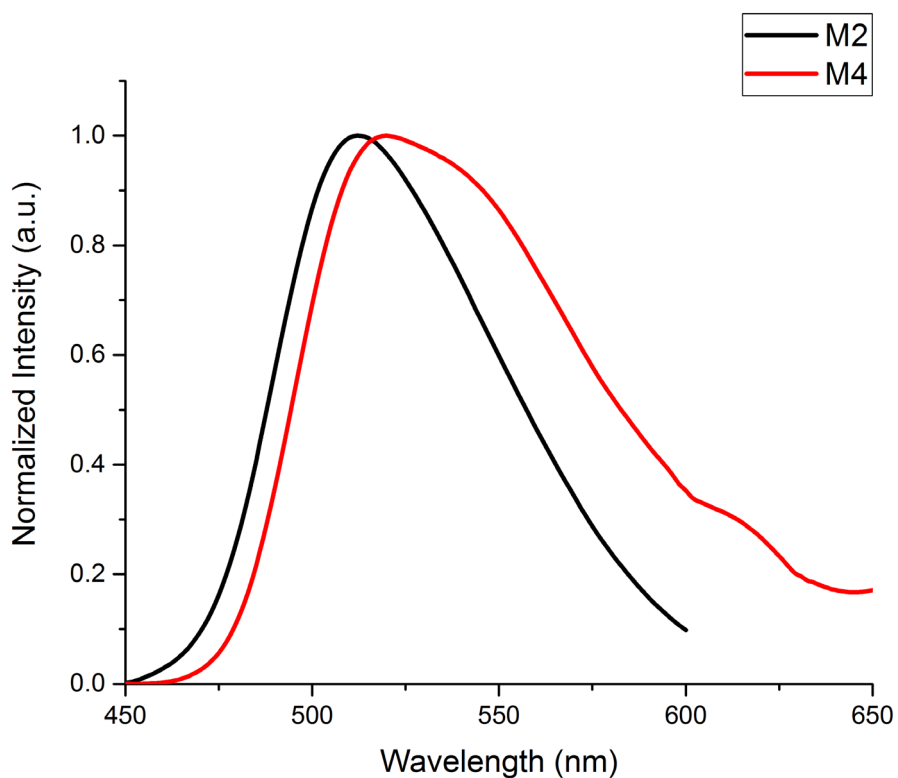


Fig. 2.25 Solid-state photoluminescence spectra of molecule **M2** and **M4**.

Table 2.2 Photoluminescence parameters of molecule **M2** and **M4** in solid state

Molecule	λ_{ex} (nm)	λ_{ems} (nm)	Stokes Shift	FWHM
M2	360	512	152	70
M4	350	520	170	88

2.3.3 Quantum Yield measurement

The fluorescence quantum yields (ϕ_S) were evaluated according to the following Equation 2.1, where Coumarin 153 in cyclohexane was used as a reference (R) for molecule **M2** and quinine sulphate in 0.5 M H_2SO_4 chosen as the reference (R) for other molecules in the series. Molecules **M1** to **M5** whose quantum yield to be determined is denoted as S. Grad corresponds to the gradient from the plot of integrated fluorescence intensity vs

absorbance at the excitation wavelength, and η the refractive index of the solvent for standard and reference (Dhami et al. 1995; Williams et al. 1983). Molecule **M2** exhibited a highest quantum yield value of 0.35 in DMSO, whereas molecules **M1** and **M4** showed a quantum yield value of 0.005 and 0.06. The estimated quantum yield of the molecules is presented in Table 2.3. Further there were no significant emissions from **M3** and **M5** with reference to the standard.

$$\phi_S = \phi_R \frac{Grad_S}{Grad_R} \frac{\eta_S^2}{\eta_R^2} \quad \text{Eq. 2.1}$$

Table 2.3 Measured quantum yield for molecule **M1**, **M2** and **M4**

Molecule	M1	M2	M3	M4	M5
ϕ_s	0.005	0.35	ND*	0.06	ND*

*ND – not determined (emission intensity is very low in comparison with standard)

2.3.4 Fluorescent lifetime measurement

Measurements of the fluorescence lifetime have been performed with standard time-correlated single-photon counting method (TCSPC). An LED with an excitation wavelength of 346 nm and a spectral width of 1.2 nm has been used to excite the molecules. The lifetime curves for **M1** to **M5** are represented in the Fig. 2.26 with their standard deviation profile is provided in Fig. 2.27. The decay curves obtained are then fitted with a DAS6 software to obtain the fluorescence lifetime of the molecules (τ_s) and the results are tabulated in Table 2.4. In general, certain materials exhibit only first order progression decay having a single lifetime component, and other materials can exhibit second or third order progression decay, resulting in two or three component lifetimes (Song et al. 2017). Decay curve with a good fit resulted in a XSQR value of lesser than 1.2 for the molecules with a three and two-component lifetime.

Table 2.4 The lifetime of molecules **M1** to **M5** and its XSQR value

Molecule	XSQR	Lifetime (ns)		
		T1	T2	T3
M1	1.095	1.3	5.59	0.079
M2	1.184	1.63	2.91	0.0763
M3	1.069	0.163	1.65	2.69
M4	1.063	0.78	4.39	-
M5	1.053	0.982	2.59	-

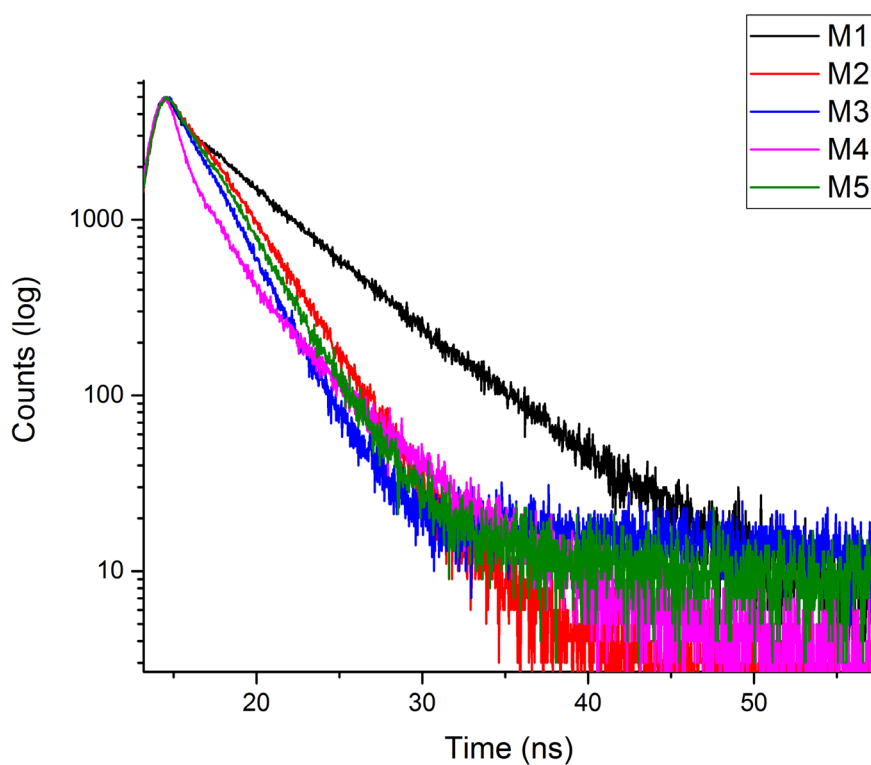


Fig. 2.26 Fluorescence decay curve of molecules **M1** to **M5** excited with a source of 346 nm

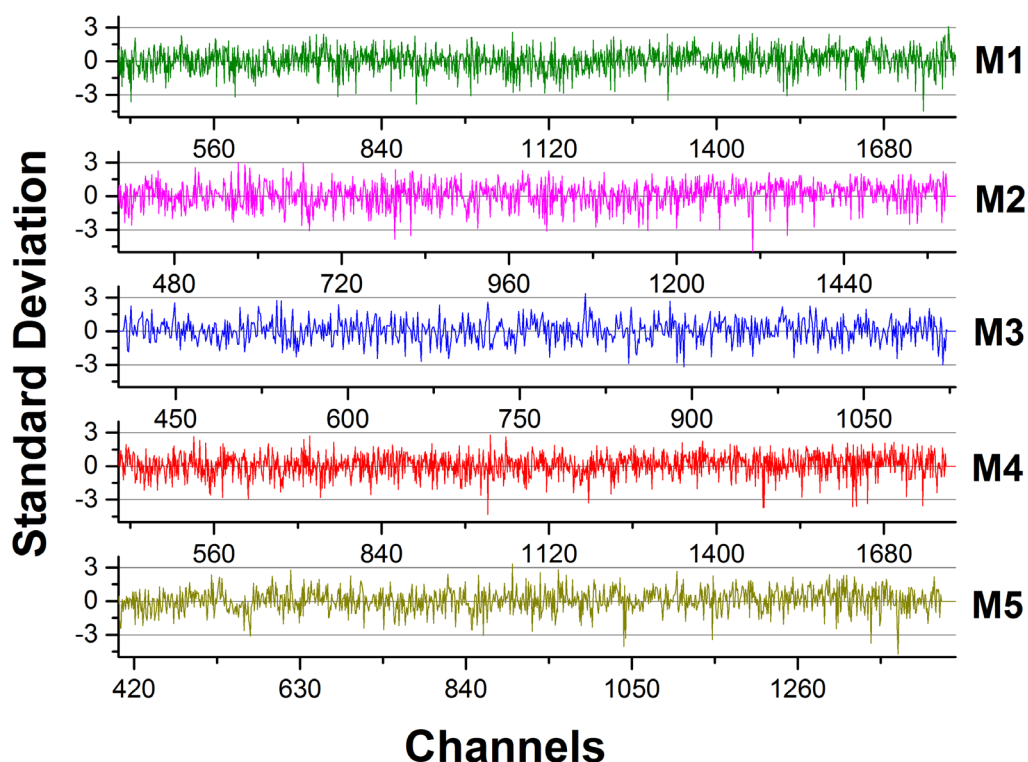


Fig. 2.27 Standard deviation profile for decay curve fitting for molecules **M1** to **M5**

2.3.5 Cyclic voltammetry

Cyclic voltammetric studies of molecules have been performed with three electrode cell in ACN medium and tetrabutylammonium perchlorate as supporting electrolyte. The anodic peak corresponds to the oxidation of $-NH$ functionality and the cathodic peak corresponds to the reduction of keto ($C=O$) functionality. Molecule **M5** has a NO_2 and a keto functionality which can undergo reduction. The cyclic voltammogram is represented in Fig. 2.28. Further, the onset potentials of oxidation and reduction of a material can be correlated to the ionization potential (I_p) and electron affinity (E_a). The highest occupied molecular orbital (HOMO) and the lowest unoccupied molecular orbital (LUMO) have been calculated (Duvenhage et al. 2015) by using Equation 2.2 and Equation 2.3 and the energy band gap E_G deduced from Equation 2.4 for the molecules are represented in Fig. 2.29. The estimated value of HOMO and LUMO for molecules **M1** to **M5** is tabulated in Table 2.5.

$$I_p = -(E_{OX} + 4.4) \text{ eV} \quad \text{Eq. 2.2}$$

$$E_a = -(E_{RED} + 4.4) \text{ eV} \quad \text{Eq. 2.3}$$

$$E_G = (E_a - I_p) \text{ eV} \quad \text{Eq. 2.4}$$

Table 2.5 Estimation of HOMO, LUMO and bandgap of molecule **M1** to **M5** from electrochemical studies

Molecule	I_{ox} (V) ^a	E_{red} (V) ^b	E_{HOMO} (eV)	E_{LUMO} (eV)	E_g (eV)
M1	0.82	-1.43	-5.22	-2.97	2.25
M2	1.41	-0.91	-5.81	-3.49	2.32
M3	1.45	-0.87	-5.85	-3.53	2.32
M4	1.4	-0.9	-5.8	-3.5	2.3
M5	2.04	-1.22	-6.44	-3.18	3.26

^a Oxidation onset measured from cyclic voltammogram

^b Reduction onset measured from cyclic voltammogram

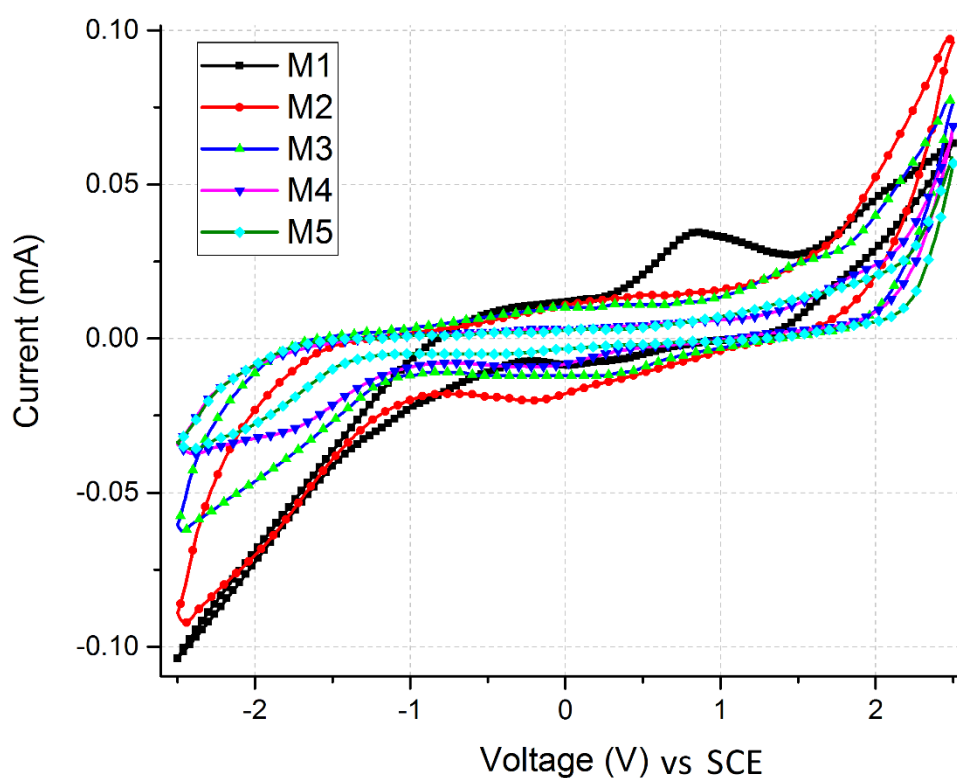


Fig. 2.28 Cyclic voltammogram of molecules **M1** to **M5**

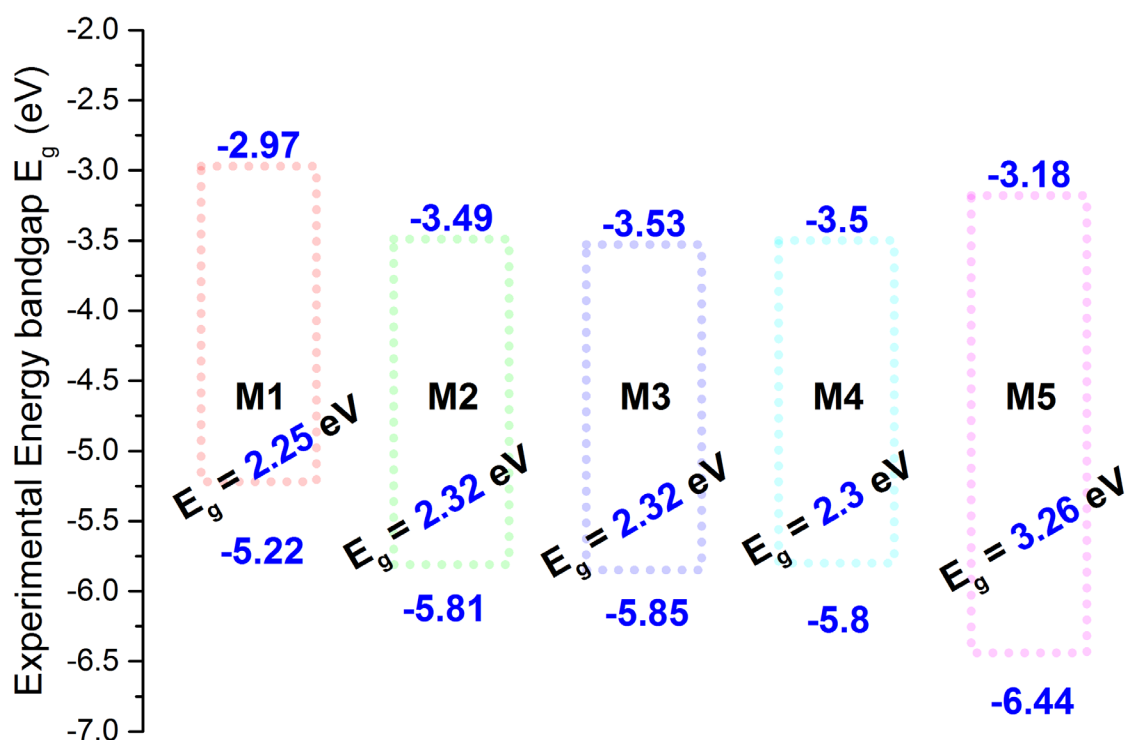


Fig. 2.29 HOMO, LUMO and band gap of molecule **M1** to **M5** by cyclic voltammetry

2.3.6 DFT studies

The geometrical and electronic properties of molecules **M1** to **M5** were performed using Gaussian 09 package (Frisch et al. 2009). The geometry optimization was achieved by means of B3LYP (Becke three parameters hybrid functional with Lee-Yang-Perdew correlation functionals) (Lee et al. 1988) with the 6-311++G (d, p) basis set (Hariharan and Pople 1973; Hehre et al. 1972). The molecules **M1** to **M5** with their optimized geometry and their dihedral angle is shown in the Fig. 2.30. Highest occupied molecular orbitals and lowest unoccupied molecular orbitals were visualized using Avogadro software (Hanwell et al. 2012). Vertical transition energies of singlet excited states in gas phase was estimated. Oscillator strengths for all the structures were estimated using time-dependent DFT method (TD-DFT) at the same level of calculation with the same basis set that was used for ground state optimization.

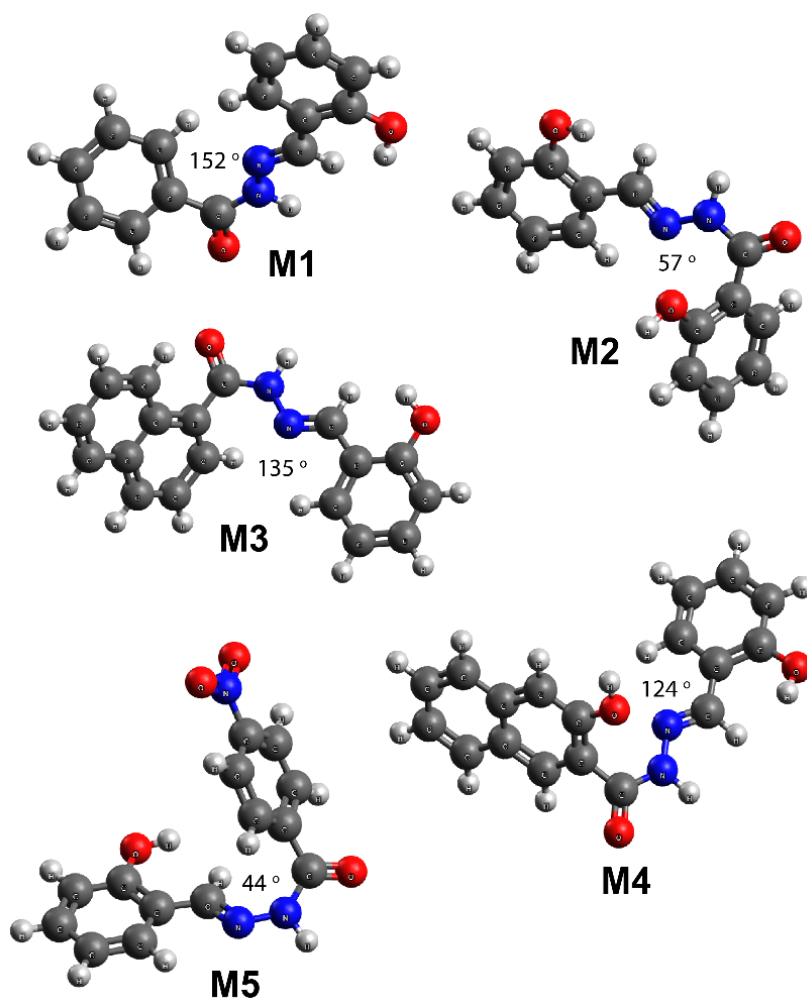


Fig. 2.30 DFT optimized structures of the molecules **M1** to **M5** with their dihedral angle.

TD-DFT calculation under the same basis set with vertical transition energies up to first 20 singlet excited states for all the molecules under various solvents have been estimated. The effect of solvent on the energy parameters has been incorporated by self-consistent reaction field using inbuilt conductor polarizable continuum model (SCRF-CPCM) (Tomasi and Persico 1994) as implemented in Gaussian 09 software. The energy distribution diagram in gas phase representing HOMO and LUMO is shown in Fig. 2.31. Molecules **M1** to **M4** have their LUMO energy distributed on the entire molecule except for **M5** where it is localized on nitro phenyl moiety. HOMO is localized on salicylaldehyde and the imine group for molecules **M1**, **M2** and **M5**, whereas it is delocalized on the entire molecule for **M3** and localized on naphthohydrazide for **M4**. Charge transfer transition is occurring between the salicylaldehyde and the entire molecular network as seen in the spatial distribution. The corresponding UV-Vis spectra are represented in Fig. 2.32 to Fig. 2.36. Computed electronic transitions obtained for the molecules **M1** to **M5** were in good

agreement with the experimentally obtained absorbance. The overall trend of the spectrum remained the same in comparison with the experimental results and the discrepancies seen in the energy transition may be attributed to the theoretical overestimation.

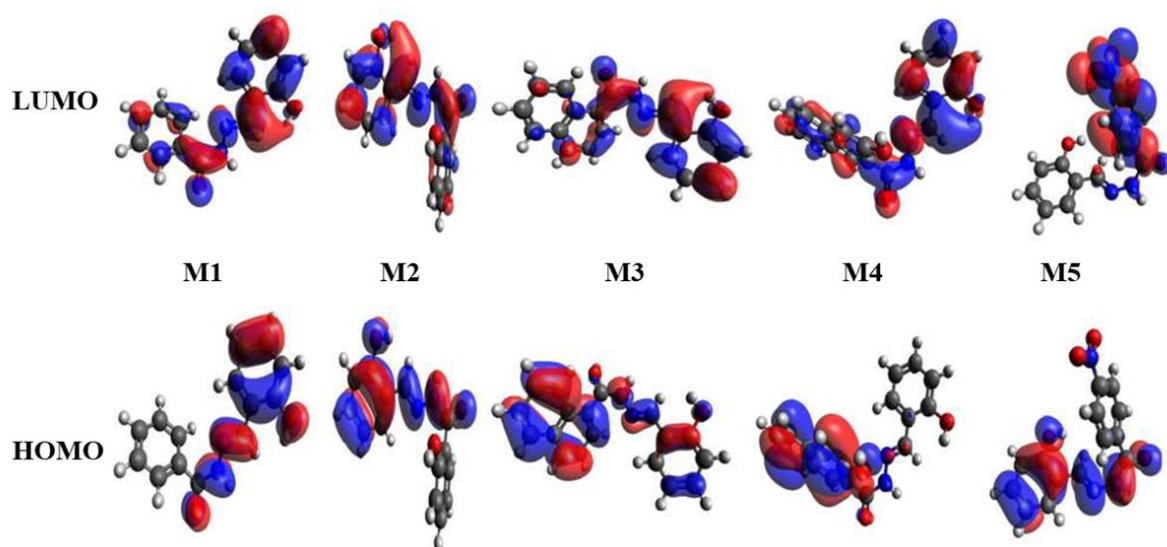


Fig. 2.31 Representation of energy distribution in molecules **M1** to **M5** in gas phase

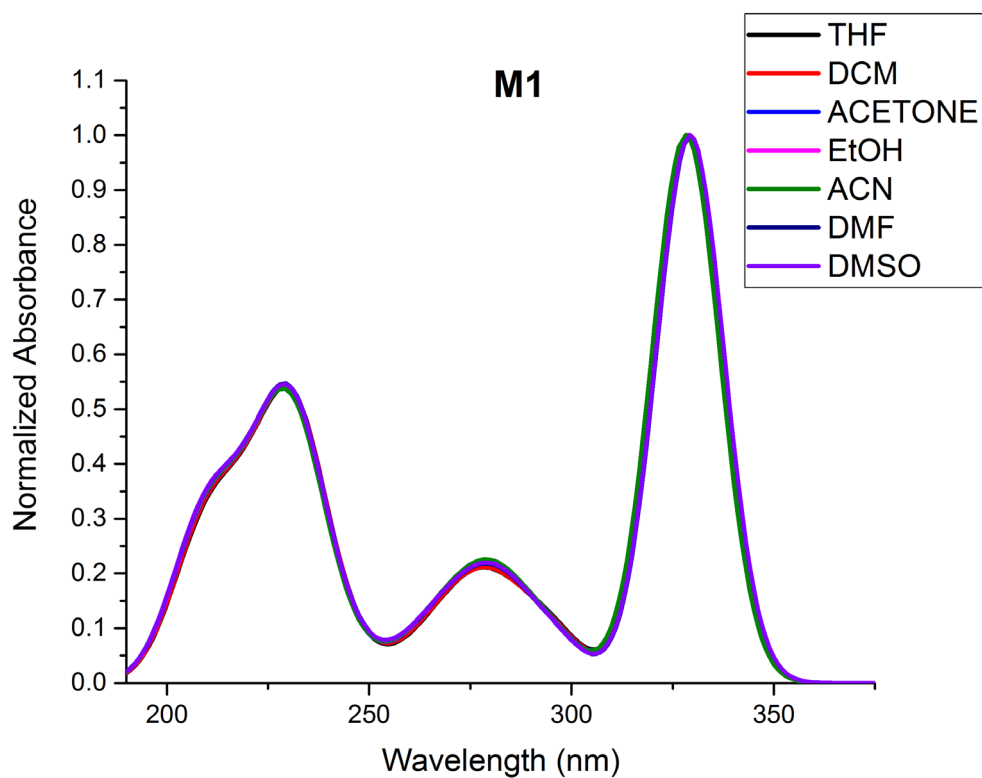


Fig. 2.32 Theoretical UV-Vis spectra of molecule **M1** in various solvent.

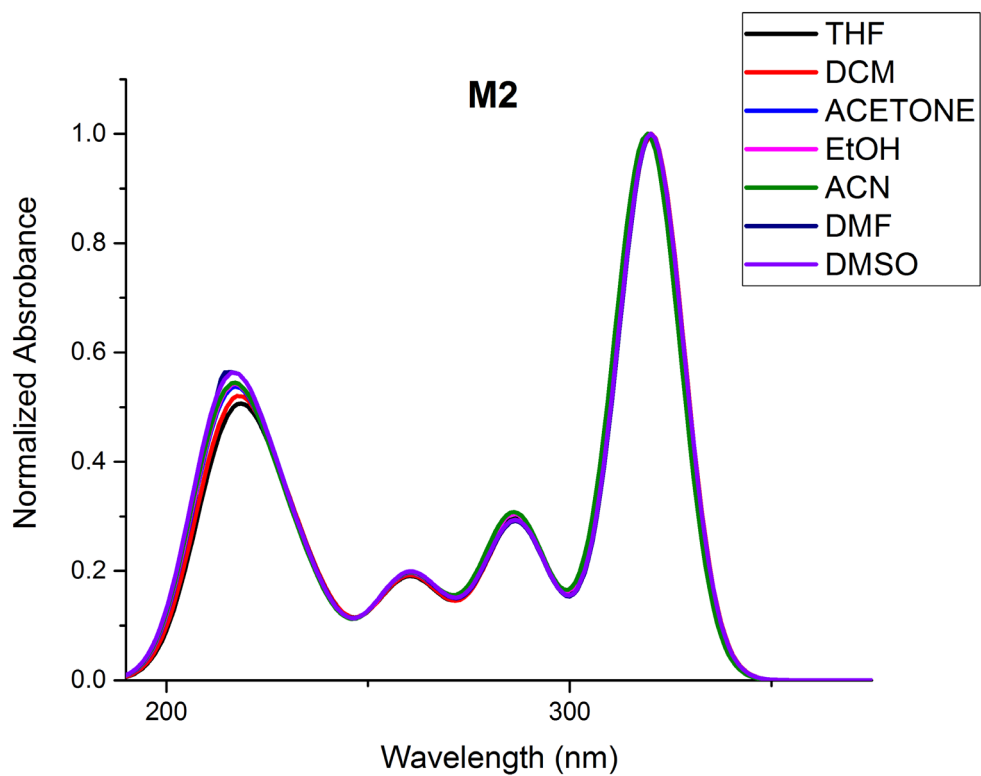


Fig. 2.33 Theoretical UV-Vis spectra of molecule **M2** in various solvents

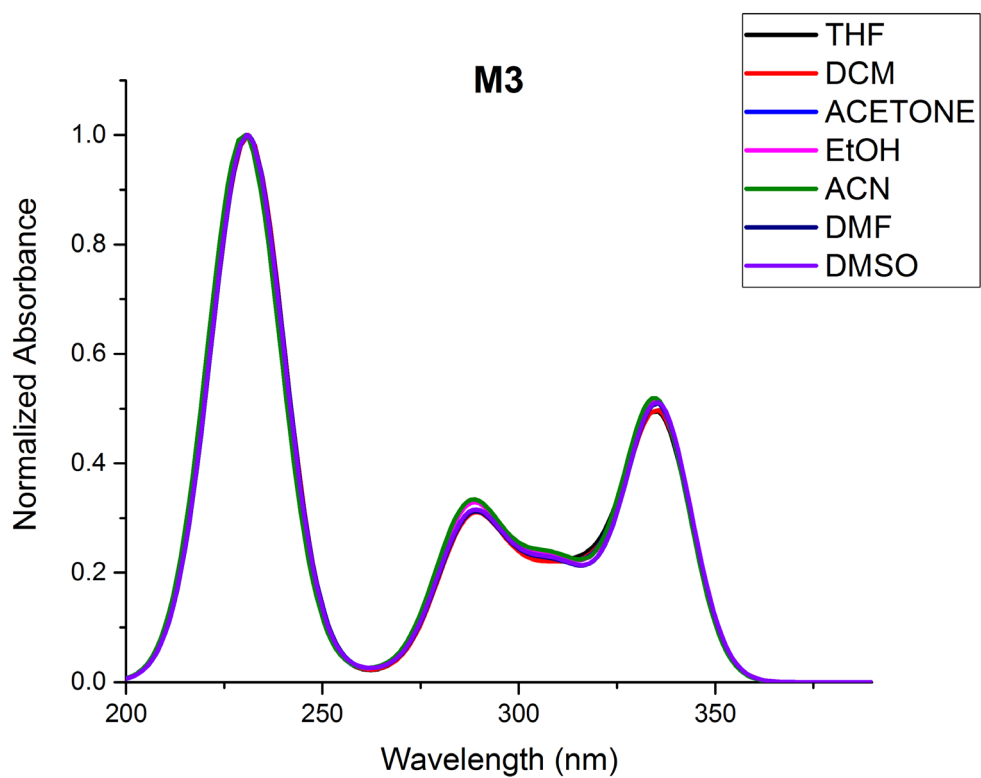


Fig. 2.34 Theoretical UV-Vis spectra of molecule **M3** in various solvents

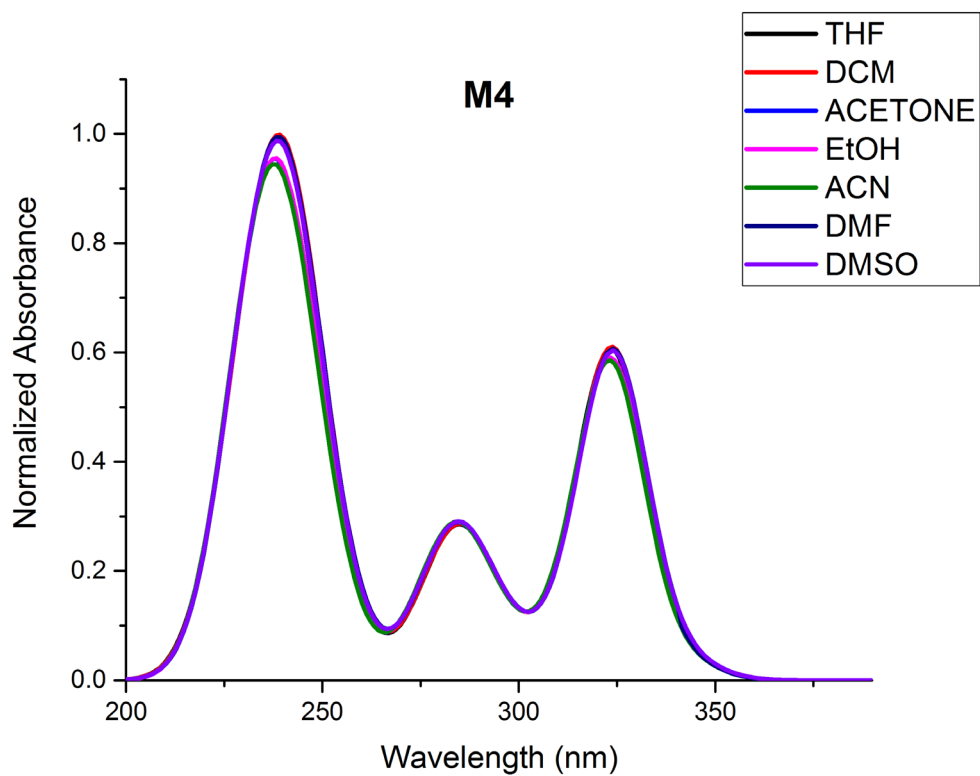


Fig. 2.35 Theoretical UV-Vis spectra of molecule **M4** in various solvents

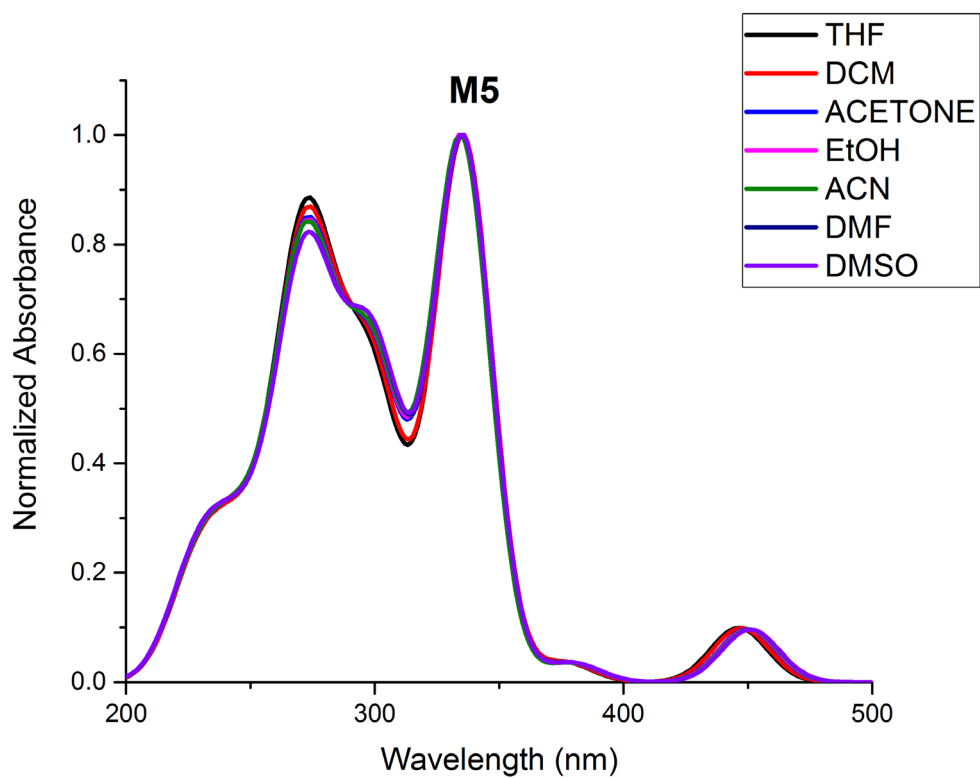


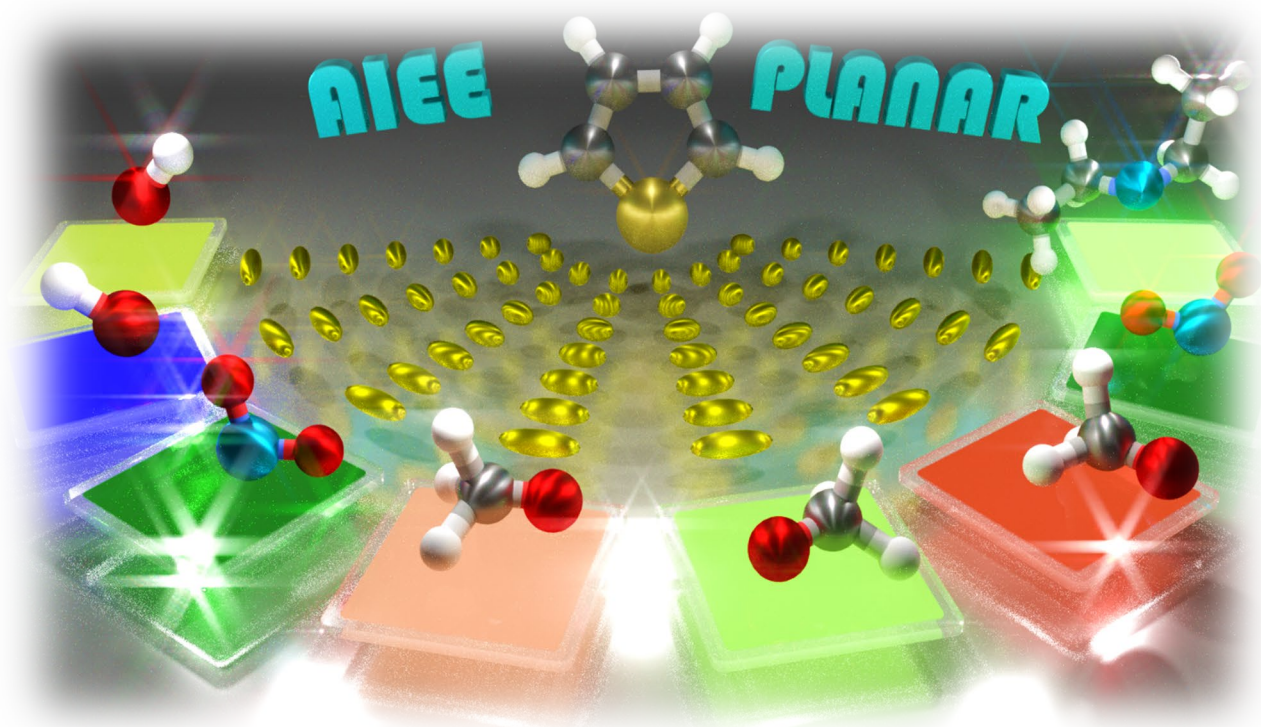
Fig. 2.36 Theoretical UV-Vis spectra of molecule **M5** in various solvents

2.4 CONCLUSIONS

Molecules **M1** to **M5** have been synthesized by Schiff's base condensation reaction in good yield and characterized by standard spectroscopic techniques like FT-IR, ¹H-NMR and DSC. Solvent dependent studies of molecules **M1** to **M5** exhibited a meager linear correlation between the solvent polarity and the observed red shift value. This confirmed the solute-solvent interaction dominating over the hydrogen bond accepting nature of the solvents. Fluorescent quantum yield determined for the molecules resulted in **M2** exhibiting a high quantum yield of 35% in comparison with the others. Fluorescent lifetime measurement carried out on all the molecules show a multicomponent lifetime value with an average lifetime of ~5 ns. Ground state optimized geometry of the molecules shows the molecules to possess a good amount of steric hindrance. Excited state energy calculations on the ground state optimized geometry estimates the probability of electronic transitions in the system that correlates well with the experimental UV-Vis spectra.

CHAPTER 3

MULTICOLOURED THIOPHENE BASED AIEGENS: SINGLE CRYSTAL STRUCTURE ELUCIDATION, SPECTRAL BEHAVIOUR AND DFT STUDIES



*Mohan, M., Pangannaya, S., Satyanarayan, M. N., and Trivedi, D. R. (2018b). "Multicoloured Thiophene Based AIEgens: Single Crystal Structure Elucidation, Spectral Behaviour and DFT Studies." **ChemistrySelect**, 3(13), 3803–3813.*

Abstract

A series of Schiff base thiophene derivatives, D1 to D9, which exhibits a phenomenon of aggregation-induced emission enhancement (AIEE) have been synthesised. Multi-coloured emission enhancement has been achieved just by introduction of electron donating and withdrawing substituent on the thiophene moiety.

3.1 INTRODUCTION

Small organic molecules that exhibit a phenomenon of aggregation induced emission enhancement (AIEE) is gaining considerable interest. Aggregation induced emission (AIE) molecules have multitude of applications in the fields of solid state electronics such as organic light emitting diodes (OLED), photovoltaic devices (Buyruk et al. 2016; Hadsadee et al. 2017; Mandal and Ramanujam 2016; Zara et al. 2017), and photofunctional materials (Asahi et al. 2008; Chan et al. 2002; Chung et al. 2009; Friend et al. 1999; Jones et al. 2017; Kumbhar et al. 2016; Samuel and Turnbull 2007; Scherf et al. 2001; Tian et al. 2017; Zhu et al. 2003). High device efficiency can be achieved if the luminophores used in devices would show an enhanced emission in solid-state supporting AIE phenomenon. Generally, conventional luminophores exhibit good emission in diluted medium and rather show a weaker emission in solid state due to the intense intermolecular π - π stacking, a phenomena generally termed as Aggregation Caused Quenching (ACQ) (Li and Li 2017). The occurrence of π - π stacking interactions lead to the formation of aggregative species such as delocalized excitons and excimer that has always been a hindrance in the development of efficient OLEDs (Hong et al. 2011). In contrast to ACQ, various mechanisms have been proposed supporting AIE behaviour in luminophores via restriction of intramolecular rotation (Chan et al. 2002; Luo et al. 2001; Tong et al. 2006; Yu et al. 2005), formation of J-aggregates, intramolecular planarization, inhibition of photoisomerization, photocyclization and blockage of nonradiative relaxation pathways of the excited species (An et al. 2002; Bao et al. 2006; Bhongale et al. 2005; Han et al. 2006; Itami and Yoshida 2006; Jayanty and Radhakrishnan 2004; Li et al. 2015; Sun et al. 2006; Toal et al. 2005; Tracy et al. 2005; Wang et al. 2005; Xie et al. 2006; Yeh et al. 2003). In general, AIE materials have twisted type structure that avoids possible intermolecular π - π interactions. However, in contrast to twisted type, certain planar type conjugated molecules do exhibit AIE wherein the excimer responsible for the emission appear to be in pairwise stacking state or the π - π stacking interactions is

absent in their resultant molecular packing arrangement. Moreover, design of a better molecular structure and their supportive solid state molecular packing arrangements play a crucial role in achieving an efficient AIEE (Li and Li 2017).

Amongst the various reported AIE fluorophores, thiophene based materials have gained a major interest due to their simplistic synthesis and excellent AIE effect. A series of thiophene derivatives that exhibit emission intensity proportional to the number of conjugated thiophene units have been reported by Shirota and coworkers (Noda et al. 1997, 1999). Moreover, thiophene moiety is reported to induce enhanced film forming ability and overall high thermal stability (Noda and Shirota 1998). Depending on the type of additional aromatic groups attached, thiophene derivatives are known to exhibit either electron transporting, hole transporting (Cho et al. 2003), or bipolar characteristics (Doi et al. 2003). Owing to the synthetic flexibility and the strong polarizability of the sulfur atoms giving rise to strong S---S and S— π intermolecular interactions for contributing high charge mobility (Hutchison et al. 2005; Muruganantham et al. 2017), thiophene based materials have been the focus of research. Researchers have extensively studied the AIE effect of various organic molecules and validated by photophysical, electrochemical and DFT studies (Arathi et al. 2016; Kothavale et al. 2017; Maragani et al. 2017; Padalkar et al. 2017; Pathak et al. 2016; Srinivasan et al. 2017; Yao and Qian 2018; Zhou et al. 2016). Suitable substitution of electron donating and electron withdrawing substituents on the aromatic ring covalently linked to the thiophene moiety, leads to multitudes of emission with varying intensity. With this in view, a series of nine derivatives have been synthesized by Schiff base condensation reaction of thiophene carboxylic acid hydrazide and various substituted aromatic aldehydes. Molecule **D1** has no substituent and is used as a control sample. In comparison with **D1**, the role of substituent on the fluorescent behaviour of molecules **D2** to **D9** was investigated. **D2** and **D3** possess electron rich —OH functionality appended at position ortho and para respectively to the covalently linked heterocyclic ring. **D4** comprising of electron withdrawing —NO₂ functionality imparts electron deficient nature to the molecule. **D5** consist of an electron donating —OC₂H₅ appended at positions meta, whereas **D6** and **D7** consists of —OCH₃ functionality, appended at para and meta positions to the covalently linked thiophene unit. Molecule **D8** differs from **D7** in possessing an electron withdrawing —NO₂ group at position para to —OH functionality. Molecule **D9** comprises of highly electron donating dimethyl amino

functionality at position para to the imine linked thiophene ring and is known to have profound influence on the fluorescent emission.

3.2 EXPERIMENTAL SECTION

3.2.1 Materials and methods

All the chemicals used in the present study were procured from Sigma-Aldrich and Alfa Aesar and were of 98% purity, used as received without further purification. All the solvents were purchased from SD Fine, India, were of HPLC grade and used without further distillation. Infrared spectrum was recorded on Bruker Apex FTIR spectrometer. UV-Vis spectroscopy was performed with analytik Jena Specord S600 spectrometer in standard 3.0 mL quartz cell with 1cm path length. The ^1H NMR spectra were recorded on Bruker Ascend (400 MHz) instrument using TMS as internal reference and DMSO- d_6 as solvent. Resonance multiplicities are described as s (singlet), d (doublet), t (triplet) and m (multiplet). Mass spectrum was recorded on Bruker Daltonics. Cyclic voltammogram was recorded on Ivium electrochemical workstation (Vertex) at a scan rate of 20 mV/s with the potential ranges from -5V to +5V. DSC analysis was performed on Shimadzu DSC-60. Single crystal X-Ray Diffraction (SCXRD) was performed on Bruker AXS APEX II system. Steady-state fluorescence emission spectra were recorded with the help of Fluoromax 4 HORIBA spectrofluorometer. Fluorescence quantum yield were determined for the series with coumarin 153 in cyclohexane as a standard. Fluorescence decay of the series was acquired employing the Time Correlated Single Photon Counting (TCSPC) technique with a nano-LED with a spectral width of 1.2 nm as an excitation source. Decay profiles were best fit with DAS6 software to estimate the fluorescence lifetime of the series. The fitting was assumed to be precise with a value of chi-sqr lower than 1.2. Molecules were thermally deposited onto chemically cleaned glass substrates under vacuum of 10^{-6} mbar to study solid state emission characteristics. All the measurements were carried out at an ambient temperature.

3.2.2 Synthesis of molecules D1 to D9

The molecules **D1** to **D9** have been synthesized by Schiff base condensation of Thiophene-2-hydrazide with various substituted aldehydes namely, benzaldehyde; salicylaldehyde; 4-hydroxy benzaldehyde; 4-nitrobenzaldehyde; 3-ethoxy 2-hydroxy benzaldehyde; 2-hydroxy, 4-methoxy benzaldehyde; 2-hydroxy 5-methoxy benzaldehyde;

2-hydroxy, 5-nitrobenzaldehyde and *p*-diethylamino 2-hydroxy benzaldehyde respectively. The reactants were weighed and transferred to round bottom flask and to it 5 ml of ethanol and a drop of acetic acid was added. The reaction mixture was refluxed for about 4 hrs at 78 °C to get the desire product. The structure of the molecules **D1** to **D9** are represented in Scheme 3.1. All the synthesized molecules have been well characterized by standard spectroscopic techniques as provided in Fig. 3.1 to Fig. 3.27. DSC analysis were carried out to measure the melting point of few of the molecules and the results are provided in the Fig. 3.28 and Fig. 3.30.

D1 (E)-N'-benzylidenethiophene-2-carbohydrazide, Yield: 80%., ¹H NMR (DMSO-d₆, 400 MHz, ppm): δ 11.89 (s, NH), 8.45 (s, Ar-H), 8.13-8.07 (dd, Ar-H), 7.98-7.89 (d, 2Ar-H), 7.82-7.71 (ddd, 2Ar-H), 7.52-7.71 (ddd, 3Ar-H), 7.2 (s, N=CH). FT-IR (cm⁻¹): (C=N) 1638, (C-H) 2951, (NH) 3233. ESI-MS Calculated: 230.05, Obtained: 231.05 (M+H⁺)

D2 (E)-N'-(2-hydroxybenzylidene)thiophene-2-carbohydrazide, Yield: 67%., ¹H NMR (DMSO-d₆, 400 MHz, ppm): δ 12.12 (s, NH), 11.11 (s, OH), 8.63 (s, N=CH), 8.44 (s, Ar-H), 7.90-7.96 (d, 2Ar-H), 7.58 (d, Ar-H), 7.25 (s, Ar-H), 6.91-6.92 (d, 2Ar-H). FT-IR (cm⁻¹): (C=N) 1610, (C-H) 3027, (NH) 3182, (OH) 3340. ESI-MS Calculated: 246.05, Obtained: 247.00 (M+H⁺)

D3 (E)-N'-(4-hydroxybenzylidene)thiophene-2-carbohydrazide, Yield: 78%., ¹H NMR (DMSO-d₆, 400 MHz, ppm): δ 11.65 (s, NH), 9.99 (s, OH), 8.33 (s, N=CH), 8.02-7.96 (ddd, 3Ar-H), 7.63--7.56 (dd, 2Ar-H), 7.24 (s, Ar-H), 6.85-6.86 (d, 2Ar-H). FT-IR (cm⁻¹): (C=N) 1597, (NH) 3116, (OH) 3225. ESI-MS Calculated: 246.05, Obtained: 247.00 (M+H⁺)

D4 (E)-N'-(4-nitrobenzylidene)thiophene-2-carbohydrazide, Yield: 83%., ¹H NMR (DMSO-d₆, 400 MHz, ppm): δ 12.17 (s, NH), 8.55 (s, OH), 8.24 (s, N=CH), 8.34-8.32 (ddd, 2Ar-H), 8.03 (dd, 4Ar-H), 7.20-7.25 (dd, Ar-H). FT-IR (cm⁻¹): (C=C) 1504, (C=N) 1644, (C-H) 2808, (NH) 2830. ESI-MS Calculated: 275.04, Obtained: 273.85 (M+H⁺)

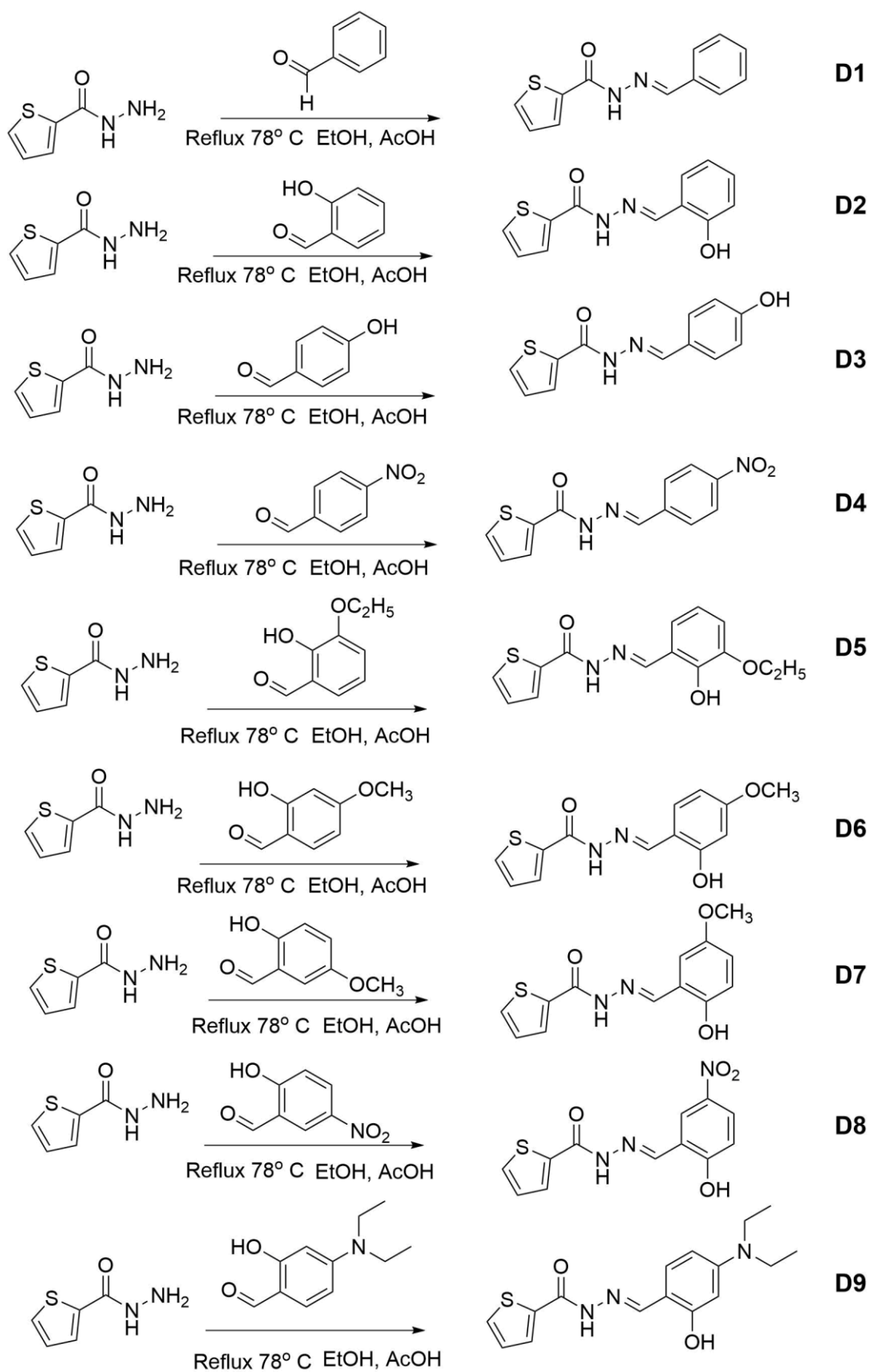
D5 (E)-N'-(3-ethoxy-2-hydroxybenzylidene)thiophene-2-carbohydrazide, Yield: 88%., ¹H NMR (DMSO-d₆, 400 MHz, ppm): δ 12.10 (s, NH), 10.76 (s, OH), 8.66 (s, N=CH), 7.92 (d, 2Ar-H), 7.26 (dd, 2Ar-H), 7.18 (d, Ar-H), 6.87 (m, 2Ar-H), 4.89 (C₂H₅, 5H). FT-IR (cm⁻¹): (C=C) 1575, (C=N) 1638, (NH) 3083, (OH) 3541. ESI-MS Calculated: 290.07, Obtained: 291.05 (M+H⁺)

D6 (E)-N'-(2-hydroxy-4-methoxybenzylidene)thiophene-2-carbohydrazide, Yield: 78%., ¹H NMR (DMSO-d₆, 400 MHz, ppm): δ 12.03 (s, NH), 11.45 (s, OH), 8.54 (s, N=CH), 7.90-7.69 (dd, 2Ar-H), 7.48 (s, Ar-H), 7.24 (s, Ar-H), 6.53-6.51 (dd, 2Ar-H), 3.79 (OCH₃, 3H). FT-IR (cm⁻¹): (C=N) 1613, (C-H) 3009, (NH) 3191, (OH) 3437. ESI-MS Calculated: 276.06, Obtained: 277.05 (M+H⁺)

D7 (E)-N'-(2-hydroxy-5-methoxybenzylidene)thiophene-2-carbohydrazide, Yield: 76%., ¹H NMR (DMSO-d₆, 400 MHz, ppm): δ 12.11 (s, NH), 10.54 (s, OH), 8.63 (s, N=CH), 8.41 (s, Ar-H), 7.99-7.94 (ddd, 2Ar-H), 7.22-7.16 (dd, 2Ar-H), 6.92-6.88 (dd, 2Ar-H), 3.76 (-OCH₃, 3H). FT-IR (cm⁻¹): (C=C) 1497, (C=N) 1573, (C-H) 2999, (NH) 3223, (OH) 3334. ESI-MS Calculated: 276.06, Obtained: 277.05 (M+H⁺)

D8 (E)-N'-(2-hydroxy-5-nitrobenzylidene)thiophene-2-carbohydrazide, Yield: 73%., ¹H NMR (DMSO-d₆, 400 MHz, ppm): δ 12.28 (s, NH), 11.99 (s, OH), 8.99-8.78 (d, Ar-H), 8.73 (s, N=CH), 8.60 (s, Ar-H), 8.43 (s, Ar-H), 8.18-8.19 (d, Ar-H), 7.27-7.26 (dd, Ar-H), 6.92-6.88 (dd, 2Ar-H), 3.76 (OCH₃, 3H). FT-IR (cm⁻¹): (C=C) 1552, (C=N) 1624, (C-H) 3025, (NH) 3063, (OH) 3289. ESI-MS Calculated: 291.03, Obtained: 289.90 (M-H⁺)

D9 (E)-N'-(4-(diethylamino)-2-hydroxybenzylidene)thiophene-2-carbohydrazide, Yield: 75%., ¹H NMR (DMSO-d₆, 400 MHz, ppm): δ 11.79 (s, NH), 11.26 (s, OH), 8.40 (s, N=CH), 7.86 (dd, Ar-H), 7.23-7.21 (dd, 2Ar-H), 6.27 (dd, Ar-H), 6.12 (d, Ar-H), 3.34(6H,(CH₃)₂) 1.12(4H,(CH₂)₂). FT-IR (cm⁻¹): (C=C) 1552, (C=N) 1624, (C-H) 3025, (NH) 3185, (OH) 3351. ESI-MS Calculated: 317.12, Obtained: 318.15 (M+H⁺)



Scheme 3.1 Structure of molecules **D1-D9**

3.2.3 Characterization data

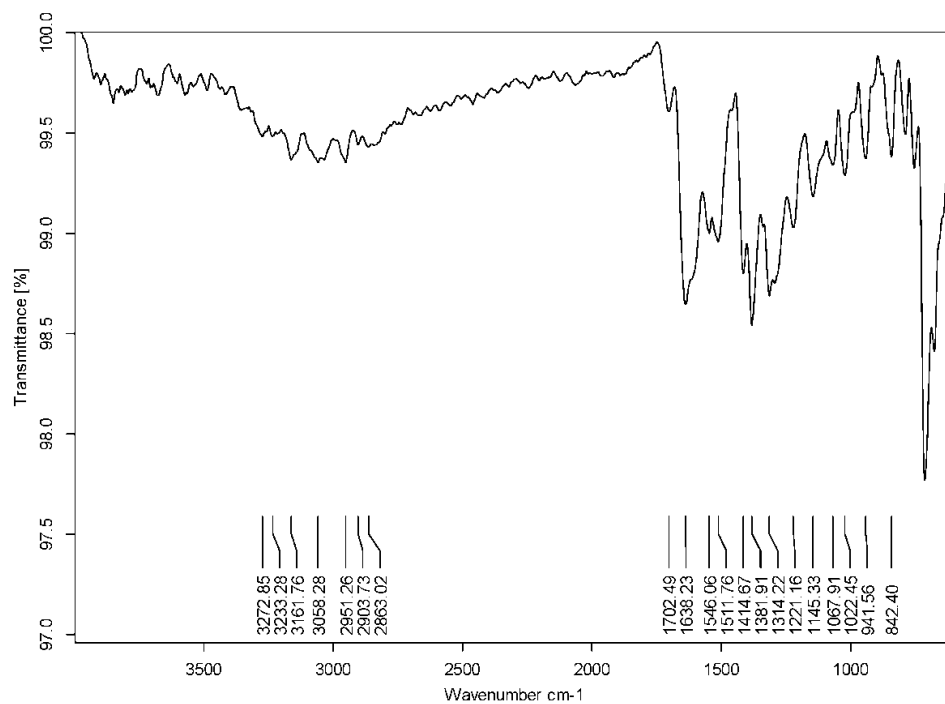


Fig. 3.1 FT-IR spectra of D1

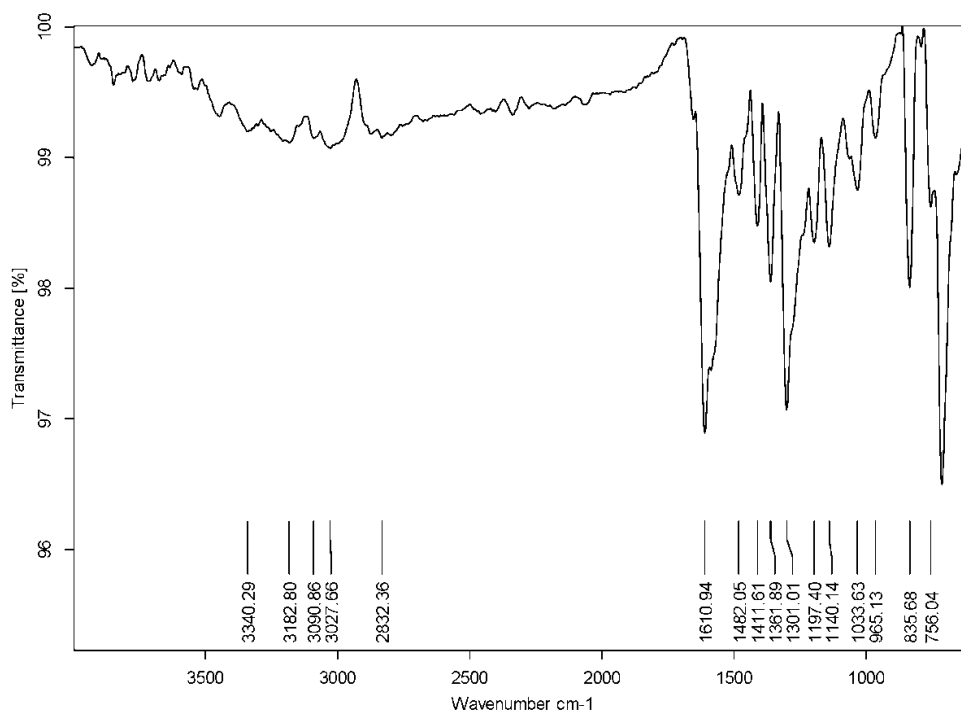


Fig. 3.2 FT-IR spectra of D2

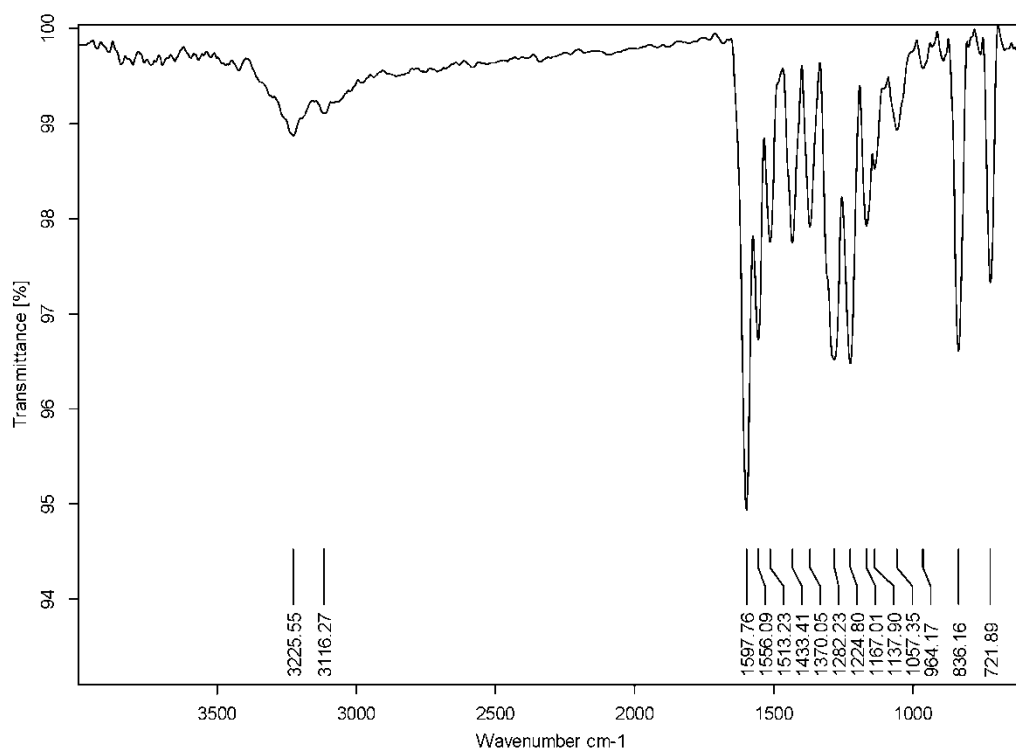


Fig. 3.3 FT-IR spectra of D3

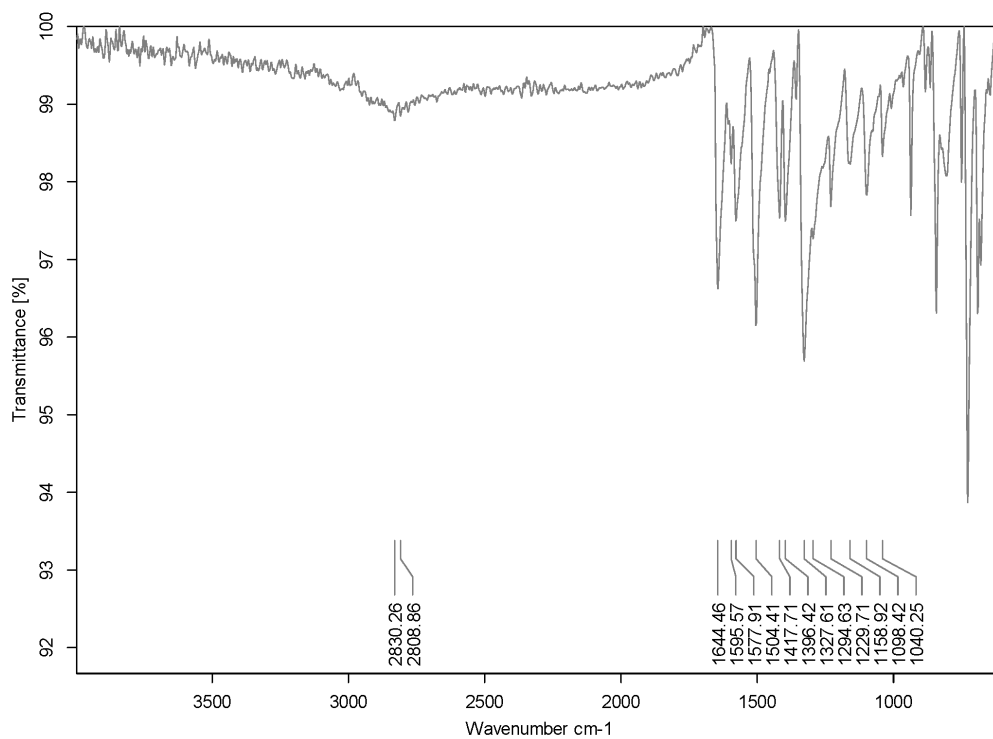


Fig. 3.4 FT-IR spectra of D4

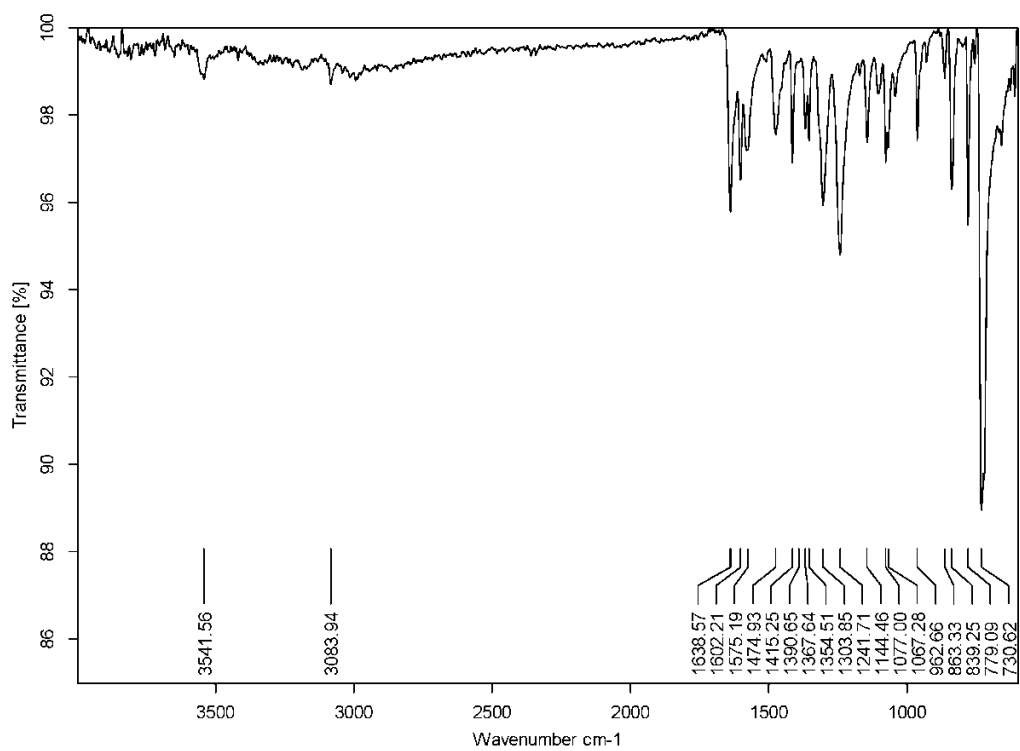


Fig. 3.5 FT-IR spectra of **D5**

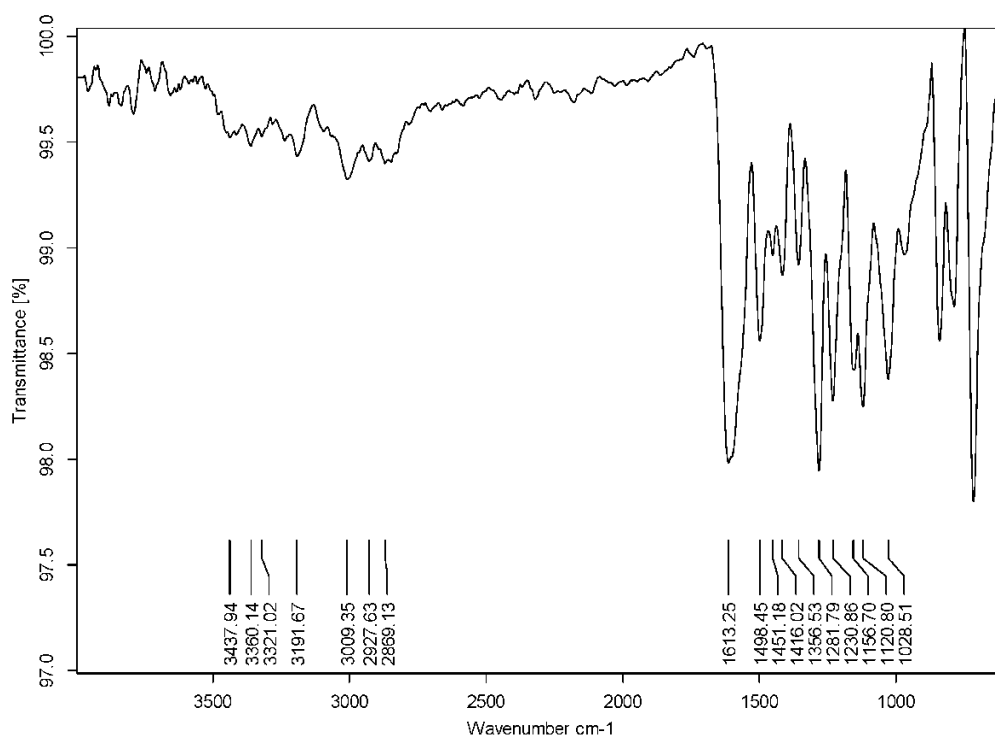


Fig. 3.6 FT-IR spectra of **D6**

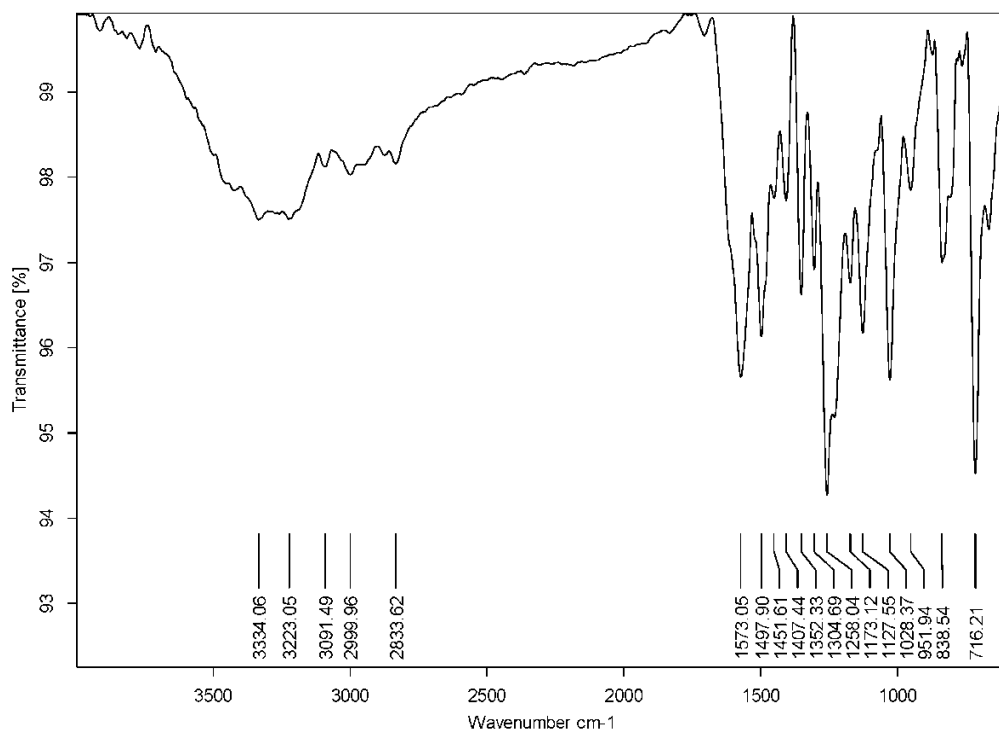


Fig. 3.7 FT-IR spectra of **D7**

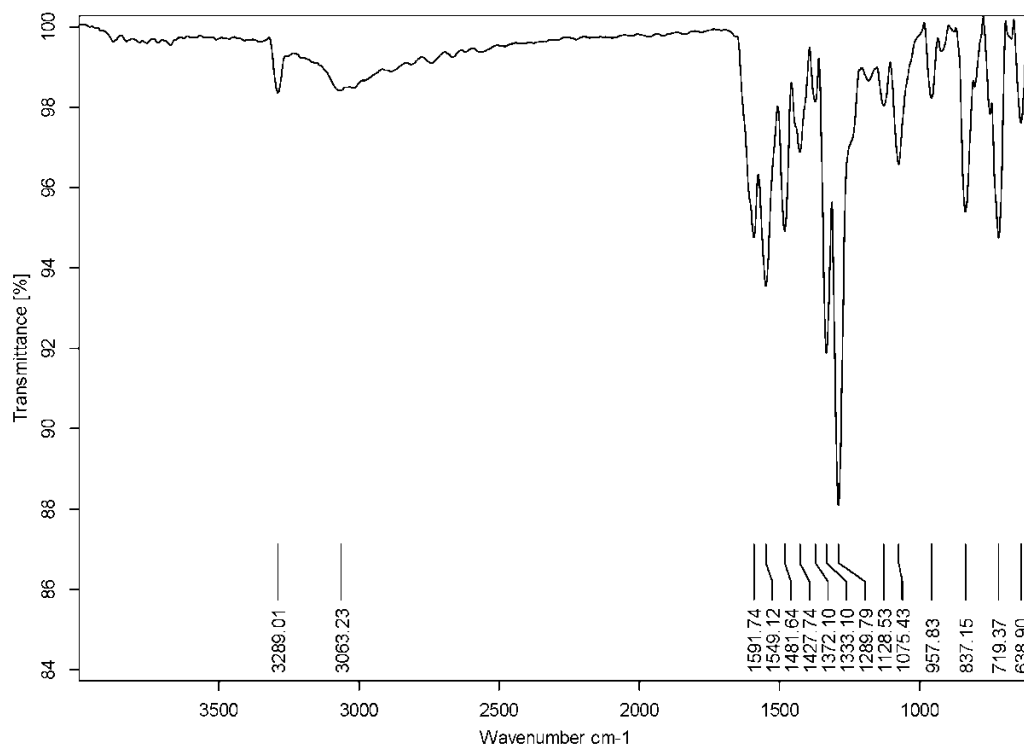


Fig. 3.8 FT-IR spectra of **D8**

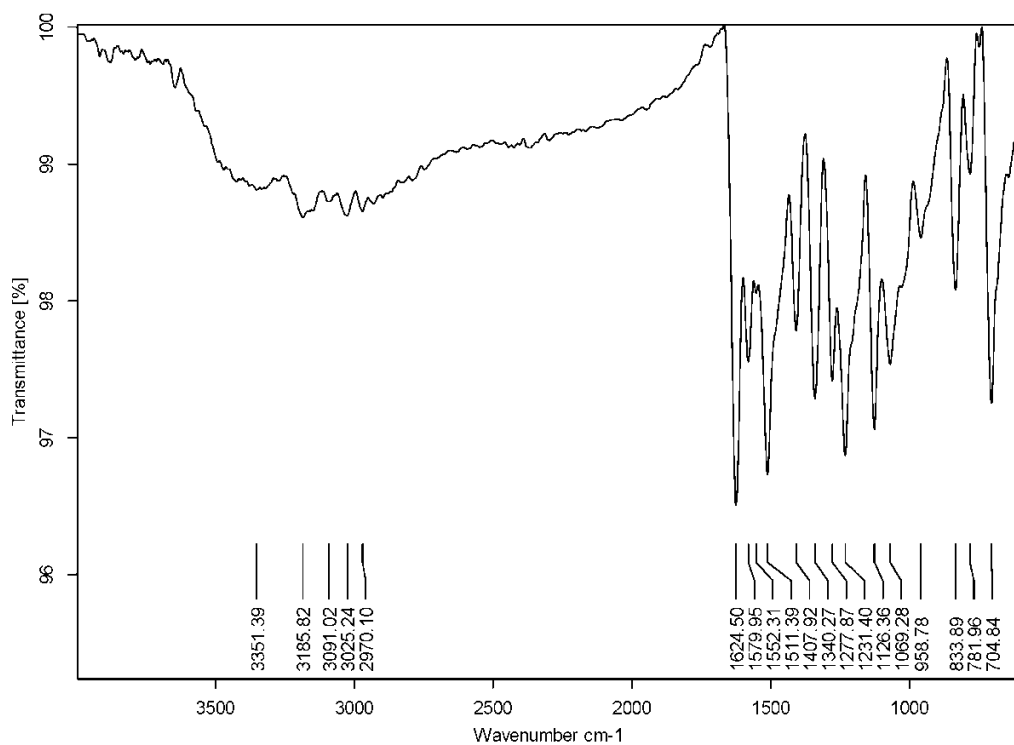


Fig. 3.9 FT-IR spectra of D9

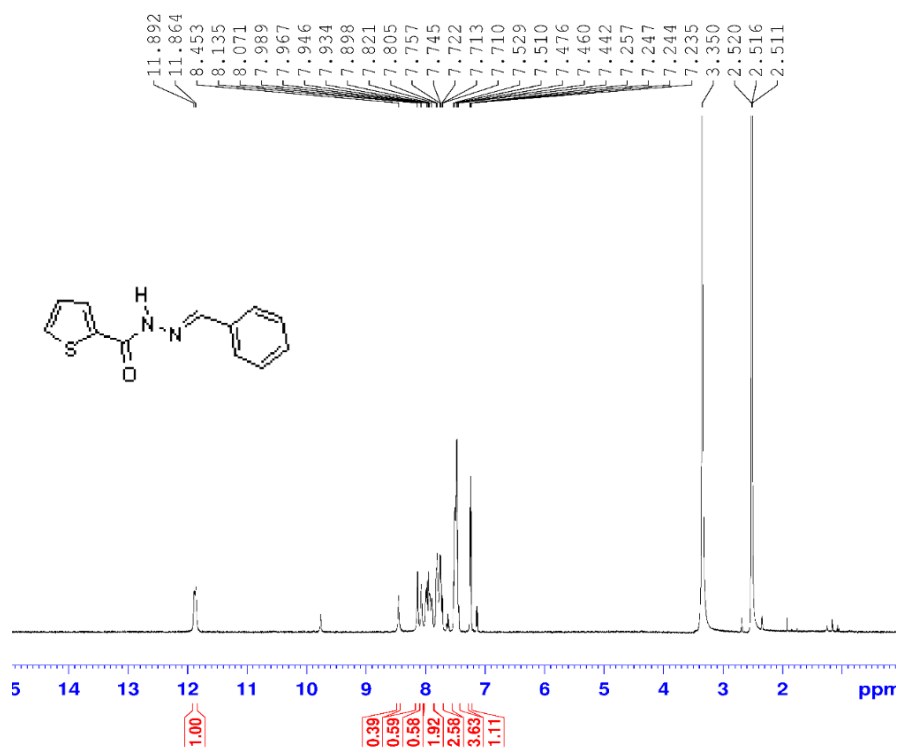


Fig. 3.10 ¹H NMR spectra of D1

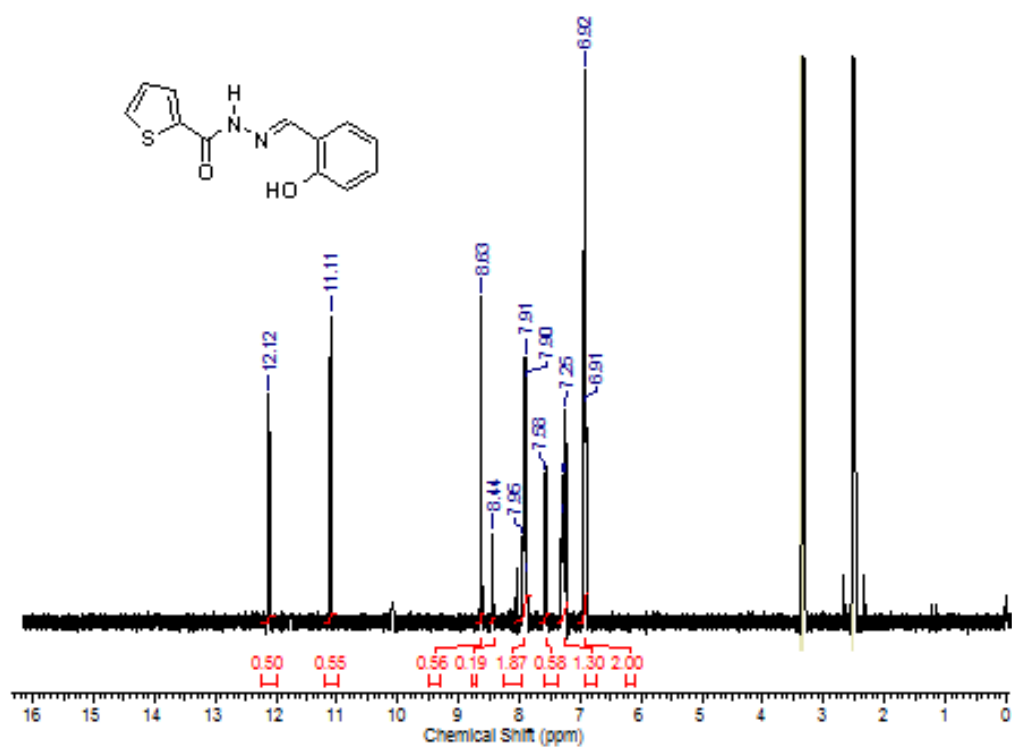


Fig. 3.11 ^1H NMR spectra of D2

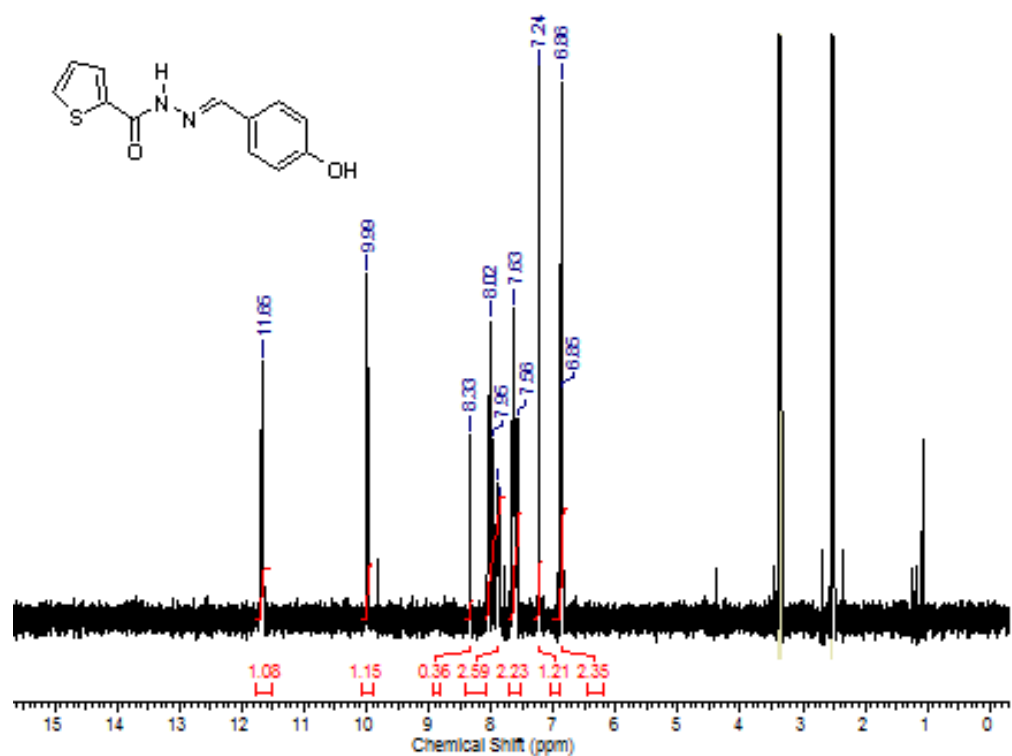


Fig. 3.12 ^1H NMR spectra of D3

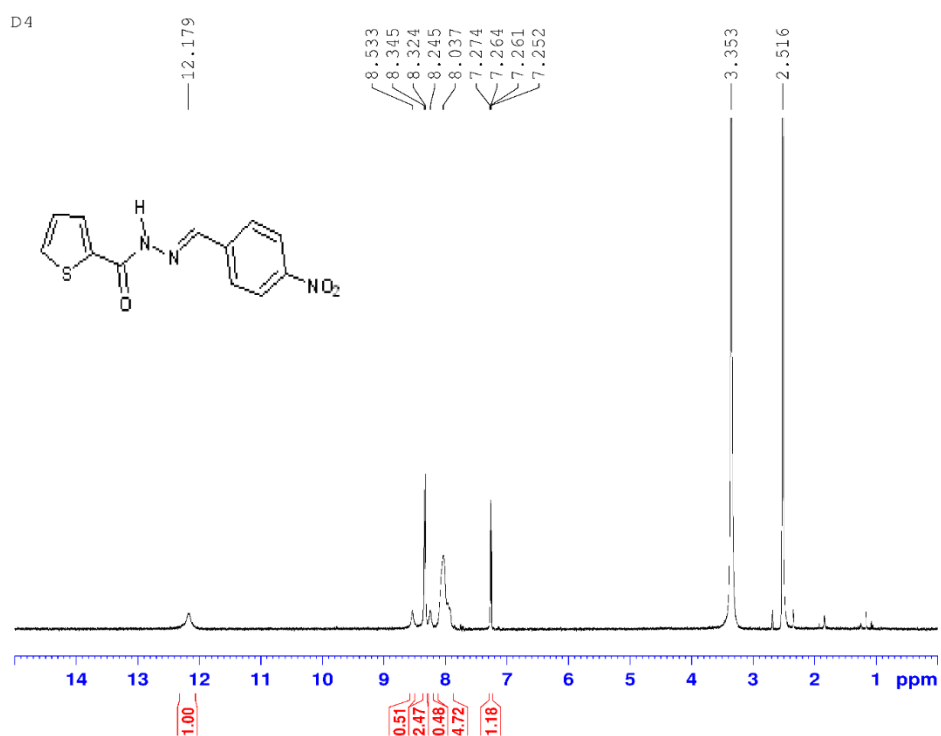


Fig. 3.13 ^1H NMR spectra of D4

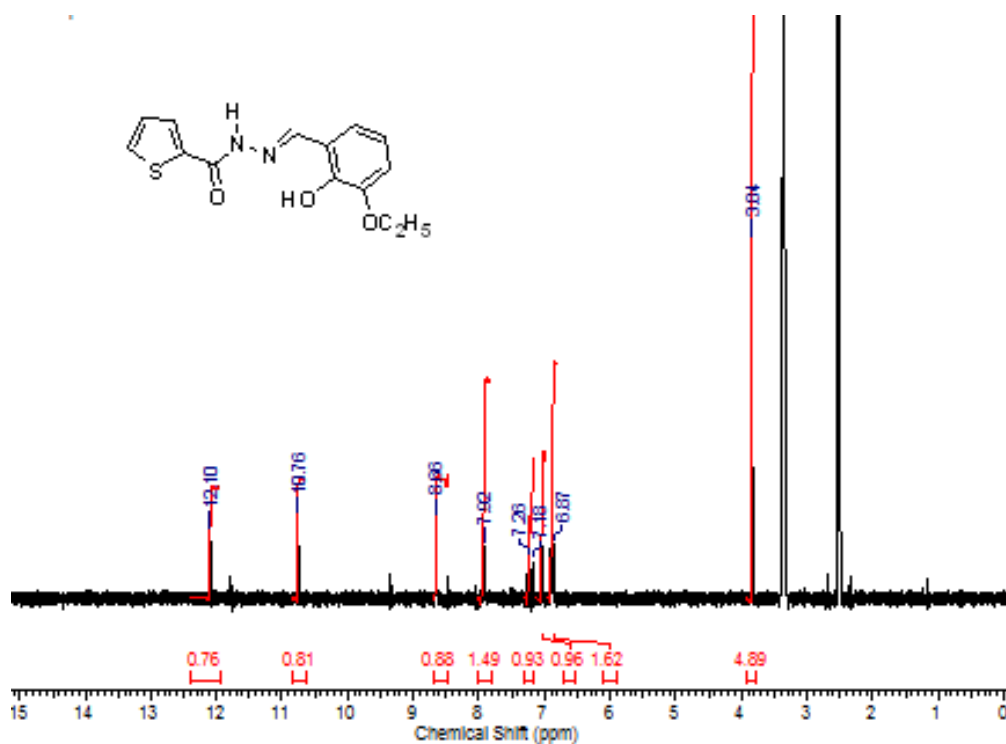


Fig. 3.14 ^1H NMR spectra of D5

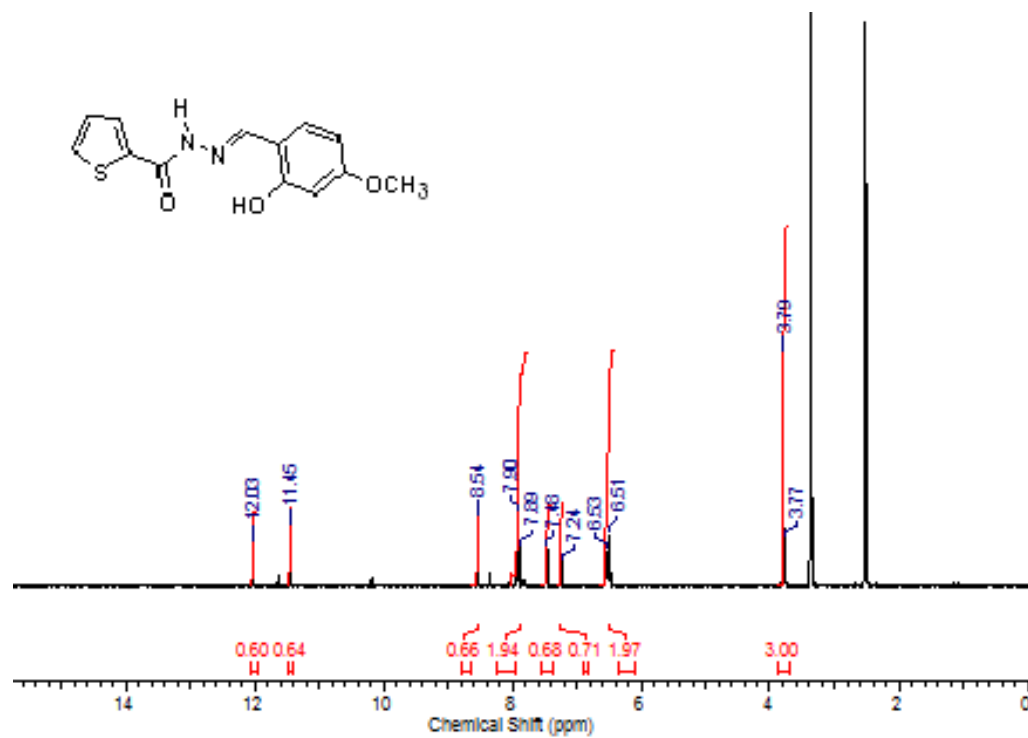


Fig. 3.15 ^1H NMR spectra of D6

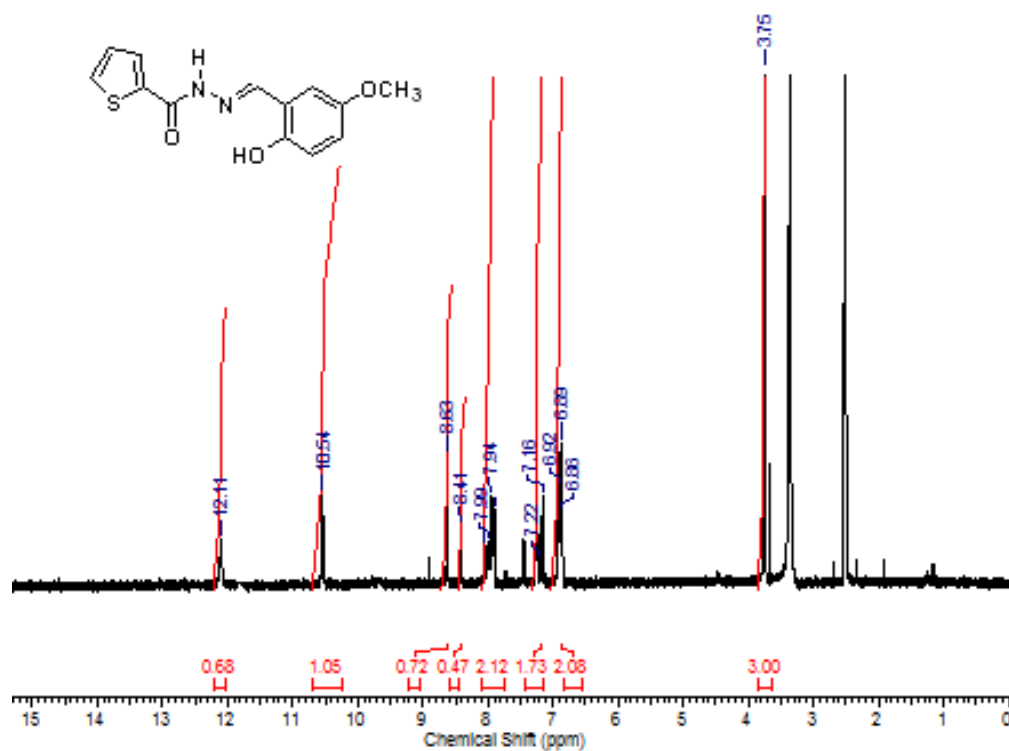


Fig. 3.16 ^1H NMR spectra of D7

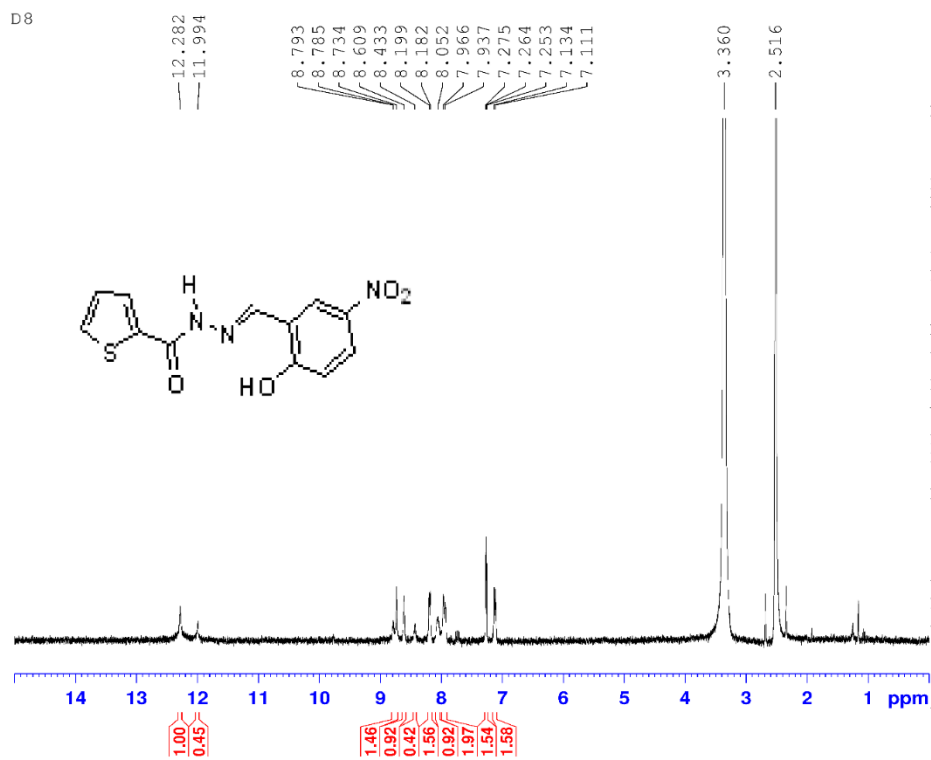


Fig. 3.17 ^1H NMR spectra of D8

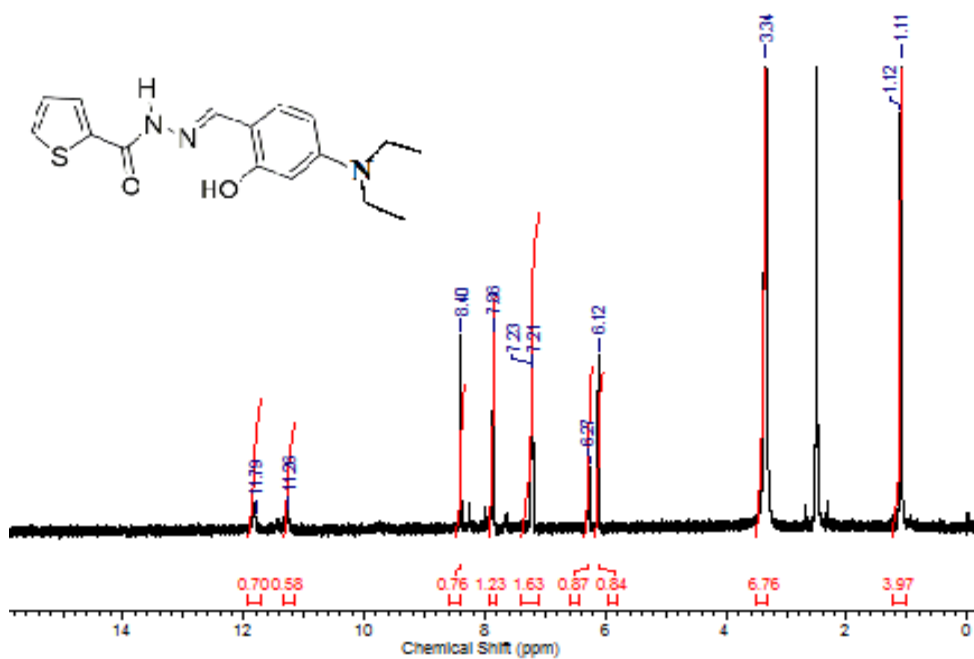


Fig. 3.18 ^1H NMR spectra of D9

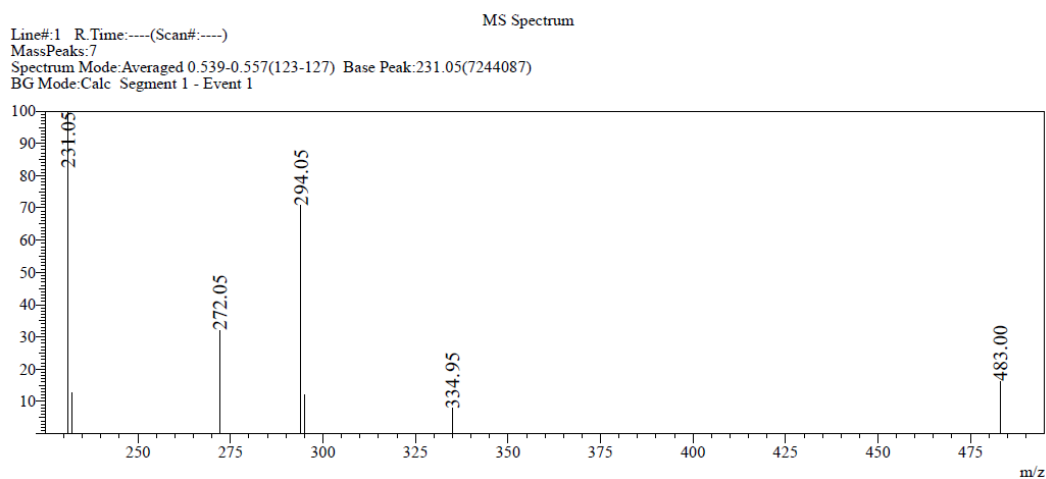


Fig. 3.19 ESI-MS spectrum of molecule **D1**

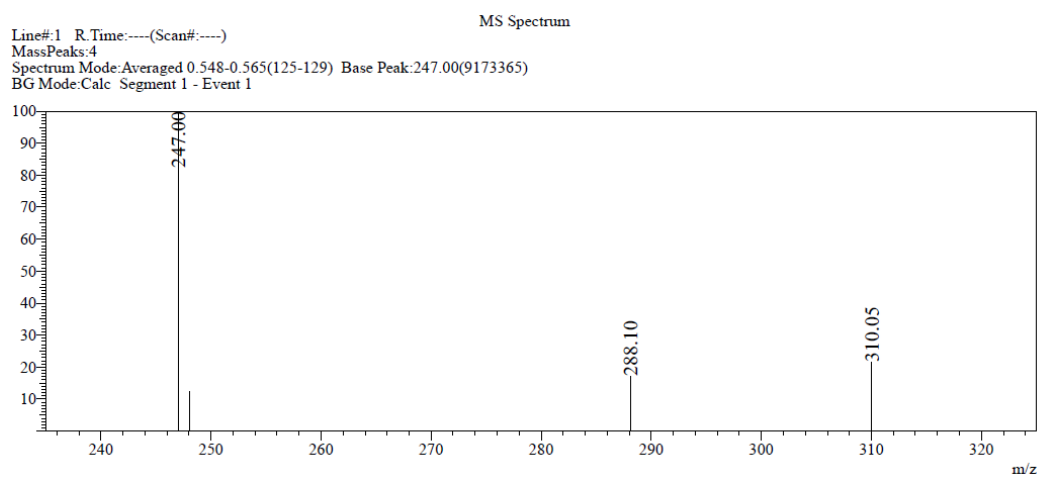


Fig. 3.20 ESI-MS spectrum of molecule **D2**

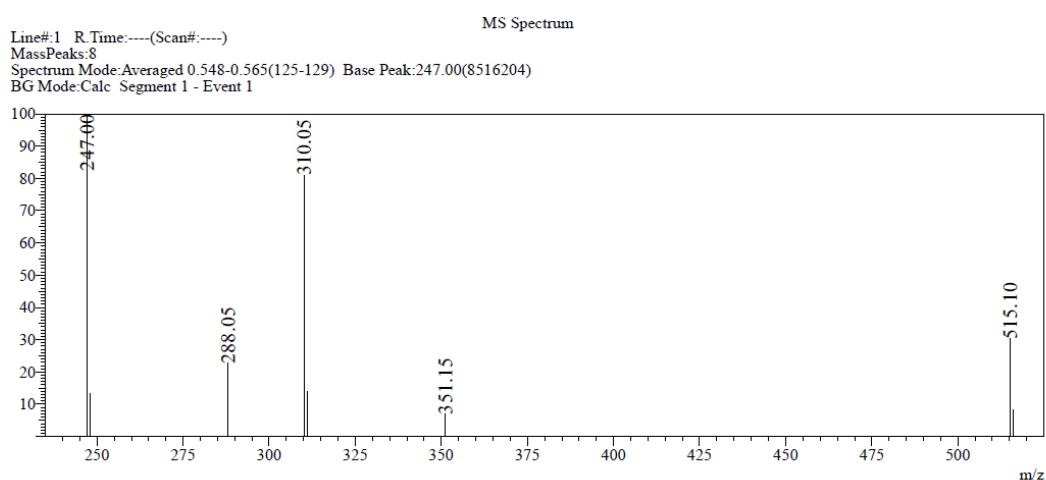


Fig. 3.21 ESI-MS spectrum of molecule **D3**

Line#:2 R.Time:----(Scan#:----)
MassPeaks:12
Spectrum Mode:Averaged 0.552-0.570(126-130) Base Peak:273.85(10565271)
BG Mode:Calc Segment 1 - Event 2

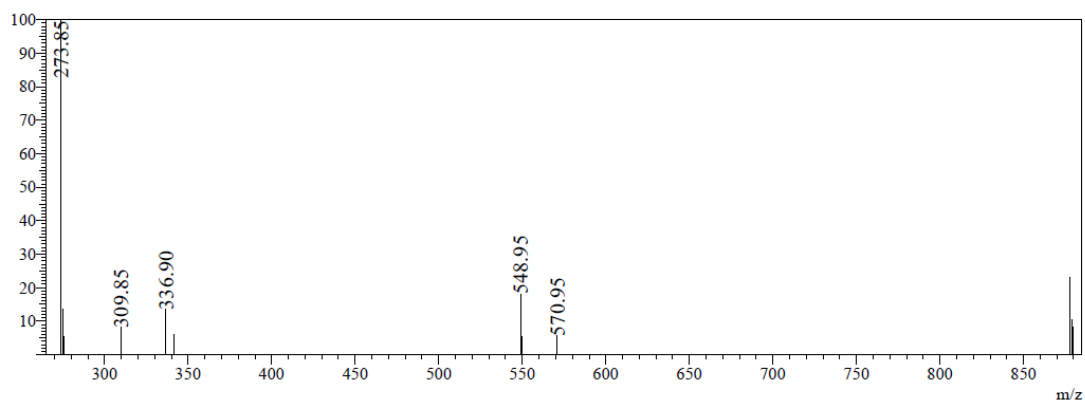


Fig. 3.22 ESI-MS spectrum of molecule D4

MS Spectrum
Line#:1 R.Time:----(Scan#:----)
MassPeaks:8
Spectrum Mode:Averaged 0.539-0.557(123-127) Base Peak:277.05(17546499)
BG Mode:Calc Segment 1 - Event 1

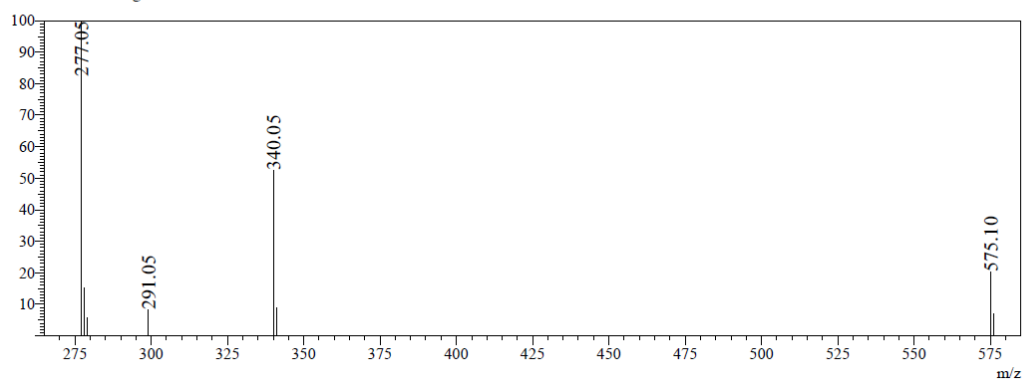


Fig. 3.23 ESI-MS spectrum of molecule D5

MS Spectrum
Line#:1 R.Time:----(Scan#:----)
MassPeaks:6
Spectrum Mode:Averaged 0.539-0.557(123-127) Base Peak:277.05(18824656)
BG Mode:Calc Segment 1 - Event 1

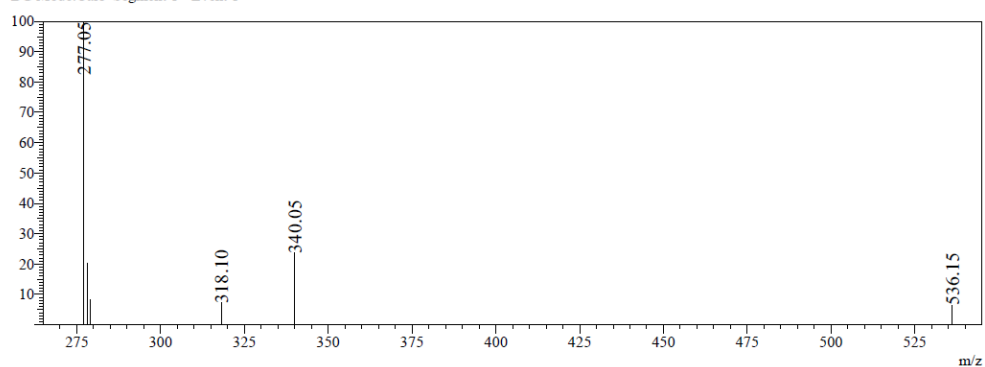


Fig. 3.24 ESI-MS spectrum of molecule D6

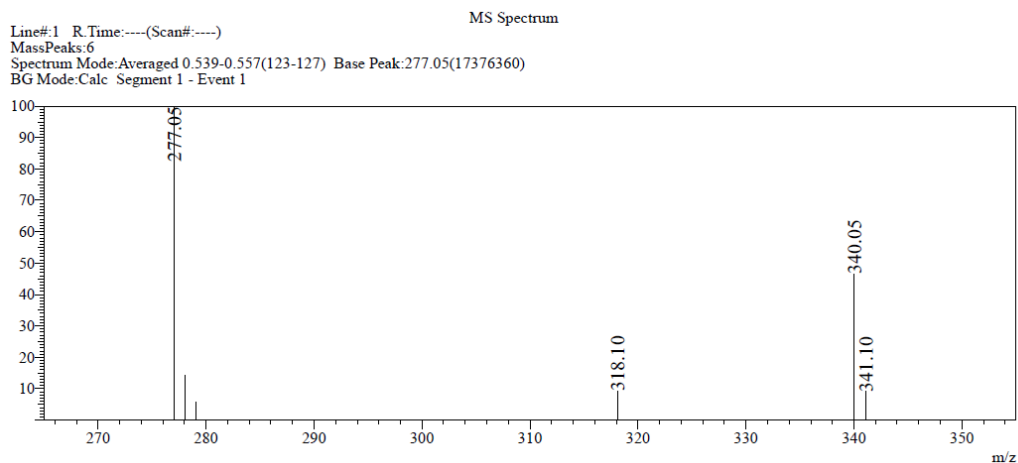


Fig. 3.25 ESI-MS spectrum of molecule **D7**

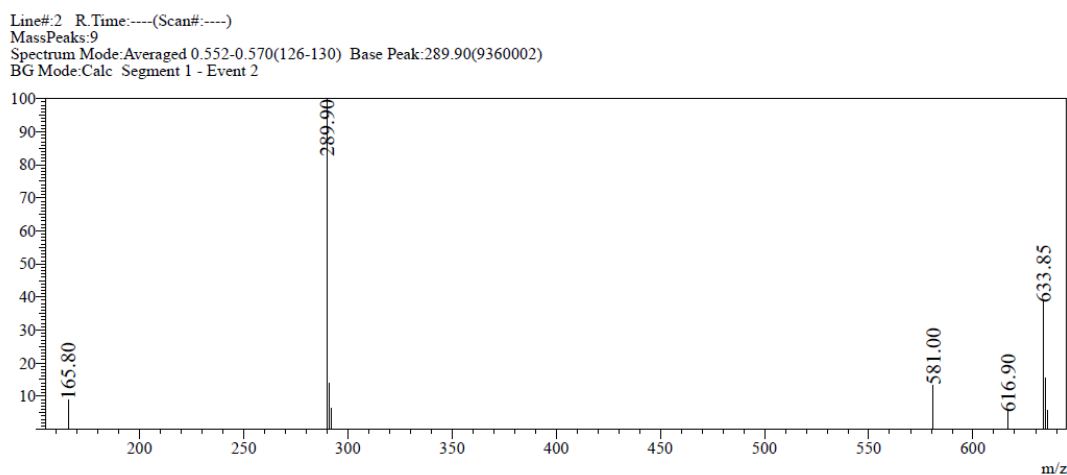


Fig. 3.26 ESI-MS spectrum of molecule **D8**

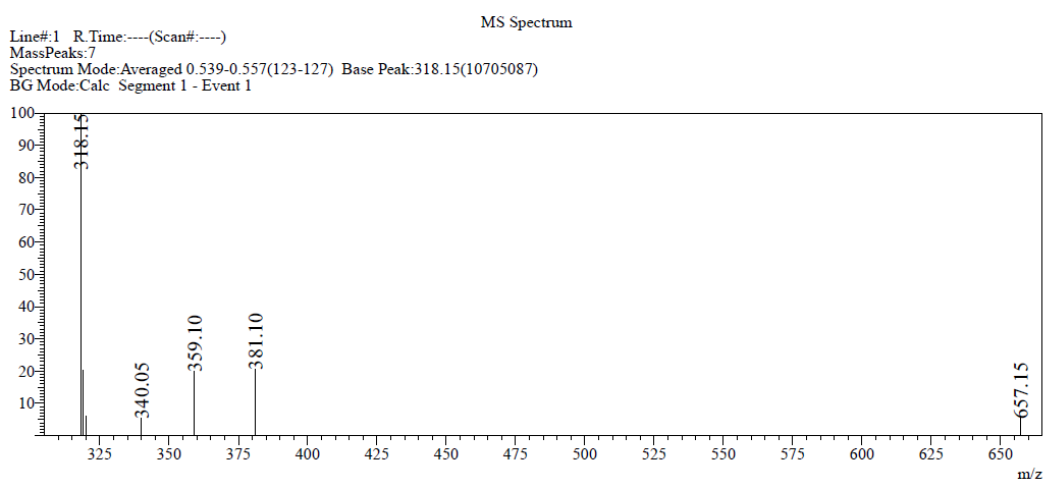


Fig. 3.27 ESI-MS spectrum of molecule **D9**

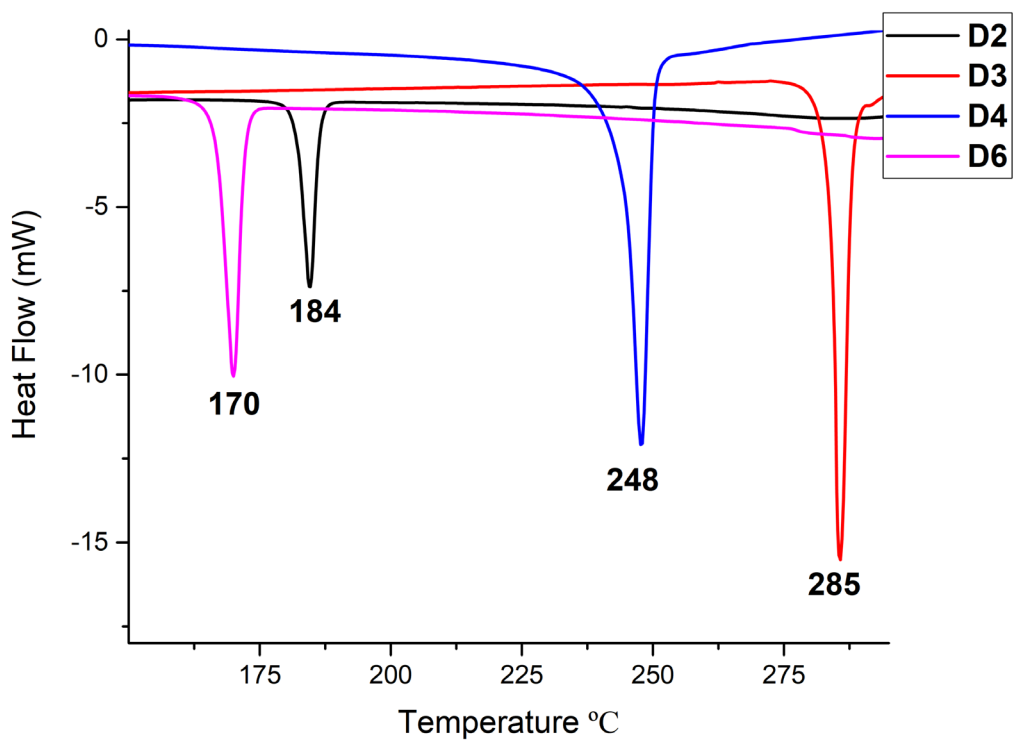


Fig. 3.28 Differential Scanning calorimetry of molecules **D2**, **D3**, **D4** and **D6**

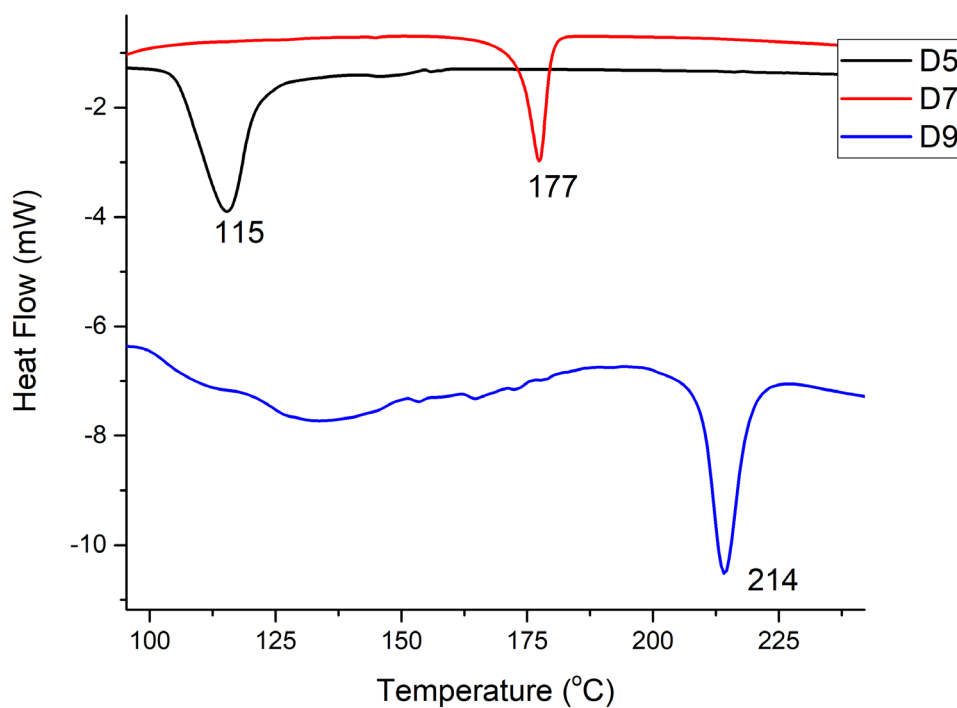


Fig. 3.29 Differential Scanning calorimetry of molecules **D5**, **D7** and **D9**

3.3 RESULTS AND DISCUSSION

3.3.1 UV-Vis Studies

With a view to understand the nature of the electronic transitions, UV-Vis studies have been performed on molecules **D1** - **D9** in solvents of varying polarity and summarized in Table 3.1. The absorption spectra of these molecules revealed the presence of absorption bands in the range 230-245 nm corresponding to the excitation of the aromatic π electrons, 260-300 nm corresponding to the π - π^* transitions of the imine linkage and 301-427 nm corresponding to the π - π^* transitions of the CONH linkage and OH functionality respectively (Gabr 1990). The presence of electron donor species was found to have direct impact on tuning the photophysical properties of the molecules. With various combination of donor and acceptor (D/A) species in the molecules, substantial red shift was observed corresponding to the charge transfer interaction between the donor and acceptor. Depending on the electron donating ability of substituents, consistent with the predicted trend, molecules **D1** to **D9** exhibited bathochromic shift possessing groups with different electron-donating abilities, in the order $N(C_2H_5)_2$, OC_2H_5 , OCH_3 and OH functionalities. This confirms the active role of intramolecular charge-transfer behaviour between the donors and acceptors in solvents of varying polarity such as THF, MeOH, DMF, ACN and DMSO. UV-Vis spectra of molecules **D1-D9** in solvents of varying polarity is provided in Fig. 3.30 – 3.38.

Table 3.1 Photophysical studies of molecules **D1** to **D9** under various solvents and its optical band gap for UV-Vis absorption spectra

Tetrahydrofuran (THF)

	λ_{abs} (nm)	λ_{ex} (nm)	λ_{ems} (nm)	Stoke Shift (nm)	FWHM (nm)
D1	301, 310	310	343	33	40
D2	297, 333, 388	333	410	77	83
D3	297, 332	332	403	71	103
D4	297, 342	342	406	64	67
D5	297, 340	340	376	36	91
D6	297, 335	335	371	36	82
D7	296, 355	355	404	49	62
D8	296, 335, 396	335	406	71	72
D9	296, 368	368	474	106	108

Methanol (MeOH)

	λ_{abs} (nm)	λ_{ex} (nm)	λ_{ems} (nm)	Stoke Shift (nm)	FWHM (nm)
D1	310	310	432	122	69
D2	270, 329, 383	383	445	62	79
D3	270, 324, 370	370	432	62	70
D4	270, 333, 370	370	432	62	70
D5	272, 333, 370	370	433	63	88
D6	271, 335, 381	381	445	64	79
D7	271, 349, 375	375	433	58	147
D8	272, 360, 380	360	433	73	73
D9	270, 384	384	463	79	73

Acetonitrile (ACN)

	λ_{abs} (nm)	λ_{ex} (nm)	λ_{ems} (nm)	Stoke Shift (nm)	FWHM (nm)
D1	300, 270, 242	300	361	61	167
D2	330, 299, 289	330	429	99	72
D3	271, 285, 297, 317	317	403	86	67
D4	271, 335	335	429	94	69
D5	301, 340	340	430	90	68
D6	272, 289, 299, 332, 397	332	430	98	63
D7	284, 353	353	430	77	60
D8	293, 332, 396	332	431	99	69
D9	369	369	531	162	120

N,N – dimethylformamide (DMF)

	λ_{abs} (nm)	λ_{ex} (nm)	λ_{ems} (nm)	Stoke Shift (nm)	FWHM (nm)
D1	271, 302	271	337	66	48
D2	277, 331, 400	400	468	68	73
D3	273, 324	324	428	104	111
D4	273, 343	343	432	89	75
D5	273, 303, 401	401	489	88	97
D6	275, 335, 396	396	474	78	101
D7	273, 297, 307, 350, 427	427	514	87	100
D8	273, 285, 393	285	333	48	43
D9	272, 372	372	510	138	122

Dimethylsulfoxide (DMSO)

	λ_{abs} (nm)	λ_{ex} (nm)	λ_{ems} (nm)	Stoke Shift (nm)	FWHM (nm)
D1	395, 410	395	442	47	63
D2	317, 384	384	488	104	107
D3	305, 334, 388	388	437	49	67
D4	275, 303, 327	275	330	55	73
D5	346	346	504	158	106
D6	323, 397	397	478	81	99
D7	276, 341, 393	393	522	129	110
D8	315, 355, 413	355	413, 435	58, 80	82
D9	392, 444	392	510	118	114

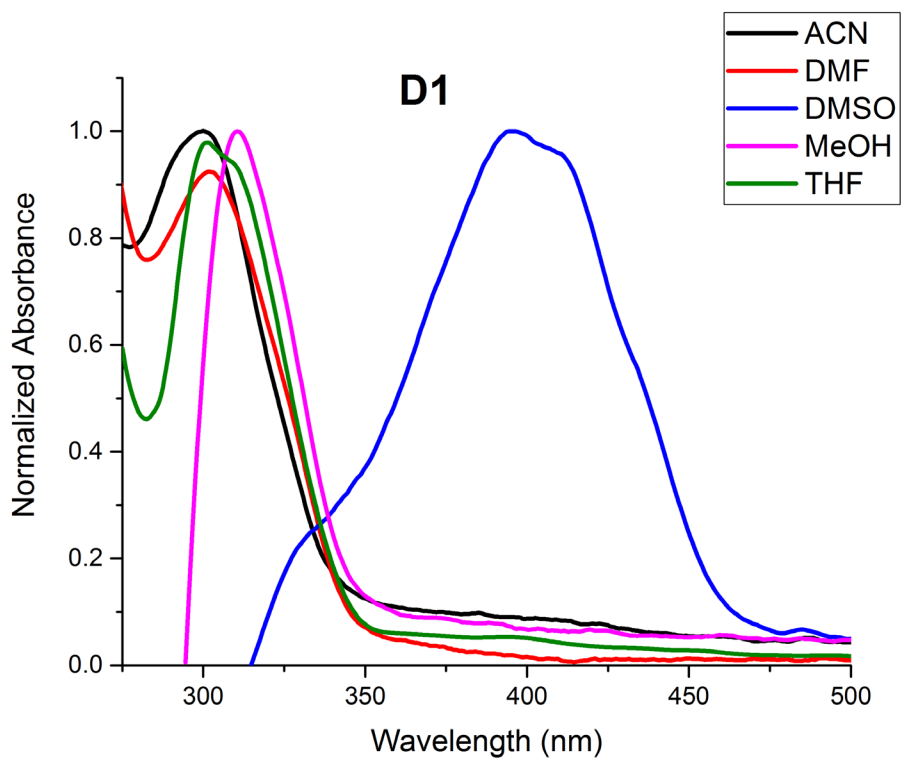


Fig. 3.30 UV-Vis absorbance spectra of molecule **D1** in solvent of varying polarity.

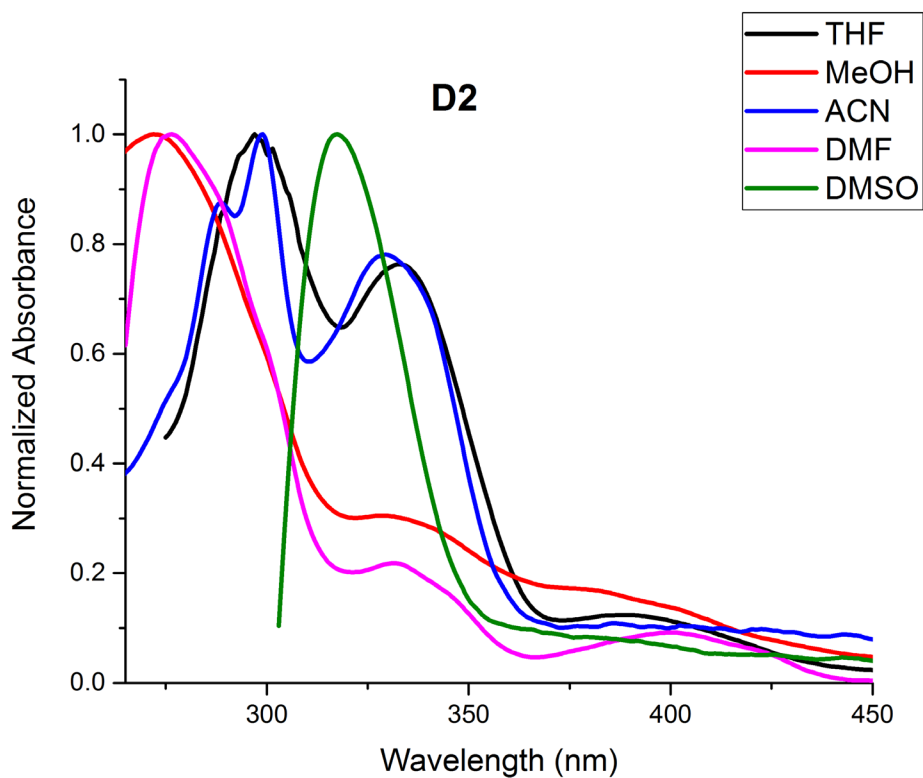


Fig. 3.31 UV-Vis absorbance spectra of molecule **D2** in solvent of varying polarity.

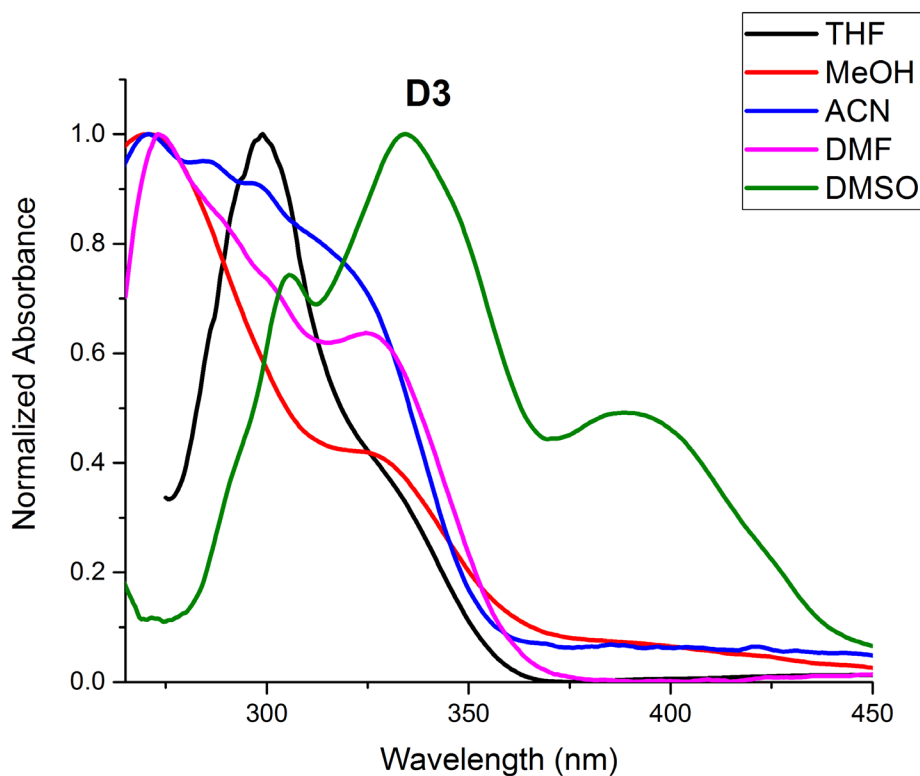


Fig. 3.32 UV-Vis absorbance spectra of molecule **D3** in solvent of varying polarity.

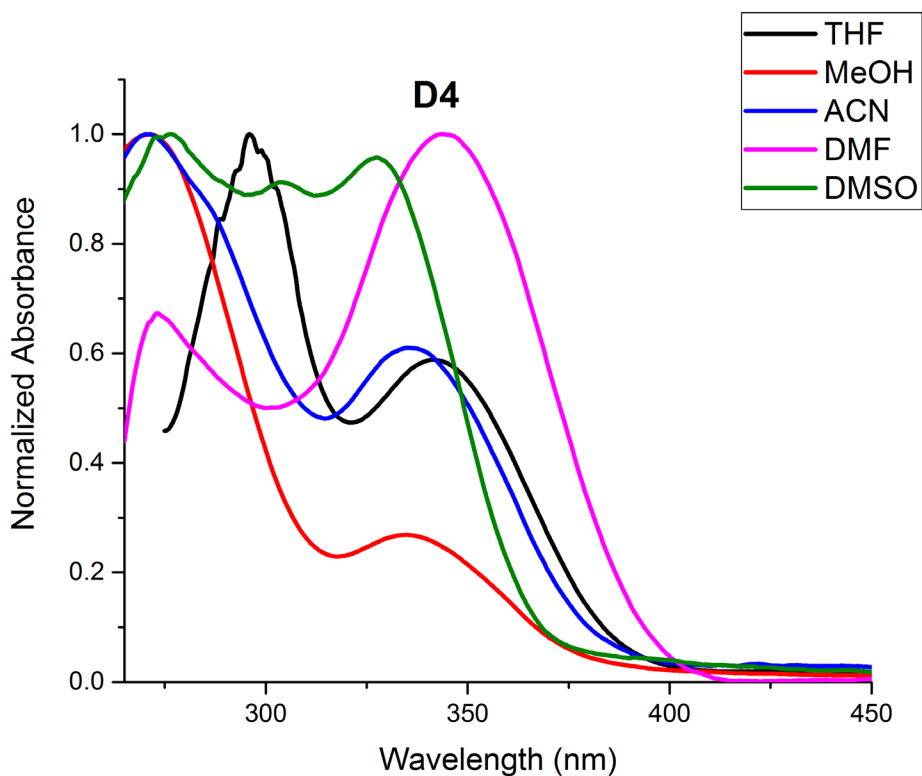


Fig. 3.33 UV-Vis absorbance spectra of molecule **D4** in solvent of varying polarity.

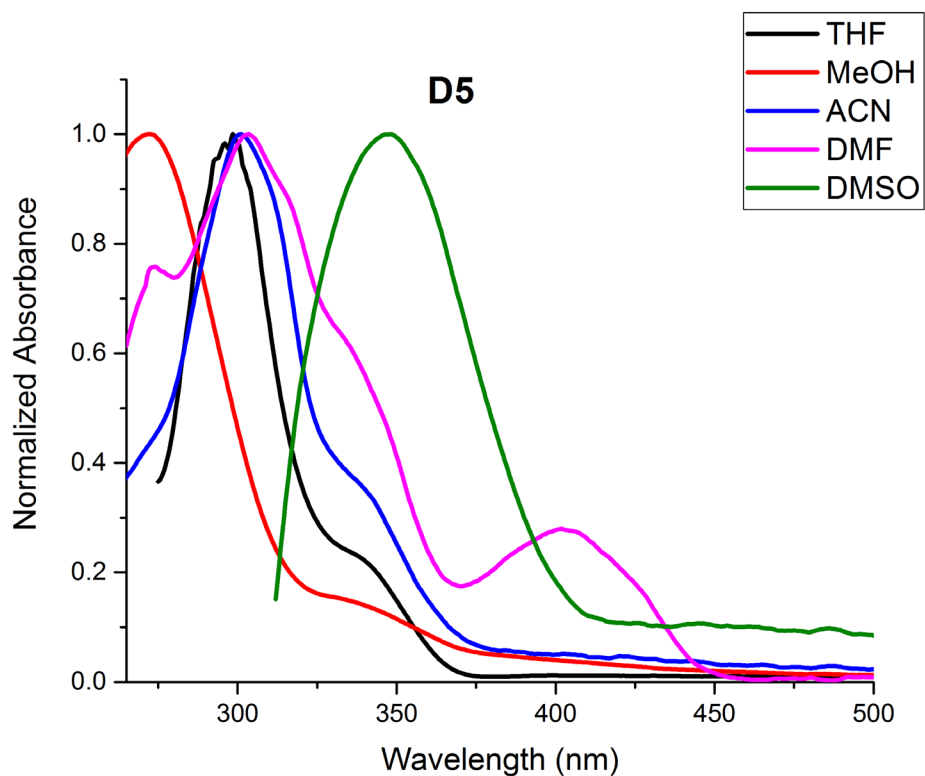


Fig. 3.34 UV-Vis absorbance spectra of molecule **D5** in solvent of varying polarity.

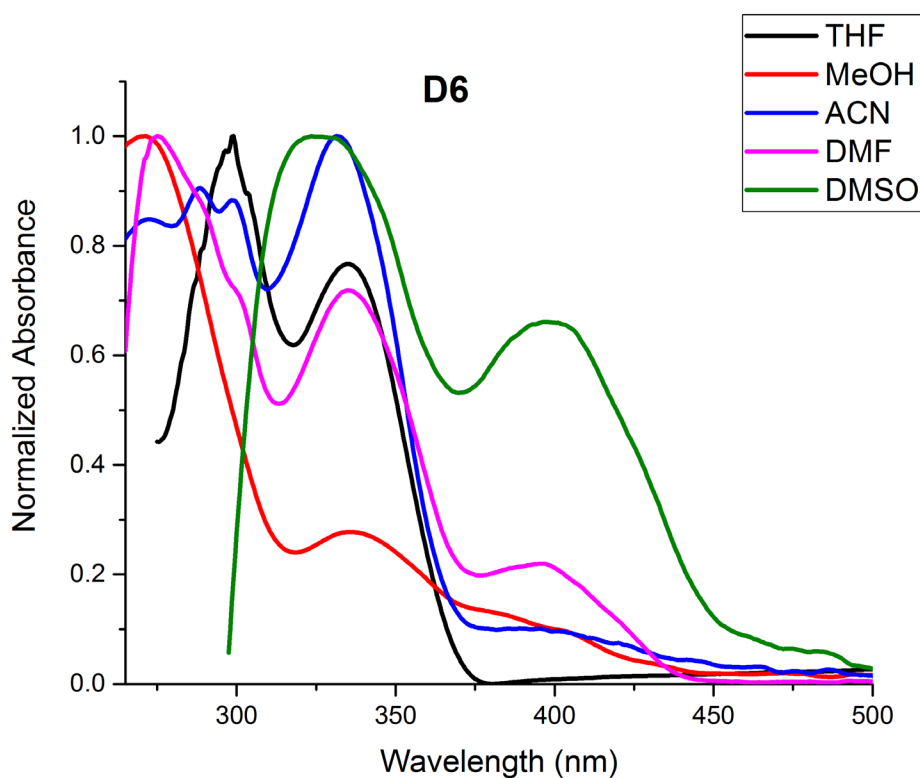


Fig. 3.35 UV-Vis absorbance spectra of molecule **D6** in solvent of varying polarity.

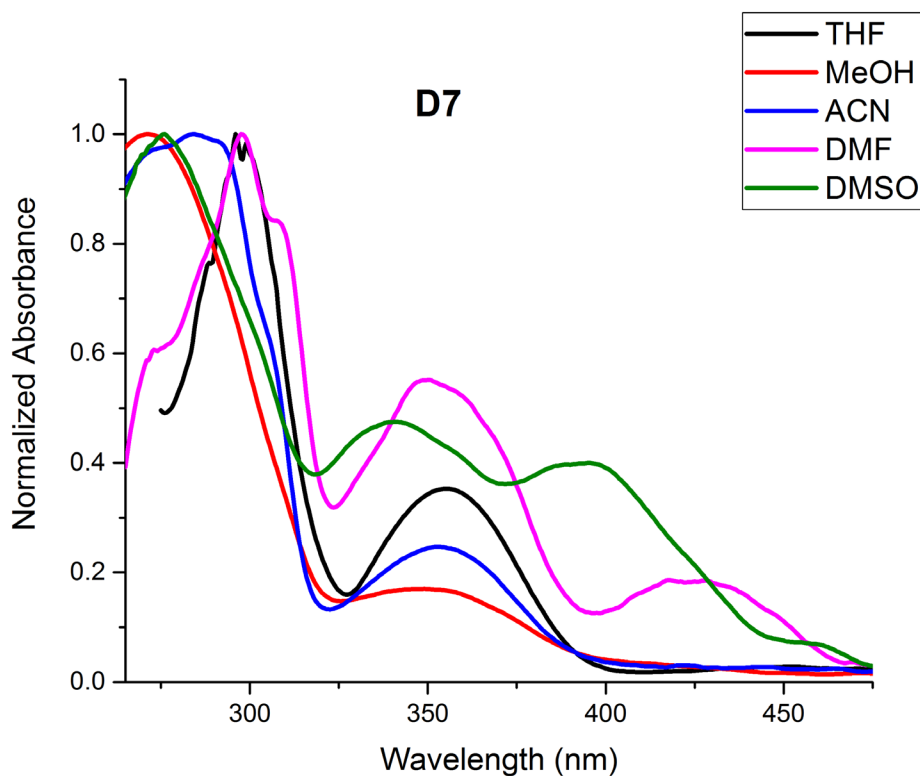


Fig. 3.36 UV-Vis absorbance spectra of molecule **D7** in solvent of varying polarity.

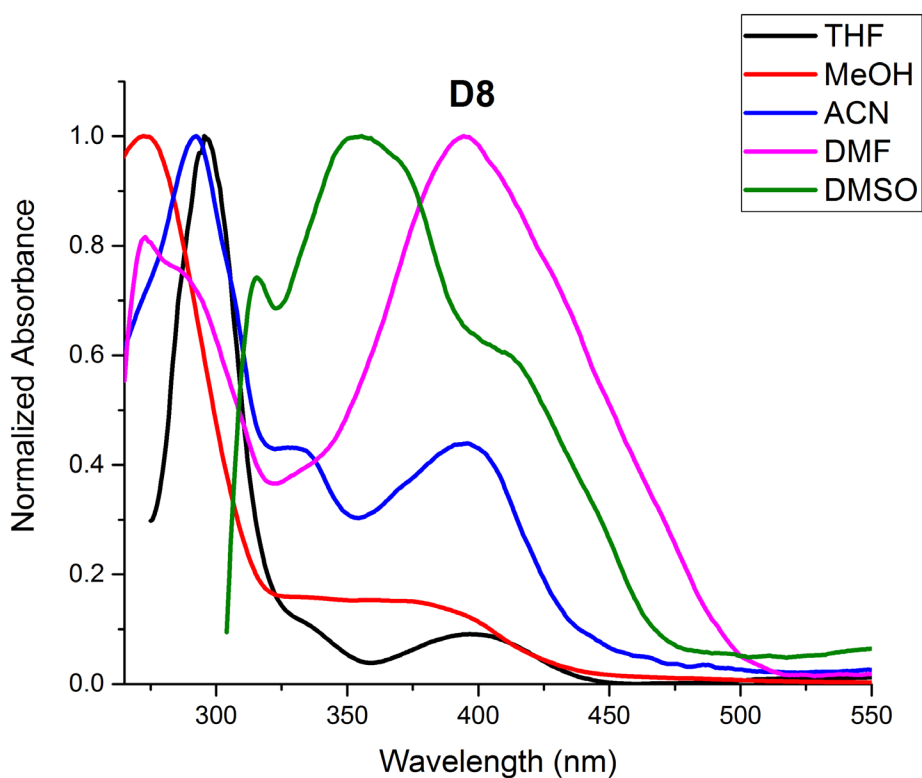


Fig. 3.37 UV-Vis absorbance spectra of molecule **D8** in solvent of varying polarity.

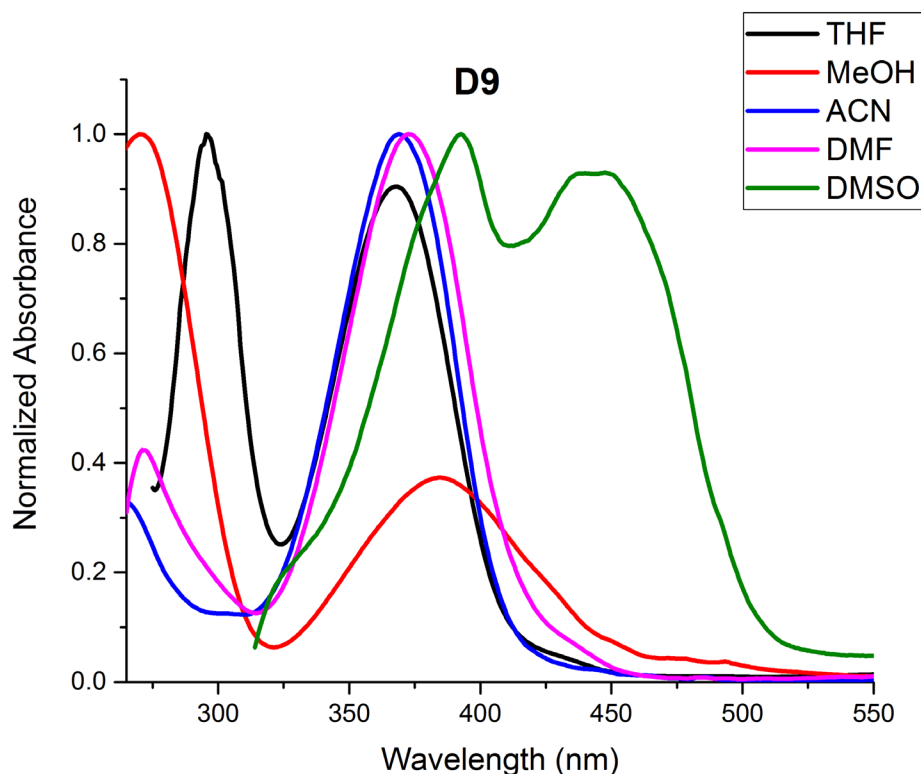


Fig. 3.38 UV-Vis absorbance spectra of molecule **D9** in solvent of varying polarity.

3.3.2 Photoluminescence Studies

Photoluminescence spectral data for molecules **D1-D9** of concentration 1×10^{-5} M in solvents of varying polarity is listed in Table 3.1 and their corresponding spectra is provided in Fig. 3.39 – 3.47. The substitution on the parent molecule **D1** via functionality and conjugation resulted in overall bathochromic shift in the emission wavelength for entire series except for **D4** and **D8**. **D4** and **D8** showed hypsochromic shift in the emission wavelength with respective emission peaks at 330 nm in DMSO and 333 nm in DMF. All molecules except **D4** and **D8** showed a bathochromic shift in the emission wavelength with the increase in the solvent polarity as shown in Fig. 3.48. It can be observed that, with increasing solvent polarity the emission wavelength shifts by a value of around 100 nm for **D1**, **D2**, **D5**, **D6** and **D7**. For molecule **D3**, only 30 nm shift was observed in emission wavelength. Excited state intramolecular proton transfer (ESIPT) is generally favoured in phototautomeric molecules with a difference of electron charge distribution between the ground state and the excited states (Forés et al. 1998). Substitution of varied functional groups both in its position and its chemical properties

influence the ESIPT process (Catalan et al. 1992). The existence of salicylaldimine derivatives as phenol-imine tautomer in polar aprotic solvents and keto-amine form in other solvents is well known (Watanabe et al. 1998). Moreover, presence of electron donating groups ortho to the phenolic -OH group generally favours the formation of intramolecular hydrogen bond interaction (Catalan et al. 1992). Molecules **D5**, **D6** and **D7** owing to the presence of electron donating groups exhibited emission corresponding to phenol imine form in the lower wavelength region. A tautomer emission band corresponding to ketoamine form appears in the higher wavelength region, as the keto form is more stable than the enol form, consequently the emission is red-shifted (Forés et al. 1998).

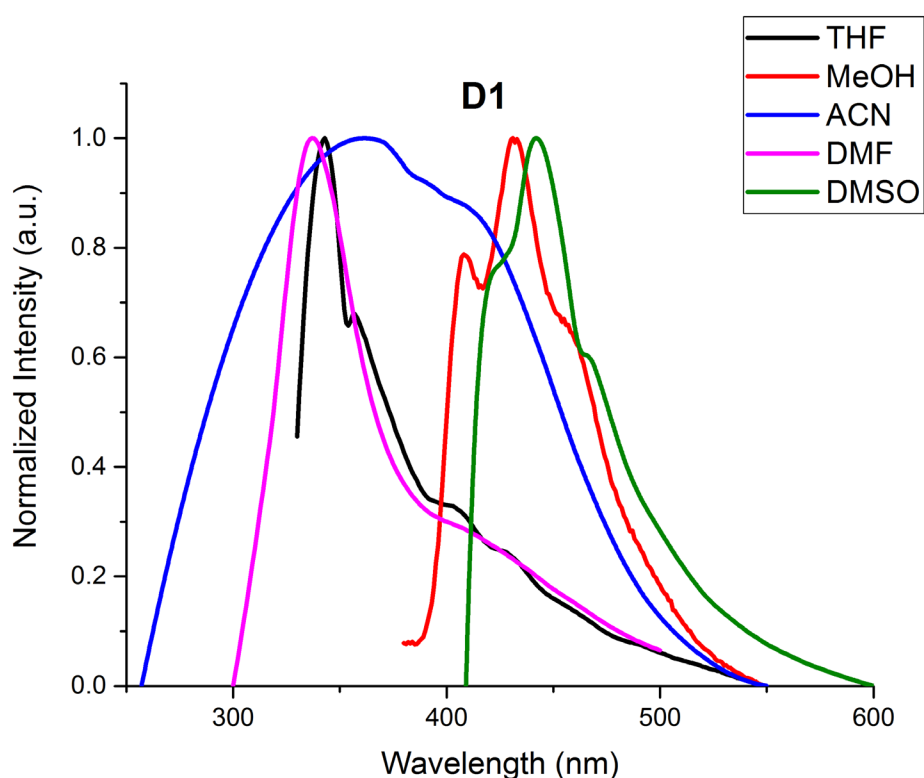


Fig. 3.39 Photoluminescence spectra of molecule **D1** in solvent of varying polarity.

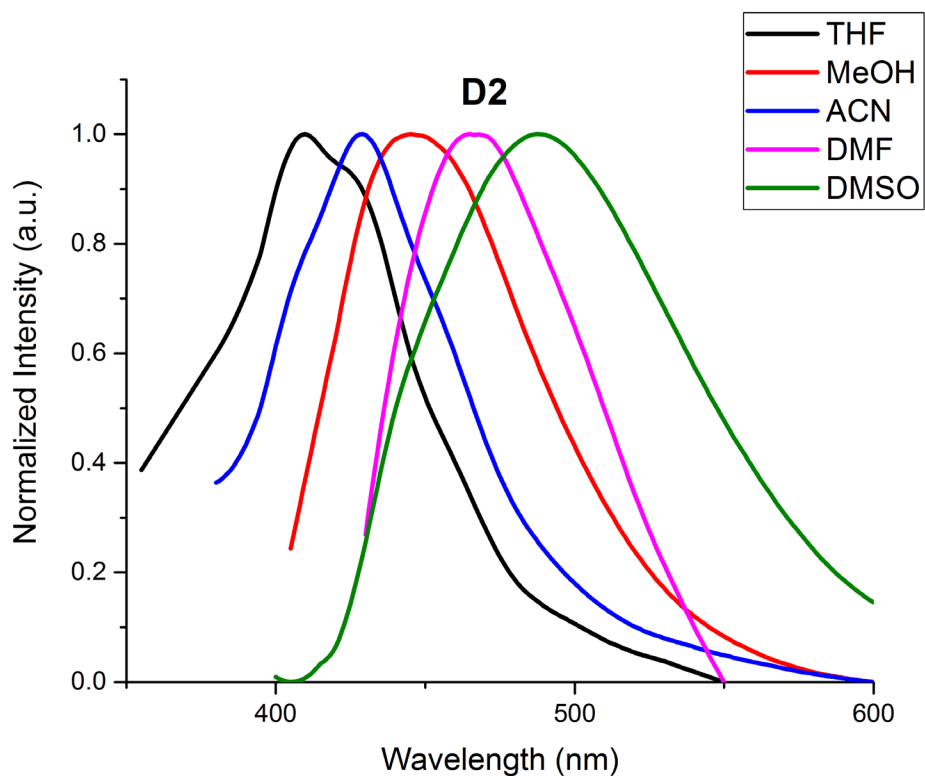


Fig. 3.40 Photoluminescence spectra of molecule **D2** in solvent of varying polarity

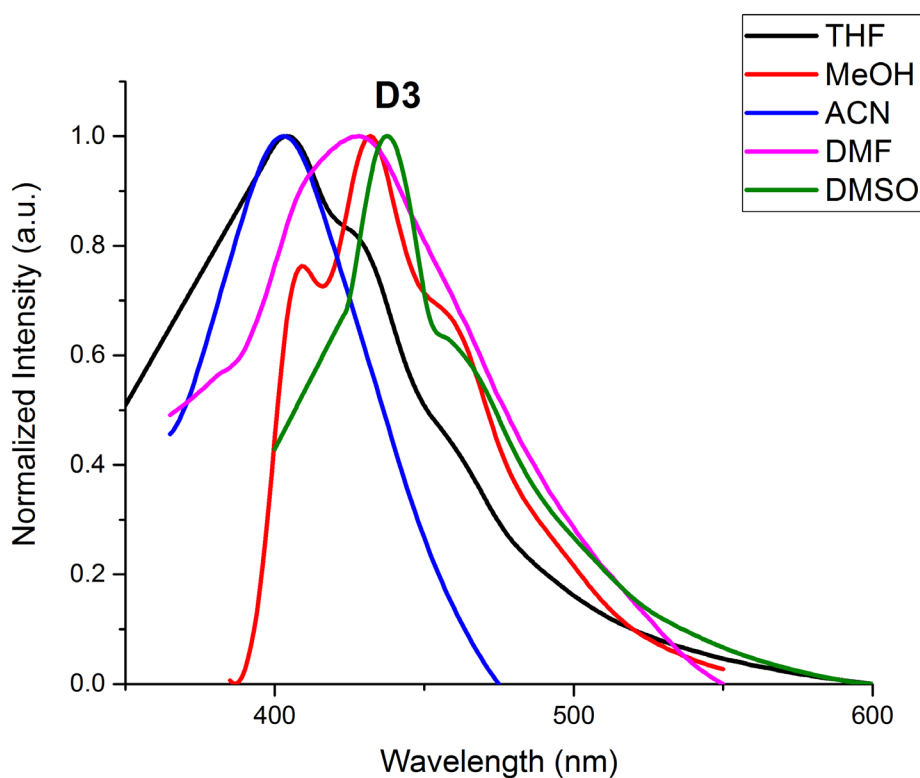


Fig. 3.41 Photoluminescence spectra of molecule **D3** in solvent of varying polarity

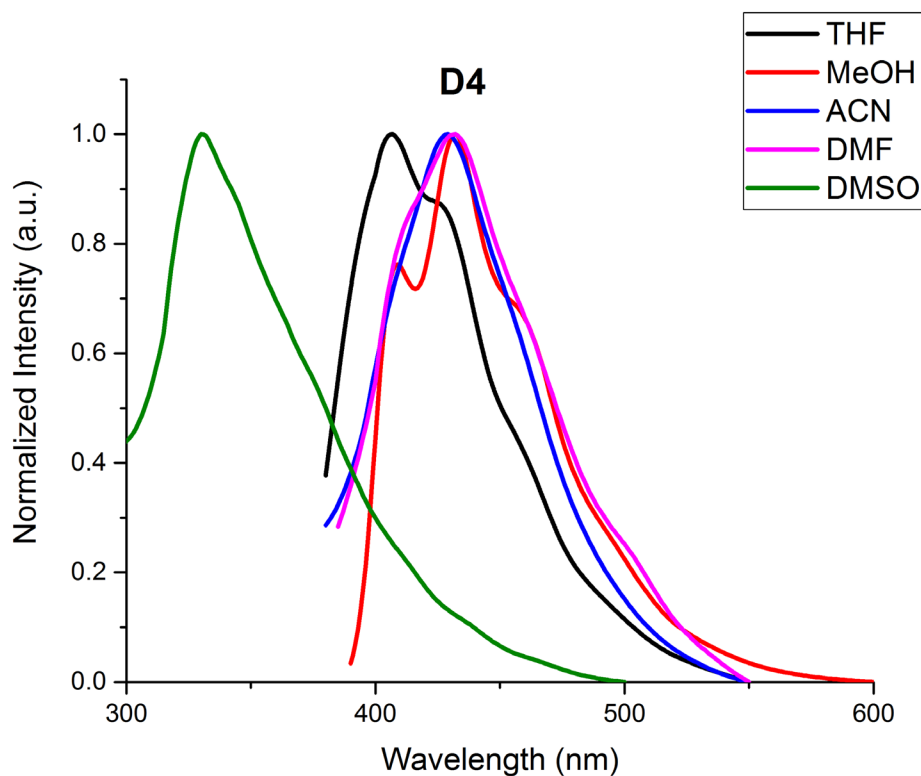


Fig. 3.42 Photoluminescence spectra of molecule **D4** in solvent of varying polarity

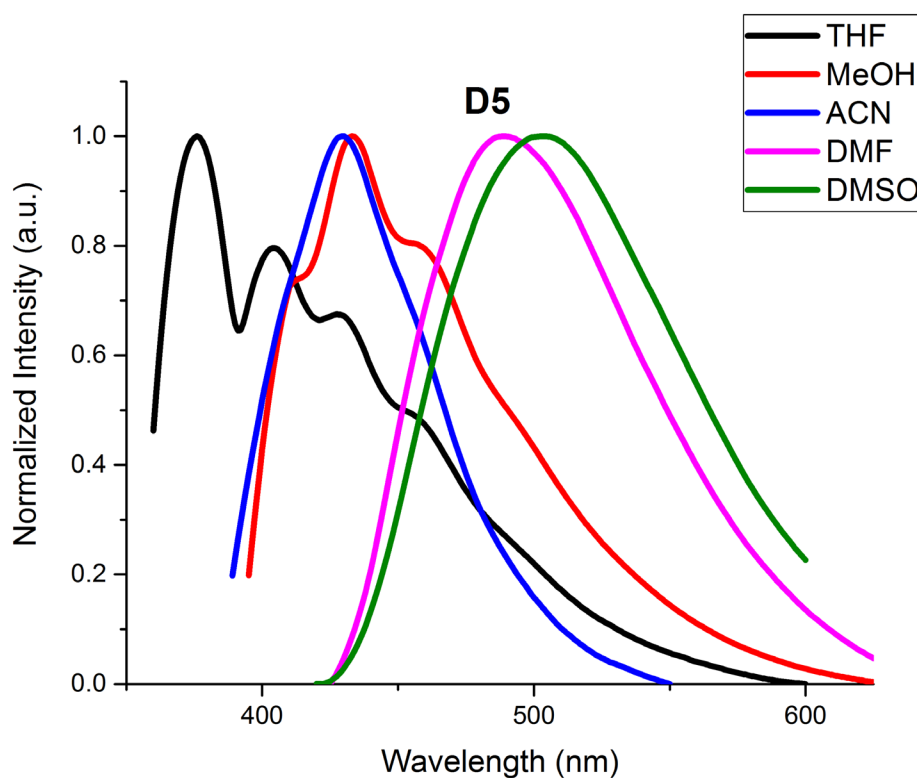


Fig. 3.43 Photoluminescence spectra of molecule **D5** in solvent of varying polarity.

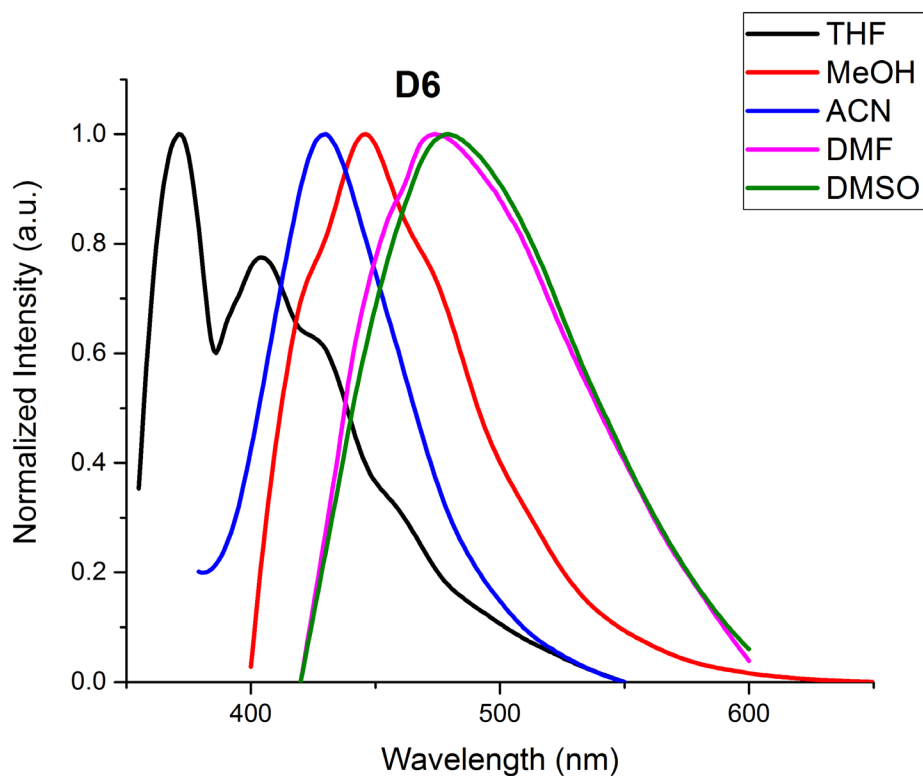


Fig. 3.44 Photoluminescence spectra of molecule **D6** in solvent of varying polarity

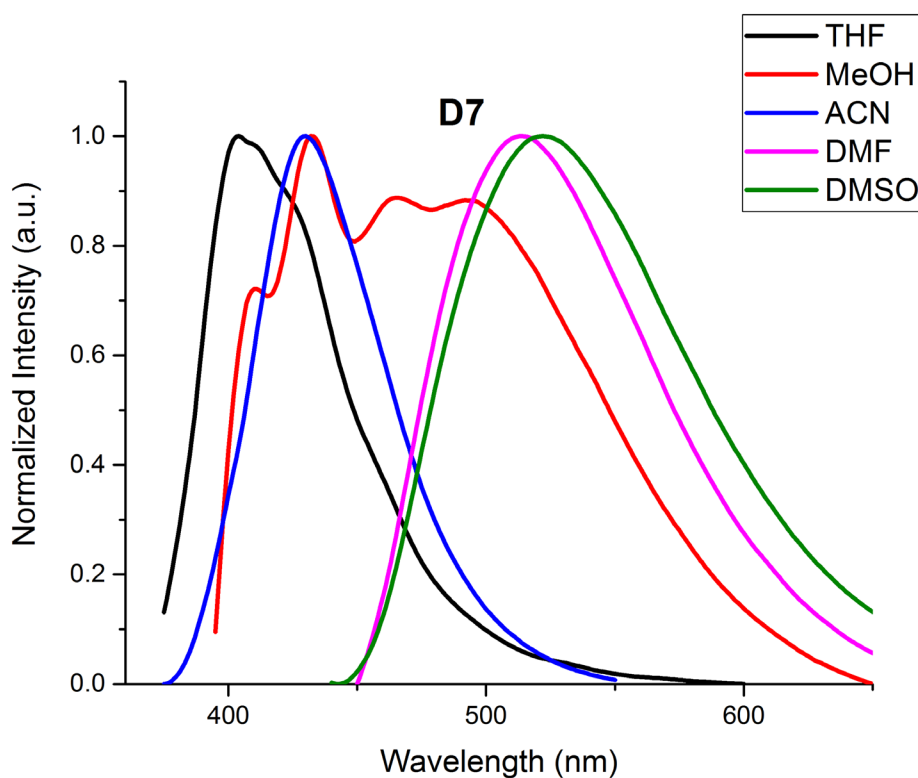


Fig. 3.45 Photoluminescence spectra of molecule **D7** in solvent of varying polarity

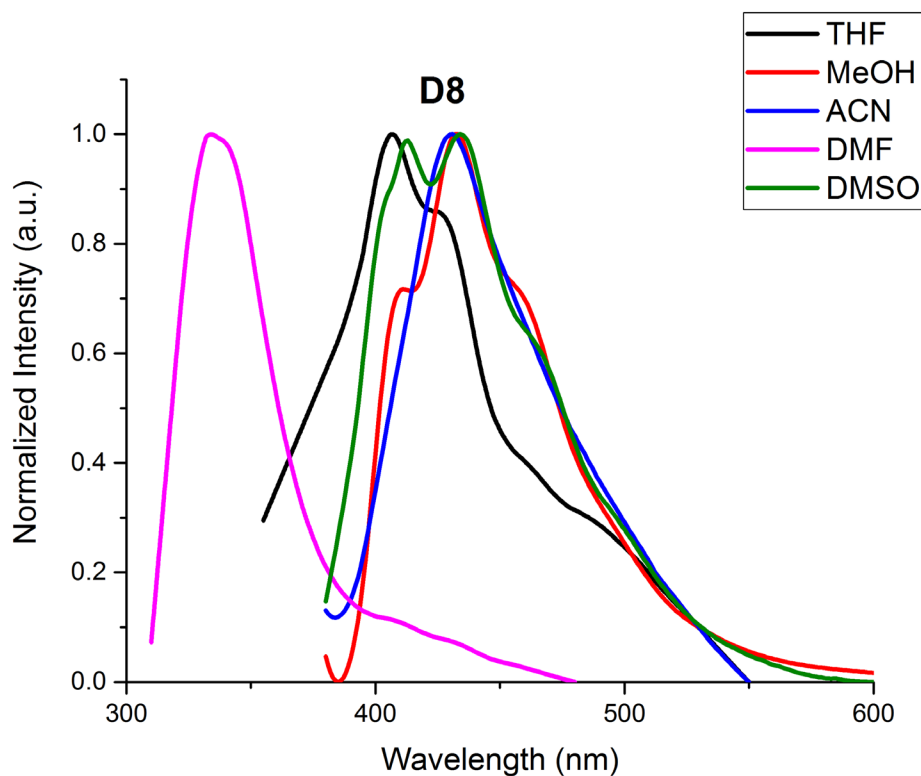


Fig. 3.46 Photoluminescence spectra of molecule **D8** in solvent of varying polarity

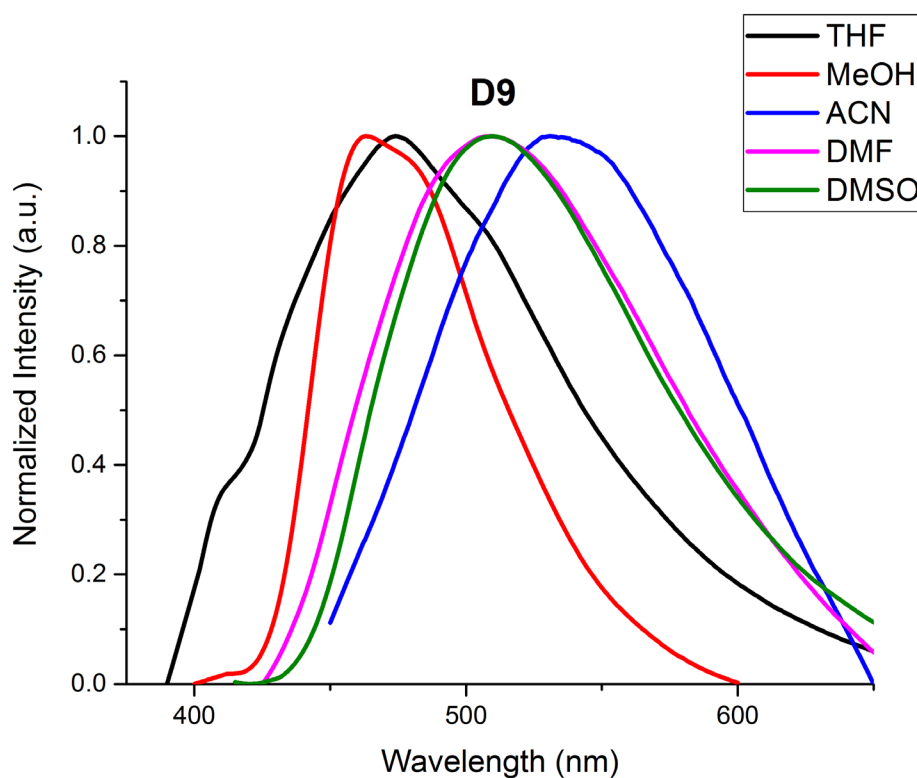


Fig. 3.47 Photoluminescence spectra of molecule **D9** in solvent of varying polarity

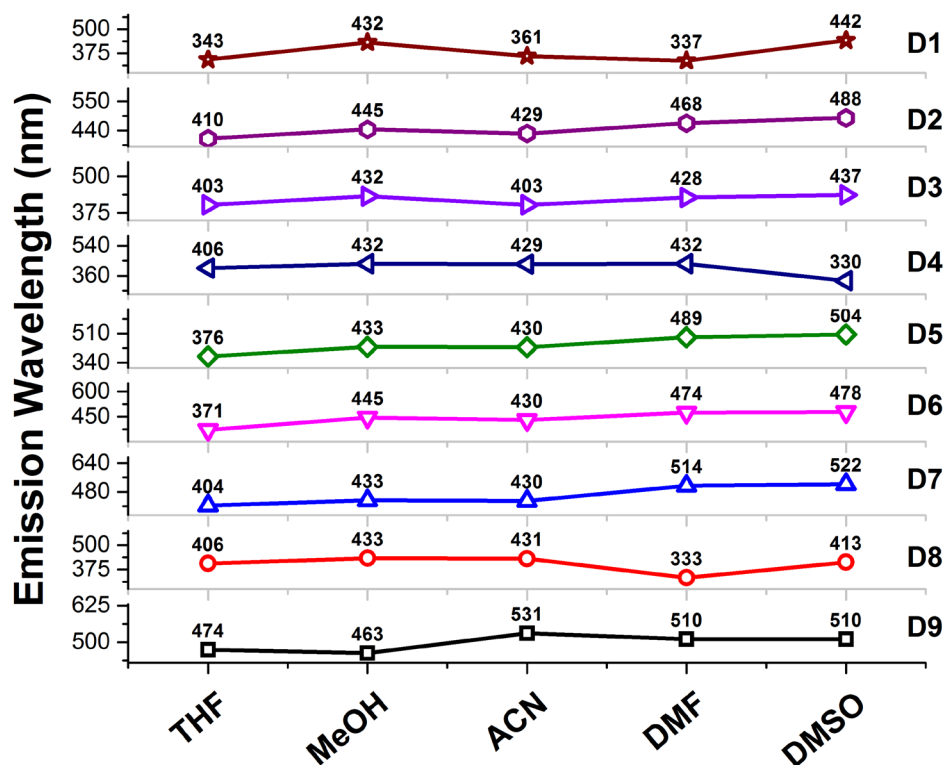


Fig. 3.48 Emission wavelength of molecule D1-D9 in solvent of varying polarity.

3.3.3 Quantum yield measurement

The fluorescence quantum yield (ϕ_s) for D1-D9 molecules in methanol were evaluated according to Equation 3.1, where Coumarin 153 is the reference denoted as (R). Grad corresponds to the gradient extracted from the plot of integrated fluorescence intensity vs absorbance at the excitation wavelength and η represents the refractive index of the solvent for standard and reference (Dhami et al. 1995; Williams et al. 1983). Molecules D6, D7 and D9 exhibited a highest quantum yield value of 3.20 %, 2.52 % and 2.40 % in comparison with the others in the series as given in the Table 3.2.

$$\phi_s = \phi_R \frac{Grad_S}{Grad_R} \frac{\eta_S^2}{\eta_R^2} \quad \text{Eq. 3.1}$$

Table 3.2 Fluorescence quantum yield of molecule D1-D9 in methanol solvent

Molecule	D1	D2	D3	D4	D5	D6	D7	D8	D9
QY (%)	0.82	2.4	0.19	0.24	0.57	3.20	2.52	0.25	2.40

3.3.4 Solid state photoluminescence studies

Thermally deposited thin films of the molecules were examined for their solid-state emission behaviour and the solid-state emission under UV illumination is shown in Fig.3.49. Molecule **D1** did not exhibit any emission in the solid state due to lack of -OH functionality in the structure which is essential to favour charge transfer transition. Molecules **D2-D9** exhibited good AIE phenomenon in comparison with the solution state. Emission wavelength (λ_{ems}) with full width half maximum (FWHM) for the entire series is tabulated in Table 3.3, a FWHM value of less than 70 accounts for good colour purity (Li et al. 2014). A good bathochromic shift was observed for all the molecules in the solid state except for **D3** that did not show any shift in comparison with the solution state. However, **D3** and **D8** showed the highest colour purity in comparison with the others in the series with an emission wavelength of 420 nm. Further, **D2**, **D4**, **D6** and **D7** exhibited a FWHM less than 90 nm in their solid state. Solid state PL spectra of molecules **D2-D9** is as shown in the Fig. 3.50.

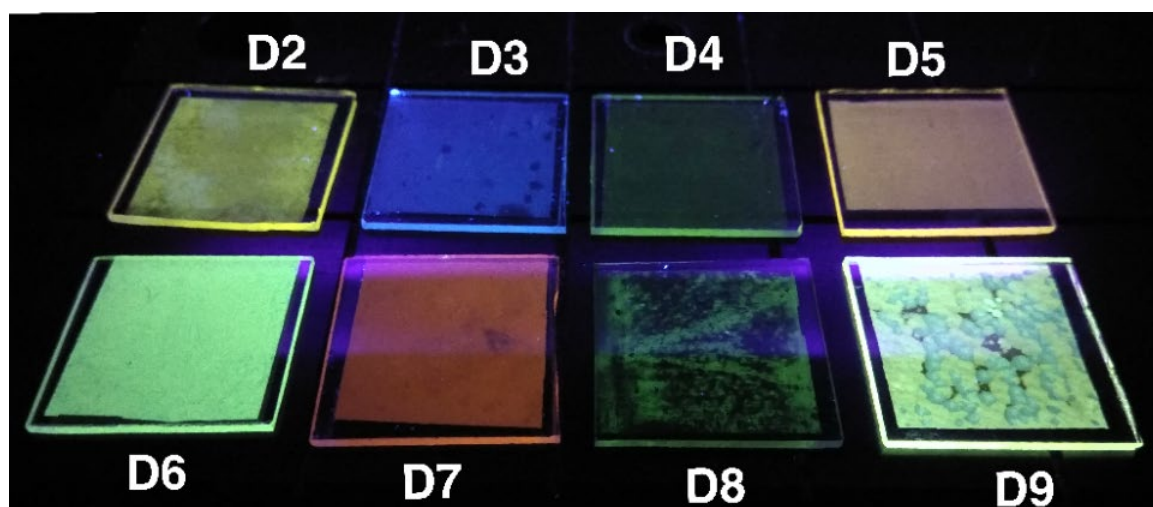


Fig. 3.49 Solid state emission of molecule **D2-D9** under UV illumination

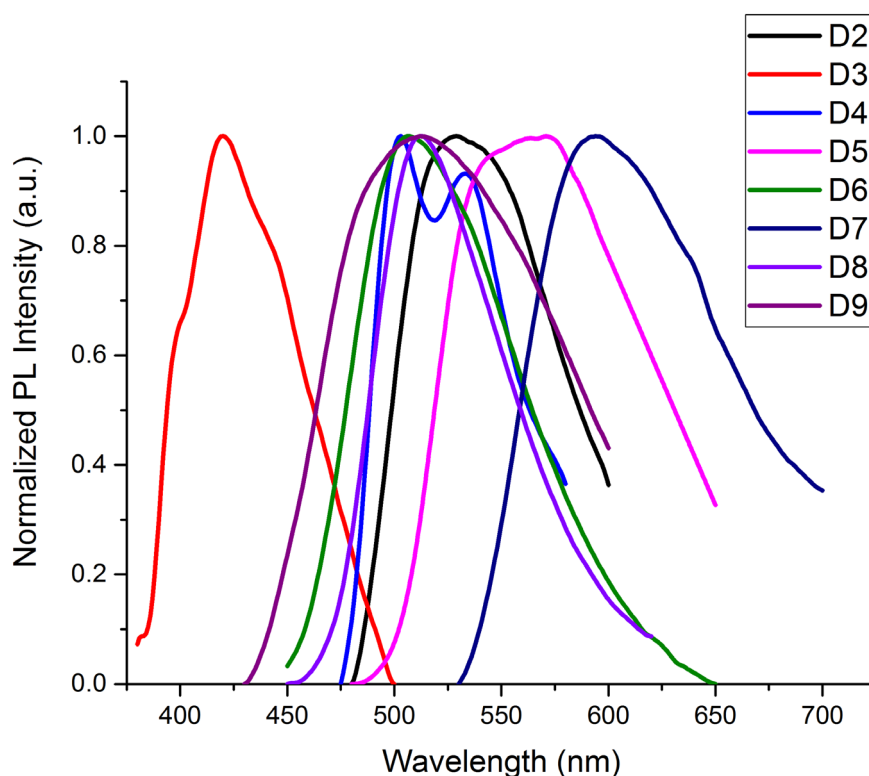


Fig. 3.50 Solid state photoluminescence spectra of molecule **D2-D9**

Table 3.3 Photophysical studies for molecule **D2-D9** in solid state

	λ_{ex} (nm)	λ_{ems} (nm)	Stokes Shift	FWHM
D2	320	528	208	88
D3	360	420	60	69
D4	370	503, 533	133, 163	75
D5	350	562	212	112
D6	380	508	128	87
D7	390	594	204	110
D8	360	512	152	70
D9	410	512	102	128

3.3.5 Fluorescent lifetime measurement

Lifetime measurements were recorded for the molecular series in methanol and the decay profile is provided in Fig. 3.51 and their standard deviation profile is given in Fig. 3.52. In general, all the molecules exhibited two component lifetimes, except for **D7** and **D8** wherein three lifetime components have been recorded as represented in Table 3.4. The multicomponent lifetime exists due to the presence of different conformations in the excited state with different spin multiplicities. For **D7** and **D8**, owing to the presence

of three lifetime components, their emission is from three excited states (Muruganatham et al. 2017).

Table 3.4 Fluorescence Lifetime for the molecules **D1** to **D9**

Lifetime (ns)				
	T1	T2	T3	X ²
D1	1.38	4.11	--	1.09
D2	1.37	3.04	--	1.03
D3	1.37	3.24	--	1.08
D4	1.34	2.93	--	1.06
D5	1.27	2.32	--	1.08
D6	1.32	2.22	--	1.13
D7	0.13	1.35	4.23	1.06
D8	1.06	1.35	3.37	1.10
D9	1.47	2.25	--	1.08

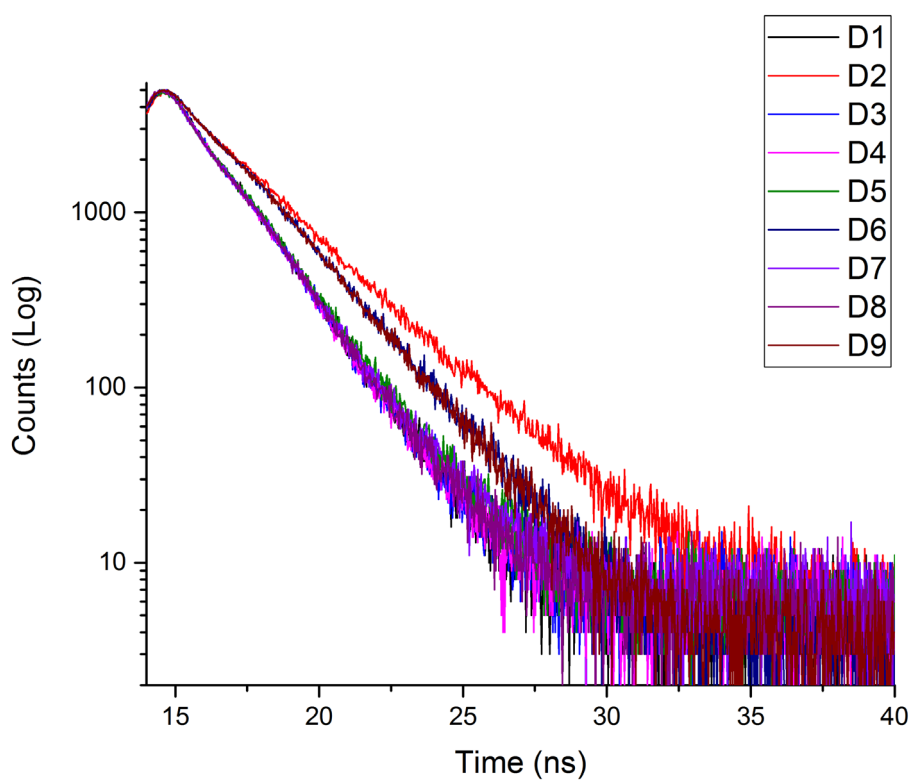


Fig. 3.51 Fluorescence Lifetime decay of molecule **D1-D9** in methanol medium

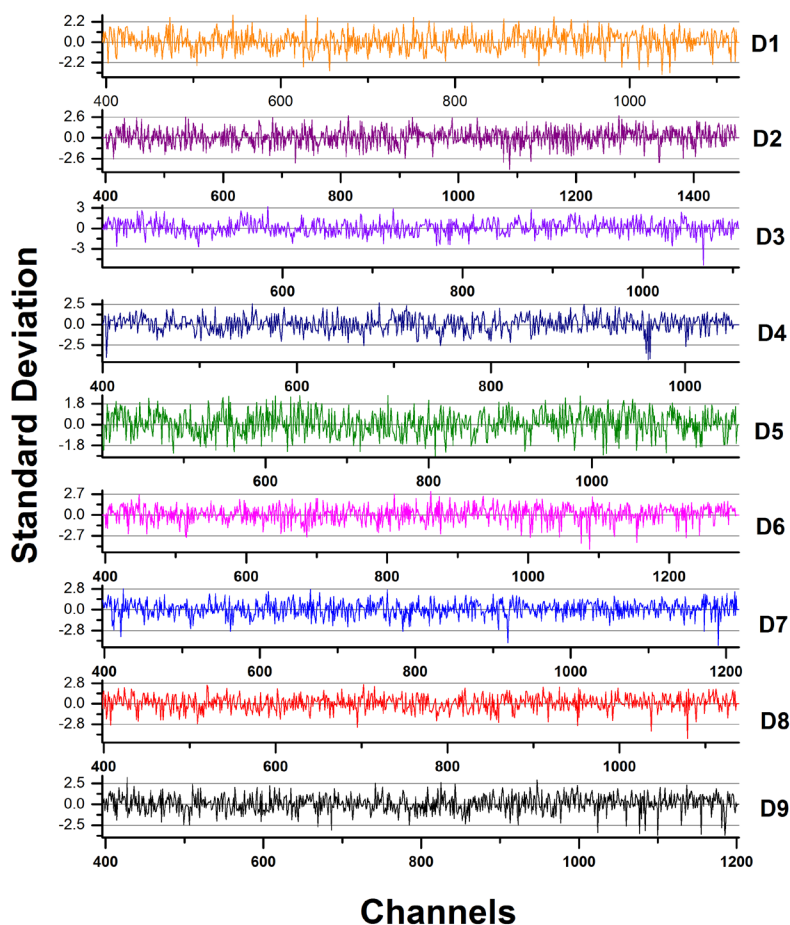


Fig. 3.52 Standard deviation profiles for the determination of fluorescence lifetime values for molecule **D1-D9**

3.3.6 Aggregation induced emission studies

Fluorescence emission intensity of the molecules are quite weak in solvents of higher polarity due to positive solvato kinetic effect and other interactions like photoinduced electron transfer (Usuki et al. 2018). Aggregation of the molecules in poor solvent mixture enhances the fluorescence emission intensity viz restriction of intramolecular motions and intramolecular rotations leading to aggregation induced emission. To quantitatively estimate the emission process of the molecules exhibiting AIEE phenomenon, fluorescence emission spectra were recorded in varying methanol/water mixtures. Solutions of molecules **D2-D9** were prepared in methanol of concentration (10^{-5} M) and their mixtures in varying water fractions f_w were considered for the fluorescence emission study. Fluorescence emission of molecules **D2-D9** with varying mixtures of f_w under ultra violet radiation is as shown in the Fig. 3.53 wherein, 0 corresponds to 0.1% f_w , 1 corresponds to 90% f_w , 2 corresponds to 80% f_w and so on with

9 corresponds to 100% f_w . **D3**, **D4** and **D8** exhibited very low emission intensity and didn't show much variation with varying f_w . Molecules **D2**, **D6**, **D7** and **D9** exhibited an emission enhancement with increase in f_w and gradual decrease on further increasing f_w . However, in contrast **D5** exhibited a drop in emission intensity upon gradual increase in f_w as provided in Fig.3.55. **D5** exhibited a good emission in pure solvent and its emission is quenched upon aggregation in solvent mixture. Molecule **D6** and **D9** attained a maximum intensity at an f_w of 50% as shown in Fig. 3.56 and Fig. 3.58 respectively. **D2** exhibited higher emission intensity at f_w 40% and **D7** at 20% as shown in the Fig. 3.54 and Fig. 3.57 respectively. The fluorescence intensities of the compounds gradually increase due to aggregation as the f_w increases and attain a maximum. Upon further increase of f_w the fluorescence emission intensity gradually diminishes and can be ascribed to a corresponding decrease in the solubility (Zhang et al. n.d.). The trend is often observed in case of AIEE molecules and **D2**, **D6**, **D7** and **D9** display a similar trend as provided in the inset plot respectively. There is small amount of redshift observed in the emission peak in addition to intensity variation upon increasing f_w . The redshift is highly predominant in molecule **D9** and a 12 nm shift was observed in the emission wavelength on increasing f_w . However, meagre redshift was observed for other molecules in the series with varying f_w . The redshift observed in the fluorescence spectrum implies the bandgap energy reduction caused due to the increased solvent polarity that enhances the HOMO energy level of the molecular system (Hu et al. 2009).

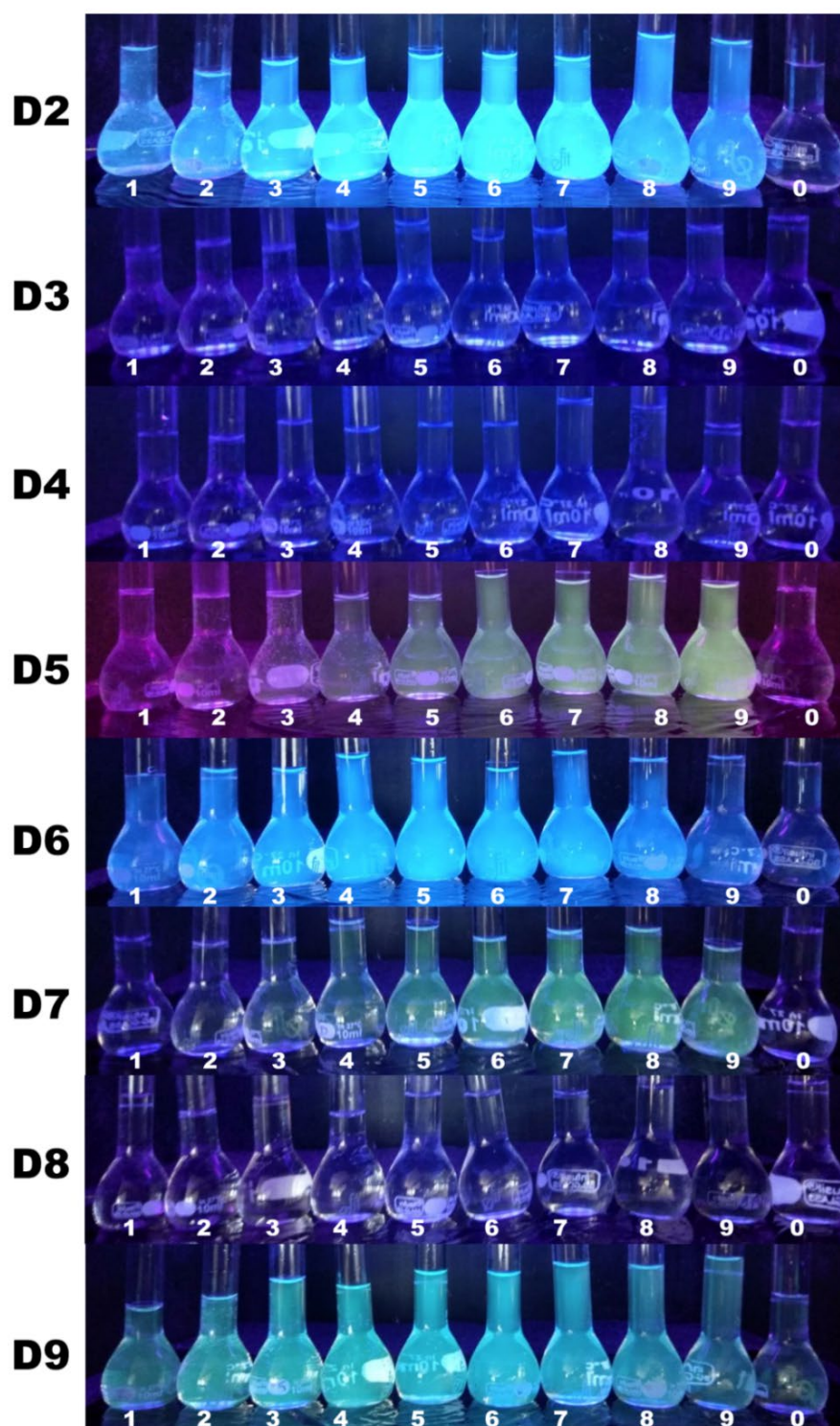


Fig. 3.53 Photographs of molecules **D2-D9** in methanol/water mixtures with different f_w taken under UV illumination at a wavelength of 365 nm

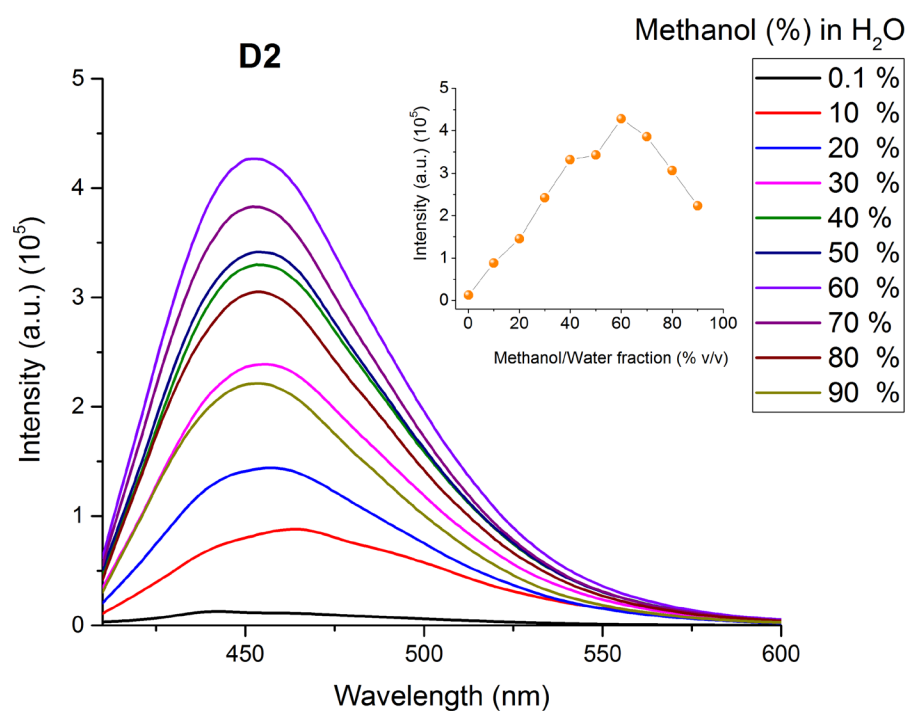


Fig. 3.54 Fluorescence emission spectrum of **D2** with varying f_w and inset gives the intensity value with varying f_w

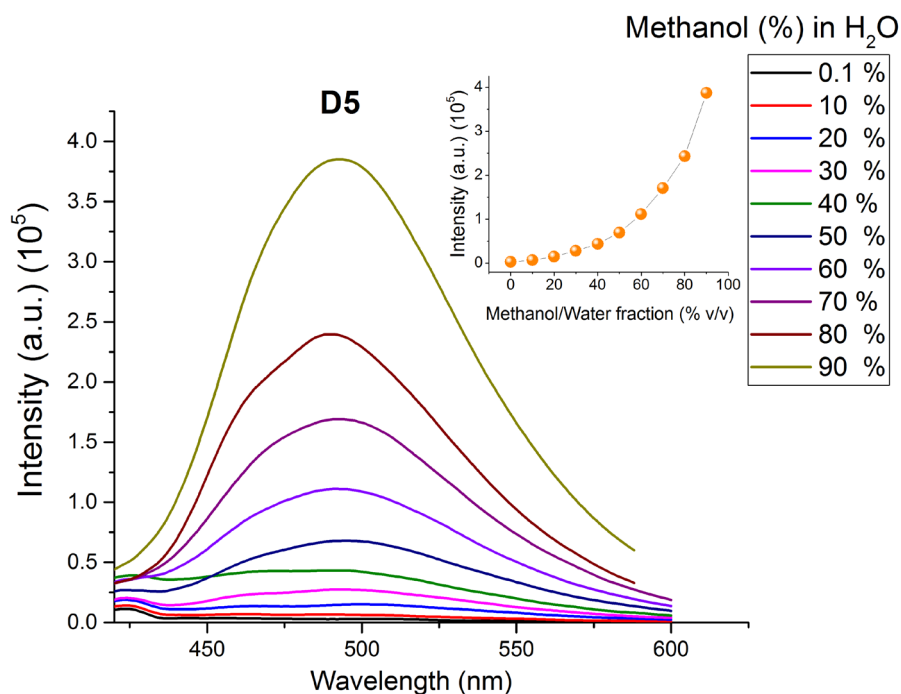


Fig. 3.55 Fluorescence emission spectrum of **D5** with varying f_w and inset gives the intensity value with varying f_w

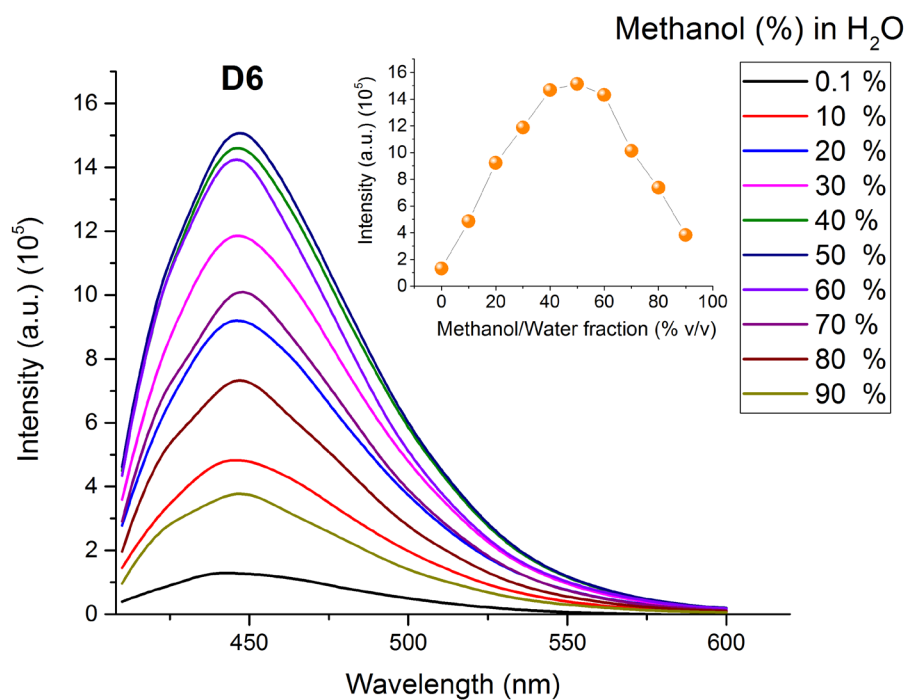


Fig. 3.56 Fluorescence emission spectrum of **D6** with varying f_w and inset gives the intensity value with varying f_w

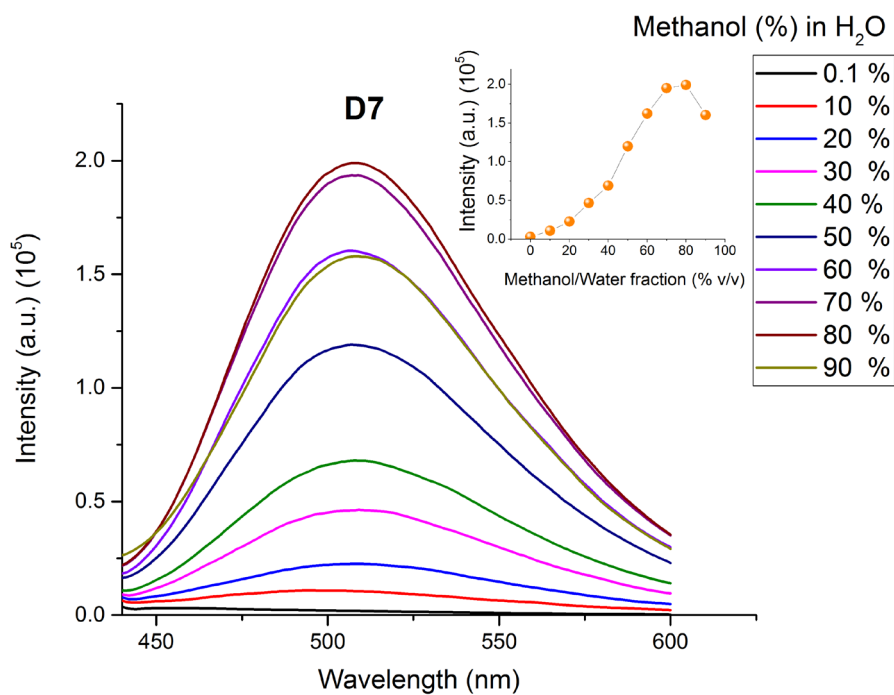


Fig. 3.57 Fluorescence emission spectrum of **D7** with varying f_w and inset gives the intensity value with varying f_w

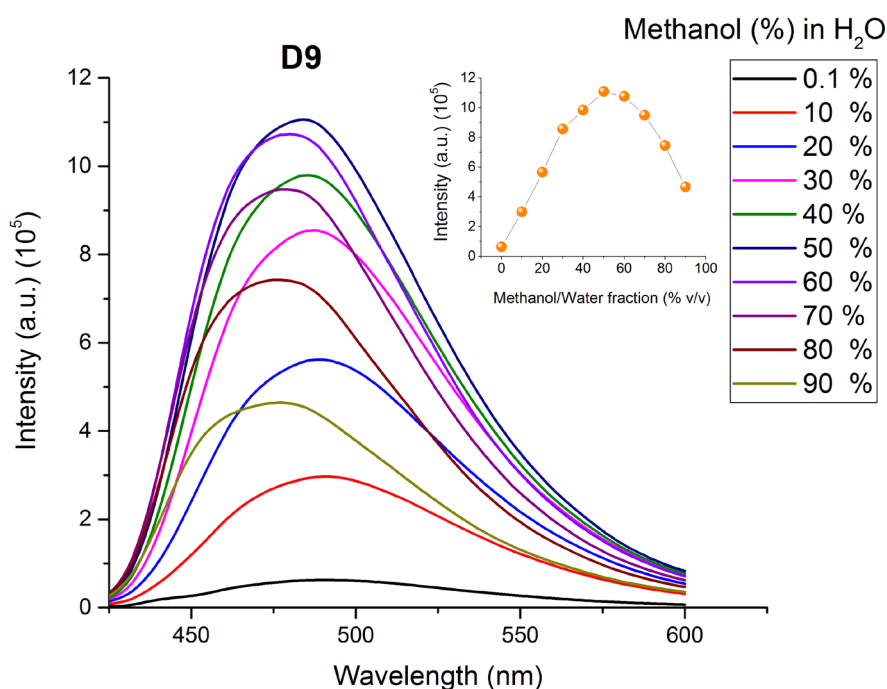


Fig. 3.58 Fluorescence emission spectrum of **D9** with varying f_w and inset gives the intensity value with varying f_w

3.3.7 Cyclic Voltammetry

The electrochemical properties of the molecules have been investigated by cyclic voltammetry to estimate their HOMO and LUMO energy levels. The presence of $-\text{OH}$ and $-\text{NH}$ functionality in the molecules **D1** to **D9** is expected to yield an oxidation peak. The cyclic voltammogram displayed an irreversible oxidation curve ascribed to the removal of electron from the conjugated system as given in the Fig. 3.59 (a) and (b). HOMO energy levels have been determined from cyclic voltammogram oxidation peak in accordance with the equation $E_{\text{HOMO}} = -(I_p + 4.4) \text{ eV}$ (Duvenhage et al. 2015). LUMO energy levels of the series were derived from the solid-state photoluminescence spectra and estimated HOMO energy level from cyclic voltammetry. The molecules possess oxidation peak in a range between 1.31 V to 2.7 V. Fig. 3.60 shows the energy level diagram of molecules **D1** to **D9**. The HOMO and LUMO levels of the molecules are listed in Table 3.5. Molecule **D2**, possessing an ortho substituted OH group exhibits a very high oxidation potential of 2.5 V leading to a high HOMO of -6.90 eV , similar to **D4** and **D8**. Molecule **D4** and **D8**, owing to the presence of NO_2 functionality that enhances electron withdrawing capability from the parent chain, exhibits a greater oxidation

potential at a positive value of 2.7 V and 2.58 V, yielding a very deep HOMO energy level of -7.1 eV and -6.98 eV respectively. Molecule **D3**, **D5**, **D6** and **D7** exhibited low oxidation peak contributed by higher electron density owing to the presence of electron donor species. The lowest oxidation peak observed in molecule **D9** is due to the highly electron donating di-ethylamino group. Such electron donating ability enhances the hole transporting nature in the system. Overall, relatively shallow HOMO, LUMO energy was observed only in **D9** molecule which is expected to facilitate a good hole and electron transport in the material.

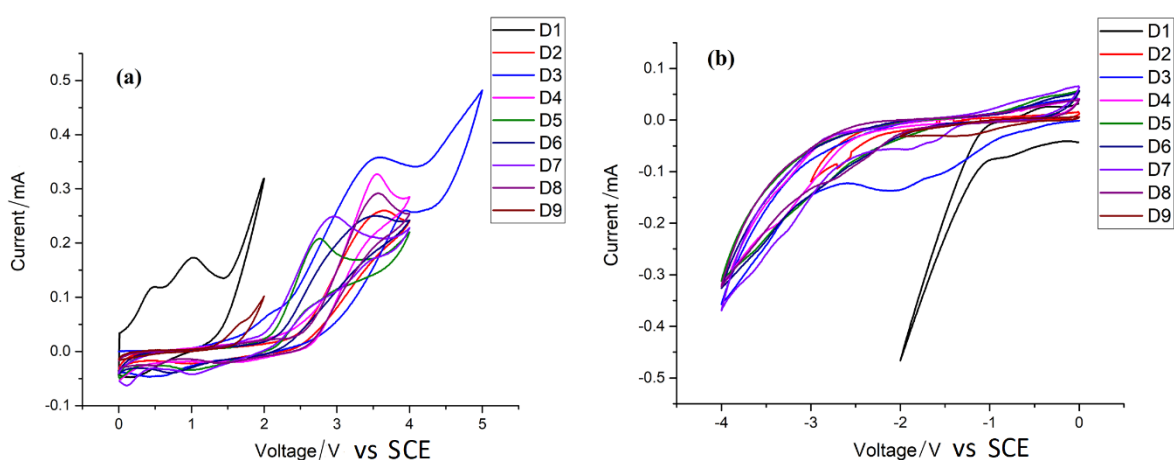


Fig. 3.59 Cyclic voltammogram representing (a) oxidation cycle and (b) reduction cycle for the molecules **D1** to **D9**

Table 3.5 Electrochemical results for the molecules **D1** to **D9**

	I_p (V)	HOMO (eV)	LUMO (eV)	E_G (eV)
D1	1.02	-5.42	-3.16	2.26
D2	2.50	-6.90	-3.57	2.35
D3	2.12	-6.52	-4.63	2.95
D4	2.70	-7.10	-4.30	2.47
D5	2.11	-6.51	-4.17	2.21
D6	2.21	-6.61	-4.33	2.44
D7	2.02	-6.42	-4.56	2.09
D8	2.58	-6.98	-3.29	2.42
D9	1.31	-5.71	-4.55	2.42

HOMO obtained from oxidation peak from cyclic voltammogram, *LUMO* – estimated from the solid-state fluorescence spectra ($LUMO = E_G - HOMO$).

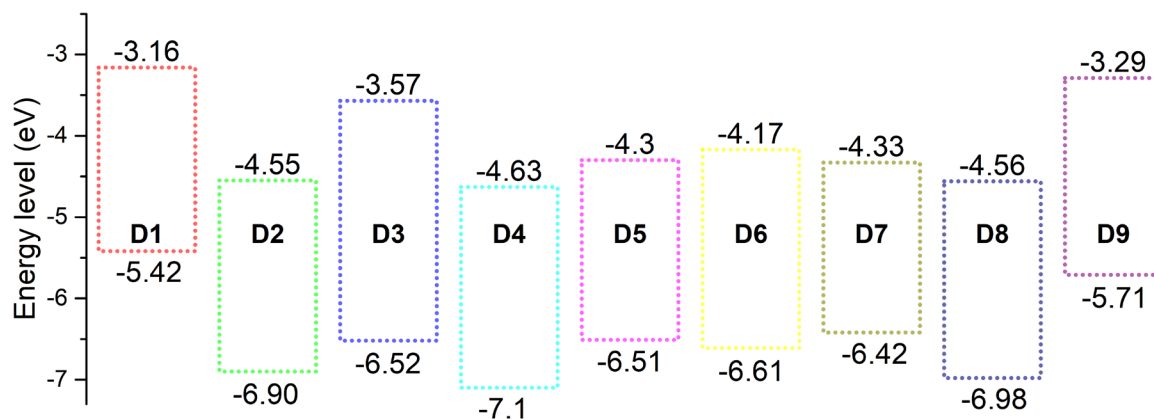


Fig. 3.60 HOMO and LUMO energy levels of molecule **D1** to **D9**

3.3.8 X-ray crystal structure analysis

The X-ray crystal structures of few molecules in the series have been analysed to understand the molecular structure and the molecular packing density in support of AIE. Crystal structures for molecule **D6** and **D7** were obtained and analysed with the help of single crystal X-ray diffraction. ORTEP diagram of molecule **D6** and **D7** is provided in Fig. 3.61 and Fig. 3.62. The crystal structures of the molecules **D1** and **D3** have been reported by J.-H. Jiang (Jiang 2011) and Yu-Feng Li (Li et al. 2010). To the best of our knowledge, the crystal structures for molecules **D6** and **D7** have not been reported earlier. Single crystal XRD analyses prove that molecules **D6** and **D7** exhibit a high amount of planarity and arrange themselves in a slipped parallel stacking arrangement in a unit cell as illustrated in the Fig. 3.63 and Fig. 3.64. The ring normal and the vector between the ring centroids form an angle of about 37° and the centroid-centroid distances of 4.636 Å. The molecules in the lattice exhibit herringbone type of molecular packing arrangements, wherein there exists π - π stacking between the C-H \cdots π and aromatic rings in the form of slipped face-face and edge to face interactions. The distances of the intermolecular π - π^* interaction play a crucial role, as it can lead to the deactivation of the photo-excited molecules via non-radiative energy transfer leading to ACQ. It is reported earlier that the influence of π - π interaction on stacking is quite strong if the distance between the aromatic ring is lesser than 3.3 Å and for a weaker interaction it is around 3.6 Å, with 3.8 Å being approximately the maximum contact for which π - π interactions are accepted (Janiak 2000). In the present study, the intermolecular π - π interaction distance between the aromatic rings for **D6** and **D7** is of the order of 4.866 Å and 4.636 Å leading to a

weaker interaction, in turn, such weak interaction would block all the pathways for non-radiative energy transfer, rather favouring AIEE.

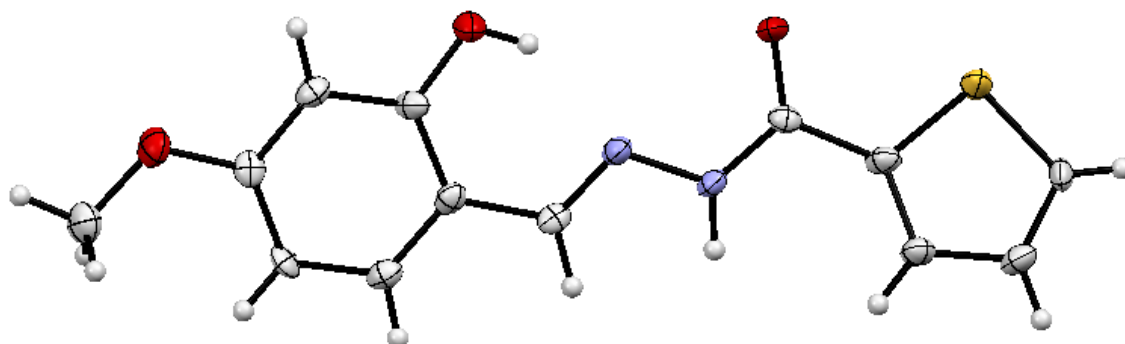


Fig. 3.61 ORTEP diagram of molecule **D6**

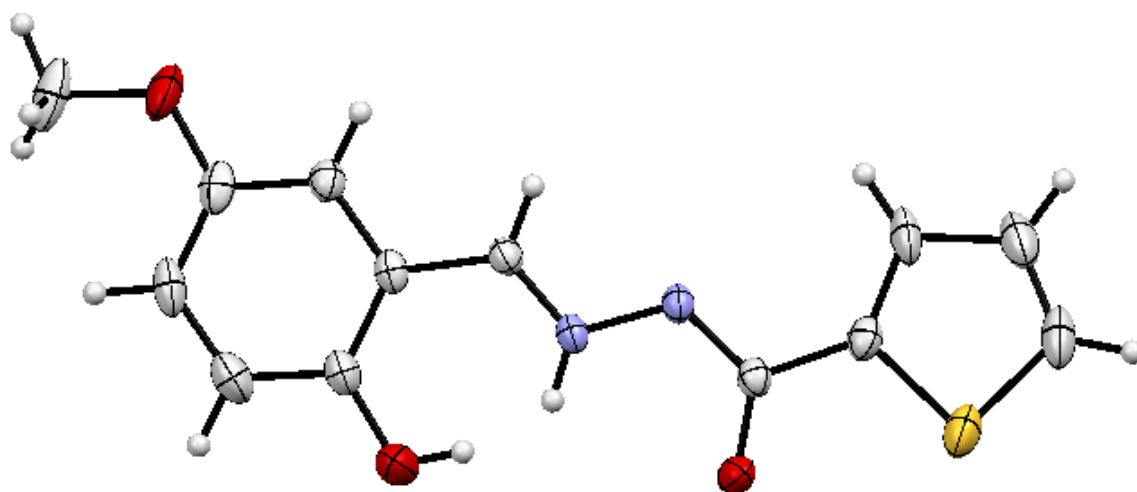


Fig. 3.62 ORTEP diagram of molecule **D7**

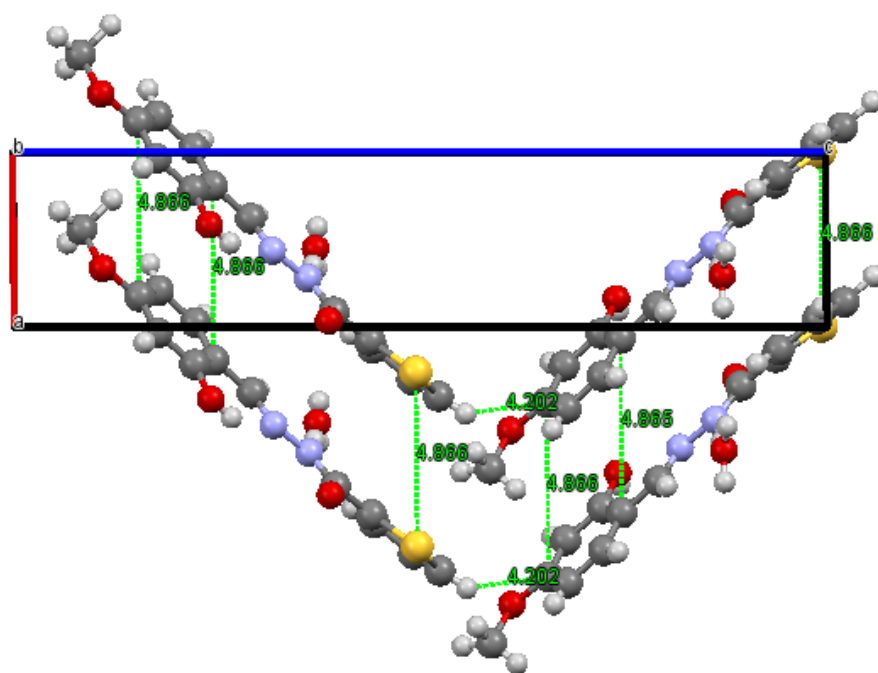


Fig. 3.63 Molecular packing arrangement of molecule of **D6** obtained by single crystal XRD

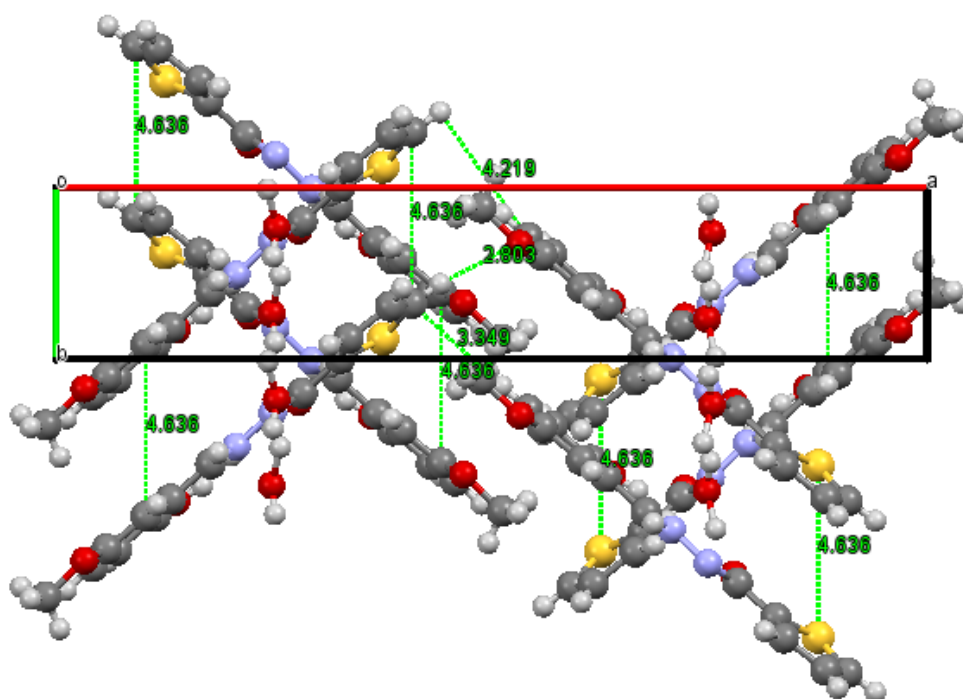


Fig. 3.64 Molecular packing arrangement of molecule of **D7** obtained by single crystal XRD

Table 3.6 Crystallographic data of molecule **D6** and **D7**

Crystal parameters	D6	D7
Empirical formula	C13 H14 N2 O4 S	C13 H14 N2 O4 S
Formula weight (g mol ⁻¹)	294.33	294.33
Temperature	296 (2) K	296 (2) K
Wavelength	0.71073	0.71073
Crystal system, space group	triclinic, 'P 1'	Orthorhombic, 'P 21'
Unit cell dimension	a = 4.8655(10), α = 89.864 ⁰ b = 6.4488(13), β = 89.453 ⁰ c = 21.972(5), γ = 75.707 ⁰	a = 23.5149(12), α = 900 b = 4.6361(3), β = 900 c = 12.4729(7), γ = 900
Volume	668(2)Å ³	1359.76 (14)Å ³
Goodness-of-fit on F ²	1.16	0.803
R indices (all data)	0.0484	0.0344
CCDC No.	1583561	1583560

3.3.9 DFT studies

The geometrical and electronic properties of the molecules were estimated using Gaussian 09 package (Frisch et al. 2013) in order to study the structure–property relationship. Singlet ground state optimization of the geometry was achieved by means of the B3LYP with the 6-311++G (d, p) basis set (Hariharan and Pople 1973; Hehre et al. 1972; Lee et al. 1988) and electronic orbitals were visualized using Avogadro software (Hanwell et al. 2012). The effect of solvent on the energy parameters of the molecules was incorporated by self-consistent reaction field using conductor polarizable continuum model (Tomasi and Persico 1994) (SCRF-CPCM). Vertical transition energies up to first 10 singlet excited states and molar extinction coefficients of the entire series both in gas and solvents phase were estimated.

Ground state optimized geometry shows that the molecule of the series adopts a highly planar structure having 0° dihedral angle, except for **D3** possessing a dihedral angle of 15°, as shown in the Fig. 3.65. DFT predictions for the molecule of the series strongly support few of the crystallographic results mentioned. Fig. 3.66 shows the spatial distributions of the orbitals of the molecules. HOMO and LUMO orbital are well distributed on the whole structure due to their high planarity, both in ground and excited states. The large overlap between HOMO and LUMO orbitals results in efficient

absorption and emission. Further, molecule **D4** and **D8** have their HOMO distributed on the entire molecular network and LUMO on aromatic ring and imine group can be attributed to the presence of NO₂ group. However, molecules **D1- D9**, in contrast have their HOMO distributed on the imine linkage and the aromatic ring and LUMO is distributed on the entire molecular network. TD-DFT calculations were carried out on molecules **D1-D9** to predict their excited state transition and the nature of absorption bands. Spatial distributions of the molecular orbitals of **D1-D9** with their oscillator strength are provided as well. Clearly, TDDFT predictions are in good agreement with the experimentally obtained absorption spectra, with the underestimated energy difference of 0.18 eV. This energy difference can be attributed to the fact that there exist many conformers in the solution state whereas such conformers may not be considered for the calculation (Linton et al. 2012). Nevertheless, the spectral trend for all the molecules is well reproduced in the computed spectra, except for series in DMSO solvent medium. Molecule **D1, D2, D3, D5** and **D9** exhibited either a single peak or a profound shift in the spectra maintaining the trend observed for other solvents, such behaviour of the solvent shift was unable to be reproduced through computational calculations. Owing to the high dielectric constant of the solvent, the solvent polarizes the electron density of the solute molecule building up many vibrational levels providing access to higher wavelength transition. Lowest energy transitions observed are assigned to the charge-transfer transitions occurring between substituted benzaldehyde donor unit and the thiophene hydrazide acceptor unit. The spectra obtained from TD-DFT calculations for the entire molecular series in solvent of varying polarity is provided in the Fig. 3.67 – Fig. 3.75.

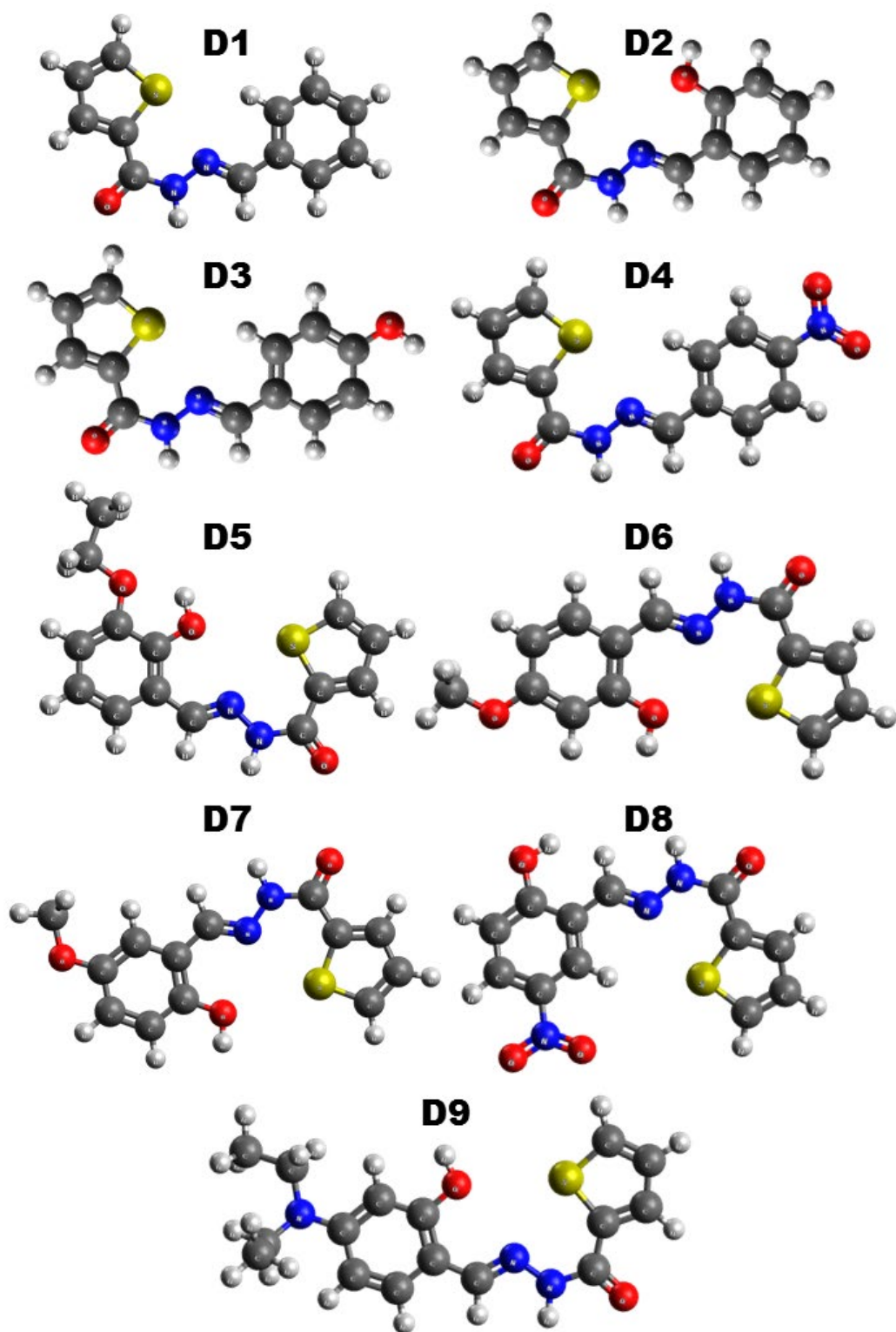


Fig. 3.65 Optimized geometry of molecules D1 - D9 using DFT B3LYP functional.

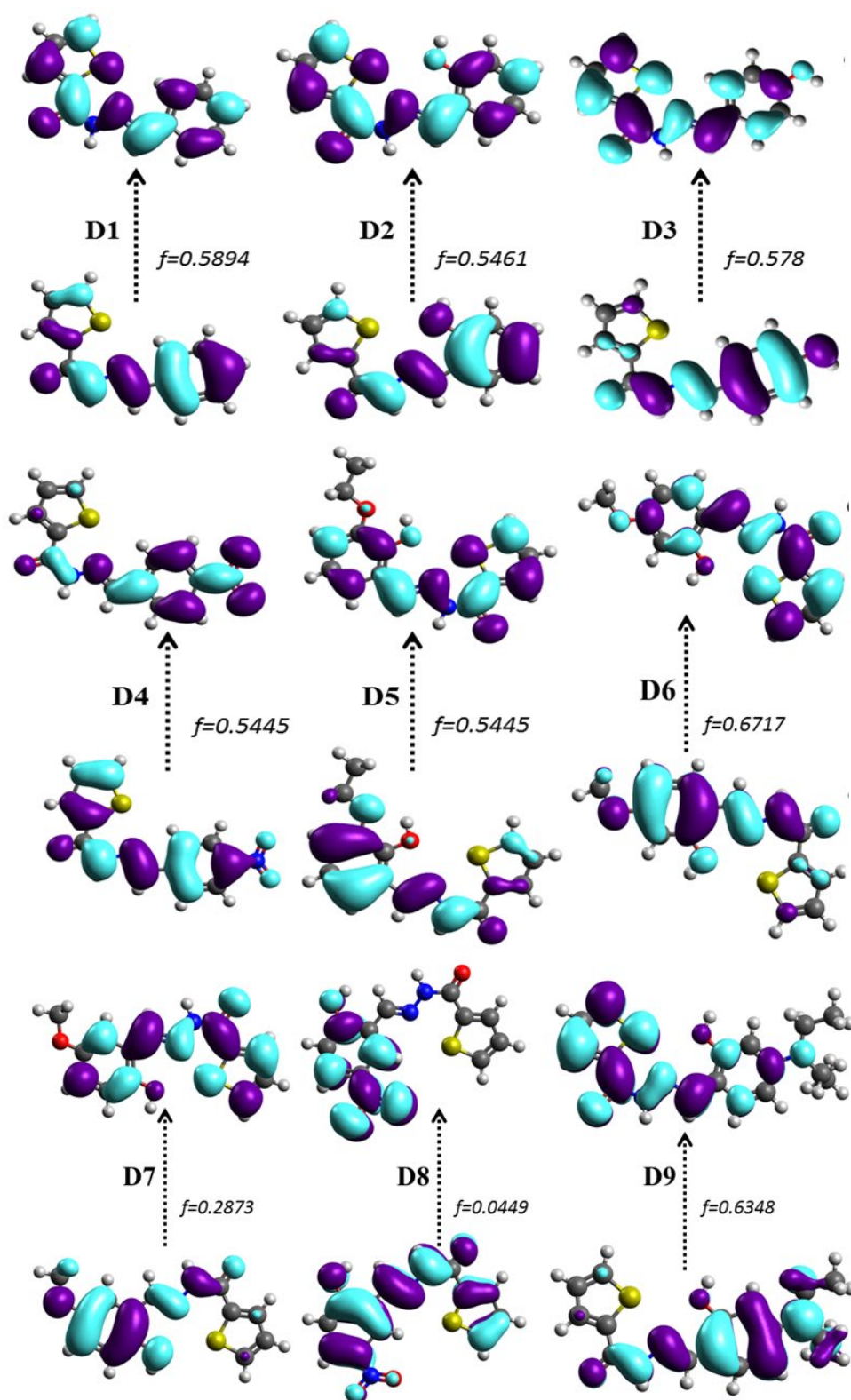


Fig. 3.66 Molecular spatial orbitals of molecule **D1** to **D9** with their oscillator strength

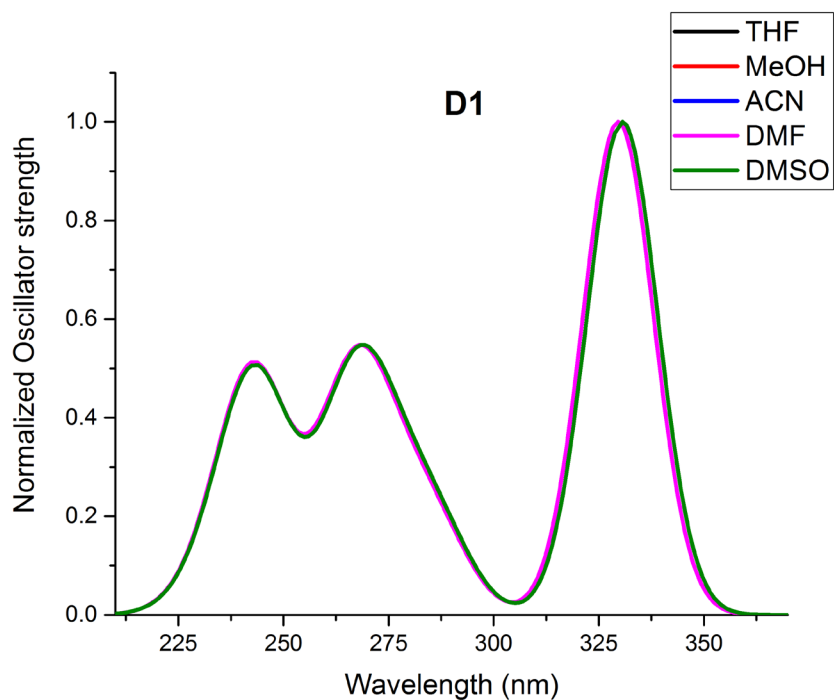


Fig. 3.67 TD-DFT absorbance spectra of molecule **D1** in solvent of varying polarity

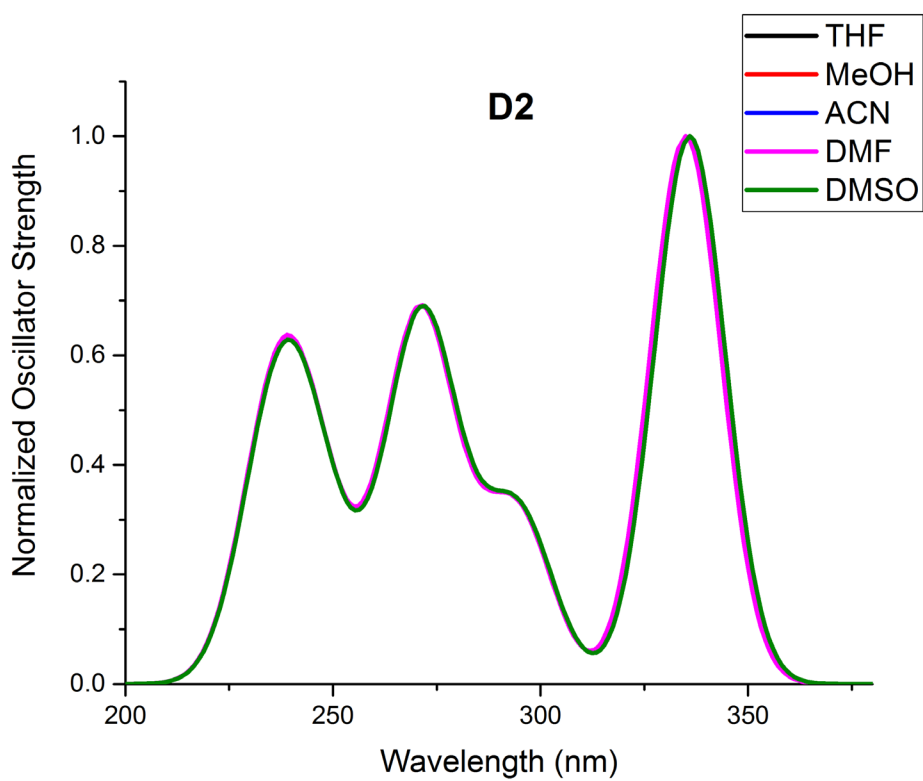


Fig. 3.68 TD-DFT absorbance spectra of molecule **D2** in solvent of varying polarity

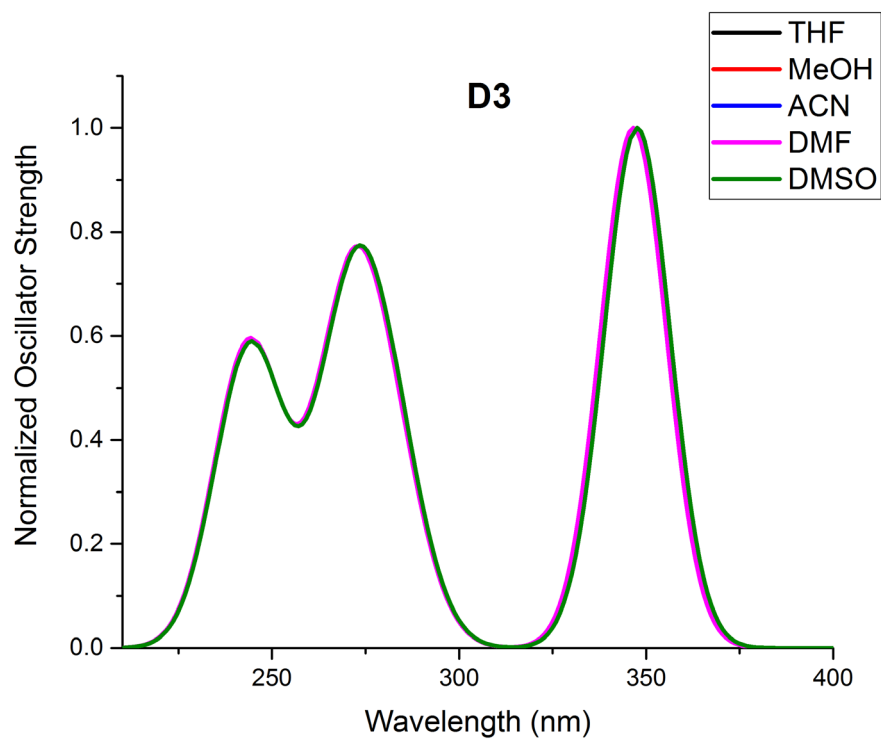


Fig. 3.69 TD-DFT absorbance spectra of molecule **D3** in solvent of varying polarity

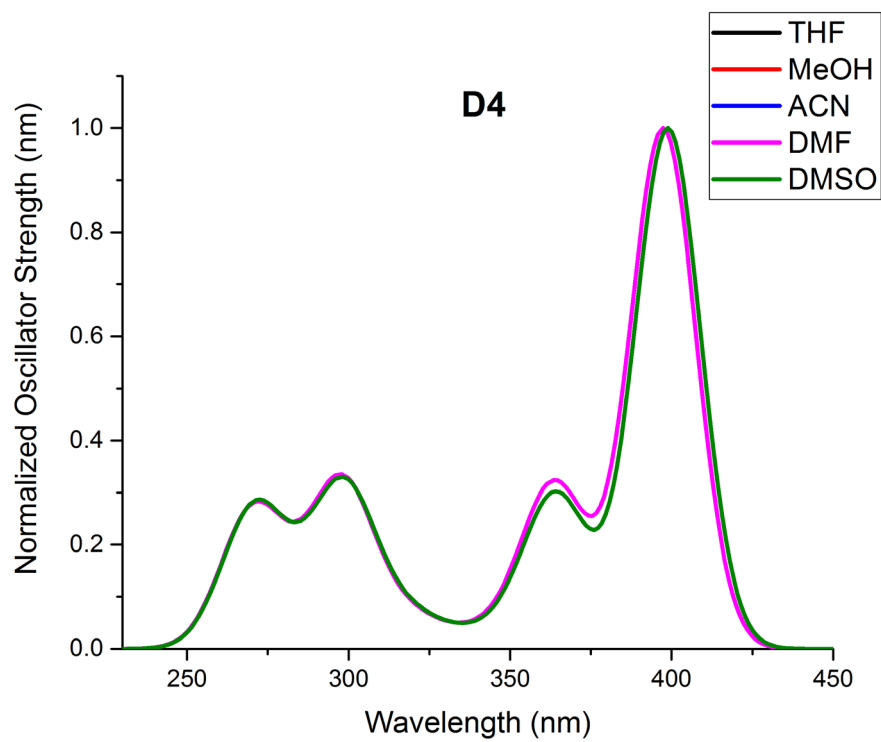


Fig. 3.70 TD-DFT absorbance spectra of molecule **D4** in solvent of varying polarity

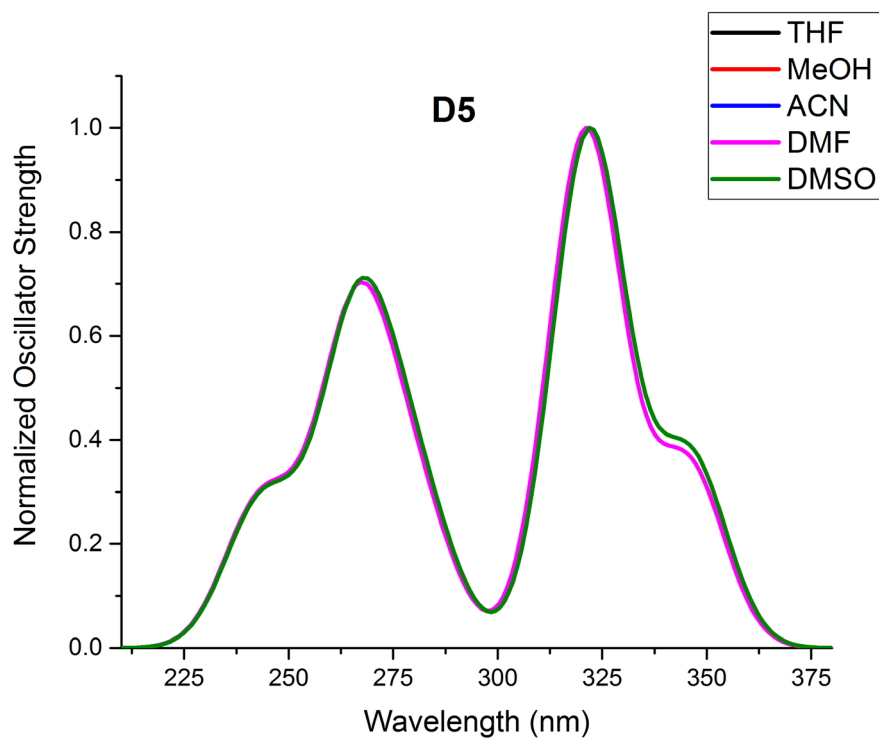


Fig. 3.71 TD-DFT absorbance spectra of molecule **D5** in solvent of varying polarity

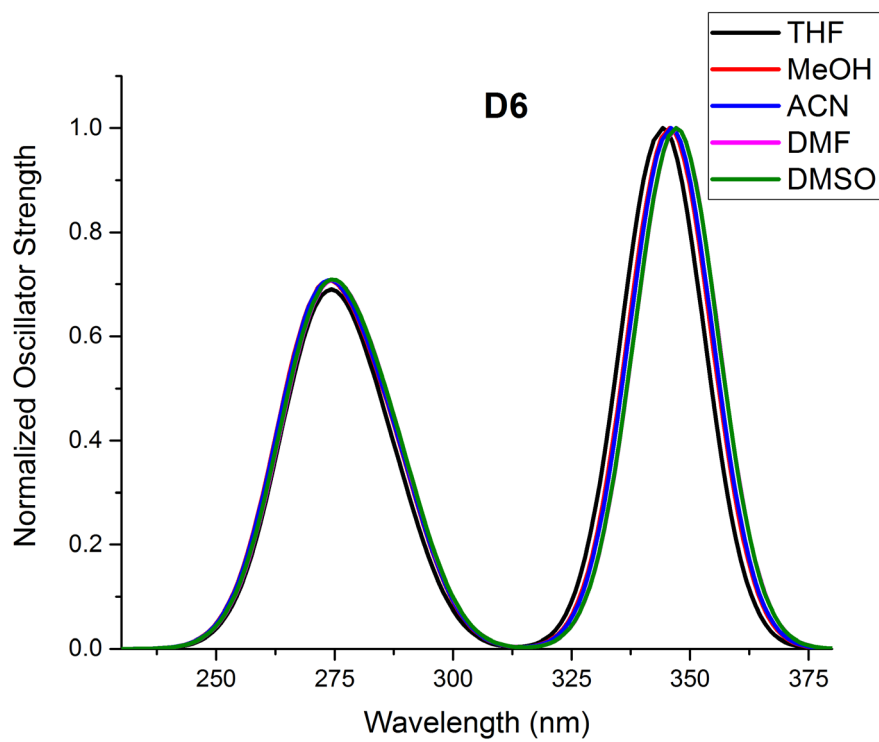


Fig. 3.72 TD-DFT absorbance spectra of molecule **D6** in solvent of varying polarity

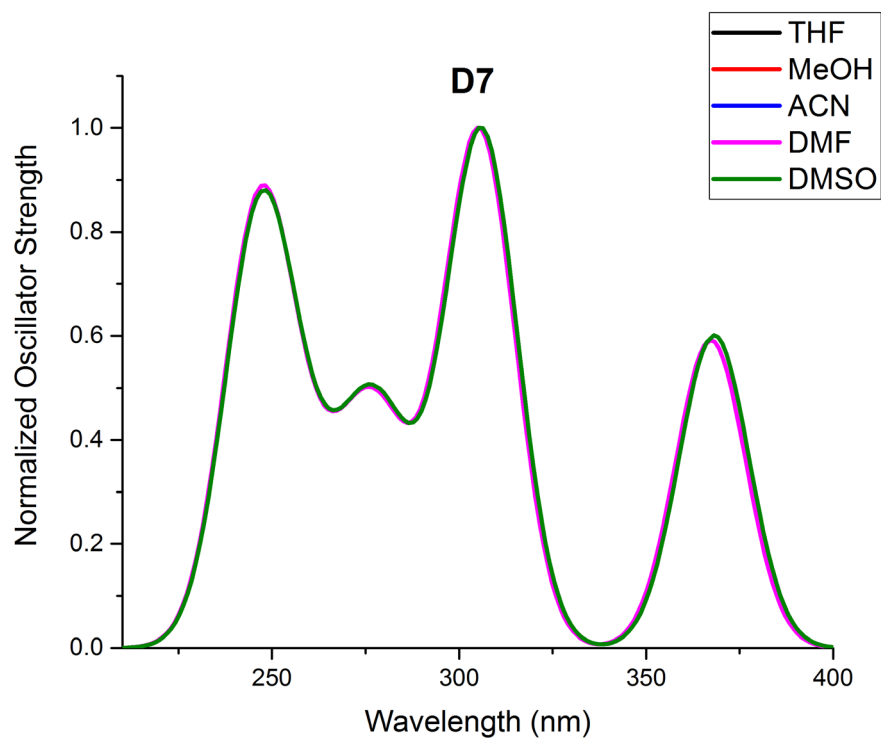


Fig. 3.73 TD-DFT absorbance spectra of molecule **D7** in solvent of varying polarity

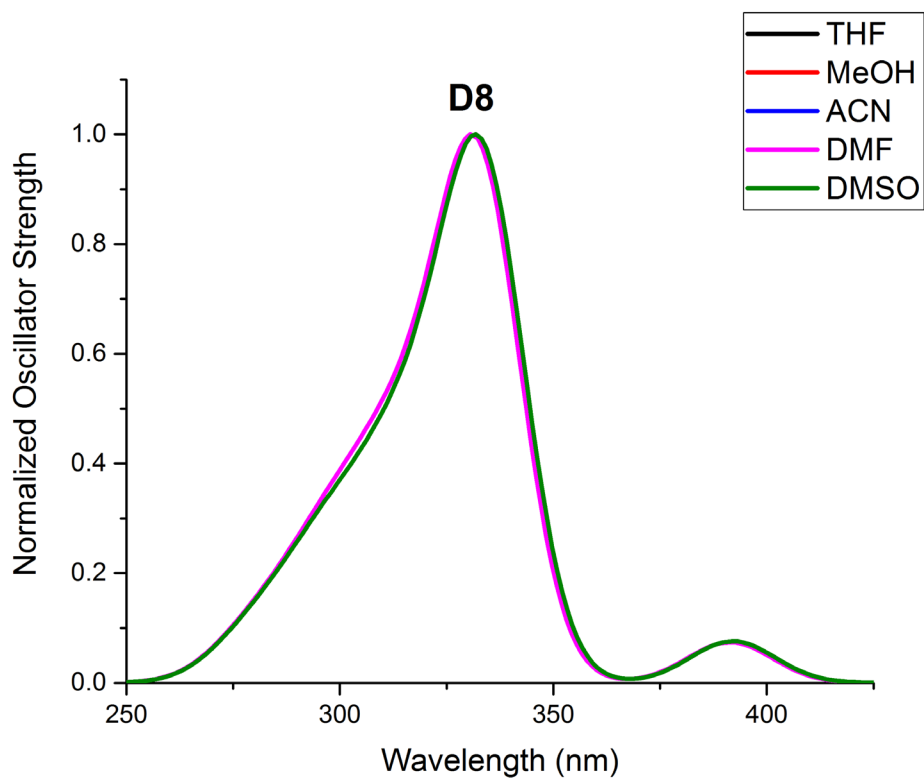


Fig. 3.74 TD-DFT absorbance spectra of molecule **D8** in solvent of varying polarity

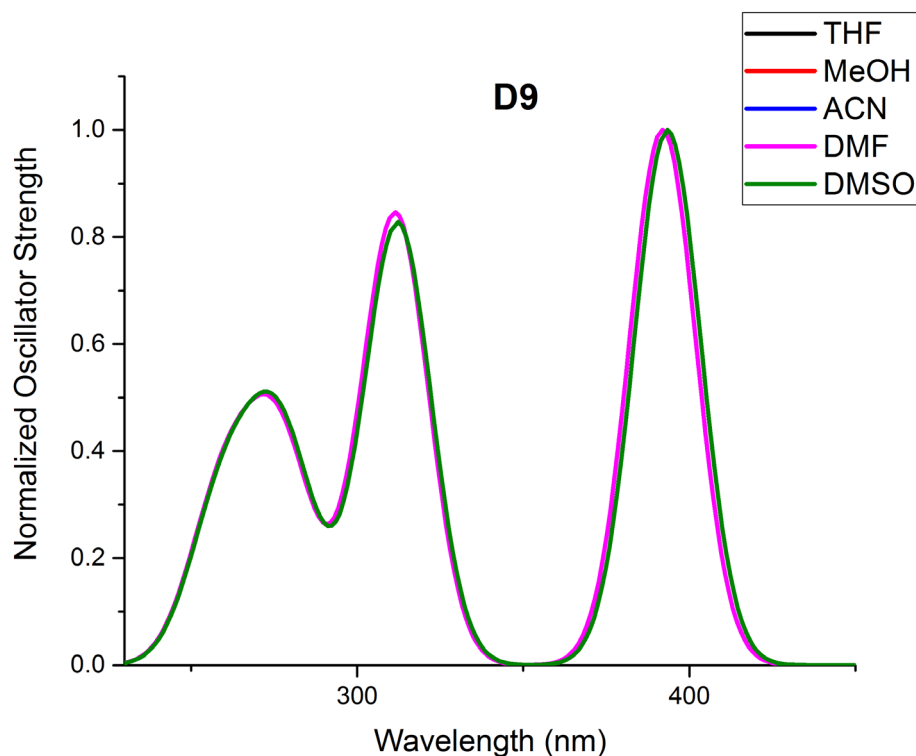


Fig. 3.75 TD-DFT absorbance spectra of molecule **D9** in solvent of varying polarity

3.4 CONCLUSIONS

A series of thiophene derivatives **D1** to **D9** have been synthesized in good yield and characterized by standard spectroscopic techniques. The positional substitution of electron donating and withdrawing groups on molecules **D2** to **D9** showed profound influence on the emission wavelength. Few of the molecules in the series exhibited AIE confirmed by comparing the emission intensities of the molecules in pure solvent and solvent/methanol mixture. Molecules of the series exhibited a fluorescence lifetime value of ~2-4 ns. SCXRD results of **D6** and **D7** shows that the molecule possesses a high amount of planarity with zero dihedral angle and a herring bone type of molecular packing arrangement that blocks the non-radiative pathways and aids in emission enhancement. Cyclic voltammogram reveals a very high redox potential resulting in higher negative values of LUMO in the system. Ground state optimized geometry of the entire series reveals the structure possesses a high amount of planarity in them, well supported by SCXRD. Excited state properties of the molecules computed are in good agreement with the experimentally observed absorption spectra, with an energy overestimation of 0.18 eV.

CHAPTER 4

DESIGN AND SYNTHESIS OF BITHIOPHENE BASED AIE EMITTERS: EXPERIMENTAL AND THEORETICAL ANALYSIS

Abstract

In this chapter, the design, syntheses, photophysical and electrochemical studies of substituted bithiophene derivatives have been described. The theoretical and experimental aspects have been elaborately discussed by DFT studies.

4.1 INTRODUCTION

Design of good solid-state emitters for organic light emitting diode applications have been a topic of interest for academic and industrial research since their development by Tang and Vanslyke. Organic light emitting diodes have attracted much attention for their use in full color flat panel displays constituting red, green and blue colors. Emission in red region by a molecule is relatively weak in comparison with blue or green region as these materials are highly susceptible to aggregation quenching and hence become either weakly emissive or non-emissive in solid state. Design of a better red emitting material that exhibit a good emission in solid-state still remains a challenge. Bithiophene based materials have been at the research forefront for their remarkable characteristics namely low oxidation potential, low energy gaps, and high thermal stability (Brzeczek et al. 2016; Fernandes et al. 2018; Gupta et al. 2015; Han et al. 2015; Karthik et al. 2016; Krishna et al. 2018; Zhang et al. 2018). The electronic rich property of thiophene rings are known to provide a good number of electrons for the whole system. In contrary, five membered heterocycle imidazole possess two distinct nitrogen atoms N1 and N3 being electron rich like pyrrole and electron deficient like pyridine respectively. In conjunction with this, lone pair from N1 occupies $2p_z$ orbital contributing to the whole aromaticity and lone pair of N3 fills the hybridized sp^2 orbital. The intrinsically bipolar electronic structure of imidazole meets the requirement of balanced charge transport leading to be more suitable for OLED applications.(Chen et al. 2018). In the present work, synthesis and photophysical properties of pyrazole and imidazole derivatives bearing the bithiophene backbone and cyano substitution have been attempted. The nature of the system is known to exhibit variant photophysical properties due to the interaction between the cyano substituent and core heterocyclic unit. Owing to the above-mentioned positives of imidazole, an attempt is made to investigate the effect of number of cyano groups on the optical property of materials. The number of cyano substituent is limited to one in pyrazole by virtue of their inherent property as electron donor and electron acceptor and is increased to two

substituents in imidazole moiety to achieve for an enhanced photophysical property. The cyano group is introduced in the system to ensure the absence of donor-acceptor interaction but enhanced electronic delocalization over the entire molecule through a conjugated backbone. Planar structure of bithiophene assists better conjugation that is otherwise reduced by twisting of the end groups. The presence of good electron delocalization yields equalized C-C bond lengths within the thiophene units. Considering these facts three molecules with bithiophene core have been designed and synthesized that shows enhanced emission in solid-state with that of the solution state.

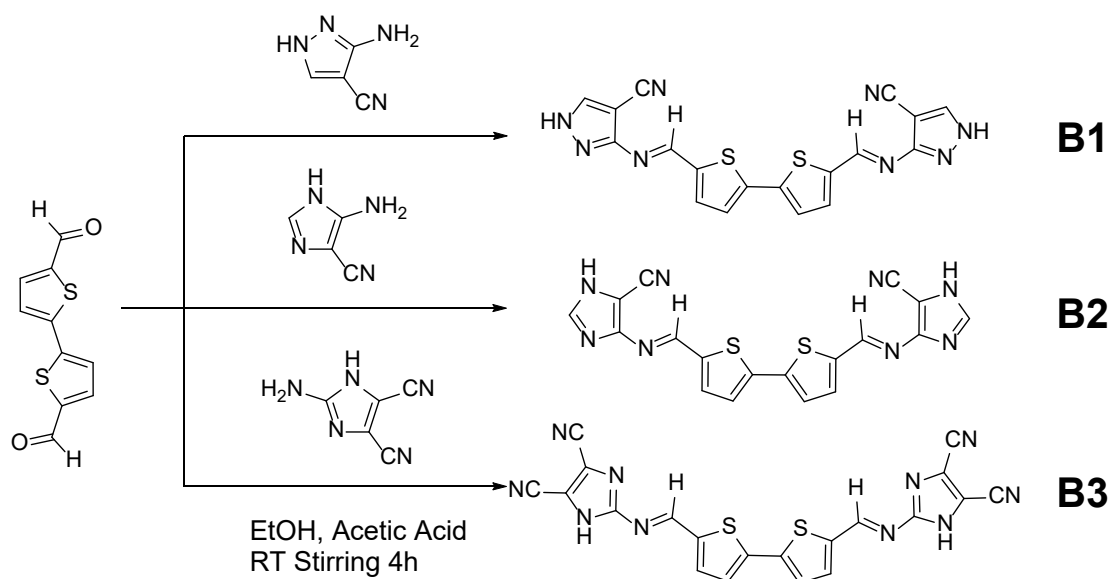
4.2 EXPERIMENTAL SECTION

4.2.1 Materials and methods

All the chemicals used in the present study were procured from Sigma-Aldrich and were used as received without further purification. All the solvents were purchased from purchased from SD Fine, India, were of HPLC grade and used without further distillation. Melting point was measured on Stuart SMP3 melting-point apparatus in open capillaries. Infrared spectrum was recorded on Bruker Apex FTIR spectrometer. UV-Vis spectroscopy was performed with Ocean optics SD2000 spectrometer in a standard 3.0 mL quartz cell with 1 cm path length. Cyclic voltammogram was recorded on IVIUM electrochemical workstation (Vertex) at a scan rate of 10 mV/s, 20 mV/s and 50 mV/s with the potential ranges from -3V to +3V. Photoluminescence studies were carried out using Horiba Jobin Yuan spectrofluorometer. All the measurements were performed under room temperature.

4.2.2 Synthesis

Molecules **B1**, **B2**, **B3** have been synthesized by Schiff base condensation of 2,2'-bithiophene-5,5'-dicarboxaldehyde (0.1 g, 0.44 mmol) with 3-amino-1H-pyrazole-4-carbonitrile (0.048 g, 0.44 mmol), 5-amino-1H-imidazole-4-carbonitrile (0.048 g, 0.44 mmol), 2-amino-1H-imidazole-4,5-dicarbonitrile (0.059 g, 0.44 mmol) respectively. All the reactions were carried out in ethanol solvent. The reaction mixtures were stirred under ambient conditions in the presence of acetic acid as a catalyst. The general scheme of synthesis is shown in Scheme 4.1.



Scheme 4.1 Synthetic scheme of molecules **B1**, **B2** and **B3**

B1 3,3'-(((1Z,1'Z)-[2,2'-bithiophene]-5,5'-diylbis(methanelylidene))bis(azaneylylidene)) bis(1H-pyrazole-4-carbonitrile) Yield: 82 %, melting point: 245°C, FTIR (ATR) (cm^{-1}): 3130 (NH), 3078 (CH), 2225 (CN), 1585 (CH=N). ^1H NMR (400 MHz, $\text{DMSO}-d_6$) δ 13.63 (s, 2H), 9.15 (d, $J = 2.6$ Hz, 2H), 8.54 (s, 2H), 7.87 (d, $J = 3.9$ Hz, 3H), 7.70 (d, $J = 3.9$ Hz, 2H). ESI-MS Calculated: 402.45, Obtained: 401.00 ($\text{M}-\text{H}^+$)

B2 5,5'-(((1Z,1'Z)-[2,2'-bithiophene]-5,5'-diylbis(methanelylidene))bis(azaneylylidene)) bis(1H-imidazole-4-carbonitrile) Yield: 76 %, melting point: 249°C, FTIR (ATR) (cm^{-1}): 3083 (NH), 2921 (CH), 2229 (CN), 1660 (CH=N). ^1H NMR (400 MHz, $\text{DMSO}-d_6$) δ 13.44 (s, 2H), 9.09 (s, 2H), 7.93 (s, 2H), 7.81 (d, $J = 4.1$ Hz, 2H), 7.68 (s, 2H). ESI-MS Calculated: 402.45, Obtained: 401.45 ($\text{M}-\text{H}^+$)

B3 2,2'-(((1Z,1'Z)-[2,2'-bithiophene]-5,5'-diylbis(methanelylidene)) bis(azaneylylidene)) bis(1H-imidazole-4,5-dicarbonitrile) Yield: 66 %, melting point: 242°C, FTIR (ATR) (cm^{-1}): 3424 (NH), 3123(CH), 2232 (CN), 1587 (CH=N). ^1H NMR (400 MHz, $\text{DMSO}-d_6$) δ 13.44 (s, 2H), 7.93 (s, 2H), 7.81 (d, $J = 4.1$ Hz, 2H), 7.68 (s, 2H). ESI-MS Calculated: 452.04, Obtained: 451.05 ($\text{M}-\text{H}^+$)

4.2.3 Characterization data

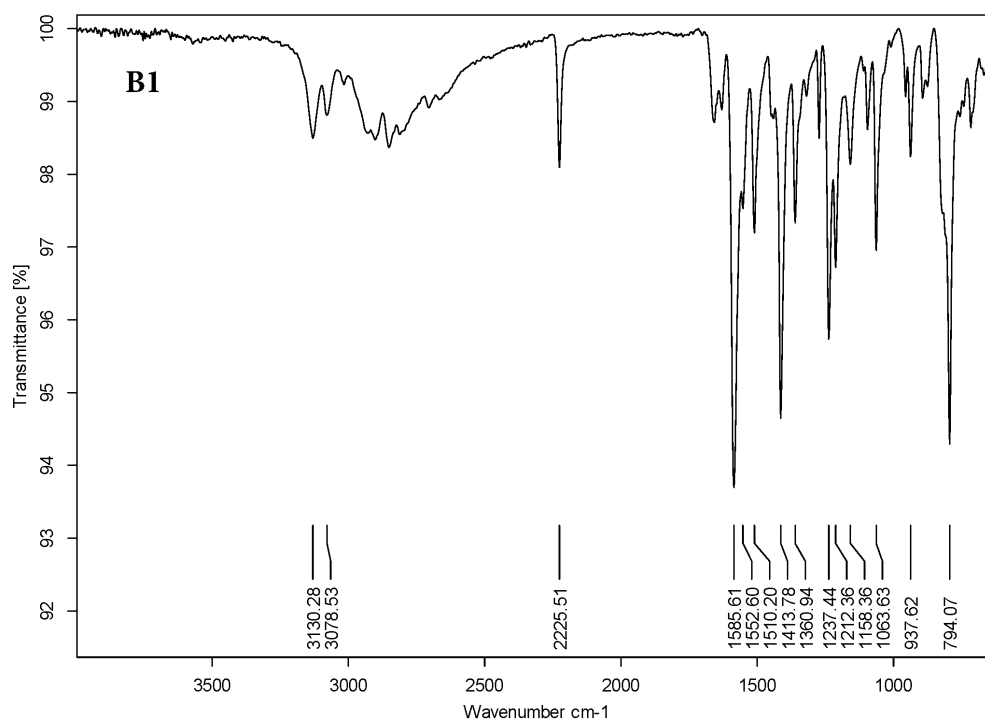


Fig. 4.1 FT-IR spectra of B1

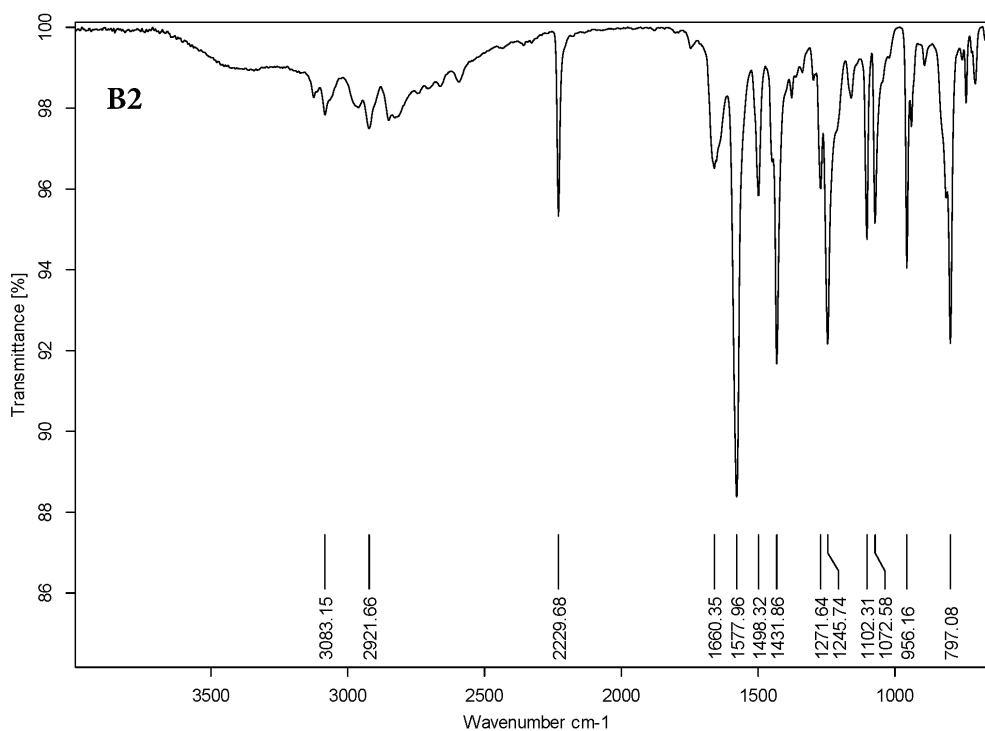


Fig. 4.2 FT-IR spectra of B2

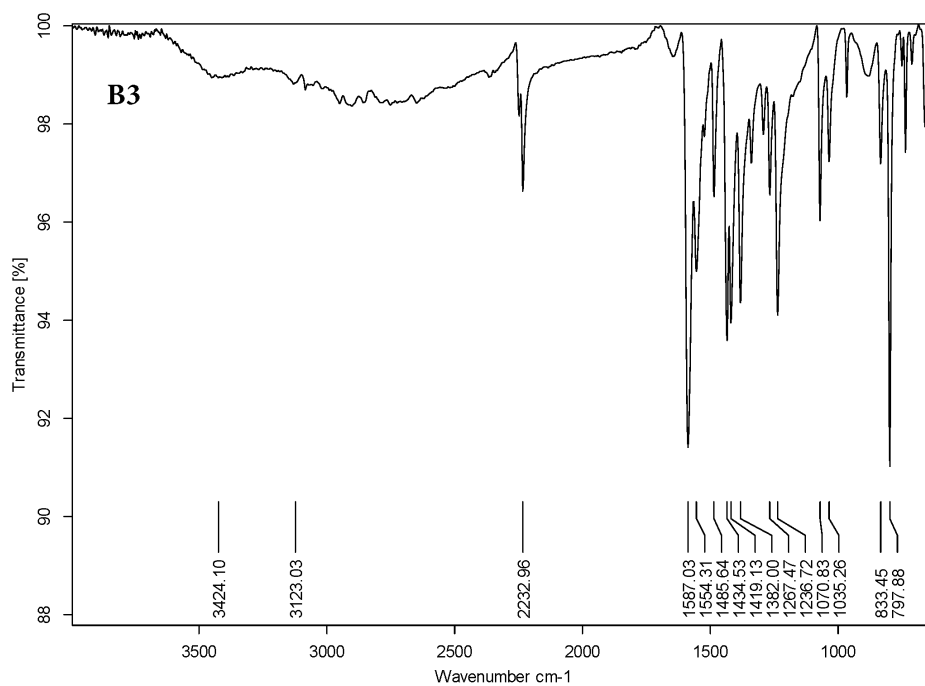


Fig. 4.3 FT-IR spectra of **B3**

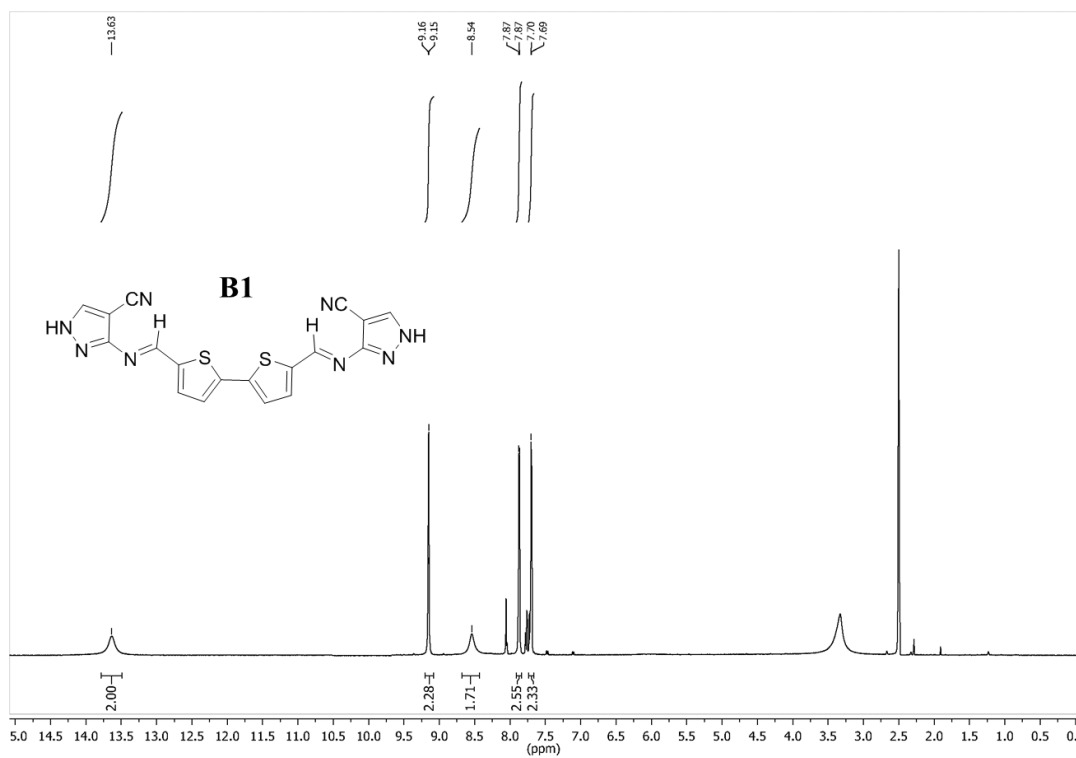


Fig. 4.4 ¹H-NMR spectra of **B1**

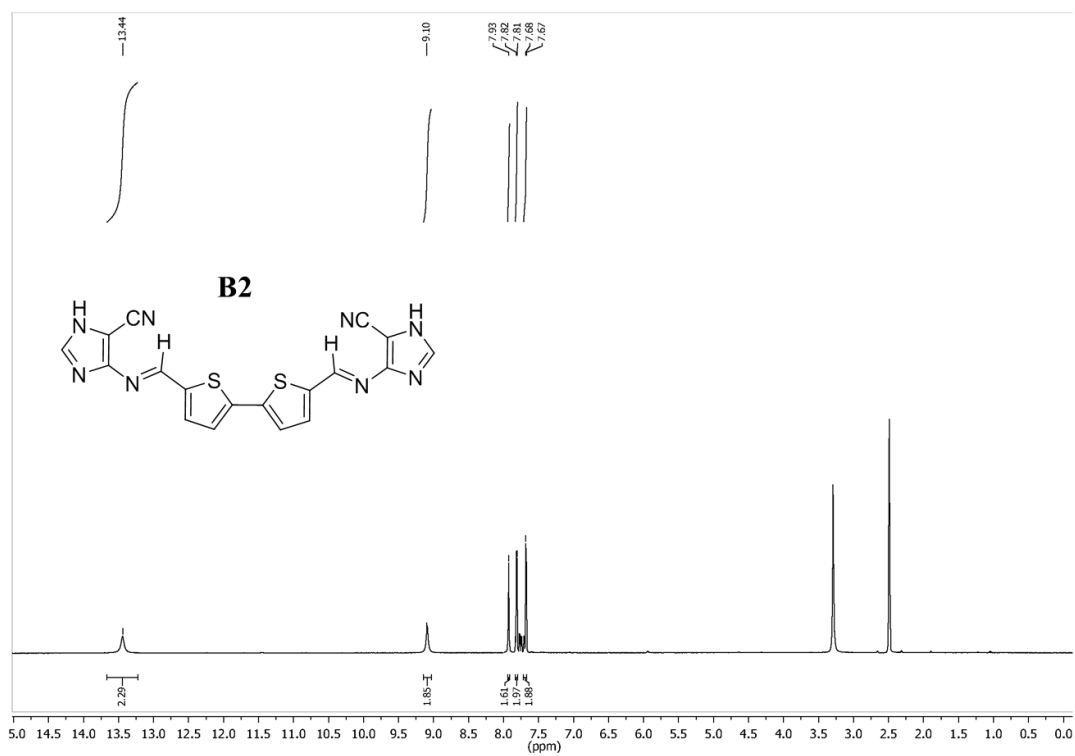


Fig. 4.5 ¹H-NMR spectra of **B2**

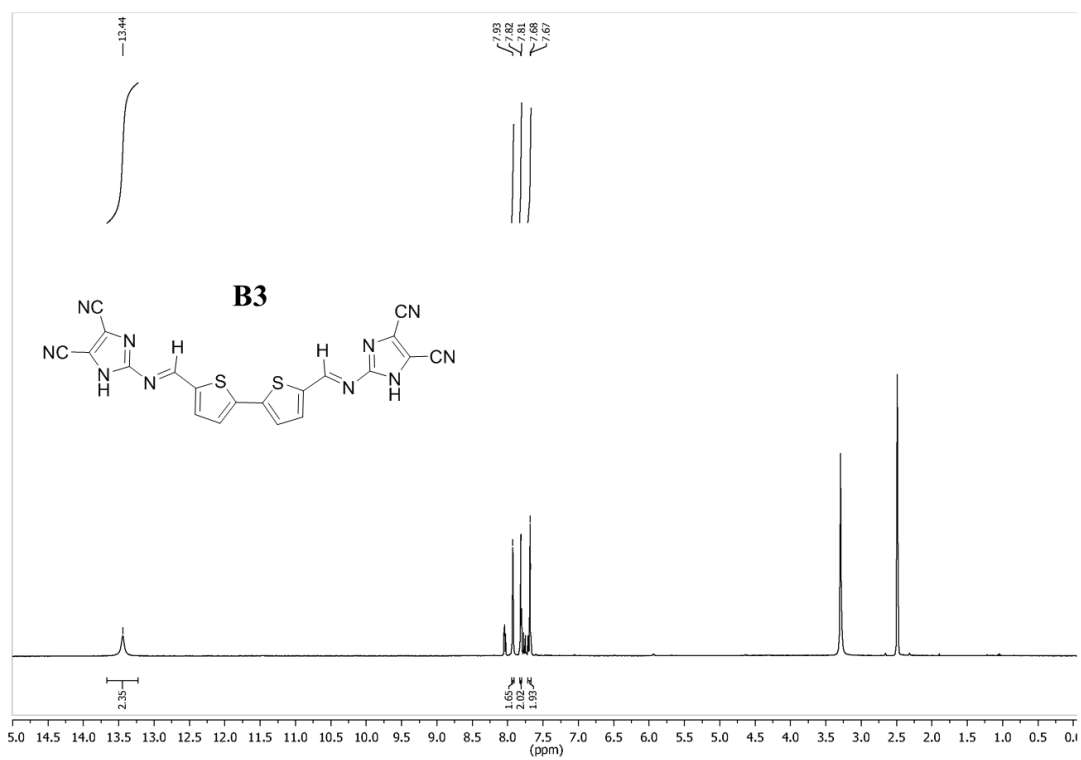


Fig. 4.6 ¹H-NMR spectra of **B3**

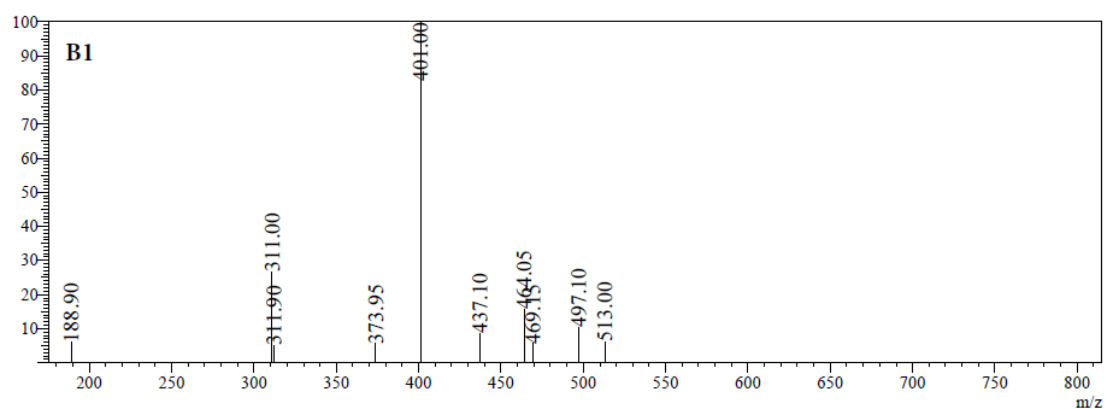


Fig. 4.7 ESI-Mass spectra of **B1**

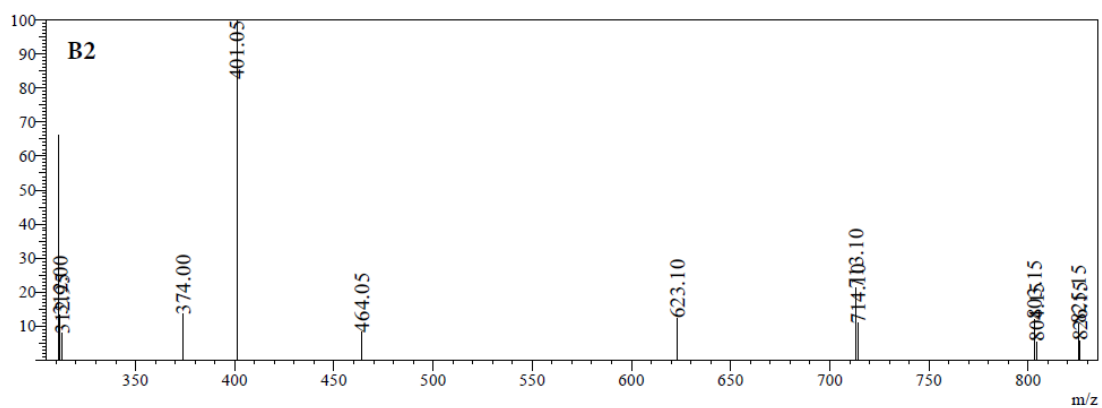


Fig. 4.8 ESI-Mass spectra of **B2**

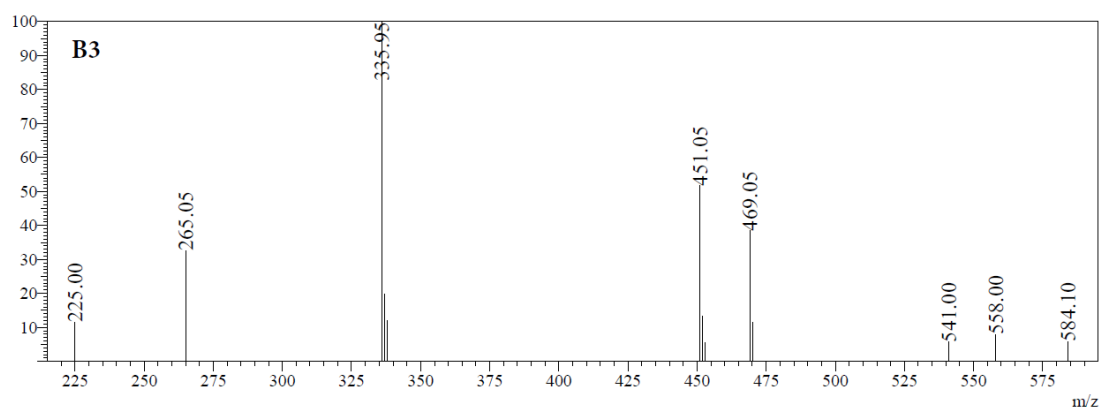


Fig. 4.9 ESI-Mass spectra of **B3**

4.3 RESULTS AND DISCUSSION

4.3.1 Photophysical studies

The optical properties of heterocyclic derivatives **B1**, **B2** and **B3** were investigated in solvents of various polarity such as THF, MeOH, ACN, DMF and DMSO to analyze the nature of ground state. The concentration of solution of the molecules were set to 10^{-5} M and all the photophysical studies were performed at this concentration. UV-Vis spectra of molecules **B1**, **B2** and **B3** are shown in Fig. 4.10 - 4.12. The high energy absorption band at ~400 to 480 nm in molecules **B1**, **B2** and **B3** can be attributed to the $n-\pi^*$ transition of the bithiophene core. This has been confirmed with the addition of acid to the solution that resulted in diminution of the peaks as seen in Fig. 4.13. After the reduction of $n-\pi^*$ peak, newer peaks start to appear at a region around 365 nm, can be assigned to $\pi-\pi^*$ transition. The corresponding data are tabulated in Table 4.1. Studies indicate that, the dependence of the absorption spectra of the molecules on the polarity of the different solvents used is less significant. This suggests the non-polar ground state for all of the molecules.

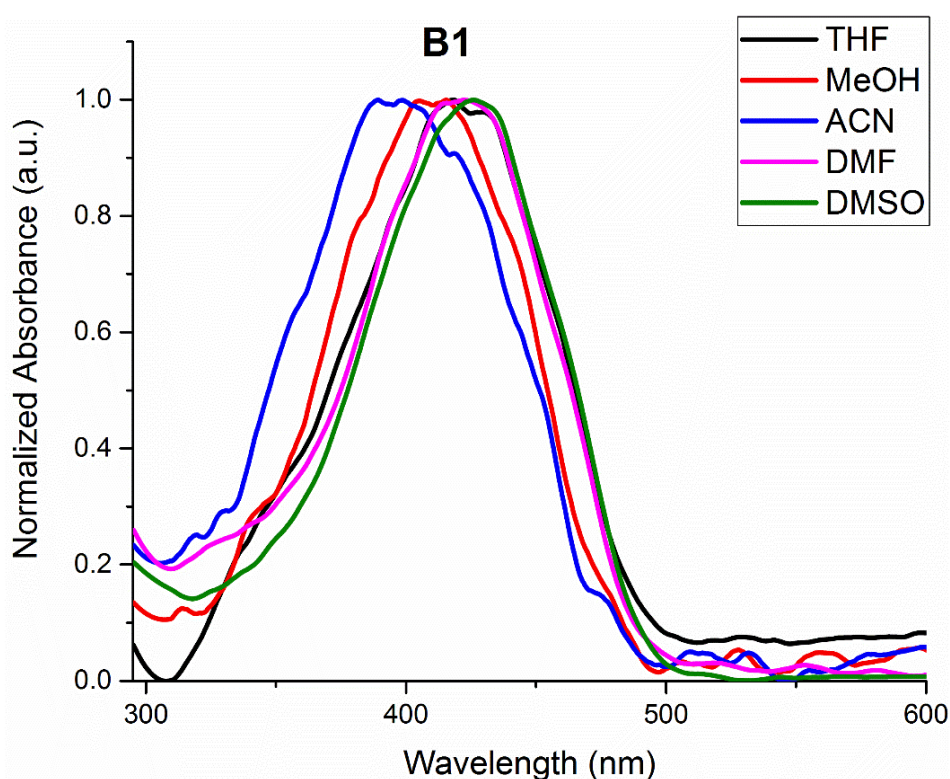


Fig. 4.10 UV-Vis spectra of molecule **B1** in solvents of varying polarity

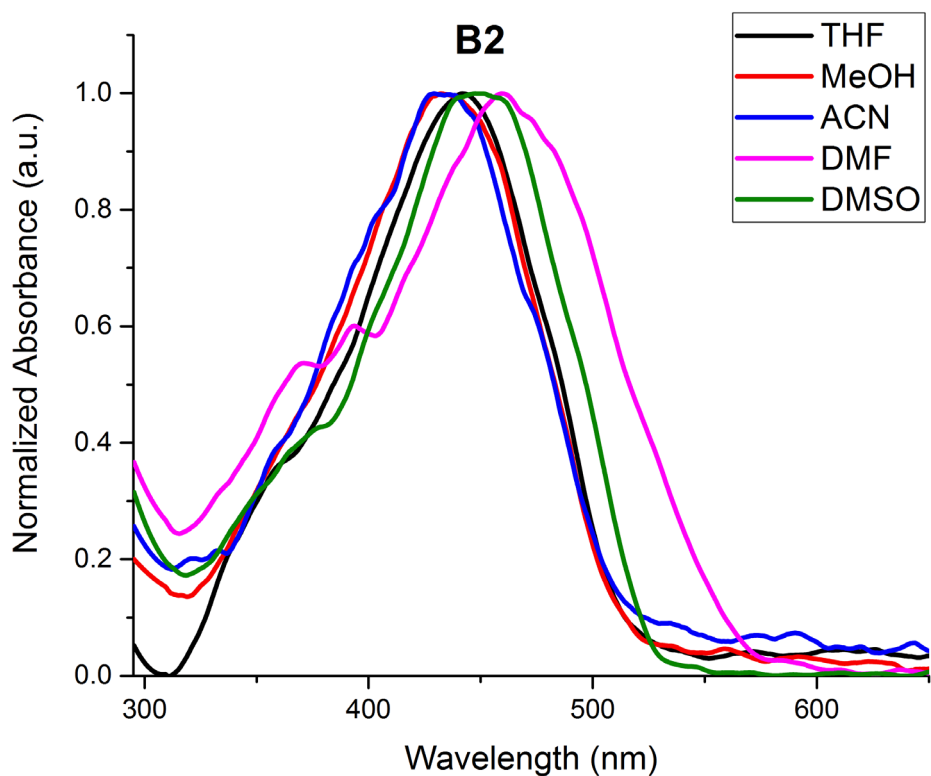


Fig. 4.11 UV-Vis spectra of molecule **B2** in solvents of varying polarity

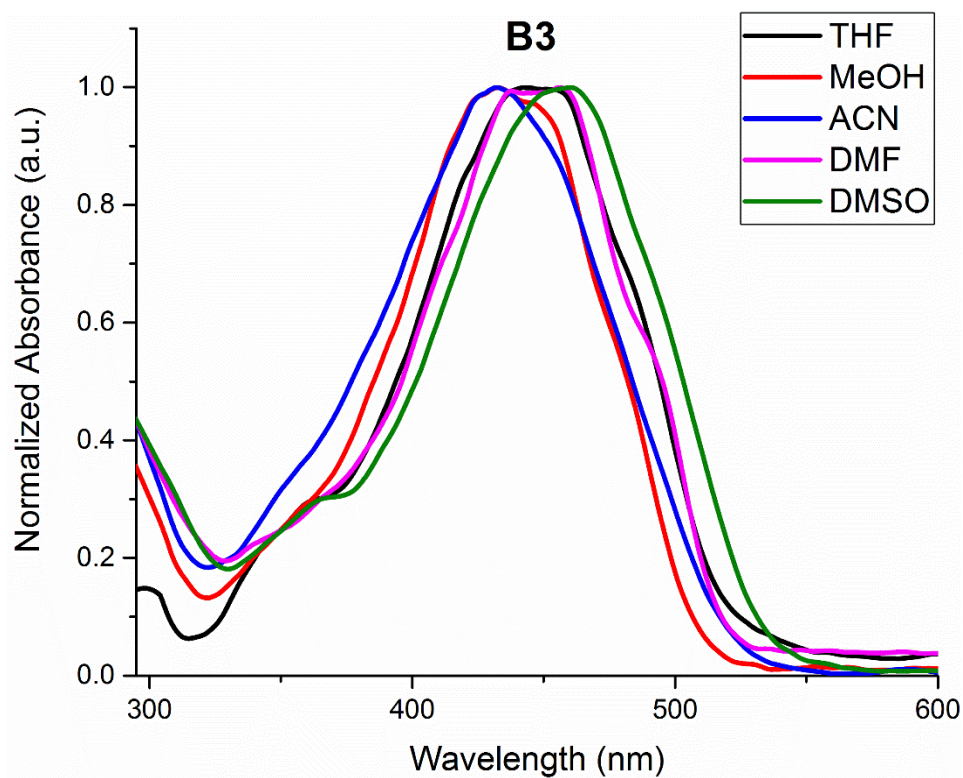


Fig. 4.12 UV-Vis spectra of molecule **B3** in solvents of varying polarity

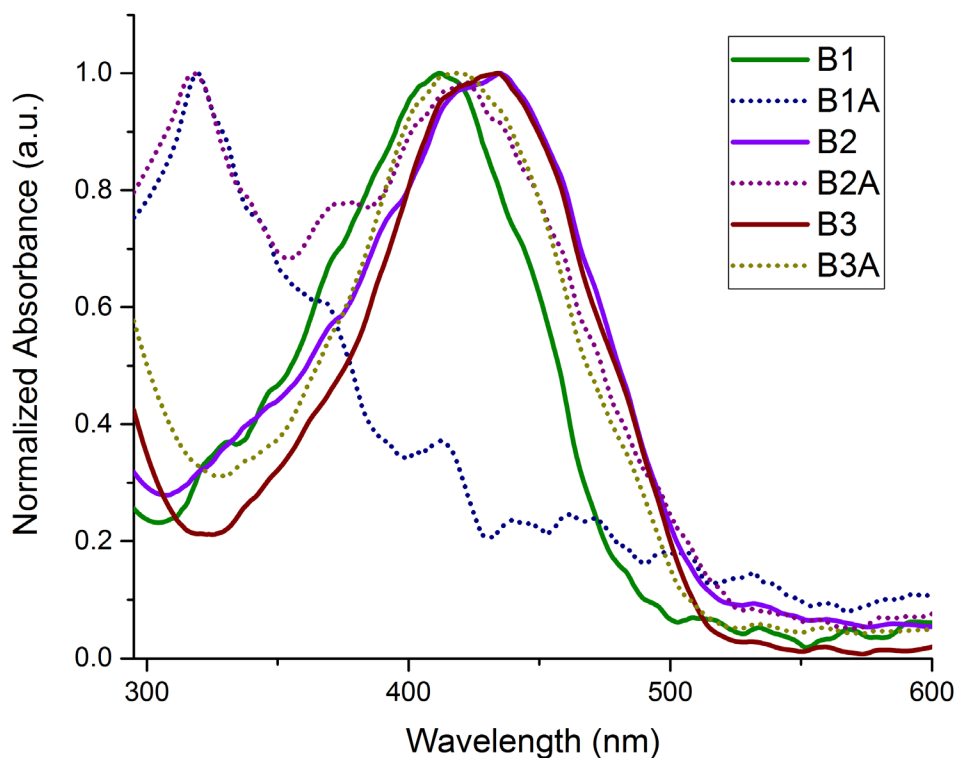


Fig. 4.13 UV-Vis spectra of molecules **B1**, **B2** and **B3** in the presence and absence of acid

The emission spectra of compounds recorded in solvents of varying polarity are displayed in Fig. 4.14 to Fig. 4.16 and the pertinent data is provided in Table 4.1. The emission spectra of the molecules show vibrational fine structure and trend similar to absorption. The vibrational fine structure indicates the rigidity of the molecules and lack of appreciable structural changes on excitation. The molecules **B1**, **B2** and **B3** exhibited emission band in the region ~ 460 nm and in particular **B3** exhibited a broad emission band at 625 nm. The broad band indicated that, substitution of bithiophene core with two cyano groups in **B3** resulted in a red shift in its emission maxima (Justin Thomas et al. 2019). Fluorescence emission of molecules in day light and under UV-irradiation are shown in Fig. 4.17. The molecules of the series were deposited onto chemically and ultrasonically cleaned glass substrates by vacuum thermal vapor deposition at a base pressure of 5×10^{-6} mbar. Thin films of thickness 50 nm obtained after deposition were investigated for their photophysical responses. UV-Vis spectra and photoluminescence spectra of the molecules are as shown in the Fig. 4.18. Solid state photophysical parameters of the molecules are provided in Table 4.2. **B1** and **B2** exhibited a solid-state emission at a wavelength of ~ 650 nm possessing a very high FWHM of 170 nm. However, **B3** possessing two cyano group exhibited a wavelength at 633 nm possessing a lower FWHM of 107 nm.

Table 4.1 Photophysical parameters of molecules in solvents of varying dielectric constant

	λ_{abs} (nm)	λ_{exe} (nm)	λ_{emi} (nm)	Stokes Shift (nm)
THF				
B1	366,418,430	366	420	54
B2	365,441	365	420	55
B3	365,441,455	365	421	56
MeOH				
B1	366,406,416	366	450	84
B2	365,430	365	449	84
B3	365, 432,448	365	449	84
ACN				
B1	366,389,400	366	428	62
B2	365,430	365	428	63
B3	365,432	365	413	48
DMF				
B1	366,419	366	424	58
B2	365,460	365	420	55
B3	366,437,460	366	430	64
DMSO				
B1	366,426	366	444	78
B2	365,449	365	441	76
B3	365,461	365	424, 611	59,246

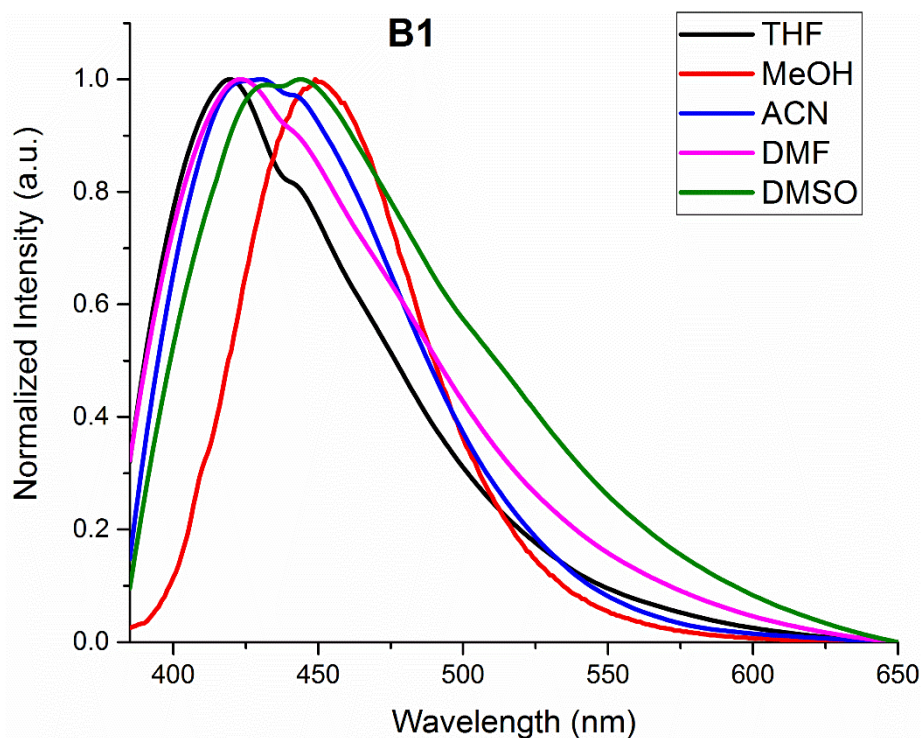


Fig. 4.14 Photoluminescence spectra of molecule **B1** in solvents of varying polarity

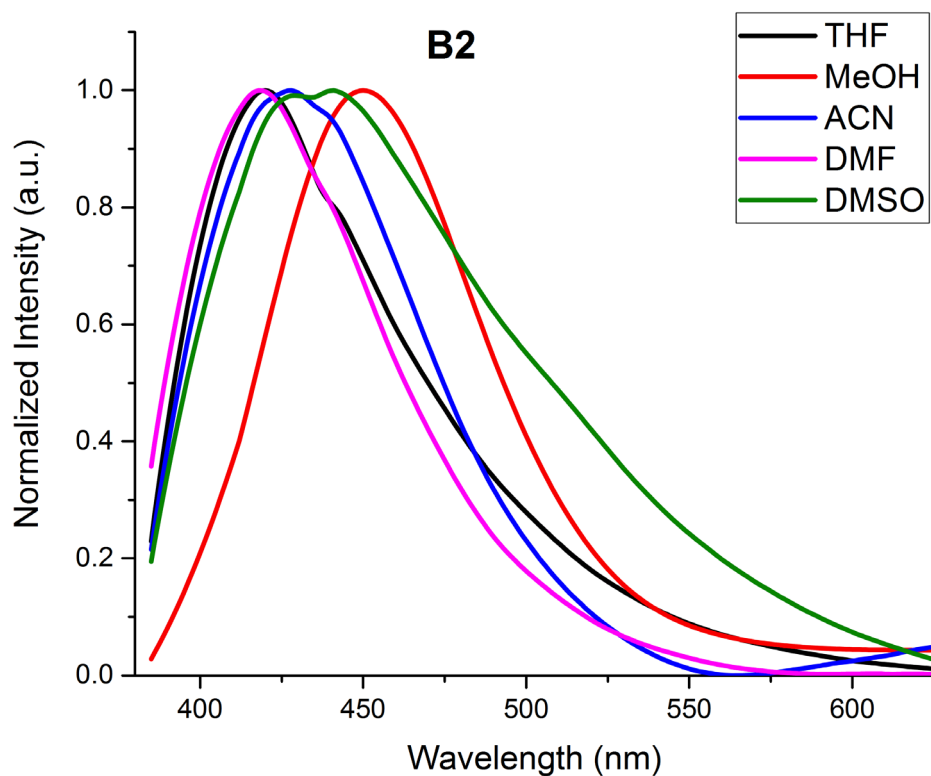


Fig. 4.15 Photoluminescence spectra of molecule **B2** in solvents of varying polarity

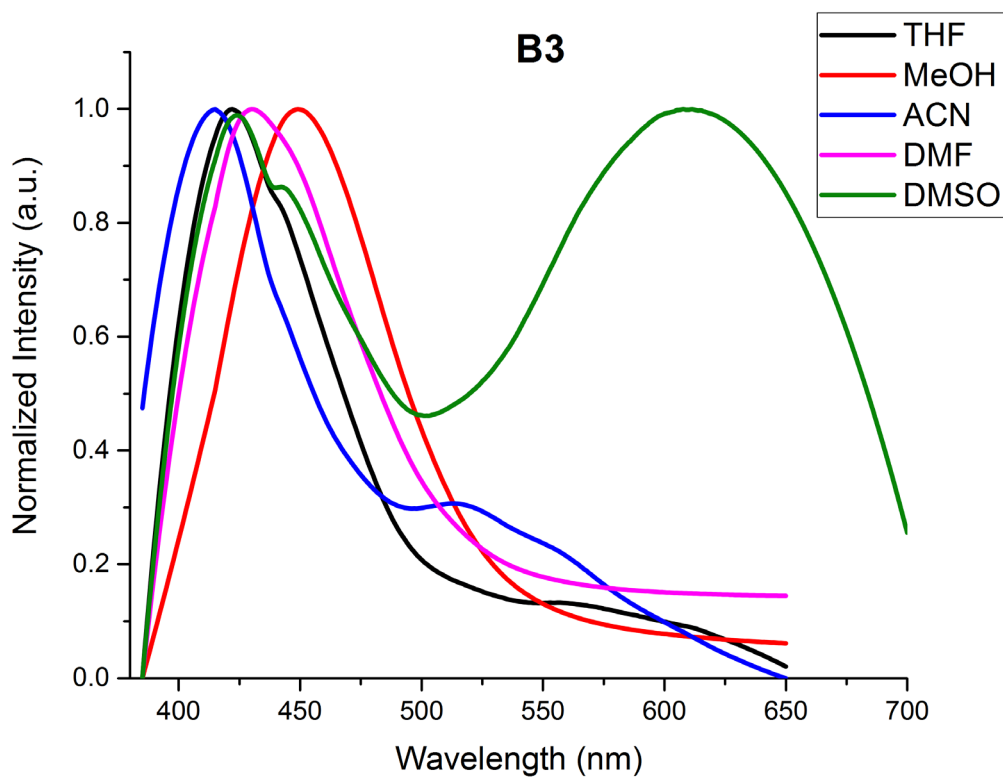


Fig. 4.16 Photoluminescence spectra of molecule **B3** in solvents of varying polarity

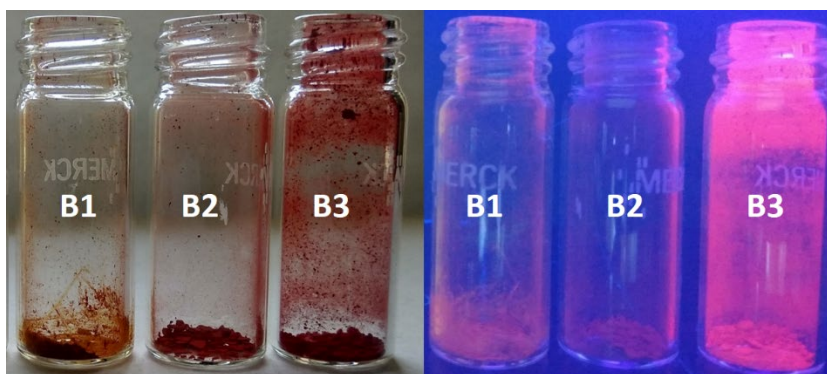


Fig. 4.17 Fluorescence emission of molecules in day light and at UV-irradiation

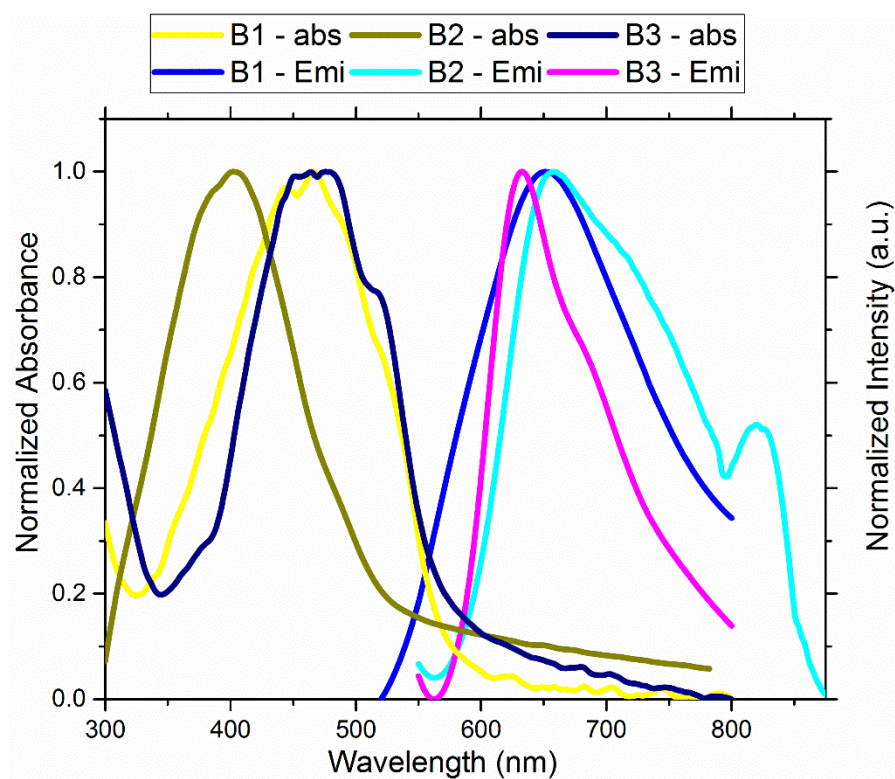


Fig. 4.18 Solid-state UV-Vis and PL spectra of molecule **B1**, **B2** and **B3**

Table 4.2 Solid state photophysical properties of all the molecules

Molecule	λ_{Abs} (nm)	λ_{Emis} (nm)	Stokes Shift (nm)	FWHM (nm)
B1	464	653	189	170
B2	402	655	253	169
B3	475	633	158	107

4.3.2 Quantum Yield measurement

Fluorescence quantum yields (ϕ_s) were evaluated according to the following Equation 4.1, wherein 9,10-diphenylanthracene in cyclohexane is considered as reference (R). Samples whose QY needs to be determined is denoted as S. Grad corresponds to the gradient from the plot of integrated fluorescence intensity vs absorbance at the excitation wavelength, and η the refractive index of the solvent for standard and reference (Dhami et al. 1995; Williams et al. 1983). The highest QY recorded for **B1** exhibited a value of 18.66% and with the lowest recorded for **B3** with 2.4% as provided in the Table.4.3.

$$\phi_S = \phi_R \frac{Grad_S}{Grad_R} \frac{\eta_S^2}{\eta_R^2} \quad \text{Eq. 4.1}$$

Table 4.3 Measured quantum yield of molecules in methanol solvent

Molecule	B1	B2	B3
QY (%)	18.66	9.05	2.4

4.3.3 Aggregation induced emission studies

Restriction of vibrational and rotational traits of a molecule when aggregated enhances the possibility of larger number of photon emission in a system. This phenomenon is highly anticipated in a system to find its application in solid-state electronics. Solid-state molecular packing that adopts various types of aggregation is an important factor that overall governs quantum efficiencies of the chromophore (Padalkar and Seki 2015). It is to better verify the effect of aggregation on the emission intensity of the molecules, AIE studies were performed for the all the molecules at different ratios of H₂O/THF mixture. Solutions were prepared with a concentration (10^{-5} M) in THF and their mixtures in varying water fractions f_w were used for AIE studies. Fig. 4.19 to Fig. 4.21, shows the fluorescence emission of the series with different H₂O/THF mixtures under UV irradiation of 365 nm. Herein, 10% of f_w implies 10:90 of the mixture with 10% of THF solution and 90% of H₂O and 20% of f_w would imply 20:80 with 20% THF solution and 80% of H₂O so on. All the molecules of the series exhibited good AIE response as shown in the Fig. 4.22. All the molecules showed an emission enhancement from 20% to 80% of f_w as observed. Molecules steadily increased its emission upon addition of water, reaches a maximum and then gradually diminishes. The drop in emission intensity at higher ratios of H₂O/THF mixtures is due to the poor solubility of the solute in solvent mixture (Zhang et al. 2016).

B1 showed good emission behavior in comparison with the others of the series. Further, the photoluminescence spectra reveals the curve to undergo a redshift upon increase in the water mixture. This is mainly attributed to the effect of polarity on the system caused due to the addition of H₂O to lessen the bandgap of the system under solvent poor-solvent mixture (Hu et al. 2009). The redshift observed at higher mixtures of water indicates the system exhibiting positive solvatochromism (Zhang et al. 2016), wherein such behavior is merely observed under solvents of lower dielectric constants.

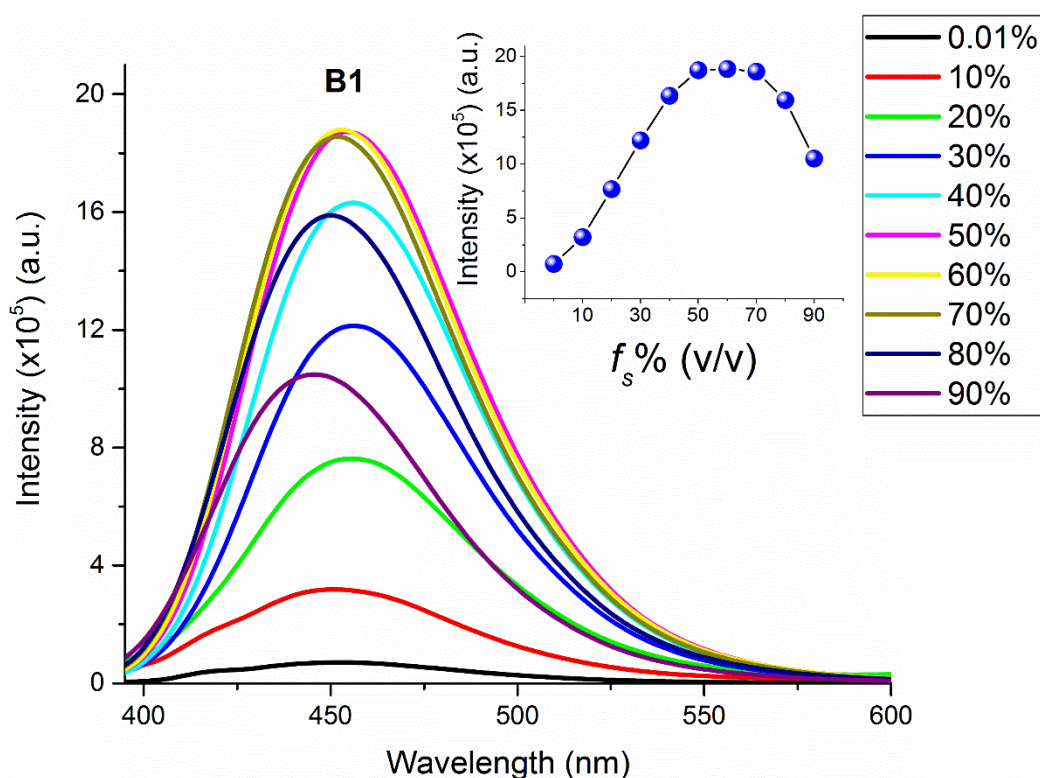


Fig. 4.19 Fluorescence spectrum of **B1** with varying f_w % and inset show intensity vs f_w

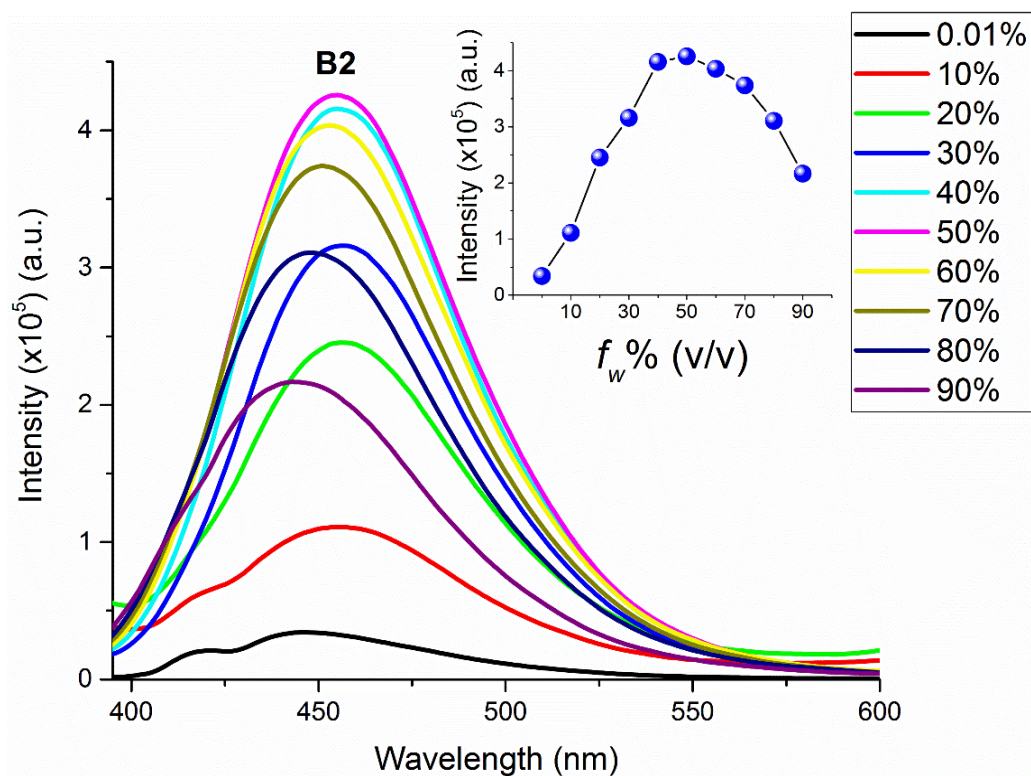


Fig. 4.20 Fluorescence spectrum of **B2** with varying f_w % and inset show intensity vs f_w

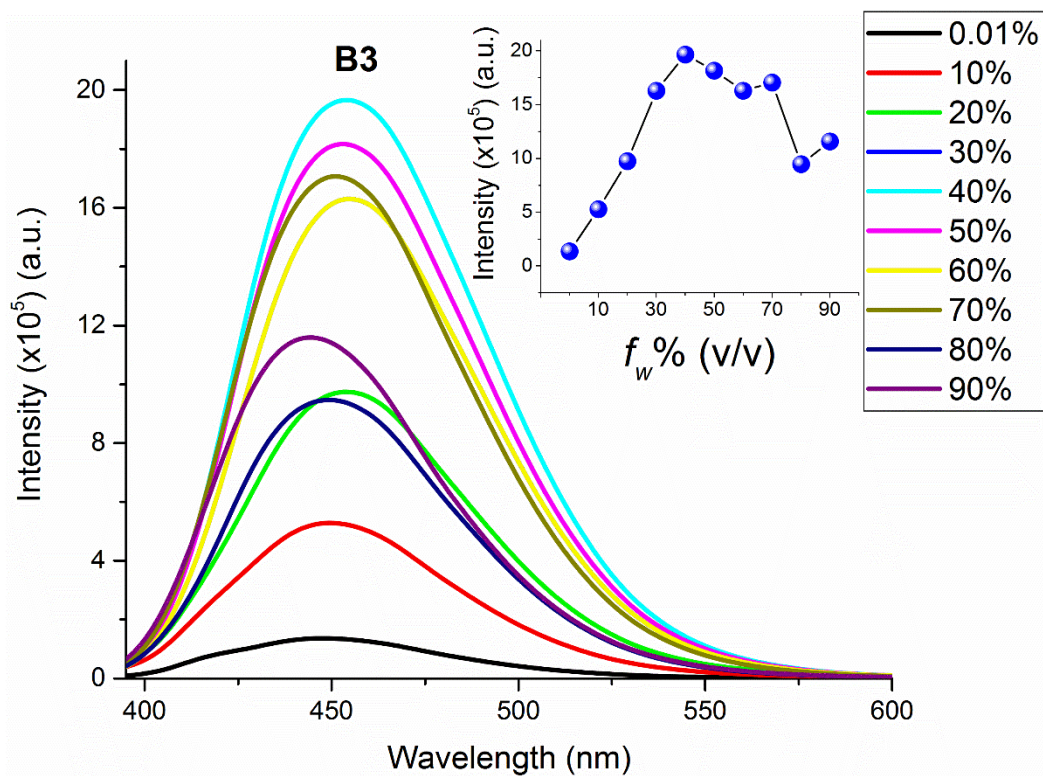


Fig. 4.21 Fluorescence spectrum of **B3** with varying f_w % and inset show intensity vs f_w

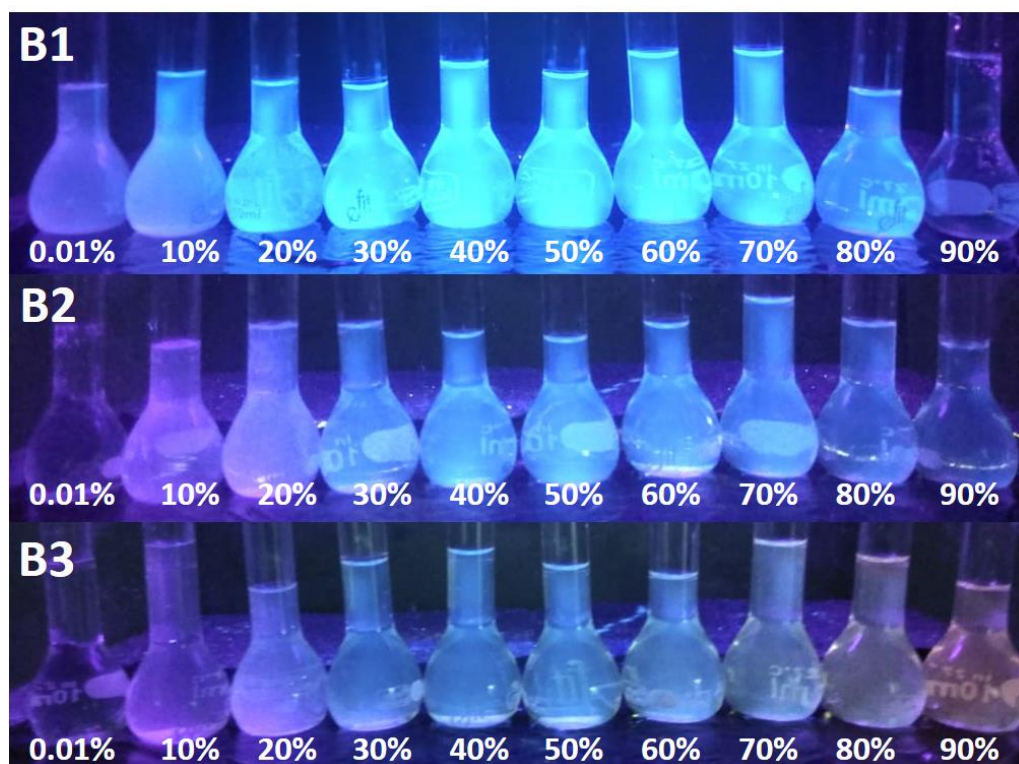


Fig. 4.22 Photographs of molecules in THF/water mixtures with different f_w under UV illumination

4.3.4 Cyclic voltammetry

The electrochemical properties of the molecules were studied by cyclic voltammetry to estimate their electronic energy levels and the bandgap thereof. Cyclic voltammogram at a varying scan rate of 10 mV/s, 20 mV/s and 50 mV/s with the potential ranges from -3V to +3V were recorded. All the molecule exhibited a good quasi reversible oxidation and reduction peak as shown in Fig. 4.23 and Fig. 4.24 respectively. Onset peak potentials for the lowest scan rate for oxidation and reduction were used for energy level estimation. The energy bandgap of **B1**, **B2** and **B3** with their HOMO is estimated using the equation $E_{\text{HOMO}} = - (I_p + 4.4) \text{ eV}$ and LUMO by $E_{\text{LUMO}} = - (E_A + 4.4) \text{ eV}$ (Duvenhage et al. 2015). A pictorial representation of electronic energy levels for all the molecules is presented in Fig. 4.25. Oxidation peak is observed in cyclic voltammogram curve corresponds to the involvement of $-\text{NH}$ functionality in oxidation process. HOMO energy level is estimated using the oxidation potential and the LUMO energy levels of the molecules were obtained from the reduction onset potential from the cyclic voltammogram curve.

OXIDATION CYCLE

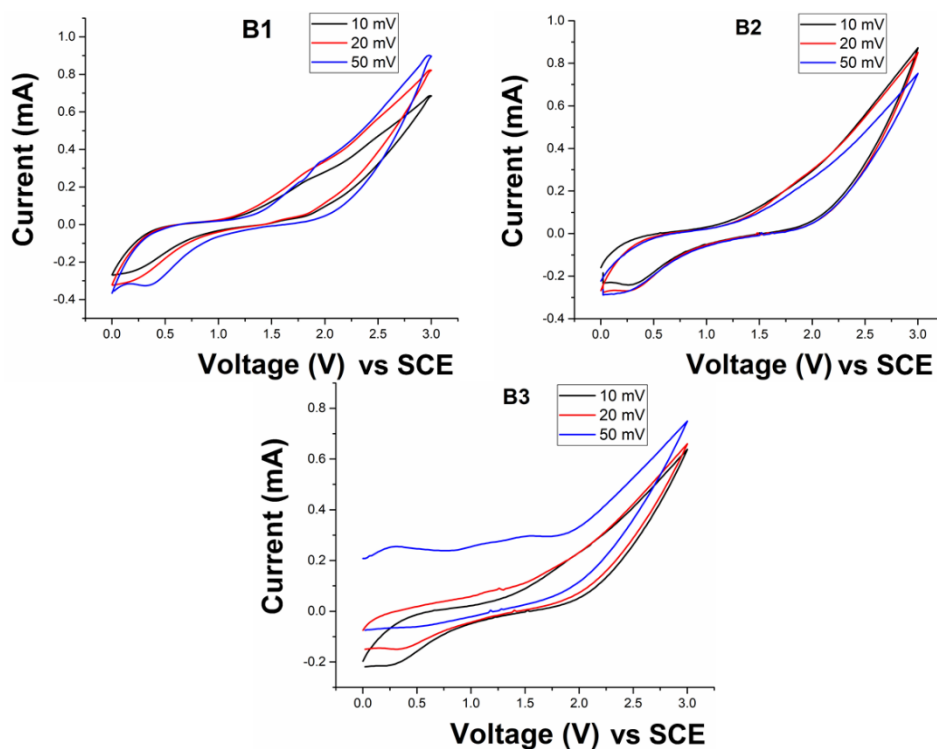


Fig. 4.23 Cyclic voltammogram representing oxidation peak for molecules **B1**, **B2** and **B3**

REDUCTION CYCLE

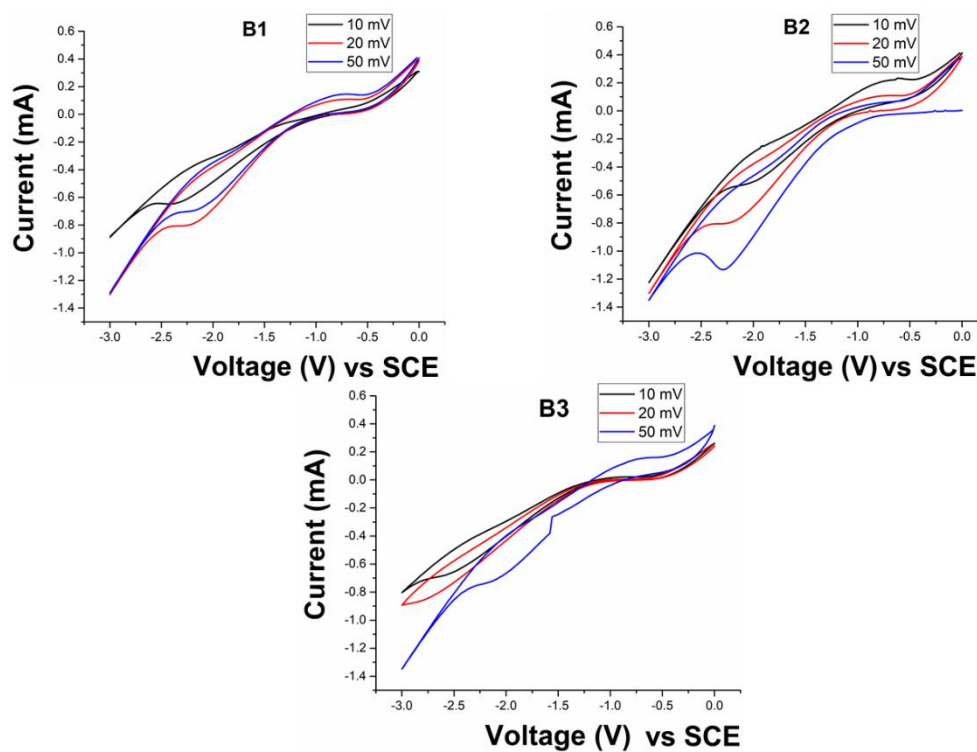


Fig. 4.24 Cyclic voltammogram representing reduction peak for molecules **B1**, **B2** and **B3**

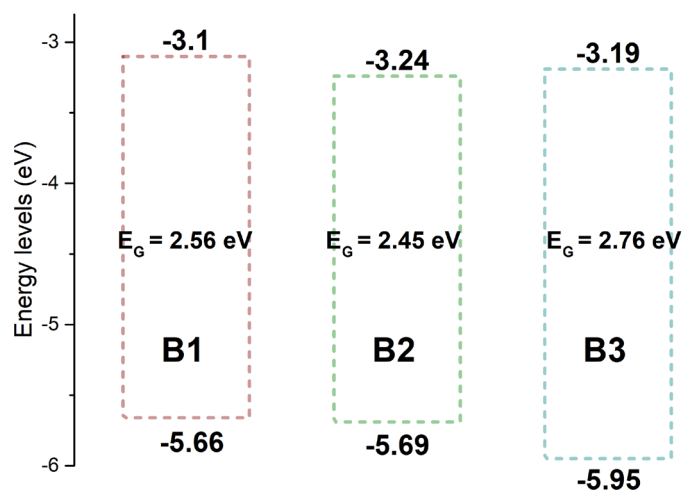


Fig. 4.25 Electronic energy levels for the molecules **B1**, **B2** and **B3**

Table 4.4 Electrochemical parameters with their energy levels for all the molecules

Molecule	V _{OX} (V)	V _{RED} (V)	HOMO (eV)	LUMO (eV)	E _G (eV)
B1	1.26	-1.3	-5.66	-3.1	2.56
B2	1.29	-1.16	-5.69	-3.24	2.45
B3	1.55	-1.21	-5.95	-3.19	2.76

4.3.5 DFT Studies

Computational calculation for the work is achieved using Gaussian 09 package (Frisch et al. 2013). Ground state calculations were carried out with DFT Becke's three-parameter hybrid exchange function with the Lee-Yang-Parr gradient-corrected correlation functional (B3LYP) (Lee et al. 1988; Miehlich et al. 1989) with 6-31G, 6-311+G (d, p) (Hariharan and Pople 1973; Hehre et al. 1972) and Def2TZVP (Schäfer et al. 1992) basis set. The excited state calculations were carried out using TD-DFT Coulomb-Attenuated Method B3LYP (Yanai et al. 2004) for 6-31G and 6-311+G(d,p), whereas for Def2TZVP method with the same basis set used for its excited state. The self-consistent field (SCF) convergence thresholds pertaining to energy minimizations for both ground and excited state optimization was set to 10^{-6} . Solvent effects on the energy parameters of the system was studied by using self-consistent reaction field based on polarizable continuum model (PCM) (Tomasi and Persico 1994) using the integral equation formalism variant (IEFPCM) (Cammi and Tomasi 1995; Cancès et al. 1997; Mennucci et al. 1997; Miertuš et al. 1981; Miertuš and Tomasi 1982). IEFPCM model studies the effect of solvent by placing the solute in a cavity of overlapping solvent and in effect reproduces the electrostatic potential arising due to the polarized dielectric created by the apparent charges surrounding the solute

(Wei et al. 2017). The selection of functional was made in accordance with previous numerous benchmarks validating their accuracy in predicting ground state energies and excited state energies (An et al. 2017; Liu et al. 2017; Zhao and Han 2008). Initially ground state optimizations were carried out in vacuum and the resultant geometry was further optimized in solvent medium. Frequency calculations were performed for the geometry optimized to confirm their geometry corresponds to a true local minimum on the ground and excited state potential energy surface. Geometry optimizations were carried out without any constraints on bond lengths, bond angles or dihedral angles. The calculation of vertical excitation energy of first singlet excited state was estimated from the ground state optimized structure based on TDDFT with IEFPCM solvation model with methanol chosen as a solvent medium. The optimized geometry and the electronic orbital distribution of all the molecules were visualized using Avogadro software (Hanwell et al. 2012). Ground state optimized geometry of all the molecules in 6-311+G(d,p) along with their side view is as given in the Fig. 4.26 along with their color codes for atomic representation. We observe that the system exhibits a high amount of planarity irrespective of the effect of side chain substituents. This implies that the molecules of the series upon aggregation is sure to acquire J-aggregate type of molecular packing supporting a larger π - π stacking distance between monomers.

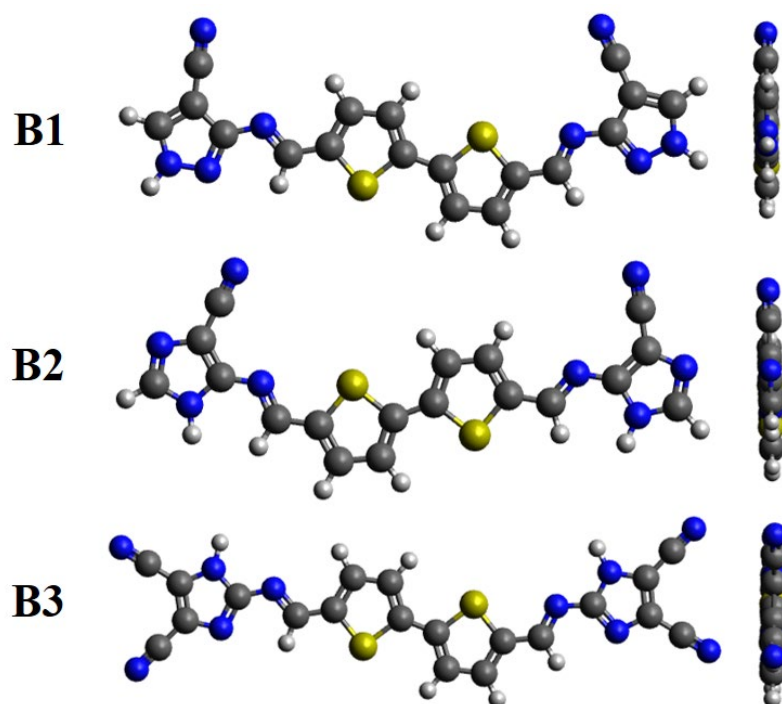


Fig. 4.26 Optimized geometry of all the molecules with B3LYP/ 6-311+G (d,p) with their side view showing structural planarity.

4.3.5.1 Spectral studies and orbital analysis

Molecular orbitals mainly highest occupied molecular orbitals (HOMO) and lowest unoccupied molecular orbitals (LUMO) play an important role that controls the chemical stability of the system (Selvaganapathi et al. 2017). Theoretically estimated HOMO, LUMO levels and energy band gap of all molecules in methanol solvent is provided in Fig. 4.27. We observe that the nature of charge transfer occurring in the system is of π - π^* type of transition mainly involving HOMO and LUMO orbitals. Further, the major contribution of electronic transitions occurring in the system is mainly from HOMO and LUMO and these orbitals provide a CI of $\sim 90\%$ for 6-31G, 6-311+G (d,p) and CI of $\sim 99\%$ for Def2TZVP basis set. The HOMO and LUMO energy levels along with their energy band gap estimated theoretically correlates well with the experimental results with an energy difference lesser than ~ 0.5 eV. We observe that molecules of the series have their HOMO and LUMO orbitals highly distributed across the entire molecular system. Calculations yielding lowest lying six singlet vertical excitations were opted with state specific approach for all the energy estimation. Fig. 4.28 shows the electronic transitions occurring in the system estimated for all the three different functional along with the vertical lines indicating the experimental values. Table 4.5 provides energy and type of electronic transitions with their oscillator strength and contribution of orbitals for such transitions. The discrete transition energies obtained after the calculations were broadened by setting the value of FWHM to 35 nm so as to better accommodate the experimental parameters in the spectra. Results reveal the major transition for the emission spectra $S_1 \rightarrow S_0$ occurring in the system is mainly from a π - π^* cloud. Oscillator strength of the emission energy is higher to that of the absorption energy in all the cases. Overall, we observe that 6-311+G(d,p) estimates energy values nearer to the experimental figures for both absorption and emission spectra with an maximum energy difference of ~ 0.3 eV (Houari et al. 2013; Lan and Liu 2015; O. Hubin et al. 2014; Yang et al. 2016). The emission energy estimated for **B1** is highly accurate and correlates well with the experimental values however their absorption energy was underestimated by a value ~ 50 nm. Further, 6-31G was closer in estimating energy absorption and emission for **B1** alone and followed a similar pattern with 6-311+G(d,p), while Def2TZVP fails to reproduce the experimental results in all the molecules and hence not suitable for our system. Theoretically estimated optical parameters pertaining to energy

transition, oscillator strength, configuration interaction using CAM-B3LYP 6-311+G(d,p) and using Def2TZVP in methanol medium are shown in Table 4.6 and 4.7.

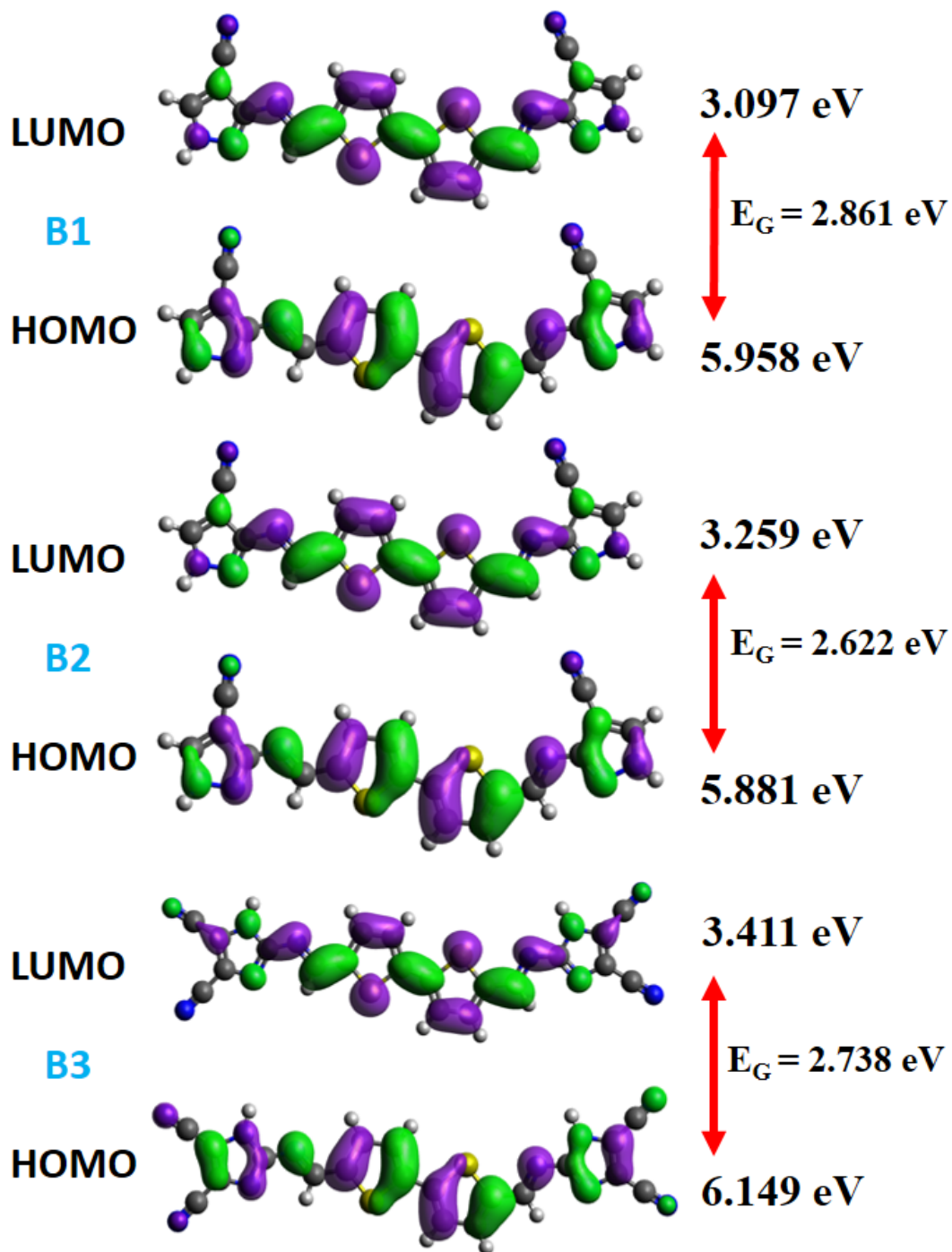


Fig. 4.27 Electronic orbital representation of the molecules B1 to B3

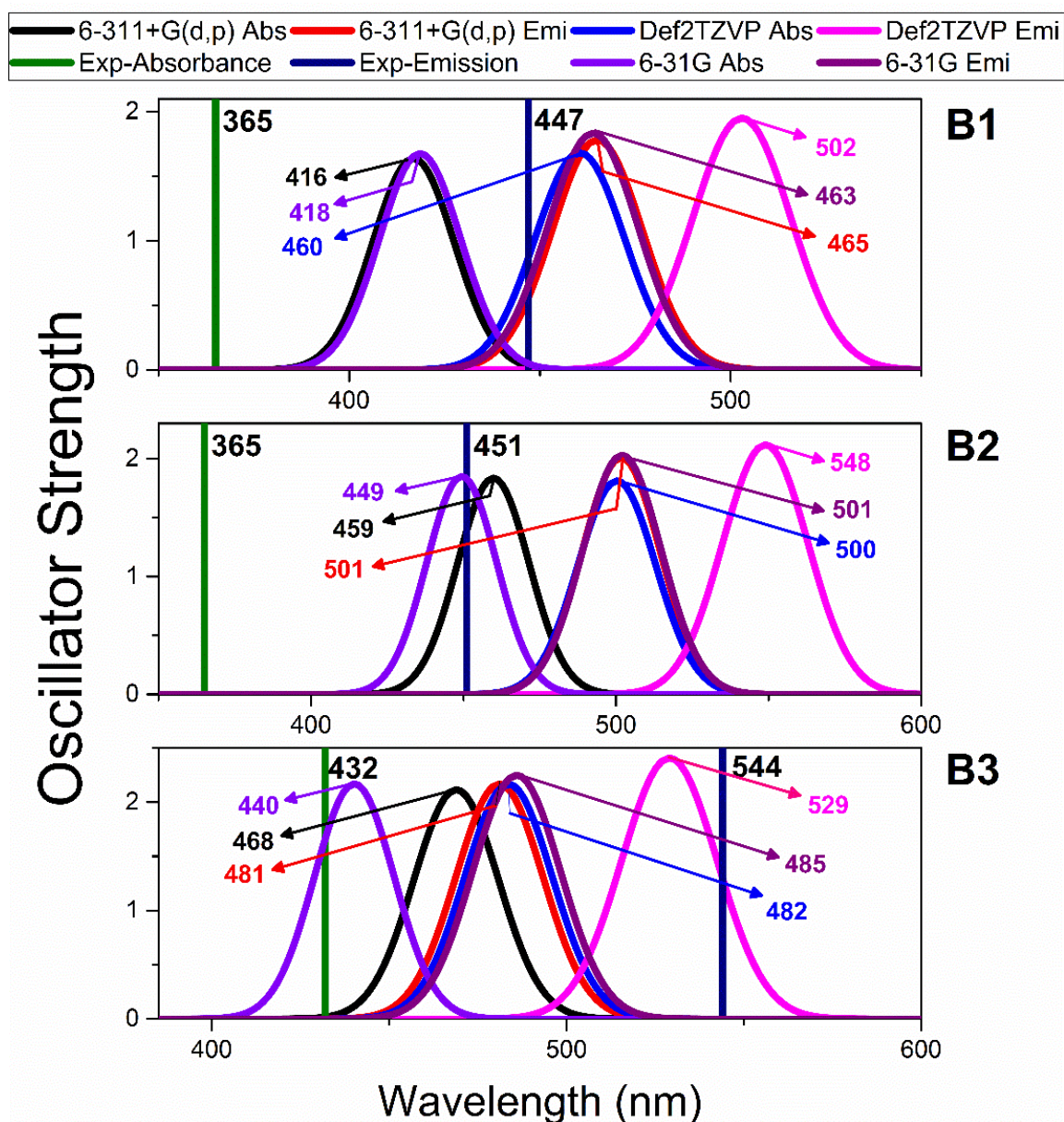


Fig. 4.28 Theoretically derived absorption and fluorescence emission spectrum of all the molecules with experimental values.

Table 4.5 Theoretically estimated optical parameters pertaining to energy transition, oscillator strength, configuration interaction using CAM-B3LYP 6-31G(d,p) in methanol medium

Molecule	Type	Energy (nm)	<i>f</i>	Type	CI (%)
B1	Absorbance	419	1.6764	H(103)→L(104)	94.51
				H-1(102)→L+1(105)	3.73
	Emission	464	1.8342	H(103)→L(104)	96.39
				H-1(102)→L+1(105)	2.3
B2	Absorbance	449	1.8506	H(103)→L(104)	92.99
				H-1(102)→L+1(105)	4.58
	Emission	502	2.0309	H(103)→L(104)	95.33
				H-1(102)→L+1(105)	2.88
B3	Absorbance	440	2.1694	H(115)→L(116)	93.2
				H-1(114)→L+1(117)	3.73
	Emission	486	2.2496	H(115)→L(116)	95.36
				H-1(114)→L+1(117)	2.39

Table 4.6 Theoretically estimated optical parameters pertaining to energy transition, oscillator strength, configuration interaction using CAM-B3LYP 6-311+G(d,p) in methanol medium

Molecule	Type	Energy (nm)	<i>f</i>	Type	CI (%)
B1	Absorbance	417	1.638	H(103)→L(104)	93.7
				H-1(102)→L+1(105)	4.06
	Emission	465	1.7829	H(103)→L(104)	95.86
				H-1(102)→L+1(105)	2.44
B2	Absorbance	460	1.8362	H(103)→L(104)	91.85
				H-1(102)→L+1(105)	5.17
	Emission	502	2.0094	H(103)→L(104)	94.54
				H-1(102)→L+1(105)	3.19
B3	Absorbance	469	2.1159	H(115)→L(116)	92.46
				H-1(114)→L+1(117)	3.96
	Emission	481	2.1686	H(115)→L(116)	94.85
				H-1(114)→L+1(117)	2.46

Table 4.7 Theoretically estimated optical parameters pertaining to energy transition, oscillator strength, and configuration interaction using Def2TZVP in methanol medium

Molecule	Type	Energy (nm)	f	Type	CI (%)
B1	Absorbance	461	1.6817	H(103)→L(104)	99.50
	Emission	503	1.9518	H(103)→L(104)	99.72
B2	Absorbance	500	1.8123	H(103)→L(104)	99.80
	Emission	549	2.1196	H(103)→L(104)	99.82
B3	Absorbance	484	2.1665	H(115)→L(116)	99.40
	Emission	529	2.4085	H(115)→L(116)	99.57

4.3.5.2 Reorganization and dimer interaction energies

Coherent band transfer and incoherent charge hopping are the two well-known models that have been widely employed to evaluate the charge mobility in a system. In coherent band model, charge carriers move as a delocalized plane wave in an energy band with a relatively long mean free path. In such system, the dynamic disorder is extremely low in comparison with charge transfer integral between a dimer. Coherent band transfer model supports inorganic system that possesses room temperature charge mobility higher than $1 \text{ cm}^2\text{V}^{-1}\text{s}^{-1}$ and such high mobility is obvious for systems interacting via strong valence bonds. On the other hand, incoherent charge hopping model well appropriates the charge transfer in organic systems. Herein, the charges are highly localized and charge transport is mainly through hopping from site to site, carrying a structural deformation along with it. Existence of strong coupling between the lattice phonons and the mobile charge carriers in organics results in non-conserved wave momentum (k) and hence the room temperature charge mobility is smaller than $1 \text{ cm}^2\text{V}^{-1}\text{s}^{-1}$. Mobility (μ) at a defined temperature (T) in organics is directly governed by activation energy E_a and is given by $\mu = -E_a/kT$, where k being a Boltzmann constant. Activation energy or reorganization energy E_a is that energy possessed by the charges to overcome the energy barrier set up by the adjacent molecular sites.

Reorganization energy determines the rate of charge transfer in a system. Electron or hole transport at a molecular level can be understood as the electron or hole transfer reactions occurring between the neighboring molecular sites. The reorganization energy for an electron is the sum of relaxation energy along the anionic state potential energy surface when a hole is removed from the neutral geometry and the relaxation energy along the ground state potential energy surface when a hole is reaccepted from the anionic geometry.

Similar approach is adopted in defining and determining the reorganization energy of hole in organic system. The illustration provided in Fig. 4.29 helps in evaluation of hole or electron reorganization energy for organic system. E_0^A is the energy of ground state neutral geometry and E_0^{A*} is the energy of cationic/anionic charged species defined at ground state geometry of neutral molecule. The term $E_{+/-}^{A*}$ is the energy of cationic or anionic geometry at charged state of geometry and $E_{+/-}^A$ is the energy of optimized cationic or anionic geometry of the charged species. The difference between energy pertaining to charged and neutral along the ground state potential energy surface determines λ_2 and along the charged state potential energy surface determines λ_1 . Finally, the reorganization energy λ would be the sum of $\lambda_1 + \lambda_2$.

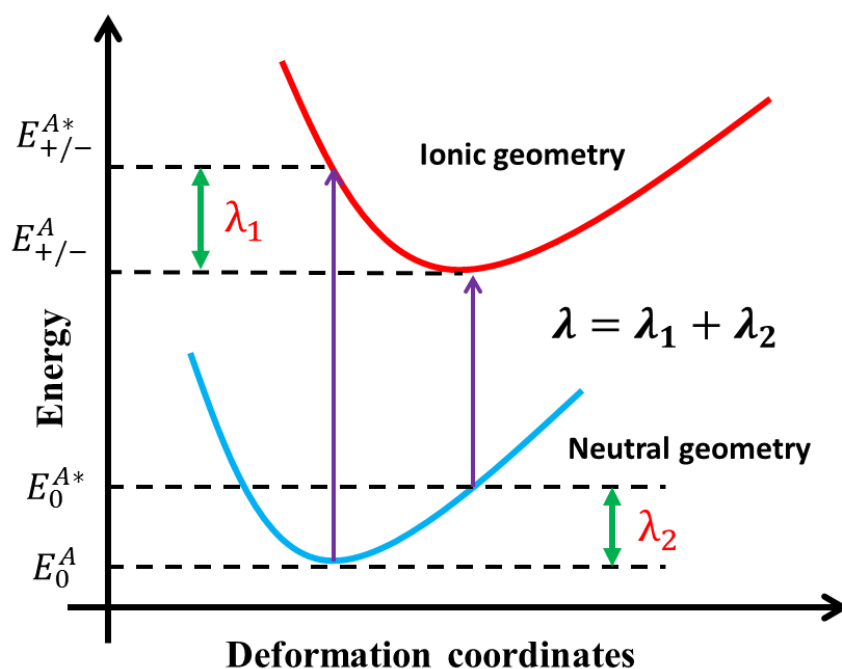


Fig. 4.29 Definition of reorganization energy in an organic system

Table 4.8 Computational evaluation of the reorganization energies k (eV) for hole and electron transport in all the molecules

Molecule	λ_1 (hole)	λ_2 (hole)	λ_1 (electron)	λ_2 (electron)	Reorganization energy	
					λ Hole	λ Electron
B1	0.1174	0.1181	0.1621	0.1596	0.2355	0.2802
B2	0.1127	0.1154	0.1539	0.1516	0.2281	0.2693
B3	0.0986	0.0998	0.166	0.1648	0.1984	0.2658

Reorganization energies were computed at B3LYP functional at 6-311+G(d,p) basis set and the computational results of hole and electron reorganization energies of all the molecules are tabulated in Table 4.8. In effect, reorganization energy is a key factor that governs the overall charge transport in organic systems. We observe that all the molecules of the series exhibited a lower hole reorganization energy in comparison with that of electron reorganization energy, suggestive of good hole transporting ability. Reorganization energy of charge carriers and mobility of charge carriers can be effectively varied by suitable functionalization of the organic molecules. **B3**, additionally possessing a -CN group in comparison with **B1** and **B2**, resulted in relatively low hole reorganization energy, in turn effectively boosting its hole transport properties.

Dimer interaction energies were computed for all the molecules using counterpoise method with basis set superposition error considered. Interaction energies were computed using long range corrected hybrid density functional wb97xd with damped dispersion corrections and 6-311+G(d,p) basis set was used for all the calculations (Chai and Head-Gordon 2008). To arrive at computing interaction energy, three different stacking modes were realized viz slip stacking (SS), face to face stacking (FF) and edge to face stacking (EF) for all the molecules as illustrated in the Fig 4.30. The interaction distance between the monomer is varied in steps and their interaction energy is computed. The plot of interaction energy vs the variation between the monomer distance for all the molecules is as shown in the Fig. 4.31 to Fig. 4.33. Interaction energies were further computed for the slipping angular variation θ , wherein, adopting FF stacking mode, one of the monomers is made to slide over the other monomer at periodic steps to arrive at optimum slip angle possessed by the dimer system. The plot of interaction energy along with the slipping angle variation θ between the monomers for all the molecules is as shown in the Fig. 4.34. It is observed that **B1** and **B3** to possess an angle of 39.6° and **B2** to possess an angle of 61° between the centroid of closest thiophene ring of the interacting monomer. Results from the plots suggests that the molecules behold a slip-stacking mode of packing arrangement at its condensed state. Further, a very minimal interaction energy exists at a monomer separation distance of 3.4 Å, 3.6 Å and 3.5 Å for the molecules **B1**, **B2** and **B3** respectively. The influence of π - π interaction on stacking is quite strong if the distance between the aromatic ring is lesser than 3.3 Å and for a weaker interaction it is around 3.6 Å, with 3.8 Å being approximately the maximum contact for which π - π interactions are accepted (Janiak 2000). Overall, results conclude the existence of a large π - π stacking distance of

~3.5 Å for all the molecules at its condensed state. This large π - π stacking would in turn activate an enhanced emission of the fluorophore at its condensed state by blocking all the non-radiative deactivation pathways.

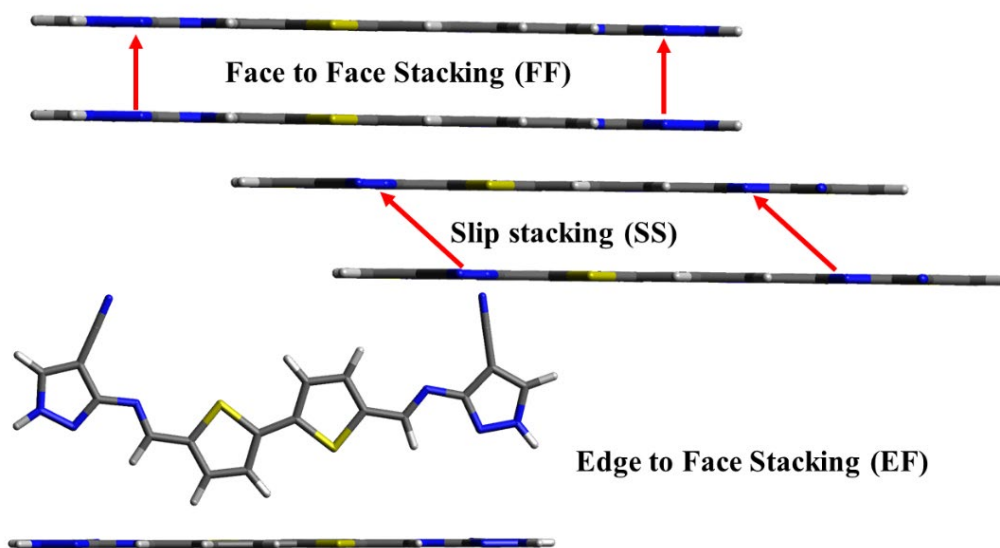


Fig. 4.30 Illustration of face to face (FF), edge to face (EF) and slip stacking (SS) modes.

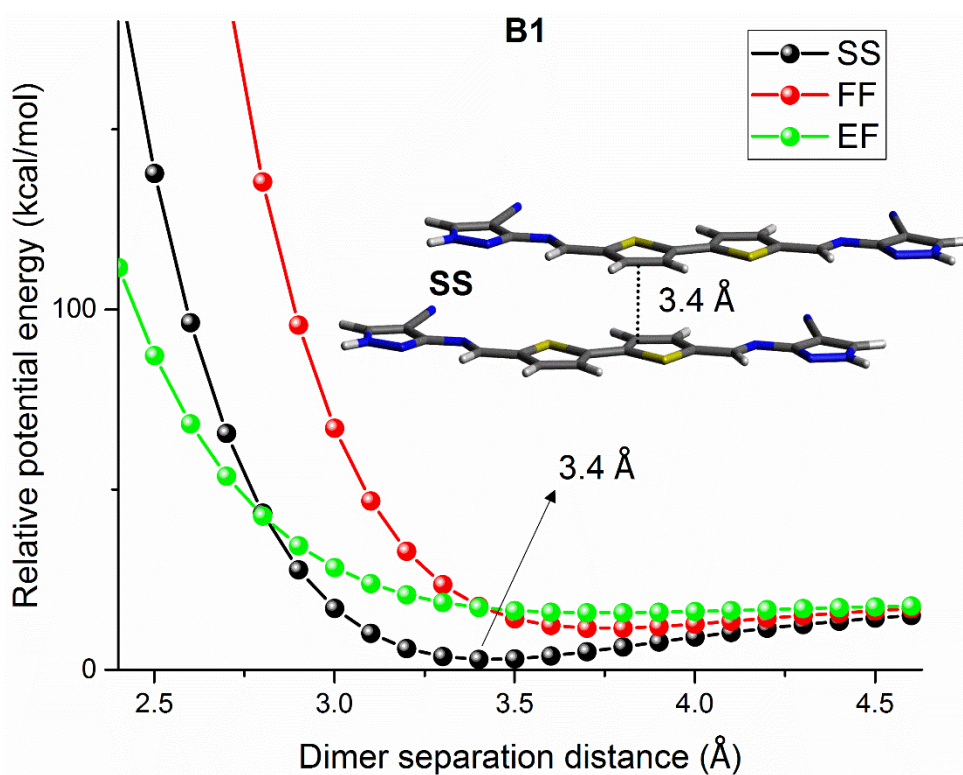


Fig. 4.31 Interaction energy of **B1** dimer for different stacking arrangement with variation in dimer separation distance

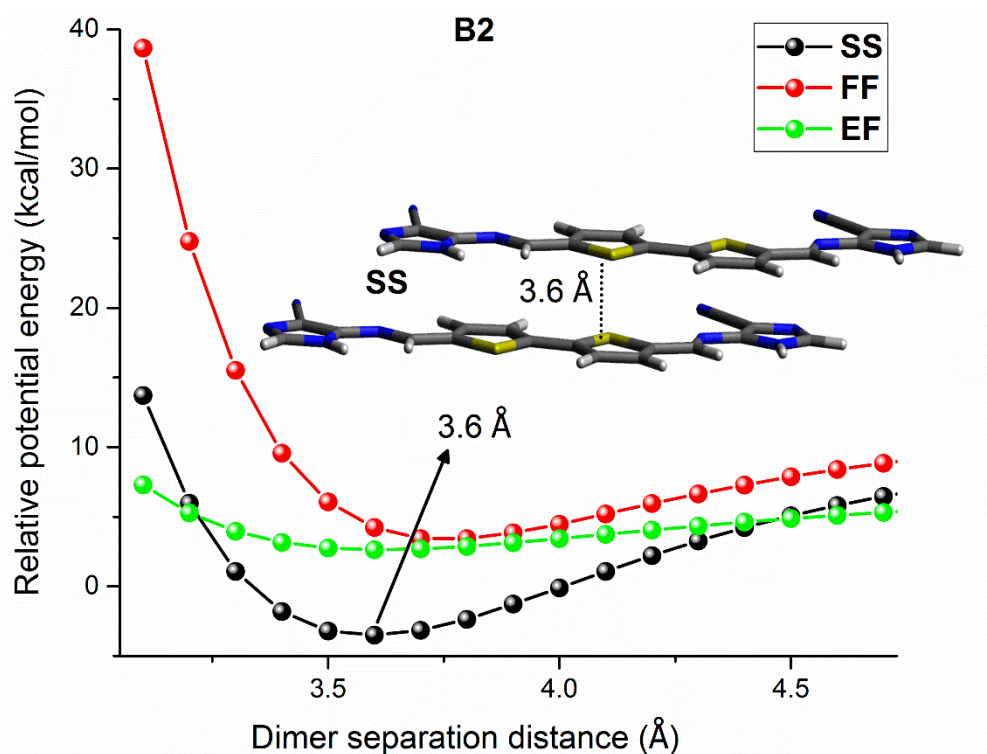


Fig. 4.32 Interaction energy of **B2** dimer for different stacking arrangement with variation in dimer separation distance

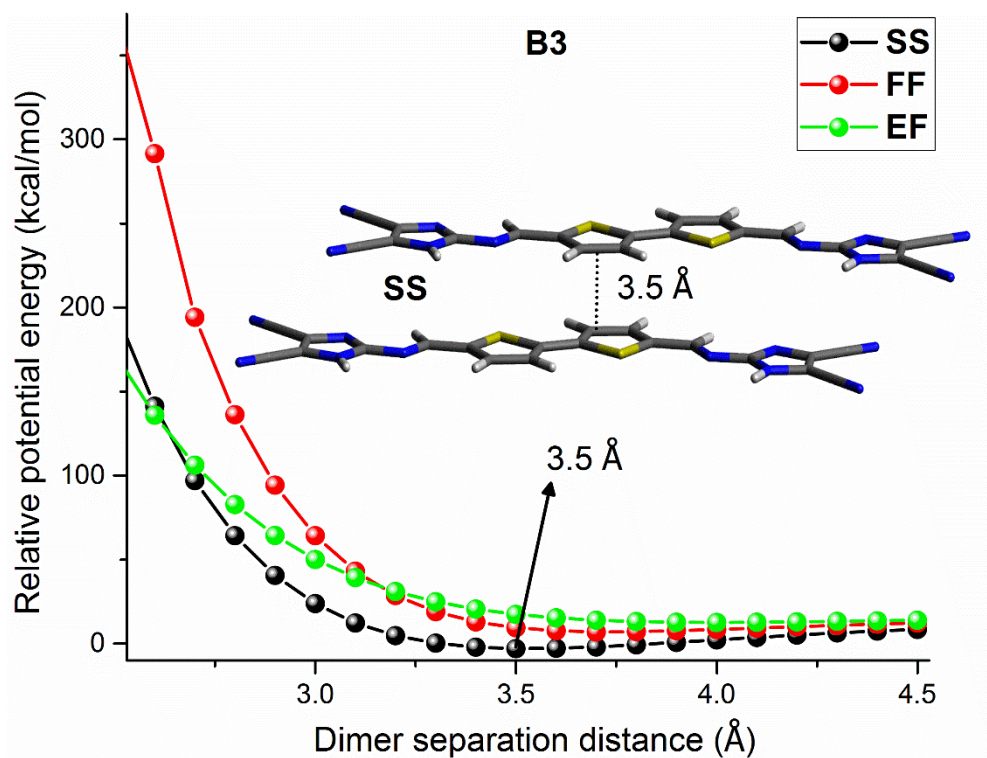


Fig. 4.33 Interaction energy of **B3** dimer for different stacking arrangement with variation in dimer separation distance

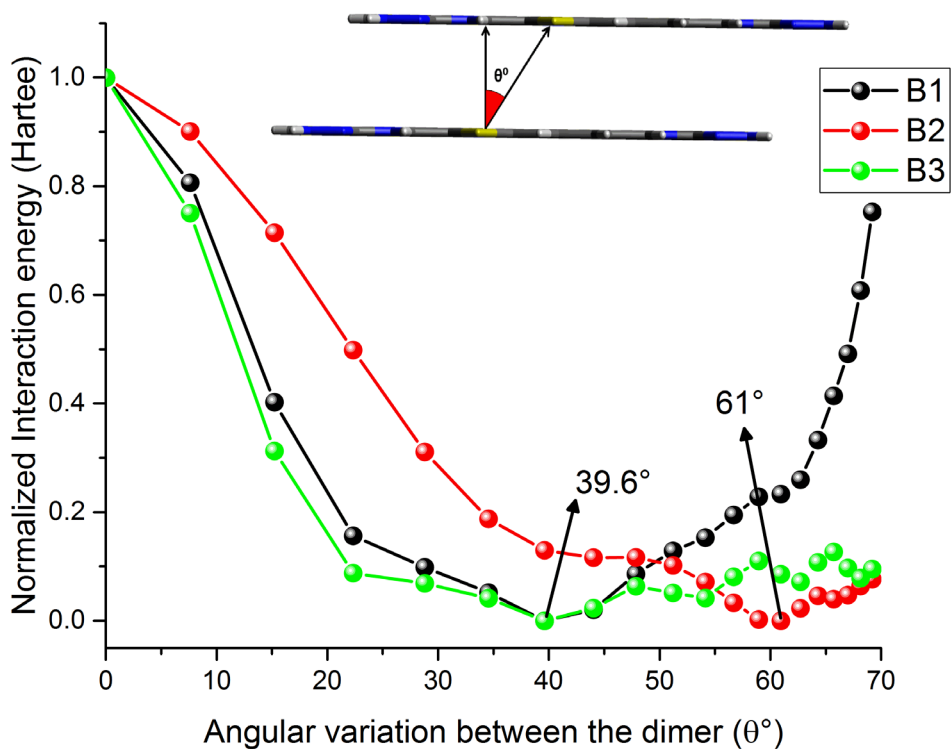


Fig. 4.34 Interaction energy of all the molecules for slip-stacking arrangement with variation in dimer angular distance

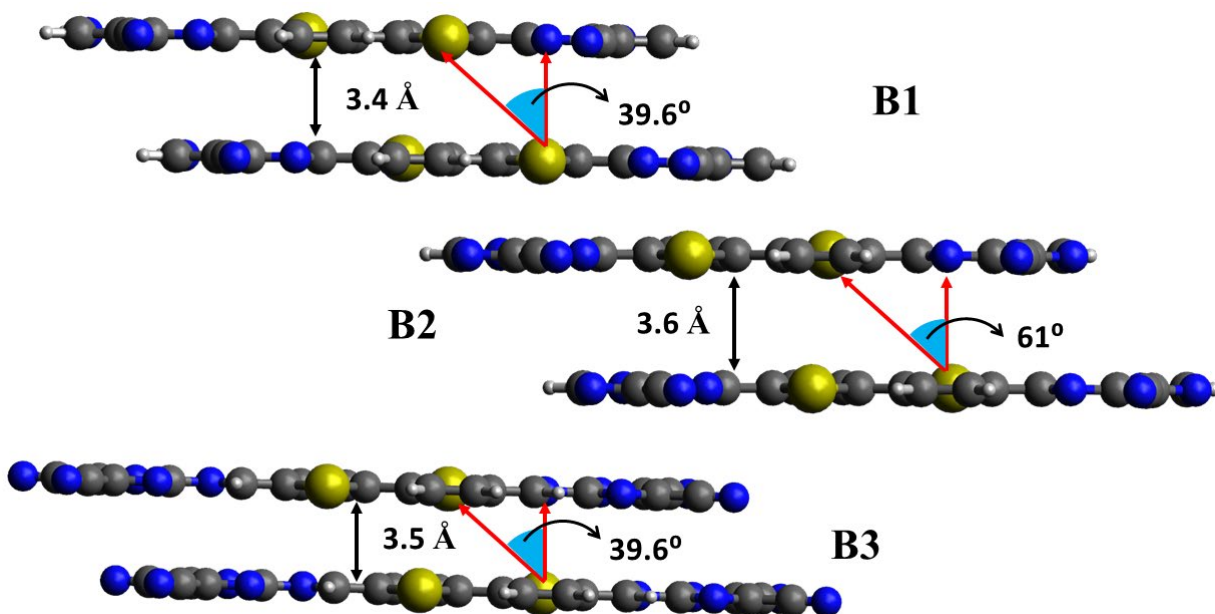


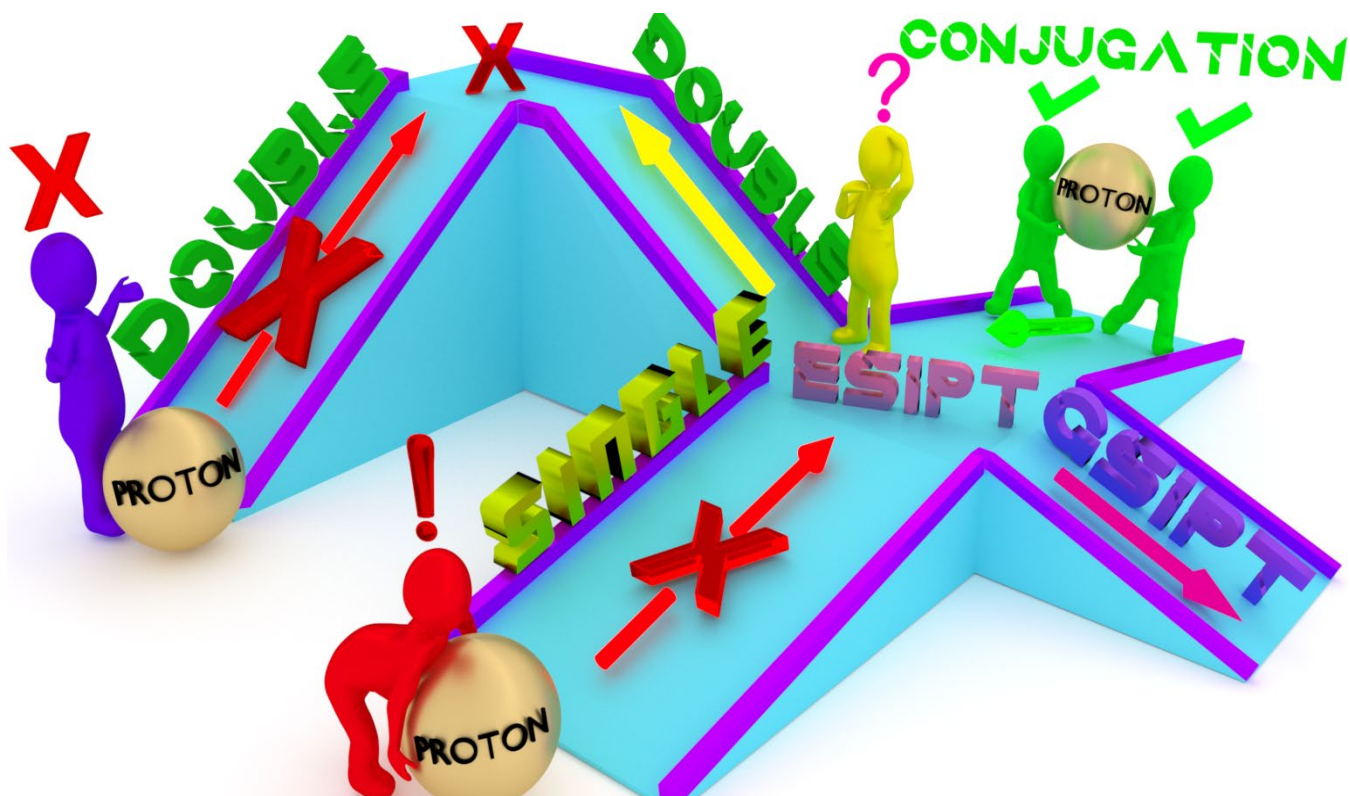
Fig. 4.35 Computed dimer geometries in slip-stacking mode with their stacking distance and slip angle

4.4 CONCLUSIONS

Three derivatives **B1**, **B2**, and **B3** based on bithiophene core substituted with heterocyclic units have been designed, synthesized, and characterized to investigate their photophysical properties. The photoluminescence spectra revealed the emission intensity upon increase in the water mixture confirmed the AIE properties of the molecules. The highest quantum yield observed for **B1** with a value of 18.66% and with the lowest recorded for **B3** with 2.4%. DFT studies have been performed and the results correlate well with the experimental data. Electron and hole reorganization energies computed for the molecular system proved **B3** to possess very low hole reorganization energy in comparison with others in the series. **B3** possessing two -CN group effectively alters the hole mobility in the system as evident from the theoretical calculations. Theoretical predictions validate all the molecules to adopt a slip stacking mode of molecular packing arrangement at condensed state. A large π - π stacking distance of 3.4 Å, 3.6 Å and 3.5 Å for **B1**, **B2** and **B3** respectively would further facilitate AIE phenomenon in the system.

CHAPTER 5

PHOTOPHYSICS OF PROTON TRANSFER IN HYDRAZIDES: A COMBINED THEORETICAL AND EXPERIMENTAL ANALYSIS TOWARDS OLED DEVICE APPLICATION



Mohan, M., Satyanarayan, M. N., and Trivedi, D. R. (2019). "Photophysics of proton transfer in hydrazides: a combined theoretical and experimental analysis towards OLED device application." New J. Chem., 43(26), 10413–10428

Abstract

In this chapter, experimental and theoretical interpretation uncovering the excited state proton transfer dynamics of hydrazides are well studied.

5.1 INTRODUCTION

Tautomerism in hydrazides at excited state is characterized by translocation of a proton from a proton donor (-NH) to a proton acceptor (-C=O) moiety with a pre-linked intramolecular hydrogen bonding (Mir et al. 2018). The energy gap between locally excited state and relaxed excited state of the system is responsible for an efficient proton transfer and the gradient of the surface connecting these two points provides activation kinetics of the system (Li and Han 2018; Zhang et al. 2016; Zhao et al. 2015). Tautomer structure exhibits exceptional photophysical properties that is highly unique for a system supporting excited state intramolecular proton transfer (ESIPT) (Barbara et al. 1980; Zhao et al. 2018). The intramolecular hydrogen bond in its normal form (N), when excited (N*) triggers the proton transfer, leading toward a structural transformation tautomer (T*) form. Tautomer T* relaxes to its tautomer ground state (T) either by a fluorescence emission or internal conversion, ensuring which tautomer rolls back to the normal (N) form via reverse ground-state proton transfer (RGSPT), realizing a four level photocyclic process (N → N* → T* → T → N) (Cheng et al. 2015; Gutiérrez-Arzaluz et al. 2015; Hayaki et al. 2013; Houari et al. 2015; Jankowska et al. 2014; Li et al. 2016, 2015; Mahanta et al. 2011; Parada et al. 2015; Park et al. 2012; Rode and Sobolewski 2010; Roohi et al. 2014; Sakai et al. 2016; Singla and Chowdhury 2012; Sobolewski et al. 2006; Stasyuk et al. 2015; Weller 1956; Xia et al. 2015; Yang and Chen 2014; Zhao et al. 2012) as presented in the Fig. 5.1. Tautomeric emission often highly red-shifted from normal absorption leads to a large Stokes shifts, that rules out the probabilities of self-absorption of generated photons (Cheng et al. 2015; Gutiérrez-Arzaluz et al. 2015; Houari et al. 2015; Li et al. 2016; Parada et al. 2015; Park et al. 2012; Sakai et al. 2016; Singla and Chowdhury 2012; Weller 1956; Zhao and Han 2012; Zhao et al. 2012). Dual fluorescence emission is highly unusual in molecules exhibiting ESIPT, that are highly fascinating for its practical applications in designing UV filters (Aparicio et al. 2011; Pinto da Silva et al. 2014; Sherin et al. 2009; Tang et al. 2011), fluorescence sensors (Aparicio et al. 2011; Chen et al. 2012; Gu et al. 2015; Kim et al. 2009; Lan et al. 2011; Pinto da Silva et al. 2014; Sherin et al. 2009; Singh et al. 2008; Song et al. 2014; Tang et al. 2011; Xu et al. 2012; Yang et al. 2009; Zhao et al.

2012) and aggregation induced emissive materials (Chen et al. 2017; Ciuciu et al. 2013; Kwon and Park 2011; Maity et al. 2015; McDonald et al. 2016; Peng et al. 2015; Qin et al. 2016; Samanta et al. 2017; Singh et al. 2016; Wu et al. 2015; Yao et al. 2014; Zhang et al. 2017). Finer tuning and systematic control over the dual emission energies has opened up research in developing a single molecule that generates white light emission for OLED device applications (Kim et al. 2011; Kundu et al. 2016; Liu et al. 2017; Samanta et al. 2017).

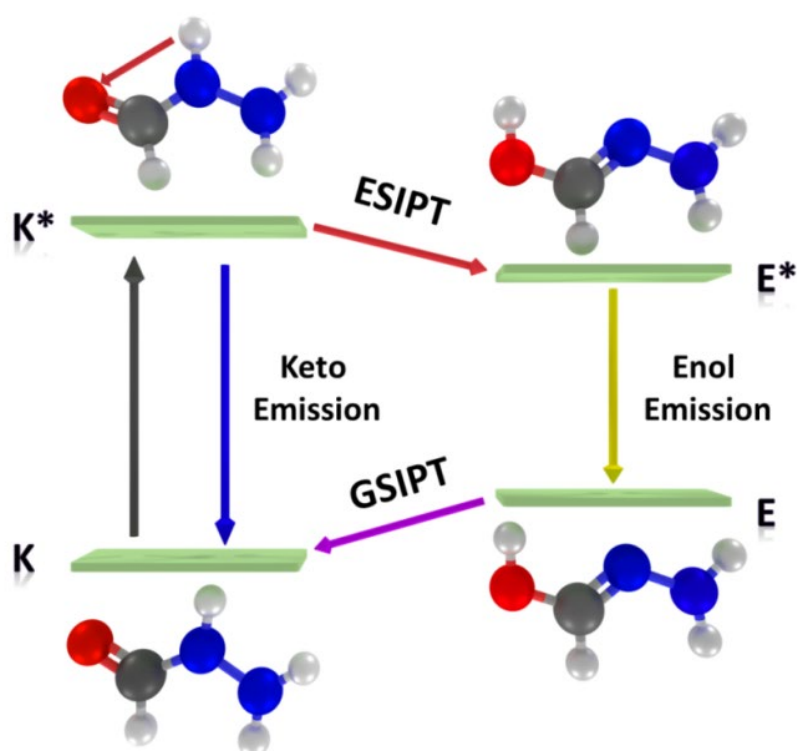


Fig. 5.1 Generic mechanism of keto-enol tautomerism exhibited in acid hydrazides

Hydrazides are a class of organic system that supports thermodynamically stable keto form and kinetically inert enolic tautomer upon photoexcitation. One of the possible reason being $-C=N$ group possessing lower bond energy of 615 kJ/mol making hydrazine N-H bond more strong, resulting in stable keto form at its ground state. Introduction of heterocyclic rings viz thiophene, furan, and pyridine will tend to alter the electronic density of the system in turn effectively governing the ESIPT of the system (Lin et al. 2012). The photophysical attributes of studied substituted hydrazides are enhanced by covalently linking with thiophene and bithiophene moiety to look into their practical applications as solid state emitters in OLEDs. Ease of synthetic modification and environmental stability

has directed thiophene and bithiophene based materials to be some of the most versatile conjugated systems for practical applications (M. et al. 1999). Hence, an attempt has been made to study the nature of excited state properties with meticulous initiation of proton transfer by incorporating extended conjugation into structures. Theoretical predictions validate the presence of extended conjugation to specifically activate proton transfer efficiently in comparison with **T1**, **P1** and **F1**. To the best of our knowledge theoretical aspects uncovering the remarkable excited state proton transfer properties of hydrazides remains a subject matter of discussion. Information relating to structures that favor simultaneous double proton transfer or step-wise double proton transfer is highly necessary to understand some of the underlying principles relating to kinetics of hydrazides.

5.2 EXPERIMENTAL SECTION

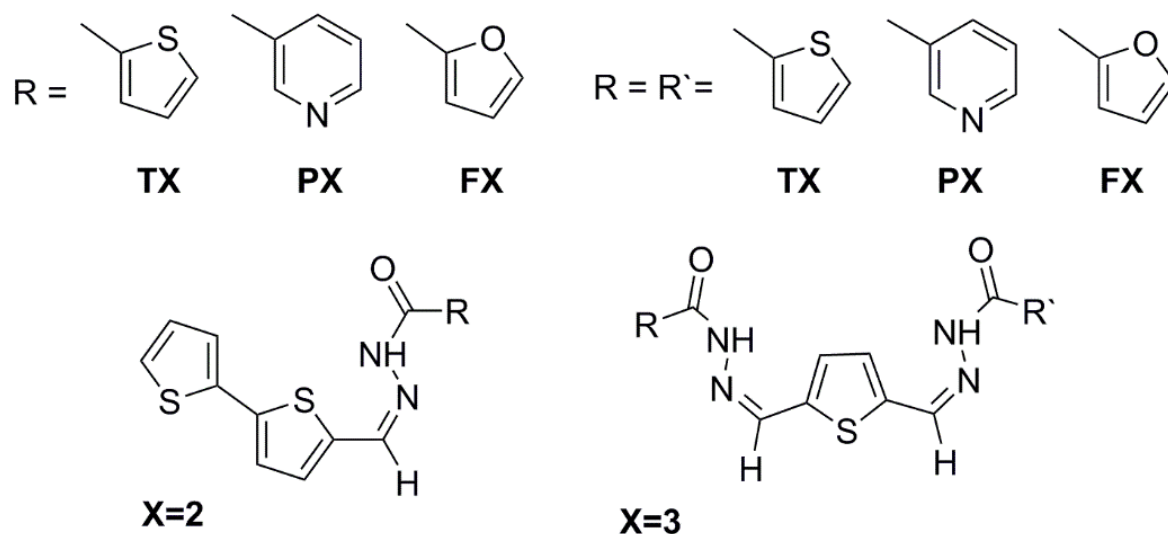
5.2.1 Materials and methods

All the chemicals used in the present study were procured from Sigma-Aldrich and were used as received without further purification. All the solvents purchased from SD Fine, India, were of HPLC grade and used without further distillation. Infrared spectrum was recorded on Bruker Apex FTIR spectrometer. UV-Vis spectra of all the molecules were carried out using Ocean optics SD2000 spectrometer and photoluminescence studies were carried out using Horiba Jobin Yvon spectrofluorometer. Cyclic voltammogram was recorded on IVIUM electrochemical workstation at a scan rate of 20mV/s with the maximum potential ranging between -5V to 5V . Device fabrication was performed using physical thermal vapor deposition at a base pressure of 5×10^{-6} Torr. Layers were deposited onto patterned indium-tin oxide (ITO) coated glass substrates with a sheet resistance of $15 \Omega/\text{square cm}$. ITO substrates were cleaned with soap solution followed by ultra-sonication in isopropyl alcohol for 20 min and followed by vapor degreasing using acetone. UV-ozone treatment was done on ITO substrates for 20 min in order to enhance the work function of ITO. The layers as per the device architecture were sequentially deposited under high vacuum condition. The deposition rate of organic materials was kept at 0.1 \AA s^{-1} to 0.5 \AA s^{-1} and for Aluminium the rate was maintained at 5 \AA s^{-1} . The total active device area measures to be 1.6 mm^2 . The EL spectra, current density–voltage–lumens (J–V–L) characteristics of the devices were measured using Keithley source-meter (Keithley 2400) and calibrated Si photodiode (SM1PD2A) equipped with an integrating sphere. All the measurements were carried out at room temperature under ambient conditions.

Computational calculation for all the molecules is achieved using Gaussian 09 package (Frisch et al. 2009). Ground state calculations S_0 were carried out with DFT Becke's three-parameter hybrid exchange function with the Lee-Yang-Parr gradient-corrected correlation functional (B3LYP) (Lee et al. 1988; Miehlich et al. 1989) with 6-311+G (d, p) (Hariharan and Pople 1973; Hehre et al. 1972) basis set and the excited state calculations S_1 were carried out using TD-DFT Coulomb-Attenuated Method B3LYP (Yanai et al. 2004) method with the same basis set used for ground state. The self-consistent field (SCF) convergence thresholds pertaining to energy minimizations for both S_0 and S_1 state optimization was set to 10^{-6} . The effect of solvent on the energy parameters of the system was studied by using self-consistent reaction field based on polarizable continuum model (PCM) (Tomasi and Persico 1994) using the integral equation formalism variant (IEFPCM) (Cammi and Tomasi 1995.; Cancès et al. 1997; Mennucci et al. 1997; Miertuš et al. 1981; Miertuš and Tomasi 1982). IEFPCM model studies the effect of solvent by placing the solute in a cavity of overlapping solvent and in effect reproduces the electrostatic potential arising due to the polarized dielectric created by the apparent charges surrounding the solute (Wei et al. 2017). The selection of functional was made in accordance with previous numerous benchmarks validating their accuracy in predicting ground state energies and excited state energies (An et al. 2017; Liu et al. 2017; Zhao and Han 2008). Initially, ground state optimizations were carried out at vacuum and the resultant geometry was further optimized in the solvent medium. The experimental results reveal ES IPT mechanism occurring at solvents of lower dielectric medium and to corroborate this effect theoretically, THF was chosen as a solvent medium for all the theoretical calculations. Frequency calculations were performed for the geometry optimized to confirm their geometry corresponds to a true local minimum on the S_0 and S_1 potential energy surface. Geometry optimizations were carried out without any constraints on bond lengths, bond angles or dihedral angles, however, such constraints were used while constructing potential energy surfaces (PESs) and potential energy curves (PECs). PESs and PECs in S_0 and S_1 states were scanned by constraining the O-H bond length fixed for a series of values with other degrees of freedom optimized without any constraint. The calculation of vertical excitation energy of first six singlet excited state S_1 was estimated from the ground state optimized structure based on TDDFT with IEFPCM solvation model. The optimized geometry and the electronic orbital distribution of all the molecules were visualized using Avogadro software (Hanwell et al. 2012).

5.2.2 Synthesis

Molecules **T2**, **P2** and **F2** have been synthesized by Schiff base condensation of 2,2'-Bithiophene-5-carboxaldehyde (0.1 g, 0.51 mmol) with 2-thiophene carboxylic acid hydrazide (0.073 g, 0.51 mmol), nicotinic acid hydrazide (0.071 g, 0.51 mmol) and 2-furoic hydrazide (0.071 g, 0.51 mmol) respectively. Molecules **T3**, **P3** and **F3** have been synthesized by Schiff base condensation of 2,5-Thiophenedicarboxaldehyde (0.1 g, 0.71 mmol) with 2-thiophene carboxylic acid hydrazide (0.2 g, 1.42 mmol), nicotinic acid hydrazide (0.196 g, 1.43 mmol) and 2-furoic hydrazide (0.18 g, 1.43 mmol) respectively. All the reactions were performed in ethanol in the presence of acetic acid as a catalyst. The structures of the representative molecules is shown in Scheme 5.1. Molecules were characterized using standard spectroscopic techniques and the results are provided in Fig. 5.2 to Fig. 5.19.



Scheme 5.1 Synthesized structures of **T2**, **P2**, **F2**, **T3**, **P3** and **F3** for the present study

T2: (*E*)-*N'*-([2,2'-bithiophen]-5-ylmethylene)thiophene-2-carbohydrazide Yield: 76 %, melting point: 210 °C, ¹H NMR (DMSO- *d*₆, 400 MHz, ppm): δ 11.88 (br. s; 1H), 8.59 (s; 1H), 8.01 (m; 1H), 7.89 (br. s; 1H), 7.6 (d; *J*=4.8, 1H), 7.45 (d; *J* = 3.8, 1H), 7.33 (d; *J* = 3.8; 1H), 7.23 (dd; *J*=4.8, 1H), 7.14 (dd; *J*=4.9, 3.8, 1H), FTIR (ATR) (cm⁻¹): 3186 (NH), 1622 (CH=N), ESI-MS Calculated: 318.00, Obtained: 318.90(M+H⁺).

P2: (*E*)-*N'*-([2,2'-bithiophen]-5-ylmethylene)nicotinohydrazide, Yield: 79 %, melting point: 234 °C, ¹H NMR (DMSO- *d*₆, 400 MHz, ppm): δ 12.03 (s; 1H), 9.05 (m; 1H), 8.77 (m; 1H), 8.6 (s; 1H), 8.25 (s; 1H), 7.59 (m; 2H), 7.47 (dd; *J* = 6.7, 3.7; 2H), 7.34 (d; *J* = 3.7; 1H), 7.14 (s; 1H), FTIR (ATR) (cm⁻¹): 1638 (CH=N), ESI-MS Calculated: 313.39, Obtained: 313.95(M+H⁺).

F2: (*E*)-*N'*-([2,2'-bithiophen]-5-ylmethylene)furan-2-carbohydrazide, Yield: 82%, melting point: 221 °C, ¹H NMR (DMSO- *d*₆, 400 MHz, ppm): δ 11.90 (br. s; 1H), 8.61 (br. s; 1H), 7.96 (s; 1H), 7.6 (d; *J* = 5; 1H), 7.46 (d; *J* = 3.5, 1H), 7.43 (d; *J* = 3.8, 1H), 7.32 (m; 2H), 7.15 (m; 1H), 6.72 (br.s; 1H), FTIR (ATR) (cm⁻¹): 3224 (NH), 3065 (Ar-CH), 1640 (CH=N), ESI-MS Calculated: 302.02, Obtained: 303.00(M+H⁺).

T3: *N',N'''*-((1*E*,1'*E*)-thiophene-2,5-diylbis(methaneylylidene))bis(thiophene-2-carbohydrazide), Yield: 72 %, melting point: 252 °C, ¹H NMR (DMSO- *d*₆, 400 MHz, ppm): δ 7.24 (br. s; 2H), 7.49 (s; 2H), 7.9 (br. s; 2H), 8.06 (d; *J* = 1.7; 2H), 8.27 (br. s; 1H), 8.65 (br. s; 1H), 11.98 (br. s; 2H). FTIR (ATR) (cm⁻¹): 2939 (NH), 2902 (Ar-CH), 1641 (CH=N). ESI-MS Calculated: 388.48, Obtained: 389(M+H⁺).

P3: *N',N'''*-((1*E*,1'*E*)-thiophene-2,5-diylbis(methaneylylidene))di(nicotinohydrazide), Yield: 78%, melting point: 276 °C, ¹H NMR (DMSO- *d*₆, 400 MHz, ppm): δ 7.58 (m; 4H), 8.26 (d; *J* = 8.1, 2H), 8.66 (s; 2H), 8.78 (m; 2H), 9.06 (s; 2H), 12.12 (m; 2H). FTIR (ATR) (cm⁻¹): 3209 (NH), 3054 (Ar-CH), 1639 (CH=N). ESI-MS Calculated: 378.41, Obtained: 379.10(M+H⁺).

F3: *N',N'''*-((1*E*,1'*E*)- thiophene- 2,5-diylbis (methaneylylidene)) bis (furan-2-carbohydrazide) Yield: 76 %, melting point: 260 °C, ¹H NMR (DMSO- *d*₆, 400 MHz, ppm): δ 6.76 (m; 2H), 7.34 (m; 2H), 7.53 (m; 2H), 7.97 (br. s; 2H), 8.65 (br. s; 2H), 11.98 (br. s; 1H), 11.89 (m; 1H). FTIR (ATR) (cm⁻¹): 3135 (NH), 1604 (CH=N). ESI-MS Calculated: 356.36, Obtained: 357(M+H⁺).

5.2.3 Characterization data

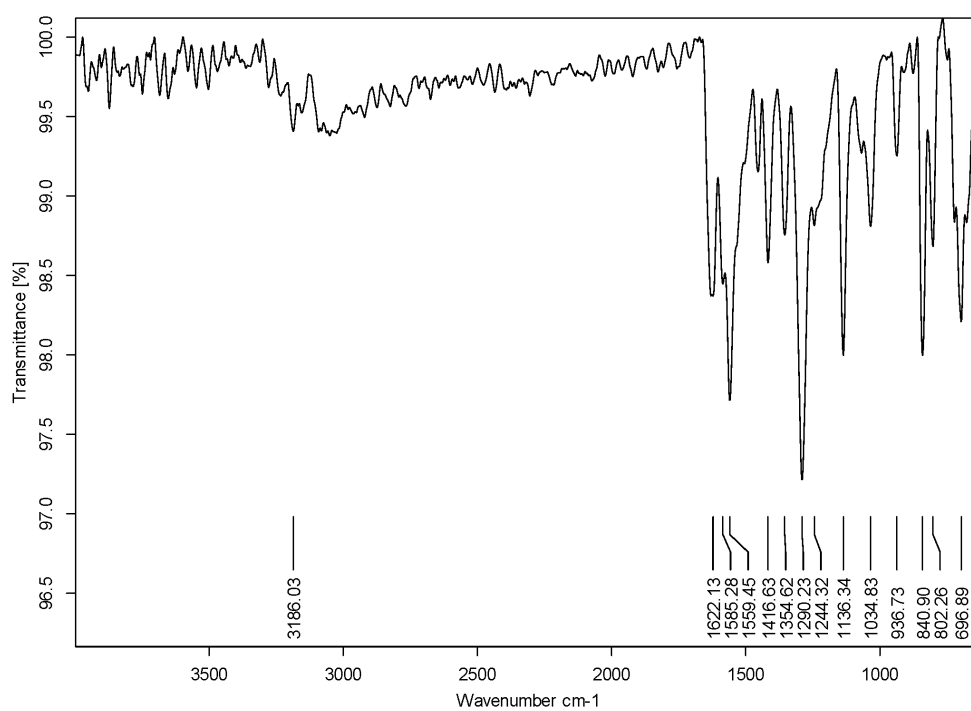


Fig. 5.2 FT-IR spectra of **T2**

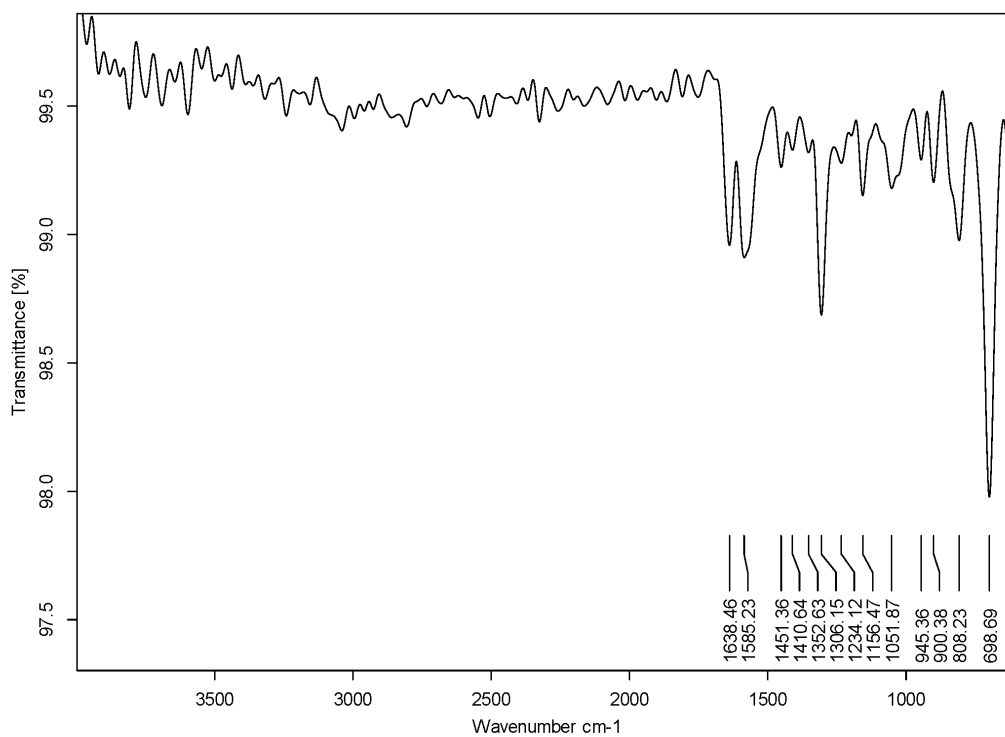


Fig. 5.3 FT-IR spectra of **P2**

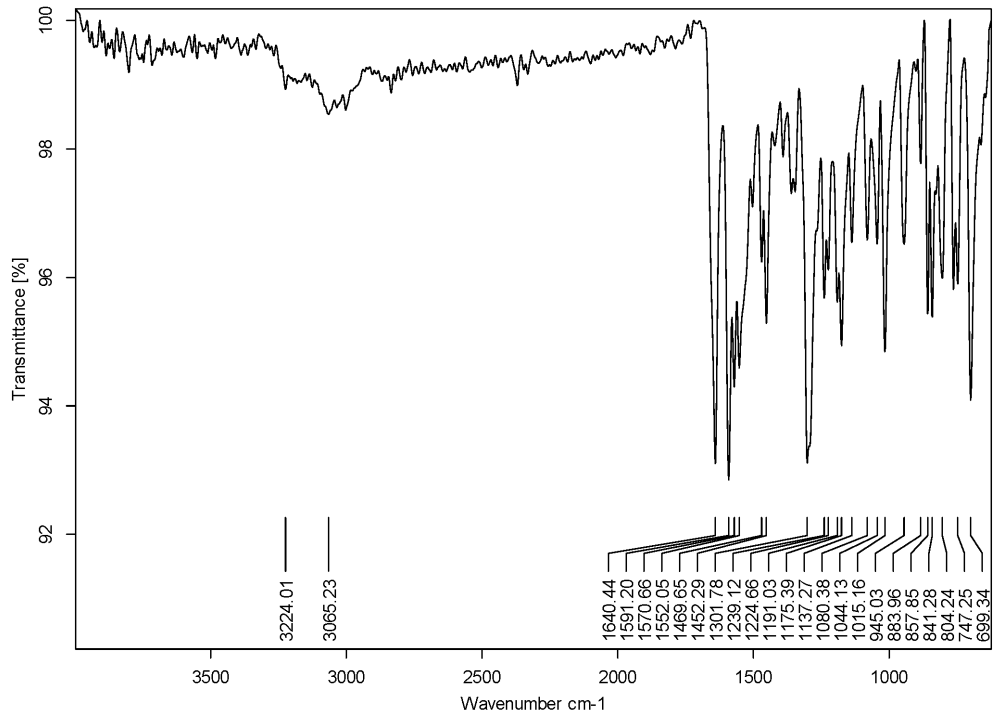


Fig. 5.4 FT-IR spectra of **F2**

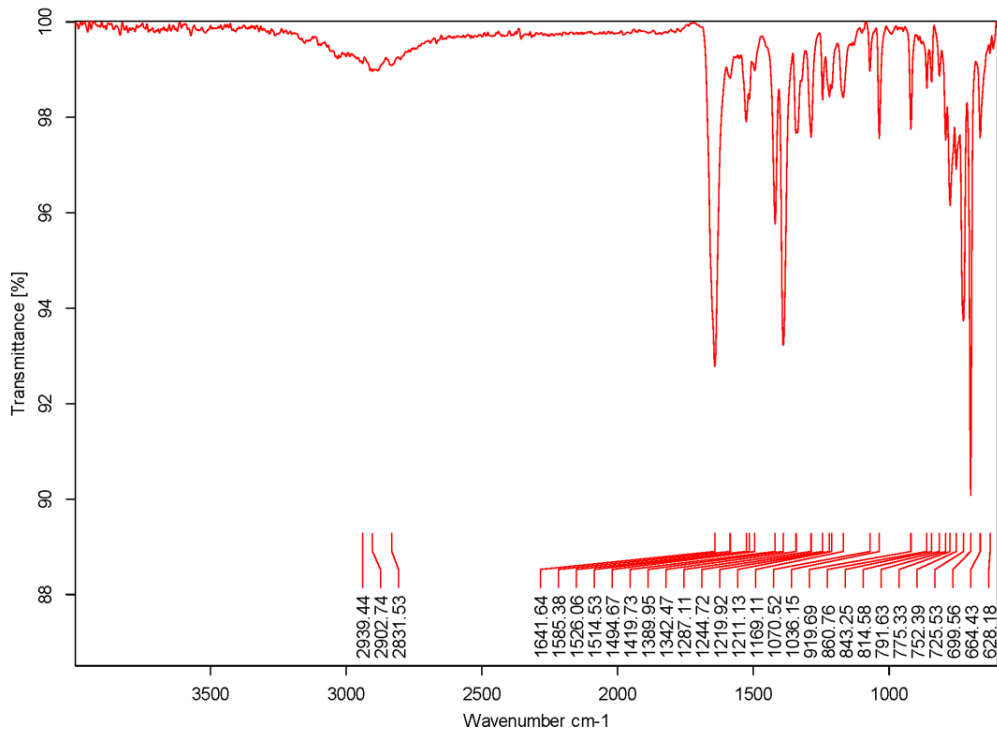


Fig. 5.5 FT-IR spectra of **T3**

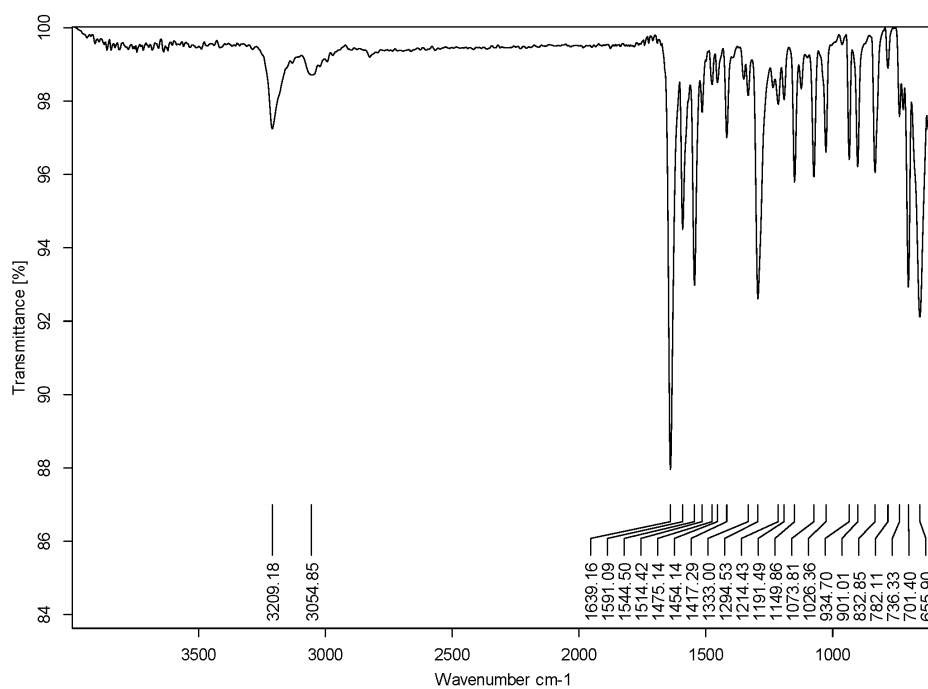


Fig. 5.6 FT-IR spectra of **P3**

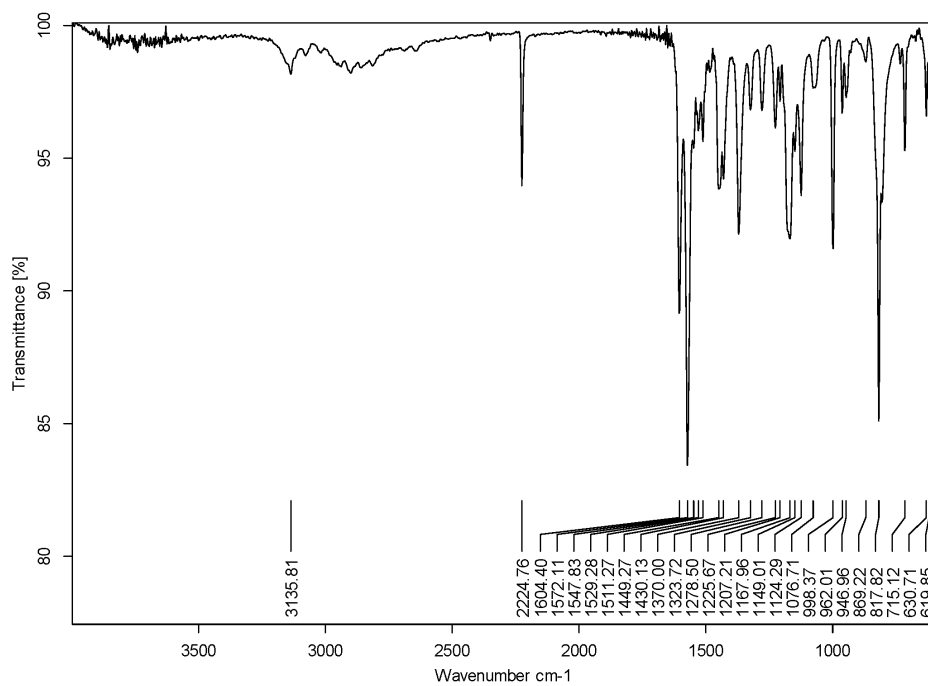


Fig. 5.7 FT-IR spectra of **F3**

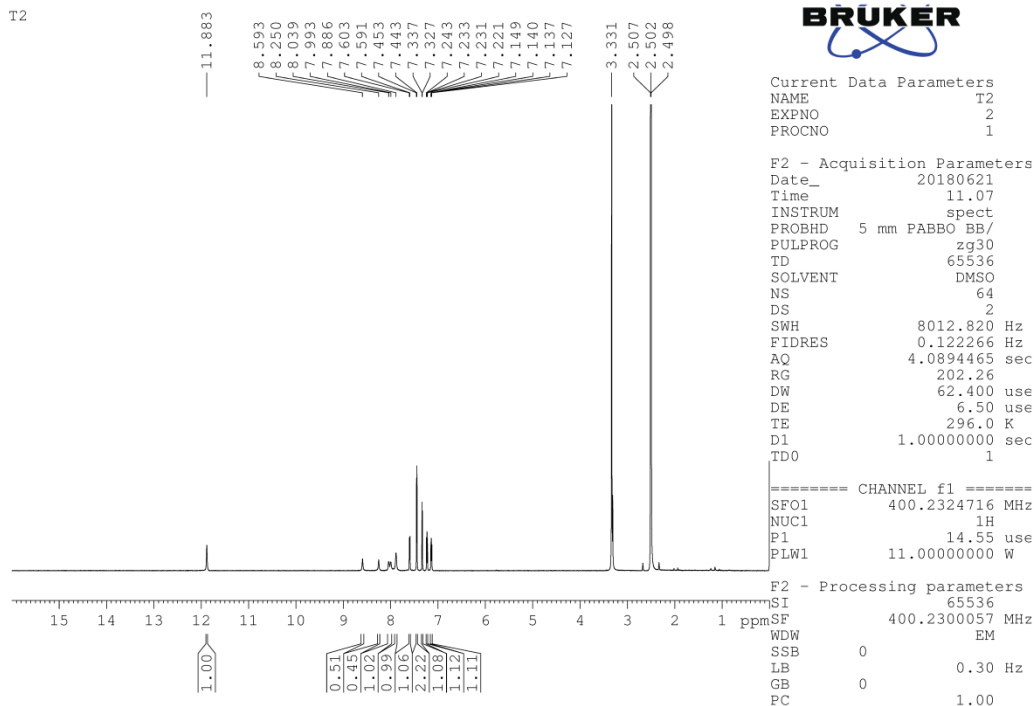


Fig. 5.8 ^1H NMR spectra of T2

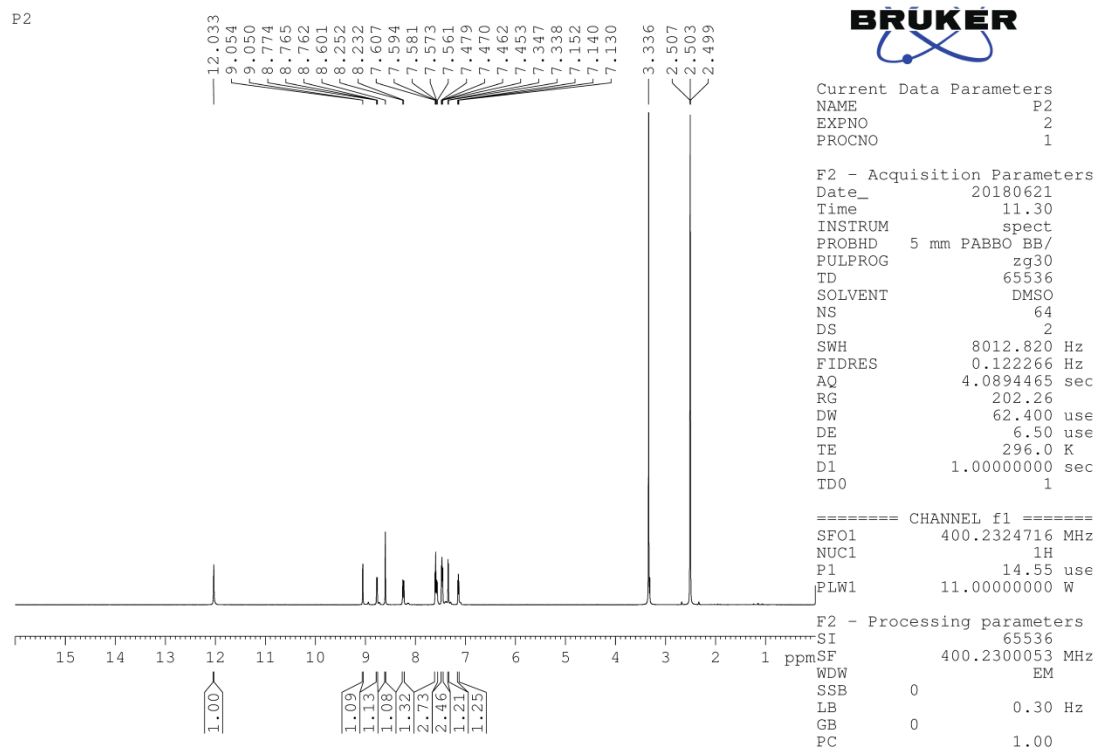


Fig. 5.9 ^1H NMR spectra of P2

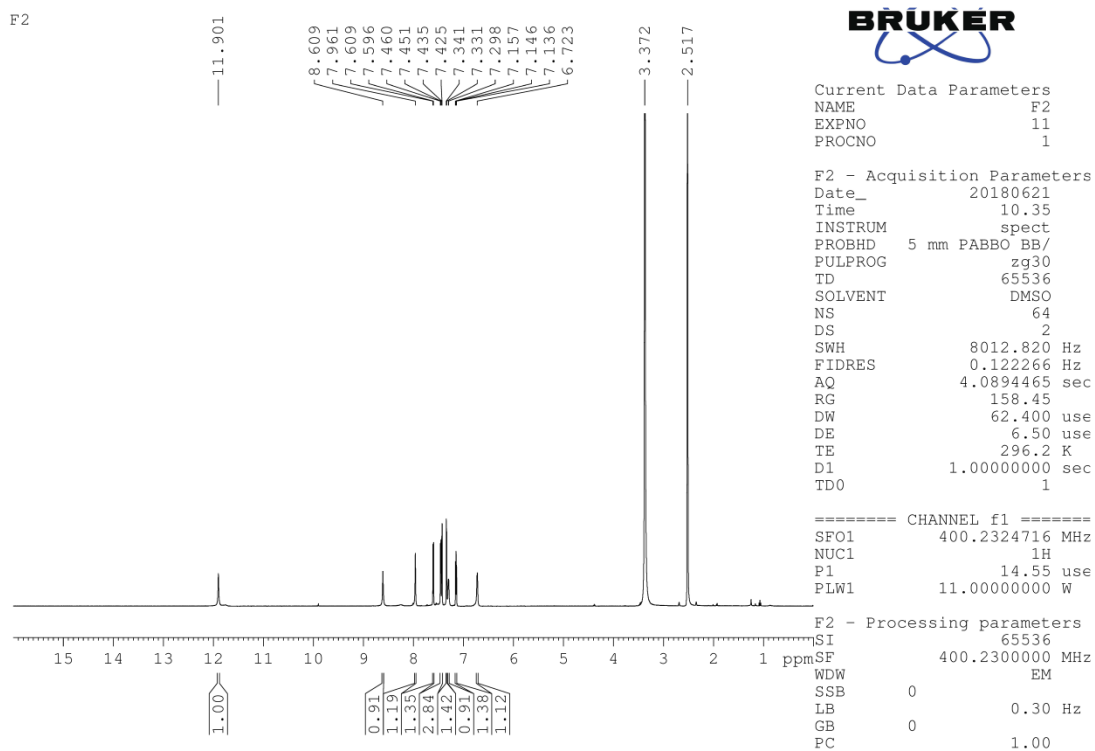


Fig. 5.10 ¹H NMR spectra of F2

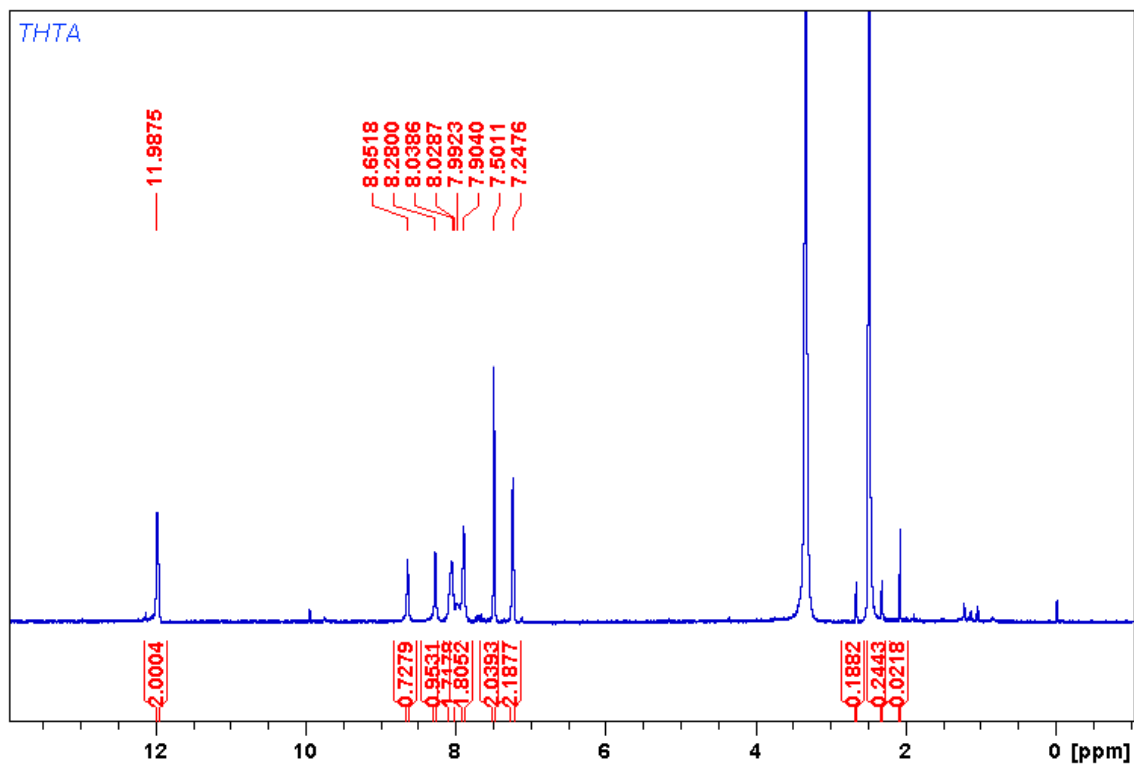


Fig. 5.11 ¹H NMR spectra of T3

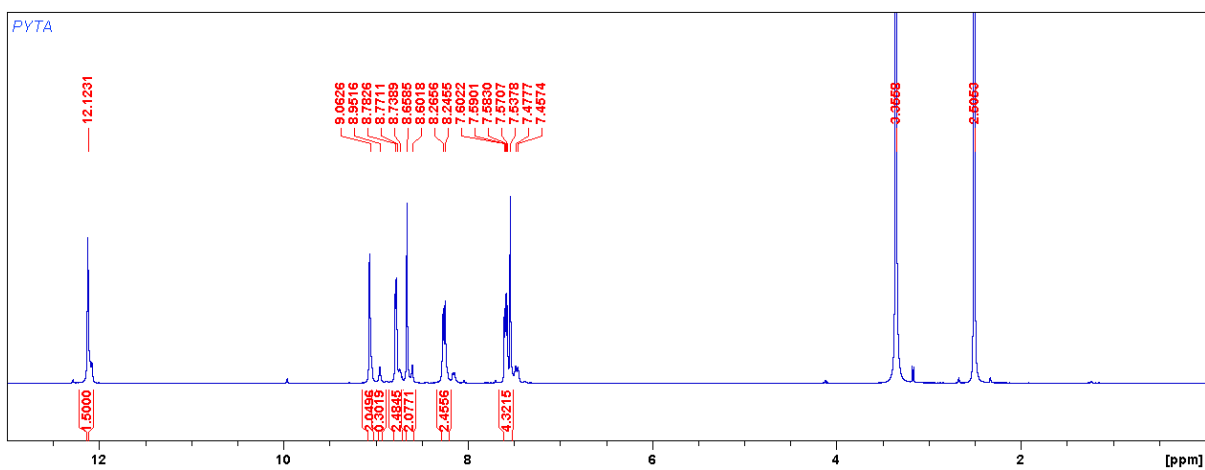


Fig. 5.12 ¹H NMR spectra of P3

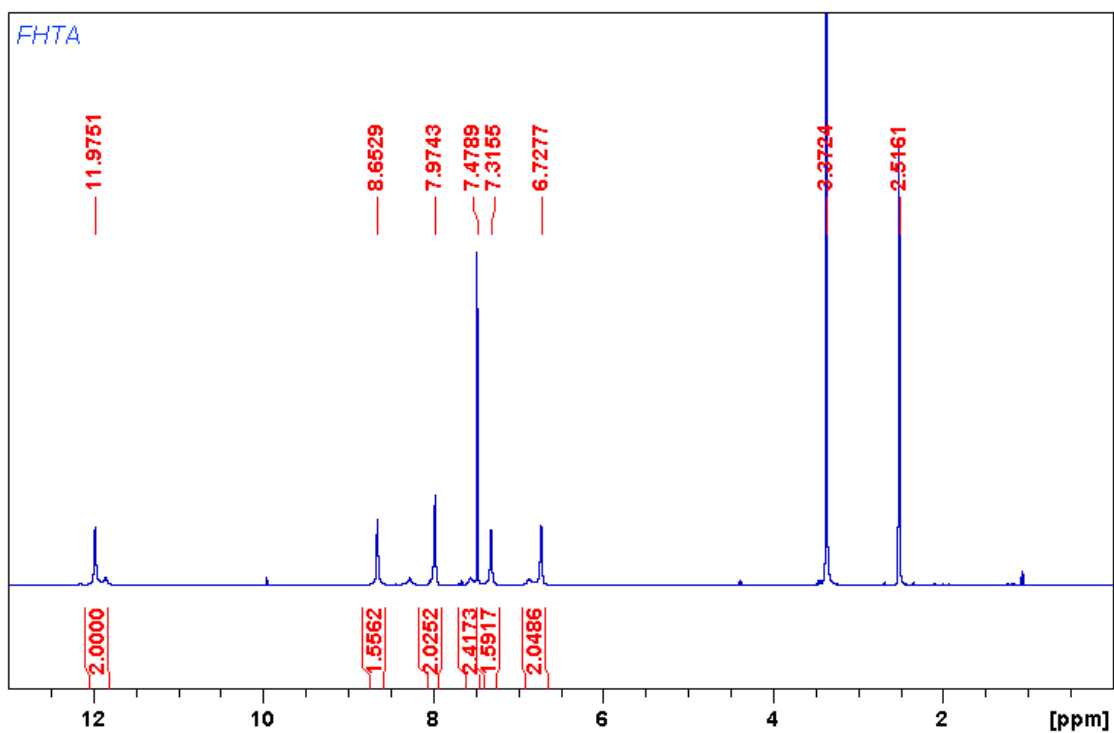


Fig. 5.13 ¹H NMR spectra of F3

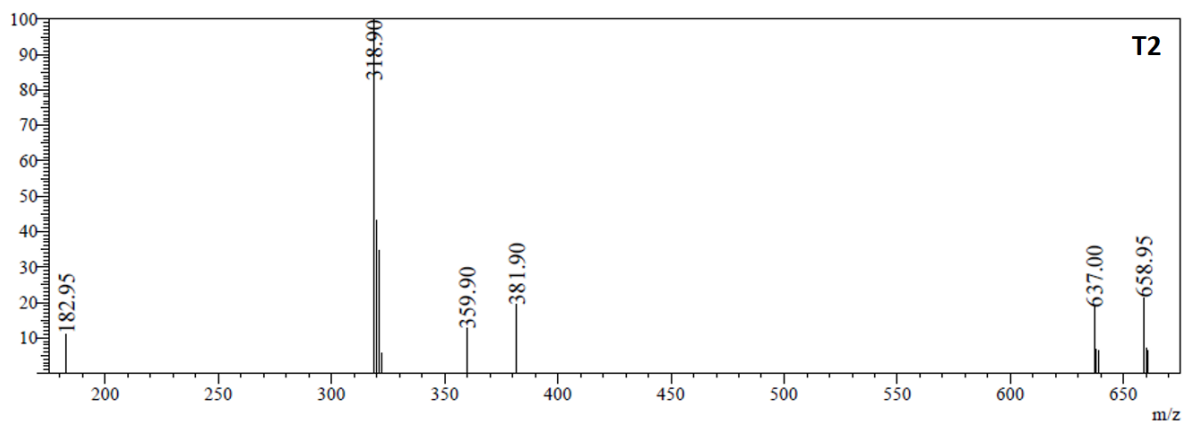


Fig. 5.14 ESI-MS spectra of T2

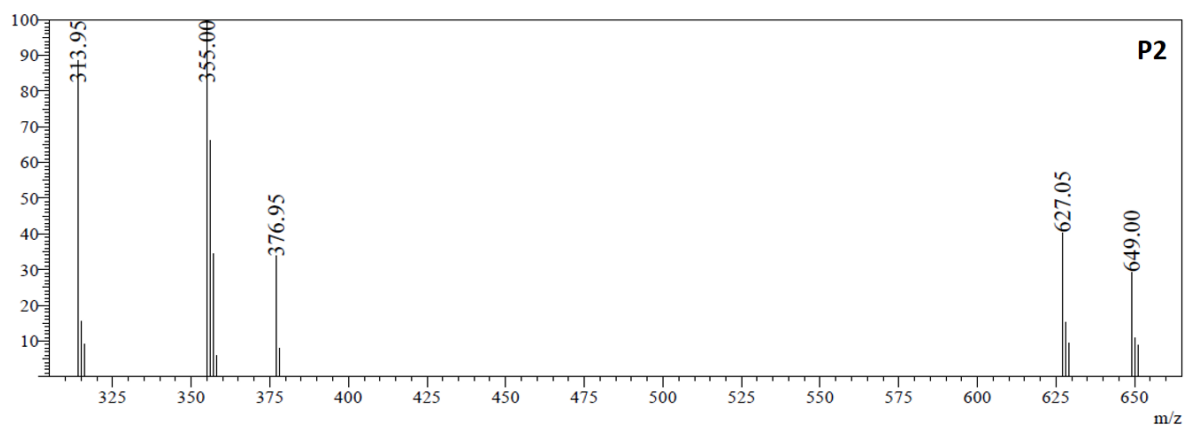


Fig. 5.15 ESI-MS spectra of P2

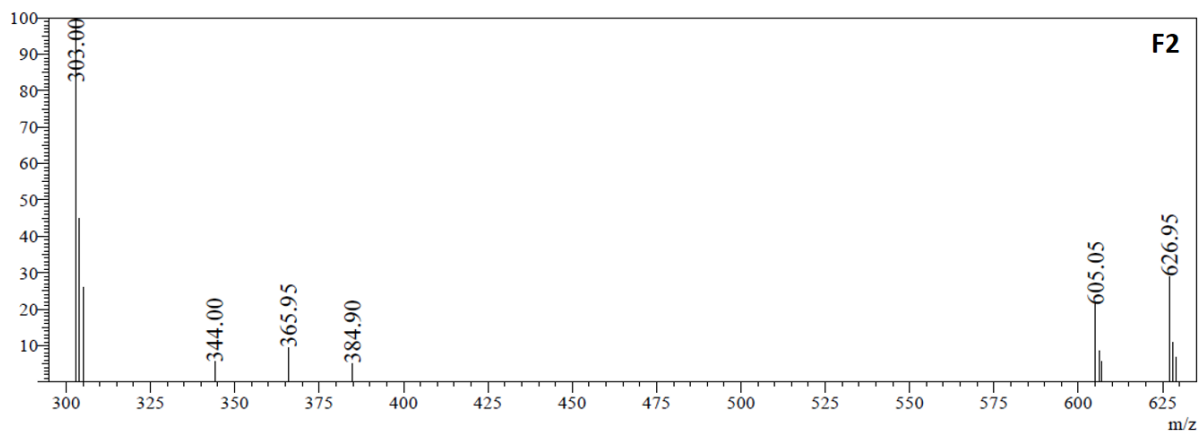


Fig. 5.16 ESI-MS spectra of F2

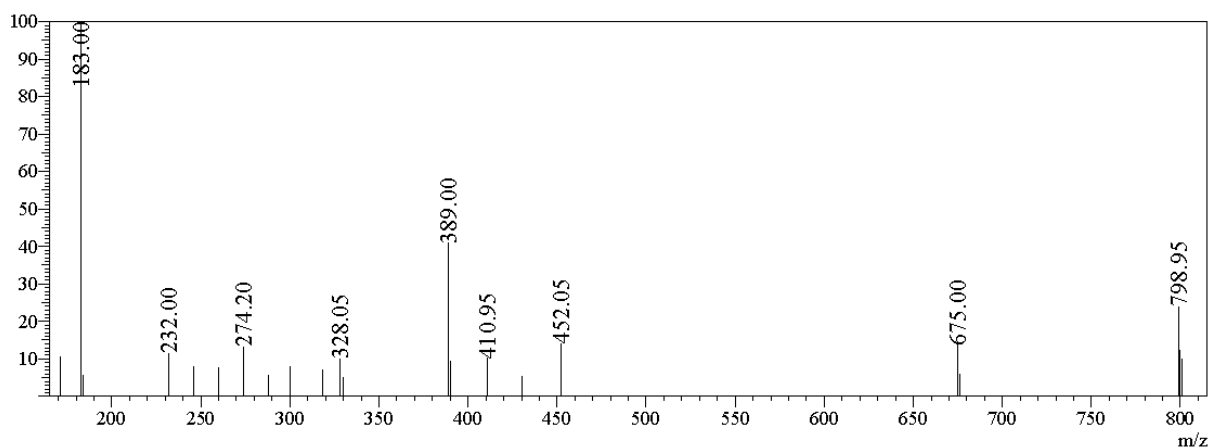


Fig. 5.17 ESI-MS spectra of T3

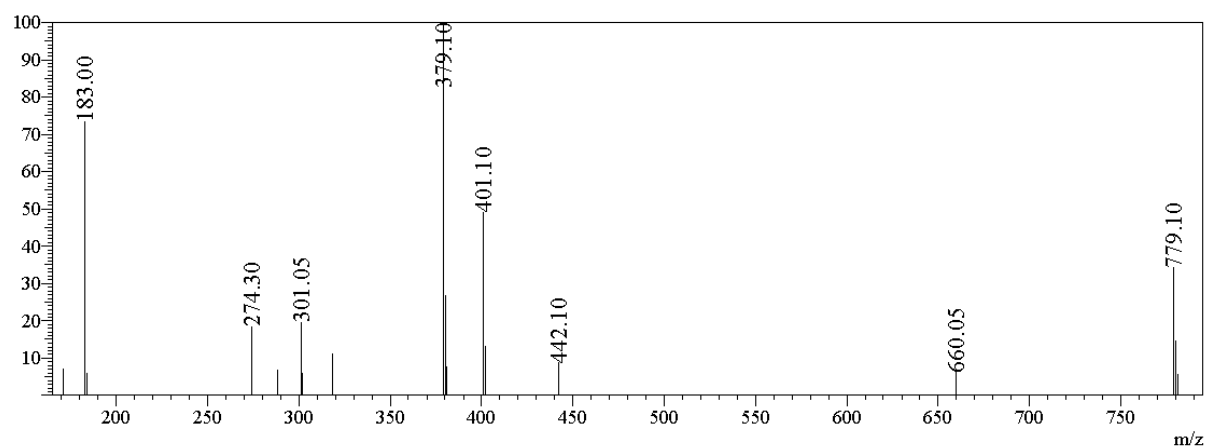


Fig. 5.18 ESI-MS spectra of P3

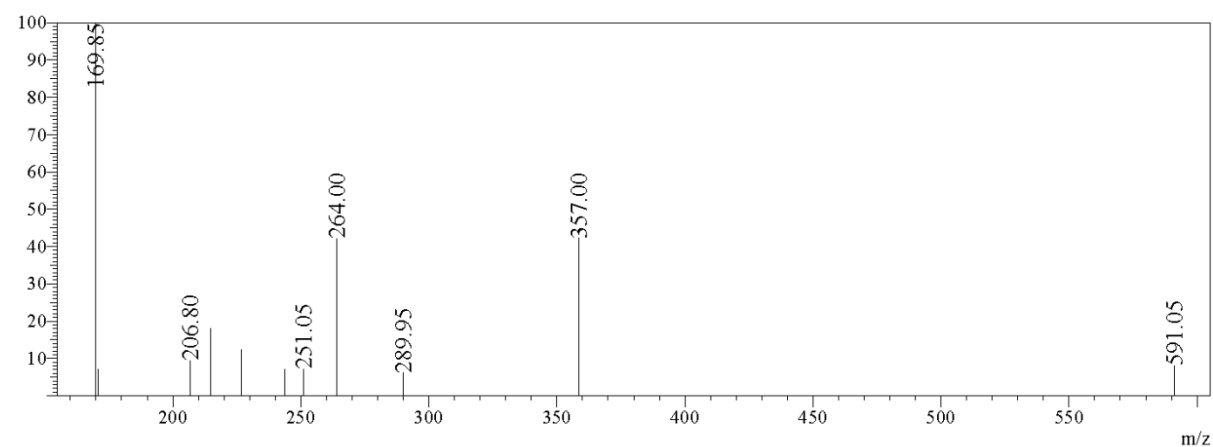


Fig. 5.19 ESI-MS spectra of F3

5.3 RESULTS AND DISCUSSION

5.3.1 UV-Vis Studies

The UV-Vis spectrum of all the molecules exhibited two main bands. The lowest lying absorption band centered at 360-370 nm could be attributed to the π - π^* transition of the aromatic rings. The second band at 400-450 nm corresponds to the n - π^* transition of the C=O and C=N groups. The second band being split and broad represents the intramolecular hydrogen bond which induces -NH proton to be acidic and carbonyl oxygen basic with respect to their ground state driving the proton-transfer reaction (Issa et al. 2005). UV-Vis spectra of all the molecules under the solvents of different dielectric constants are provided in Fig. 5.20 – Fig. 5.25. The observed bathochromic shift in polar protic solvents is indicative of strengthening of intermolecular hydrogen bond between solute and solvent molecules at their excited state (Song and Ma 2013).

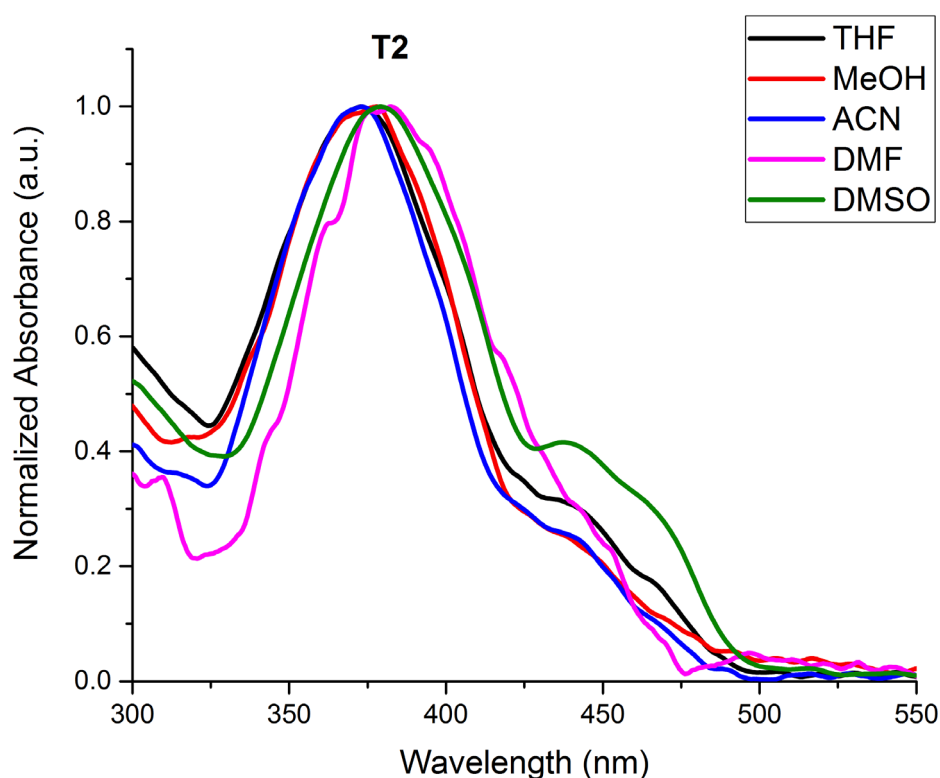


Fig. 5.20 UV-Vis absorbance spectra of molecule **T2** in solvent of varying polarity.

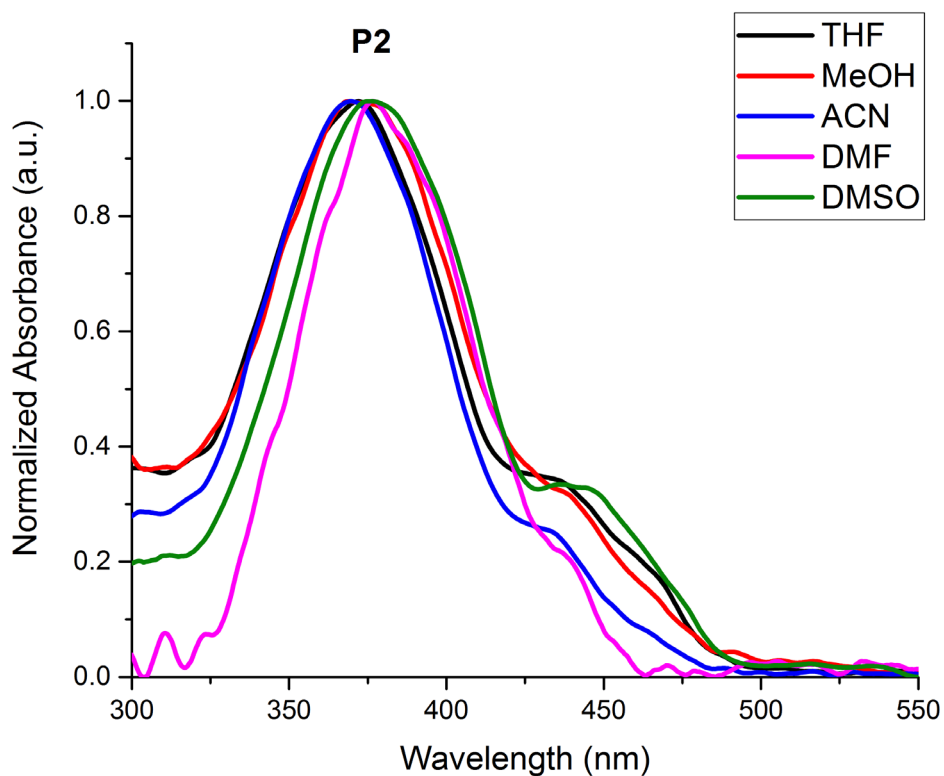


Fig. 5.21 UV-Vis absorbance spectra of molecule **P2** in solvent of varying polarity.

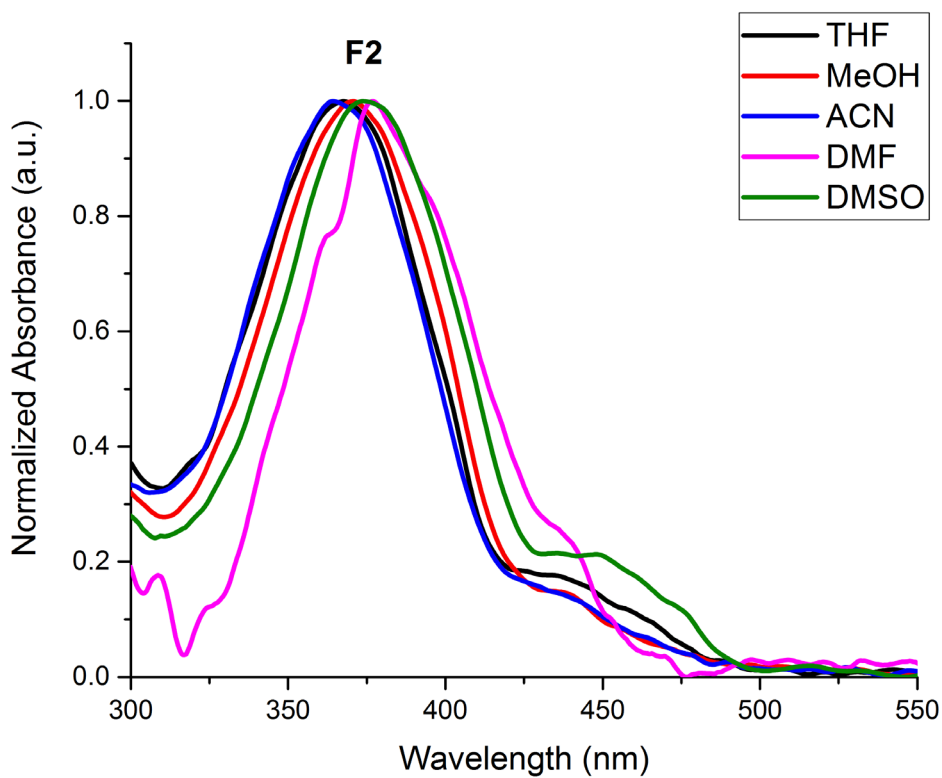


Fig. 5.22 UV-Vis absorbance spectra of molecule **F2** in solvent of varying polarity.

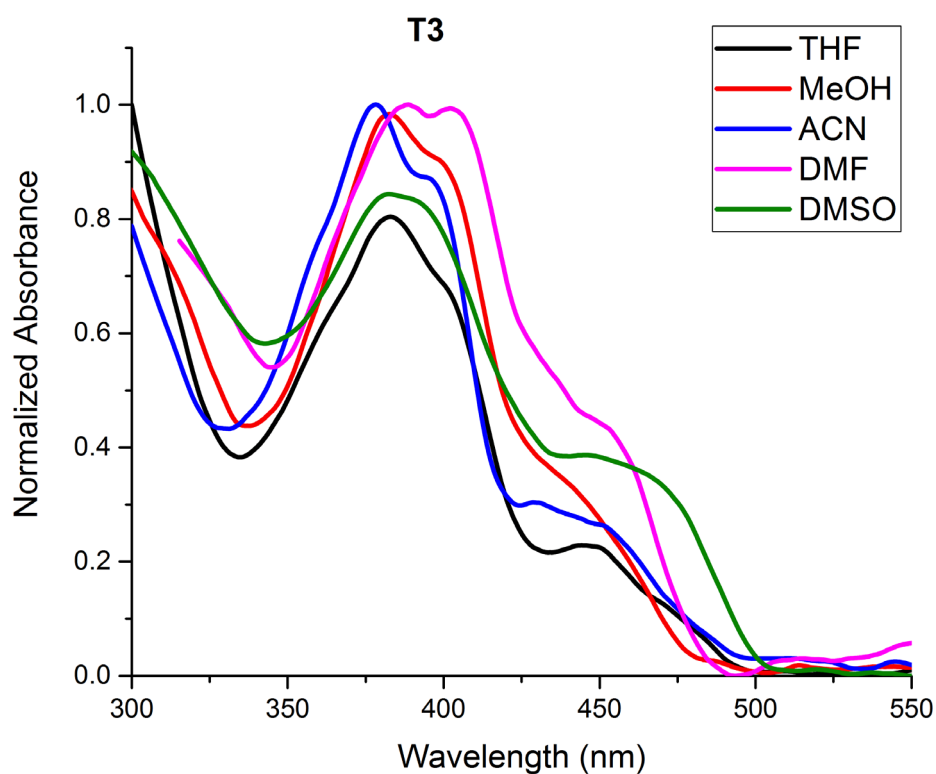


Fig. 5.23 UV-Vis absorbance spectra of molecule **T3** in solvent of varying polarity.

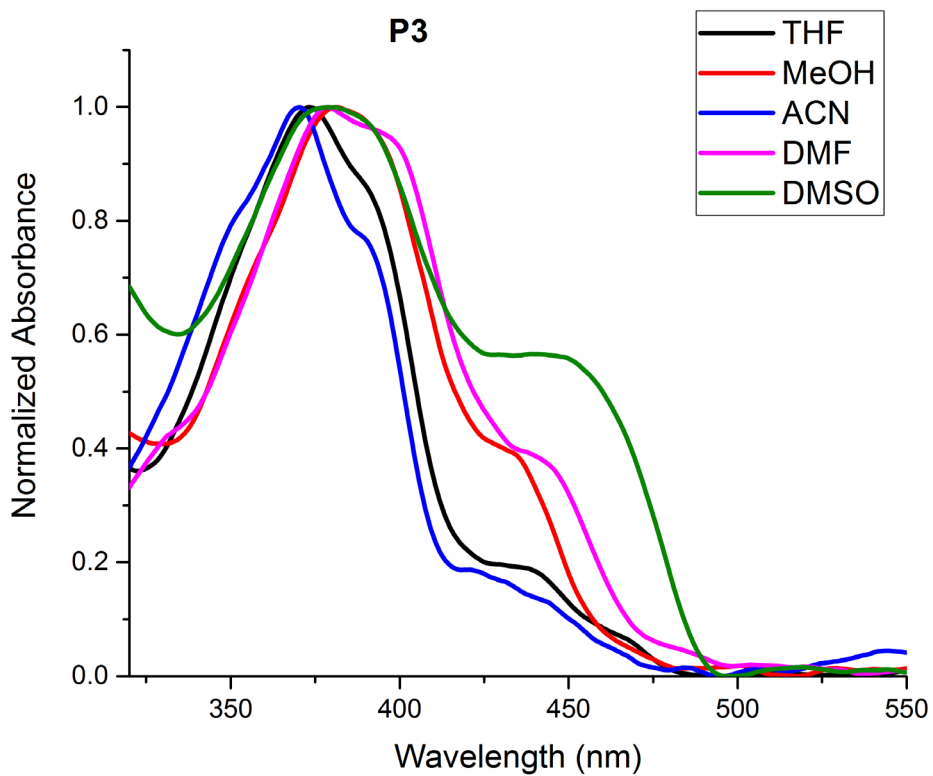


Fig. 5.24 UV-Vis absorbance spectra of molecule **P3** in solvent of varying polarity.

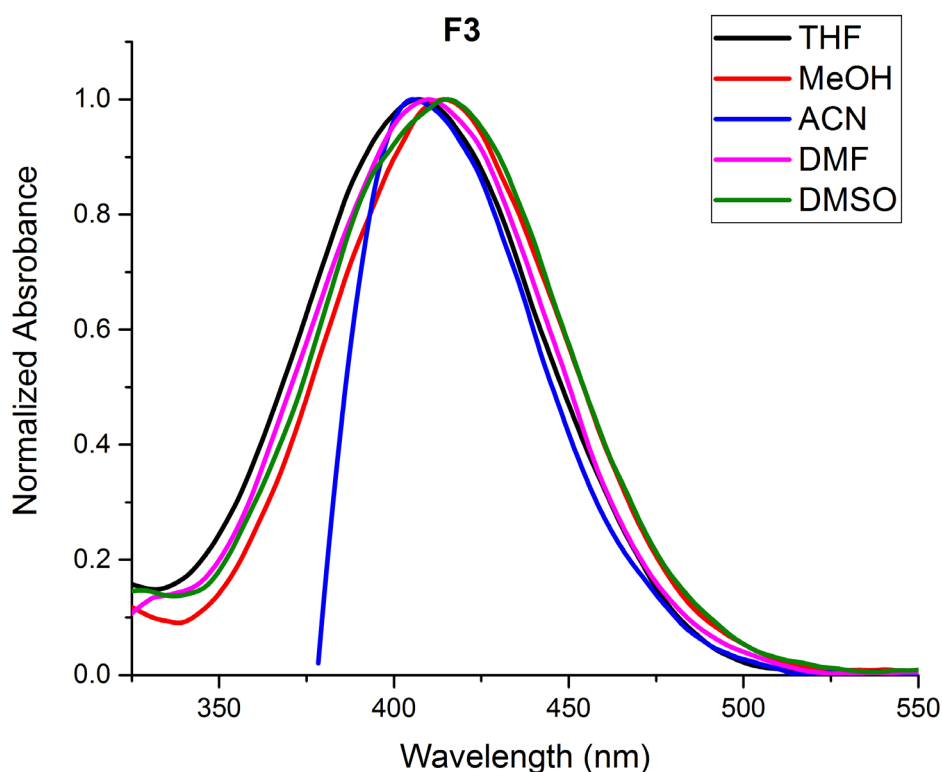


Fig. 5.25 UV-Vis absorbance spectra of molecule **F3** in solvent of varying polarity.

5.3.2 Photoluminescence studies

Fluorescence emission studies were carried out in solvents of varying polarities to gain a better understanding of the nature of ESIPT under different solvent medium. Molecules of the series exhibited a general photoluminescence response of double peak that links to keto (k^*) and enol (e^*) emissions characterized by a four level photo cyclic process triggered due to intramolecular H-bonding. The photophysical property of the molecules in solvents of varying polarity is summarized in the Table 5.1 and the spectral images are provided in Fig. 5.26 – Fig. 5.31. In specific, THF possessing a very low dielectric constant supports ESIPT with a distinct keto-enol emission for all the molecules of the series as evident from the spectra. Conjugation enhanced structural backbone of **T3**, **P3** and **F3** with acyl substituted hydrazides on both the arms show a red-shifted keto emission in all the solvents in comparison with others in the series. Methanol, a polar protic solvent has the tendency to form H-bonding with solute molecules, this being the reason; molecules of the series did not show dual emission in methanol. In polar solvents, apart from intramolecular H-bonding, intermolecular H-bonding is quite probable between solute and solvent molecules (Cheng et al. 2015). Polar solvents acting as hydrogen bond

acceptors can impede the ESIPT process by bonding with the proton donor species, resulting in suppression of tautomer emission (Kasha 1986). Emission energy of the organic system is pivoted on the nature of H-bonding occurring between solute and solvent molecules (Zhao and Han 2008). The solvent induced bathochromic shift observed at the emission energy indicates the strengthening of the intermolecular hydrogen bond and hypsochromic shift indicates the weakening of hydrogen bond (Song and Ma 2013). This is highly prevalent in this case, where molecules showed a red-shifted emission in comparison with other solvents superseding the linearity, otherwise expected. All the molecules showed a bathochromic emission wavelength from THF to ACN excluding methanol, exhibiting positive solvatochromic behavior. Polar solvents inducing positive solvatochromism in solute-solvent interaction substantiates better stabilization of the excited state as compared to that of the ground state; in turn, redistribution of the charges occur supporting multi-dimensional intramolecular charge transfer (MDICT) between the core and peripheral moieties (Brunel et al. 2003). **T2**, **F2**, and **F3** furthered positive solvatochromic effect in DMF in contrast with the others in the series exhibiting negative solvatochromism. **P2** and **P3** possessing nicotinic hydrazide moiety exhibited similar emission pattern supporting positive solvatochromism, however, neglecting slight changes offered due to closer dielectric constants offered by ACN and DMF. **F3** exhibited a peculiar emission characteristic and failed to show tautomer emission in any solvent other than THF. The sensitivity of emission energy due to the changes in solvent polarity is highly evident for all molecules of the series. Solvent polarity induces a greater charge separation in the excited state, in turn, provokes higher dipole moment at the excited state than that possessed in the ground state (Wang et al. 2011). Normal Stokes shift measured considering the excitation energy, and keto emission is roughly 132 nm for **T3** in ACN solvent. The so-called large Stokes shift recorded between keto emission, and enol emission is around 30 nm in the series, and the highest observed for **P2** is 40 nm in DMF solvent.

TABLE 5.1 Photophysical parameters of the molecules in solvents of different polarities

	λ_{abs} (nm)	λ_{exe} (nm)	λ_{emi} (nm)		Normal Stokes Shift (nm)	Large Stokes Shift (nm)
			Keto (k)	Enol (e)		
THF						
T2	372, 438	372	418	450	46	32
P2	368, 435	368	413	444	45	31
F2	372, 436	372	415	441	43	26
T3	382, 401, 449	382	425	447	43	22
P3	373, 388, 438	373	417	451	44	34
F3	407	407	456	484	49	28
MeOH						
T2	378, 435	378	461	—	83	—
P2	370, 435	370	463	—	93	—
F2	370, 435	370	450	—	80	—
T3	381, 400, 443	381	506	—	125	—
P3	380, 391, 433	391	481	—	90	—
F3	413	413	535	—	122	—
ACN						
T2	372, 440	372	422	450	50	28
P2	370, 432	370	423	450	53	27
F2	364, 440	364	446	—	82	—
T3	378, 396, 438	378	510	—	132	—
P3	370, 390, 434	370	465	486	95	21
F3	405	405	517	—	112	—
DMF						
T2	385, 440	385	462	490	77	28
P2	376, 440	376	420	460	44	40
F2	376, 440	376	459	483	83	24
T3	387, 402, 455	387	484	505	97	21
P3	378, 398, 441	379	463	487	84	24
F3	410	410	518	—	108	—
DMSO						
T2	379, 439	379	432	461	53	29
P2	374, 439	374	427	453	53	26
F2	374, 439	374	426	451	52	25
T3	381, 448	381	455	—	74	—
P3	378, 446	378	478	503	100	25
F3	415	415	508	—	93	—

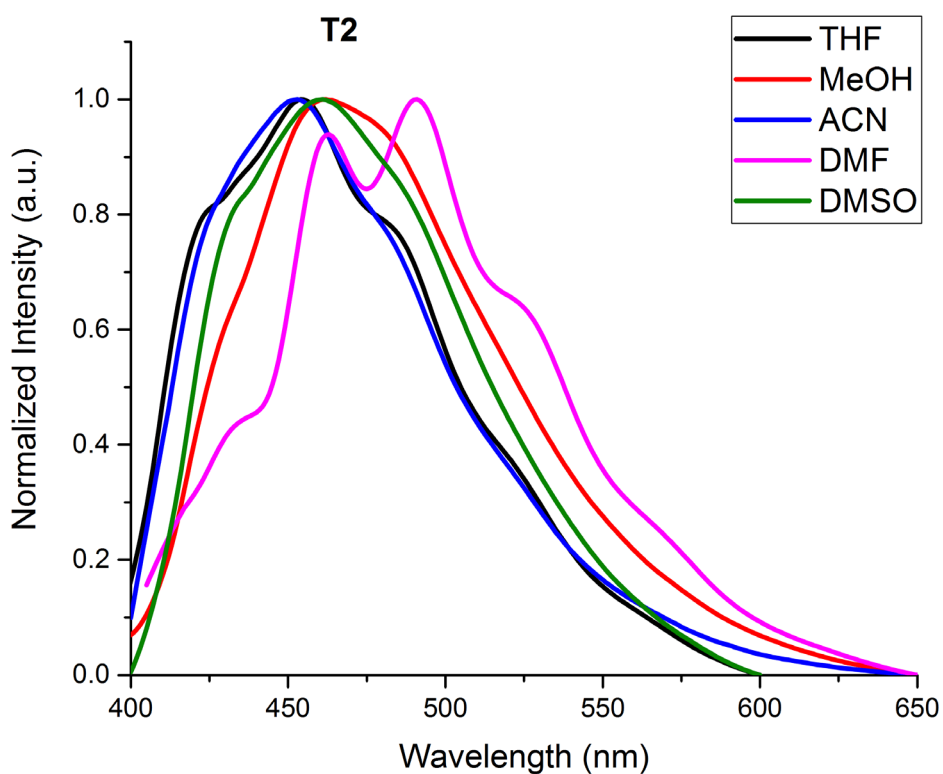


Fig. 5.26 PL spectra of molecule **T2** in solvent of varying polarity.

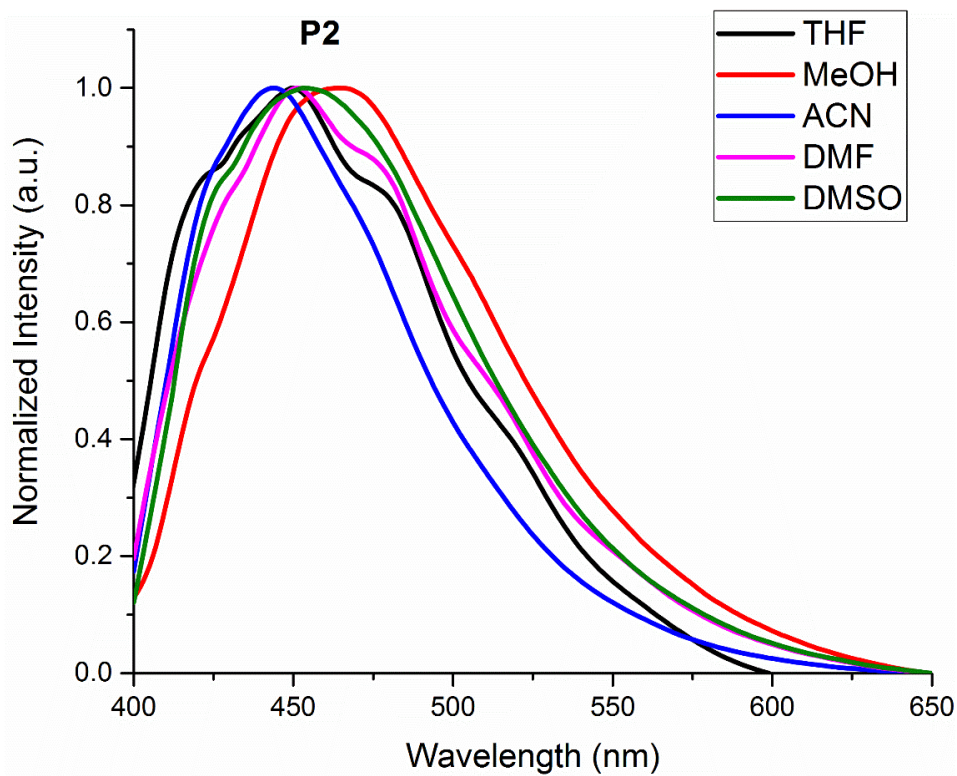


Fig. 5.27 PL spectra of molecule **P2** in solvent of varying polarity.

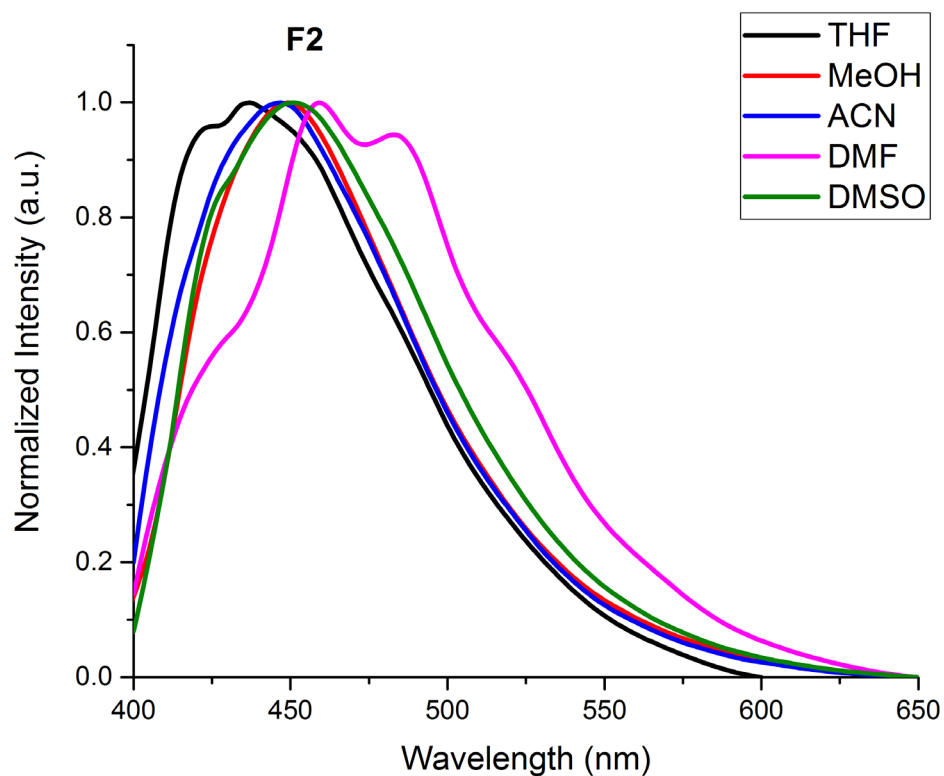


Fig. 5.28 PL spectra of molecule **F2** in solvent of varying polarity.

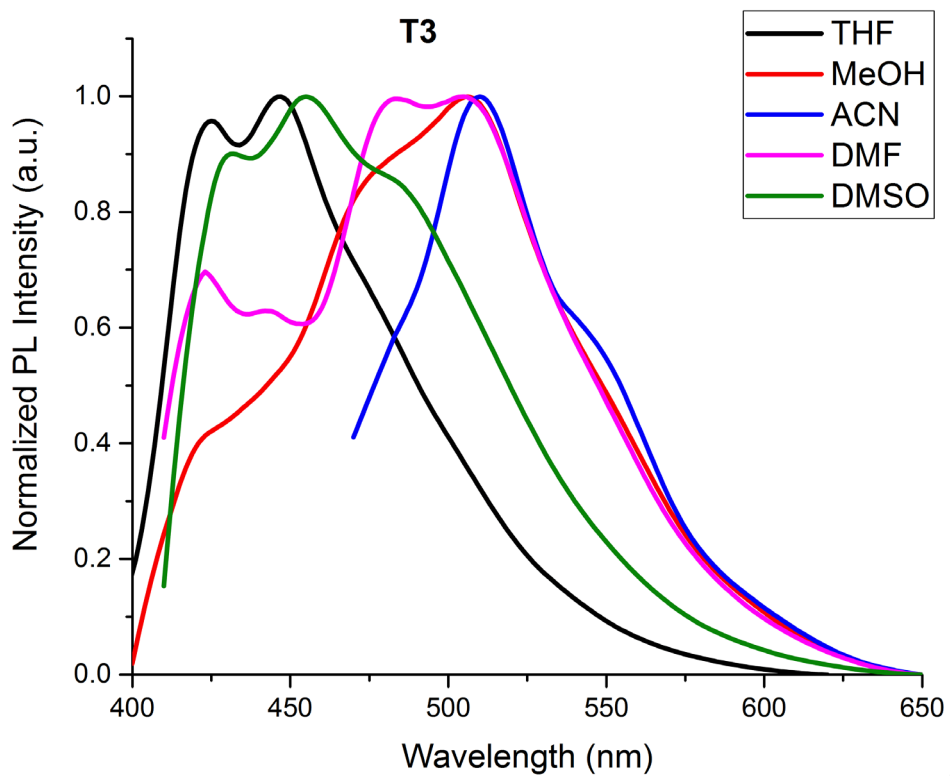


Fig. 5.29 PL spectra of molecule **T3** in solvent of varying polarity.

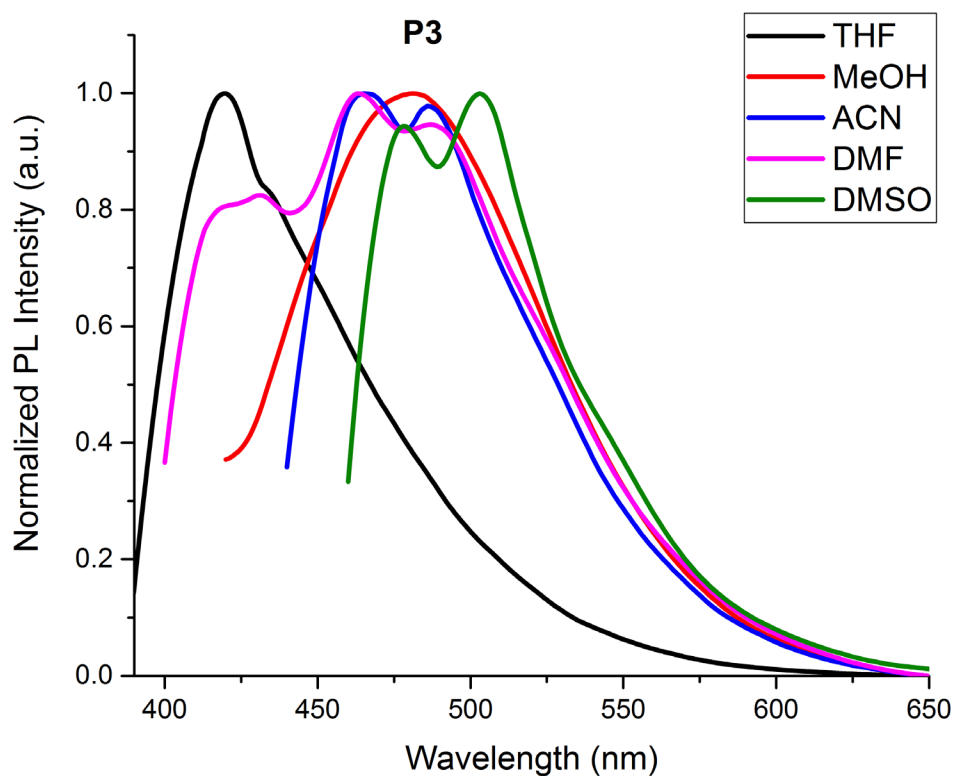


Fig. 5.30 PL spectra of molecule **P3** in solvent of varying polarity.

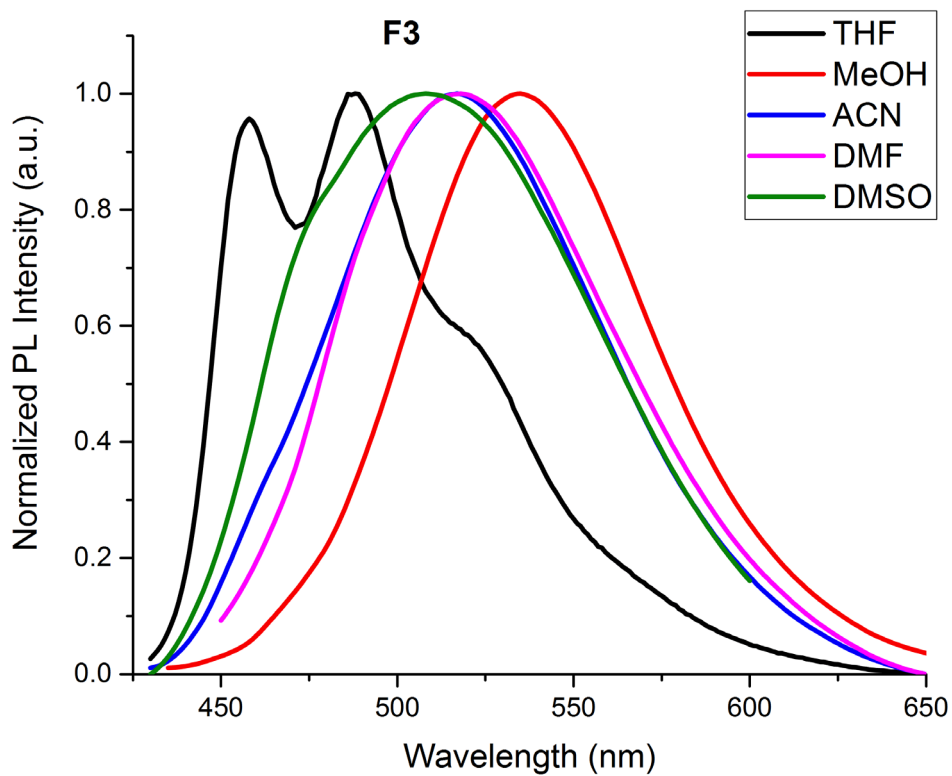


Fig. 5.31 PL spectra of molecule **F3** in solvent of varying polarity.

5.3.3 Solid state studies

An enormous amount of work published covers the ESIPT mechanism of molecules in the solvent medium. However, solid state emitters undergoing ESIPT have not been explored much to a greater extent. The mechanism supporting excited state proton transfer in a solid state remains unclear (Padalkar and Seki 2015). The molecules of the series were deposited onto chemically and ultrasonically cleaned glass substrates by vacuum thermal vapor deposition at a base pressure of 5×10^{-6} mbar. Thin films of thickness 50 nm obtained after deposition were investigated for their photophysical responses. Solid state UV-Vis spectra of all the molecules are provided in Fig. 5.32 and its fluorescence spectra shown in Fig. 5.33 with the inset showing fluorescence emission under UV irradiation. Solid state photophysical parameters of the molecules are provided in Table 5.2. Solid state emission of **T2**, **P2**, **P3**, and **F2** exhibited a small stokes shift between keto and enol emission. **T3** exhibited a clear well resolved double peak with a yellow emission and **F3** exhibited a single emission peak centered at 690 nm with a highest normal stokes shift of 270 nm. Large stokes shift observed only for **T3** exhibited 106 nm, whereas, the rest of the molecules showed a value of ~ 25 nm.

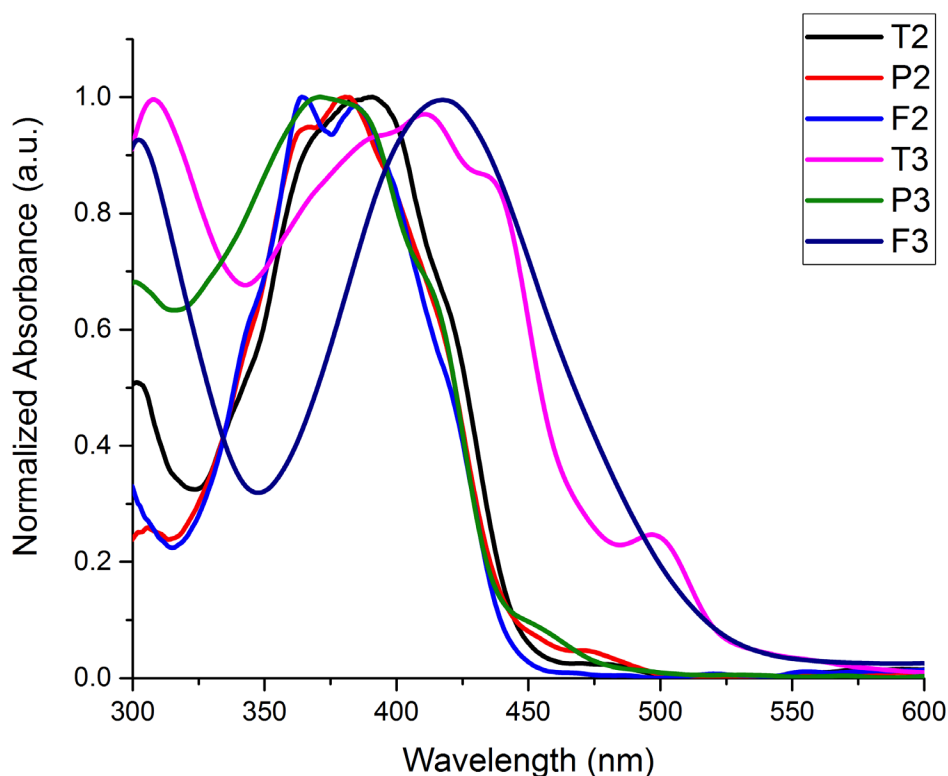


Fig. 5.32 Solid State UV-Vis absorbance spectra of all the molecules of the series

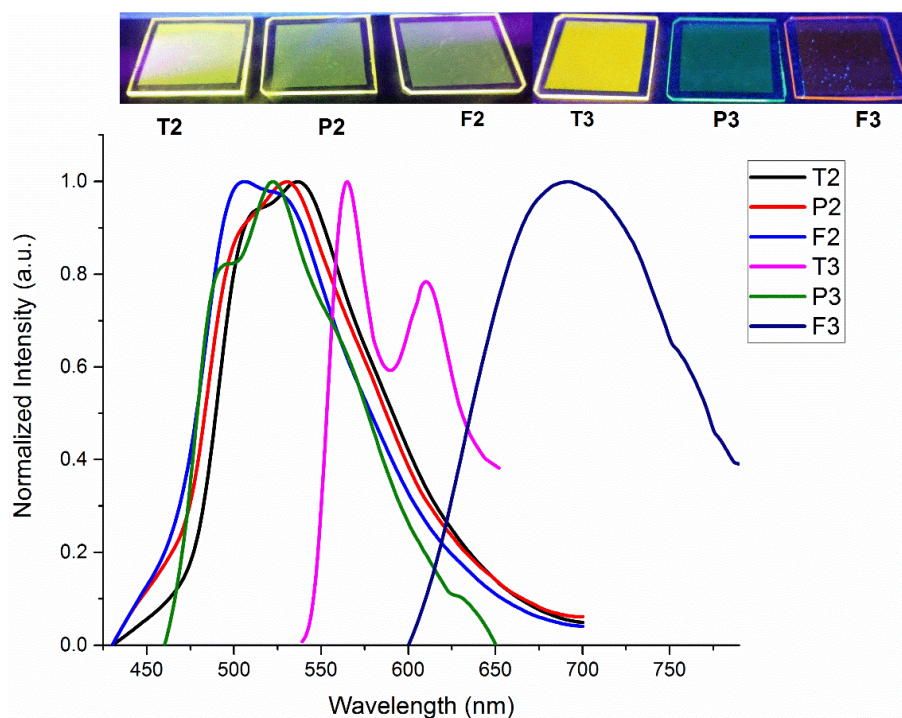


Fig. 5.33 Solid state PL spectra of molecules. Inset shows solid state emission under UV illumination

TABLE 5.2 Photophysical parameters of the molecules in thin film

	$\lambda_{\text{excitation}}$ (nm)	$\lambda_{\text{emission}}$ (nm)		Normal Stokes Shift (nm)	Large Stokes Shift (nm)	FWHM (nm)
		keto	enol			
T2	385	451	475	66	24	102
P2	376	463	491	87	28	104
F2	376	459	482	83	23	100
T3	435	504	610	69	106	78
P3	387	494	523	107	29	98
F3	420	690	–	270	–	136

5.3.4 Quantum yield measurement

The fluorescence quantum yields (ϕ_s) were evaluated according to the following Equation 5.1, where Coumarin 153 in cyclohexane is considered as a reference (R) for molecule **T3**, **P3**, **F3** while for **T2**, **P2** and **F2**, 9,10-diphenyl anthracene was taken as reference. Samples whose QY needs to be determined is denoted as S. Grad corresponds to the gradient from the plot of integrated fluorescence intensity vs. absorbance at the excitation wavelength, and η the refractive index of the solvent for standard and reference

(Dhami et al. 1995; Williams et al. 1983). As observed from the table the value of QY increases upon an increase in the number of thiophene core unit. The highest QY recorded is for **T2** with a value of 1.8% and with the lowest recorded for **F2** with 0.014% as given in Table 5.3. However, amongst the series thiophene substituent present on the side chain of the central core gives a better quantum yield in comparison with furan and pyridine.

$$\phi_S = \phi_R \frac{Grad_S}{Grad_R} \frac{\eta_S^2}{\eta_R^2} \quad \text{Eq. 5.1}$$

TABLE 5.3 The measured quantum yield of all the molecules

Molecule	T2	P2	F2	T3	P3	F3
QY (%)	1.80	0.15	0.014	0.273	0.02	0.08

5.3.5 Ratiometric studies

Restriction of vibrational and rotational components in a system upon aggregation enhances the emission intensity at solid state over the solution. However, solid-state molecular packing and aggregation type decides the quantum efficiencies of ESIPT chromophores (Padalkar and Seki 2015). In order to better understand the effect of aggregation on the emission intensity of the molecules, AIE studies were performed for the series at different ratios of H₂O/THF mixture. Solutions were prepared with a concentration (10⁻⁵ M) in THF, and their mixtures in varying water fractions f_w were used for AIE studies. Fig. 5.34 shows the fluorescence emission of the series with different H₂O/THF mixtures under UV irradiation of 365 nm. Herein, 10% of f_w implies 10:90 of the mixture with 10% of H₂O and 90% of THF and 20% of f_w would imply 20:80 with 20% of H₂O and 80% of THF and so on. **F3** exhibited good AIE characteristics as shown in Fig. 5.40 in contrast with the others in the series that showed Aggregation caused quenching (ACQ) as shown in Fig. 5.35 – Fig. 5.39. Aggregation of **F3** under poorer solvent medium shows an enhancement in emission intensity and achieves a maximum at 80% of H₂O/THF ratio and then drops down rapidly upon further increase of f_w . The drop in emission intensity at higher ratios of H₂O/THF mixtures is due to the poor solubility of the solute in solvent mixture (Zhang et al. n.d.). The polarity of the mixture increases upon an increase in the ratio of f_w , further, lessens the energy bandgap in the system and hence, the redshift observed at higher f_w (Hu et al. 2009). The redshift is highly predominant in **F3**, and a value of 45 nm shift is

observed in the emission wavelength with increasing f_w is indicative of positive solvatochromism (Zhang et al. 2016b). On the other hand, **F2** at initial ratios exhibited an increasing trend in the intensity and stabilized to a fixed value with increase in f_w and drops down at higher f_w ratios. The absence of double peaks at higher ratios of f_w is indicative of nonoccurrence of proton transfer at excited state owing to an increase in the solvent polarity.

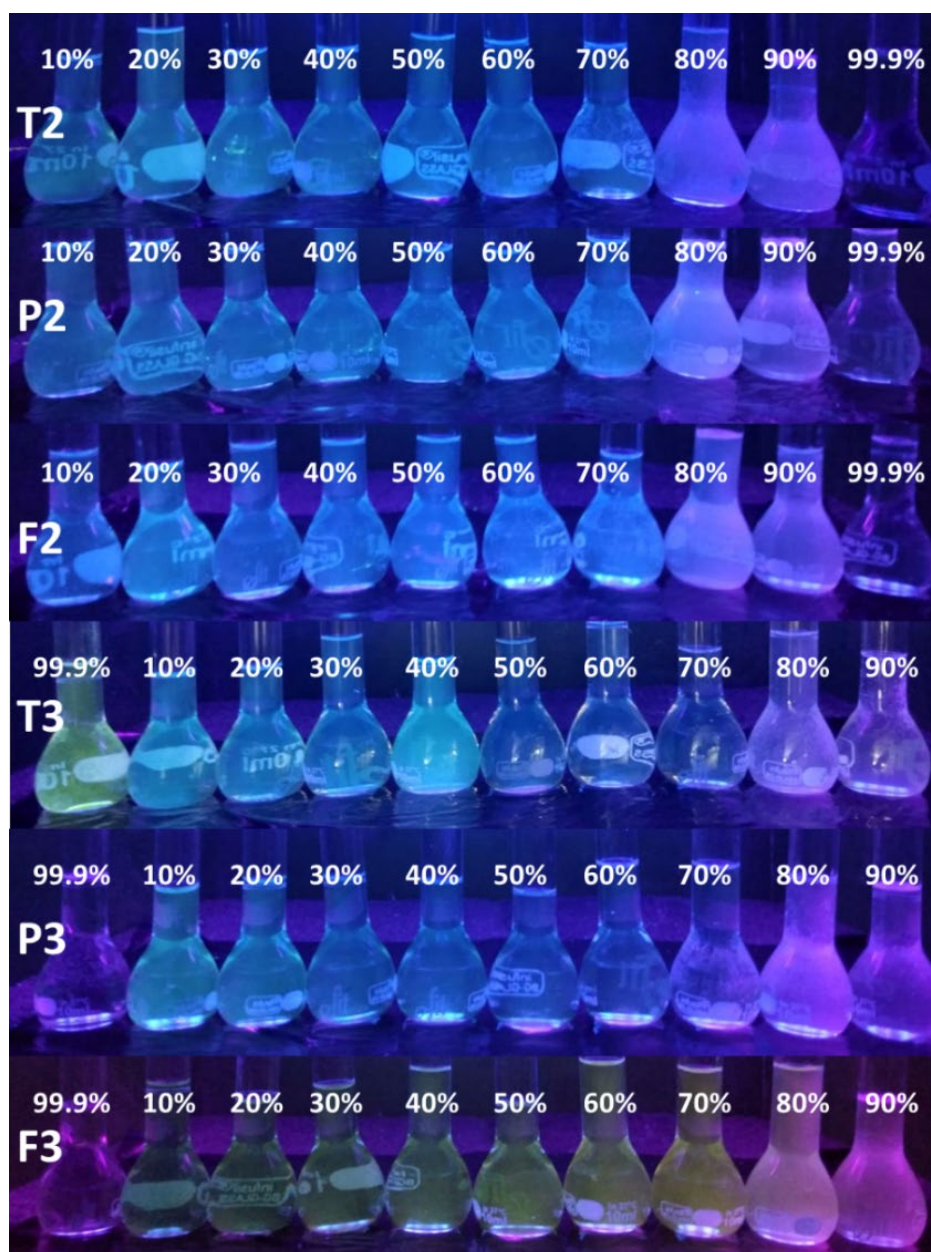


Fig. 5.34 Photographs of molecules in THF/water mixtures with different f_w under UV illumination

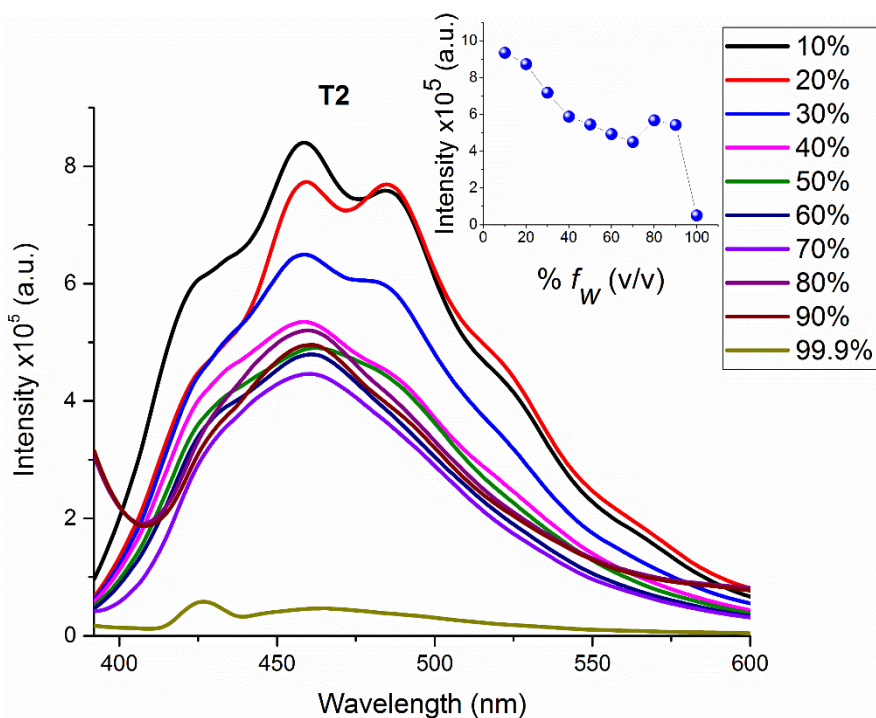


Fig. 5.35 Fluorescence emission spectrum of **T2** with varying f_w and inset gives the intensity value with varying f_w

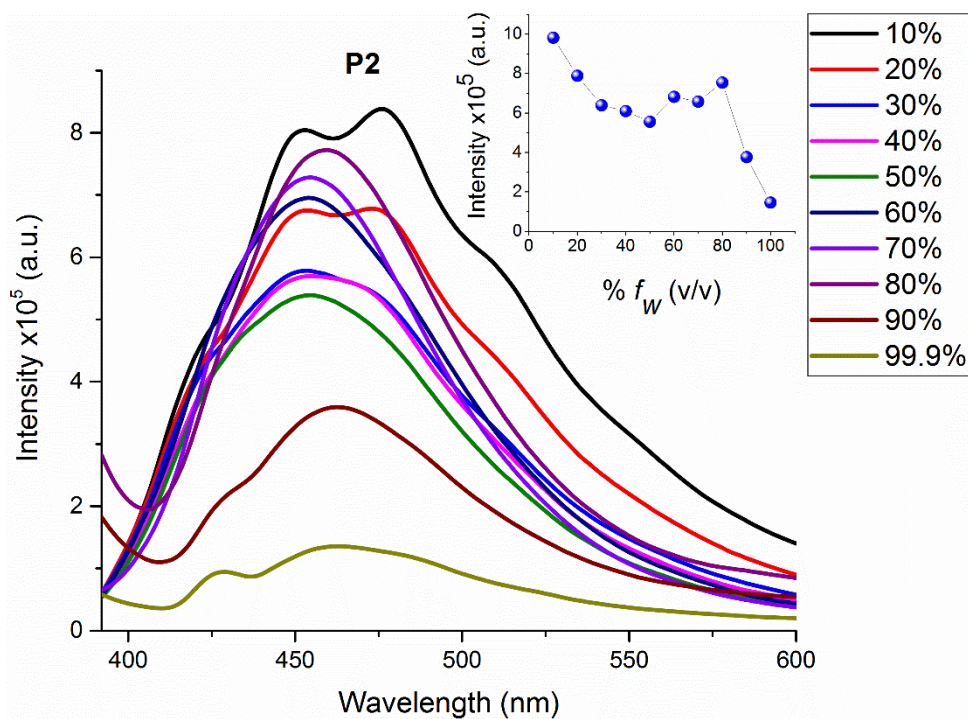


Fig. 5.36 Fluorescence emission spectrum of **P2** with varying f_w and inset gives the intensity value with varying f_w

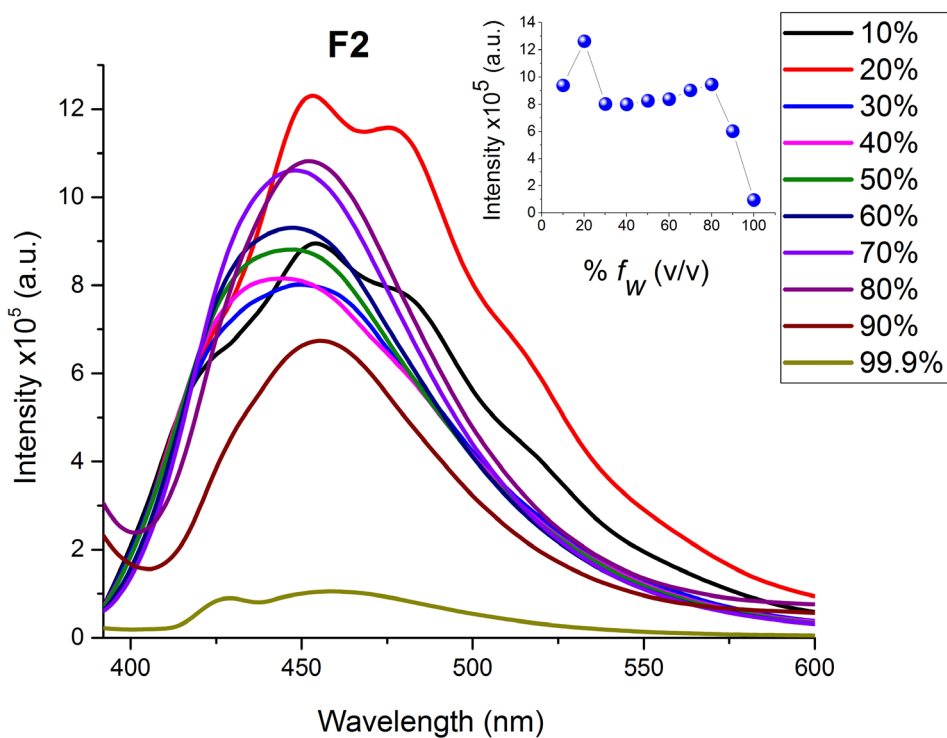


Fig. 5.37 Fluorescence emission spectrum of **F2** with varying f_w and inset gives the intensity value with varying f_w

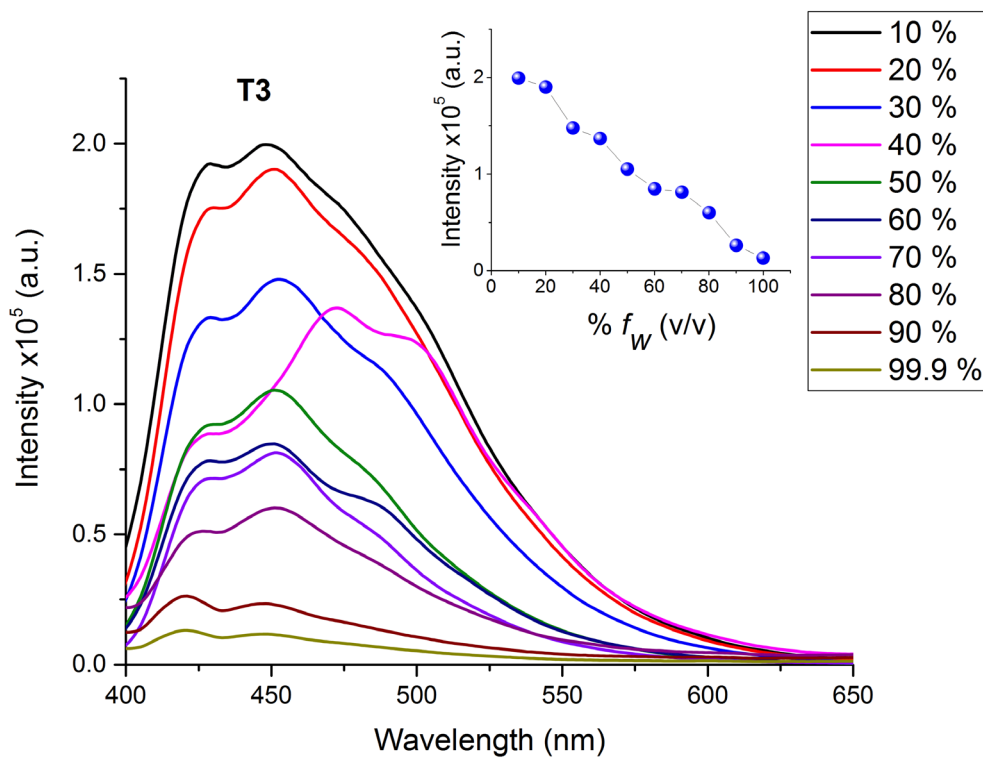


Fig. 5.38 Fluorescence emission spectrum of **T3** with varying f_w and inset gives the intensity value with varying f_w

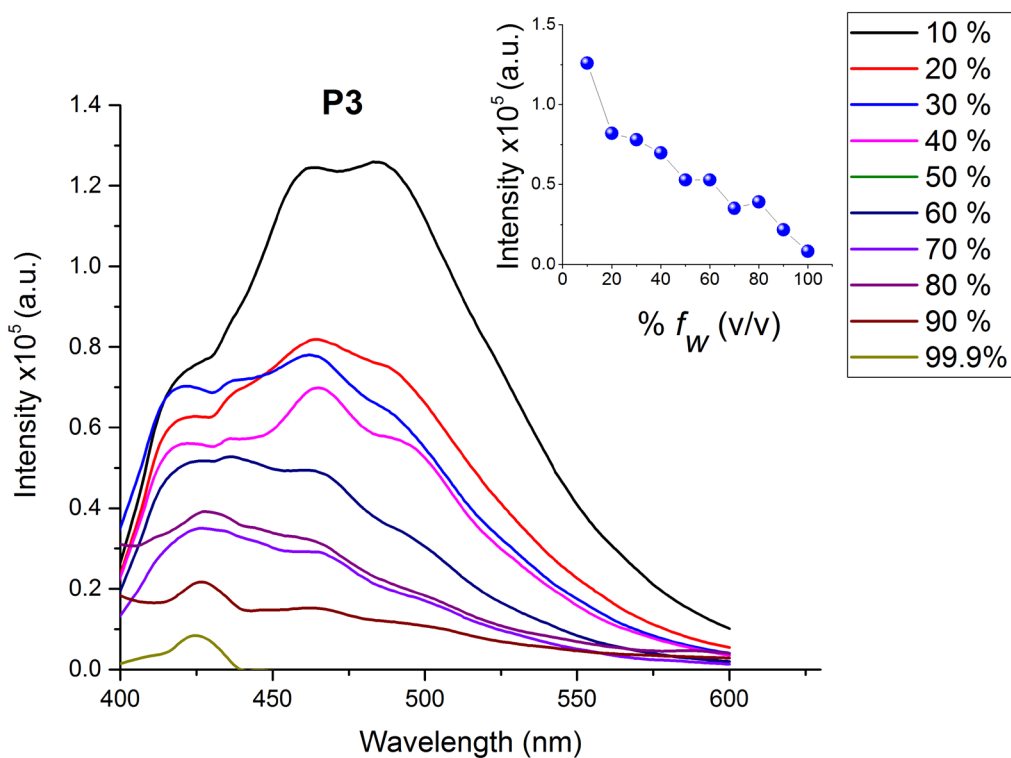


Fig. 5.39 Fluorescence emission spectrum of **P3** with varying f_w and inset gives the intensity value with varying f_w

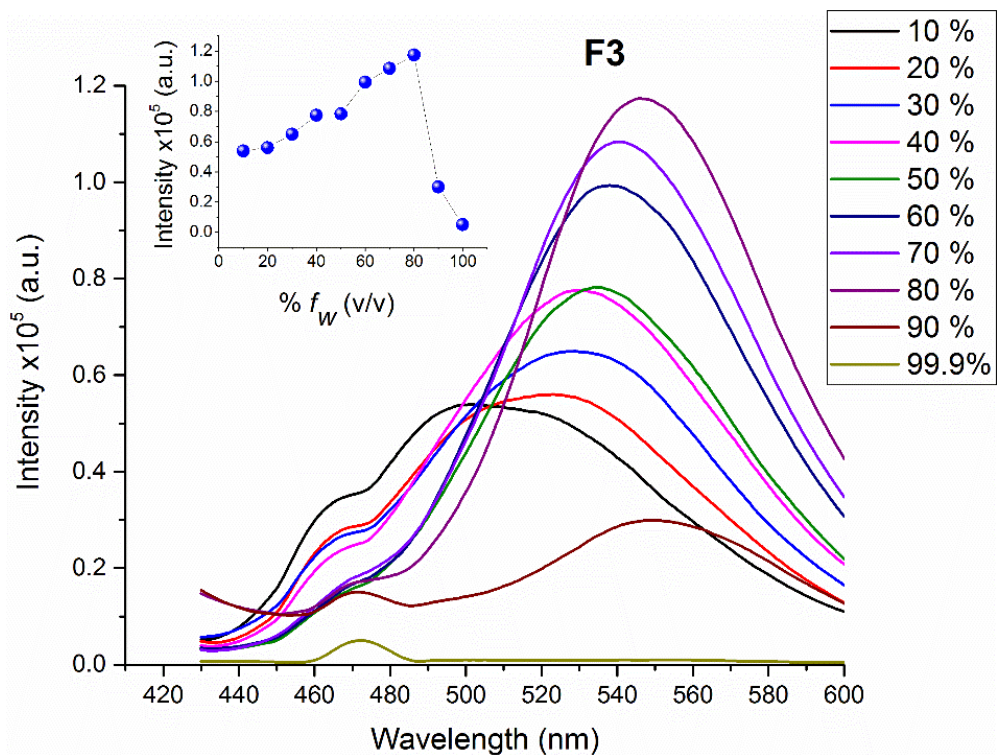


Fig. 5.40 The fluorescence emission spectrum of **F3** with varying f_w and inset gives the intensity value with varying f_w

5.3.6 Cyclic Voltammetry

The electrochemical properties of the molecules were studied by cyclic voltammetry to estimate their electronic energy levels and the bandgap thereof. **T2**, **P2**, and **F2** showed a good quasi-reversible oxidation and reduction peak as shown in Fig. 5.41, whereas, **T3**, **P3** and **F3** exhibited quasi-irreversible curves as shown in Fig. 5.42 with their estimated energy level is given in the inset plot. Enhanced conjugation in structure found in **T3**, **P3** and **F3** with hydrazides on both the arms chemically connected with thiophene di-aldehyde group hampered peaks during reduction cycle. Oxidation peak corresponds to the involvement of $-NH$ functionality in oxidation and reduction peak corresponds to $-C=O$ functionality involved in the reduction process of the series. The energy levels of HOMO, LUMO and band gap of **T2**, **P2** and **F2** are closely analogous, and hence the substituted hydrazides on the bi-thiophene moiety had no significant role in altering the energy levels of the molecule. The energy bandgap of all the molecules is estimated using the equation $E_{HOMO} = -(I_p+4.4)$ eV and LUMO by $E_{LUMO} = -(E_A+4.4)$ eV (Duvenhage et al. 2015) with their results tabulated in Table 5.4. The energy level of HOMO for **T3**, **P3**, and **F3** were obtained from cyclic voltammogram following the equation mentioned above. LUMO energy levels of the series were derived from the energy gap of solid-state photoluminescence spectra and the estimated HOMO level from cyclic voltammogram. The HOMO of **T3** and **F3** showed a similar energy value of around ~ -6.3 eV with **T3** having a LUMO level of -4.16 eV and that of **F3** is -4.34 eV. **P3** exhibited a slightly higher negative value of HOMO of -6.65 eV in comparison with **T3** and **F3** and a shallow LUMO level of -4.85 eV. The highest energy bandgap E_G obtained in the series is for **T2** with 2.27 eV, and the lowest obtained for **P3** is 1.8 eV respectively.

TABLE 5.4 Electrochemical parameters and their electronic energy levels of all the molecules

	I_p (V)	E_A (V)	HOMO (eV)	LUMO (eV)	E_G (eV)
T2	1.38	-0.89	-5.78	-3.51	2.27
P2	1.27	-0.86	-5.67	-3.54	2.13
F2	1.13	-0.93	-5.69	-3.47	2.22
T3	1.95	*	-6.35	-4.16	2.16
P3	2.25	*	-6.65	-4.85	1.80
F3	1.92	*	-6.32	-4.34	1.98

**reduction not obtained from the cyclic voltammogram*

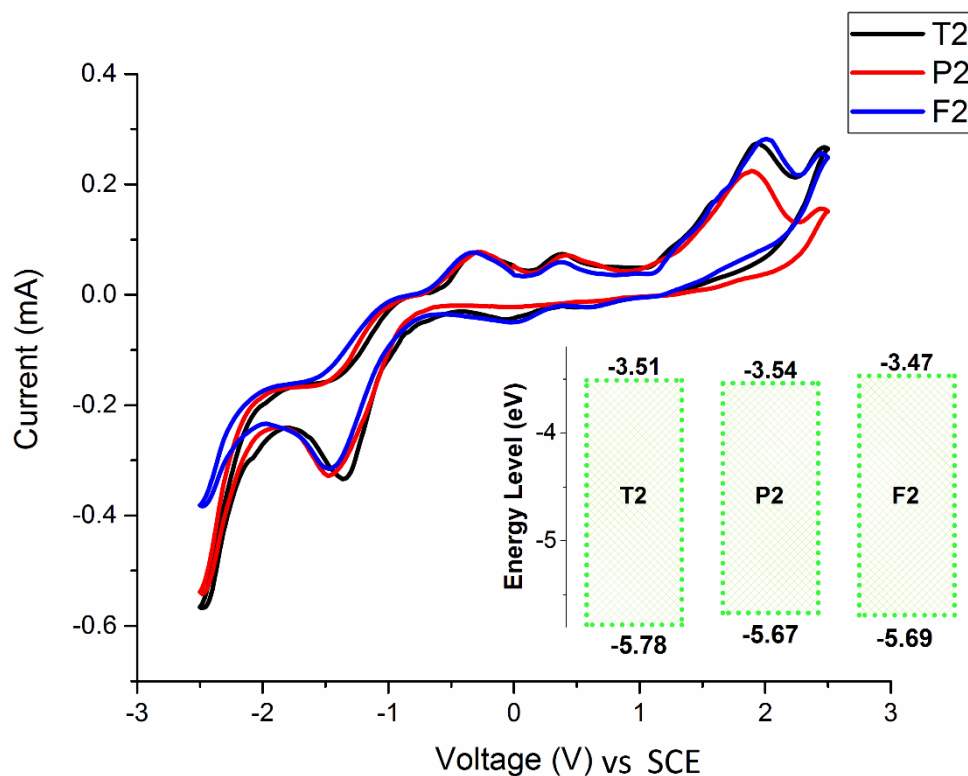


Fig. 5.41 Cyclic voltammogram for the molecules **T2**, **P2**, and **F2** with their energy levels

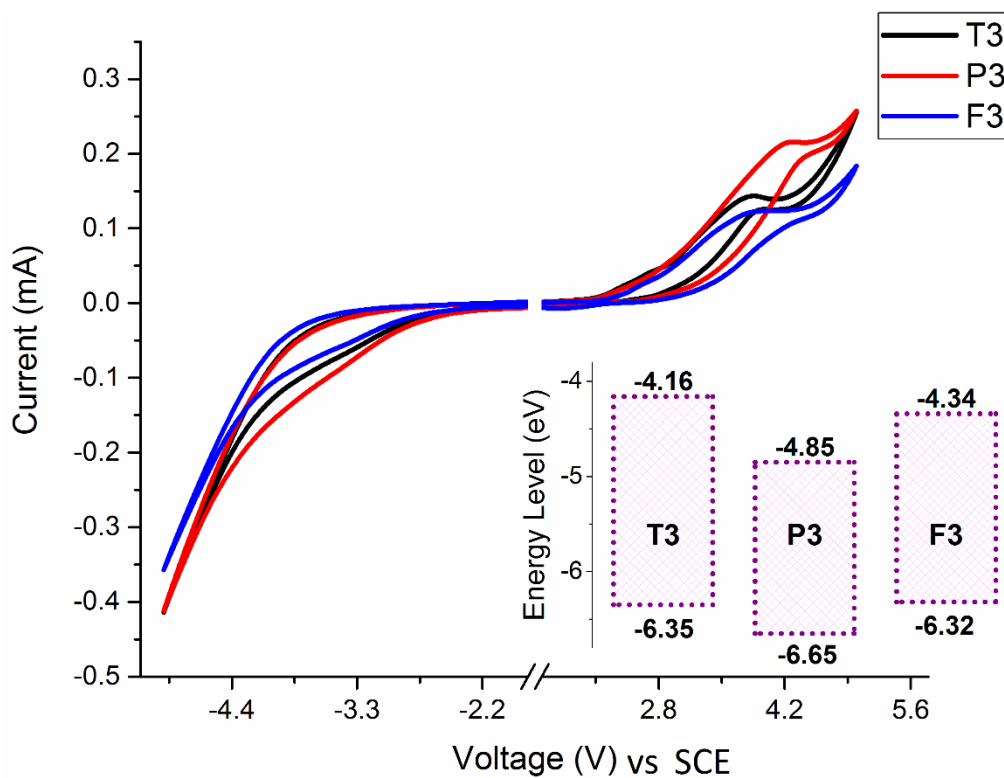


Fig. 5.42 Cyclic voltammogram for the molecules **T3**, **P3**, and **F3** with their energy levels

5.3.7 DFT Studies

Fig. 5.43 shows the possible normal and tautomeric structures of all the molecules, specifically, **T2**, **P2**, and **F2**, can solely support a single proton translocation. Keto form is believed to be thermodynamically stable structure denoted as (k), while the enol form (e) is believed to be kinetically stable entity corresponds to a tautomeric form occurring after photoexcitation of the molecules. **T3**, **P3**, and **F3**, possessing dual hydrazide may undergo three different possible structures, firstly, both the arms exhibiting keto form (k); secondly, one of the arm exhibiting keto and the other arm exhibiting enol represented as (e). Hypothetical tautomeric form denoted as (o) with both the arms showing enol is strictly impossible. Supposing, if such a transformation occurs in a system, the system might mutate to keto and enol across the arms (i.e., e form) and hence a double enol structure is difficult to realize. Zhang et al. provided proof for impossible double proton transfer concurrently occurring in the system, despite their structural attributes supporting double proton transfer (Zhang et al. 2016).

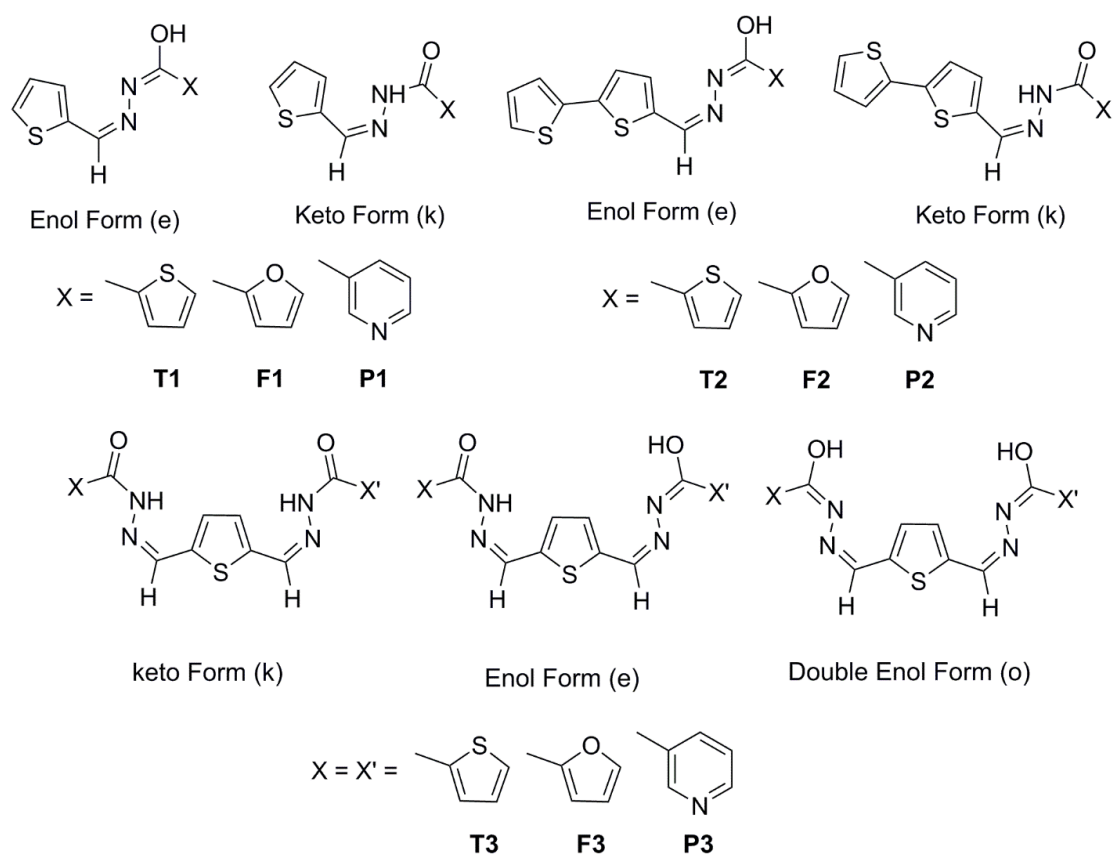


Fig. 5.43 Probable tautomeric structures with keto (k), enol (e) and double enol (o) form

Structures possessing single substituted hydrazide covalently linked with single thiophene moiety termed as **T1**, **P1** and **F1** were also studied. **T1** and **F1** have been designed and synthesized to look into their practical cation sensing applications⁹². **T1**, **P1**, and **F1** exhibit extremely weak fluorescence emission in solution and solid state, hence difficult to ascertain their keto-enol transition energies. Theoretical aspects dealing with excited state dynamics of these molecules were not reported so far and has been solely discussed herein for comparison with the present study. Computed ground state vibrational spectra of **T1**, **P1**, and **F1** in comparison with their excited state is redshifted by a finite value as shown in Fig. 5.44. This redshift indicates the weakening of intramolecular hydrogen bond at their excited state and hence can assure a difficult excited state proton translocation. Emission energy transition estimated for k-form is around ~340 nm and of e-form is ~ 375 nm. The probability of enolic transition is more in number in comparison with that of the keto, and hence the oscillator strength of the e-form is higher than k-form. Potential energy scans were attempted to verify any possibility of proton transfer at the excited state. However, repeated attempts failed to estimate transition structure of these molecules at the excited state. With the above-mentioned reasons, we conclude **T1**, **P1**, and **F1** don't support excited state intramolecular proton transfer in them.

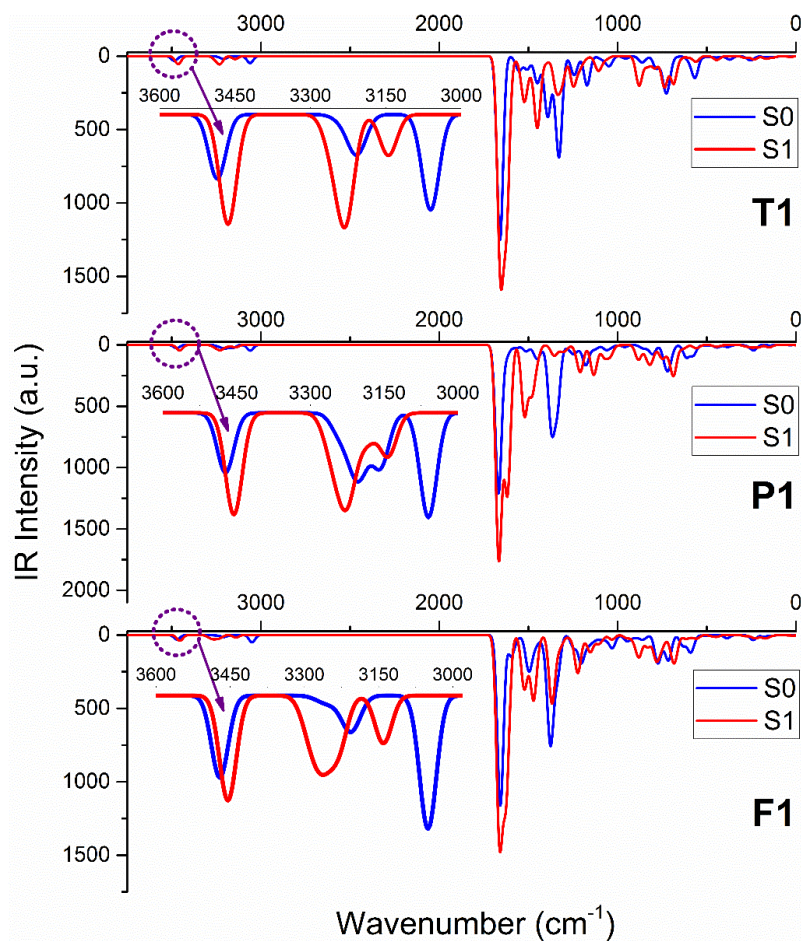


Fig. 5.44 Vibrational stretching frequency of **T1**, **P1** and **F1** in S_0 and S_1 states; specifically focusing N-H stretching frequency

5.3.7.1 Geometry

Ground state geometry optimized normal form (k) of all the structures is shown in Fig. 5.45 and their structural attributes are summarized in Table 5.5. The N-H distance of normal form (k) for all the structures remains unaffected to a value of 1.020 Å in both S_0 and S_1 . The intramolecular hydrogen bond distance d and d' , however, is shortened at the excited state S_1 in comparison with that of the ground state S_0 . The value of R reduces from 2.340 Å and 2.378 Å to 2.324 Å and 2.359 Å for **P2** and **F2**, while there was no change observed for **T2** in S_0 and S_1 . Similarly, the value of d and d' show a reduction in their intramolecular hydrogen bonding distance for **T3**, **P3** and **F3** at S_1 in comparison with that at S_0 , however, a single proton is expected to translocate from donor to acceptor. The lowering of hydrogen bond distance at the excited state S_1 in comparison with S_0 is highly supportive of possible excited state intramolecular proton transfer (Kanlayakan et al. 2017;

Zhao et al. 2015). Interestingly, **P3** shows a phenomenal reduction in **d** and **d'** in comparison to the other five-membered ring of the series. One of the possible reasons is that the effect of a six-membered heterocyclic ring tends to stabilize the structure by gaining greater control over the distance of H-bonding interaction. **P3** possesses a dihedral angle of 39° at S_0 and reduces to 32.6° at S_1 between extended thiophene core and pyridine moiety. Molecules of the series with bithiophene moiety possess certain minimal dihedral angle between the bithiophene core, and at their excited state, this angle turns to zero to support ESIPT in the system. **T2** and **F2** possessing a dihedral angle of 19° and 27° between the bithiophene rings at S_0 , changes to 0.1° at S_1 . Structural planarity might better support and eases proton transfer in a system than for a non-planar structure(Kanlayakan et al. 2017).

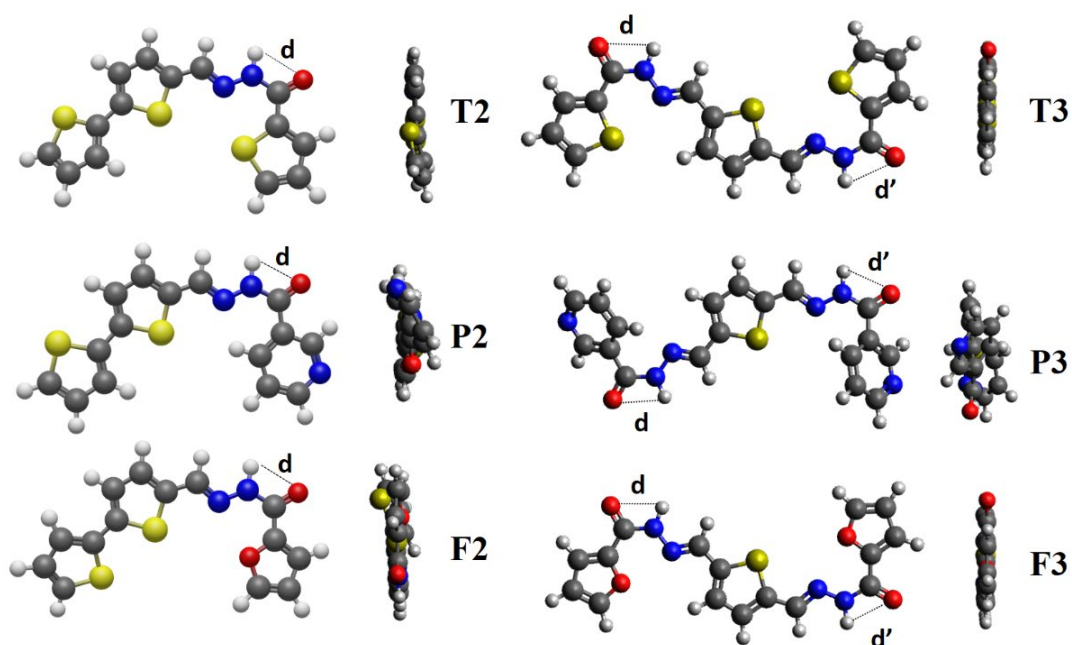


Fig. 5.45 Intermolecular associations of molecules of the series with O--H bond distances. Color code: O-atoms, red; C-atoms, grey; N-atom: blue, S- atoms, green).

TABLE 5.5 Geometrical parameters of the molecules at S_0 and S_1

	N-H distance (Å)		d (Å)		d' (Å)	
	S_0	S_1	S_0	S_1	S_0	S_1
T2	1.019	1.018	2.401	2.401	-	-
P2	1.020	1.020	2.340	2.324	-	-
F2	1.020	1.020	2.378	2.359	-	-
T3	1.019	1.020	2.396	2.377	2.396	2.380
P3	1.020	1.020	2.404	2.369	2.406	2.370
F3	1.019	1.020	2.375	2.353	2.377	2.359

5.3.7.2 Spectral quality and frontier molecular orbitals

Molecular orbitals, especially the highest occupied molecular orbitals (HOMO) and lowest unoccupied molecular orbitals (LUMO) play an essential role that governs the overall chemical reactivity of the system (Selvaganapathi et al. 2017). The energy gap between HOMO and LUMO determines the dynamic stability, chemical hardness, and chemical reactivity; it further provides an overall understanding of the reaction pathway and molecular activity of the complex. Theoretically estimated HOMO, LUMO levels and energy band gap of all molecules in THF solvent is provided in Fig. 5.46. The significant contribution of electronic transitions (CI ~93% to 97%) occurring within the system for both the normal form and the tautomeric form is governed by HOMO and LUMO. Hence, the discussion herein is restricted to HOMO and LUMO, corresponds to π - π^* orbitals. Computed energy levels and the energy band gap values of all the molecules lie around ~3.3 eV. The significant contribution of HOMO and LUMO is from π orbitals and the core moiety. Theoretical estimation of energy bandgap for conjugation enhanced structure of **T3** and **F3** exhibited a seemingly small energy reduction in comparison with **T2** and **F2** supporting experimental facts, while, such differences were not distinguishable in **P3**. The HOMO and LUMO of **T2** are completely distributed on the entire molecular network, while, **T3**, **P3**, and **F3** majorly centered on the thiophene and a portion of it is on the keto moiety. Orbitals of the series exhibit a size reduction of electron cloud engulfing proton donor moiety (N-H) in LUMO level in comparison with that of the HOMO, while there was almost no change in the electron density on the O atom belonging to carbonyl moiety (Hao and Yang 2018). Such changes in electron density suggest the enhanced interaction between hydrogen donor and acceptor moiety at the excited state and can better induce alienation of proton from a donor moiety (Kanlayakan et al. 2017; Li et al. 2016). The effect of intramolecular charge transfer (ICT) is highly evident in **P2** and **F2**, which further helps easy separation of a proton from a donor moiety (Kanlayakan et al. 2017). Further, upon comparing the HOMO and LUMO electronic distributions of all the system, it can be seen that proton acceptor oxygen exhibits an σ type of orbital, whereas -NH exhibits a π - π^* type of distribution. Observed distribution around -NH at HOMO level clearly indicates strong electron withdrawing capability of nitrogen moiety, readily giving up proton upon photoexcitation from S_0 to S_1 state (Zhao et al. 2017).

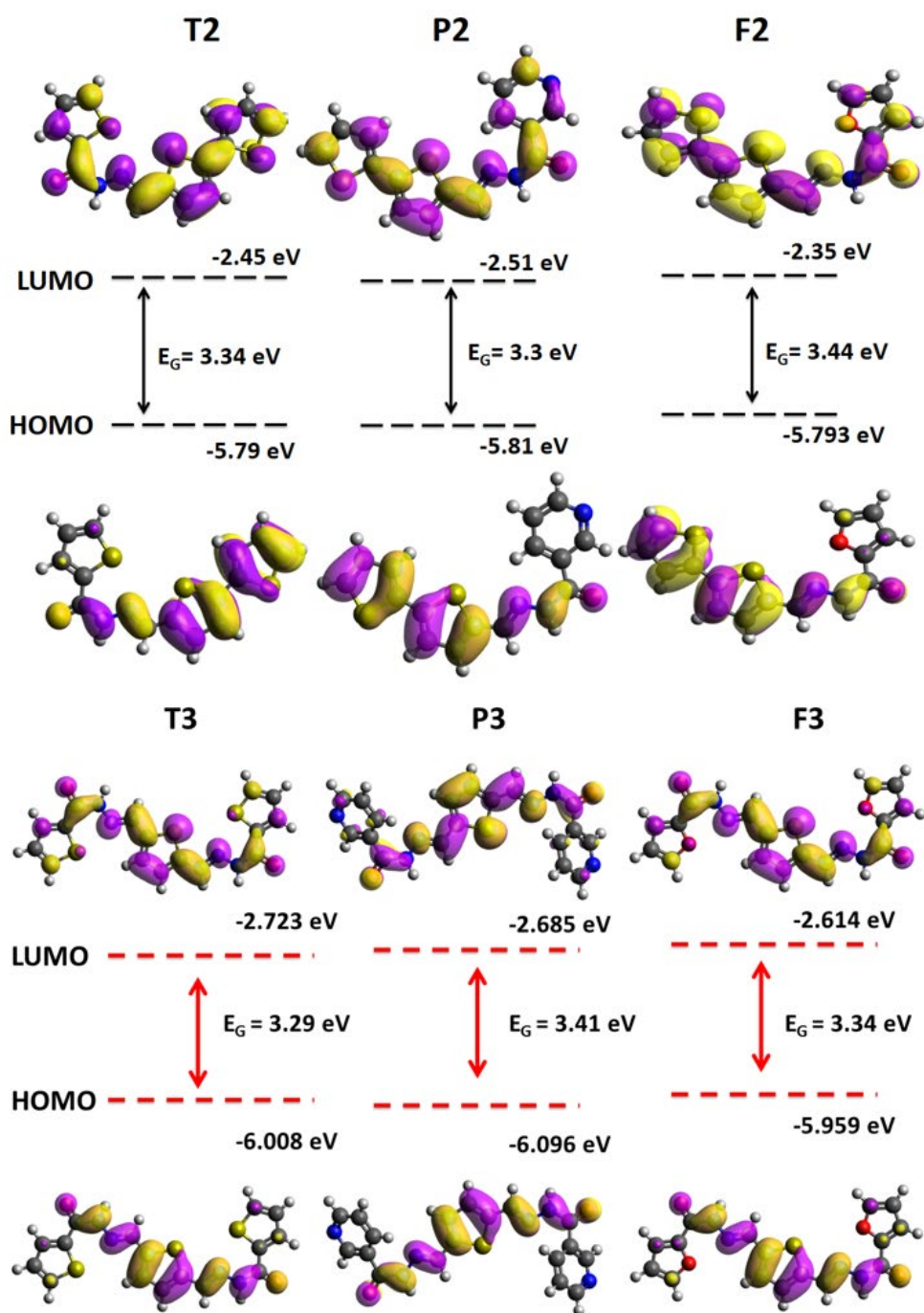


Fig. 5.46 Electronic orbital representations of all the molecules with their energy levels

Analysis of vibrational stretching frequencies of proton donor moiety involved in intramolecular hydrogen bonding could provide effective information on the dynamics of hydrogen bonding at the excited state (Chansen et al. 2017; Lan and Liu 2015; O. Hubin et al. 2014; Zhao et al. 2015). Stretching vibrational frequencies of N-H moiety in S_0 and S_1 were analyzed to predict ESIPT mechanism occurring in the system. Vibrational spectra reveal the peak corresponding to N-H stretching red-shifted at the excited state in

comparison with the ground state as shown in Fig. 5.47 and the Table 5.6 provides the –NH stretching frequency at S_0 and S_1 state. Han and co-worker proposed the strengthening of the intramolecular hydrogen bond at the excited state is strongly related to the observed red-shift in the stretching vibrations of proton donor moiety (Zhao and Han 2007). The redshift observed for bithiophene series is higher in comparison with that of thiophene series. The reason may be attributed to the extended conjugation possessed in the thiophene series enhances their influence over binding hydrogen stronger than bithiophene moieties. Higher the red-shift observed at the excited state, lower is the potential energy barrier for an efficient proton transfer (Chansen et al. 2017). N-H stretching vibration is relaxed at the excited state with that of rigid stretching at the ground state as is evident from the intensity of the N-H stretching vibration is higher at the excited state in comparison with the ground state.

TABLE 5.6 Vibrational –NH stretching frequency of all molecules at state S_0 and S_1

Molecule	N-H Stretching (cm^{-1})		Shift (cm^{-1})
	S_0	S_1	
T1	3488	3464	-23
P1	3477	3456	-21
F1	3473	3455	-18
T2	3473	3486	13
P2	3473	3488	15
F2	3471	3486	15
T3	3485	3489	4
P3	3475	3482	7
F3	3469	3477	8

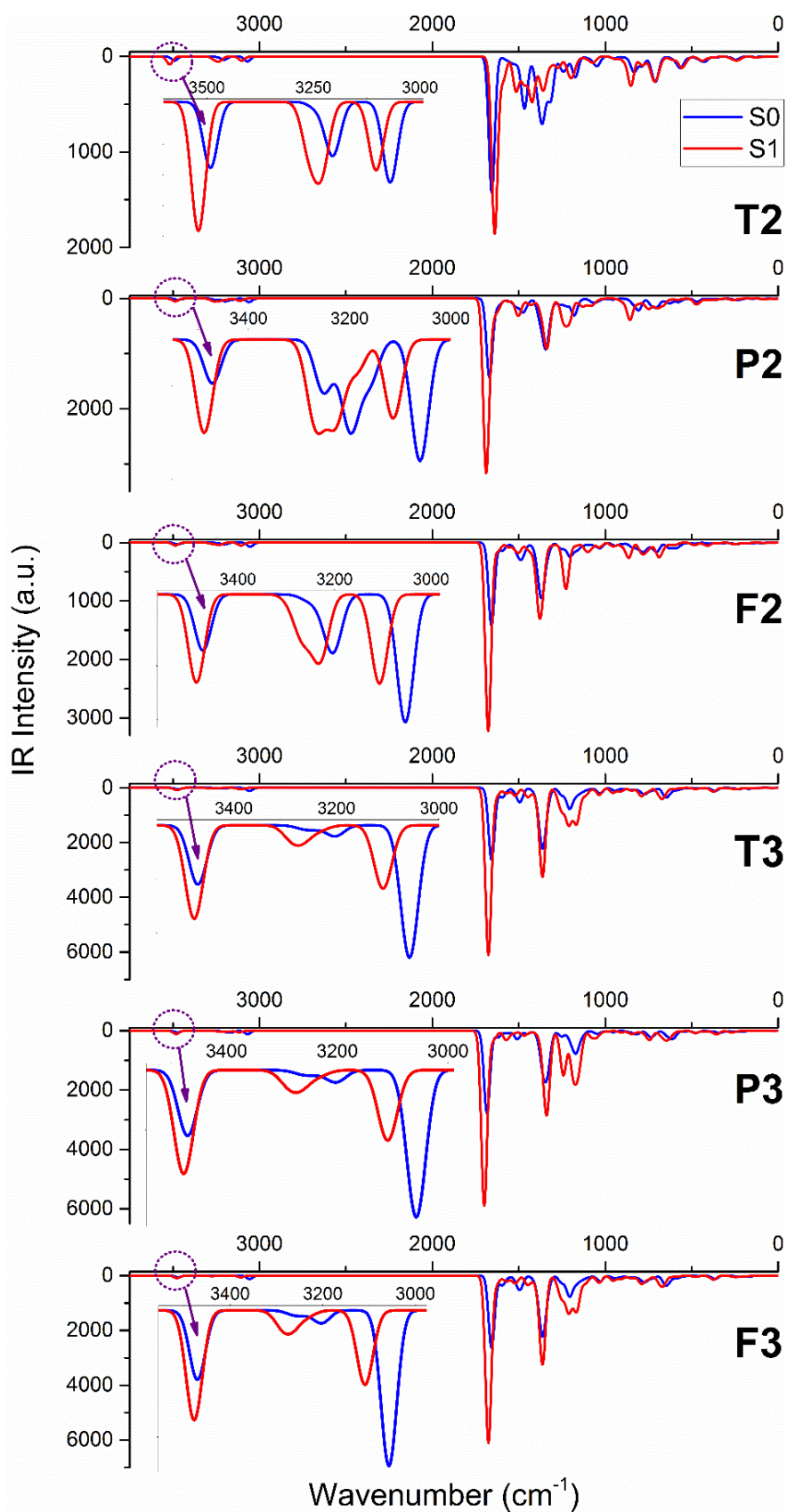


Fig. 5.47 Vibrational stretching frequency of all the molecules in S₀ and S₁ states; specifically focusing N-H stretching frequency

Calculations yielding six lowest lying singlet vertical excitations and the energy of that transition along with their oscillator strength for all the molecules of the series is reported in Table 5.7. The electronic transitions associated with keto absorbance (k abs), keto emission (k emi) and tautomer enol emission (e emi) for all the molecules are given in Fig. 5.48, wherein, k abs*, k emi* and e emi* represents the experimental values. The discrete transition energies obtained after the calculations were broadened by setting the value of FWHM to 50 nm to better accommodate the experimental parameters in the spectra. Results reveal the major transition for the emission spectra occurring in the system is mainly from $S_1 \rightarrow S_0$ proposing a $\pi-\pi^*$ nature. The spectroscopic nature of the absorption spectrum for k form follow similar trend obtained experimentally, and their absorption peak centered around 350-370 nm for all the molecules are near the experimental figures. Emission energy obtained from the k form and e form correlate well with the experimentally observed spectra with a little overestimated energy difference of ~ 0.3 eV (Houari et al. 2013; Lan and Liu 2015; O. Hubin et al. 2014; Yang et al. 2016). Oscillator strength of the e form estimated theoretically is higher in comparison with that of the k form for few of the molecules, in line with the experimental pieces of evidence. Moreover, it is essential to note that the energy emission of the k form for all the series is higher in energy in comparison to e form, establishing k form as the thermodynamically stable state. The energy difference of the emission spectrum between the k form and the e form of the series is analogous to the experimentally obtained values.

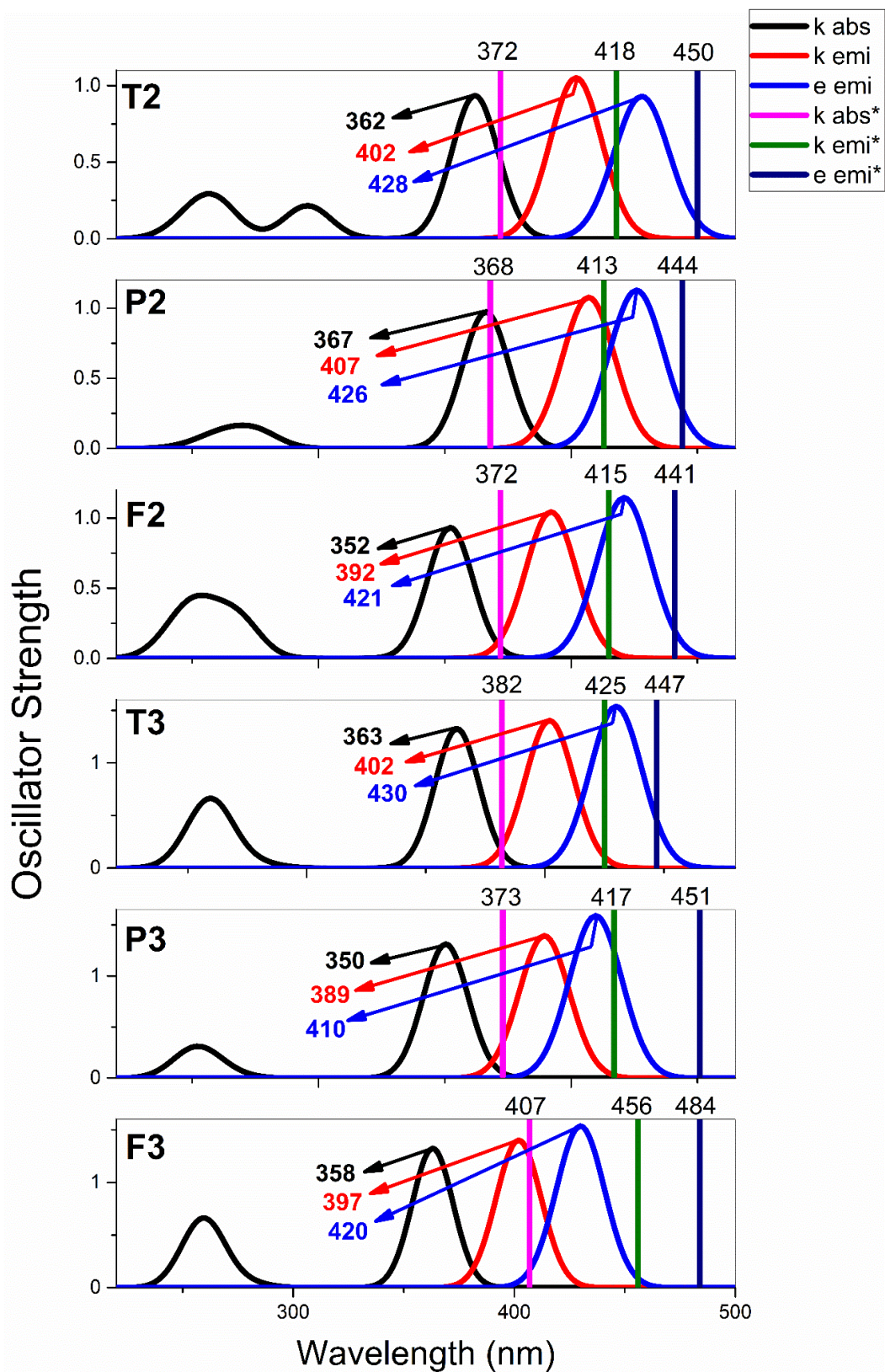


Fig. 5.48 Experimentally observed and theoretically estimated absorption and emission spectra for keto and enol forms of all the molecules.

TABLE 5.7 Computed optical parameters of molecules, keto absorbance and emission, enol emission, oscillator strengths, composition and CI(%) calculated at DFT/B3LYP and TD-DFT/CAM-B3LYP for ground and excited state

Molecule	Type	Transition	Energy (nm)	Oscillator strength	Composition	CI (%)
T2	k abs	$S_0 \rightarrow S_1$	362	0.9357	H(82) \rightarrow L(83)	93.37
	k emission	$S_1 \rightarrow S_0$	402	1.0520	H(82) \rightarrow L(83)	96.76
	e emission	$S_1 \rightarrow S_0$	428	0.9304	H(82) \rightarrow L(83)	96.34
H-1(81) \rightarrow L+1(84)					2.33	
P2	k abs	$S_0 \rightarrow S_1$	367	0.9721	H(81) \rightarrow L(82)	93.61
	k emission	$S_1 \rightarrow S_0$	407	1.0776	H(81) \rightarrow L(82)	96.74
	e emission	$S_1 \rightarrow S_0$	426	1.1281	H(81) \rightarrow L(82)	96.51
F2	k abs	$S_0 \rightarrow S_1$	352	0.9325	H(78) \rightarrow L(79)	94.00
	k emission	$S_1 \rightarrow S_0$	392	1.044	H(78) \rightarrow L(79)	97.02
	e emission	$S_1 \rightarrow S_0$	421	1.145	H(78) \rightarrow L(79)	96.62
H-1(77) \rightarrow L+1(80)					2.15	
T3	k abs	$S_0 \rightarrow S_1$	363	1.3251	H(100) \rightarrow L(101)	93.36
	k emission	$S_1 \rightarrow S_0$	402	1.4021	H(100) \rightarrow L(101)	96.2
	e emission	$S_1 \rightarrow S_0$	430	1.5366	H(100) \rightarrow L(101)	94.65
H-1(99) \rightarrow L+1(102)					3.05	
P3	k abs	$S_0 \rightarrow S_1$	350	1.3135	H(98) \rightarrow L(99)	95.05
	k emission	$S_1 \rightarrow S_0$	389	1.3953	H(98) \rightarrow L(99)	96.81
	e emission	$S_1 \rightarrow S_0$	410	1.5919	H(98) \rightarrow L(99)	96.52
F3	k abs	$S_0 \rightarrow S_1$	358	1.3541	H(92) \rightarrow L(93)	93.73
	k emission	$S_1 \rightarrow S_0$	397	1.4234	H(92) \rightarrow L(93)	96.38
	e emission	$S_1 \rightarrow S_0$	420	1.6346	H(92) \rightarrow L(93)	96.23
H-1(91) \rightarrow L+1(94)					2.14	

5.3.7.3 Potential energy curve

Owing to molecules of the series to support single proton transfer alone at the excited state, potential energy curves (PECs) for both the ground and the excited state is

estimated. PEC is a useful technique that nurtures the subtleties of molecular properties and gives information about the nature of hydrogen transfer reactions along the proton transfer path. PEC was simulated using B3LYP functional with 6-31G basis set for a complete rotation of 0° – 180° between the carbonyl and –NH group. Variation in potential energy as a function of dihedral angle for all the molecules is provided in Fig. 5.49 and Fig. 5.50. The optimized structures with zero dihedral angles between the plane connecting –NH and –C=O seems to be energetically more stable than that with 180° dihedral as evident from the values at the extremities of the curve. The results show that **F3** tend to acquire a geometry that does not favor for optimal intramolecular hydrogen bonding between the donor and acceptor moieties, in turn, hinders ESIPT in comparison with other types.

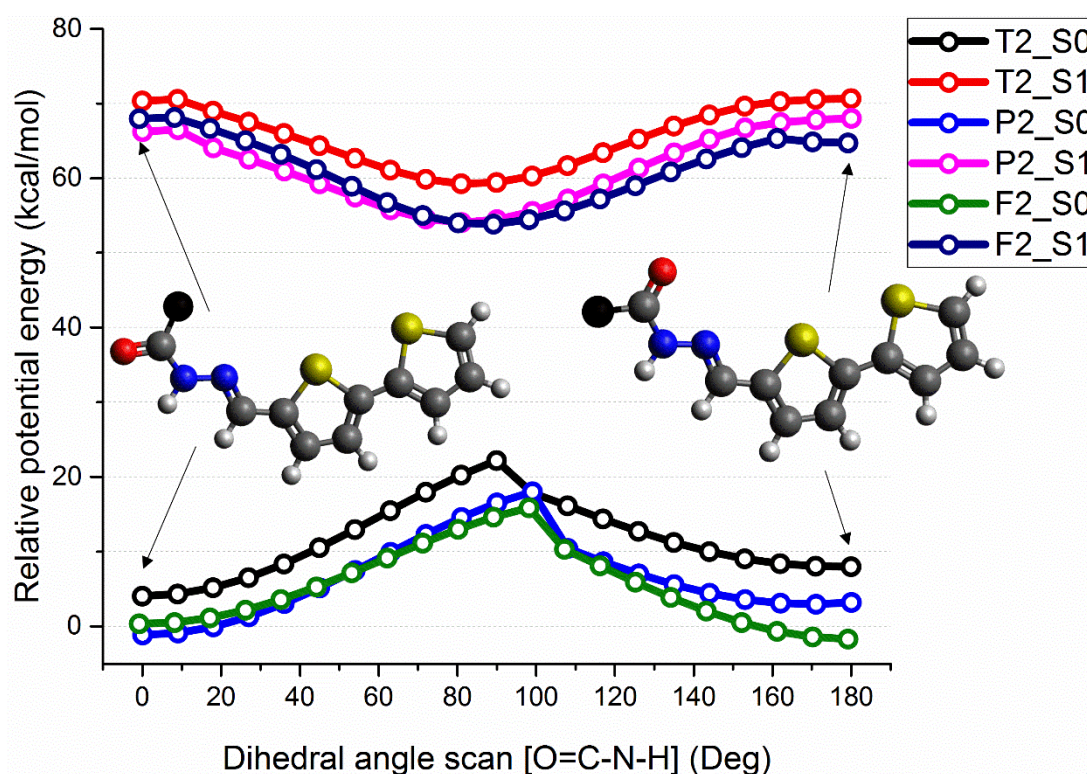


Fig. 5.49 Single point energies of molecule **T2**, **P2** and **F2** as a function of rotation of dihedral angle for both S_0 and S_1 . Black colored atom - Thiophene, Furan or Pyridine

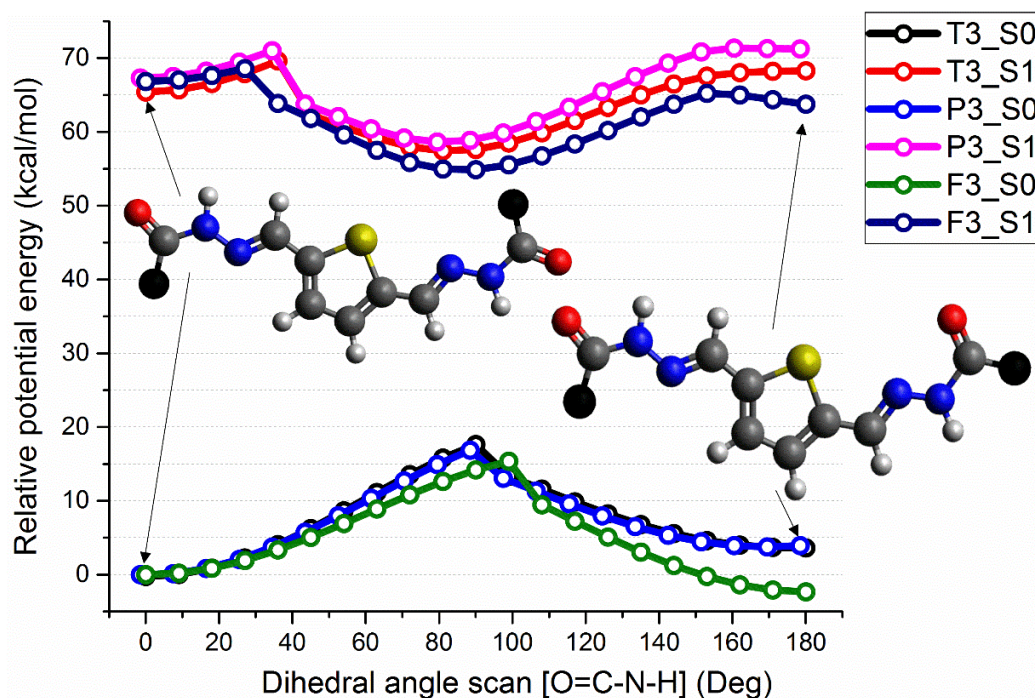


Fig. 5.50 Single point energies of molecule **T3**, **P3**, and **F3** as a function of rotation of dihedral angle for both S_0 and S_1 . Black colored atom - Thiophene, Furan or Pyridine

Potential energy scans were acquired on constrained optimization of geometry at their corresponding electronic states with fixed O-H bond length. The consistency in the reproduction of the results by DFT with that of the experimental may not be precise, however, the previous calculations have proven effective in providing qualitative results for accurate pathways supporting proton transfer (Saga et al. 2010; Serrano-Andrés and Merchán 2009; Sobolewski and Domcke 1999; Song and Ma 2013). Potential energy curve of all the molecule are provided in is provided in Fig. 5.51 – Fig. 5.55, wherein, the term FB indicates forward barrier and the RB indicates the reverse barrier for both S_0 and S_1 states. FB refers to the difference between the stable keto state and the point at which the potential reaches a maximum along the proton transfer pathway. Similarly, RB refers to the difference between the maximum potential and the stable enol tautomer along the proton transfer pathway. Estimation of transition structure for **F3** on the potential energy curve at excited state was difficult to realize. The molecules of the series at their ground state prefer keto form and upon excitation changes to tautomer e-form undergoing ES IPT. The scans pertaining to proton transfer were estimated using DFT to realize the FB and RB potential in both S_0 and S_1 state. Results illustrate the FB for all the molecules of the series at their excited state were comparatively lesser in magnitude than that of the ground state. The

lessened FB at their respective excited state indicates possible proton transfer at S_1 in comparison with S_0 . On an average ~ 3.57 to ~ 3.78 kcal/mol of energy barrier required for a molecule to undergo ESIPT to adopt a tautomer form. The reverse barrier at their ground state for all the molecules is lower in energy in comparison with that of their FB, reveals the possible ground state intramolecular proton transfer (GSIPT). **T3** showed a RB higher to FB at its S_0 may account for stringent GSIPT. Further, to summarize the whole ESIPT mechanism for the present system with $-C=O$ acting as a proton acceptor and $-NH$ acting as the proton donor. Initially, $-C=O$ capable of capturing a proton from the nearest $-NH$ donor and forms an intramolecular hydrogen bond at the ground state. Upon photo-excitation, the intramolecular hydrogen bond is strengthened, and a proton translocates from $-NH$ to $-C=O$ group through a significant forward energy barrier. At an approximate O-H distance of 1.35\AA , the system exhibits maximum potential energy, and beyond this point, the energy minimizes, and the system possesses desired tautomeric structure. The tautomeric structure at S_1 undergoes a spontaneous emission either radiative or non-radiative to reach its ground state S_0 and reverts to normal form by crossing over a significant RB potential.

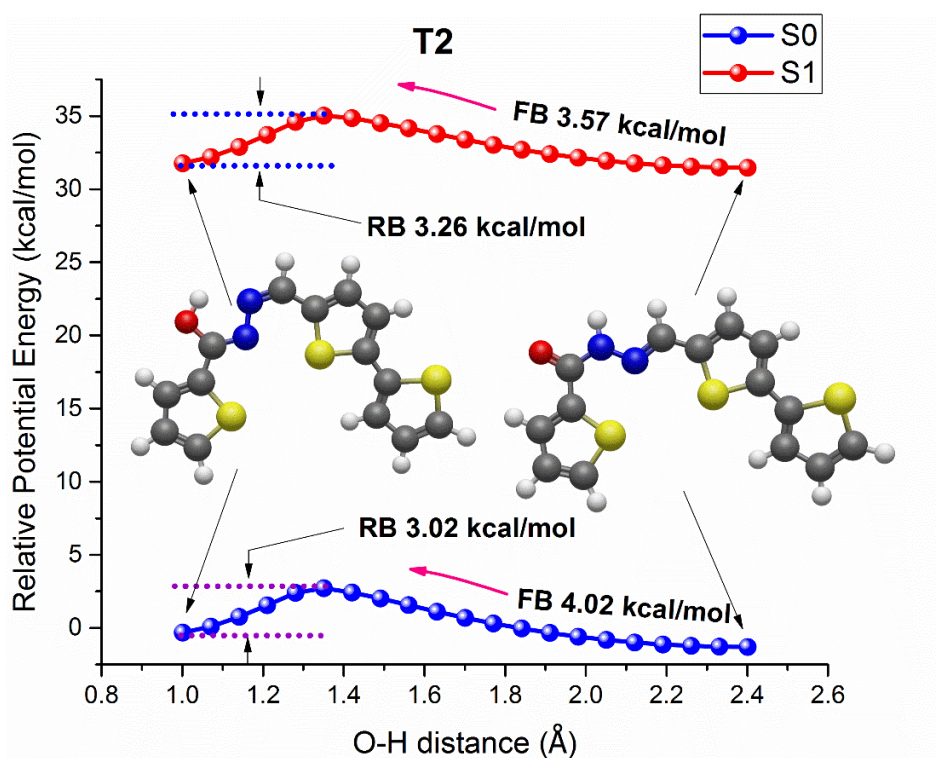


Fig. 5.51 Single point energies of molecule **T2** in the S_0 and S_1 states calculated by B3LYP and CAM-B3LYP

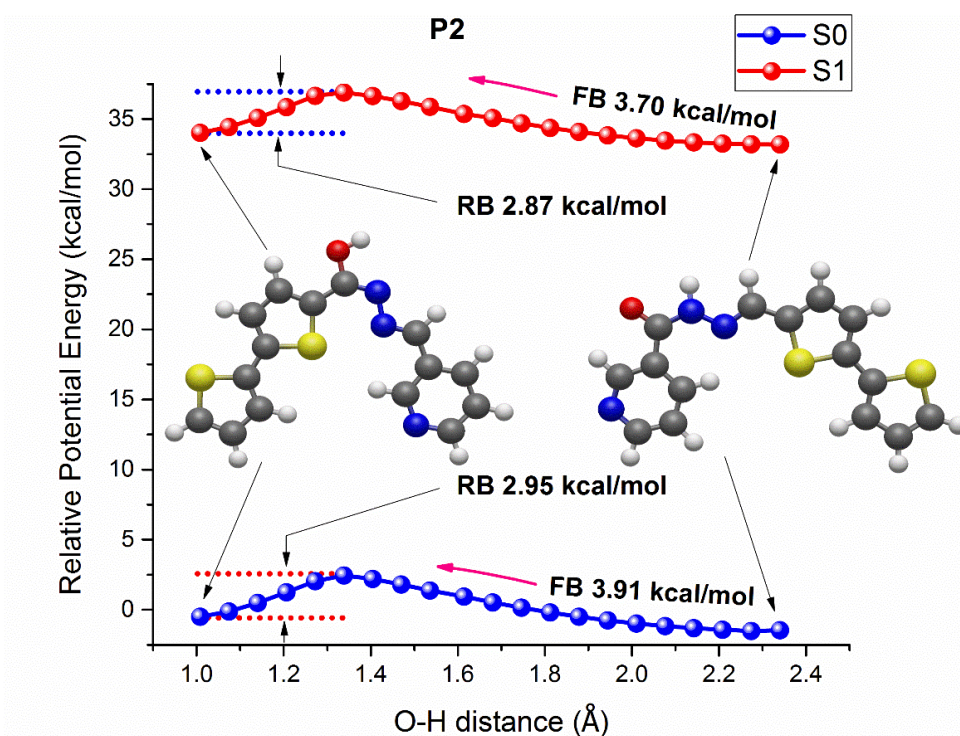


Fig. 5.52 Single point energies of molecule P2 in the S₀ and S₁ states calculated by B3LYP and CAM-B3LYP

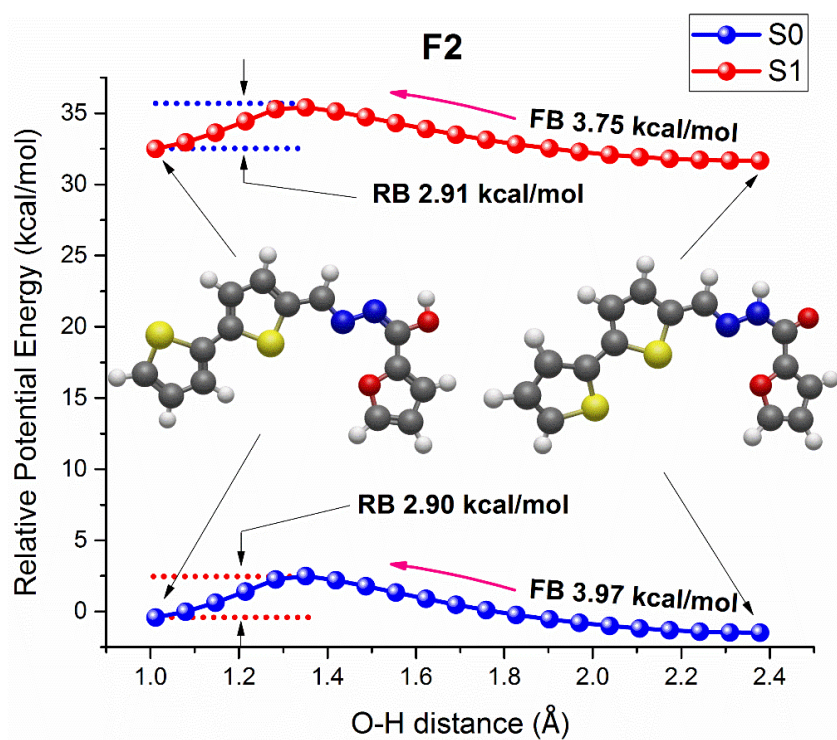


Fig. 5.53 Single point energies of molecule F2 in the S₀ and S₁ states calculated by B3LYP and CAM-B3LYP

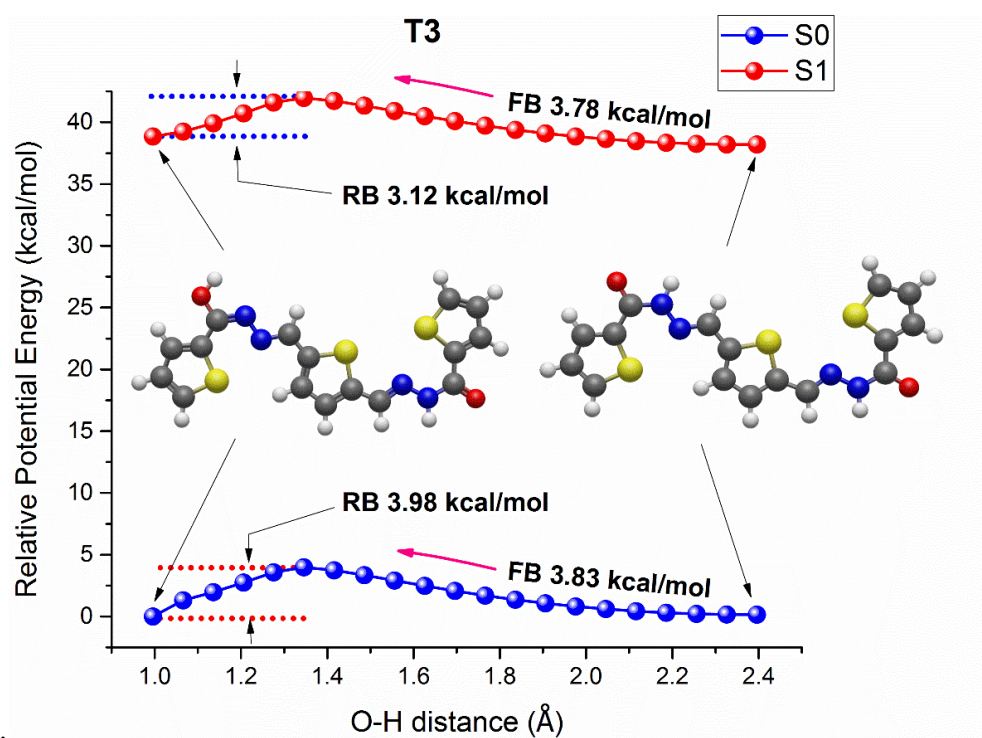


Fig. 5.54 Single point energies of molecule T3 in the S₀ and S₁ states calculated by B3LYP and CAM-B3LYP

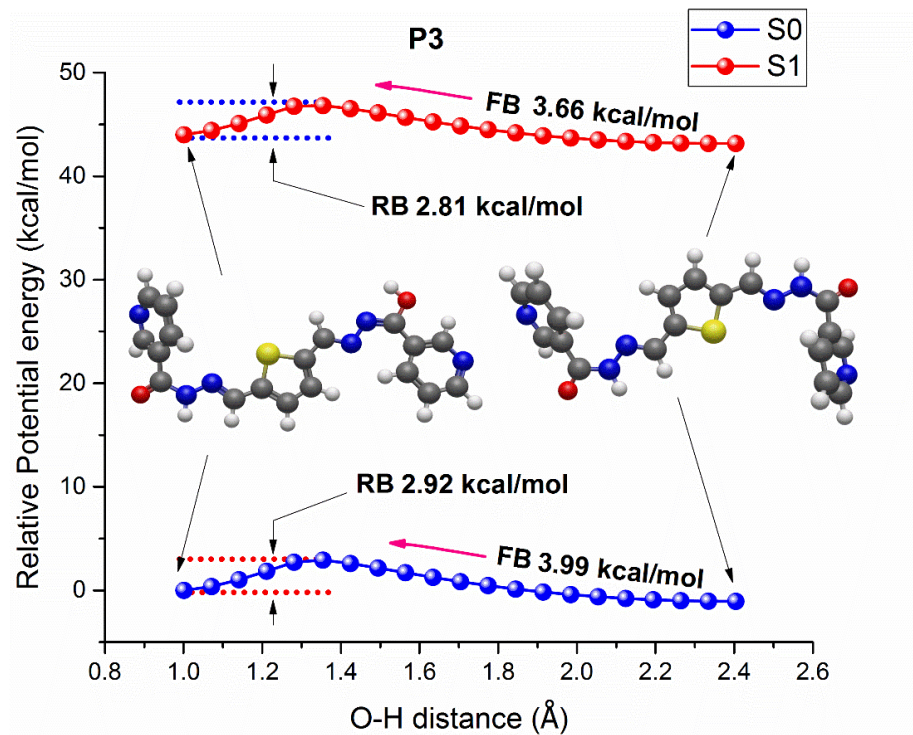


Fig. 5.55 Single point energies of molecule P3 in the S₀ and S₁ states calculated by B3LYP and CAM-B3LYP

5.3.7.4 PES Surface studies

PES scans were performed on the system to verify the possibility of double proton translocation arising due to the presence of substituted hydrazides present on both the arms of thiophene core. Potential energy scans were performed with DFT-B3LYP functional with 6-31G basis set for ground state and CAM-B3LYP with the same basis set for the excited state. The selection of the function is expected to estimate qualitative energetic pathways for ESIPT process (Liu et al. 2017; Padalkar and Seki 2015; Wang et al. 2015; Zhao and Zheng 2017; Zhou et al. 2015). Potential energy surface of **T3** and **P3** for both the ground and excited state is provided in Fig. 5.56 and Fig. 5.57 with inset providing the surface contour profile. There exist a high amount of symmetry in the surface along the diagonal line connecting the ends of normal and double enol form. It is important to note that the potential energy surface remains the same irrespective of the change in the heteroatom present in the ring. There exist four minima on the PES surface that relates to k-form, e-form and o-form, wherein, the estimated potential energy follows an order of $E_k < E_e < E_o$, signifying GSIPT is an endothermic process. A very high potential barrier of value ~ 8 kcal/mol exists for the molecules at S_0 and S_1 traced along the path (a \rightarrow d). This high potential barrier exhibited by the system validates the impossible simultaneous double proton transfer at their excited state. System after photoexcitation induces a proton to translocate from proton donor to an proton acceptor species guided along the path (a \rightarrow c) or (a \rightarrow b) with a minimal potential energy barrier attaining tautomer e-form. Second proton transfer or a step-wise double proton transfer can occur provided if the system gets much higher external energy to overcome a significant barrier potential of ~ 4.2 kcal/mol along the path (c \rightarrow e) or (b \rightarrow e). Higher barrier potential traversed along the path (c \rightarrow e) or (b \rightarrow e) does not support second proton transfer, thus hindering the step-wise double proton transfer kinetically. Further, supposing a step-wise double proton transfer occurs in the system (a \rightarrow b \rightarrow e or a \rightarrow c \rightarrow e), the reverse barrier of ~ 2.8 kcal/mol from (e \rightarrow c) or (e \rightarrow b) is significantly far lesser compared to the forward barrier and the system quickly achieves e-form. Based on the above discussions, we conclude that the system with hetero substituted hydrazides to support single proton transfer at their excited state and an impossible double proton transfer or step-wise double proton transfer.

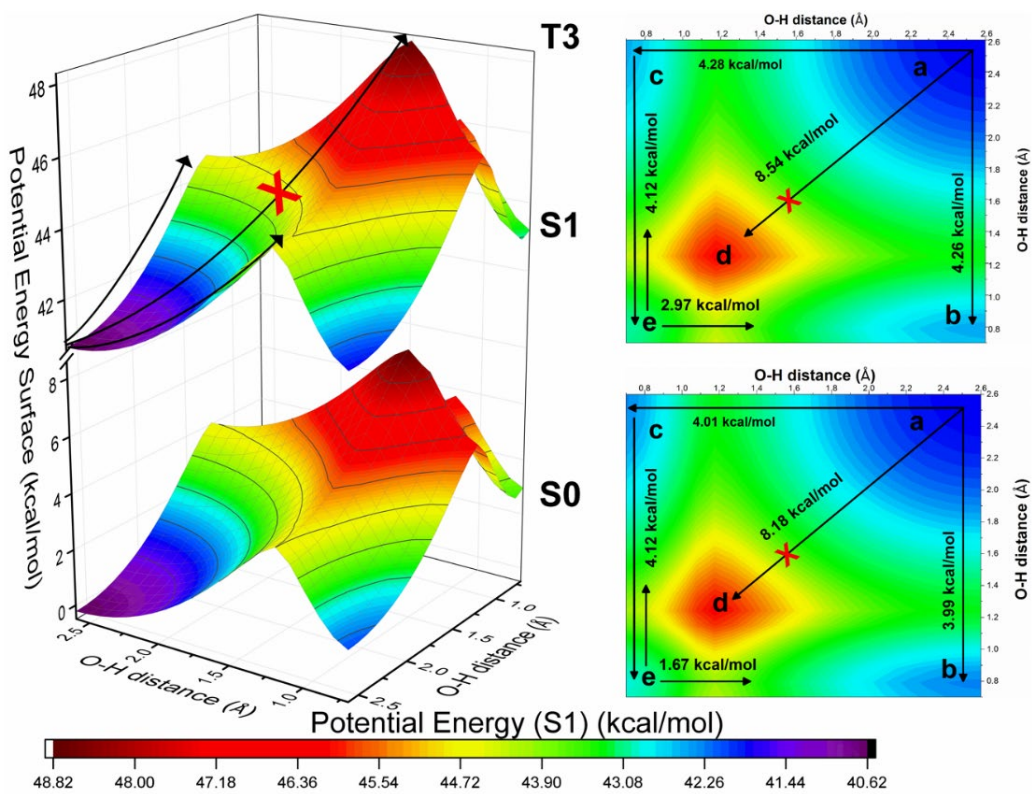


Fig. 5.56 PES scan of T3 in S₀ and S₁ states with their contour profile

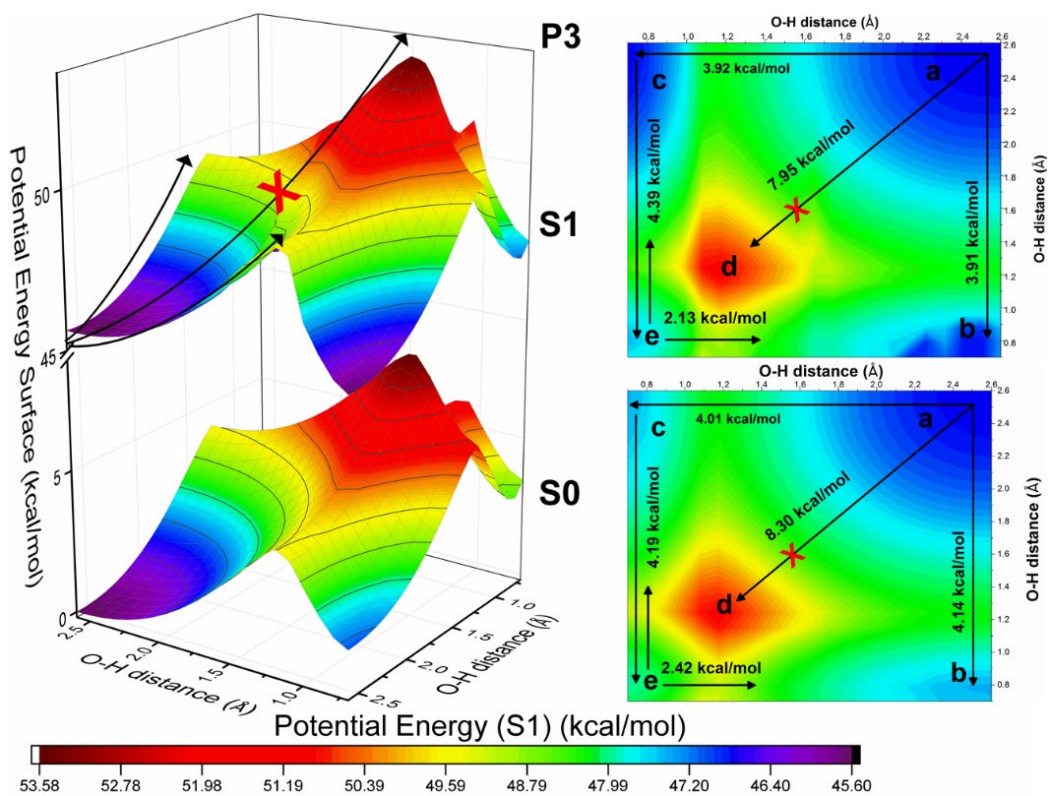


Fig. 5.57 PES scan of P3 in S₀ and S₁ states with their contour profile

5.3.8 Device fabrication and characterization

Amongst the series **T2** exhibited good quantum yield of value 1.8% and the energy levels determined from cyclic voltammogram signifies that **T2**, **P2**, and **F2** can function as emitter material for organic light emitting diode applications in comparison to **T3**, **P3** and **F3** possessing a high HOMO level. To evaluate the electroluminescence performances of the synthesized materials, non-doped OLEDs were fabricated with a device structure: ITO/N,N'-Bis(3-methylphenyl)-N,N'-diphenylbenzidine [TPD] (40 nm)/ **T2** or **P2** or **F2** (60 nm)/ 4,4'-Bis(N-carbazolyl)-1,1'-biphenyl [CBP] (6 nm)/ Tris(8-hydroxyquinolino) aluminum [Alq₃] (35 nm)/ Lithium fluoride [LiF] (1 nm)/ Aluminium (150 nm) as shown in Fig. 5.58. The adopted device architecture is well reported to result in good charge injection and recombination at the emitter material (Zucchi et al. 2010). TPD acts as a hole-injection and hole-transport layer, CBP acts as a hole blocking layer, Alq₃ acting as an electron transport layer and Aluminium used as a cathode material. Fig. 5.59 shows voltage vs. current density plots for devices with **T2** and **P2** as emitters with inset showing electroluminescence and device emission. As observed the device requires a very high turn-on voltage ~15V for initiating electroluminescence. Voltage vs. luminous flux for **T2** and **P2** is as shown in Fig. 5.60, wherein we observe the device exhibits a maximum luminous flux of value 0.035 and 0.015 lumens for **T2** and **P2**. However, **F2** possessing a low quantum yield amongst the series failed to produce any light. Current efficiency of 0.94 Cd/A and power efficiency of 0.94 lm/W is exhibited by molecule **T2** while **P2** exhibited a current efficiency of 0.23 Cd/A and power efficiency of 0.18 lm/W as shown in Fig. 5.61 and Fig. 5.62 respectively.

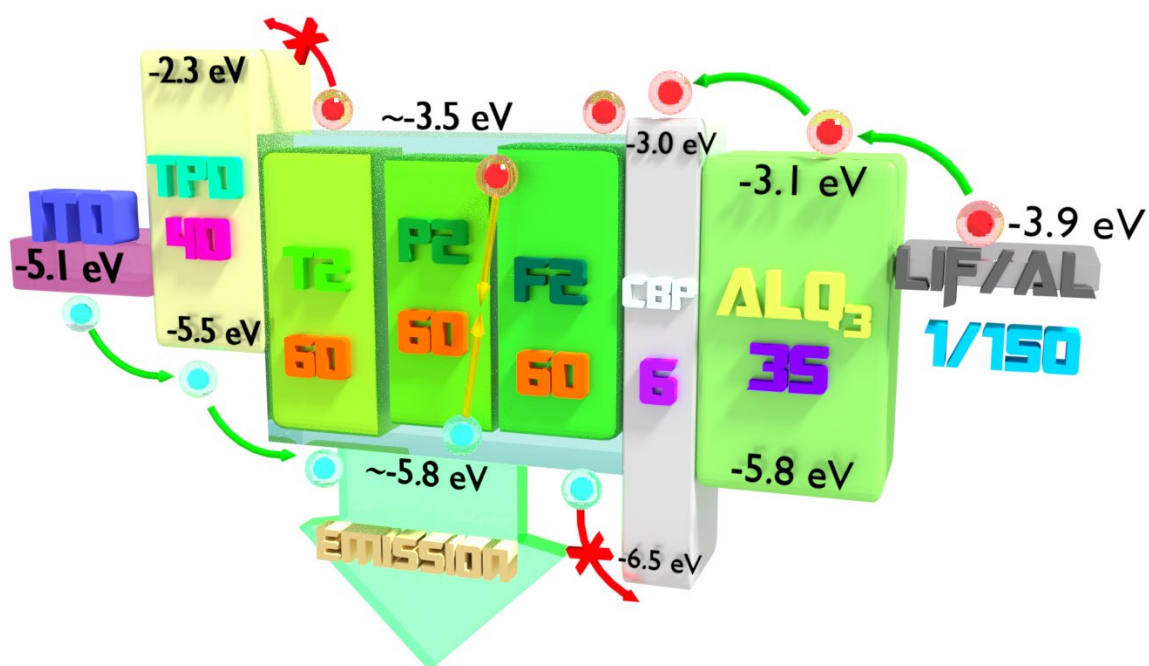


Fig. 5.58 Device architecture for molecule T2, P2, and F2 as an emitter layer

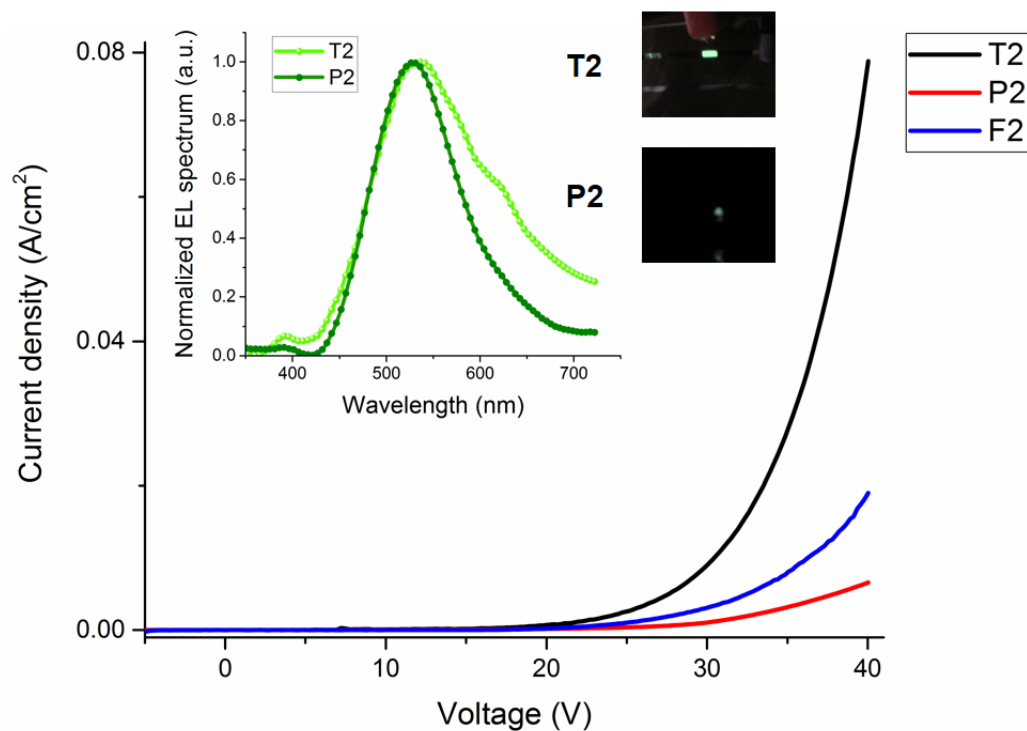


Fig. 5.59 J-V characteristics of the device with T2, P2, and F2 as emitter material. Inset showing the EL spectrum and image showing the light emission from the device.

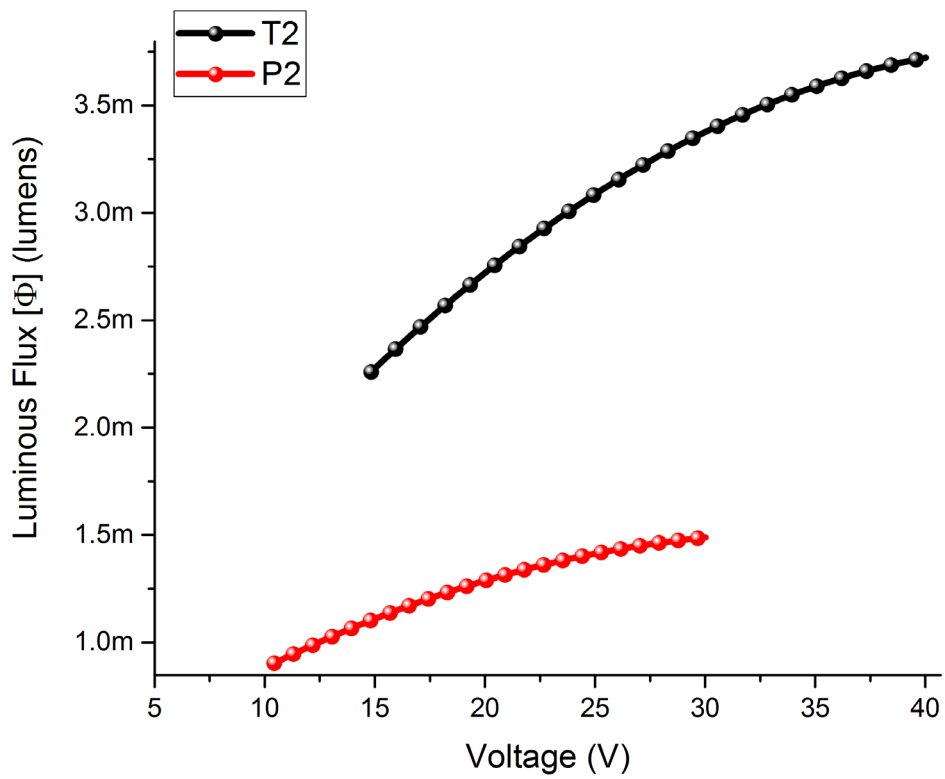


Fig. 5.60 Voltage luminous flux characteristics of molecule T2 and P2

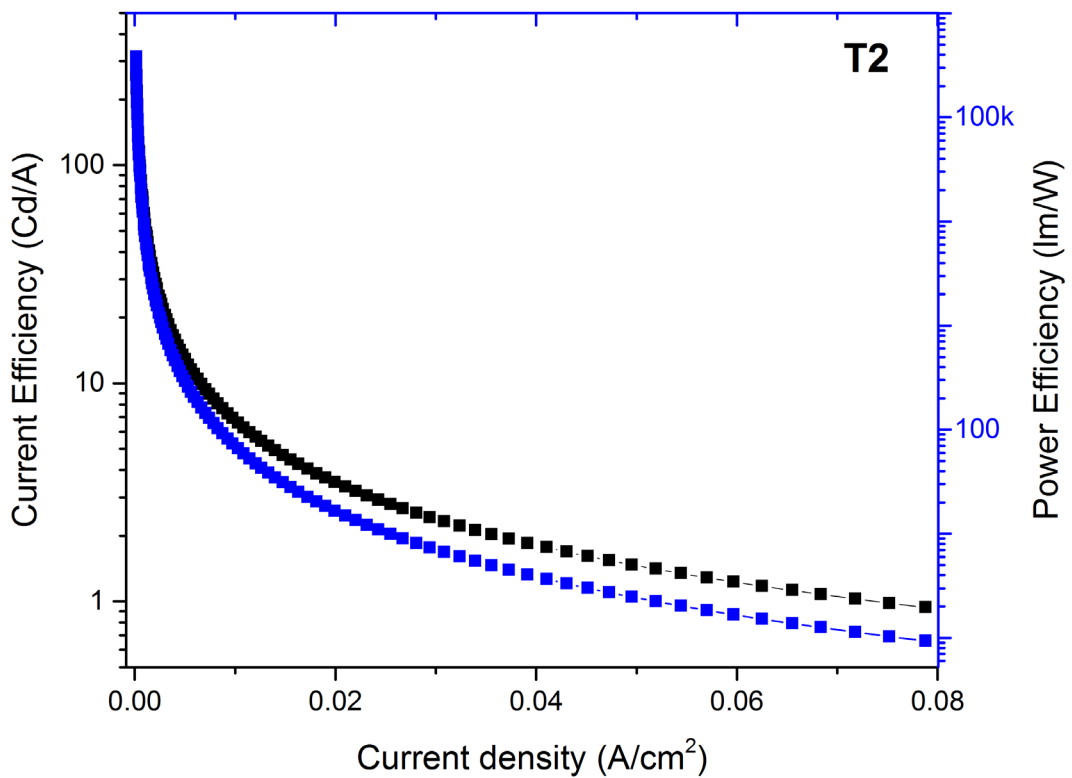


Fig. 5.61 Current Efficiency and power efficiencies of the device with T2 as an emitter layer

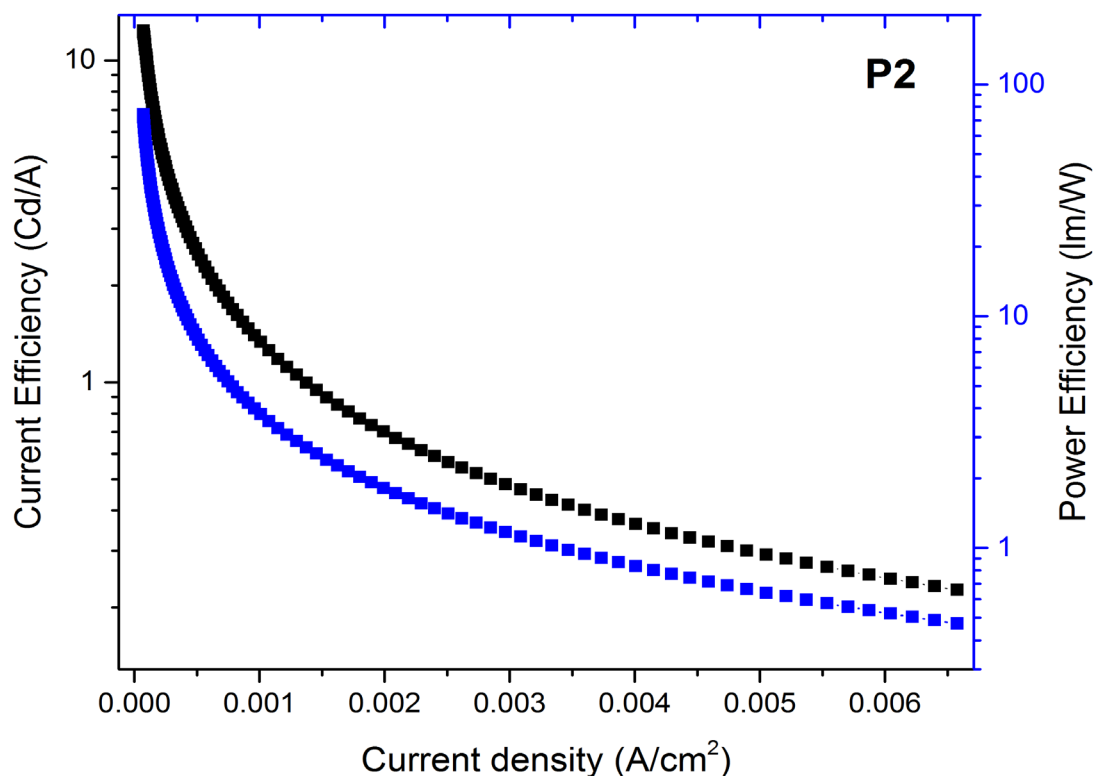


Fig. 5.62 Current Efficiency and power efficiencies of the device with **P2** as an emitter layer

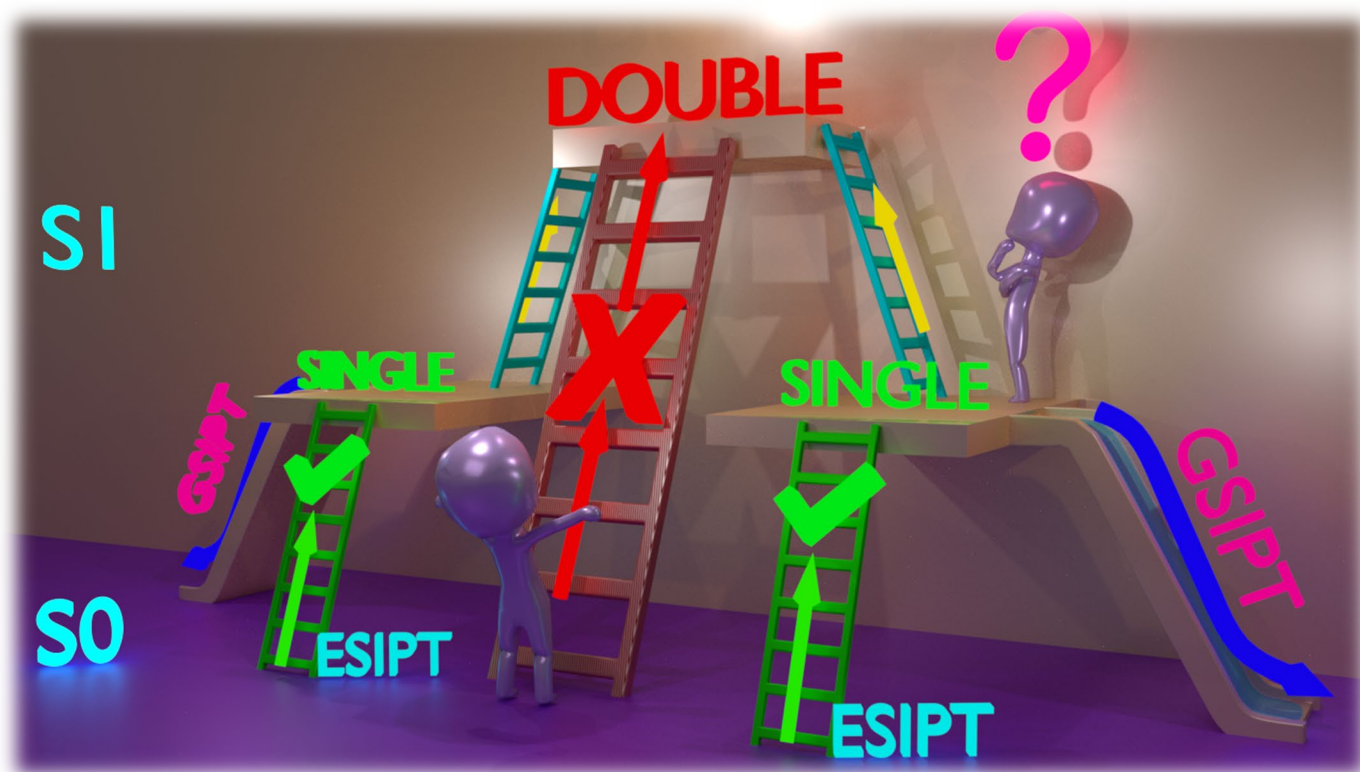
5.4 CONCLUSIONS

Six heterocyclic substituted hydrazides have been designed and synthesized that initiate intramolecular excited state proton translocation. Photophysical characterization in solvents of varying dielectric constants signifies the occurrence of the double peak that correlates to keto and enol transitions. Molecules of the series exhibited good ESIPT in solvents of lower dielectric constants, this being the reason, molecules of the series exhibited a distinct double peak in THF solvent. AIE studies revealed, molecules bereft of furan moiety to have their emission intensity quenched upon aggregation. **F3** possessing furoic hydrazide exhibited a good AIE effect and failed to support ESIPT in the solid state. **T2** exhibited the highest quantum yield of 1.8% amongst the series, and this value scales down upon aggregation. Cyclic voltammetry study reveals bithiophene covalently linked with substituted hydrazide possesses energetically favorable HOMO-LUMO level for efficient device application. OLEDs were realized using **T2** and **P2** as emitter material embedded in a device architecture with ITO / TPD / **T2** or **P2** / CBP / Alq₃/ LiF/ Al. Current efficiency of 0.94 Cd/A and 0.23 Cd/A for **T2** and **P2** along with their power efficiency

value of 0.94 lm/W and 0.18 lm/W respectively. Energy-optimized ground state geometry of all the tautomer and their electronic orbital distribution well supports the excited state intramolecular proton transfer phenomenon. Theoretically derived vibrational spectra of **T1**, **P1** and **F1** did not favor ESIPT. However, conjugation enhanced structure possessed in synthesized molecules supports ESIPT. Theoretical energy transitions of keto-enol tautomer well correlate with the pertinent energy transitions experimentally observed. Potential energy scans performed on the molecules revealed the existence of the lower forward barrier at its excited state in comparison with its ground state, suggestive of excited state proton translocation. Potential energy surface scan performed on **T3**, **P3** and **F3** affirm impossible double proton transfer and difficult step-wise double proton transfer.

CHAPTER 6

EXPLORING THE POSSIBILITIES OF DOUBLE PROTON TRANSFER IN HYDRAZIDES: A THEORETICAL APPROACH



Mohan, M., Satyanarayan, M. N., and Trivedi, D. R. (2019). "Exploring the possibilities of double proton transfer in hydrazides: A theoretical approach." J. Phys. Org. Chem., 32(11), e4003.

Abstract

In this chapter, theoretical aspects uncovering excited state intramolecular proton transfer (ESIPT) of N-acylsubstituted hydrazides with bithiophene and trithiophene core have been investigated.

6.1 INTRODUCTION

It is quite interesting to know that hydrazides exhibit keto – enol tautomerism upon photoexcitation (Chohan et al. 2000; Cigáň et al. 2015; Mir et al. 2018). Tautomerism in hydrazides is characterized by translocation of a proton from a donor (N–H) moiety to an acceptor moiety (C=O) with a pre-established intramolecular hydrogen bond giving birth to a phototautomer phenomenon, commonly termed as excited state intramolecular proton transfer (ESIPT). Proton transfer is primly induced by the energy difference pertaining to locally excited state and the relaxed excited state, and the gradient spread over potential energy surface connecting these two extremities governs the relative kinetics of the system (Tong et al. 2018; Yang et al. 2018; Yin and Shi 2018; Zhang et al. 2016; Zhao et al. 2018). ESIPT properties of various functional small organic systems have attracted research community for its extensive applications in the field of biological molecular probes (Deng et al. 2016; Paul and Guchhait 2010), organic light-emitting diodes (Kundu et al. 2016; Liu et al. 2017; Samanta et al. 2017), fluorescent sensors (Aparicio et al. 2011; Pinto da Silva et al. 2014; Tang et al. 2011; Zhao et al. 2012) and UV stabilizers (Sobolewski and Domcke 2006). ESIPT materials are renowned potent luminescent systems that invariantly exhibit a large Stokes shift between their keto and enol emission, hindering self-absorption of generated photons (Hao and Yang 2019; Sobolewski and Domcke 2006; Wu 2015; Yang et al. 2017, 2018; Zhang et al. 2019). Finer tuning and precise control over the emission energies has opened up research in developing a single molecule that generates while light emission for OLED device applications (Kim et al. 2011; Kundu et al. 2016; Liu et al. 2017; Samanta et al. 2017). Interestingly, solid-state luminescent materials that are ESIPT active is highly challenging and intricacies of the scientific mechanism of such occurrences remains a subject for discussion until today (Padalkar and Seki 2015; Tong et al. 2018; Yang et al. 2018).

Jedryka-Jarczyk and co-workers have meticulously designed and synthesized Schiff's base symmetrical N-acylsubstituted dihydrazones containing bithiophene core to

look into practical solar cell applications (Jarczyk-Jedryka et al. 2016). Amongst the molecules designed, bithiophene coupled with furoic hydrazide turns out to be the best competitor as an active solar energy harvester. Scientific observations and evidence were intimately supported by photophysical and electrochemical characterizations, supported with valid reasons and discussions. Optical signatures reveal molecules show dual emission in DMF; however, in solvents of lower dielectric constants, this dual emission is profound and distinct (Cheng et al. 2015). Further, some of the necessary DFT studies were carried out to realize ground state optimized geometry and to understand the effective variation of acylsubstituted dihydrazones on the nature of electronic density. However, the revelation of excited state properties arising out of conformational changes and alterations in electronic distributions is highly essential to theorize principles based on some of the experimentally observed phenomena. Theoretical aspects discussing the nature of excited state dynamics and the excited state proton transfer pathways providing necessary information on potential barrier can enrich concepts on mechanistic details. Owing to the presence of bithiophene equipped with hydrazides on both the arm, an exploration into possible double proton transfer or step-wise double proton transfer can be enlivening.

With the above in view, an attempt is made to uncover a few of the interesting theoretical fundamentals of ES IPT occurring in substituted hydrazides and correlate the experimental findings with the theoretical counterpart. We would like to present further a few of the experimental results that were not done and reported earlier by Jedryka-Jarczyk et al., to provide necessary support for the theoretical validation. Jarczyk-Jedryka reported TBTH, FBTH (herein referred to as **T4** and **F4** respectively) (Jarczyk-Jedryka et al. 2016). **P4** varies from NBTH in possessing hydrazide unit at position meta to the pyridine ring nitrogen. Additionally, in the current work **P4** has been synthesized and characterized by various spectroscopic techniques and its necessary experimental details and discussions are discussed in details. Further, to understand the limits of proton transfer in substituted hydrazides, theoretical aspects of excited state proton transfer dynamics of substituted hydrazides on trithiophene core is also studied. Structures supporting double proton transfer in substituted hydrazides present over both the arms of trithiophene core were computationally verified and results pertaining to such mechanism are well discussed.

6.2 EXPERIMENTAL SECTION

6.2.1 Materials and methods

All the chemicals used in the present study were procured from Sigma-Aldrich and were used as received without further purification. All the solvents were purchased from SD Fine, India was of HPLC grade and used without further distillation. Melting point was measured on Stuart SMP3 melting-point apparatus in open capillaries. The infrared spectrum was recorded on Bruker Apex FTIR spectrometer. UV-Vis spectroscopy was performed with Ocean Optics SD2000 spectrometer in a standard 3.0 mL quartz cell with 1 cm path length. Cyclic voltammogram was recorded on IVIUM electrochemical workstation at a scan rate of 20mV/s with the potential range 5V to -5V. Photoluminescence studies were carried out using Horiba Jobin Yvan spectrofluorometer. All the measurements were performed under room temperature.

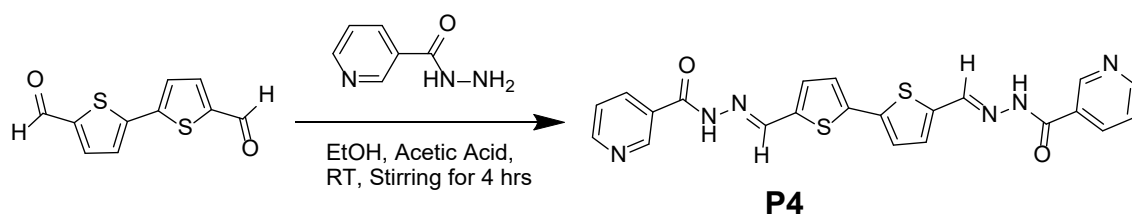
Computational calculation for the work is achieved using Gaussian 09 package (Frisch et al. 2009). Ground state calculations S0 were carried out with DFT Becke's three-parameter hybrid exchange function with the Lee-Yang-Parr gradient-corrected correlation functional (B3LYP) (Lee et al. 1988; Miehlich et al. 1989) with 6-311+G (d, p) (Hariharan and Pople 1973; Hehre et al. 1972) basis set and the excited state calculations S1 were carried out using TD-DFT Coulomb-Attenuated Method B3LYP (Yanai et al. 2004) with the same basis set used for ground state. The molecular system herein exhibits a good amount of delocalization owing to their structure possessing good amount of planarity, and hence CAM-B3LYP were carefully chosen to predict the nature of electronic transition at excited state. CAM-B3LYP functionals for excited state calculations is known to reproduce experimental values with greater accuracy. Further, owing to the presence of long-range correction scheme present in CAM-B3LYP can predict excited state dynamics accurately to a greater extent than B3LYP (Egidi et al. 2014; Gong et al. 2016; Liu et al. 2017; Muriel et al. 2019; Yang et al. 2016; Zhao and Zheng 2017). The self-consistent field (SCF) convergence thresholds pertaining to energy minimizations for both S0 and S1 state optimizations were set to 10^{-6} . The effect of solvent on the energy parameters of the system was studied by using self-consistent reaction field based on polarizable continuum model (PCM) (Tomasi and Persico 1994) using the integral equation formalism variant (IEFPCM) (Cammi and Tomasi 2001.; Cancès et al. 1997; Mennucci et al. 1997; Miertuš et al. 1981; Miertuš and Tomasi 1982). IEFPCM model studies the effect of the solvent by placing the

solute in a cavity of overlapping solvent and the effect reproduces the electrostatic potential arising due to the polarized dielectric created by the apparent charges surrounding the solute (Wei et al. 2017). The selection of the functional was made following numerous previous benchmarks validating their accuracy in predicting ground state energies and excited state energies (An et al. 2017; Liu et al. 2017; Zhao and Han 2008). Initially, ground state optimizations were carried out under vacuum and the resultant geometry was further optimized in a solvent medium. The experimental results reveal ESIPT mechanism occurring at solvents of lower dielectric medium and to corroborate this effect theoretically, THF was chosen as a solvent medium for all the theoretical calculations. Frequency calculations were performed for the geometry optimized to confirm their geometry corresponds to a true local minimum on the S0 and S1 potential energy surface. Geometry optimizations were carried out without any constraints on bond lengths, bond angles or dihedral angles, however, such constraints were used while constructing potential energy surfaces (PESs) and potential energy curves (PECs). PESs and PECs in S0 and S1 states were scanned by constraining the O-H bond length fixed for a series of values with other degrees of freedom optimized without any constraint. The calculation of vertical excitation energy of first singlet excited state S1 was estimated from the ground state optimized structure based on TDDFT with IEFPCM solvation model. The optimized geometry and the electronic orbital distribution of all the molecules were visualized using Avogadro software (Hanwell et al. 2012).

6.2.2 Synthesis of molecule P4

To a solution of 2,2'-Bithiophene-5,5-carboxaldehyde (0.1 g, 0.51 mmol) in ethanol (10 ml), nicotinic acid hydrazide (0.071 g, 0.51 mmol) was added. Acetic acid was used as a catalyst and stirred for 4 h to get a thick pale brown curdy precipitate. The product was confirmed with TLC. The residue was then washed with cold ethanol, filtered and dried at 65 °C to obtain a bright yellow solid compound. The synthesis scheme is as shown in Scheme 6.1.

Yield: 82%, melting point: 220 °C - 224 °C, ¹H NMR (DMSO- *d*₆, 400 MHz, ppm): δ 12.1 (br. s; 2H), 9.07 (br. s; 2H), 8.79 (m; 2H), 8.64 (s; 2H), 8.26 (d; J= 7.6, 2H), 7.55 (m; 6H), FTIR (ATR) (cm⁻¹): 3067 (Ar-CH), 1641 (CH=N).



Scheme 6.1 Synthesis of molecule **P4**

6.2.3 Characterization data

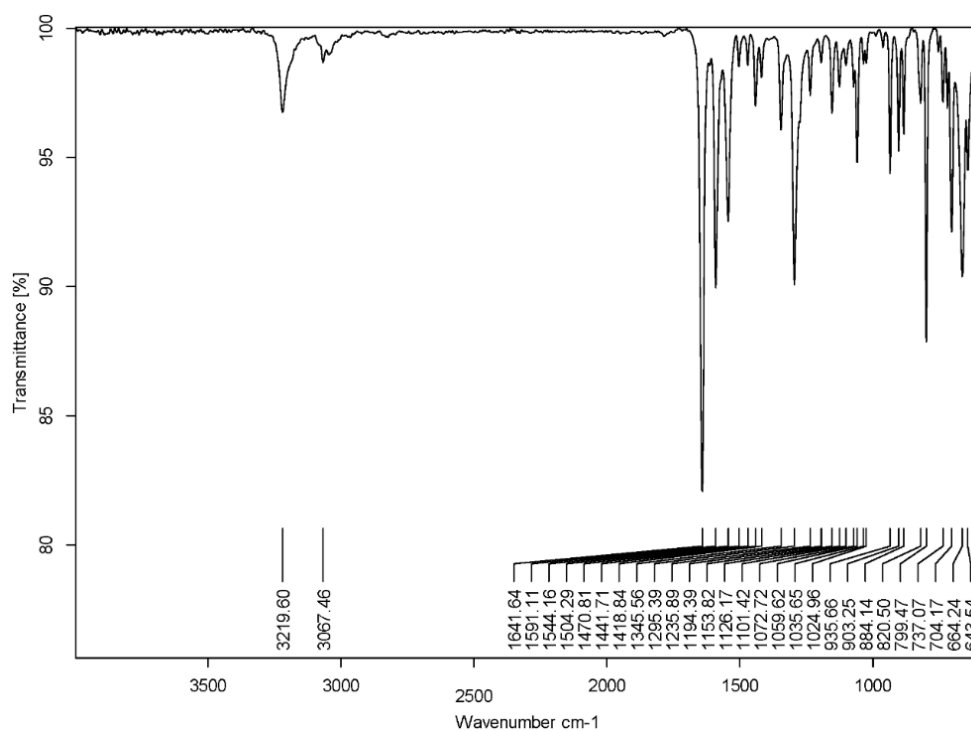


Fig. 6.1 FT-IR spectra of **P4**

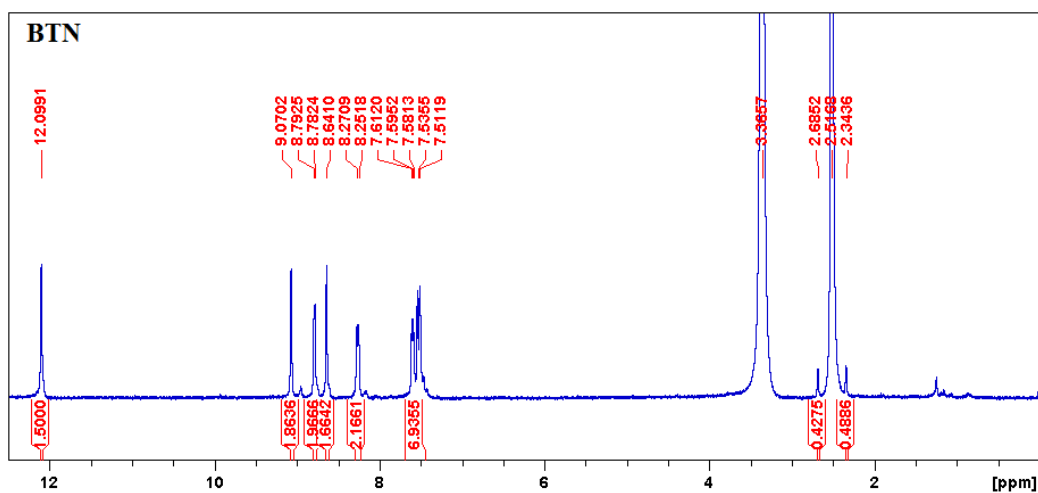


Fig. 6.2 ¹H NMR spectra of **P4**

6.3 RESULTS AND DISCUSSION

6.3.1 UV-Vis and photoluminescence studies

Spectroscopic characterizations were carried out on few of the molecules of the series to record the nature of electronic transitions in the system. Solutions of concentration (10^{-5} M) of **TX**, **PX** and **FX**, where X=4 in THF solvent were considered for all solvent related optical characterization. UV-Vis spectra and photoluminescence spectra of **T4**, **P4** and **F4** under THF solvent is as shown in Fig. 6.3. UV-Vis spectra confirm a band centered around 391-410 nm that corresponds π - π^* type of transition prominently contributed by HOMO and LUMO orbitals.

Photoluminescence spectra of molecules show a distinct double peak that corresponds to normal and tautomer emission generated from keto and enol conformers, validated by theoretical results. Methanol being a polar protic solvent has a tendency to form intermolecular hydrogen bonding with the solute system (Cheng et al. 2015). In polar solvents, solute-solvent interactions can support both the intermolecular and intramolecular hydrogen bonding (Kasha 1986). This hydrogen bonding further restricts the molecules to undergo structure tautomerism and hence, molecular system exhibits a single emission peak in polar solvents in comparison with the distinct double peak seen in other solvent medium. The detailed experimental photophysical parameters of all the molecules is provided in the Table 6.1 and the photoluminescence spectra of **T4**, **P4** and **F4** in various solvents is provided in Fig. 6.4 to Fig. 6.6. The emission behavior of all the molecular system didn't exhibit any variation in spectral behavior supporting solvatochromism. The solvent induced bathochromic shift observed at the emission energy clearly indicates the strengthening of the intramolecular hydrogen bond and hypsochromic shift indicates weakening of hydrogen bond (Song and Ma 2013). This is highly prevalent in our systems, wherein, molecules showed a red-shifted emission in comparison with other solvents superseding the linearity. **T4** showed a pronounced bathochromic shift in the emission wavelength from THF to ACN excluding methanol, exhibiting positive solvatochromic behavior in comparison with **P4** and **F4**. Excited state stabilization of the molecules is highly predominant in solvents of higher polarity inducing positive solvatochromism during solute-solvent interaction. This leads to a redistribution of the charges supporting multi-dimensional intramolecular charge transfer (MDICT) between the core and peripheral moieties (Brunel et al. 2003). The

highest large stokes shift value of 43 nm was recorded for **T4** in DMF solvent and the lowest recorded value is 27 nm for **F4** in the same solvent.

Table 6.1 Photophysical parameters of **T4**, **P4** and **F4** in solvent of varying polarities

	SOLVENT	λ_{Abs}^* (nm)	λ_{exi}^* (nm)	KETO (nm)	ENOL (nm)	Normal Stokes Shift* (nm)	Large Stokes Shift* (nm)	FWHM* (nm)
T4	THF	415,487	415	462	493	47	31	79
	MeOH	415,437,473	415	496	--	81	--	110
	ACN	490,549	490	547	585	57	38	71
	DMF	424,446,486	424	465	508	41	43	95
	DMSO	424,449,498	424	470	500	46	30	83
P4	THF	397	397	454	486	57	32	87
	MeOH	412,432,473	412	490	--	78	--	93
	ACN	405,483	405	455	487	50	32	120
	DMF	441,476	441	461	495	20	34	81
	DMSO	421,445,493	421	466	495	45	29	85
F4	THF	406,481	406	458	487	52	29	83
	MeOH	412,476	412	491	--	79	--	86
	ACN	531,553	531	458	485	73	27	76
	DMF	423,443,482	423	501	528	78	27	125
	DMSO	418,496	418	469	497	51	28	77

** λ_{Abs} – UV-Vis absorption peaks, * λ_{exi} – UV-Vis excitation values, *KETO and ENOL – Corresponds to Keto emission and enol emission, *Normal Stokes Shift – Refers to the difference between keto absorption and keto emission, *Large Stokes shift – Refers to the difference between keto and enol emission, *FWHM – Full width half maximum*

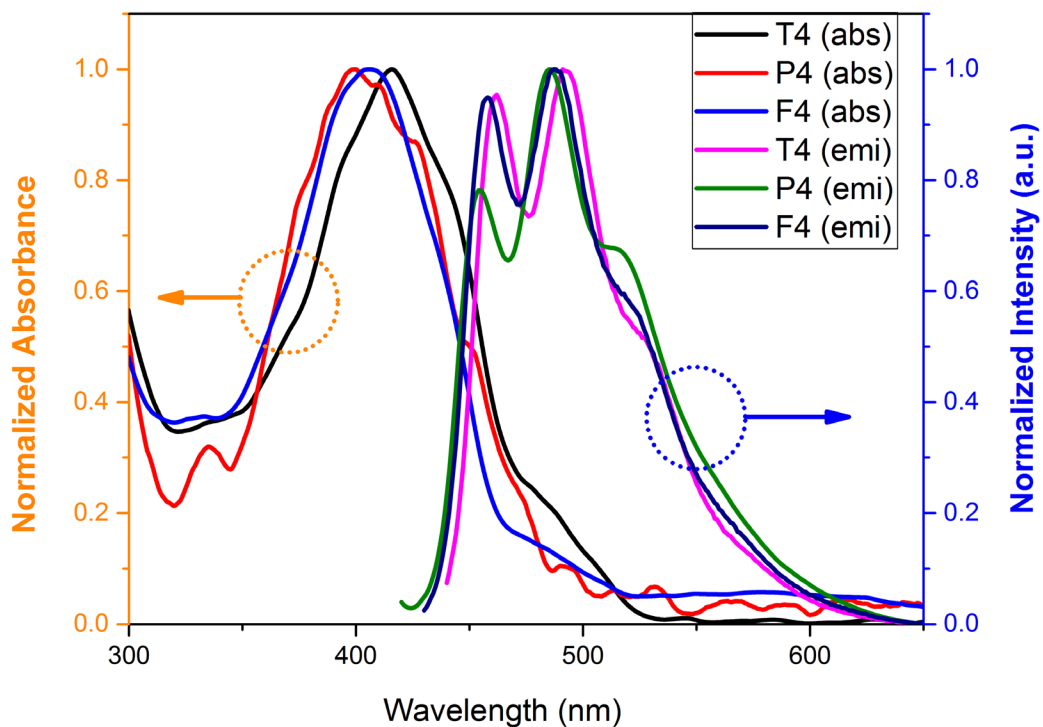


Fig. 6.3 Experimental UV-Vis absorbance spectra and fluorescence emission spectra of **T4**, **P4** and **F4** in THF solvent

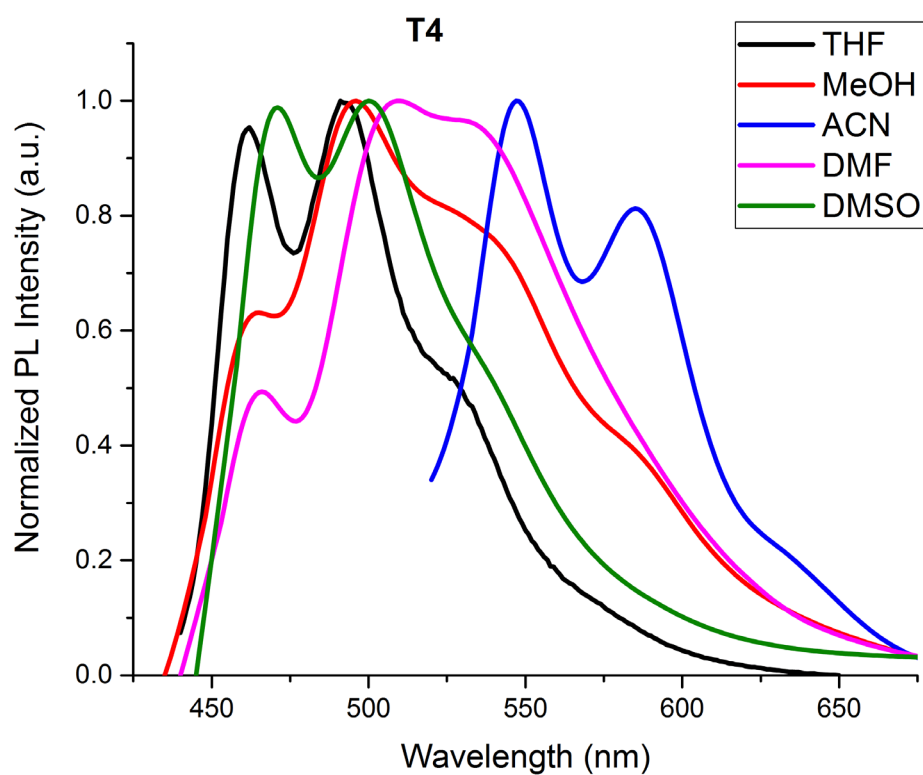


Fig. 6.4 Photoluminescence spectra of **T4** in solvents of varying dielectric constants

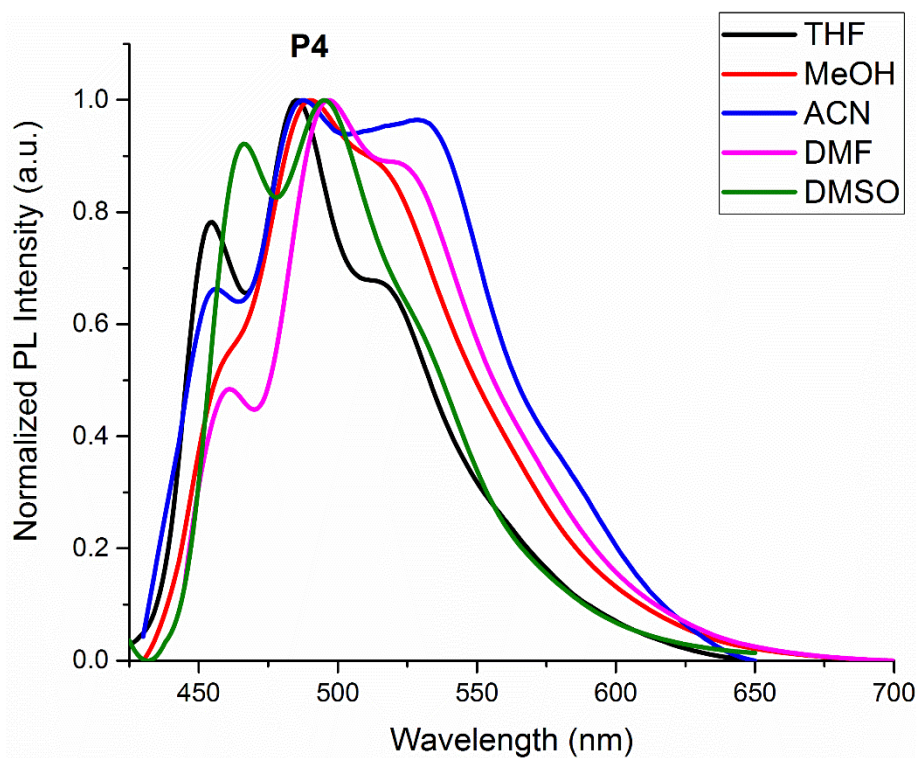


Fig. 6.5 Photoluminescence spectra of **P4** in solvents of varying dielectric constants

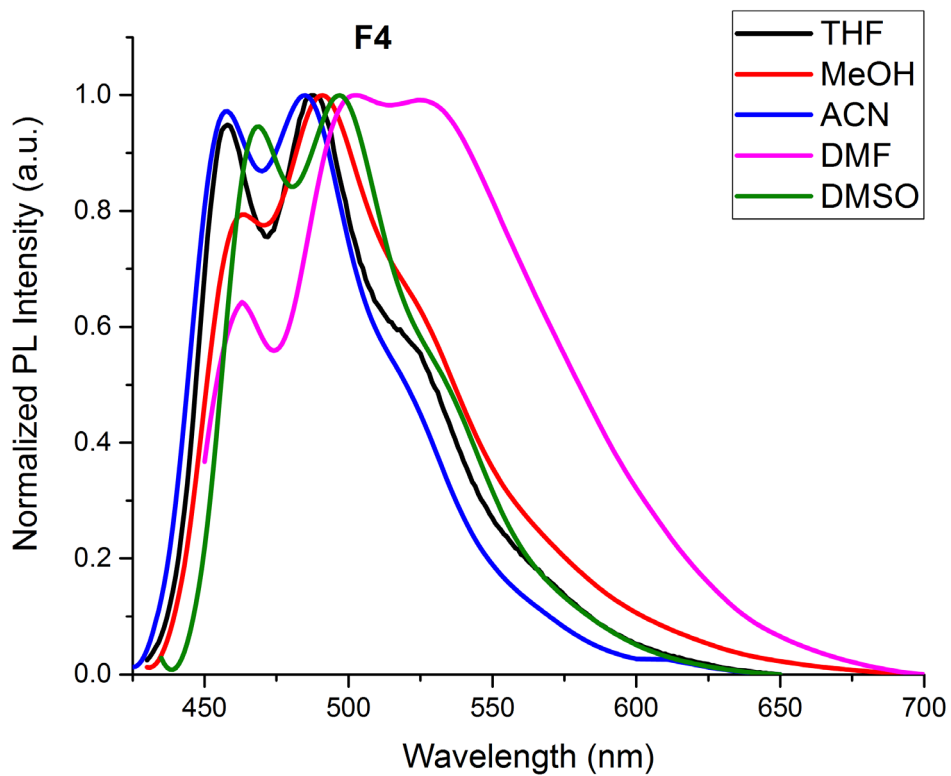


Fig. 6.6 Photoluminescence spectra of **F4** in solvents of varying dielectric constants

6.3.2 Quantum yield measurement

The fluorescence quantum yields (Φ_S) were evaluated according to the following Equation 6.1 given, where Coumarin 153 in cyclohexane is considered as reference (R) for all the molecules. Samples whose QY needs to be determined is denoted as S. Grad corresponds to the gradient from the plot of integrated fluorescence intensity vs absorbance at the excitation wavelength, and η the refractive index of the solvent for standard and reference (Dhami et al. 1995; Williams et al. 1983). As observed from the table the value of QY increases upon increase in the number of thiophene core unit. The highest QY recorded is for **T4** with a value of 6.17 %, whereas **F4** and **P4** exhibited 3.70 % and 3.74 % respectively. However, amongst the series thiophene substituent present on the side chains of the central core gives a better quantum yield in comparison with furan and pyridine.

$$\Phi_S = \Phi_R \frac{Grad_S}{Grad_R} \frac{\eta_S^2}{\eta_R^2} \quad \text{Eq. 6.1}$$

6.3.3 Solid state photoluminescence studies

Enormous amount of work published covers the ESIPT mechanism of molecules in solvent medium, however, solid state emitters undergoing ESIPT haven't been explored much to a greater extent. Jedryka-Jarczyk and co-workers have spin coated **T4** and **F4** with a polymer binder for solar cell applications. However, their ESIPT properties in solid state were not studied and with this in view, thin films of molecules were prepared by thermal vapor deposition under vacuum for solid state photoluminescence studies. The mechanism explaining the excited state proton transfer in solid-state still remains undefined (Padalkar and Seki 2015). The results of this characterization is provided in the Fig. 6.7 and the inset shows images of thin films under UV illumination. We observe that **T4** and **F4** exhibited a double peak supporting ESIPT in its condensed state; however, **P4** failed to exhibit a keto and enol emission in solid form. There may be possibility of keto and enol emissions getting overlapped to give out a broad spectrum in solid state as observed. Photoluminescence parameters of thin films of **T4**, **P4** and **F4** is provided in the Table 6.2. The lowest FWHM value of 95 nm was observed for **T4** and the highest value of 166 nm seen for molecules **P4**. The largest stokes shift between keto and enol emission is approximately around 35 nm observed for the molecules **T4** and **P4**.

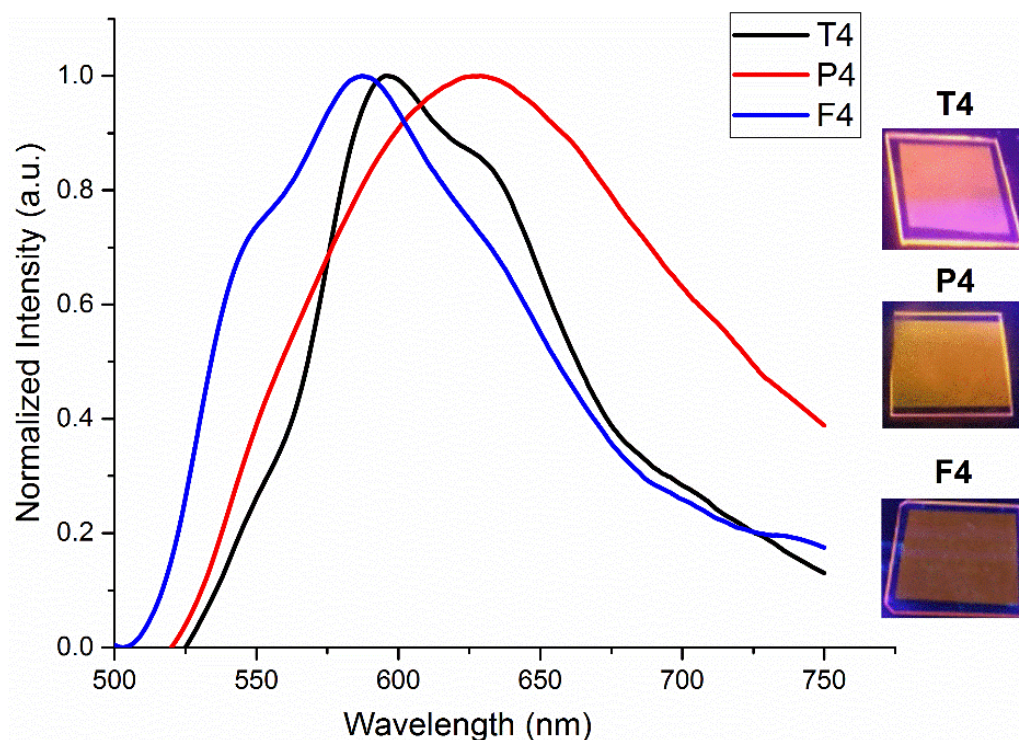


Fig. 6.7 Fluorescence emission spectra of **T4**, **P4** and **F4** thin films

Table 6.2 Photoluminescence parameters of thin films of **T4**, **P4** and **F4**

Molecule	Keto Emission (nm)	Enol Emission (nm)	Large stokes shift (nm)	FWHM (nm)
T4	595	630	35	95
P4	629	-	-	166
F4	549	587	38	122

6.3.4 Ratiometric studies

Restriction of vibrational and rotational components in a system upon aggregation enhances the emission intensity at solid state over solution, however, solid state molecular packing and aggregation type governs the overall quantum efficiencies of ESIPT chromophores (Padalkar and Seki 2015). Solutions were prepared with a concentration (10^{-5} M) in THF and their mixtures in varying water fractions f_w were used for AIE studies. Ratiometric studies of all the molecules with varying THF:H₂O mixture were considered to test the molecules for aggregation-induced emission behaviour. Fig. 6.8 shows photographs of **T4**, **P4** and **F4** exhibiting fluorescence response with varying solvent-water mixture. Herein, 10% of f_w implies 10:90 of the mixture with 10% of H₂O and 90% of THF and 20% of f_w would imply 20:80 with 20% of H₂O and 80% of THF and so on. Fig. 6.9 to

Fig. 6.11 shows the photoluminescence spectra with varying solvent-water mixture and the inset plot provides intensity vs ratiometric increase. Noticeably, **F4** shows an increase in emission intensity slightly higher than its initial value and retains there until THF:H₂O mixture of 30%, then falls back on further increase in THF:H₂O mixture exhibiting good aggregation induced emission. Further, we observe the disappearance of double peak at higher THF:H₂O mixture clearly establishing the fact that at higher polarity or at higher dielectric constant, intermolecular hydrogen bonding overrides intramolecular hydrogen bonding. **T4** and **P4** fails to exhibit an aggregation induced emission behaviour as evident from their corresponding spectra.



Fig. 6.8 Photographs of molecules in THF/water mixtures with different fw under UV illumination

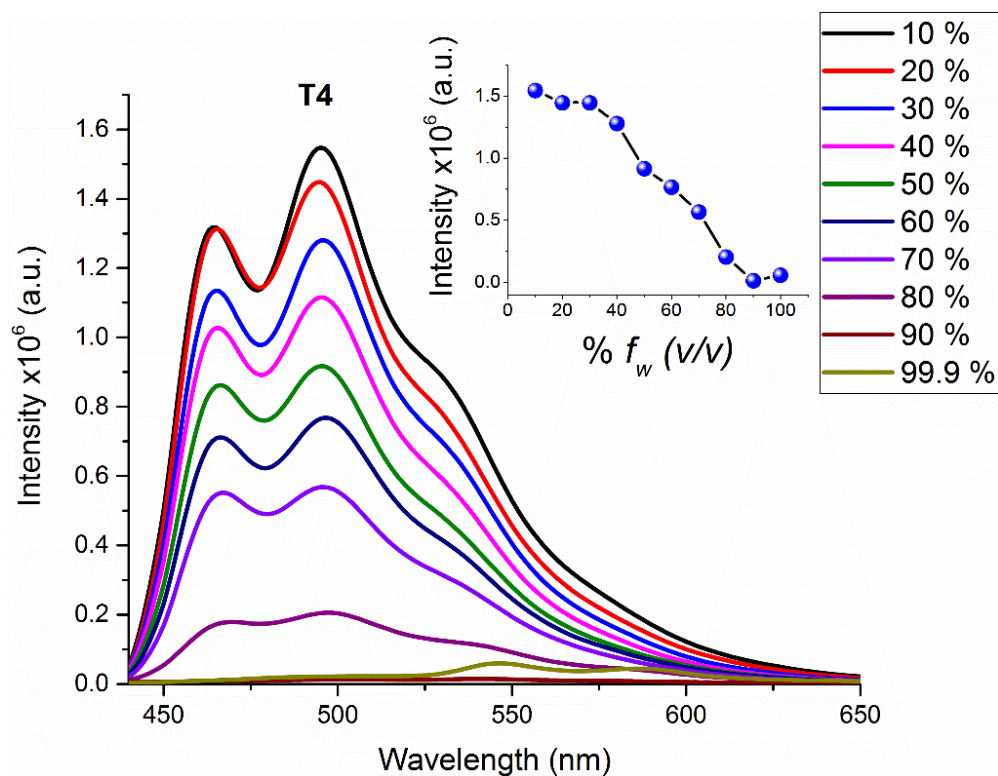


Fig. 6.9 Fluorescence emission spectrum of **T4** with varying f_w and inset gives the intensity value with varying f_w

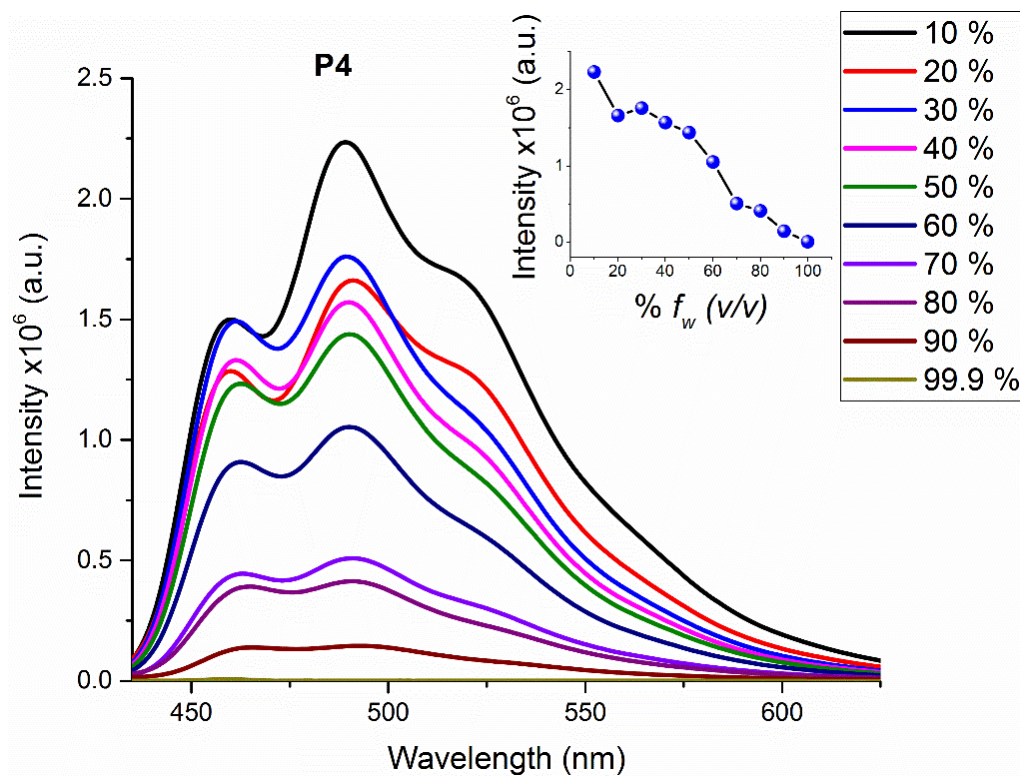


Fig. 6.10 Fluorescence emission spectrum of **P4** with varying f_w and inset gives the intensity value with varying f_w

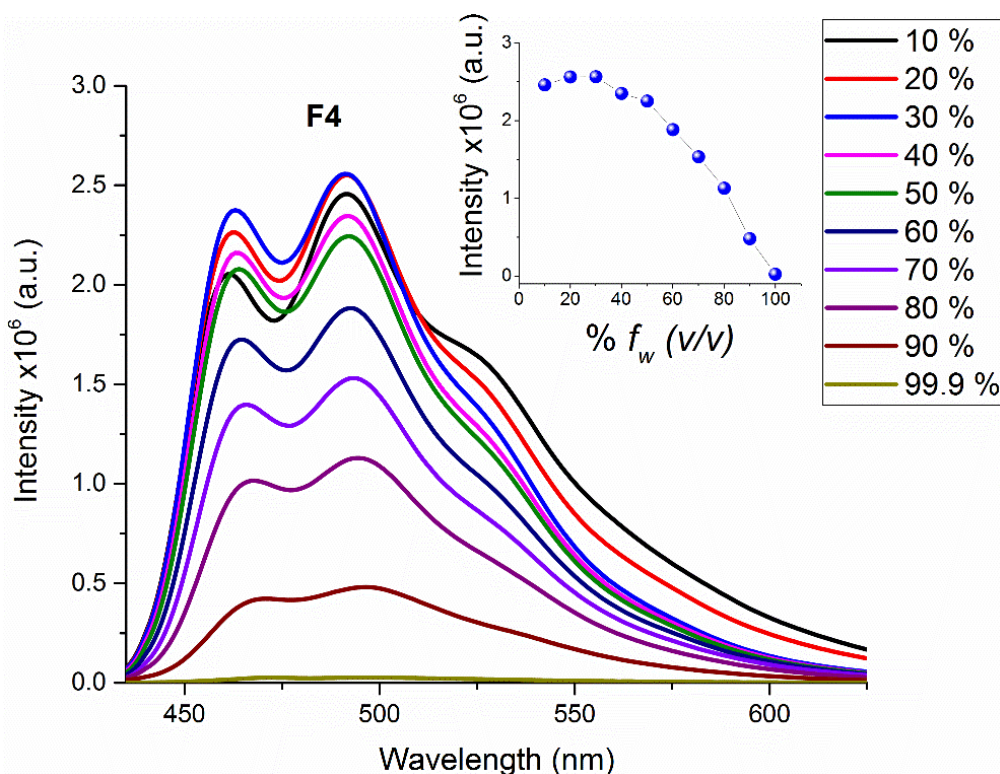


Fig. 6.11 Fluorescence emission spectrum of **F3** with varying f_w and inset gives the intensity value with varying f_w

6.3.5 Cyclic voltammetry

The electrochemical properties of the **P4** were studied by cyclic voltammetry to estimate their electronic energy levels and the bandgap. However, **T4** and **F4** have been reported previously by Jedryka-Jarczyk and co-workers (Jarczyk-Jedryka et al. 2016). Cyclic voltammetry studies reveal a good oxidation peak of value 1.89 yielding a HOMO around 6.29 eV calculated in accordance with equation reported as $E_{\text{HOMO}} = -(I_p + 4.4)$ eV and $E_{\text{LUMO}} = -(E_A + 4.4)$ eV (Duvnhage et al. 2015). Cyclic voltammogram curve for **P4** is as shown in the Fig. 6.12, and inset illustrate an estimated HOMO and LUMO levels corresponding to -6.29 eV and -4.34 eV with a band gap value of 1.95 eV.

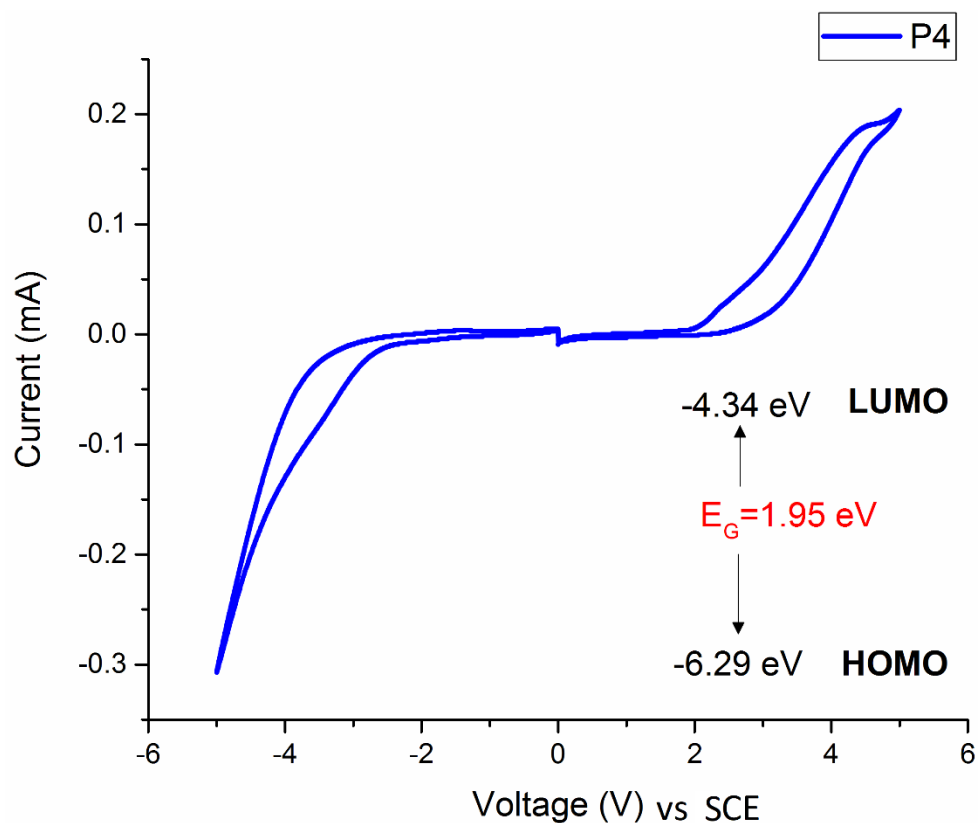


Fig. 6.12 Cyclic voltammogram of molecule **P4** in acetonitrile solvent

6.3.6 DFT studies

Fig. 6.13 shows the possible stable conformations for **TX**, **PX**, and **FX** where X=4,5,6 at their ground and excited state. Herein, keto (k) form refers to a thermodynamically stable entity possessing keto conformation on both the arm. Enol (e) form corresponds to one of the arm exhibiting enol with respect to other possessing keto form, wherein, a single proton translocates from a proton donor to an acceptor upon photoexcitation. Final conformation is double enol (o) form, which is a hypothetical form, wherein, both the proton translocates at their excited state from the proton donor to the proton acceptor species as represented.

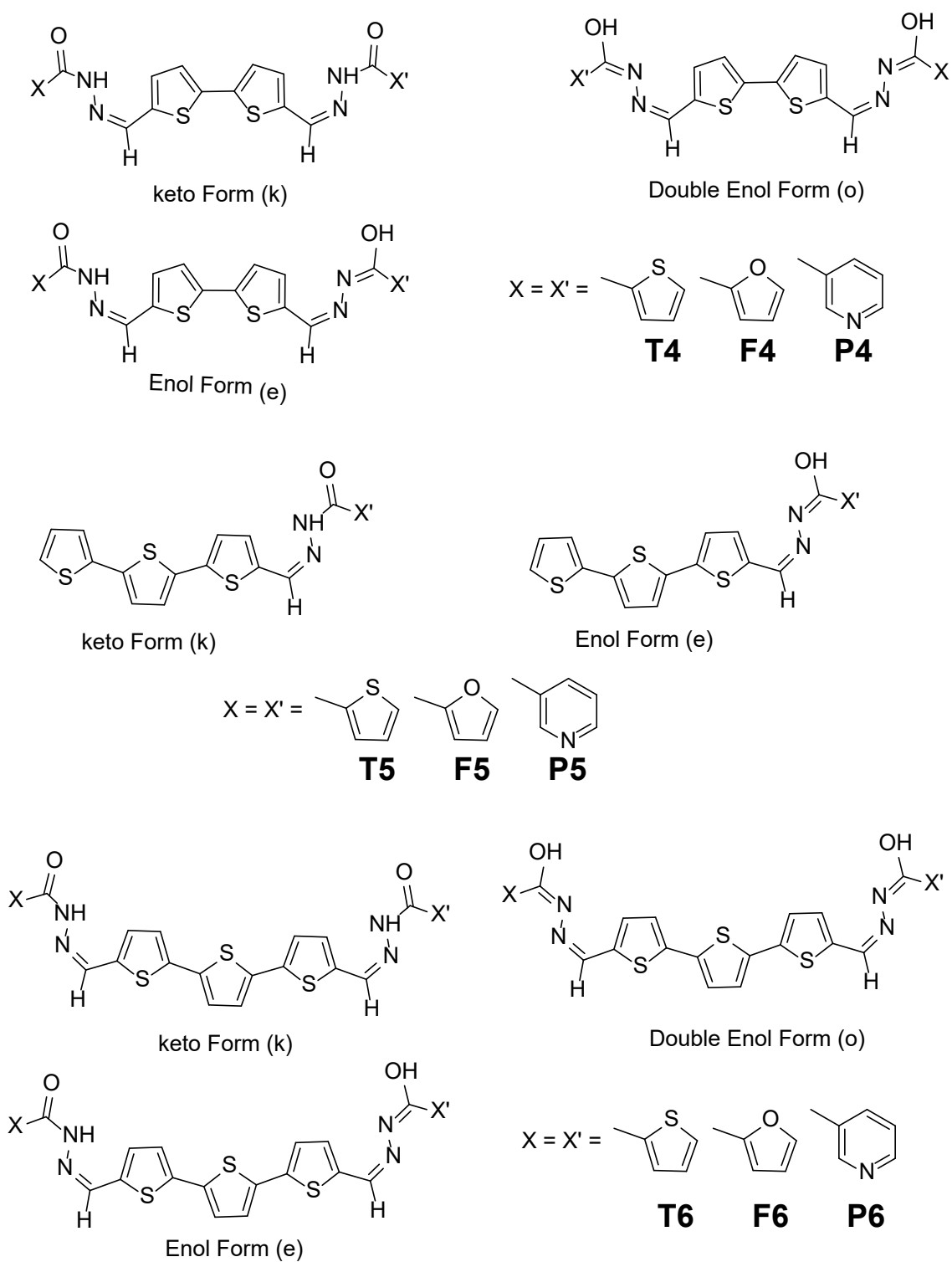


Fig. 6.13 Possible conformations of **TX**, **PX**, and **FX** where $X=4,5,6$ at its S_0 and S_1 state,

6.3.7 Structural analysis

Ground state optimizations of keto (k) form for all the molecules is provided in Fig. 6.14 to Fig. 6.16 with their structural parameters summarized in Table 6.3. We observe that at ground state **TX** and **FX** possesses a high amount of planarity and adheres to planarity even at their excited state. However, **PX**, where X=4,5, owing to the presence of six-membered nitrogen ring gives in a certain minimal steric hindrance disturbing planarity of the structure. **P4** and **P5** possesses a dihedral angle of 39.9° at its ground state, however, this dihedral angle reduces to 36.8° and 33.4° at its excited state between the planes connecting the bithiophene unit and the pyridine ring. **P6** possessing a trithiophene core exhibits a complete planar structure in both ground and the excited state as observed. The planar structure might well support the proton transfer process in a system in comparison with a sterically hindered structure (Kanlayakan et al. 2017). The dihedral angle between the planes possessing N-H and -C=O is 1.7° for **P4** at S0 and increases to a value of 2.3° at S1, whereas, **F4** exhibits 0.0° at S0 and increases to a value of 0.8° at S1 with the rest of the molecules maintaining 0.0° for both S0 and S1. Change in geometrical parameters of the system at its excited state signifies a better stabilization of the structure to support ESIPT.

The N-H bond length remains unaltered with a value of ~1.019Å for k form at S0 and S1 for all the molecules; however, the difference in bond length tabulated at S0 and S1 are too insignificant for practical discussion. Intramolecular hydrogen bond distance denoted as R and R' is shortened at excited state in comparison with that of ground state for all the molecules. The shortening of intramolecular hydrogen bond distance is highly suggestive of possible proton transfer via pre-linked hydrogen bond pathway (Kanlayakan et al. 2017; Zhao et al. 2015). System possessing pyridine moiety shows a substantial change in the R and R' at their excited state in comparison with that of the ground state possibly owing to the effect of six-membered pyridine spreading its influence over the proton donor-acceptor moiety. All the molecules of the series exhibited a reduction in the proton transfer distance at its excited state suggestive of hydrogen bond strengthening at the excited state leading to efficient excited state proton transfer in the system.

Vibrational frequency analysis of N-H proton donor involved in intramolecular hydrogen bonding substantiates the nature of possible ESIPT present in the system (Chansen et al. 2017; Lan and Liu 2015; O. Hubin et al. 2014; Zhao et al. 2015). Han and co-workers proposed that the observed bathochromic shift or hypsochromic shift at excited

state in vibrational spectra strongly correlates with the corresponding strengthening or weakening of intramolecular hydrogen bonding (Zhao and Han 2007, 2008). N-H stretching vibrations were recorded for all the molecules at S0 and at S1 to evaluate ESIPT process. The peak at $\sim 3473\text{ cm}^{-1}$ corresponds to N-H stretching exhibited a bathochromic shift of approximately 23 cm^{-1} at S1 with intensity higher in comparison with S0 for all the molecules as shown in Fig. 6.17 and Fig. 6.18. The observed bathochromic shift supports the strengthening of intramolecular hydrogen bond and probable excited state proton transfer concurrent in the system (Lu et al. 2018; Wang et al. 2018, 2019). The effect of redshift observed is strongly connected to the proton transfer barrier, the stronger the redshift, the lower is the potential barrier and the easier the proton transfer (Chansen et al. 2017). The stronger the red-shift the weaker the energy of interaction between proton and proton donor. The weakening of energy further favors proton acceptor moiety to capture the proton that is leaving the donor. Further, higher the intensity or the stronger the oscillation of the vibrational modes suggest that the bonds tend to become less rigid, in turn favoring the proton transfer. Table 6.4 provides the computed vibrational stretching frequencies for all the molecules at ground and excited state with their relative frequency shift.

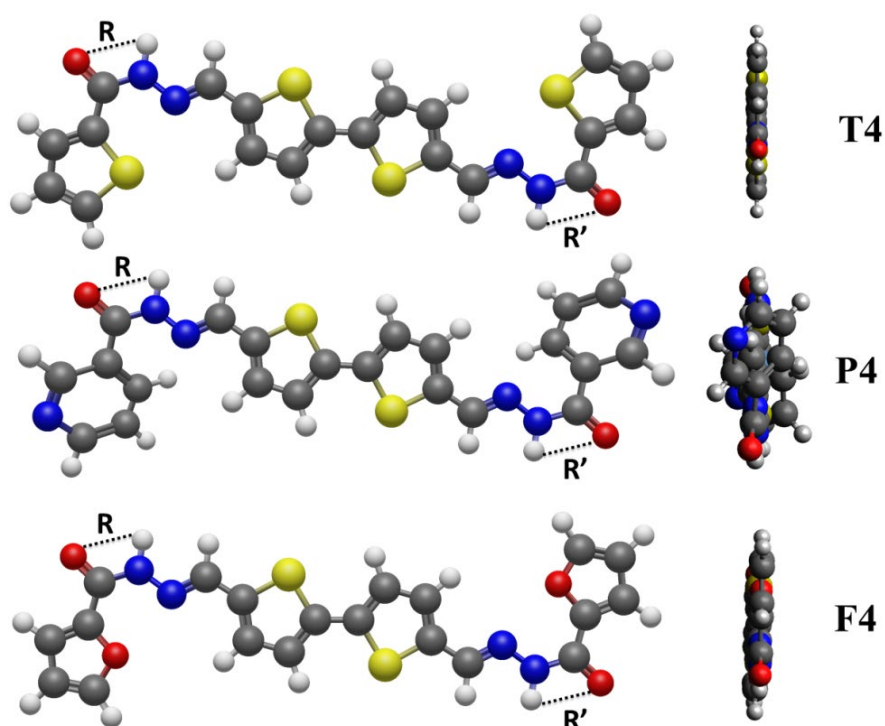


Fig. 6.14 Ground state geometry optimized normal form (k) of TX, PX, FX, where X=4, Color code: O-atoms, red; C-atoms, grey; N-atom: blue, S- atoms, yellow; H-atoms, white.

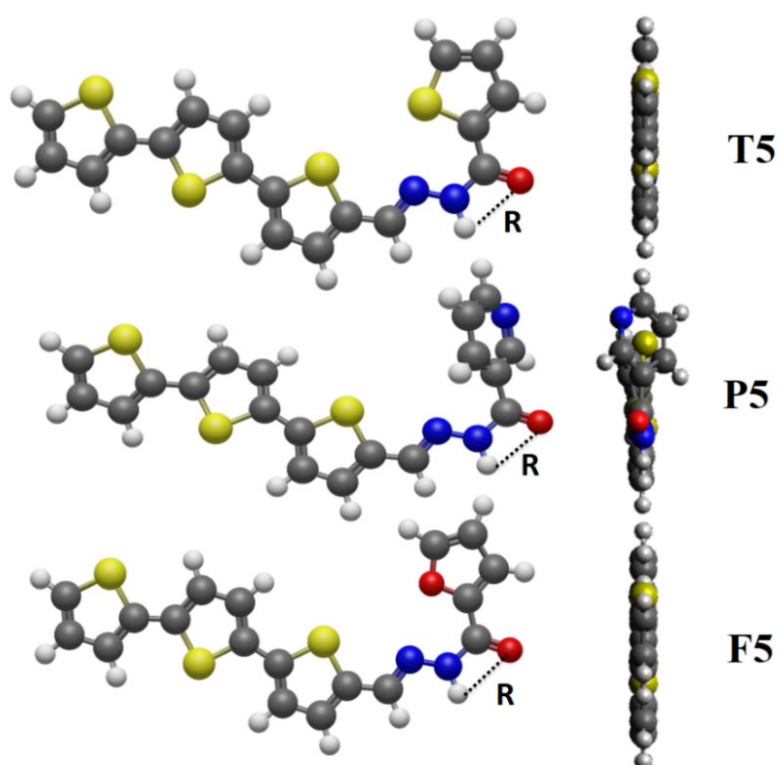


Fig. 6.15 Ground state geometry optimized normal form (k) of TX, PX, FX, where X=5
Color code: O-atoms, red; C-atoms, grey; N-atom: blue, S- atoms, yellow; H-atoms, white.

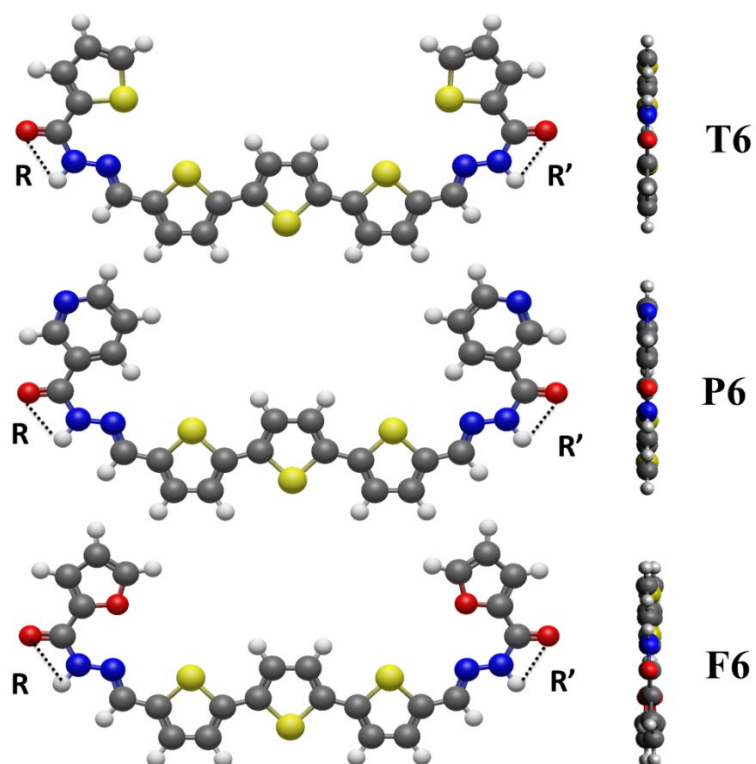


Fig. 6.16 Ground state geometry optimized normal form (k) of TX, PX, FX, where X=6,
Color code: O-atoms, red; C-atoms, grey; N-atom: blue, S- atoms, yellow; H-atoms, white

Table 6.3 Geometrical parameters of the molecules at S0 and S1

Molecule	N-H distance (Å)		R (Å)		R' (Å)	
	S0	S1	S0	S1	S0	S1
T4	1.0189	1.0186	2.3963	2.3888	2.3963	2.3888
P4	1.0196	1.0191	2.4066	2.3890	2.4066	2.3890
F4	1.0198	1.0196	2.3759	2.3643	2.3759	2.3643
T5	1.019	1.018	2.396	2.390	-	-
P5	1.019	1.019	2.405	2.389	-	-
F5	1.020	1.019	2.376	2.366	-	-
T6	1.019	1.0177	2.395	2.3914	2.395	2.3914
P6	1.020	1.0182	2.397	2.3942	2.397	2.3942
F6	1.020	1.0186	2.376	2.3696	2.376	2.3696

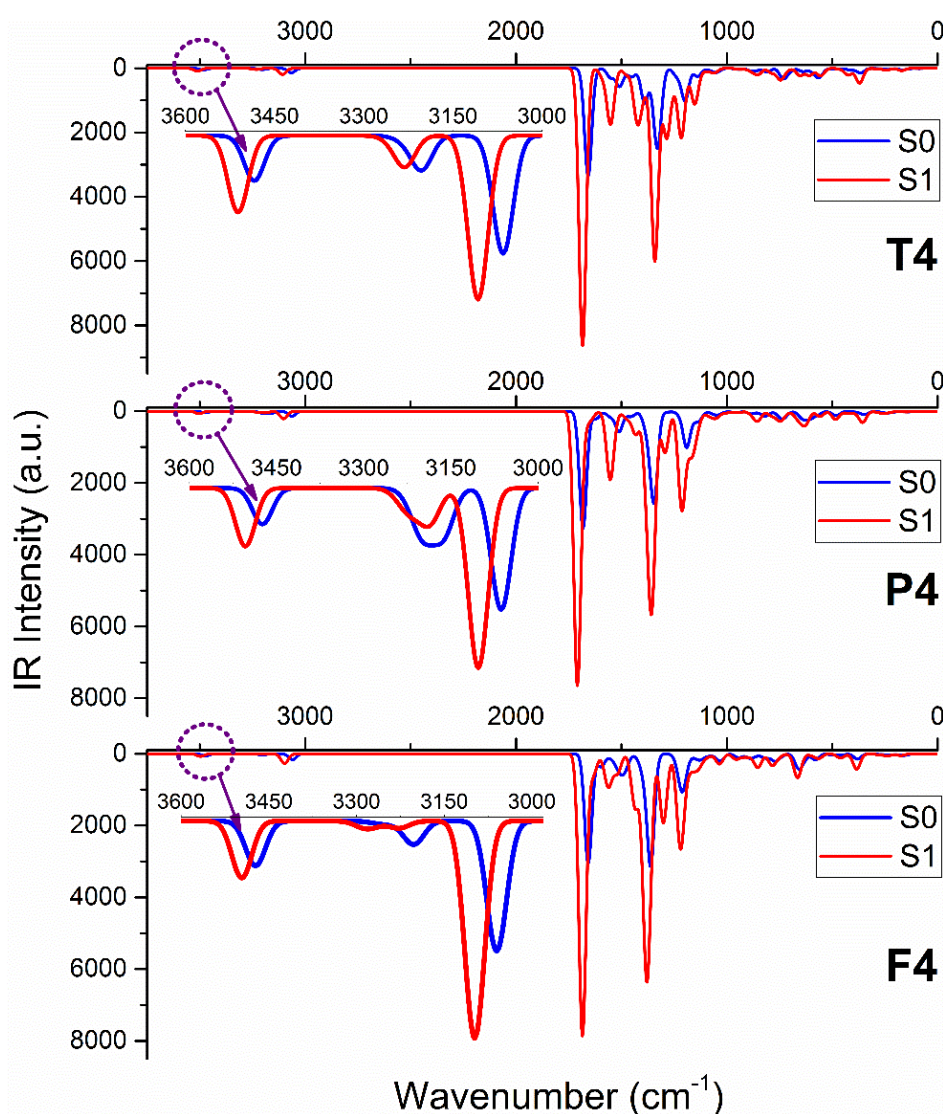


Fig. 6.17 Vibrational stretching frequency of TX, PX, FX, where X=4, in S0 and S1 states; specifically focusing N-H stretching frequency

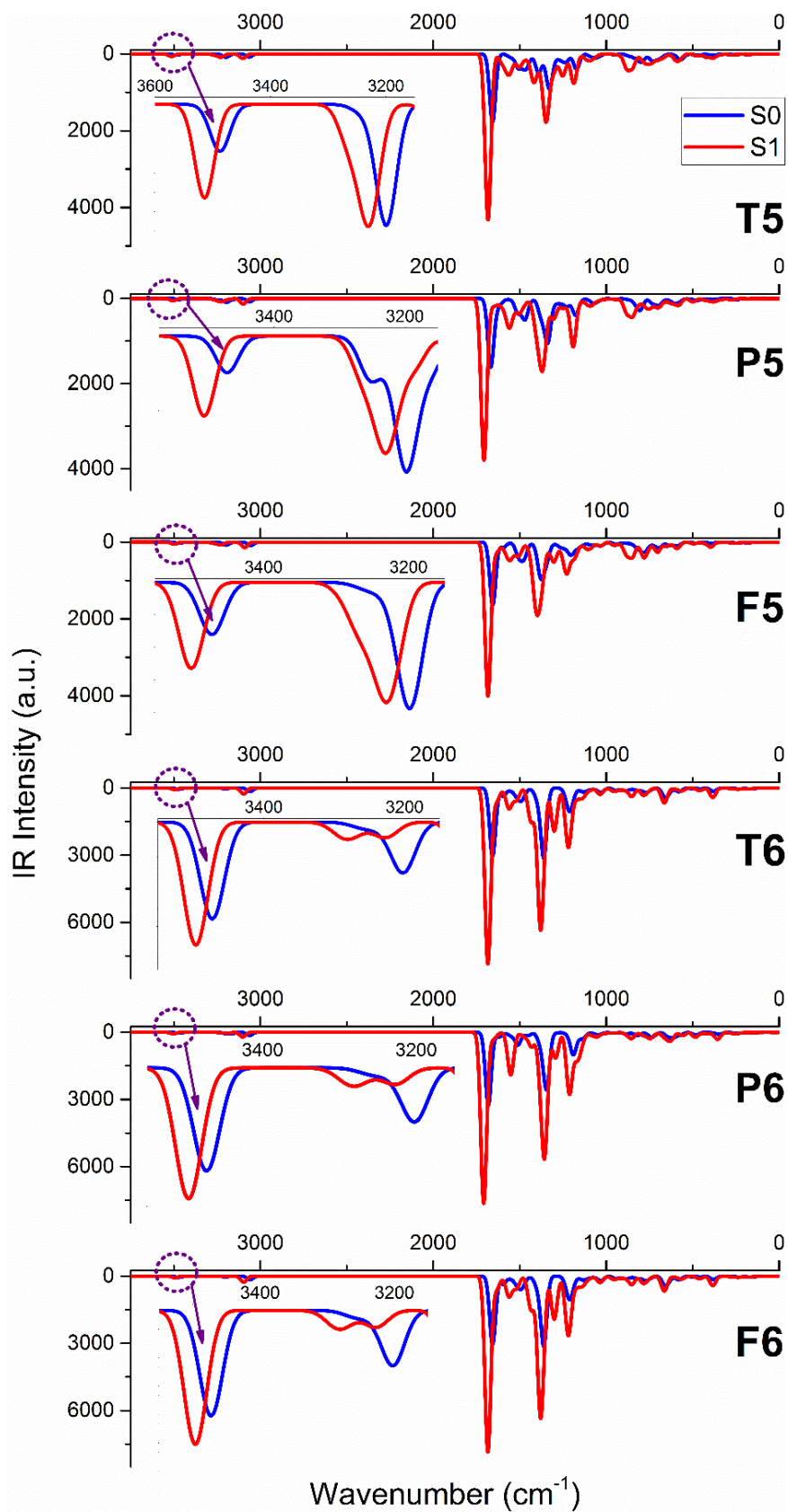


Fig. 6.18 Vibrational stretching frequency of TX, PX, FX, where X=5,6, in S0 and S1 states; specifically focusing N-H stretching frequency

Table 6.4 Computed vibrational NH stretching frequency at ground and excited state

Mol	N-H Stretching (cm ⁻¹)		Shift (cm ⁻¹)	Mol	N-H Stretching (cm ⁻¹)		Shift (cm ⁻¹)	Mol	N-H Stretching (cm ⁻¹)		Shift (cm ⁻¹)
	S0	S1			S0	S1			S0	S1	
T4	3473	3496	23	T5	3488	3514	27	T6	3473	3496	23
P4	3473	3497	24	P5	3471	3507	35	P6	3473	3496	23
F4	3473	3496	23	F5	3473	3500	27	F6	3473	3496	23

6.3.8 Electronic spectra and molecular orbitals analysis

To corroborate the concept of ESIPT, the nature of electronic transition arising due to the contribution of electronic density and frontier molecular orbitals were visualized. Energy gap plays a crucial role in governing the kinetic stability, chemical hardness and chemical reactivity of the system. Highest occupied molecular orbitals (HOMO), lowest unoccupied molecular orbitals (LUMO) and the energy gap (E_G) of all the molecules is provided in Fig. 6.19. Jarczyk-Jedryka and co-workers have optimized **T4** and **F4** using PCM solvation model with dichloromethane as a solvation medium (Jarczyk-Jedryka et al. 2016). The HOMO and LUMO values reported by Jarczyk-Jedryka is identical with the results reported herein; however, the slight energy differences observed arise due to the selection of basis set and the solvent medium considered. The major contribution of electronic transitions from $S_0 \rightarrow S_1$ and $S_1 \rightarrow S_0$ observed for k form and e form is governed by HOMO and LUMO orbitals with CI ~92% to ~96% as provided in Table 6.5. The contribution from HOMO-1 and LUMO+1 orbitals are quite insignificant and hence the discussion herein is solely restricted to HOMO and LUMO orbitals. The electronic distribution of HOMO and LUMO is mainly distributed over bithiophene and trithiophene core, and a portion of the hydrazide group excluding the heterocyclic ring on either side as observed (Jarczyk-Jedryka et al. 2016). The nature of electronic transition arising from HOMO and LUMO is of $\pi-\pi^*$ type, and one can conclude that the transitions occurring within the system is mainly supported by the central core. The energy gap of **T4**, **F4**, and **P4** is nearly the same owing to their structure possessing similar compositions (Jarczyk-Jedryka et al. 2016) and a similar trend is observed for trithiophene core as illustrated in the Fig. 6.20 and Fig. 6.21. Electronic cloud surrounding (N-H) proton donor at LUMO level shrinks to a larger extent in comparison to that observed at the HOMO level, and such

changes were not observed for the proton acceptor moiety (C=O) (Hao and Yang 2018). Such observed changes over electronic cloud support good interactions between proton donor and acceptor moieties heading towards a better proton translocation at the S1 as observed for all the molecules (Hao and Yang 2018, 2019; Kanlayakan et al. 2017).

Ground state optimized geometries of the molecules were considered for spectral calculations under THF solvent medium. Solvents of higher polarity tend to form hydrogen bonding with solute particles, in turn altering the spectral behavior of the system (Cheng et al. 2015). Such tendencies can be easily suspended by careful selection of solvent medium, this being the reason, both the theoretical and the experimental studies were carried out in THF solvent. The experimental emission spectra of **T4**, **P4**, and **F4** exhibited pronounced dual emission bands in THF solvent supportive of ES IPT. However, this dual emission was curbed when the system is treated with solvents of higher dielectric constants supporting intermolecular hydrogen bonding (Kasha 1986). The simulated spectra associated with keto absorbance (k abs), keto emission (k emi) and enol emission (e emi) for **T4**, **P4** and **F4** is as shown in Fig. 6.22, while, k abs*, k emi* and e emi* highlights the experimental values. The simulated discrete energy values obtained were then broadened by scaling up the value of FWHM to 30 nm. Theoretically estimated absorption spectra for **T4**, **P4** and **F4** centered at 404 nm, 394 nm and 398 nm respectively correlate well with experimental values centered at 415 nm, 397 nm and 406 nm. The energy difference estimated using CAM-B3LYP functional at excited state for all **T4**, **P4** and **F4** falls below an overestimated energy difference of less than 0.08 eV. Experimentally observed electronic transitions from S1→S0 giving rise to tautomer emission is higher in magnitude in comparison with the emission recorded for the normal form. This trend is perfectly reproduced in theoretically estimated emission spectra for k form and e form. Further, theoretical calculation of **TX**, **PX** and **FX**, where X=5,6 were also performed to estimate the energy transition involving keto absorption, keto emission and enol emission in THF solvent medium. **T6**, **P6** and **F6** in comparison with **T4**, **P4** and **F4**, show a red shifted emission caused due to the presence of extended conjugation brought about by inclusion of a thiophene ring. Molar extinction coefficient of enol tautomer emission is higher in intensity in comparison with that of the keto tautomer emission, establishing the fact that the number of transitions corresponding to enol species is higher compared to keto tautomer.

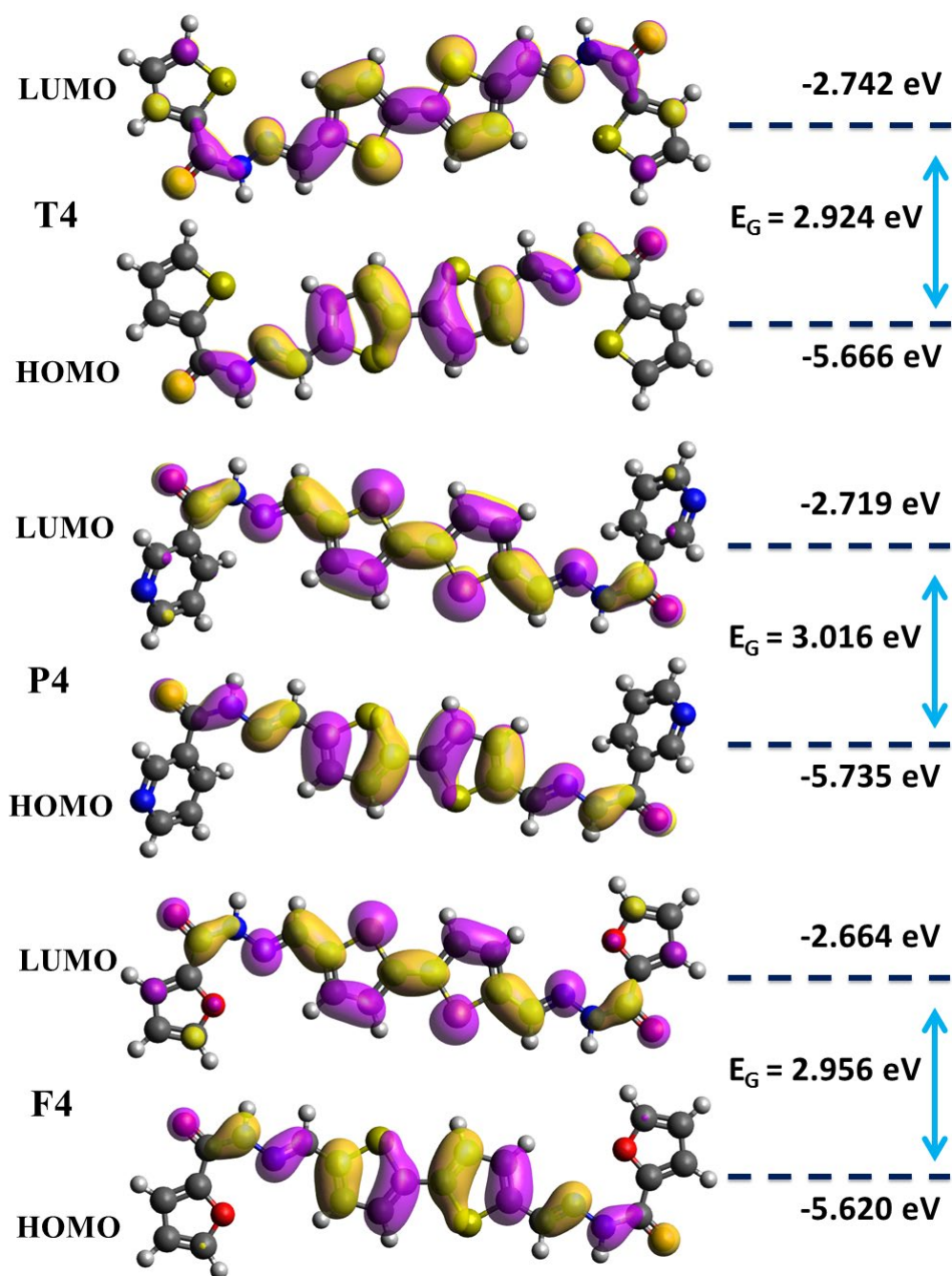


Fig. 6.19 Frontier molecular orbitals of T4, P4 and F4 in keto form

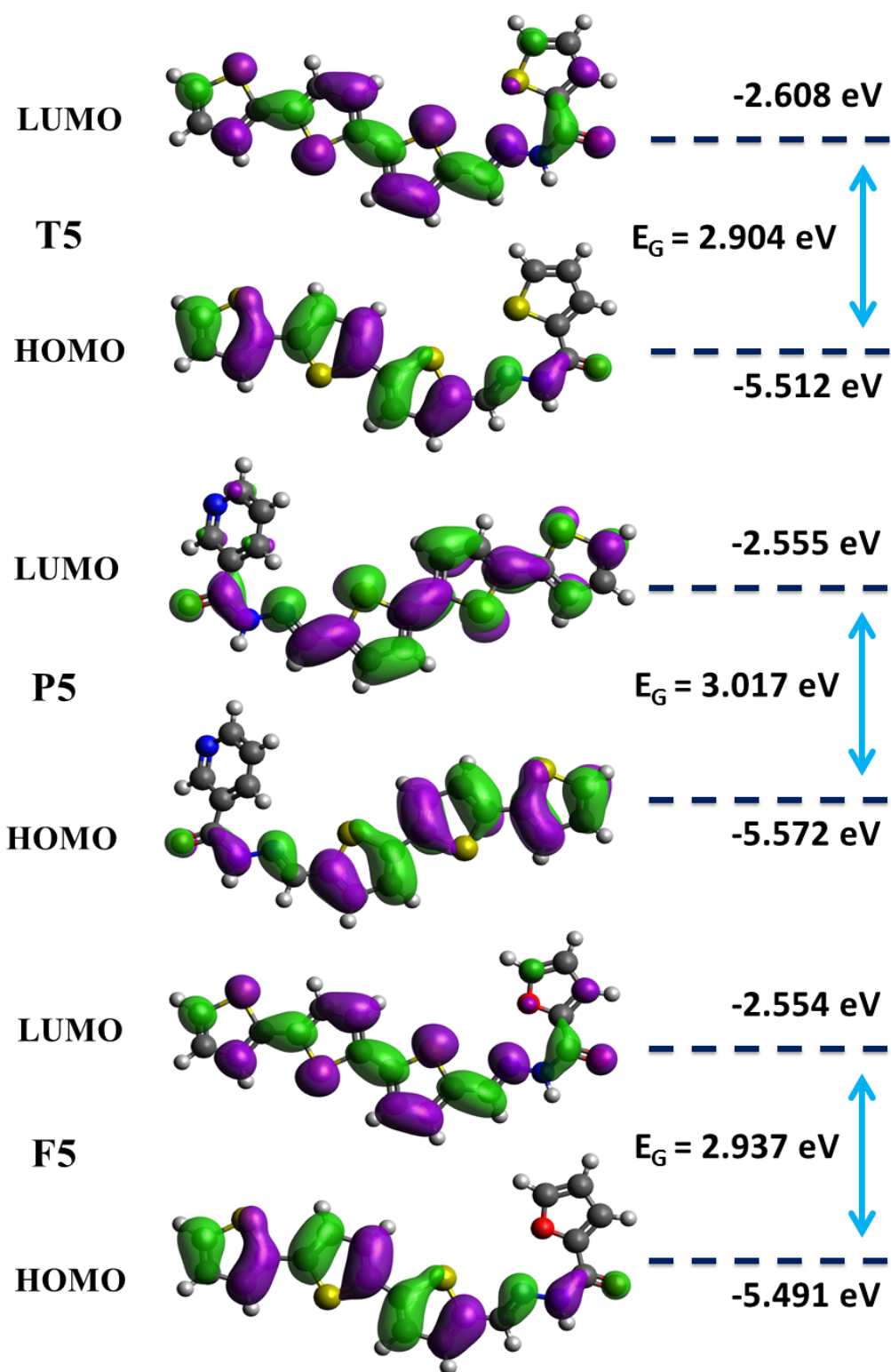


Fig. 6.20 Frontier molecular orbitals of T5, P5 and F5 in keto form

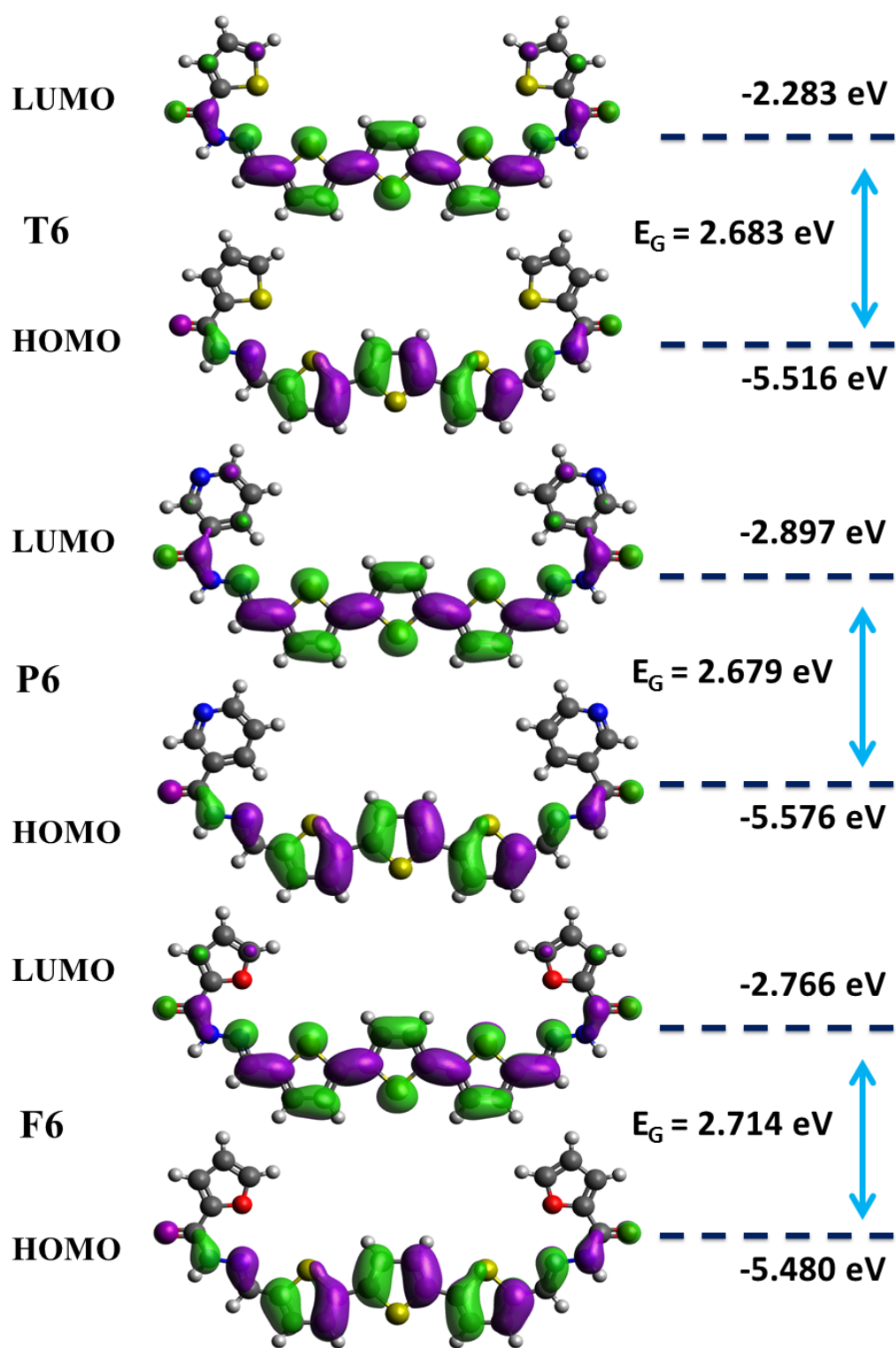


Fig. 6.21 Frontier molecular orbitals of T6, P6 and F6 in keto form

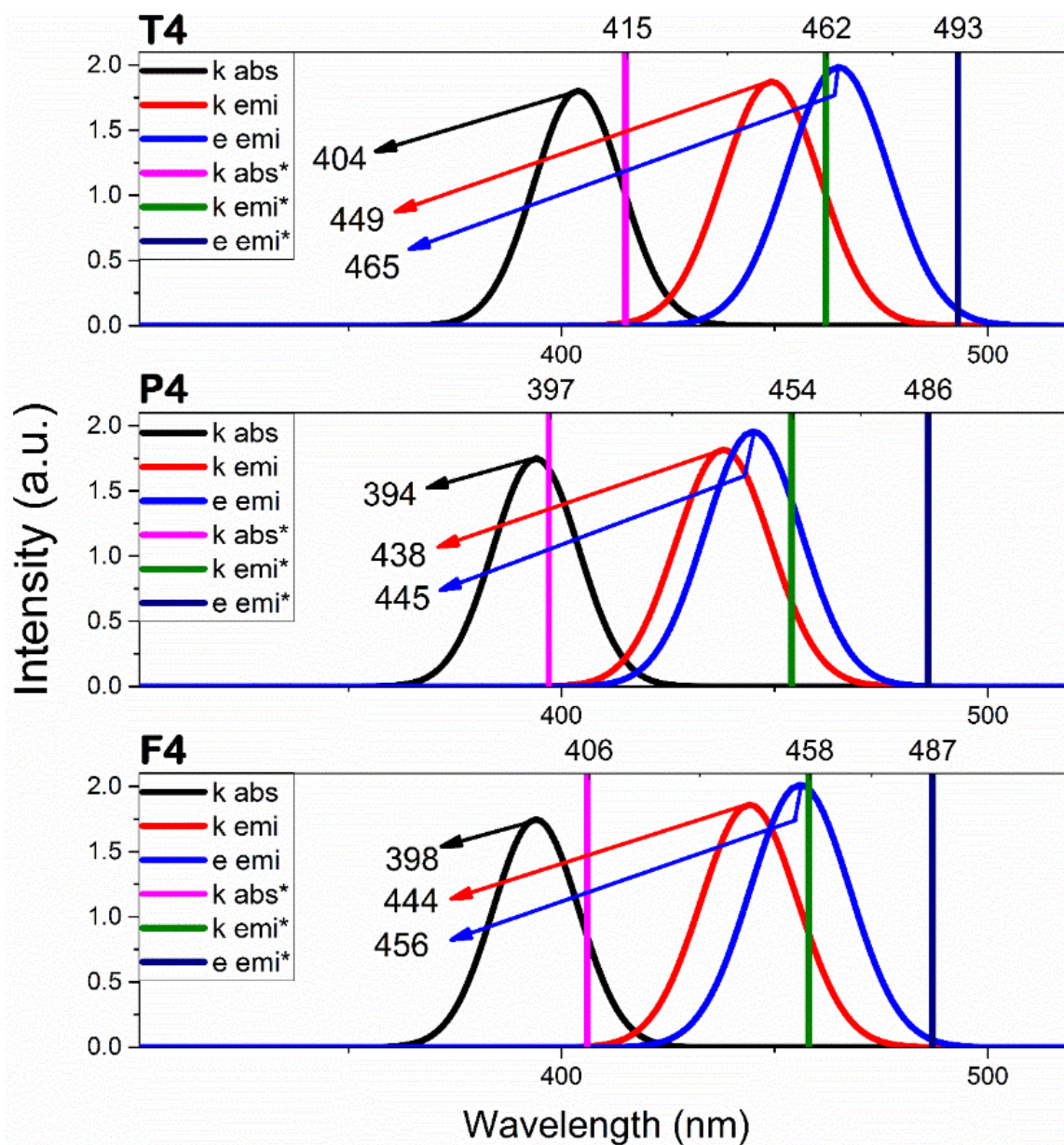


Fig. 6.22 Absorption and Fluorescence emission spectrum of all the TX, PX and FX, where X=4 with experimental values

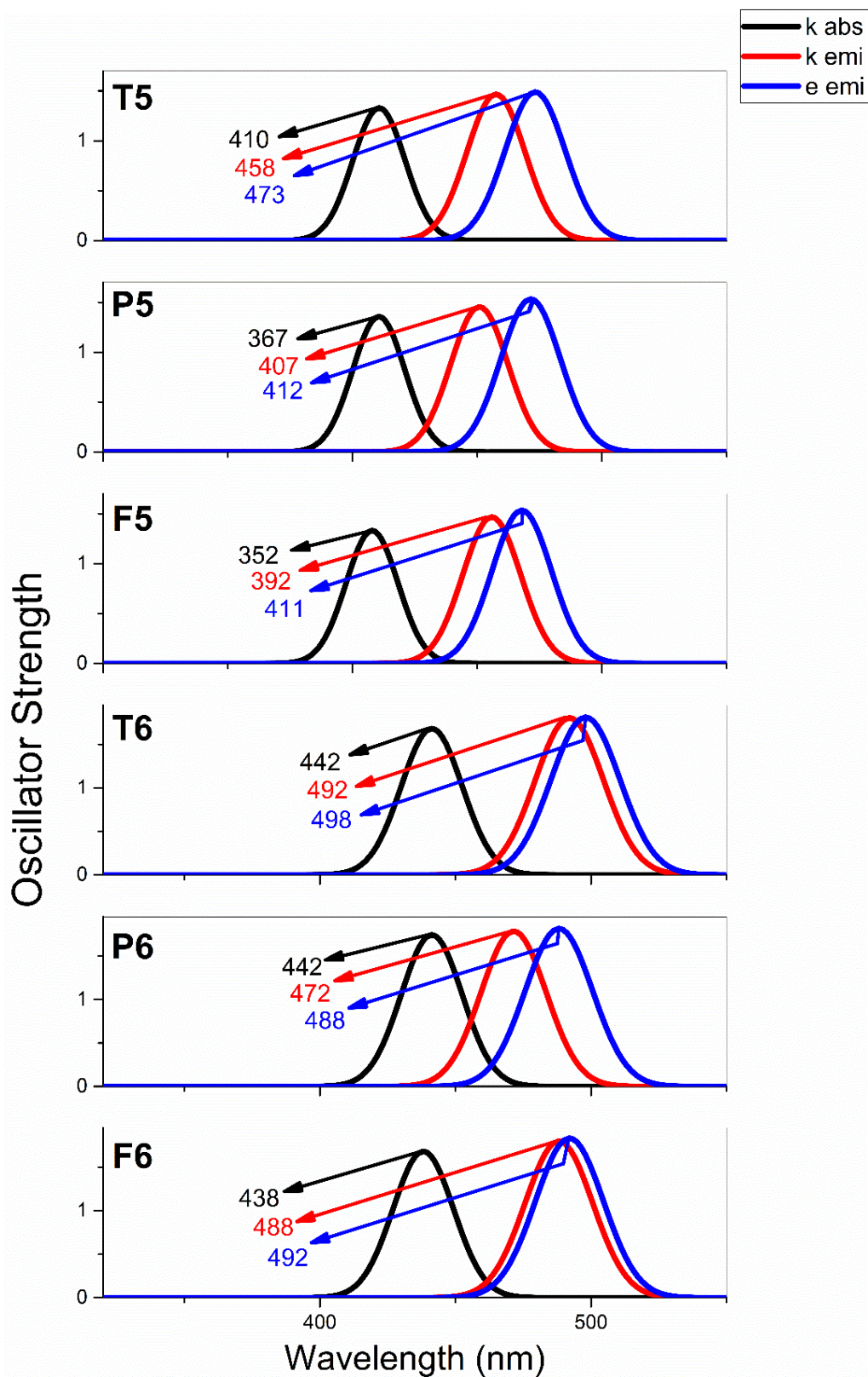


Fig. 6.23 Absorption and Fluorescence emission spectrum of all the TX, PX and FX, where X=5,6 with experimental values

Table 6.5 Computed optical parameters of molecules: keto absorbance and emission, enol emission, oscillator strengths, composition and CI(%) calculated at DFT/B3LYP and TD-DFT/CAM-B3LYP for ground and excited state

Mol	Type	Transition	Energy (nm)	Oscillator strength	Composition	CI (%)
T4	k abs	S0→S1	404	1.802	H(121)→L(122)	92.06
					H-1(120)→L+1(123)	4.11
	k emission	S1→S0	449	1.8717	H(121)→L(122)	95.35
					H-1(120)→L+1(123)	2.41
	e emission	S1→S0	465	1.9835	H(121)→L(122)	94.64
				H-1(120)→L+1(123)	3.05	
P4	k abs	S0→S1	394	1.7488	H(119)→L(120)	93.46
					H-1(118)→L+1(121)	3.41
	k emission	S1→S0	438	1.8173	H(119)→L(120)	95.95
	e emission	S1→S0	445	1.9562	H(119)→L(120)	95.37
					H-1(118)→L+1(121)	2.56
F4	k abs	S0→S1	398	1.8031	H(113)→L(114)	92.43
					H-1(112)→L+1(115)	4.24
	k emission	S1→S0	444	1.8611	H(113)→L(114)	95.6
					H-1(112)→L+1(115)	2.41
	e emission	S1→S0	456	2.0131	H(113)→L(114)	94.95
				H(112)→L(115)	2.93	
T5	keto A	S0→S1	411	1.3293	H(103)→L(104)	92.01
					H-1(102)→L+1(105)	2.54
	Keto E	S1→S0	459	1.467	H(103)→L(104)	95.82
	Enol E	S1→S0	475	1.4892	H(103)→L(104)	95.16
					H-1(102)→L+1(105)	2.74
P5	keto A	S0→S1	411	1.3573	H(102)→L(103)	91.81
					H(101)→L+1(104)	2.12
	Keto E	S1→S0	451	1.4555	H(102)→L(103)	96.24
	Enol E	S1→S0	472	1.5332	H(102)→L(103)	95.21
					H(101)→L+1(104)	2.31
F5	keto A	S0→S1	408	1.3324	H(99)→L(100)	92.92
					H(98)→L+1(101)	3.02
	Keto E	S1→S0	456	1.4677	H(99)→L(100)	96.06
	Enol E	S1→S0	469	1.5352	H(99)→L(100)	95.42
					H(98)→L+1(101)	2.68
T6	keto A	S0→S1	442	1.6814	H(142)→L(143)	90.51
	Keto E	S1→S0	492	1.805	H-1(142)→L+1(143)	94.44

					H-1(141)→L+1(144)	3.00
	Enol E	S1→S0	498	1.8124	H(142)→L(143)	93.77
					H-1(141)→L+1(144)	3.44
P6	keto A	S0→S1	441	1.7426	H(140)→L(141)	90.68
	Keto E	S1→S0	472	1.7855	H-1(140)→L+1(141)	94.98
					H-1(139)→L+1(142)	2.86
	Enol E	S1→S0	489	1.8154	H(140)→L(141)	94.54
					H-1(139)→L+1(142)	3.04
F6	keto A	S0→S1	438	1.6823	H(134)→L(135)	90.96
	Keto E	S1→S0	488	1.7996	H-1(134)→L+1(135)	94.68
					H-1(133)→L+1(136)	3.02
	Enol E	S1→S0	493	1.8339	H(134)→L(135)	94.08
					H-1(133)→L+1(136)	3.35

6.3.9 Potential Energy Scan

Potential Energy Curve (PECs) reveals the dynamics of proton transfer and provides valuable information concerning the proton transfer pathway upon photoexcitation. Potential energy scans were recorded for S0 with B3LYP and S1 with CAM-B3LYP to assess the forward and reverse potential barrier for proton translocation between donor and acceptor moieties. Scans were performed with constrained O-H bond length following optimization of geometry under THF solvation sphere. Approximations of the results derived from computational methods may not be precise with the experimental values; however, the previous reports have significantly validated the method to produce qualitative proton transfer pathways (Saga et al. 2010; Serrano-Andrés and Merchán 2009; Sobolewski and Domcke 1999; Song and Ma 2013). Potential energy curves have been constructed for a complete rotation of 0°-180° between the carbonyl and –NH group. Variation in potential energy as a function of dihedral angle for all the molecules is given in Fig. 6.24 to Fig. 6.26. The optimized structures with zero dihedral angles between the plane connecting –NH and –C=O seems to be energetically more stable than that with 180° dihedral as evident from the values at the extremities of the curve. The nature of the graph validates the possible occurrence of ESIPT for hydrazides possessing thiophene and pyridine. However, structure possessing furoic hydrazide seems to show different behavior and establishes difficulties in ESIPT.

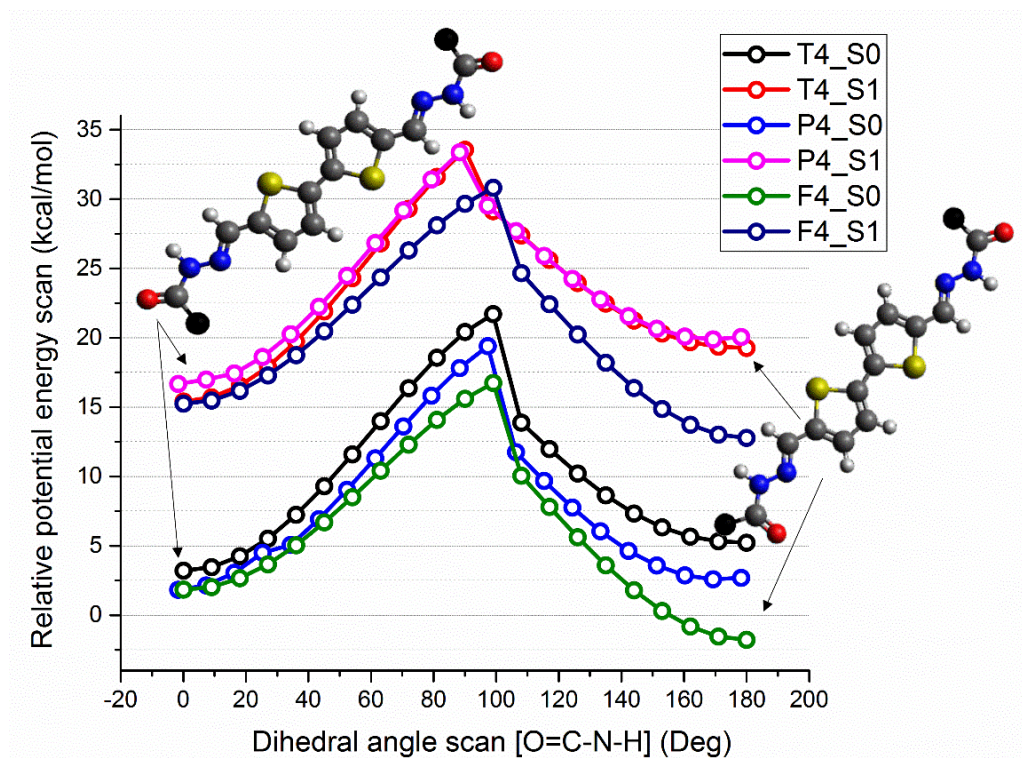


Fig. 6.24 SP energies of T4, P4, F4 as a function of rotation of dihedral angle for S0 and S1

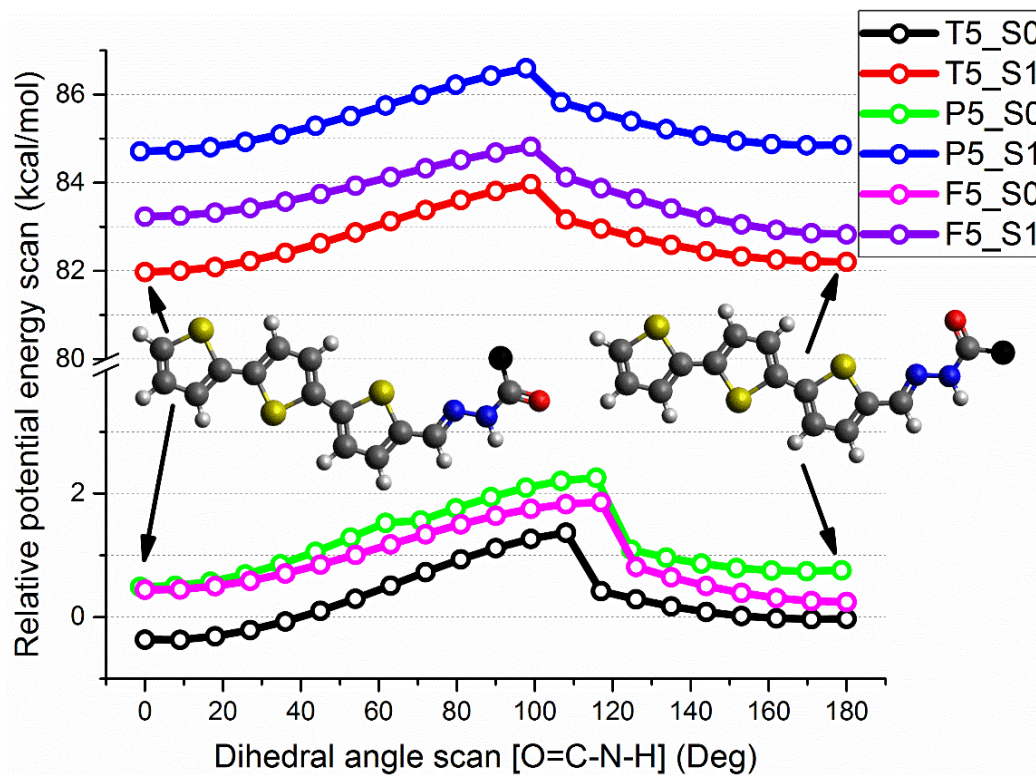


Fig. 6.25 SP energies of T5, P5, F5 as a function of rotation of dihedral angle for S0 and S1

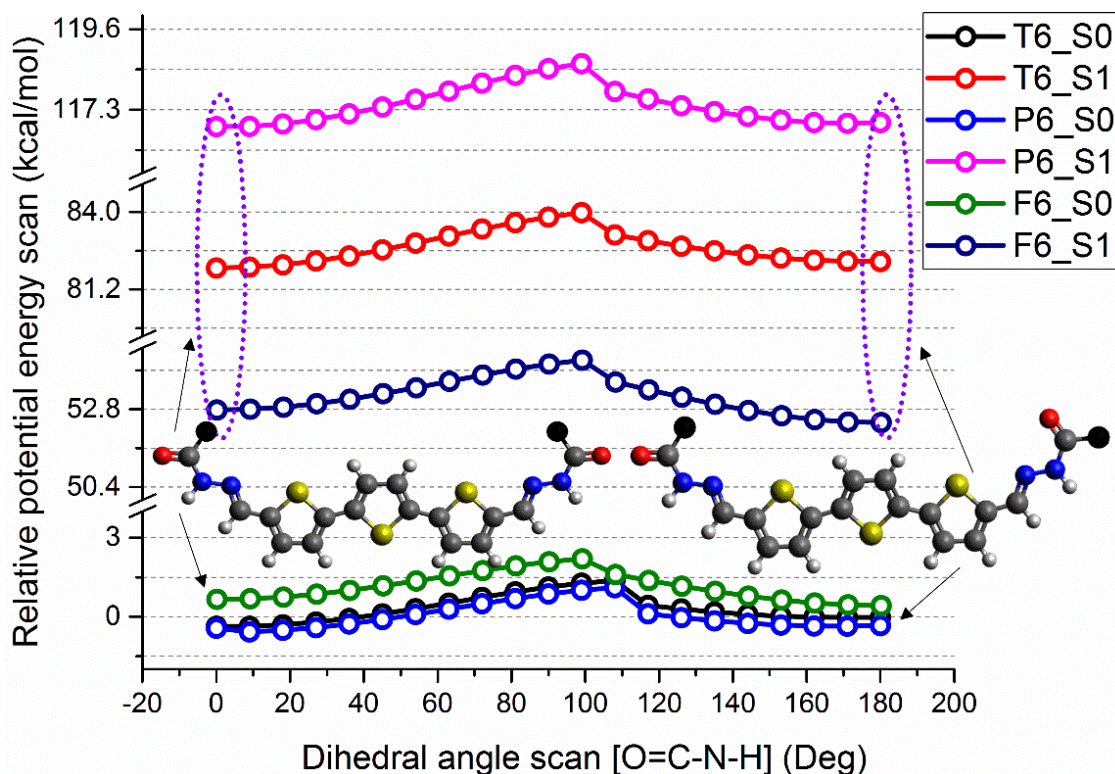


Fig. 6.26 SP energies of **T6**, **P6**, **F6** as a function of rotation of dihedral angle for S0 and S1

Potential energy curve of all the molecules is given in Fig. 6.27 to Fig. 6.35, wherein, the forward barrier is termed as FB and that of the reverse barrier as RB for both S0 and S1 states. Molecules of the series at their ground state acquire a thermodynamically stable k form, and upon photoexcitation alters to e form assisting ESIPT mechanism. Analysis of the PECs shows that the molecules need to overcome a FB potential of ~ 4.0 kcal/mol at their ground state to translocate a proton from a donor to an acceptor; however, this value comes down to ~ 3.95 kcal/mol at its excited state for **T4**, **P4** and **F4**. Reduction in potential barrier along the reaction pathway reveals a proton transfer likely to occur upon photoexcitation. However, addition of thiophene ring in the structure causes excited state FB of the system to show a greater value in comparison with that of its ground state. Results reveal that the extension of thiophene rings in the system may result in harder proton transfer at the excited state. The reverse barrier of all the molecules at their ground state is comparatively lower in energy with that of their excited state, and this further supports the reverse proton transfer termed as ground state intramolecular proton transfer (GSIPT). The reverse barrier for **P4** remains the same in both S0 and S1, may result in a harder GSIPT. Forward and reverse barrier potential of all the molecules estimated in ground and excited

state is provided in Table 6.6. In gist, the ESIPT mechanism for hydrazides with $-N-H$ acting as a proton donor and $-C=O$ acting as a proton acceptor could be understood as follows. At their ground state, intramolecular hydrogen bond formation occurs between the $-C=O$ acceptor group and the nearest $-N-H$ donor group. This intramolecular hydrogen bond then strengthens upon photoexcitation leading to translocation of a proton between the donor and acceptor moiety with a significant potential barrier. The system experiences maximum potential energy at an approximate O-H distance of 1.35\AA , and beyond this point, the energy of the system minimizes to acquire desired tautomeric structure. Excited state tautomer then undergoes spontaneous emission either radiative or non-radiative to reach its tautomer ground state. The structure further reverts to normal form by reverse proton transfer from $-C=O$ to $N-H$ moiety by crossing over a significant RB potential.

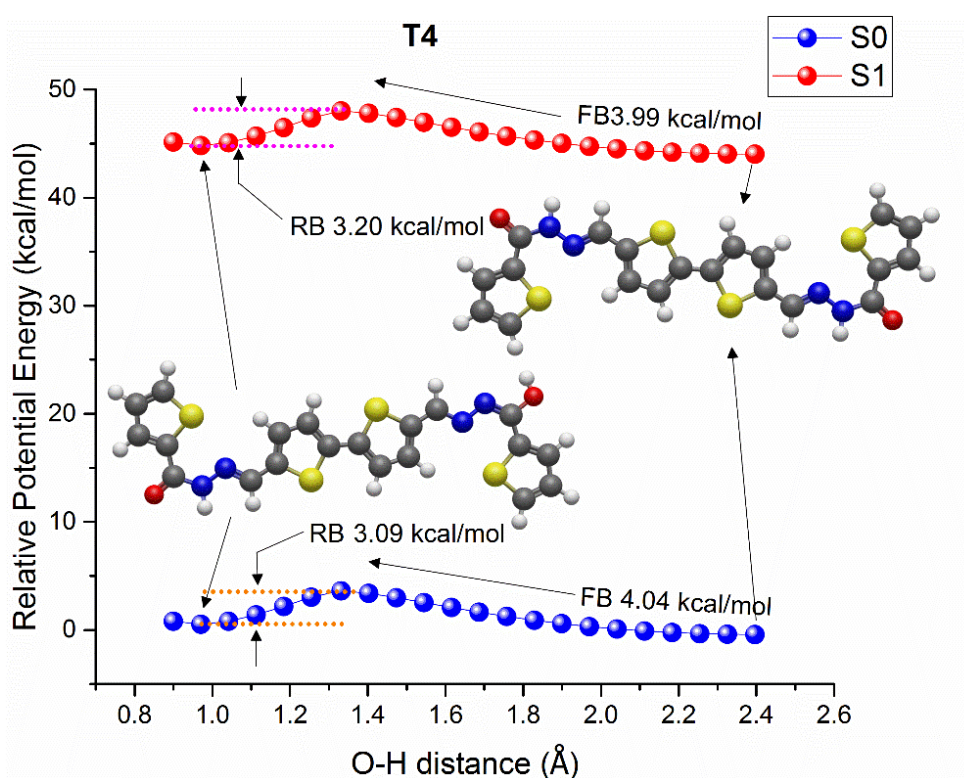


Fig. 6.27 SP energies of T4 in the S0 and S1 states calculated by B3LYP and CAM-B3LYP

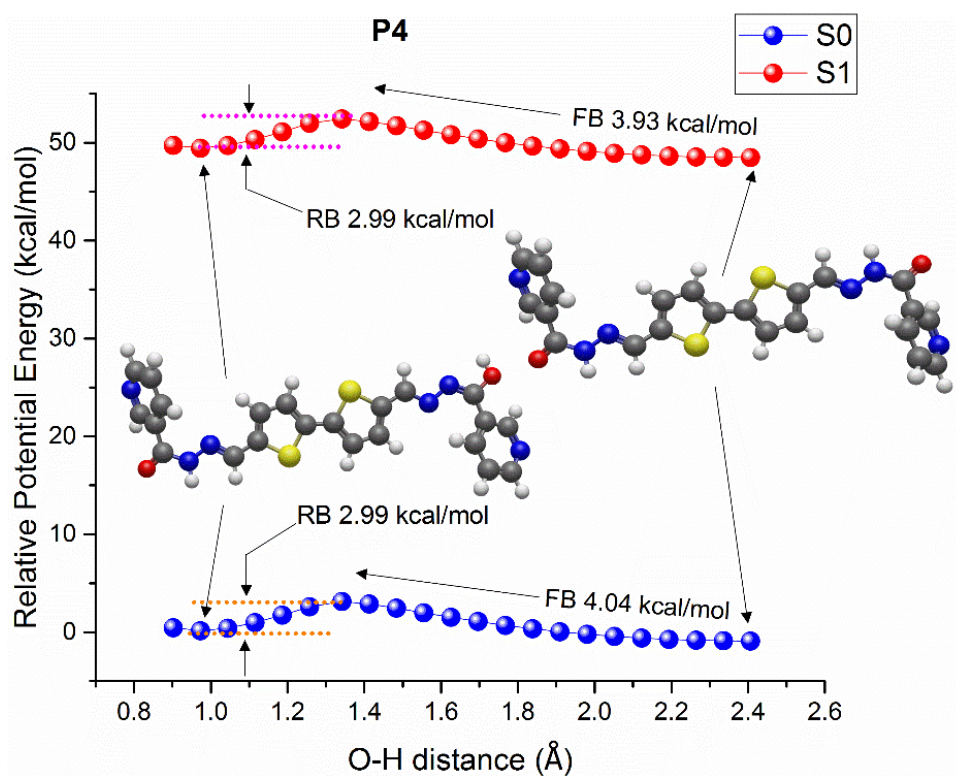


Fig. 6.28 SP energies of P4 in the S₀ and S₁ states calculated by B3LYP and CAM-B3LYP

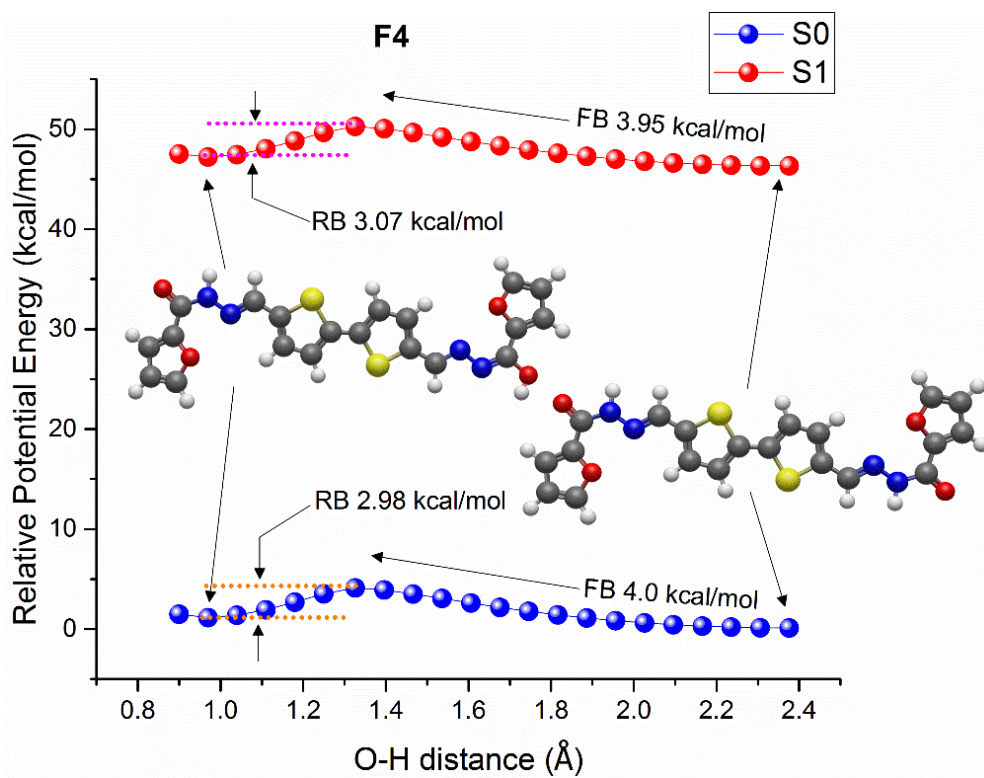


Fig. 6.29 SP energies of F4 in the S₀ and S₁ states calculated by B3LYP and CAM-B3LYP

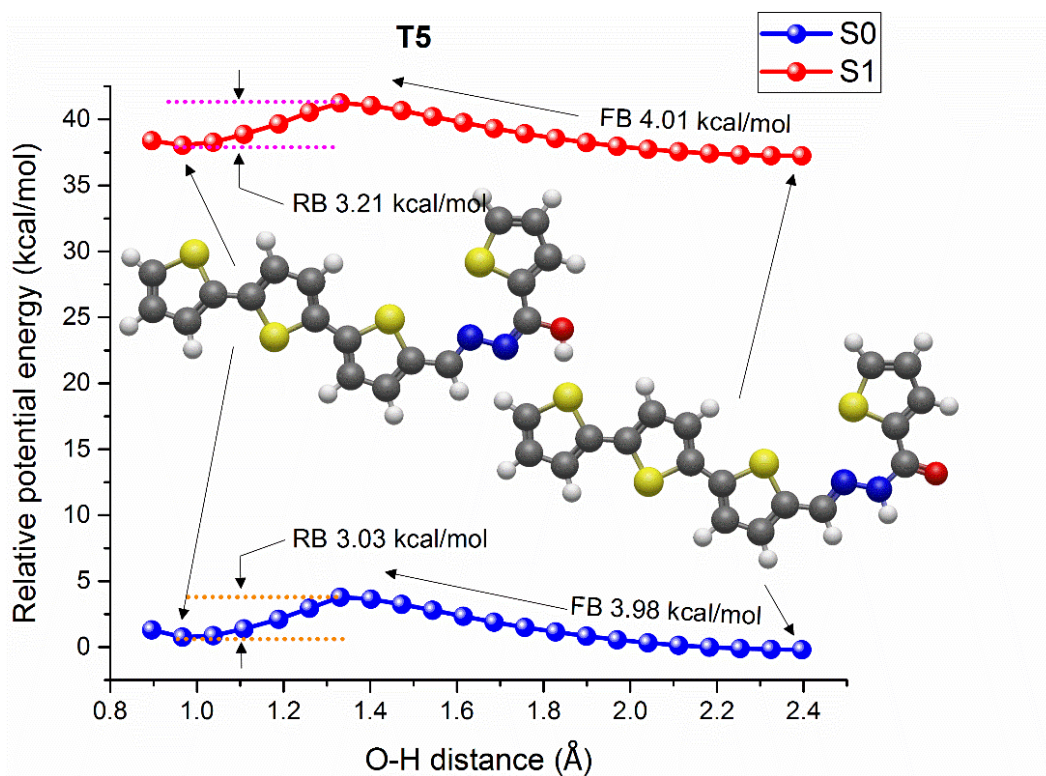


Fig. 6.30 SP energies of **T5** in the S0 and S1 states calculated by B3LYP and CAM-B3LYP

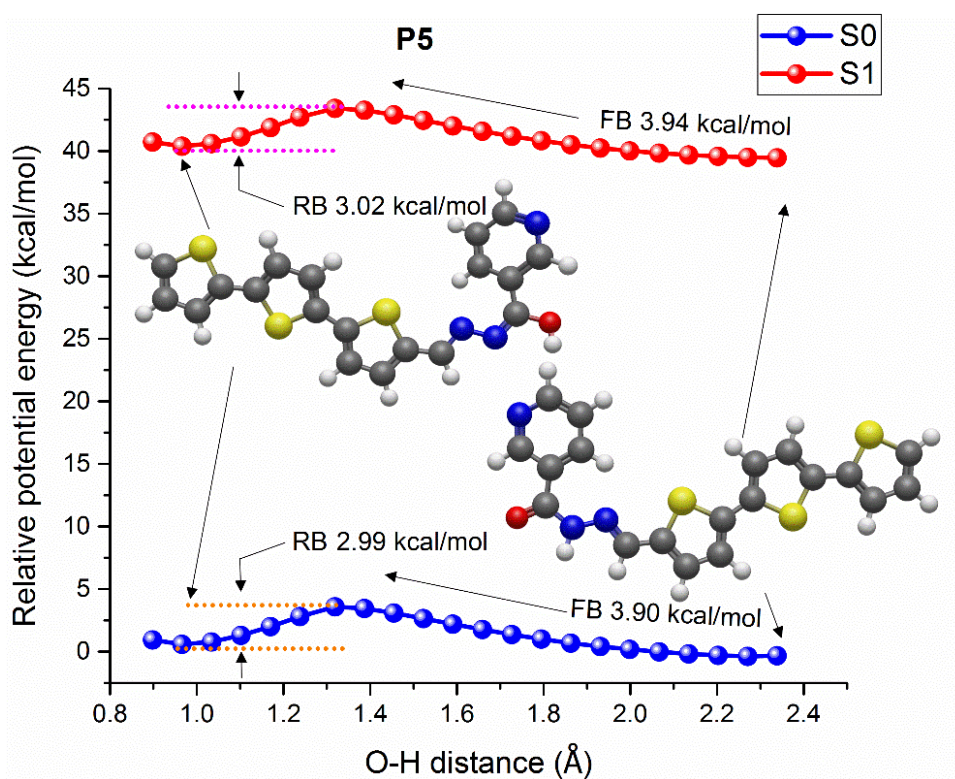


Fig. 6.31 SP energies of **P5** in the S0 and S1 states calculated by B3LYP and CAM-B3LYP

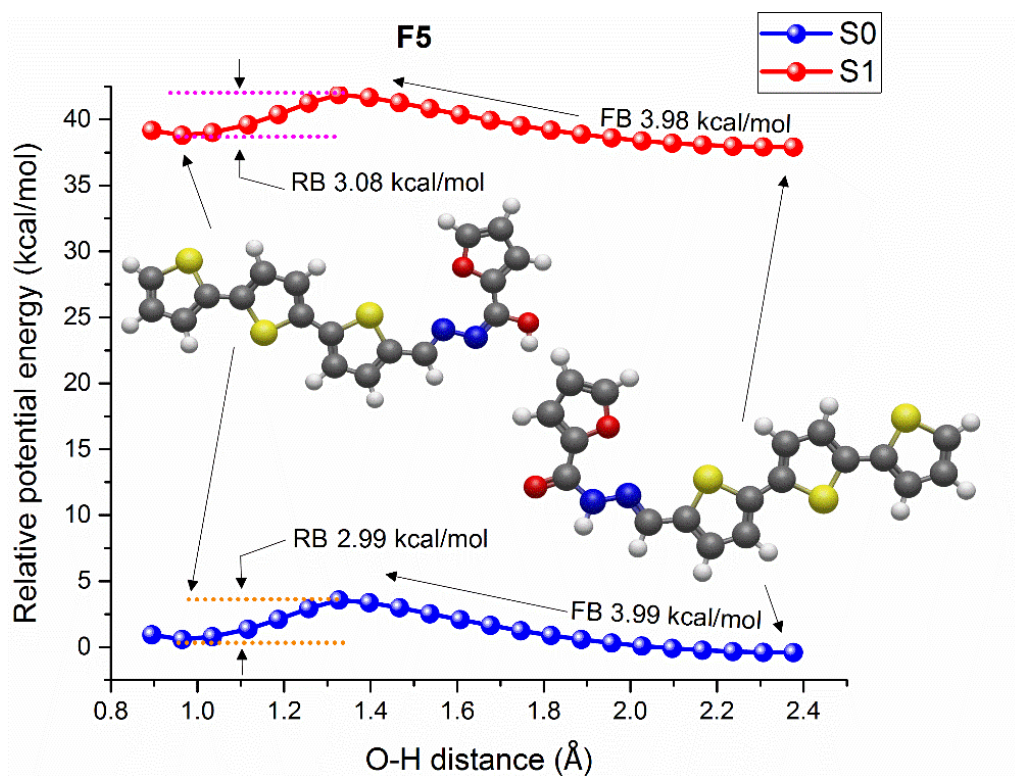


Fig. 6.32 SP energies of F5 in the S0 and S1 states calculated by B3LYP and CAM-B3LYP

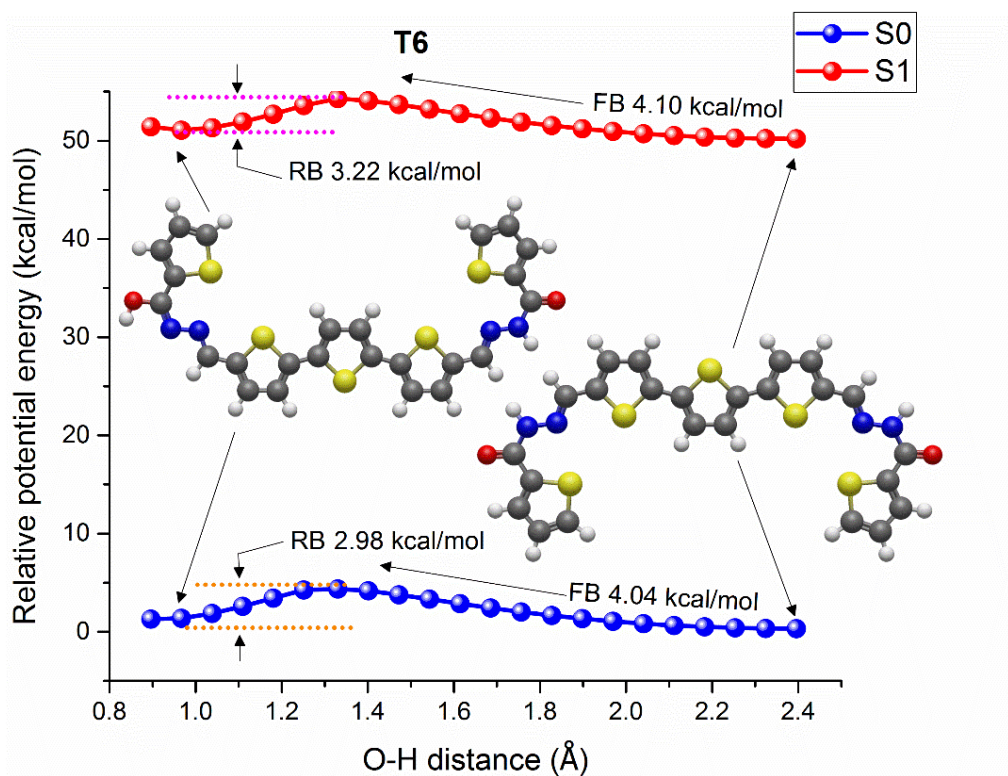


Fig. 6.33 SP energies of T6 in the S0 and S1 states calculated by B3LYP and CAM-B3LYP

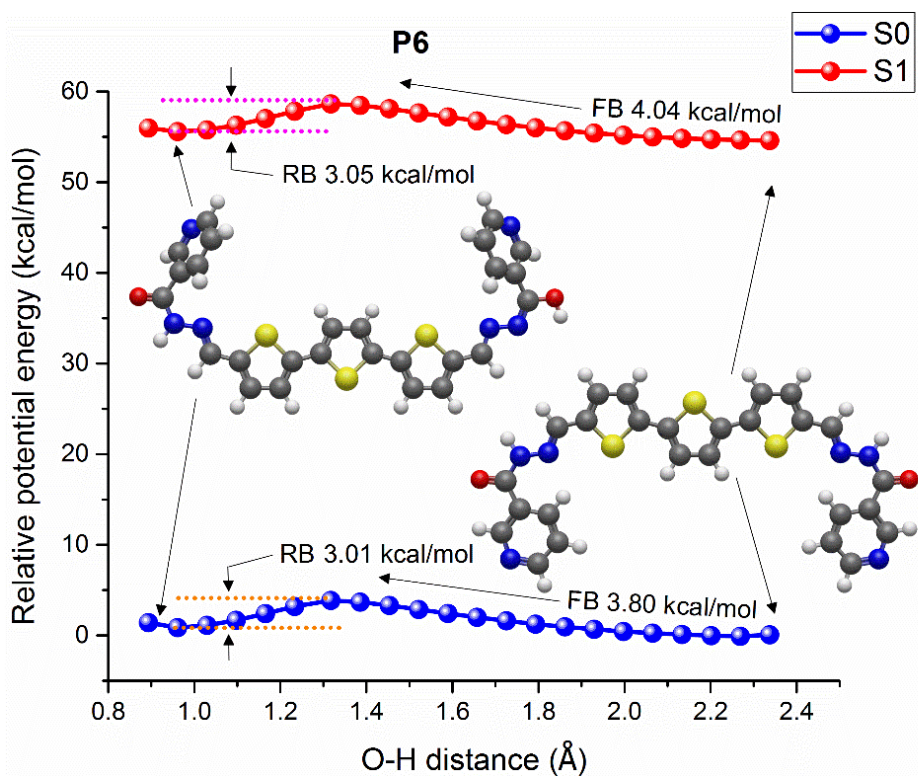


Fig. 6.34 SP energies of P6 in the S0 and S1 states calculated by B3LYP and CAM-B3LYP

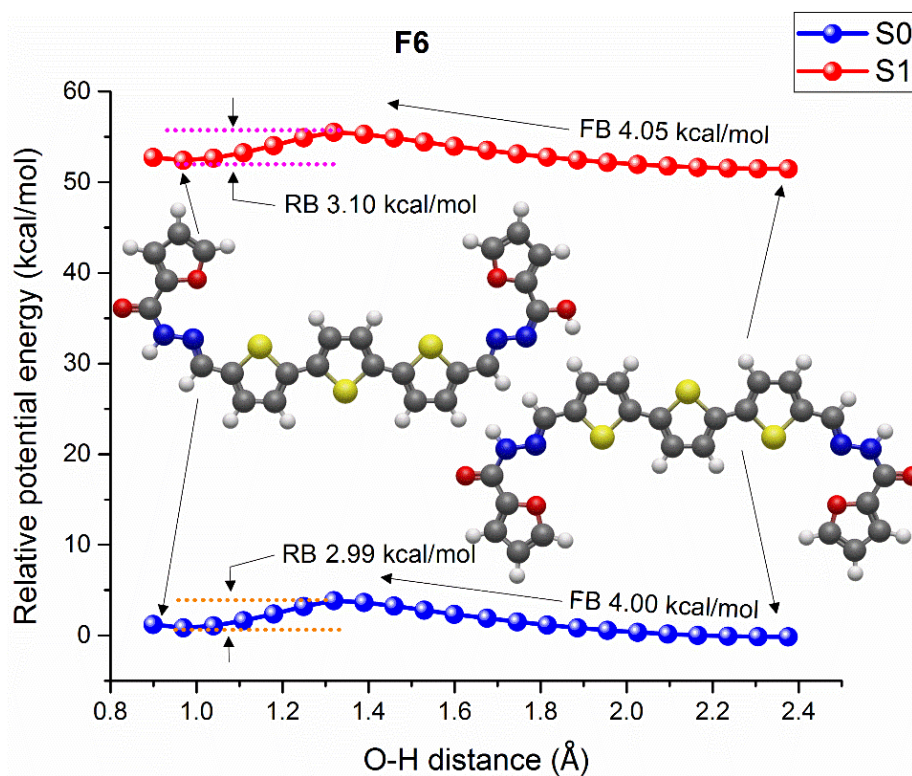


Fig. 6.35 SP energies of F6 in the S0 and S1 states calculated by B3LYP and CAM-B3LYP

Table 6.6 Forward and Reverse potential barrier at ground state S0 and excited state S1 for all the molecules of the series

Molecule	Forward Barrier (kcal/mol)		Reverse Barrier (kcal/mol)	
	S0	S1	S0	S1
T4	4.04	3.99	3.09	3.20
T5	3.98	4.01	3.03	3.21
T6	4.04	4.10	2.98	3.22
P4	4.04	3.93	2.99	2.99
P5	3.90	3.94	2.99	3.02
P6	3.80	4.04	3.01	3.05
F4	4.00	3.95	2.98	3.07
F5	3.99	3.96	2.99	3.08
F6	4.00	4.05	2.99	3.10

6.3.10 Potential Energy Surface Scan

Potential energy surface scans were performed to verify the occurrence of ambiguous double proton transfer initiated by the presence of hydrazides over both the arm. Scans were performed with DFT-B3LYP functional with 6-31G basis set for ground state and CAM-B3LYP with the same basis set for the excited state. This selection of the functional and basis set is expected to be reliable in providing qualitative energetic pathways for excited state proton transfer process. Nonetheless, an obvious error arises due to the mismatch in recognizing the order of closely spaced excited states (Du et al. 2019; Padalkar and Seki 2015; Wang et al. 2015; Zhou et al. 2015). The 3D potential energy surface for all the molecules for both S0 and S1 with their respective contour profile is provided in Fig. 6.36 to Fig. 6.41. The potential energy surfaces in both of their ground and excited states are highly symmetrical along the diagonal line. Further, the heteroatoms present in the ring did not have much influence on the shape of PES. The four minima present in PES correspond to k-form, e-form, and o-form, the estimated potential energy is in the order of $E_k < E_e < E_o$, which signifies that GSIPT is an endothermic process. In S0 and S1 state there exist a very high potential barrier of value ~ 8.2 kcal/mol for **TX** and **FX** for $X=4,6$ traced along the path (a→d). While this value of barrier potential is 7.9 kcal/mol for **P4** and **P6** traced along the same path. The double proton transfer in S0 or S1 is highly improbable due to the reaction pathway experiencing a very high potential barrier. Photoexcitation triggers the system to S1 state, wherein, one proton is likely to translocate with a minimal potential energy barrier traversing the path (a→c) or (a→b) to attain

tautomer e-form. When e form is attained, the second proton transfer process may occur via a step-wise double proton transfer provided the system gets sufficient energy to overcome a significantly higher barrier potential of 4.12 kcal/mol along the path (c→e) or (b→e). Higher barrier potential along the path (c→e) or (b→e) is not in favor of second proton translocation, thus hindering the step-wise double proton transfer kinetically, observed in all the systems. Even at instance if we suppose a step-wise double proton transfer occurs and the system achieves o-form viz (a→b→e or a→c→e), the reverse barrier of ~2.8 kcal/mol from (e→c) or (e→b) is significantly less compared to the forward barrier, this in-turn reverts the structure back to e-form. The reverse barrier from (e→c) or (e→b) is comparatively less than (b→a) or (c→a) leading to a faster GSIPT. Hence, based on the above discussion we claim the hetero-substituted hydrazides to support single proton transfer alone at their excited state with a relatively tricky double proton transfer or step-wise double proton transfer.

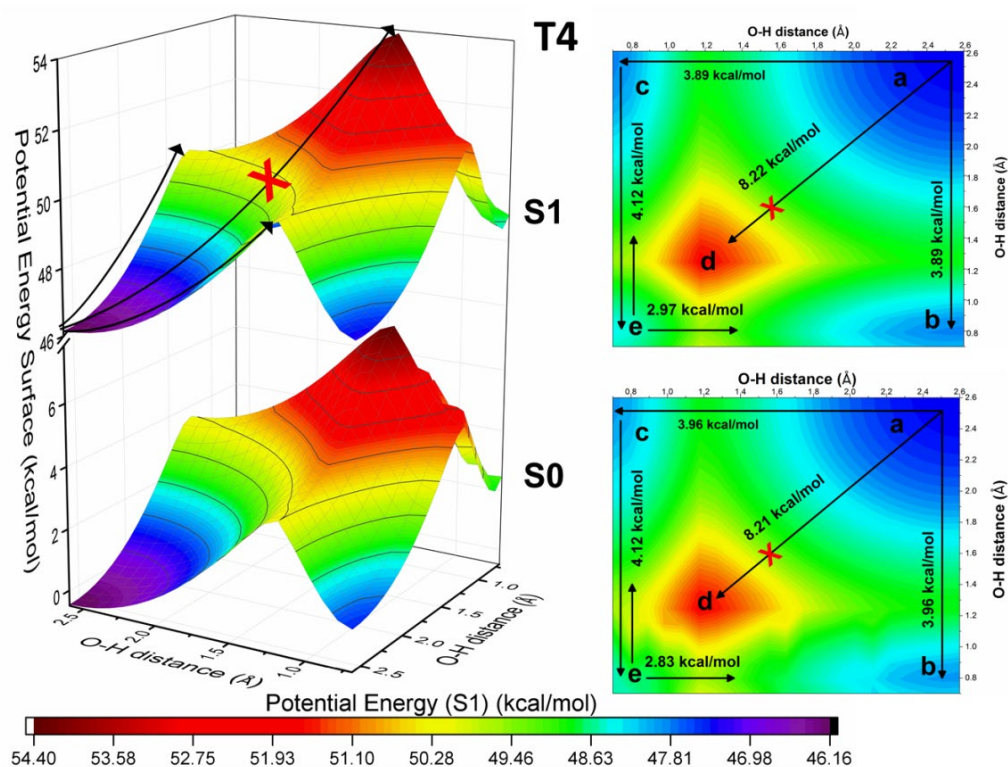


Fig. 6.36 PES scan of T4 in S0 and S1 states with their contour profile

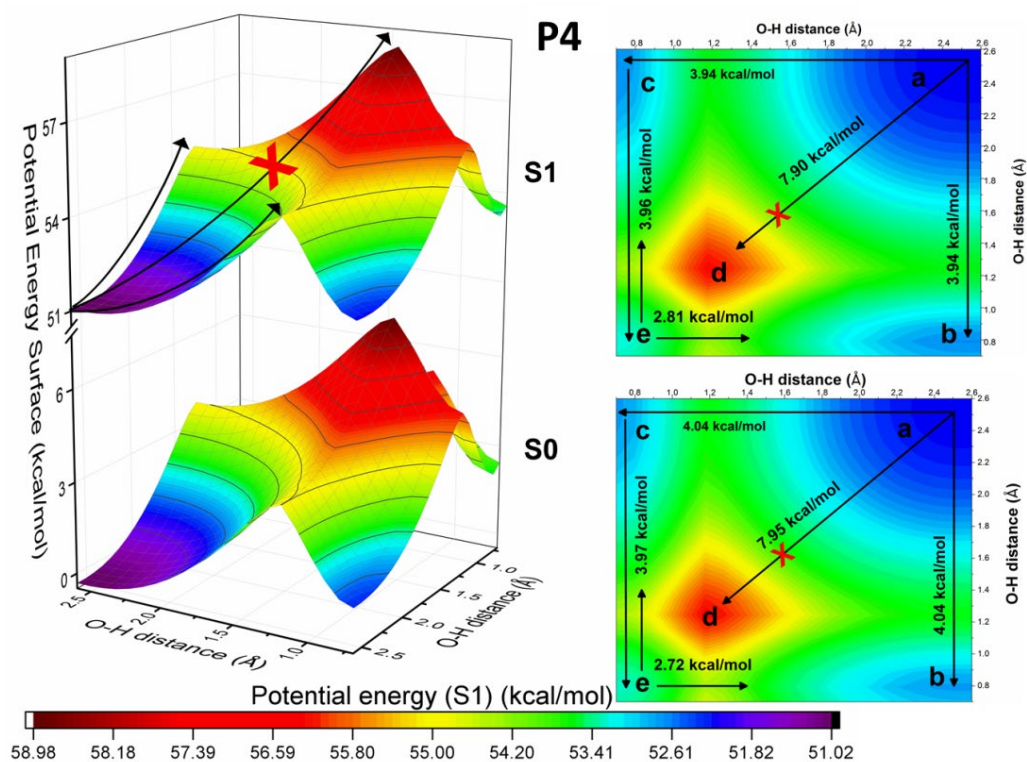


Fig. 6.37 PES scan of P4 in S0 and S1 states with their contour profile

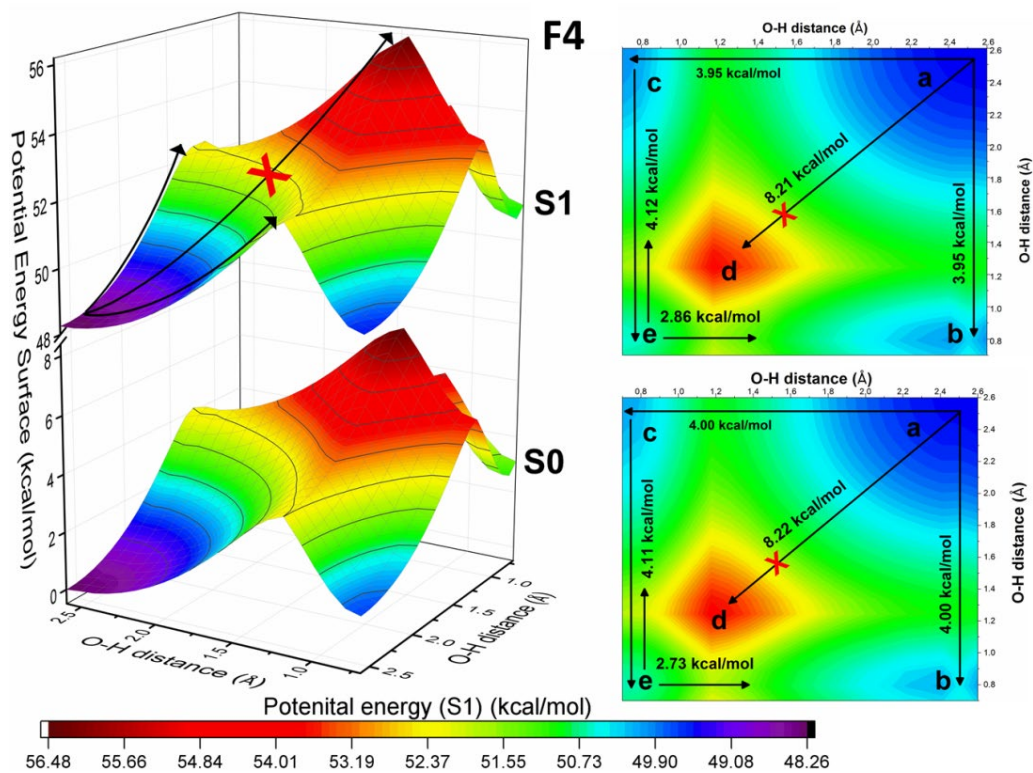


Fig. 6.38 PES scan of F4 in S0 and S1 states with their contour profile

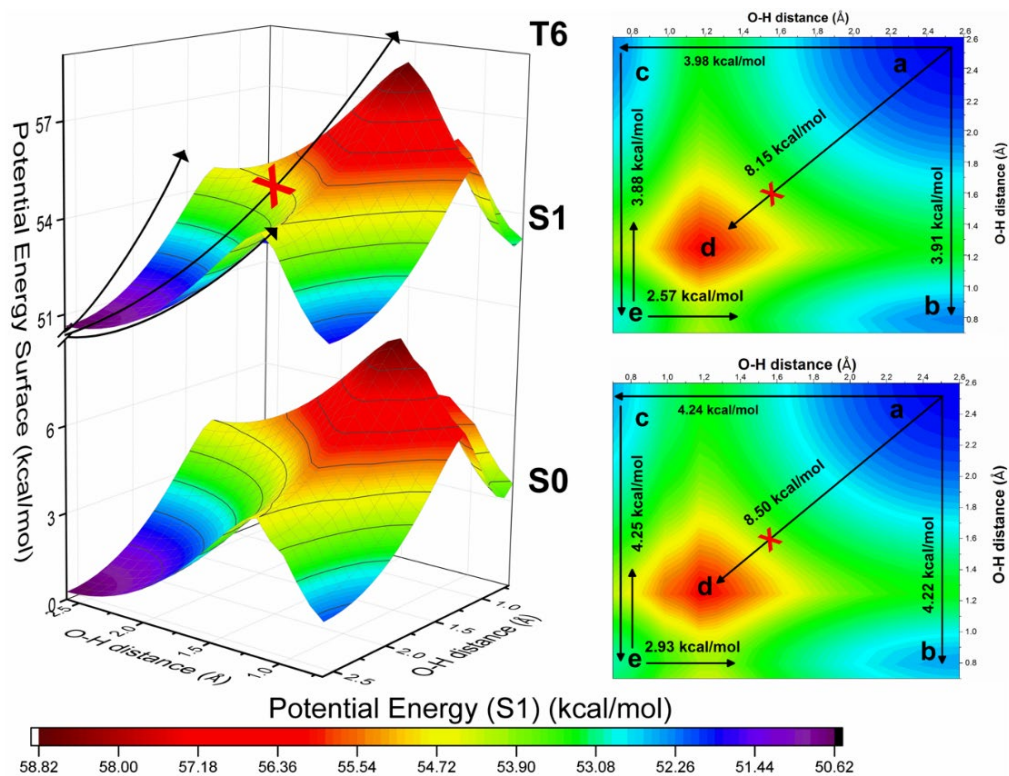


Fig. 6.39 PES scan of T6 in S0 and S1 states with their contour profile

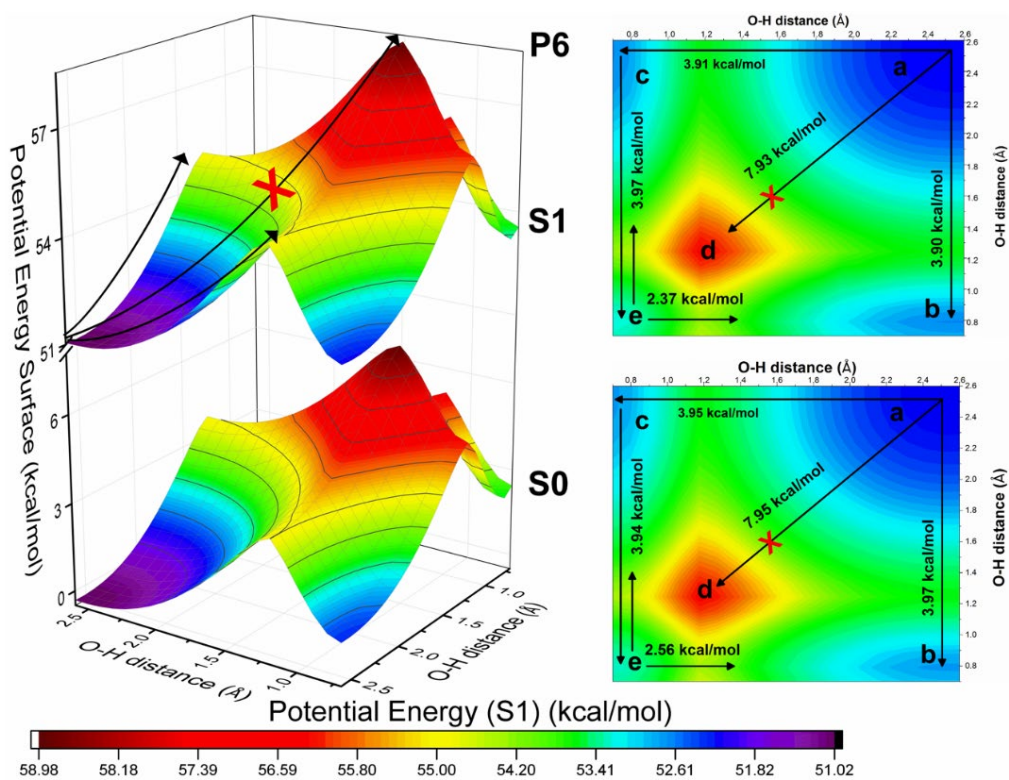


Fig. 6.40 PES scan of P6 in S0 and S1 states with their contour profile

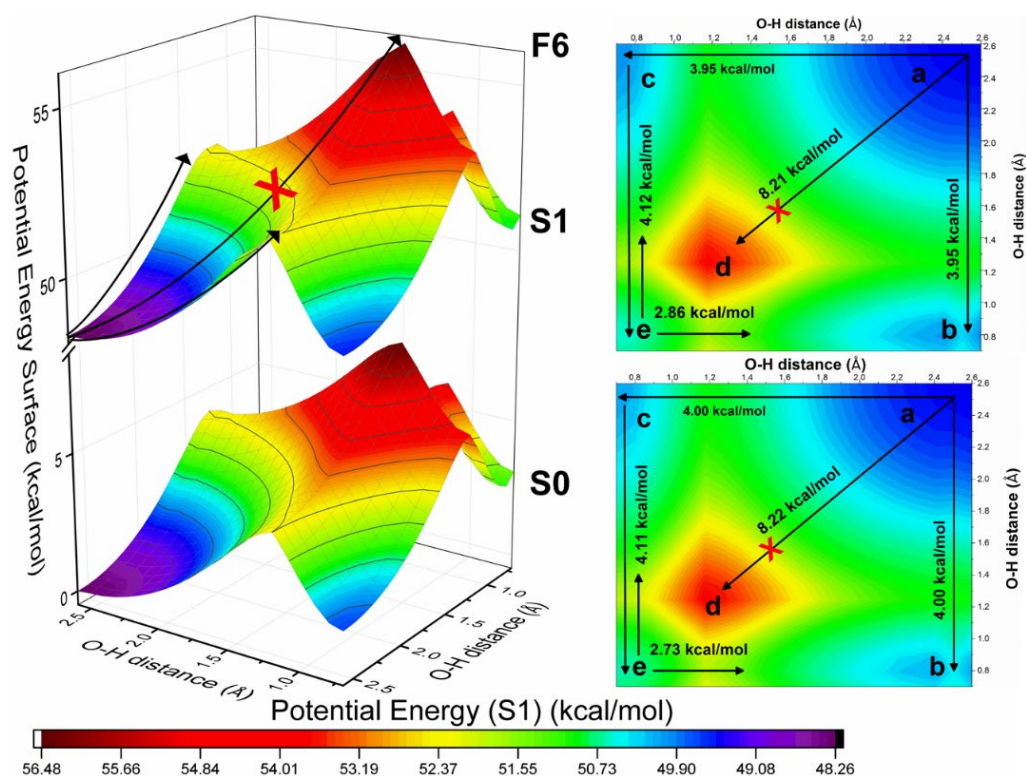


Fig. 6.41 PES scan of **F6** in **S0** and **S1** states with their contour profile

6.4 CONCLUSIONS

In summary, theoretical investigation of excited state intramolecular proton transfer phenomena in N-acylsubstituted hydrazides have been discussed. Analysis of subtle details of geometries at its ground and excited state confirms the feasible ESIPT well supported with spectral shift observed in N-H stretching frequency. Visualization of electronic density at the ground and excited state hints possible excited state proton translocation in the system. Theoretical estimation of electronic transition energies with their oscillator strength correlates well with the experimental absorption and emission spectra possessing trifling overestimation energy <0.17 eV. Potential energy scans performed on the molecules well supports the excited state single proton transfer in the system. Potential energy surface studies on the molecules confirm impossible simultaneous double proton transfer and hard step-wise double proton transfer. Hence, we conclude that N-acyl substituted hydrazides chemically coupled with bithiophene and terthiophene unit supports excited state single proton transfer alone.

CHAPTER 7

SUMMARY AND CONCLUSIONS

7.1 SUMMARY

- The main objective of the present work was to strategically design small organic molecules that exhibit solid-state fluorescence for OLED device application.
- To this end, five different series comprising 24 molecules have been designed and synthesized by Schiff's base condensation reaction. Synthesized organic molecules exhibited fluorescence emission and were characterized by standard spectroscopic techniques such as FT-IR, ¹H-NMR and ESI-MS to confirm their structural aspects.
- Solvatochromic response of all the systems have been examined, to study the effective optical response of the system brought about by microenvironmental changes. To accomplish this, UV-Vis and photoluminescence spectra were recorded for all the systems in solvents of varying dielectric constants. Fluorescent lifetime measurement for selected molecules exhibited a lifetime of order of nanoseconds. Relative quantum yield measurements were performed for all the molecules of the series to estimate quantum efficiency of the system. Further, optical characterizations of molecular thin films were recorded that corroborate the designed system as potential solid-state emitters. Cyclic voltammetry has been done on molecular systems to estimate HOMO, LUMO and the energy bandgap of the system.
- Aggregation induced emission mechanism were confirmed for few of the molecules by ratiometric studies of solvent-poor-solvent mixture. Molecular system exhibited a maximum emission intensity at a 50% ratiometric v/v of solvent and poor solvent.
- Excited state intramolecular proton transfer mechanism was studied for few of the designed and synthesized molecules. Proton transfer at excited state were highly prevalent at solvents of lower dielectric constants. THF solvent facilitated proton transfer in the system with photoluminescence spectra containing double peaks pertaining to keto and enol emission.
- Few of the synthesized materials were employed as an active emitter material for organic light emitting diode application. Active light emitters were successful in photon generation brought about by electrical excitations.
- Density functional theory calculations were carried out for all the molecules of the system to find correlation between structure and optoelectronic properties. Electronic orbital densities were computed to analyze the nature of electronic

transitions brought about by hybridized orbitals and the type of transitions. Emission energies were computed that correlates well with the experimental spectra. Dimer interaction energies and reorganization energies were computationally determined for few of the molecules. Potential energies with constrained geometry were computed to extract various parameters supportive of ESIPT in the system. Excited state potential energy barrier for a proton transfer in ESIPT system were estimated with theoretical calculations. Structures favoring double proton transfer were proven to support single proton transfer alone at the excited state.

7.2 CONCLUSIONS

The present work appends to the field of organic electronics, wherein, organic molecules were designed and synthesized aiming towards OLED device application. Emphasis on studies pertaining to some of the interesting phenomenon such as aggregation induced emission and excited state intramolecular proton transfer, exhibited by designed system is highly supportive to hypothesize theories based on experimental observances. Such theories and concepts would in turn assists in tuning the photophysical property aiming at designing a better material for device application.

Five different series of fluorescent organic small molecules have been designed, synthesized and characterized by standard spectroscopic techniques. Photophysical and electrochemical characterizations were performed on the synthesized molecules and following conclusions have been derived out it. Ring systems possessing sulphur atom exhibits a heavier S---S and S— π intermolecular interactions that would enhance charge injection and charge transport in a system. Bithiophene core appended with substituted heteroaromatics on either side exhibits a good amount of structure planarity and adopts a J-aggregate type of molecular packing arrangement supporting AIE. However, AIE phenomenon wasn't observed for system with bithiophene core and substituted hydrazides that favors excited state proton transfer phenomena. ESIPT luminophores with bithiophene core displayed an optimal HOMO and LUMO energy levels well suited for a device application. Undoped OLEDs were realized using hydrazides appended with bithiophene core as an active

light emitting material. Some of the scientific findings pertaining to absorption and emission transitions were adequately supported by theoretical calculations correlating well with the experimental results.

7.3 SCOPE FOR THE FUTURE WORK

The availability of wide variety of organic materials, and the feasibility of fine tuning of electronic properties through various chemical means have gathered great attention in the recent times and emerged as an attracting area of research. Organic molecules generally tend to exhibit weaker emission in solid state in comparison with the solution state. This has certainly been a challenge to realize their full potential towards solid-state application. Strategic design and control of molecular structure could certainly lead to enhanced emission in organic solid-state light emitters. Design of organic molecules focusing on quantum yield enhancement in solid-state is highly desirable to combat the shortcomings and to promote solid state lighting applications.

Further, organic systems that undergo a four-level photo-cyclic process of excited state intramolecular proton transfer (ESIPT) have gained immense interest with their mechanistic aspects driving the photophysical aspects to greater heights. Researchers have designed organic emitters that undergo ESIPT phenomenon to generate emission energy over a broad range of spectrum and to achieve a white light emission from a single molecule. Although many solid-state ESIPT luminophores have been reported, yet the mechanism of proton transfer at excited state in condensed media remains open for discussion. Extensive research in this field is vital to gain insight into some of the core concepts that govern the operation of these devices, thereby enhancing the field of OLEDs. Considering all the above interesting challenges, there is an immense scope for future work in this direction as an ever-exciting field aiming towards greater efficiency for OLED applications.

REFERENCES

- Adachi, C., Baldo, M. A., Thompson, M. E., and Forrest, S. R. (2001). “Nearly 100% internal phosphorescence efficiency in an organic light-emitting device.” *J. Appl. Phys.*, 90(10), 5048–5051.
- Alvarado, S. F., Seidler, P. F., Lidzey, D. G., and Bradley, D. D. C. (1998). “Direct determination of the exciton binding energy of conjugated polymers using a scanning tunneling microscope.” *Phys. Rev. Lett.*, 81(5), 1082.
- An, B., Yuan, H., Zhu, Q., Li, Y., Guo, X., and Zhang, J. (2017). “Theoretical insight into the excited-state intramolecular proton transfer mechanisms of three amino-type hydrogen-bonding molecules.” *Spectrochim. Acta. A. Mol. Biomol. Spectrosc.*, 175, 36–42.
- An, B.-K., Kwon, S.-K., Jung, S.-D., and Park, S. Y. (2002). “Enhanced Emission and Its Switching in Fluorescent Organic Nanoparticles.” *J. Am. Chem. Soc.*, 124(48), 14410–14415.
- Aparicio, F. J., Holgado, M., Borrás, A., Blaszczyk-Lezak, I., Griol, A., Barrios, C. A., Casquel, R., Sanza, F. J., Sohlström, H., Antelius, M., González-Elipe, A. R., and Barranco, A. (2011). “Transparent Nanometric Organic Luminescent Films as UV-Active Components in Photonic Structures.” *Adv. Mater.*, 23(6), 761–765.
- Arathi, A. S., Mallick, S., and Koner, A. L. (2016). “Tuning Aggregation-Induced Emission of 2,3-Naphthalimide by Employing Cyclodextrin Nanocavities.” *ChemistrySelect*, 1(13), 3535–3540.
- Arias, A. C., MacKenzie, J. D., McCulloch, I., Rivnay, J., and Salleo, A. (2010). “Materials and Applications for Large Area Electronics: Solution-Based Approaches.” *Chem. Rev.*, 110(1), 3–24.
- Arnaut, L. G., and Formosinho, S. J. (1993). “Excited-state proton transfer reactions I. Fundamentals and intermolecular reactions.” *J. Photochem. Photobiol. Chem.*, 75(1), 1–20.
- Asahi, T., Sugiyama, T., and Masuhara, H. (2008). “Laser Fabrication and Spectroscopy of Organic Nanoparticles.” *Acc. Chem. Res.*, 41(12), 1790–1798.
- Ashcroft, N. W., and Mermin, N. D. (1976). “Solid State Physics (Saunders College, Philadelphia).” *Google Sch.*, 404.
- Baldo, M. A., Adachi, C., and Forrest, S. R. (2000). “Transient analysis of organic electrophosphorescence. II. Transient analysis of triplet-triplet annihilation.” *Phys. Rev. B*, 62(16), 10967.
- Banal, J. L., White, J. M., Ghiggino, K. P., and Wong, W. W. (2014). “Concentrating aggregation-induced fluorescence in planar waveguides: a proof-of-principle.” *Sci. Rep.*, 4, 4635.

- Bao, C., Lu, R., Jin, M., Xue, P., Tan, C., Xu, T., Liu, G., and Zhao, Y. (2006). "Helical Stacking Tuned by Alkoxy Side Chains in π -Conjugated Triphenylbenzene Discotic Derivatives." *Chem. - Eur. J.*, 12(12), 3287–3294.
- Barbara, P. F., Walsh, P. K., and Brus, L. E. (1989). "Picosecond kinetic and vibrationally resolved spectroscopic studies of intramolecular excited-state hydrogen atom transfer." *J. Phys. Chem.*, 93(1), 29–34.
- Barman, S., Mukhopadhyay, S. K., Gangopadhyay, M., Biswas, S., Dey, S., and Singh, N. P. (2015). "Coumarin–benzothiazole–chlorambucil (Cou–Benz–Cbl) conjugate: an ESIPT based pH sensitive photoresponsive drug delivery system." *J. Mater. Chem. B*, 3(17), 3490–3497.
- Barth, S., and Bässler, H. (1997). "Intrinsic photoconduction in PPV-type conjugated polymers." *Phys. Rev. Lett.*, 79(22), 4445.
- Benelhadj, K., Massue, J., Retailleau, P., Ulrich, G., and Ziessel, R. (2013). "2-(2'-Hydroxyphenyl) benzimidazole and 9, 10-phenanthroimidazole chelates and borate complexes: solution-and solid-state emitters." *Org. Lett.*, 15(12), 2918–2921.
- Bhongale, C. J., Chang, C.-W., Lee, C.-S., Diao, E. W.-G., and Hsu, C.-S. (2005). "Relaxation Dynamics and Structural Characterization of Organic Nanoparticles with Enhanced Emission." *J. Phys. Chem. B*, 109(28), 13472–13482.
- Braslavsky, S. E., Fron, E., Rodríguez, H. B., San Román, E., Scholes, G. D., Schweitzer, G., Valeur, B., and Wirz, J. (2008). "Pitfalls and limitations in the practical use of Förster's theory of resonance energy transfer." *Photochem. Photobiol. Sci.*, 7(12), 1444–1448.
- Brown, R. E., Singer, L. A., and Parks, J. H. (1972). "Prompt and delayed fluorescence from benzophenone." *Chem. Phys. Lett.*, 14(2), 193–195.
- Brunel, J., Mongin, O., Jutand, A., Ledoux, I., Zyss, J., and Blanchard-Desce, M. (2003). "Propeller-Shaped Octupolar Molecules Derived from Triphenylbenzene for Nonlinear Optics: Synthesis and Optical Studies." *Chem. Mater.*, 15(21), 4139–4148.
- Brütting, W. (2006). "Introduction to the Physics of Organic Semiconductors." *Phys. Org. Semicond.*, John Wiley & Sons, Ltd, 1–14.
- Brütting, W., and Adachi, C. (2012). *Physics of Organic Semiconductors*.
- Brzeczek, A., Karon, K., Higginbotham, H., Jędrysiak, R. G., Lapkowski, M., Walczak, K., and Golba, S. (2016). "Synthesis and characterization of 1,3,5-triphenylamine derivatives with star-shaped architecture." *Dyes Pigments*, 133, 25–32.
- Bulović, V., Baldo, M. A., and Forrest, S. R. (2001). "Excitons and energy transfer in doped luminescent molecular organic materials." *Org. Electron. Mater.*, Springer, 391–441.

- Bünau, G. V. (1970). "J. B. Birks: Photophysics of Aromatic Molecules. Wiley-Interscience, London 1970. 704 Seiten. Preis: 210s." *Berichte Bunsenges. Für Phys. Chem.*, 74(12), 1294–1295.
- Buyruk, A., Cinar, M. E., Eroglu, M. S., and Ozturk, T. (2016). "Polymerization of Thienothiophenes and Dithienothiophenes via Click-Reaction for Electronic Applications." *ChemistrySelect*, 1(12), 3028–3032.
- C. Rasmussen, S., Ogawa, K., and Rothstein, S. D. (2008). *Handb. Org. Electron. Photonics*, Stevenson Ranch, CA, 2008: American Scientific Publishers.
- Cai, M., Gao, Z., Zhou, X., Wang, X., Chen, S., Zhao, Y., Qian, Y., Shi, N., Mi, B., and Xie, L. (2012). "A small change in molecular structure, a big difference in the AIEE mechanism." *Phys. Chem. Chem. Phys.*, 14(15), 5289–5296.
- Cammi, R., and Tomasi, J. (1995). "Remarks on the use of the apparent surface charges (ASC) methods in solvation problems: Iterative versus matrix-inversion procedures and the renormalization of the apparent charges." *J. Comput. Chem.*, 16(12), 1449–1458.
- Cancès, E., Mennucci, B., and Tomasi, J. (1997). "A new integral equation formalism for the polarizable continuum model: Theoretical background and applications to isotropic and anisotropic dielectrics." *J. Chem. Phys.*, 107(8), 3032–3041.
- Catalan, J., Perez, P., Fabero, F., Wilshire, J. F. K., Claramunt, R. M., and Elguero, J. (1992). "Photophysical properties of some 2-(2'-hydroxyaryl)benzotriazoles: dramatic effect of an ortho-located bulky tert-butyl group." *J. Am. Chem. Soc.*, 114(3), 964–966.
- Chai, J.-D., and Head-Gordon, M. (2008). "Long-range corrected hybrid density functionals with damped atom–atom dispersion corrections." *Phys. Chem. Chem. Phys.*, 10(44), 6615–6620.
- Chan, L.-H., Lee, R.-H., Hsieh, C.-F., Yeh, H.-C., and Chen, C.-T. (2002). "Optimization of High-Performance Blue Organic Light-Emitting Diodes Containing Tetraphenylsilane Molecular Glass Materials." *J. Am. Chem. Soc.*, 124(22), 6469–6479.
- Chansen, W., Salaeh, R., Prommin, C., Kerdpol, K., Daengngern, R., and Kungwan, N. (2017). "Theoretical study on influence of geometry controlling over the excited-state intramolecular proton transfer of 10-hydroxybenzo[h]quinoline and its derivatives." *Comput. Theor. Chem.*, 1113, 42–51.
- Chen, J., Law, C. C. W., Lam, J. W. Y., Dong, Y., Lo, S. M. F., Williams, I. D., Zhu, D., and Tang, B. Z. (2003). "Synthesis, Light Emission, Nanoaggregation, and Restricted Intramolecular Rotation of 1,1-Substituted 2,3,4,5-Tetraphenylsiloles." *Chem. Mater.*, 15(7), 1535–1546.
- Chen, L., Wu, D., Lim, C. S., Kim, D., Nam, S.-J., Lee, W., Kim, G., Kim, H. M., and Yoon, J. (2017). "A two-photon fluorescent probe for specific detection of hydrogen sulfide

based on a familiar ESIPT fluorophore bearing AIE characteristics.” *Chem. Commun.*, 53(35), 4791–4794.

Chen, S., Hou, P., Wang, J., and Song, X. (2012). “A highly sulfite -selective ratiometric fluorescent probe based on ESIPT.” *RSC Adv.*, 2(29), 10869–10873.

Chen, W.-C., Zhu, Z.-L., and Lee, C.-S. (2018). “Organic Light-Emitting Diodes Based on Imidazole Semiconductors.” *Adv. Opt. Mater.*, 6(18), 1800258.

Cho, J.-S., Kojima, Y., and Yamamoto, K. (2003). “A novel oligothiophene derivative as a hole-transport with emitting material for OLED.” *Polym. Adv. Technol.*, 14(1), 52–57.

Chohan, Z. H., Farooq, M. A., and Iqbal, M. S. (2000). “Synthesis, Characterization and Biological Properties of Anions of Bivalent Transition Metal [Co(II) and Ni(II)] Complexes With Acylhydrazine Derived ONO Donor Schiff Bases.” *Met.-Based Drugs*, <<https://www.hindawi.com/journals/mbd/2000/321636/abs/>> (Oct. 19, 2018).

Chung, J. W., Yang, H., Singh, B., Moon, H., An, B., Lee, S. Y., and Park, S. Y. (2009). “Single-crystalline organic nanowires with large mobility and strong fluorescence emission: a conductive-AFM and space-charge-limited-current study.” *J. Mater. Chem.*, 19(33), 5920–5925.

Cigáň, M., Jakusová, K., Donovalová, J., Filo, J., Horváth, M., and Gáplovský, A. (2015). “Fluorescence of isatin *N* -phenylsemicarbazones: aggregation and hydrazide-hydrazone tautomerism: KETO-ENOL TAUTOMERISM.” *J. Phys. Org. Chem.*, 28(5), 337–346.

Ciuciu, A. I., Flamigni, L., Skonieczny, K., and Gryko, D. T. (2013). “Blue-green emitting sulphonamido-imidazole derivatives: ESIPT based excited state dynamics.” *Phys. Chem. Chem. Phys.*, 15(39), 16907–16916.

Costa, R. D., Ortí, E., and Bolink, H. J. (2011). “Recent advances in light-emitting electrochemical cells.” *Pure Appl. Chem.*, 83(12), 2115–2128.

Das, R., Duportail, G., Ghose, A., Richert, L., Klymchenko, A., Chakraborty, S., Yesylevskyy, S., and Mely, Y. (2014). “Tuning excited-state proton transfer dynamics of a 3-hydroxychromone dye in supramolecular complexes via host–guest steric compatibility.” *Phys. Chem. Chem. Phys.*, 16(2), 776–784.

Datt, S. C. (1969). “Conduction Mechanism in Organic Semiconductors.” *J. Sci. Ind. Res.*, 28(1), 5-.

Deng, B., Ren, M., Kong, X., Zhou, K., and Lin, W. (2016). “An ESIPT based fluorescent probe for imaging hydrogen sulfide with a large turn-on fluorescence signal.” *RSC Adv.*, 6(67), 62406–62410.

Dhami, S., Mello, A. J. D., Rumbles, G., Bishop, S. M., Phillips, D., and Beeby, A. (1995b). “Phthalocyanine Fluorescence at High Concentration: Dimers or Reabsorption Effect?” *Photochem. Photobiol.*, 61(4), 341–346.

- Ding, D., Li, K., Liu, B., and Tang, B. Z. (2013). "Bioprobes based on AIE fluorogens." *Acc. Chem. Res.*, 46(11), 2441–2453.
- Doi, H., Kinoshita, M., Okumoto, K., and Shirota, Y. (2003). "A Novel Class of Emitting Amorphous Molecular Materials with Bipolar Character for Electroluminescence." *Chem. Mater.*, 15(5), 1080–1089.
- Douhal, A., Lahmani, F., and Zewail, A. H. (1996). "Proton-transfer reaction dynamics." *Chem. Phys.*, 207(2–3), 477–498.
- Douvali, A., Papaefstathiou, G. S., Gullo, M. P., Barbieri, A., Tsipis, A. C., Malliakas, C. D., Kanatzidis, M. G., Papadas, I., Armatas, G. S., and Hatzidimitriou, A. G. (2015). "Alkaline earth metal ion/dihydroxy-terephthalate MOFs: structural diversity and unusual luminescent properties." *Inorg. Chem.*, 54(12), 5813–5826.
- Du, C., Zhou, Q., Zhang, M., Song, P., and Ma, F. (2019). "Excited-state intramolecular proton transfer of 6-amino-2-(2'-hydroxyphenyl) benzoxazole (6A-HBO) in different solvents." *J. Phys. Org. Chem.*, 32(2), e3901.
- Duvenhage, M.-M., Ntwaeaborwa, M., Visser, H. G., Swarts, P. J., Swarts, J. C., and Swart, H. C. (2015). "Determination of the optical band gap of Alq₃ and its derivatives for the use in two-layer OLEDs." *Opt. Mater.*, 42(Supplement C), 193–198.
- Egidi, F., Segado, M., Koch, H., Cappelli, C., and Barone, V. (2014). "A benchmark study of electronic excitation energies, transition moments, and excited-state energy gradients on the nicotine molecule." *J. Chem. Phys.*, 141(22), 224114.
- El Kouari, Y., Migalska-Zalas, A., Arof, A. K., and Sahraoui, B. (2015). "Computations of absorption spectra and nonlinear optical properties of molecules based on anthocyanidin structure." *Opt. Quantum Electron.*, 47(5), 1091–1099.
- Feng, L., Zhu, C., Yuan, H., Liu, L., Lv, F., and Wang, S. (2013). "Conjugated polymer nanoparticles: preparation, properties, functionalization and biological applications." *Chem. Soc. Rev.*, 42(16), 6620–6633.
- Feng, Y., Cheng, J., Zhou, L., Zhou, X., and Xiang, H. (2012). "Ratiometric optical oxygen sensing: a review in respect of material design." *Analyst*, 137(21), 4885–4901.
- Fernandes, S. S. M., Pereira, A., Ivanou, D., Mendes, A., and Raposo, M. M. M. (2018). "Benzothiadiazole derivatives functionalized with two different (hetero)aromatic donor groups: Synthesis and evaluation as TiO₂ sensitizers for DSSCs." *Dyes Pigments*, 151, 89–94.
- Fernández-Moreira, V., Thorp-Greenwood, F. L., and Coogan, M. P. (2009). "Application of d₆ transition metal complexes in fluorescence cell imaging." *Chem. Commun.*, 46(2), 186–202.

Forés, M., Duran, M., and Solà, M. (1998). “Intramolecular proton transfer in the ground and the two lowest-lying singlet excited states of 1-amino-3-propenal and related species. This paper is dedicated to Albert, son of M. Solà, born during the elaboration of this paper.1.” *Chem. Phys.*, 234(1), 1–19.

Forrest, S. R., Burrows, P. E., Shen, Z., Gu, G., Bulovic, V., and Thompson, M. E. (1997). “The stacked OLED (SOLED): a new type of organic device for achieving high-resolution full-color displays.” *Synth. Met.*, International Conference on Electroluminescence of Molecular Materials and Related Phenomena, 91(1), 9–13.

Förster, T., and Kasper, K. (1954). “Ein konzentrationsumschlag der fluoreszenz.” *Z Phys Chem*, 1, 275–277.

Frackowiak, D. (1988). “The Jablonski diagram.” *J. Photochem. Photobiol. B*, 2(3), 399.

Friend, R. H., Gymer, R. W., Holmes, A. B., Burroughes, J. H., Marks, R. N., Taliani, C., Bradley, D. D. C., Santos, D. A. D., Brédas, J. L., Lögdlund, M., and Salaneck, W. R. (1999). “Electroluminescence in conjugated polymers.” *Nature*, 397(6715), 121–128.

Frisch, M., Trucks, G., Schlegel, H., Scuseria, G., Robb, M., Cheeseman, J., Scalmani, G., Barone, V., Mennucci, B., Petersson, G., Nakatsuji, H., Caricato, M., Li, X., Hratchian, H., Izmaylov, A., Bloino, J., Zheng, G., Sonnenberg, J., Hada, M., Ehara, M., Toyota, K., Fukuda, R., Hasegawa, J., Ishida, M., Nakajima, T., Honda, Y., Kitao, O., Nakai, H., Vreven, T., Montgomery, J., Peralta, J., Ogliaro, F., Bearpark, M., Heyd, J., Brothers, E., Kudin, K., Staroverov, V., Kobayashi, R., Normand, J., Raghavachari, K., Rendell, A., Burant, J., Iyengar, S., Tomasi, J., Cossi, M., Rega, N., Millam, J., Klene, M., Knox, J., Cross, J., Bakken, V., Adamo, C., Jaramillo, J., Gomperts, R., Stratmann, R., Yazyev, O., Austin, A., Cammi, R., Pomelli, C., Ochterski, J., Martin, R., Morokuma, K., Zakrzewski, V., Voth, G., Salvador, P., Dannenberg, J., Dapprich, S., Daniels, A., Farkas, Foresman, J., Ortiz, J., Cioslowski, J., and Fox, D. (2009). “Gaussian 09, Revision B.01.” *Gaussian 09 Revis. B01 Gaussian Inc Wallingford CT*.

Furukawa, K., Yamamoto, N., Nakabayashi, T., Ohta, N., Amimoto, K., and Sekiya, H. (2012). “Changes in the electric dipole moments and molecular polarizabilities of enol and keto forms of 2-(2'-hydroxyphenyl) benzimidazole along the proton transfer reaction path in a PMMA film.” *Chem. Phys. Lett.*, 539, 45–49.

Gabr, A. A. (1990). “Spectrophotometric studies on some Schiff bases derived from benzidine.” *Spectrochim. Acta Part Mol. Spectrosc.*, 46(12), 1751–1757.

Gao, F., Liao, Q., Xu, Z.-Z., Yue, Y.-H., Wang, Q., Zhang, H.-L., and Fu, H.-B. (2010). “Strong Two-Photon Excited Fluorescence and Stimulated Emission from an Organic Single Crystal of an Oligo (Phenylene Vinylene).” *Angew. Chem. Int. Ed.*, 49(4), 732–735.

Gaspar, D. J., and Polikarpov, E. (2015). *OLED fundamentals: materials, devices, and processing of organic light-emitting diodes*. CRC press.

- Geffroy, B., Le Roy, P., and Prat, C. (2006). "Organic light-emitting diode (OLED) technology: materials, devices and display technologies." *Polym. Int.*, 55(6), 572–582.
- Ghosh, D., Batuta, S., Das, S., Begum, N. A., and Mandal, D. (2015). "Proton transfer dynamics of 4'-N, N-dimethylamino-3-hydroxyflavone observed in hydrogen-bonding solvents and aqueous micelles." *J. Phys. Chem. B*, 119(17), 5650–5661.
- Giebink, N. C., and Forrest, S. R. (2008). "Quantum efficiency roll-off at high brightness in fluorescent and phosphorescent organic light emitting diodes." *Phys. Rev. B*, 77(23), 235215.
- Gondek, E., Kityk, I. V., Danel, A., Wisla, A., Pokladko, M., Sanetra, J., and Sahraoui, B. (2006). "Electroluminescence of several pyrazoloquinoline and quinoksaline derivatives." *Mater. Lett.*, 60(27), 3301–3306.
- Gong, Y., Wang, Z., Zhang, S., Luo, Z., Gao, F., and Li, H. (2016). "New ESIPT-Inspired Photostabilizers of Two-Photon Absorption Coumarin–Benzotriazole Dyads: From Experiments to Molecular Modeling." *Ind. Eng. Chem. Res.*, 55(18), 5223–5230.
- Goushi, K., Kawamura, Y., Sasabe, H., and Adachi, C. (2004). "Unusual phosphorescence characteristics of Ir (ppy) 3 in a solid matrix at low temperatures." *Jpn. J. Appl. Phys.*, 43(7A), L937.
- Grabowski, Z. R., Rotkiewicz, K., and Rettig, W. (2003). "Structural Changes Accompanying Intramolecular Electron Transfer: Focus on Twisted Intramolecular Charge-Transfer States and Structures." *Chem. Rev.*, 103(10), 3899–4032.
- Gu, B., Huang, L., Mi, N., Yin, P., Zhang, Y., Tu, X., Luo, X., Luo, S., and Yao, S. (2015). "An ESIPT-based fluorescent probe for highly selective and ratiometric detection of mercury(II) in solution and in cells." *Analyst*, 140(8), 2778–2784.
- Guezguez, I., Ayadi, A., Ordon, K., Iliopoulos, K., Branzea, D. G., Migalska-Zalas, A., Makowska-Janusik, M., El-Ghayoury, A., and Sahraoui, B. (2014). "Zinc Induced a Dramatic Enhancement of the Nonlinear Optical Properties of an Azo-Based Iminopyridine Ligand." *J. Phys. Chem. C*, 118(14), 7545–7553.
- Gupta, A., Ali, A., Gao, M., Singh, Th. B., Bilic, A., Watkins, S. E., Bach, U., and Evans, R. A. (2015). "Small molecules containing rigidified thiophenes and a cyanopyridone acceptor unit for solution-processable bulk-heterojunction solar cells." *Dyes Pigments*, 119, 122–132.
- Gutiérrez-Arzaluz, L., Cortés-Guzmán, F., Rocha-Rinza, T., and Peón, J. (2015). "Ultrafast excited state hydrogen atom transfer in salicylideneaniline driven by changes in aromaticity." *Phys. Chem. Chem. Phys.*, 17(47), 31608–31612.
- Gutman, F., and Lyons, L. E. (1981). *Organic Semiconductors, Part A*. Malabar, Florida, USA.

- Hadjoudis, E., and Mavridis, I. M. (2004). "Photochromism and thermochromism of Schiff bases in the solid state: structural aspects." *Chem. Soc. Rev.*, 33(9), 579–588.
- Hadsadee, S., Rattanawan, R., Tarsang, R., Kungwan, N., and Jungsuttiwong, S. (2017). "Push-Pull N-Annulated Perylene-Based Sensitizers for Dye-Sensitized Solar Cells: Theoretical Property Tuning by DFT/TDDFT." *ChemistrySelect*, 2(30), 9829–9837.
- Han, J., Thirupathaiah, B., Kwon, G., Kim, C., and Seo, S. (2015). "Synthesis and characterization of carbazole- and α -carboline-based thiophene derivatives as organic semiconductors for organic thin-film transistors." *Dyes Pigments*, 114, 78–84.
- Han, M. R., Hirayama, Y., and Hara, M. (2006). "Fluorescence Enhancement from Self-Assembled Aggregates: Substituent Effects on Self-Assembly of Azobenzenes." *Chem. Mater.*, 18(12), 2784–2786.
- Hanwell, M. D., Curtis, D. E., Lonie, D. C., Vandermeersch, T., Zurek, E., and Hutchison, G. R. (2012). "Avogadro: an advanced semantic chemical editor, visualization, and analysis platform." *J. Cheminformatics*, 4, 17.
- Hao, J., and Yang, Y. (2018). "Exploring the ESIPT dynamical processes of two novel chromophores: symmetrical structure CHC and asymmetric structure CHN." *Org. Chem. Front.*, 5(8), 1330–1341.
- Hao, J., and Yang, Y. (2019). "The theoretical study about the ESIPT mechanism for 2,4-bis(benzooxazol-2'-yl)hydroquinone: Single or double?" *J. Phys. Org. Chem.*, 32(3), e3903.
- Hariharan, P. C., and Pople, J. A. (1973). "The influence of polarization functions on molecular orbital hydrogenation energies." *Theor. Chim. Acta*, 28(3), 213–222.
- Harris, T. D., Buzby, P. R., Babcock, H., Beer, E., Bowers, J., Braslavsky, I., Causey, M., Colonell, J., DiMeo, J., and Efcavitch, J. W. (2008). "Single-molecule DNA sequencing of a viral genome." *Science*, 320(5872), 106–109.
- Hayaki, S., Kimura, Y., and Sato, H. (2013). "Ab Initio Study on an Excited-State Intramolecular Proton-Transfer Reaction in Ionic Liquid." *J. Phys. Chem. B*, 117(22), 6759–6767.
- Hehre, W. J., Ditchfield, R., and Pople, J. A. (1972). "Self—Consistent Molecular Orbital Methods. XII. Further Extensions of Gaussian—Type Basis Sets for Use in Molecular Orbital Studies of Organic Molecules." *J. Chem. Phys.*, 56(5), 2257–2261.
- Hill, I. G., Kahn, A., Soos, Z. G., and Pascal Jr, R. A. (2000). "Charge-separation energy in films of π -conjugated organic molecules." *Chem. Phys. Lett.*, 327(3–4), 181–188.
- Hong, Y., Lam, J. W., and Tang, B. Z. (2011). "Aggregation-induced emission." *Chem. Soc. Rev.*, 40(11), 5361–5388.

Hong, Y., Lam, J. W. Y., and Tang, B. Z. (2009). "Aggregation-induced emission: phenomenon, mechanism and applications." *Chem. Commun.*, 0(29), 4332–4353.

Houari, Y., Charaf-Eddin, A., Laurent, A. D., Massue, J., Ziessel, R., Ulrich, G., and Jacquemin, D. (2013). "Modeling optical signatures and excited-state reactivities of substituted hydroxyphenylbenzoxazole (HBO) ESIPT dyes." *Phys. Chem. Chem. Phys.*, 16(4), 1319–1321.

Houari, Y., Chibani, S., Jacquemin, D., and Laurent, A. D. (2015). "TD-DFT Assessment of the Excited State Intramolecular Proton Transfer in Hydroxyphenylbenzimidazole (HBI) Dyes." *J. Phys. Chem. B*, 119(6), 2180–2192.

Hsieh, C.-C., Jiang, C.-M., and Chou, P.-T. (2010). "Recent experimental advances on excited-state intramolecular proton coupled electron transfer reaction." *Acc. Chem. Res.*, 43(10), 1364–1374.

Hu, R., Lager, E., Aguilar-Aguilar, A., Liu, J., Lam, J. W., Sung, H. H., Williams, I. D., Zhong, Y., Wong, K. S., and Pena-Cabrera, E. (2009). "Twisted intramolecular charge transfer and aggregation-induced emission of BODIPY derivatives." *J. Phys. Chem. C*, 113(36), 15845–15853.

Huang, Y., Cheng, T., Li, F., Huang, C.-H., Hou, T., Yu, A., Zhao, X., and Xu, X. (2002). "Photophysical Studies on the Mono- and Dichromophoric Hemicyanine Dyes I. Photoelectric Conversion from the Dye Modified ITO Electrodes." *J. Phys. Chem. B*, 106(39), 10020–10030.

Hung, L. S., and Chen, C. H. (2002). "Recent progress of molecular organic electroluminescent materials and devices." *Mater. Sci. Eng. R Rep.*, 39(5), 143–222.

Hutchison, G. R., Ratner, M. A., and Marks, T. J. (2005). "Intermolecular Charge Transfer between Heterocyclic Oligomers. Effects of Heteroatom and Molecular Packing on Hopping Transport in Organic Semiconductors." *J. Am. Chem. Soc.*, 127(48), 16866–16881.

El-Mellouhi, F., Bentría, E. T., Marzouk, A., Rashkeev, S. N., Kais, S., and Alharbi, F. H. (2016). "Hydrogen bonding: a mechanism for tuning electronic and optical properties of hybrid organic–inorganic frameworks." *Npj Comput. Mater.*, 2, 16035.

Ignasiak, M. T., Houée-Levin, C., Kciuk, G., Marciniak, B., and Pedzinski, T. (2015). "A Reevaluation of the Photolytic Properties of 2-Hydroxybenzophenone-Based UV Sunscreens: Are Chemical Sunscreens Inoffensive?" *ChemPhysChem*, 16(3), 628–633.

Iijima, T., Momotake, A., Shinohara, Y., Sato, T., Nishimura, Y., and Arai, T. (2010). "Excited-state intramolecular proton transfer of naphthalene-fused 2-(2'-hydroxyaryl) benzazole family." *J. Phys. Chem. A*, 114(4), 1603–1609.

Ikegami, M., and Arai, T. (2002). "Photoinduced intramolecular hydrogen atom transfer in 2-(2-hydroxyphenyl) benzoxazole and 2-(2-hydroxyphenyl) benzothiazole studied by laser flash photolysis." *J. Chem. Soc. Perkin Trans. 2*, (7), 1296–1301.

Issa, R. M., Khedr, A. M., and Rizk, H. F. (2005). "UV–vis, IR and ¹H NMR spectroscopic studies of some Schiff bases derivatives of 4-aminoantipyrine." *Spectrochim. Acta. A. Mol. Biomol. Spectrosc.*, 62(1), 621–629.

Itami, K., and Yoshida, J. (2006). "Multisubstituted Olefins: Platform Synthesis and Applications to Materials Science and Pharmaceutical Chemistry." *Bull. Chem. Soc. Jpn.*, 79(6), 811–824.

Janiak, C. (2000). "A critical account on π – π stacking in metal complexes with aromatic nitrogen-containing ligands †." *J. Chem. Soc. Dalton Trans.*, (21), 3885–3896.

Jankowska, J., Rode, M. F., Sadlej, J., and Sobolewski, A. L. (2014). "Excited-State Intramolecular Proton Transfer: Photoswitching in Salicylidene Methylamine Derivatives." *ChemPhysChem*, 15(8), 1643–1652.

Jarczyk-Jedryka, A., Filapek, M., Malecki, G., Kula, S., Janeczek, H., Boharewicz, B., Iwan, A., and Schab-Balcerzak, E. (2016). "Symmetrical N-acylsubstituted dihydrazones containing bithiophene core - Photophysical, electrochemical and thermal characterization." *Spectrochim. Acta. A. Mol. Biomol. Spectrosc.*, 159, 169–176.

Jayanty, S., and Radhakrishnan, T. P. (2004). "Enhanced Fluorescence of Remote Functionalized Diaminodicyanoquinodimethanes in the Solid State and Fluorescence Switching in a Doped Polymer by Solvent Vapors." *Chem. - Eur. J.*, 10(3), 791–797.

Jiang, J.-H. (2011). "N'-Benzyl-idene-thio-phene-2-carbohydrazide." *Acta Crystallogr. Sect. E Struct. Rep. Online*, 67(1), o50–o50.

Jin, X., Liu, C., Wang, X., Huang, H., Zhang, X., and Zhu, H. (2015). "A flavone-based ESIPT fluorescent sensor for detection of N₂H₄ in aqueous solution and gas state and its imaging in living cells." *Sens. Actuators B Chem.*, 216, 141–149.

Jones, L., Pask, C. M., Kazlauciusas, A., Gulcur, M., and Lin, L. (2017). "Synthesis and Characterisation of Fused Heterocyclic Molecular Rods: A Combined Experimental and Theoretical Study on Diethynyl Dithienothiophenyl Derivatives." *ChemistrySelect*, 2(21), 5958–5964.

Justin Thomas, K. R., Venkateswararao, A., Joseph, V., Kumar, S., and Jou, J.-H. (2019). "Polarity tuning of fluorene derivatives by chromophores to achieve efficient blue electroluminescent materials." *Org. Electron.*, 64, 266–273.

Kafafi, Z. H. (2018). *Organic electroluminescence*. CRC Press.

- Kalinin, S., Speckbacher, M., Langhals, H., and Johansson, L. B.-Å. (2001). “A new and versatile fluorescence standard for quantum yield determination.” *Phys. Chem. Chem. Phys.*, 3(2), 172–174.
- Kalinowski, J., Stampor, W., Mężyk, J., Cocchi, M., Virgili, D., Fattori, V., and Di Marco, P. (2002). “Quenching effects in organic electrophosphorescence.” *Phys. Rev. B*, 66(23), 235321.
- Kamaldeep, K. S. nee, Kaur, S., Bhalla, V., Kumar, M., and Gupta, A. (2014). “Pentacenequinone derivatives for preparation of gold nanoparticles: facile synthesis and catalytic application.” *J. Mater. Chem. A*, 2(22), 8369–8375.
- Kanlayakan, N., Kerdpol, K., Prommin, C., Salaeh, R., Chansen, W., Sattayanon, C., and Kungwan, N. (2017). “Effects of different proton donor and acceptor groups on excited-state intramolecular proton transfers of amino-type and hydroxy-type hydrogen-bonding molecules: theoretical insights.” *New J. Chem.*, 41(17), 8761–8771.
- Karakas, A., Migalska-Zalas, A., El Kouari, Y., Gozutok, A., Karakaya, M., and Touhtouh, S. (2013). “Quantum chemical calculations and experimental studies of third-order nonlinear optical properties of conjugated TTF–quinones.” *Opt. Mater.*, 36(1), 22–26.
- Karimov, Kh. S., Senin, H. B., Qazi, I., and Sadrai, M. (2008). “Organic Semiconductors: Conduction Mechanisms and some Applications.” *AIP Conf. Proc.*, 1017(1), 25–34.
- Karthik, D., Thomas, K. R. J., Jou, J.-H., and Chen, Y.-L. (2016). “Synthesis, characterization and electroluminescence of carbazole-benzimidazole hybrids with thiophene/phenyl linker.” *Dyes Pigments*, 133, 132–142.
- Kasha, M. (1986). “Proton-transfer spectroscopy. Perturbation of the tautomerization potential.” *J. Chem. Soc. Faraday Trans. 2 Mol. Chem. Phys.*, 82(12), 2379–2392.
- Kaur, K., Saini, R., Kumar, A., Luxami, V., Kaur, N., Singh, P., and Kumar, S. (2012). “Chemodosimeters: An approach for detection and estimation of biologically and medically relevant metal ions, anions and thiols.” *Coord. Chem. Rev.*, 256(17), 1992–2028.
- Khimich, M. N., Ivanov, V. L., Melnikov, M. Ya., Shelaev, I. V., Gostev, F. E., Nadtochenko, V. A., and Uzhinov, B. M. (2017). “Dynamics of excited-state intramolecular proton-transfer in 2-amino-3-(2'-benzazolyl)quinoline cations.” *Photochem. Photobiol. Sci.*, 16(7), 1139–1145.
- Kim, H. N., Lee, M. H., Kim, H. J., Kim, J. S., and Yoon, J. (2008). “A new trend in rhodamine-based chemosensors: application of spirolactam ring-opening to sensing ions.” *Chem. Soc. Rev.*, 37(8), 1465–1472.
- Kim, S. H., Park, S., Kwon, J. E., and Park, S. Y. (2011). “Organic Light-Emitting Diodes with a White-Emitting Molecule: Emission Mechanism and Device Characteristics.” *Adv. Funct. Mater.*, 21(4), 644–651.

- Kim, T.-I., Kang, H. J., Han, G., Chung, S. J., and Kim, Y. (2009). "A highly selective fluorescent ESIPT probe for the dual specificity phosphatase MKP-6." *Chem. Commun.*, 0(39), 5895–5897.
- Knupfer, M., Fink, J., Zojer, E., Leising, G., Scherf, U., and Müllen, K. (1998). "Localized and delocalized singlet excitons in ladder-type poly (paraphenylene)." *Phys. Rev. B*, 57(8), R4202.
- Kothavale, S., Erande, Y., and Sekar, N. (2017). "Triphenylamine-Based Bis- and Tris-ESIPT Compounds and Their Boron Complexes: Synthesis, Photophysical Properties and DFT Study of ICT and ESIPT Emissions." *ChemistrySelect*, 2(18), 5013–5024.
- Krishna, A., Varathan, E., Sreedevi, P., Subramanian, V., Karunakaran, V., and Varma, R. L. (2018). "Design, synthesis and photophysical investigation of triphenylamine-bithiophene dyes as RGB emitters for white light applications." *Dyes Pigments*, 159, 77–84.
- Kula, S., Szlapa-Kula, A., Kotowicz, S., Filapek, M., Bujak, K., Siwy, M., Janeczek, H., Maćkowski, S., and Schab-Balcerzak, E. (2018). "Phenanthro[9,10-d]imidazole with thiophene rings toward OLEDs application." *Dyes Pigments*, 159, 646–654.
- Kumbhar, H. S., Deshpande, S. S., and Shankarling, G. S. (2016). "Aggregation induced emission (AIE) active carbazole styryl fluorescent molecular rotor as viscosity sensor." *ChemistrySelect*, 1(9), 2058–2064.
- Kundu, A., Hariharan, P. S., Prabakaran, K., Moon, D., and Anthony, S. P. (2016). "Aggregation Induced Emission of Excited-State Intramolecular Proton Transfer Compounds: Nanofabrication Mediated White Light Emitting Nanoparticles." *Cryst. Growth Des.*, 16(6), 3400–3408.
- Kwok, R. T., Leung, C. W., Lam, J. W., and Tang, B. Z. (2015). "Biosensing by luminogens with aggregation-induced emission characteristics." *Chem. Soc. Rev.*, 44(13), 4228–4238.
- Kwon, J. E., and Park, S. Y. (2011). "Advanced Organic Optoelectronic Materials: Harnessing Excited-State Intramolecular Proton Transfer (ESIPT) Process." *Adv. Mater.*, 23(32), 3615–3642.
- Lamansky, S., Djurovich, P., Murphy, D., Abdel-Razzaq, F., Lee, H.-E., Adachi, C., Burrows, P. E., Forrest, S. R., and Thompson, M. E. (2001). "Highly phosphorescent bis-cyclometalated iridium complexes: synthesis, photophysical characterization, and use in organic light emitting diodes." *J. Am. Chem. Soc.*, 123(18), 4304–4312.
- Lan, M., Wu, J., Liu, W., Zhang, H., Zhang, W., Zhuang, X., and Wang, P. (2011). "Highly sensitive fluorescent probe for thiols based on combination of PET and ESIPT mechanisms." *Sens. Actuators B Chem.*, 156(1), 332–337.

- Lan, S.-C., and Liu, Y.-H. (2015). "TDDFT study on the excited-state proton transfer of 8-hydroxyquinoline: Key role of the excited-state hydrogen-bond strengthening." *Spectrochim. Acta. A. Mol. Biomol. Spectrosc.*, 139, 49–53.
- Langhals, H., Karolin, J., and Johansson, L. B.-Å. (1998). "Spectroscopic properties of new and convenient standards for measuring fluorescence quantum yields." *J. Chem. Soc. Faraday Trans.*, 94(19), 2919–2922.
- Leclerc, N., Sanaur, S., Galmiche, L., Mathevet, F., Attias, A.-J., Fave, J.-L., Roussel, J., Hapiot, P., Lemaître, N., and Geffroy, B. (2005). "6-(Arylvinylylene)-3-bromopyridine Derivatives as Lego Building Blocks for Liquid Crystal, Nonlinear Optical, and Blue Light Emitting Chromophores." *Chem. Mater.*, 17(3), 502–513.
- Lee, C., Yang, W., and Parr, R. G. (1988). "Development of the Colle-Salvetti correlation-energy formula into a functional of the electron density." *Phys. Rev. B*, 37(2), 785–789.
- Leung, N. L., Xie, N., Yuan, W., Liu, Y., Wu, Q., Peng, Q., Miao, Q., Lam, J. W., and Tang, B. Z. (2014). "Restriction of intramolecular motions: the general mechanism behind aggregation-induced emission." *Chem. Eur. J.*, 20(47), 15349–15353.
- Li, B., Lan, J., Wu, D., and You, J. (2015). "Rhodium (III)-Catalyzed ortho-Heteroarylation of Phenols through Internal Oxidative C–H Activation: Rapid Screening of Single-Molecular White-Light-Emitting Materials." *Angew. Chem. Int. Ed.*, 54(47), 14008–14012.
- Li, C., Ma, C., Li, D., and Liu, Y. (2016). "Excited state intramolecular proton transfer (ESIPT) of 6-amino-2-(2'-hydroxyphenyl)benzoxazole in dichloromethane and methanol: A TD-DFT quantum chemical study." *J. Lumin.*, 172, 29–33.
- Li, G.-Y., and Han, K.-L. (2018). "The sensing mechanism studies of the fluorescent probes with electronically excited state calculations." *Wiley Interdiscip. Rev. Comput. Mol. Sci.*, 8(2), e1351.
- Li, J., Yan, F., Gao, J., Li, P., Xiong, W.-W., Zhao, Y., Sun, X. W., and Zhang, Q. (2015). "Synthesis, physical properties and OLED performance of azatetracenes." *Dyes Pigments*, 112(Supplement C), 93–98.
- Li, Q., and Li, Z. (2017). "The Strong Light-Emission Materials in the Aggregated State: What Happens from a Single Molecule to the Collective Group." *Adv. Sci.*, 4(7), 1600484.
- Li, W., and Kwok, H. (2012). "Conduction Mechanisms in Organic Semiconductors." *Encycl. Nanotechnol.*, B. Bhushan, ed., Dordrecht: Springer Netherlands, 493–500.
- Li, W., Yao, L., Liu, H., Wang, Z., Zhang, S., Xiao, R., Zhang, H., Lu, P., Yang, B., and Ma, Y. (2014). "Highly efficient deep-blue OLED with an extraordinarily narrow FWHM of 35 nm and a y coordinate <0.05 based on a fully twisting donor–acceptor molecule." *J Mater Chem C*, 2(24), 4733–4736.

- Li, X., Shan, D., Kim, C., and Son, Y.-A. (2016). “The excited-state intramolecular proton transfer fluorescence of HBT derivative induced by solvent polarity.” *Mol. Cryst. Liq. Cryst.*, 635(1), 158–166.
- Li, Y., Wang, L., Guo, X., and Zhang, J. (2015c). “A CASSCF/CASPT2 insight into excited-state intramolecular proton transfer of four imidazole derivatives.” *J. Comput. Chem.*, 36(32), 2374–2380.
- Li, Y.-F., Jiang, J.-H., and Jian, F.-F. (2010). “N’-(4-Hydroxy-benzyl-ylidene)thio-phenene-2-carbohydrazide.” *Acta Crystallogr. Sect. E Struct. Rep. Online*, 66(Pt 7), o1719.
- Lin, Y., Fan, H., Li, Y., and Zhan, X. (2012). “Organic Semiconductors: Thiazole-Based Organic Semiconductors for Organic Electronics (Adv. Mater. 23/2012).” *Adv. Mater.*, 24(23), 3081–3081.
- Linton, K. E., Fisher, A. L., Pearson, C., Fox, M. A., Pålsson, L.-O., Bryce, M. R., and Petty, M. C. (2012). “Colour tuning of blue electroluminescence using bipolar carbazole-oxadiazole molecules in single-active-layer organic light emitting devices (OLEDs).” *J. Mater. Chem.*, 22(23), 11816–11825.
- Liu, H., Cheng, X., Zhang, H., Wang, Y., Zhang, H., and Yamaguchi, S. (2017). “ESIPT-active organic compounds with white luminescence based on crystallization-induced keto emission (CIKE).” *Chem. Commun.*, 53(55), 7832–7835.
- Liu, J., Meng, Q., Zhang, X., Lu, X., He, P., Jiang, L., Dong, H., and Hu, W. (2013). “Aggregation-induced emission enhancement based on 11, 11, 12, 12-tetracyano-9, 10-anthraquinodimethane.” *Chem. Commun.*, 49(12), 1199–1201.
- Liu, X., Zhao, J., and Zheng, Y. (2017b). “Insight into the excited-state double proton transfer mechanisms of doxorubicin in acetonitrile solvent.” *RSC Adv.*, 7(81), 51318–51323.
- Lu, X., Zhai, Y., Zhang, M., and Song, Y. (2018b). “A theoretical study on the ESPT mechanism for a novel Bis-HPBT fluorophore.” *J. Phys. Org. Chem.*, 31(6), e3821.
- Luo, J., Xie, Z., Lam, J. W. Y., Cheng, L., Chen, H., Qiu, C., Kwok, H. S., Zhan, X., Liu, Y., Zhu, D., and Tang, B. Z. (2001). “Aggregation-induced emission of 1-methyl-1,2,3,4,5-pentaphenylsilole.” *Chem. Commun.*, 0(18), 1740–1741.
- M., G., M. G., H., and R. H., F. (1999). *Handb. Oligo- Polythiophene*, New York: Wiley-VCH.
- Ma, J., Zhao, J., Yang, P., Huang, D., Zhang, C., and Li, Q. (2012). “New excited state intramolecular proton transfer (ESIPT) dyes based on naphthalimide and observation of long-lived triplet excited states.” *Chem. Commun.*, 48(78), 9720–9722.
- Mahanta, S., Paul, B. K., Singh, R. B., and Guchhait, N. (2011). “Inequivalence of substitution pairs in hydroxynaphthaldehyde: A theoretical measurement by intramolecular

hydrogen bond strength, aromaticity, and excited-state intramolecular proton transfer reaction.” *J. Comput. Chem.*, 32(1), 1–14.

Maity, A., Ali, F., Agarwalla, H., Anothumakkool, B., and Das, A. (2015). “Tuning of multiple luminescence outputs and white-light emission from a single gelator molecule through an ESIPT coupled AIEE process.” *Chem. Commun.*, 51(11), 2130–2133.

Mallesham, G., Balaiah, S., Reddy, M. A., Sridhar, B., Singh, P., Srivastava, R., Bhanuprakash, K., and Rao, V. J. (2014). “Design and synthesis of novel anthracene derivatives as n-type emitters for electroluminescent devices: a combined experimental and DFT study.” *Photochem. Photobiol. Sci.*, 13(2), 342–357.

Mandal, S., and Ramanujam, K. (2016). “DFT/TD-DFT Studies of Metal-Free N-Annulated Perylene Based Organic Sensitizers for Dye-Sensitized Solar Cells: Is Thiophene Spacer Essential for Improving the DSSC Performance?” *ChemistrySelect*, 1(18), 5854–5862.

Maragani, R., Sharma, R., and Misra, R. (2017). “Donor-Acceptor Triphenylvinyl and Tetraphenyl Conjugates: Synthesis, Aggregation and Computational Studies.” *ChemistrySelect*, 2(31), 10033–10037.

Martínez-Máñez, R., and Sancenón, F. (2003). “Fluorogenic and Chromogenic Chemosensors and Reagents for Anions.” *Chem. Rev.*, 103(11), 4419–4476.

Maxim, C., Pasatoiu, T. D., Kravtsov, V. C., Shova, S., Muryn, C. A., Winpenny, R. E., Tuna, F., and Andruh, M. (2008). “Copper (II) and zinc (II) complexes with Schiff-base ligands derived from salicylaldehyde and 3-methoxysalicylaldehyde: Synthesis, crystal structures, magnetic and luminescence properties.” *Inorganica Chim. Acta*, 361(14–15), 3903–3911.

McDonald, L., Wang, J., Alexander, N., Li, H., Liu, T., and Pang, Y. (2016). “Origin of Water-Induced Fluorescence Turn-On from a Schiff Base Compound: AIE or H-Bonding Promoted ESIPT?” *J. Phys. Chem. B*, 120(4), 766–772.

Mei, J., Hong, Y., Lam, J. W., Qin, A., Tang, Y., and Tang, B. Z. (2014). “Aggregation-induced emission: the whole is more brilliant than the parts.” *Adv. Mater.*, 26(31), 5429–5479.

Mei, J., Leung, N. L., Kwok, R. T., Lam, J. W., and Tang, B. Z. (2015). “Aggregation-induced emission: together we shine, united we soar!” *Chem. Rev.*, 115(21), 11718–11940.

Mennucci, B., Cancès, E., and Tomasi, J. (1997). “Evaluation of Solvent Effects in Isotropic and Anisotropic Dielectrics and in Ionic Solutions with a Unified Integral Equation Method: Theoretical Bases, Computational Implementation, and Numerical Applications.” *J. Phys. Chem. B*, 101(49), 10506–10517.

- Miehlich, B., Savin, A., Stoll, H., and Preuss, H. (1989). "Results obtained with the correlation energy density functionals of Becke and Lee, Yang and Parr." *Chem. Phys. Lett.*, 157(3), 200–206.
- Miertuš, S., Scrocco, E., and Tomasi, J. (1981). "Electrostatic interaction of a solute with a continuum. A direct utilization of AB initio molecular potentials for the prevision of solvent effects." *Chem. Phys.*, 55(1), 117–129.
- Miertuš, S., and Tomasi, J. (1982). "Approximate evaluations of the electrostatic free energy and internal energy changes in solution processes." *Chem. Phys.*, 65(2), 239–245.
- Mir, J. M., Roy, S., Vishwakarma, P. K., and Maurya, R. C. (2018). "cis-Dioxomolybdenum(VI) complex of N-o-hydroxyacetophenone-isonicotinic acid hydrazide as nosocomial anti-infectious agent: experimental and theoretical study." *J. Chin. Adv. Mater. Soc.*, 6(3), 282–300.
- Mishra, A. K., and Dogra, S. K. (1983). "Effect of solvents and pH on the absorption and fluorescence spectra of 2-phenylbenzimidazole." *Spectrochim. Acta Part Mol. Spectrosc.*, 39(7), 609–611.
- Mitschke, U., and Bäuerle, P. (2000). "The electroluminescence of organic materials." *J. Mater. Chem.*, 10(7), 1471–1507.
- Montes, V. A., Li, G., Pohl, R., Shinar, J., and Anzenbacher, P. (2004). "Effective Color Tuning in Organic Light-Emitting Diodes Based on Aluminum Tris(5-aryl-8-hydroxyquinoline) Complexes." *Adv. Mater.*, 16(22), 2001–2003.
- Morin, J.-F., Drolet, N., Tao, Y., and Leclerc, M. (2004). "Syntheses and Characterization of Electroactive and Photoactive 2,7-Carbazolenevinylene-Based Conjugated Oligomers and Polymers." *Chem. Mater.*, 16(23), 4619–4626.
- Müllen, K., and Scherf, U. (2006). *Organic Light Emitting Devices: Synthesis, Properties and Applications*. John Wiley & Sons.
- Muriel, W. A., Morales-Cueto, R., and Rodríguez-Córdoba, W. (2019). "Unravelling the solvent polarity effect on the excited state intramolecular proton transfer mechanism of the 1- and 2-salicylideneanthrylamine. A TD-DFT case study." *Phys. Chem. Chem. Phys.*, 21(2), 915–928.
- Muruganatham, S., Nagarajan, N., Velmurugan, G., Prakash, A., Katiyar, M., Venuvanalingam, P., and Renganathan, R. (2017). "Green light-emitting 2-(1H-indol-3-yl)acetonitrile-based D–A fluorophores – a combined theoretical and experimental study." *Mater. Chem. Front.*, 1(7), 1373–1383.
- Mutai, T., Tomoda, H., Ohkawa, T., Yabe, Y., and Araki, K. (2008). "Switching of polymorph-dependent ESIPt luminescence of an imidazo [1, 2-a] pyridine derivative." *Angew. Chem. Int. Ed.*, 47(49), 9522–9524.

- Nakane, Y., Takeda, T., Hoshino, N., Sakai, K., and Akutagawa, T. (2015). "Cation–Anion Dual Sensing of a Fluorescent Quinoxalinone Derivative Using Lactam–Lactim Tautomerism." *J. Phys. Chem. A*, 119(24), 6223–6231.
- Noda, T., Ogawa, H., Noma, N., and Shirota, Y. (1997). "A novel family of amorphous molecular materials containing an oligothiophene moiety as color-tunable emitting materials for organic electroluminescent devices." *Adv. Mater.*, 9(9), 720–722.
- Noda, T., Ogawa, H., Noma, N., and Shirota, Y. (1999). "Organic light-emitting diodes using a novel family of amorphous molecular materials containing an oligothiophene moiety as colour-tunable emitting materials." *J. Mater. Chem.*, 9(9), 2177–2181.
- Noda, T., and Shirota, Y. (1998). "5,5'-Bis(dimesitylboryl)-2,2'-bithiophene and 5,5'-Bis(dimesitylboryl)-2,2':5',2'-terthiophene as a Novel Family of Electron-Transporting Amorphous Molecular Materials." *J. Am. Chem. Soc.*, 120(37), 9714–9715.
- Nolan, E. M., and Lippard, S. J. (2008). "Tools and Tactics for the Optical Detection of Mercuric Ion." *Chem. Rev.*, 108(9), 3443–3480.
- Ohmori, Y., Fujii, A., Uchida, M., Morishima, C., and Yoshino, K. (1993). "Observation of spectral narrowing and emission energy shift in organic electroluminescent diode utilizing 8-hydroxyquinoline aluminum/aromatic diamine multilayer structure." *Appl. Phys. Lett.*, 63(14), 1871–1873.
- O. Hubin, P., D. Laurent, A., P. Vercauteren, D., and Jacquemin, D. (2014). "Investigation of ESIPT in a panel of chromophores presenting N–H···N intramolecular hydrogen bonds." *Phys. Chem. Chem. Phys.*, 16(46), 25288–25295.
- Oliveira, F. F., Santos, D. C., Lapis, A. A., Corrêa, J. R., Gomes, A. F., Gozzo, F. C., Moreira Jr, P. F., Oliveira, V. C. de, Quina, F. H., and Neto, B. A. (2010). "On the use of 2, 1, 3-benzothiadiazole derivatives as selective live cell fluorescence imaging probes." *Bioorg. Med. Chem. Lett.*, 20(20), 6001–6007.
- Padalkar, V. S., Kuwada, K., Sakamaki, D., Tohnai, N., Akutagawa, T., Sakai, K., Sakurai, T., and Seki, S. (2017). "AIE Active Carbazole-Benzothiazole Based ESIPT Motifs: Positional Isomers Directing the Optical and Electronic Properties." *ChemistrySelect*, 2(5), 1959–1966.
- Padalkar, V. S., Ramasami, P., and Sekar, N. (2014). "A comprehensive spectroscopic and computational investigation of intramolecular proton transfer in the excited states of 2-(2'-hydroxyphenyl) benzoxazole and its derivatives." *J. Lumin.*, 146, 527–538.
- Padalkar, V. S., and Seki, S. (2015). "Excited-state intramolecular proton-transfer (ESIPT)-inspired solid state emitters." *Chem. Soc. Rev.*, 45(1), 169–202.
- Padalkar, V. S., Tathe, A., Gupta, V. D., Patil, V. S., Phatangare, K., and Sekar, N. (2012). "Synthesis and photo-physical characteristics of ESIPT inspired 2-substituted

benzimidazole, benzoxazole and benzothiazole fluorescent derivatives.” *J. Fluoresc.*, 22(1), 311–322.

Parada, G. A., Markle, T. F., Glover, S. D., Hammarström, L., Ott, S., and Zietz, B. (2015). “Control over Excited State Intramolecular Proton Transfer and Photoinduced Tautomerization: Influence of the Hydrogen-Bond Geometry.” *Chem. – Eur. J.*, 21(17), 6362–6366.

Park, S., Kwon, J. E., and Park, S. Y. (2012). “Strategic emission color tuning of highly fluorescent imidazole-based excited-state intramolecular proton transfer molecules.” *Phys. Chem. Chem. Phys.*, 14(25), 8878–8884.

Parker, C. A., and Hatchard, C. G. (1961). “Triplet-singlet emission in fluid solutions. Phosphorescence of eosin.” *Trans. Faraday Soc.*, 57, 1894–1904.

Paterson, M. J., Robb, M. A., Blancafort, L., and DeBellis, A. D. (2004). “Theoretical study of benzotriazole UV photostability: ultrafast deactivation through coupled proton and electron transfer triggered by a charge-transfer state.” *J. Am. Chem. Soc.*, 126(9), 2912–2922.

Pathak, S. K., Gupta, M., Pal, S. K., and Achalkumar, A. S. (2016). “Hexacatenars Exhibiting π - π Driven Supergelation, Aggregation Induced Blue Light Emission and Thermochromism.” *ChemistrySelect*, 1(16), 5107–5120.

Patil, V. S., Padalkar, V. S., Tathe, A. B., and Sekar, N. (2013). “ESIPT-inspired benzothiazole fluorescein: Photophysics of microenvironment pH and viscosity.” *Dyes Pigments*, 98(3), 507–517.

Paul, B. K., and Guchhait, N. (2010). “Modulated Photophysics of an ESIPT Probe 1-Hydroxy-2-naphthaldehyde within Motionally Restricted Environments of Liposome Membranes Having Varying Surface Charges.” *J. Phys. Chem. B*, 114(39), 12528–12540.

Peng, L., Gao, M., Cai, X., Zhang, R., Li, K., Feng, G., Tong, A., and Liu, B. (2015). “A fluorescent light-up probe based on AIE and ESIPT processes for β -galactosidase activity detection and visualization in living cells.” *J. Mater. Chem. B*, 3(47), 9168–9172.

Peng, L., Xu, S., Zheng, X., Cheng, X., Zhang, R., Liu, J., Liu, B., and Tong, A. (2017). “Rational Design of a Red-Emissive Fluorophore with AIE and ESIPT Characteristics and Its Application in Light-Up Sensing of Esterase.” *Anal. Chem.*, 89(5), 3162–3168.

Pham, T. H. N., and Clarke, R. J. (2008). “Solvent Dependence of the Photochemistry of the Styrylpyridinium Dye RH421.” *J. Phys. Chem. B*, 112(20), 6513–6520.

Pinto da Silva, L., Ferreira, P. J. O., Duarte, D. J. R., Miranda, M. S., and Esteves da Silva, J. C. G. (2014). “Structural, Energetic, and UV–Vis Spectral Analysis of UVA Filter 4-tert-Butyl-4'-methoxydibenzoylmethane.” *J. Phys. Chem. A*, 118(8), 1511–1518.

- Pope, M., and Swenberg, C. E. (1999). *Electronic processes in organic crystals and polymers*. Oxford University Press on Demand.
- Pribat, D., and Plais, F. (2001). "Matrix addressing for organic electroluminescent displays." *Thin Solid Films*, 383(1–2), 25–30.
- Qian, Y., Li, S., Zhang, G., Wang, Q., Wang, S., Xu, H., Li, C., Li, Y., and Yang, G. (2007). "Aggregation-induced emission enhancement of 2-(2'-Hydroxyphenyl) benzothiazole-based excited-state intramolecular proton-transfer compounds." *J. Phys. Chem. B*, 111(21), 5861–5868.
- Qin, J., Wang, B., Yang, Z., and Yu, K. (2016). "A ratiometric fluorescent chemosensor for Zn²⁺ in aqueous solution through an ESIPT coupled AIE process." *Sens. Actuators B Chem.*, 224, 892–898.
- Qiu, Y., Gao, Y., Wang, L., Wei, P., Duan, L., Zhang, D., and Dong, G. (2002). "High-efficiency organic light-emitting diodes with tunable light emission by using aromatic diamine/5, 6, 11, 12-tetraphenylnaphthacene multiple quantum wells." *Appl. Phys. Lett.*, 81(19), 3540–3542.
- Rahulan, K. M., Balamurugan, S., Meena, K. S., Yeap, G.-Y., and Kanakam, C. C. (2014). "Synthesis and nonlinear optical absorption of novel chalcone derivative compounds." *Opt. Laser Technol.*, 56(Supplement C), 142–145.
- Reineke, S., Schwartz, G., Walzer, K., and Leo, K. (2007). "Reduced efficiency roll-off in phosphorescent organic light emitting diodes by suppression of triplet-triplet annihilation." *Appl. Phys. Lett.*, 91(12), 123508.
- Ren, Y., Lam, J. W., Dong, Y., Tang, B. Z., and Wong, K. S. (2005). "Enhanced emission efficiency and excited state lifetime due to restricted intramolecular motion in silole aggregates." *J. Phys. Chem. B*, 109(3), 1135–1140.
- Rode, M. F., and Sobolewski, A. L. (2010). "Effect of Chemical Substituents on the Energetical Landscape of a Molecular Photoswitch: An Ab Initio Study." *J. Phys. Chem. A*, 114(44), 11879–11889.
- Roohi, H., Hejazi, F., Mohtamedifar, N., and Jahantab, M. (2014). "Excited state intramolecular proton transfer (ESIPT) in 2-(2'-hydroxyphenyl)benzoxazole and its naphthalene-fused analogs: A TD-DFT quantum chemical study." *Spectrochim. Acta. A. Mol. Biomol. Spectrosc.*, 118, 228–238.
- Saga, Y., Shibata, Y., and Tamiaki, H. (2010). "Spectral properties of single light-harvesting complexes in bacterial photosynthesis." *J. Photochem. Photobiol. C Photochem. Rev.*, 11(1), 15–24.
- Sajoto, T., Djurovich, P. I., Tamayo, A. B., Oxgaard, J., Goddard III, W. A., and Thompson, M. E. (2009). "Temperature dependence of blue phosphorescent cyclometalated Ir (III) complexes." *J. Am. Chem. Soc.*, 131(28), 9813–9822.

- Sakai, K., Tsuchiya, S., Kikuchi, T., and Akutagawa, T. (2016). “An ESIPT fluorophore with a switchable intramolecular hydrogen bond for applications in solid-state fluorochromism and white light generation.” *J. Mater. Chem. C*, 4(10), 2011–2016.
- Samanta, S., Manna, U., and Das, G. (2017). “White-light emission from simple AIE–ESIPT-excimer tripled single molecular system.” *New J. Chem.*, 41(3), 1064–1072.
- Samuel, I. D. W., and Turnbull, G. A. (2007). “Organic Semiconductor Lasers.” *Chem. Rev.*, 107(4), 1272–1295.
- Schäfer, A., Horn, H., and Ahlrichs, R. (1992). “Fully optimized contracted Gaussian basis sets for atoms Li to Kr.” *J. Chem. Phys.*, 97(4), 2571–2577.
- Scherf, U., Riechel, S., Lemmer, U., and Mahrt, R. F. (2001). “Conjugated polymers: lasing and stimulated emission.” *Curr. Opin. Solid State Mater. Sci.*, 5(2), 143–154.
- Schmidtke, S. J., Underwood, D. F., and Blank, D. A. (2004). “Following the solvent directly during ultrafast excited state proton transfer.” *J. Am. Chem. Soc.*, 126(28), 8620–8621.
- Selvaganapathi, P., Thirumaran, S., and Ciattini, S. (2017). “Synthesis, spectral, crystal structures, Hirshfeld surface analysis and DFT studies on phenylmercury(II) dithiocarbamate complexes and their utility for the preparation of mercury sulfide nanoparticles.” *J. Mol. Struct.*, 1148, 547–556.
- Sensors, F. (2006). “Biosensors; Thompson, RB, Ed.” *CRC Boca Raton FL*.
- Serrano-Andrés, L., and Merchán, M. (2009). “Are the five natural DNA/RNA base monomers a good choice from natural selection?: A photochemical perspective.” *J. Photochem. Photobiol. C Photochem. Rev.*, 10(1), 21–32.
- Shaikh, M., Mohanty, J., Singh, P. K., Bhasikuttan, A. C., Rajule, R. N., Satam, V. S., Bendre, S. R., Kanetkar, V. R., and Pal, H. (2010). “Contrasting Solvent Polarity Effect on the Photophysical Properties of Two Newly Synthesized Aminostyryl Dyes in the Lower and in the Higher Solvent Polarity Regions.” *J. Phys. Chem. A*, 114(13), 4507–4519.
- Sherin, P. S., Grilj, J., Tsentalovich, Y. P., and Vauthey, E. (2009). “Ultrafast Excited-State Dynamics of Kynurenine, a UV Filter of the Human Eye.” *J. Phys. Chem. B*, 113(14), 4953–4962.
- Shigemitsu, Y., Mutai, T., Houjou, H., and Araki, K. (2012). “Excited-state intramolecular proton transfer (ESIPT) emission of hydroxyphenylimidazopyridine: computational study on enhanced and polymorph-dependent luminescence in the solid state.” *J. Phys. Chem. A*, 116(49), 12041–12048.
- Shigemitsu, Y., Mutai, T., Houjou, H., and Araki, K. (2014). “Influence of intermolecular interactions on solid state luminescence of imidazopyridines: theoretical interpretations

using FMO-TDDFT and ONIOM approaches.” *Phys. Chem. Chem. Phys.*, 16(28), 14388–14395.

Singh, H., Sindhu, J., and Khurana, J. M. (2014). “Determination of dipole moment, solvatochromic studies and application as turn off fluorescence chemosensor of new 3-(4-(dimethylamino)phenyl)-1-(5-methyl-1-(naphthalen-1-yl)-1H-1,2,3-triazol-4-yl)prop-2-en-1-one.” *Sens. Actuators B Chem.*, 192(Supplement C), 536–542.

Singh, N., Kaur, N., Mulrooney, R. C., and Callan, J. F. (2008). “A ratiometric fluorescent probe for magnesium employing excited state intramolecular proton transfer.” *Tetrahedron Lett.*, 49(47), 6690–6692.

Singh, P., Singh, H., Sharma, R., Bhargava, G., and Kumar, S. (2016). “Diphenylpyrimidinone–salicylideneamine – new ESIPT based AIEgens with applications in latent fingerprinting.” *J. Mater. Chem. C*, 4(47), 11180–11189.

Singh-Rachford, T. N., and Castellano, F. N. (2010). “Photon upconversion based on sensitized triplet–triplet annihilation.” *Coord. Chem. Rev.*, 18th International Symposium on the Photochemistry and Photophysics of Coordination Compounds Sapporo, 2009, 254(21), 2560–2573.

Singla, N., and Chowdhury, P. (2012). “Role of hydrogen bonding in excited state intramolecular proton transfer of Indole-7-Carboxaldehyde: A theoretical and experimental study.” *Chem. Phys. Lett.*, 548, 71–79.

Slinker, J. D., Rivnay, J., Moskowitz, J. S., Parker, J. B., Bernhard, S., Abruña, H. D., and Malliaras, G. G. (2007). “Electroluminescent devices from ionic transition metal complexes.” *J. Mater. Chem.*, 17(29), 2976–2988.

So, F. F., and Forrest, S. R. (1991). “Evidence for exciton confinement in crystalline organic multiple quantum wells.” *Phys. Rev. Lett.*, 66(20), 2649.

Sobolewski, A. L., and Domcke, W. (1999). “Ab initio potential-energy functions for excited state intramolecular proton transfer: a comparative study of o - hydroxybenzaldehyde, salicylic acid and 7-hydroxy-1-indanone.” *Phys. Chem. Chem. Phys.*, 1(13), 3065–3072.

Sobolewski, A. L., and Domcke, W. (2006). “Photophysics of intramolecularly hydrogen-bonded aromatic systems: ab initio exploration of the excited-state deactivation mechanisms of salicylic acid.” *Phys. Chem. Chem. Phys.*, 8(29), 3410–3417.

Sobolewski, A. L., Domcke, W., and Hättig, C. (2006). “Photophysics of Organic Photostabilizers. Ab Initio Study of the Excited-State Deactivation Mechanisms of 2-(2'-Hydroxyphenyl)benzotriazole.” *J. Phys. Chem. A*, 110(19), 6301–6306.

Song, M.-S., Nguyen, Q. P. B., Song, C.-H., Lee, D., and Chai, K. Y. (2013). “Synthesis of Some Green Dopants for OLEDs Based on Arylamine 2,3-disubstituted Bithiophene Derivatives.” *Molecules*, 18(11), 14033–14041.

- Song, P., and Ma, F.-C. (2013). “Intermolecular hydrogen-bonding effects on photophysics and photochemistry.” *Int. Rev. Phys. Chem.*, 32(4), 589–609.
- Song, S., Chen, J., Pan, W., Song, H., Shi, H., Mai, Y., and Wen, W. (2017). “LED based on alternating benzene-furan oligomers.” *Spectrochim. Acta. A. Mol. Biomol. Spectrosc.*, 170(Supplement C), 157–166.
- Song, Z., Kwok, R. T. K., Zhao, E., He, Z., Hong, Y., Lam, J. W. Y., Liu, B., and Tang, B. Z. (2014). “A Ratiometric Fluorescent Probe Based on ESIPT and AIE Processes for Alkaline Phosphatase Activity Assay and Visualization in Living Cells.” *ACS Appl. Mater. Interfaces*, 6(19), 17245–17254.
- Srinivas, M., Vijayakumar, G. R., Mahadevan, K. M., Nagabhushana, H., and Naik, H. B. (2017). “Synthesis, photoluminescence and forensic applications of blue light emitting azomethine-zinc (II) complexes of bis (salicylidene) cyclohexyl-1, 2-diamino based organic ligands.” *J. Sci. Adv. Mater. Devices*, 2(2), 156–164.
- Srinivasan, V., Jhonsi, M. A., Dhenadhayalan, N., Lin, K.-C., Jaccob, M., and Kathiravan, A. (2017). “AIE Nanodots Obtained from a Pyrene Schiff Base and Their Applications.” *ChemistrySelect*, 2(4), 1353–1359.
- Stasyuk, A. J., Cyrański, M. K., Gryko, D. T., and Solà, M. (2015). “Acidic C–H Bond as a Proton Donor in Excited State Intramolecular Proton Transfer Reactions.” *J. Chem. Theory Comput.*, 11(3), 1046–1054.
- Sun, R. W.-Y., and Che, C.-M. (2009). “The anti-cancer properties of gold(III) compounds with dianionic porphyrin and tetradentate ligands.” *Coord. Chem. Rev., Bioinorganic and Biomedical Chemistry of Gold*, 253(11), 1682–1691.
- Sun, Y.-Y., Liao, J.-H., Fang, J.-M., Chou, P.-T., Shen, C.-H., Hsu, C.-W., and Chen, L.-C. (2006). “Fluorescent Organic Nanoparticles of Benzofuran–Naphthyridine Linked Molecules: Formation and Fluorescence Enhancement in Aqueous Media.” *Org. Lett.*, 8(17), 3713–3716.
- “Synthesis, crystal structures and two-photon absorption properties of a series of terpyridine-based chromophores.” (2012). *Dyes Pigments*, 95(1), 149–160.
- Szlapa-Kula, A., Kula, S., Filapek, M., Fabianczyk, A., Bujak, K., Siwy, M., Kotowicz, S., Janeczek, H., Smolarek, K., Maćkowski, S., Krompiec, S., and Schab-Balcerzak, E. (2018). “Synthesis, electrochemistry and optical properties with electroluminescence ability of new multisubstituted naphthalene derivatives with thiophene and carbazole motifs.” *J. Lumin.*, 196, 244–255.
- Takagi, K., Yamada, Y., Fukuda, R., Ehara, M., and Takeuchi, D. (2018). “ESIPT emission behavior of methoxy-substituted 2-hydroxyphenylbenzimidazole isomers.” *New J. Chem.*, 42(8), 5923–5928.

Tang, B. Z., and Qin, A. (2013). *Aggregation-Induced Emission: Fundamentals*. John Wiley & Sons.

Tang, B. Z., Zhan, X., Yu, G., Lee, P. P. S., Liu, Y., and Zhu, D. (2001). "Efficient blue emission from siloles." *J. Mater. Chem.*, 11(12), 2974–2978.

Tang, C. W., and VanSlyke, S. A. (1987). "Organic electroluminescent diodes." *Appl. Phys. Lett.*, 51(12), 913–915.

Tang, C. W., and VanSlyke, S. A. (1998). "Organic electroluminescent diodes." *Appl. Phys. Lett.*, APLCLASS2019(1), 913–915.

Tang, K.-C., Chang, M.-J., Lin, T.-Y., Pan, H.-A., Fang, T.-C., Chen, K.-Y., Hung, W.-Y., Hsu, Y.-H., and Chou, P.-T. (2011). "Fine Tuning the Energetics of Excited-State Intramolecular Proton Transfer (ESIPT): White Light Generation in A Single ESIPT System." *J. Am. Chem. Soc.*, 133(44), 17738–17745.

Tang, W., Xiang, Y., and Tong, A. (2009). "Salicylaldehyde azines as fluorophores of aggregation-induced emission enhancement characteristics." *J. Org. Chem.*, 74(5), 2163–2166.

Tekuri, V., and Trivedi, D. R. (2017). "A new colorimetric chemosensors for Cu²⁺ and Cd²⁺ ions detection: Application in environmental water samples and analytical method validation." *Anal. Chim. Acta*, 972, 81–93.

Tian, D., Zhou, Y., Li, Z., Liu, S., Shao, J., Yang, X., Shao, J., Huang, W., and Zhao, B. (2017). "Thieno[3,2-b]thiophene-Based Discotic Liquid Crystal Mesogens: Rational Synthesis, Physical Properties and Self-Assembly." *ChemistrySelect*, 2(26), 8137–8145.

Toal, S. J., Jones, K. A., Magde, D., and Trogler, W. C. (2005). "Luminescent Silole Nanoparticles as Chemoselective Sensors for Cr(VI)." *J. Am. Chem. Soc.*, 127(33), 11661–11665.

Tomasi, J., and Persico, M. (1994). "Molecular Interactions in Solution: An Overview of Methods Based on Continuous Distributions of the Solvent." *Chem. Rev.*, 94(7), 2027–2094.

Tong, H., Hong, Y., Dong, Y., Häußler, M., Lam, J. W. Y., Li, Z., Guo, Z., Guo, Z., and Tang, B. Z. (2006). "Fluorescent 'light-up' bioprobes based on tetraphenylethylene derivatives with aggregation-induced emission characteristics." *Chem. Commun.*, 0(35), 3705–3707.

Tong, Y., Mei, W., and Ma, J. (2018). "Theoretical insight into the excited-state proton transfer process: Role of the substituent -CN on HBT system." *J. Phys. Org. Chem.*, 31(7), e3832.

- Tracy, H. J., Mullin, J. L., Klooster, W. T., Martin, J. A., Haug, J., Wallace, S., Rudloe, I., and Watts, K. (2005). “Enhanced Photoluminescence from Group 14 Metalloles in Aggregated and Solid Solutions.” *Inorg. Chem.*, 44(6), 2003–2011.
- Usuki, T., Shimada, M., Yamanoi, Y., Ohto, T., Tada, H., Kasai, H., Nishibori, E., and Nishihara, H. (2018). “Aggregation-Induced Emission Enhancement from Disilane-Bridged Donor–Acceptor–Donor Luminogens Based on the Triarylamine Functionality.” *ACS Appl. Mater. Interfaces*.
- Wang, B., Wang, Y., Hua, J., Jiang, Y., Huang, J., Qian, S., and Tian, H. (2011). “Starburst Triarylamine Donor–Acceptor–Donor Quadrupolar Derivatives Based on Cyano-Substituted Diphenylaminestyrylbenzene: Tunable Aggregation-Induced Emission Colors and Large Two-Photon Absorption Cross Sections.” *Chem. – Eur. J.*, 17(9), 2647–2655.
- Wang, M., Zhang, G., Zhang, D., Zhu, D., and Tang, B. Z. (2010). “Fluorescent bio/chemosensors based on silole and tetraphenylethene luminogens with aggregation-induced emission feature.” *J. Mater. Chem.*, 20(10), 1858–1867.
- Wang, Y., Shi, Y., Cong, L., and Li, H. (2015). “TDDFT study of twisted intramolecular charge transfer and intermolecular double proton transfer in the excited state of 4'-dimethylaminoflavonol in ethanol solvent.” *Spectrochim. Acta. A. Mol. Biomol. Spectrosc.*, 137, 913–918.
- Wang, Y., Yang, G., Jia, M., Song, X., Zhang, Q., and Yang, D. (2019). “Insights into the excited state dynamical process for 3-hydroxy-2-(5-(5-(5-(3-hydroxy-4-oxo-4H-chromen-2-yl)thiophen-2-yl)thiophen-2-yl)thiophen-2-yl)-4H-chromen-4-one.” *J. Phys. Org. Chem.*, 32(3), e3911.
- Wang, Y., Yang, G., and Yang, D. (2018). “Theoretical insights into the ESIPT process for π -conjugated benzimidazole compounds.” *J. Phys. Org. Chem.*, 31(11), e3868.
- Wang, Z., Shao, H., Ye, J., Tang, L., and Lu, P. (2005). “Dibenzosuberonylidene-Ended Fluorophores: Rapid and Efficient Synthesis, Characterization, and Aggregation-Induced Emissions.” *J. Phys. Chem. B*, 109(42), 19627–19633.
- Watanabe, S., Onogawa, O., Komatsu, Y., and Yoshida, K. (1998). “Luminescent Metalloceptor with a Neutral Bis(Acylaminoimidazoline) Binding Site: Optical Sensing of Anionic and Neural Phosphodiesterases.” *J. Am. Chem. Soc.*, 120(1), 229–230.
- Wei, Q., Zhou, Q., Zhao, M., Zhang, M., and Song, P. (2017). “Theoretical study on ESIPT mechanism of 2-acetylcyclohexane-1,3-dione in hexane and acetonitrile solvents.” *J. Lumin.*, 183, 7–12.
- Weller, A. (1956). “Inermolekularer Protonenübergang im angeregten Zustand.” *Z. Für Elektrochem. Berichte Bunsenges. Für Phys. Chem.*, 60(9–10), 1144–1147.

- Wilbraham, L., Savarese, M., Rega, N., Adamo, C., and Ciofini, I. (2014). “Describing excited state intramolecular proton transfer in dual emissive systems: a density functional theory based analysis.” *J. Phys. Chem. B*, 119(6), 2459–2466.
- Williams, A. T. R., Winfield, S. A., and Miller, J. N. (1983a). “Relative fluorescence quantum yields using a computer-controlled luminescence spectrometer.” *Analyst*, 108(1290), 1067–1071.
- Williams, A. T. R., Winfield, S. A., and Miller, J. N. (1983b). “Relative fluorescence quantum yields using a computer-controlled luminescence spectrometer.” *Analyst*, 108(1290), 1067–1071.
- Wirth, M. J. (1982). “Solvation effects on spectroscopic measurements.” *TrAC Trends Anal. Chem.*, 1(16), 383–386.
- Wong, M. S., Li, Z. H., Tao, Y., and D’Iorio, M. (2003). “Synthesis and Functional Properties of Donor–Acceptor π -Conjugated Oligomers.” *Chem. Mater.*, 15(5), 1198–1203.
- Wu, D.-E., Yao, Q.-C., and Xia, M. (2015). “How is the AIE mechanism profoundly changed in an ESIPT family: the novel introduction of a tetraphenylethene group onto (Z)-3-(quinolin-2-ylmethylene)-3,4-dihydroquinoxalin-2(1H)-one.” *Phys. Chem. Chem. Phys.*, 17(5), 3287–3294.
- Wu, J., Liu, W., Ge, J., Zhang, H., and Wang, P. (2011). “New sensing mechanisms for design of fluorescent chemosensors emerging in recent years.” *Chem. Soc. Rev.*, 40(7), 3483–3495.
- Wu, Q., Peng, Q., Niu, Y., Gao, X., and Shuai, Z. (2012). “Theoretical insights into the aggregation-induced emission by hydrogen bonding: a QM/MM study.” *J. Phys. Chem. A*, 116(15), 3881–3888.
- Wu, W.-R. (2015). “Theoretical investigation on the excited-state intramolecular proton transfer mechanism of 2-(2'-benzofuryl)-3-hydroxychromone: The Excited-State Intramolecular Proton Transfer Mechanism of 2-(2'-Benzofuryl)-3-Hydroxychromone.” *J. Phys. Org. Chem.*, 28(9), 596–601.
- Xia, S.-H., Xie, B.-B., Fang, Q., Cui, G., and Thiel, W. (2015). “Excited-state intramolecular proton transfer to carbon atoms: nonadiabatic surface-hopping dynamics simulations.” *Phys. Chem. Chem. Phys.*, 17(15), 9687–9697.
- Xiang, H., Cheng, J., Ma, X., Zhou, X., and Chruma, J. J. (2013). “Near-infrared phosphorescence: materials and applications.” *Chem. Soc. Rev.*, 42(14), 6128–6185.
- Xiao, H., Chen, K., Cui, D., Jiang, N., Yin, G., Wang, J., and Wang, R. (2014). “Two novel aggregation-induced emission active coumarin-based Schiff bases and their applications in cell imaging.” *New J. Chem.*, 38(6), 2386–2393.

Xie, Z., Yang, B., Xie, W., Liu, L., Shen, F., Wang, H., Yang, X., Wang, Z., Li, Y., Hanif, M., Yang, G., Ye, L., and Ma, Y. (2006). "A Class of Nonplanar Conjugated Compounds with Aggregation-Induced Emission: Structural and Optical Properties of 2,5-Diphenyl-1,4-distyrylbenzene Derivatives with All Cis Double Bonds." *J. Phys. Chem. B*, 110(42), 20993–21000.

Xu, X., Zhao, Y., Dang, J., Yang, X., Zhou, G., Ma, D., Wang, L., Wong, W.-Y., Wu, Z., and Zhao, X. (2012a). "Simple Tuning of the Optoelectronic Properties of IrIII and PtII Electrophosphors Based on Linkage Isomer Formation with a Naphthylthiazolyl Moiety." *Eur. J. Inorg. Chem.*, 2012(13), 2278–2288.

Xu, Z., Xu, L., Zhou, J., Xu, Y., Zhu, W., and Qian, X. (2012). "A highly selective fluorescent probe for fast detection of hydrogen sulfide in aqueous solution and living cells." *Chem. Commun.*, 48(88), 10871–10873.

Yanai, T., Tew, D. P., and Handy, N. C. (2004). "A new hybrid exchange–correlation functional using the Coulomb-attenuating method (CAM-B3LYP)." *Chem. Phys. Lett.*, 393(1), 51–57.

Yang, D., Yang, G., Jia, M., Song, X., and Zhang, Q. (2018). "Theoretical insight into the excited-state behavior of a novel Compound 1: A TDDFT investigation." *J. Phys. Org. Chem.*, 31(6), e3828.

Yang, D., Yang, G., Zhao, J., Zheng, R., Wang, Y., and Lv, J. (2017). "A theoretical assignment on excited-state intramolecular proton transfer mechanism for quercetin." *J. Phys. Org. Chem.*, 30(11), e3684.

Yang, D., Zheng, R., Wang, Y., and Lv, J. (2016). "Theoretical investigation on ESIPT mechanism of a new fluorescent sensor in different solvents." *Spectrochim. Acta. A. Mol. Biomol. Spectrosc.*, 159, 30–34.

Yang, W., and Chen, X. (2014). "Dual fluorescence of excited state intra-molecular proton transfer of HBFO: mechanistic understanding, substituent and solvent effects." *Phys. Chem. Chem. Phys.*, 16(9), 4242–4250.

Yang, X., Zhao, Y., Zhang, X., Li, R., Dang, J., Li, Y., Zhou, G., Wu, Z., Ma, D., Wong, W.-Y., Zhao, X., Ren, A., Wang, L., and Hou, X. (2012). "Thiazole-based metallophosphors of iridium with balanced carrier injection/transporting features and their two-colour WOLEDs fabricated by both vacuum deposition and solution processing-vacuum deposition hybrid strategy." *J. Mater. Chem.*, 22(15), 7136–7148.

Yang, X.-F., Qi, H., Wang, L., Su, Z., and Wang, G. (2009). "A ratiometric fluorescent probe for fluoride ion employing the excited-state intramolecular proton transfer." *Talanta*, 80(1), 92–97.

Yang, Y., Zhao, J., and Li, Y. (2016). "Theoretical Study of the ESIPT Process for a New Natural Product Quercetin." *Sci. Rep.*, 6, 32152.

- Yang, Y., Zhao, Q., Feng, W., and Li, F. (2013). “Luminescent chemodosimeters for bioimaging.” *Chem Rev*, 113(1), 192–270.
- Yao, C., Jiao, B., Yang, X., Xu, X., Dang, J., Zhou, G., Wu, Z., Lv, X., Zeng, Y., and Wong, W.-Y. (2013). “Tris(cyclometalated) Iridium(III) Phosphorescent Complexes with 2-Phenylthiazole-Type Ligands: Synthesis, Photophysical, Redox and Electrophosphorescent Behavior.” *Eur. J. Inorg. Chem.*, 2013(27), 4754–4763.
- Yao, L., Zhang, S., Wang, R., Li, W., Shen, F., Yang, B., and Ma, Y. (2014). “Highly Efficient Near-Infrared Organic Light-Emitting Diode Based on a Butterfly-Shaped Donor–Acceptor Chromophore with Strong Solid-State Fluorescence and a Large Proportion of Radiative Excitons.” *Angew. Chem. Int. Ed.*, 53(8), 2119–2123.
- Yao, Q.-C., Lu, X.-L., and Xia, M. (2014b). “(Z)-3-(Quinolin-2-ylmethylene)-3,4-dihydroquinoxalin-2(1H)-one derivatives: AIE-active compounds with pronounced effects of ESIPT and TICT.” *New J. Chem.*, 38(6), 2693–2700.
- Yao, S., and Qian, Y. (2018). “Aggregation-Induced Emission, Functionalized Fluorescent Nanoparticles and Cells Imaging of a Water-Soluble Pyridyl-Naphthalimide Dendron.” *ChemistrySelect*, 3(1), 308–313.
- Yeh, H.-C., Yeh, S.-J., and Chen, C.-T. (2003). “Readily synthesised arylamino fumaronitrile for non-doped red organic light-emitting diodes.” *Chem. Commun.*, 0(20), 2632–2633.
- Yersin, H. (2008). *Highly Efficient OLEDs with Phosphorescent Materials*. John Wiley & Sons.
- Yin, H., and Shi, Y. (2018). “Theoretical investigation on the excited state intramolecular proton coupled charge transfer phenomenon for a novel fluorophore.” *J. Phys. Org. Chem.*, 31(10), e3856.
- Yoo, S.-J., Yun, H.-J., Kang, I., Thangaraju, K., Kwon, S.-K., and Kim, Y.-H. (2013). “A new electron transporting material for effective hole-blocking and improved charge balance in highly efficient phosphorescent organic light emitting diodes.” *J. Mater. Chem. C*, 1(11), 2217–2223.
- Yu, G., Yin, S., Liu, Y., Chen, J., Xu, X., Sun, X., Ma, D., Zhan, X., Peng, Q., Shuai, Z., Tang, B., Zhu, D., Fang, W., and Luo, Y. (2005). “Structures, Electronic States, Photoluminescence, and Carrier Transport Properties of 1,1-Disubstituted 2,3,4,5-Tetraphenylsiloles.” *J. Am. Chem. Soc.*, 127(17), 6335–6346.
- Yu, T., Liu, L., Xie, Z., and Ma, Y. (2015). “Progress in small-molecule luminescent materials for organic light-emitting diodes.” *Sci. China Chem.*, 58(6), 907–915.
- Zara, Z., Iqbal, J., BiBi, S., Sadaf, S., and Eliasson, B. (2017). “Designing Benzodithiophene-Based Donor Materials with Favorable Photovoltaic Parameters for Bulk Heterojunction Organic Solar Cells.” *ChemistrySelect*, 2(20), 5628–5639.

- Zhang, J. F., Zhou, Y., Yoon, J., and Kim, J. S. (2011). “Recent progress in fluorescent and colorimetric chemosensors for detection of precious metal ions (silver, gold and platinum ions).” *Chem. Soc. Rev.*, 40(7), 3416–3429.
- Zhang, M., Zhou, Q., Du, C., Ding, Y., and Song, P. (2016). “Detailed theoretical investigation on ESIPT process of pigment yellow 101.” *RSC Adv.*, 6(64), 59389–59394.
- Zhang, N., Hu, Y., and Liu, X. (2013). “Transparent organic thin film transistors with WO₃/Ag/WO₃ source-drain electrodes fabricated by thermal evaporation.” *Appl. Phys. Lett.*, 103(3), 033301.
- Zhang, P., Nie, X., Gao, M., Zeng, F., Qin, A., Wu, S., and Zhong Tang, B. (2017). “A highly selective fluorescent nanoprobe based on AIE and ESIPT for imaging hydrogen sulfide in live cells and zebrafish.” *Mater. Chem. Front.*, 1(5), 838–845.
- Zhang, Q., Luo, L., Xu, H., Hu, Z., Brommesson, C., Wu, J., Sun, Z., Tian, Y., and Uvdal, K. (2016). “Design, synthesis, linear and nonlinear photophysical properties of novel pyrimidine-based imidazole derivatives.” *New J. Chem.*, 40(4), 3456–3463.
- Zhang, Q., Zhang, T., Cheng, S., Yang, G., Jia, M., and Song, X. (2019a). “A detailed theoretical simulation about the excited state dynamical process for the novel (benzo[d]thiazol-2-yl)-5-(9H-carbazol-9-yl)phenol molecule.” *J. Phys. Org. Chem.*, e3942.
- Zhang, W., Wang, N., Yu, Y., Shan, Y.-M., Wang, B., Pu, X.-M., and Yu, X.-Q. (n.d.). “Synthetic Regulation of 1,4-Dihydropyridines for the AIE or AIEE Effect: From Rational Design to Mechanistic Views.” *Chem. – Eur. J.*, n/a-n/a.
- Zhang, Y., Ren, F., Li, Q., Zhang, Z., He, X., Chen, Z., Shi, J., and Tu, G. (2018). “Novel N-heteroacene small molecules as electron donors for organic bulk heterojunction photovoltaics.” *Org. Electron.*, 57, 93–97.
- Zhao, G.-J., and Han, K.-L. (2007). “Early Time Hydrogen-Bonding Dynamics of Photoexcited Coumarin 102 in Hydrogen-Donating Solvents: Theoretical Study.” *J. Phys. Chem. A*, 111(13), 2469–2474.
- Zhao, G.-J., and Han, K.-L. (2008). “Effects of Hydrogen Bonding on Tuning Photochemistry: Concerted Hydrogen-Bond Strengthening and Weakening.” *ChemPhysChem*, 9(13), 1842–1846.
- Zhao, G.-J., and Han, K.-L. (2012). “Hydrogen Bonding in the Electronic Excited State.” *Acc. Chem. Res.*, 45(3), 404–413.
- Zhao, J., Chen, J., Liu, J., and R. Hoffmann, M. (2015). “Competitive excited-state single or double proton transfer mechanisms for bis-2,5-(2-benzoxazolyl)-hydroquinone and its derivatives.” *Phys. Chem. Chem. Phys.*, 17(18), 11990–11999.

- Zhao, J., Dong, H., and Zheng, Y. (2018). "Theoretical Insights Into the Excited State Double Proton Transfer Mechanism of Deep Red Pigment Alkannin." *J. Phys. Chem. A*, 122(5), 1200–1208.
- Zhao, J., Dong, H., and Zheng, Y. (2018). "Elaborating the excited state multiple proton transfer mechanism for 9H-pyrido[3,4-b]indole." *J. Lumin.*, 195, 228–233.
- Zhao, J., Ji, S., Chen, Y., Guo, H., and Yang, P. (2012). "Excited state intramolecular proton transfer (ESIPT): from principal photophysics to the development of new chromophores and applications in fluorescent molecular probes and luminescent materials." *Phys. Chem. Chem. Phys.*, 14(25), 8803–8817.
- Zhao, J., Ji, S., and Guo, H. (2011). "Triplet–triplet annihilation based upconversion: from triplet sensitizers and triplet acceptors to upconversion quantum yields." *RSC Adv.*, 1(6), 937–950.
- Zhao, J., Liu, X., and Zheng, Y. (2017). "Controlling Excited State Single versus Double Proton Transfer for 2,2'-Bipyridyl-3,3'-diol: Solvent Effect." *J. Phys. Chem. A*, 121(20), 4002–4008.
- Zhao, J., Liu, X., and Zheng, Y. (2017). "Deciphering the excited state behavior for 2-(4'-N,N-Dimethylaminophenyl)imidazo[4,5-b]pyridine." *J. Lumin.*, 188, 1–6.
- Zhao, J., Wu, W., Sun, J., and Guo, S. (2013). "Triplet photosensitizers: from molecular design to applications." *Chem. Soc. Rev.*, 42(12), 5323–5351.
- Zhao, J., and Zheng, Y. (2017). "Elaboration and controlling excited state double proton transfer mechanism of 2,5-bis(benzoxazol-2-yl)thiophene-3,4-diol." *Sci. Rep.*, 7(1).
- Zhao, Q., Huang, C., and Li, F. (2011). "Phosphorescent heavy-metal complexes for bioimaging." *Chem. Soc. Rev.*, 40(5), 2508–2524.
- Zhao, Q., Li, F., and Huang, C. (2010). "Phosphorescent chemosensors based on heavy-metal complexes." *Chem. Soc. Rev.*, 39(8), 3007–3030.
- Zhao, Z., Lam, J. W., and Tang, B. Z. (2012). "Tetraphenylethene: a versatile AIE building block for the construction of efficient luminescent materials for organic light-emitting diodes." *J. Mater. Chem.*, 22(45), 23726–23740.
- Zhelev, Z., Ohba, H., and Bakalova, R. (2006). "Single quantum dot-micelles coated with silica shell as potentially non-cytotoxic fluorescent cell tracers." *J. Am. Chem. Soc.*, 128(19), 6324–6325.
- ZhongTang, B. (2008). "Photoluminescence and electroluminescence of hexaphenylsilole are enhanced by pressurization in the solid state." *Chem. Commun.*, (26), 2989–2991.
- Zhou, J., He, B., Xiang, J., Chen, B., Lin, G., Luo, W., Lou, X., Chen, S., Zhao, Z., and Tang, B. Z. (2016). "Tuning the AIE Activities and Emission Wavelengths of Tetraphenylethene-Containing Luminogens." *ChemistrySelect*, 1(4), 812–818.

Zhou, P., Hoffmann, M. R., Han, K., and He, G. (2015). “New Insights into the Dual Fluorescence of Methyl Salicylate: Effects of Intermolecular Hydrogen Bonding and Solvation.” *J. Phys. Chem. B*, 119(6), 2125–2131.

Zhou, T., Li, F., Fan, Y., Song, W., Mu, X., Zhang, H., and Wang, Y. (2009). “Hydrogen-bonded dimer stacking induced emission of aminobenzoic acid compounds.” *Chem. Commun.*, (22), 3199–3201.

Zhu, M., and Yang, C. (2013). “Blue fluorescent emitters: design tactics and applications in organic light-emitting diodes.” *Chem. Soc. Rev.*, 42(12), 4963–4976.

Zhu, X., Gindre, D., Mercier, N., Frère, P., and Nunzi, J.-M. (2003). “Stimulated Emission from a Needle-like Single Crystal of an End-Capped Fluorene/Phenylene Co-oligomer.” *Adv. Mater.*, 15(11), 906–909.

Zucchi, G., Jeon, T., Tondelier, D., Aldakov, D., Thuéry, P., Ephritikhine, M., and Geffroy, B. (2010). “White electroluminescence of lanthanide complexes resulting from exciplex formation.” *J. Mater. Chem.*, 20(11), 2114–2120.

LIST OF PUBLICATIONS

Papers published/communicated in international journals

- Mohan, M., Pangannaya, S., Satyanarayan, M. N., and Trivedi, D. R. (2018). “Photophysical and electrochemical properties of organic molecules: Solvatochromic effect and DFT studies.” *Opt. Mater.*, **77**, 211–220.
- Mohan, M., Pangannaya, S., Satyanarayan, M. N., and Trivedi, D. R. (2018). “Multicoloured Thiophene Based AIEgens: Single Crystal Structure Elucidation, Spectral Behaviour and DFT Studies.” *ChemistrySelect*, **3(13)**, 3803–3813.
- Mohan, M., Satyanarayan, M. N., and Trivedi, D. R. (2019). “Photophysics of proton transfer in hydrazides: a combined theoretical and experimental analysis towards OLED device application.” *New J. Chem.*, **43(26)**, 10413–10428.
- Mohan, M., Satyanarayan, M. N., and Trivedi, D. R. (2019). “Exploring the possibilities of double proton transfer in hydrazides: A theoretical approach.” *J. Phys. Org. Chem.*, **32(11)**, e4003.

Papers published in conference proceedings

- Mohan, M., Satyanarayan, M. N., and Trivedi, D. R. (2019). “Bithiophene based red light emitting material-Photophysical and DFT studies.” *AIP Conf. Proc.*, AIP Publishing, 030577.

Papers presented in national/international conferences

- Makesh Mohan., Satyanarayan M. N., Trivedi, D. R. (2016). “Design, synthesis, characterization of new fluorescent molecule for OLED device applications” Paper presented in “International conference on Science and Technology: Future Challenges and Solutions and 7th Annual Conference of Indian JSPS Alumni Association” August 08-09, Mysore University, Mysore.
- Makesh Mohan., Satyanarayan M. N., Trivedi, D. R. (2017). “AIE based new thiophene derivative for OLEDs: electrooptical and DFT studies” Paper presented in “Crystal ball vision on science and engineering for societal upliftment” and 8th Annual Conference of Indian JSPS Alumni Association” August 07-08, CSIR-National Institute of Oceanography (NIO), Dona Paula, Goa.

CURRICULUM VITAE

Name: MAKESH MOHAN

Email: maheshbavm@gmail.com

Mobile +91-7259135726

Research Interests

Synthesis and characterization of a few organic small molecules as OLED materials for device applications

Academic qualifications

January 2015 – August 2020	Ph.D. in physics under the guidance of Prof. M. N. Satyanarayan, Department of physics and Dr. Darshak R. Trivedi, Department of Chemistry, National Institute of Technology Karnataka, Surathkal, Mangalore, Karnataka, INDIA
June 2010 - May 2012	Masters in Electronics, Vellore Institute of Technology, VIT, Vellore, Tamil Nadu, India, First class with distinction
June 2007 - May 2010	Bachelor in Electronics (Specialization) Ancillary subjects: Physics and Mathematics, St. Aloysius college (autonomous), Mangalore, Karnataka, India, First class with distinction

Achievements and Awards

1. Served the Students council as class representative during Bachelor of science.
2. Witness to Excellence Merit certificate for securing Distinction in Bachelor of science.
3. First Prize in “Inter-collegiate Science Seminar Competition 2010” conducted by Materials Science Forum, Mangalore University.

Papers published/communicated in international journals

1. **Mohan, M.**, Satyanarayan, M. N., and Trivedi, D. R. (2019). “Photophysics of proton transfer in hydrazides: a combined theoretical and experimental analysis towards OLED device application.” *New J. Chem.*, 43(26), 10413–10428.

2. **Mohan, M.**, Pangannaya, S., Satyanarayan, M. N., and Trivedi, D. R. (2018). "Multicoloured Thiophene Based AIEgens: Single Crystal Structure Elucidation, Spectral Behaviour and DFT Studies." *ChemistrySelect*, 3(13), 3803–3813.
3. **Mohan, M.**, Pangannaya, S., Satyanarayan, M. N., and Trivedi, D. R. (2018). "Photophysical and electrochemical properties of organic molecules: Solvatochromic effect and DFT studies." *Opt. Mater.*, 77, 211–220.
4. **Mohan, M.**, Satyanarayan, M. N., and Trivedi, D. R., "Exploring the Possibilities of Double Proton Transfer in Hydrazides: A Theoretical Approach," *J. Phys. Org. Chem.*, 32(11), e4003.
5. **Mohan, M.**, James, J., Satyanarayan, M. N., and Trivedi, D. R. (2019). "Functionalized pyrene-based AIEgens: synthesis, photophysical characterization and density functional theory studies." *Luminescence*, 1–9.
6. **Mohan, M.**, John, R., Nagarajan, S. M., and Trivedi, D. R. (2020). "Design, Synthesis and Characterization of N-Substituted Heteroaromatics: DFT-Studies and Organic Light Emitting Device Application." *ChemistrySelect*, 5(20), 5903–5915.
7. Pangannaya, S., **Mohan, M.**, and Trivedi, D. R. (2018). "Colorimetric and fluorometric turn-on sensor for selective detection of fluoride ions: sol–gel transition studies and theoretical insights." *New J. Chem.*, 42(12), 10406–10413.
8. TG, A. K., Tekuri, V., **Mohan, M.**, and Trivedi, D. R. (2019). "Selective colorimetric chemosensor for the detection of Hg²⁺ and arsenite ions using Isatin based Schiff's bases; DFT Studies and Applications in test strips." *Sens. Actuators B Chem.*, 284, 271–280.
9. Vikram Thimaradka, Srikala Pangannaya, **Makesh Mohan**, Darshak R. Trivedi, (2018) "Hydrazinylpyridine Based Highly Selective Optical Sensor for Aqueous Source of Carbonate Ions: Electrochemical and DFT studies" *Spectrochim. Acta Mol. Biomol. Spectrosc.*, 193, 330-337.
10. Srikala Pangannaya, Arshiya Kaur, **Makesh Mohan**, Keyur Raval, Dillip Kumar Chand and Darshak R. Trivedi. (2017) "Synthesis and Spectral Investigation of Colorimetric Receptors for the Dual Detection of Copper and Acetate ions: Application in Molecular Logic Gates." *Supramolecular Chemistry*, 29:8, 561-574.
11. Singh, A., **Mohan, M.**, and R. Trivedi, D. (2019). "Chemosensor Based on Hydrazinyl Pyridine for Selective Detection of F⁻ Ion in Organic Media and CO₃²⁻ Ions in Aqueous Media: Design, Synthesis, Characterization and Practical Application." *ChemistrySelect*, 4(48), 14120–14131.

12. Singh, A., **Mohan, M.**, and Trivedi, D. R. (2019). “Design and synthesis of malonohydrazide based colorimetric receptors for discrimination of maleate over fumarate and detection of F-, AcO- and AsO₂- ions.” *Spectrochimica Acta Part A: Molecular and Biomolecular Spectroscopy*, 117883.
13. Singh, A., **Mohan, M.**, and Trivedi, D. R. (2020). “Design and synthesis new colorimetric receptors for naked-eye detection of biologically important fluoride and acetate anions in organic and arsenite in aqueous medium based on ICT mechanism: DFT study and test strip application.” *Spectrochimica Acta Part A: Molecular and Biomolecular Spectroscopy*, 225, 117522.
14. Tekuri, V., **Mohan, M.**, and Trivedi, D. R. (2020). “Smart Colorimetric Chemosensors for Multi-Analyte Signaling: Recognition of Heavy Metal Ions in an Aqueous Medium and DFT Studies.” *ChemistrySelect*, 5(17), 5289–5299.

Papers published in conference proceedings

1. **Mohan, M.**, Satyanarayan, M. N., and Trivedi, D. R. (2019). “Bithiophene based red light emitting material-Photophysical and DFT studies.” *AIP Conf. Proc.*, AIP Publishing, 030577.
2. Trivedi, D. R., Singh, A., and **Mohan, M.** (2019). “Colorimetric detection of biologically important anion based on ICT Between Donor–Acceptor (D–A): Experimental and DFT studies.” *International Journal of Photochemistry*, 5(1), 49–56

Papers presented in national/international conferences

1. **Makeesh Mohan.**, Satyanarayan M. N., Trivedi, D. R. (2016). “Design, synthesis, characterization of new fluorescent molecule for OLED device applications” Paper presented in “International conference on Science and Technology: Future Challenges and Solutions and 7th Annual Conference of Indian JSPS Alumni Association” August 08-09, Mysore University, Mysore.
2. **Makeesh Mohan.**, Satyanarayan M. N., Trivedi, D. R. (2017). “AIE based new thiophene derivative for OLEDs: electrooptical and DFT studies” Paper presented in “Crystal ball vision on science and engineering for societal upliftment” and 8th Annual Conference of Indian JSPS Alumni Association” August 07-08, CSIR-National Institute of Oceanography (NIO), Dona Paula, Goa.

3. Srikala Pangannaya, Goutam Pawaskar, **Makesh Mohan**, Keyur Raval, Ritu Raval, Darshak R. Trivedi, (2018). “Application of colorimetric receptor in biological screening: Experimental and theoretical studies”, Paper presented in “XXXII Gujarat Science Congress – 2018, Science and Technology for Capacity Building & Inclusive Growth: The Role of Academies and Academia” 4-5, February, CSIR-Central Salt and Marine Chemicals Research Institute, Bhavnagar, Gujarat.
4. Darshak R Trivedi, Raganjali John, **Makesh Mohan**, Satyanarayan M N, (2019). “Design and Synthesis of Dimethyl-Phenylenediamine based Greenish-Yellow Fluorescent Emitter: Photophysical and DFT Studies”, Paper presented in “International conference on Emerging Advancements in Science and Technology & 10th India-Japan Science and Technology conclave” September 05-06, 2019 New Delhi, India.

Software & Hardware skills

- Computational Chemistry packages – Gaussian 09 package, Schrodinger - Materials Science suite, Turbomole, GaussView, Gabedit, Avogadro, Gausssum, ArgusLab, IQmol, Vesta, Nanotube Modeler.
- Chemical drawing software – Chemdraw professional
- Programming Language - C, C++, VB.net, Embedded C for PIC Microcontroller, MPLAB IDE, Basics of MATLAB, Proteus Professional, LABVIEW. Arduino
- Good Experience in PCB designing and hands on experience with PCB Fabrication.
- Graphics – Blender, Photoshop, Inkscape, GIMP, MS paint
- General Software – MS Word, MS Powerpoint, MS Excel, Origin, MesterNova
- Operating System – Windows, Ubuntu and Mac

Instrumentation skills

Hands-on experience in handling and usage of UV-Vis spectrophotometer (Ocean Optics), Cyclic voltammetry-IVIUM electrochemical workstation (Vertex), HORIBA Jobin Yvan Fluorescence spectrophotometer, TCSPC Lifetime measurement unit, Thermal physical vapor deposition, Keithley 2400 source meter.

Specialized skills

Mentored three post graduate project students and assisting practical laboratory for engineering graduates and post graduate science students

Workshop attended

- Short Course on “Flexible Electronics 2017”, 3rd – 8th July at IIT Kanpur
- National workshop High Performance Computing and Applications 2019 August 12th -17th, 2019 organized by Department of Information Technology, NITK Surathkal.

Personal Details

Date of birth 06th July 1984
Nationality Indian
Marital Status Married
Languages known English, Hindi, Kannada, Sanskrit, Tamil,
Permanent address #162, 4th Cross, Bhashyamnagar, Sreerampuram, Bangalore-560021

References

Prof. M. N. Satyanarayan (Research supervisor)

Professor
Department of Physics,
National Institute of Technology Karnataka
(NITK), Surathkal-575025,
Mangalore, Karnataka, India
Mob: +91-9686146138
Email: satya_mn@nitk.edu.in

Dr. Darshak R. Trivedi (Research co-supervisor)

Associate Professor
Department of Chemistry,
National Institute of Technology Karnataka
(NITK), Surathkal-575025,
Mangalore, Karnataka, India
Mob: +91-9481271272; Tel.: +91-824-
2473205; Fax: +91 824 2474033
E-mail: darshak_rtrivedi@yahoo.co.in

